FKFS
RESEARCH IN MOTION.

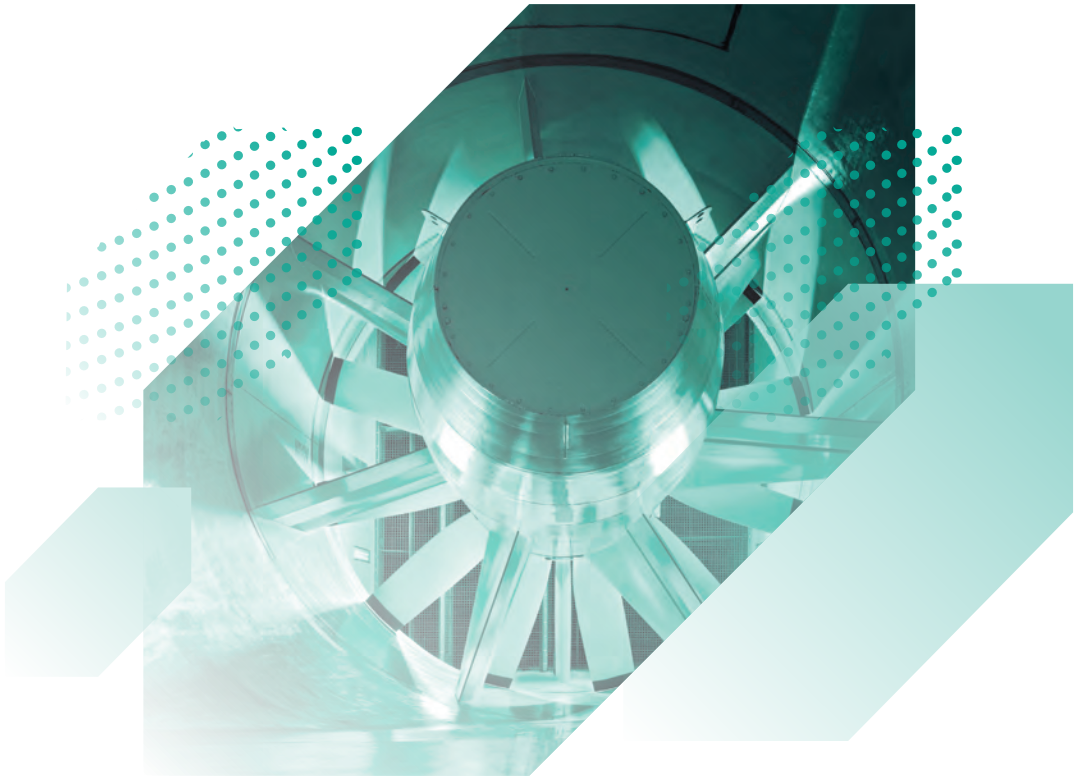

Contributions of:

2025 FKFS Conference on Vehicle Aerodynamics and Thermal Management

15 – 16 October 2025

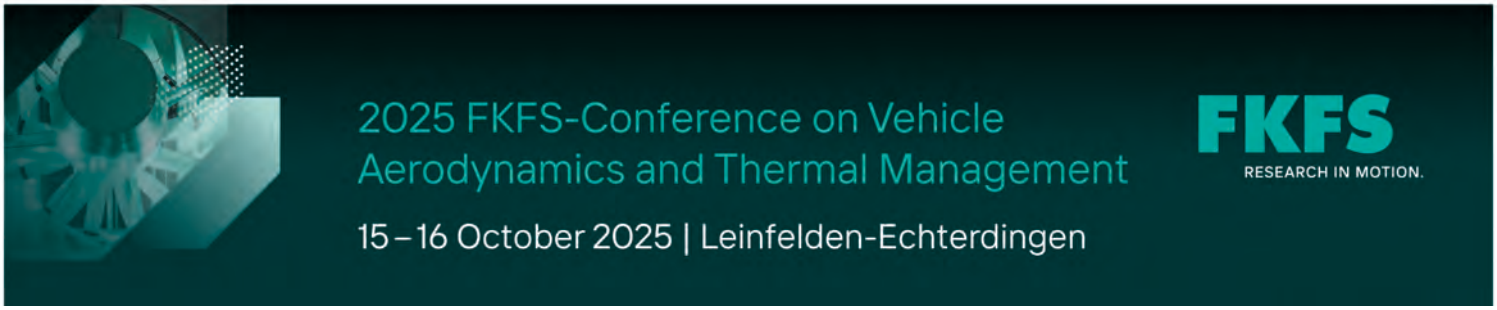

2026 Contributions

Transient Aero

Progress Towards On-Road Aerodynamic-State Estimation in Traffic
Brian McAuliffe, National Research Council Canada et. al.

Relationship between the Effect of Natural Wind Specifications on Aerodynamic Drag
Yasuyuki Onishi, Honda R&D Co., Ltd.

On the Origin of Low Frequency Pressure Fluctuations in Passenger Compartments of Vehicles
Laura Breitenbücher, Dr. Ing. h.c. F. Porsche AG

Climate Comfort

Comparative Analysis and Integration of MPC and RL-Control for Cabin Comfort in Heavy-Duty BEVs
Daniel Linse, RWTH Aachen et. al.

Optimized Cabin Heating Strategy for Battery Electric CEP Vehicles (available through SAE)
Dominik Rehm, Mercedes Benz AGet. al.

User-Centric Comfort Optimization with AI-Supported Methods
Daniel Braun, AVL Deutschland GmbH et. al.

CFD Methods

Use of Low-Order Simulations to Predict Proximity Interactions in Traffic

Fa Ghorbanishohrat, National Research Council Canada et. al.

Transformer-Based Prediction of Vehicle Aerodynamics
Faron Hesse, Dassault Systèmes et. al.

Thermal Systems

Investigation on Thermal Management of Heavy-Duty Commercial FCEV with Focus on Vehicle System Efficiency (available through SAE)
Sophia Uhde, Robert Bosch GmbHet. al.

Simulation-Based Investigation and its Experimental Validation of the Thermal Behavior of a BEV Bus
Henrik Schäfer, Helmut-Schmidt-University et. al.

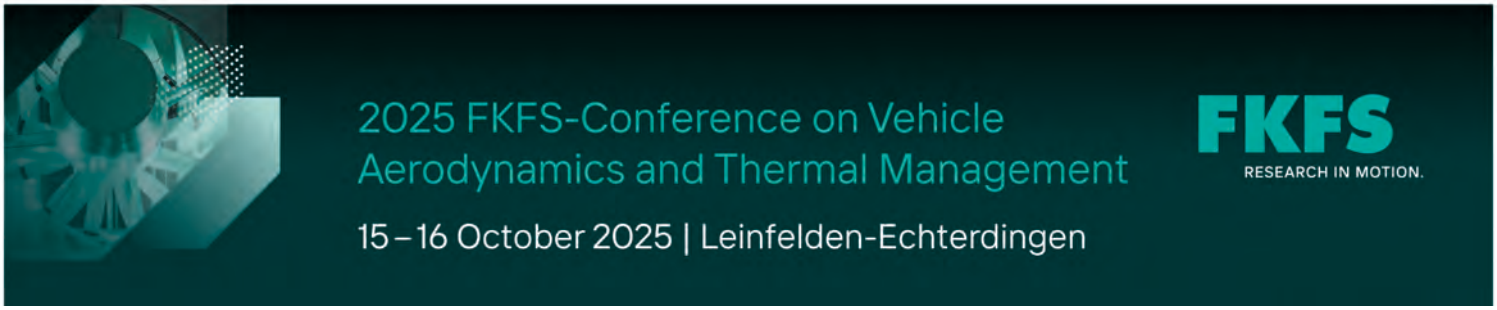

Acoustics

Numerical Investigation of Whistling Noise from Vehicle Side Mirrors'
Peng Xing, Tongji University

Modulated Aeroacoustics Cabin Noise Under Controlled Unsteady Flow Conditions for Different Vehicle Geometries
Nur Syafiqah Jamaluddin, Jaguar Landrover et. al.

Thermal Modelling I

How do Thermal Optimisations on the CCS Charging Inlet Affect the Charging Time?
Jochen Krings, Daimler Truck AG et. al.

Advances in Multiphase HVB Modelling: Coupling of Particle Depositions and Channel Blocking
David Koti, Magna Steyr Fahrzeugtechnik GmbH & Co. KG et. al.

Wind Tunnel Technologies

Efficient Pulsation Mitigation Modeling for Low-Speed Open-Jet Wind Tunnels with Helmholtz Resonator
Joseph Yen, Amentum Technology, Inc.et. al.

Numerical Study on a Boundary Layer Control System and Vortex Generator to Alleviate a Static Pressure Gradient
Seung Hun Lee, Hyundai Motor Group et. al.

How Software Keeps your Wind Tunnel Up to Date for Efficiency and New Use Case
Jan Jacob, Werum Software & Systems AG

The New BMW Acoustic Wind Tunnel Centre
Peter Waudby-Smith, Aiolos Engineering Group et. al.

Thermal Modelling II

Numerical Design and Optimization of Underhood Cooling System Based on Coupled 1D and 3D Flow Modeling
Dig Vijay, Gamma Technologies GmbH et. al.

Coupled Aero-Thermal Simulation into a Structural Simulation with Fatigue Analysis, Automatically
Gabor Matulik, Dassault Systèmes

Lumped Parameter Thermal Network Identification for Transient System Response Prediction of Automotive Components
Maximilian Kehe, BMW et. al.

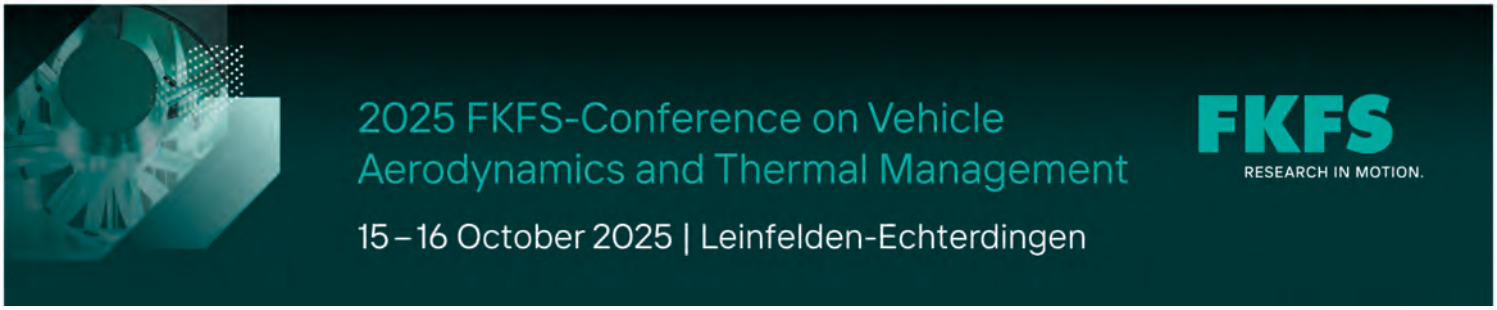

Topology and Sizing Optimization of Thermal and Electric Energy Systems for Battery Electric Vehicle
Fakher Belkacem, Helmut-Schmidt-University

Tire and Wheel Aerodynamics

Experimental Aerodynamic Investigation of Tire Geometries
Aleix Lazaro Prat, BMW Group and TU Darmstadt et. al.

Measuring Time-Averaged and Dynamic Surface Pressures on Passenger Car Wheels Using Fast-Response PSP
Jan Marcel Hübner, Volkswagen AG et. al.

Environmental Testing

Efficient Hybrid Approach for Vehicle Soiling Simulations
Kevin Posch, MAGNA STEYR Fahrzeugtechnik GmbH & Co KG

Advancing Wind Tunnel Vehicle Soiling Studies with a Realistic Dynamic Rain Simulation System
Long Li, Ontario Tech University et. al.

CFD Simulations of Vehicle Self-Soiling
Martin Sevcik, ICON Technology & Process Consulting

Aero Development

Reconstruction of Road Vehicle Wake by Physics Informed Neural Networks
Sanghyek Kim, Hyundai Motor Group

Developments in Road Testing Methods for Novel Drag Reduction Devices
Michael Gerard Connolly, University College Dublin et. al.

Development of Aerodynamics of the Facelifted Enyaq and Enyaq Coupe Models
Jiri Novak, Skoda Auto

Thermal Test & Validation

Optimisation of Chassis Dynamometer Force Variability for Floor Anchor Restraint Systems
Luke Williams, Jaguar Landrover

Multi Element Integration Technology for Thermal Hazard Simulation Calibration Based on Full-Scale Automotive Climate Numerical Wind Tunnel
Dan Wang, China Automotive Engineering Research Institute (Tianjin) Co., Ltd et. al.

A Novel Approach to Highly Integrated Thermal Management Rig and Facility for Vehicle Applications
Paul Cromback-Dugény, Jaguar Landrover

Progress Towards
On-Road Aerodynamic-State Estimation in Traffic

Brian R. McAuliffe[1], Moira Barnes[2], Taufiq Rahman[1], Abdullah Jirjees[1], Faegheh Ghorbanishohrat[1], David Rival[2]

[1]National Research Council Canada
1200 Montreal Rd., Ottawa, Ontario, Canada, K1A 0R6

[2]RivalLab/ Queen's University
99 University Avenue, Kingston, Ontario, Canada, K7L 3N6

Email: Brian.McAuliffe@ nrc-cnrc.gc.ca

Abstract: By exploiting aerodynamic interactions among road vehicles, driving-automation technologies have the potential to reduce energy use and emissions. Traditional platooning concepts consider multiple vehicles travelling in close longitudinal proximity within the same road lane, but recent research suggests that lateral offsetting and adjacent-lane positioning can provide additional benefits in the complex traffic-and-wind climate experienced in everyday driving. On-road aerodynamic-state estimation will be a critical feedback metric for such autonomous-vehicle systems. A small sample of multi-vehicle wind-tunnel results is used to introduce a concept for using surface-pressure differences to infer aerodynamic states, and measurements from on-road in-traffic tests highlight ways to differentiate between wake effects from leading vehicles and close-proximity pressure-field influences from adjacent-lane vehicles. Complex conditions and varied positions of other vehicles in traffic highlight the need to track temporal changes in states, and to use multiple metrics to predict aerodynamic states.

1 Concept and Objectives

Instantaneous aerodynamic load prediction, whether for air or ground vehicles, has vast applications related to performance, energy use, stability, and safety. Transient disturbances from wind gusts, dynamic body motion, or relative motion to proximate objects pose significant challenges. Current advances in autonomous aerial and road mobility are pushing the limits of necessary environmental feedback to ensure reliable control of vehicle motion and to ensure safety, while exploiting or avoiding aerodynamic interactions with other bodies. Examples include: urban air-mobility applications for human and goods transportation, for which navigating buildings and associated wind disturbances is important [1], and autonomous road-traffic systems,

Contribution: 2025 FKFS Conference on Vehicle Aerodynamics and Thermal Management
15 – 16 October 2025 | Leinfelden-Echterdingen

for which close-proximity driving can reduce congestion and save energy via speed harmonization and aerodynamic interactions [2]. Sensing the aerodynamic state of a vehicle directly may improve real-time control strategies. Biological systems use sensory feedback in this manner, such as fish or birds adapting in real time to exploit local aero/hydro-dynamic phenomena [3]. Drones and ground vehicles are bluff bodies (non-streamlined), for which surface-pressure changes, rather than air friction, are highly correlated with overall aerodynamic performance, and can be used to infer local wind conditions and aerodynamic behaviour [4]. Recent work has demonstrated the feasibility of using sparse arrays of surface-pressure measurements to infer the aerodynamic state of a body, by making use of data-driven methods via transition-network concepts [5]. This approach is particularly useful for non-linear aerodynamic environments with separated/stalled flows, characteristic of bluff bodies.

Emerging traffic-aerodynamics research and the accelerating deployment of connected-and-automated-vehicle (CAV) and intelligent-transportation-systems (ITS) technologies suggests that road-vehicle aerodynamic drag, and associated energy use, can be optimized via two approaches: 1) optimized multi-lane mixed-traffic patterns that minimize traffic-system drag [6]; and 2) active aerodynamic technologies that adapt to their traffic environment [7]. This paper describes the preliminary steps of a project examining the first of these approaches, namely traffic-aerodynamic optimization using CAV technologies. Within this project, named *AeroCAV*, an attempt is being made to apply wireless surface-pressure sensing with a transition-network approach to estimate real-time aerodynamic performance. Section 2 provides some context to the necessity of the approaches being applied, while Sections 3 and 4 document the on-road demonstrator and some preliminary measurements, respectively.

2 The Challenge of Characterizing Aerodynamic Boundary Conditions

Based on a previous proof-of-concept investigation using a wireless-surface-pressure measurement system [8], pressure-difference coefficients calculated using a vehicle-speed-based dynamic pressure showed suitability as indicators of aerodynamic boundary conditions. Building upon that experience, with additional knowledge from wind tunnel tests of traffic interactions [6,9], three pressure-coefficient parameters have been selected for the current on-road investigations, based on six locations around the perimeter of the test vehicle. Specific locations are the Front centre (F), the Back/Base centre (B), the Left-side door (L), the Right-side door (R), the Front Left bumper (FL), and the Front Right bumper (FR). The (F)ront position is intended to be as close to the stagnation point as possible. Pressure-difference coefficients are defined based on the front-to-back difference ($\Delta\bar{C}_{\mathrm{p}}^{FB}$), the left-to-right-door difference ($\Delta\bar{C}_{\mathrm{p}}^{LR}$), and the front-bumper left-to-right difference ($\Delta\bar{C}_{\mathrm{p}}^{FLR}$). Challenges, and potential solutions, using these parameters are described to provide some context for the on-road data presented in a later section.

The three pressure-difference metrics have been calculated and presented in this section for four traffic scenarios that were simulated using a 30%-scale DrivAer model

in the NRC 9 m Wind Tunnel. Configuration 1 consists of the isolated DrivAer Notchback model in uniform flow. Configurations 2 and 3 consist of the DrivAer in proximity to an AeroSUV model, in a side-by-side arrangement (see Figure 1) and a longitudinal-following arrangement (following the AeroSUV at 2 vehicle-length spacing). Configuration 4 consists of a side-by-side arrangement with a heavy-duty-vehicle (HDV) model, with the base of the two model nearly coincident (see [10] for details of the HDV model).

Figure 1: 30%-scale DrivAer and AeroSUV models in a side-by-side configuration in the NRC 9 m Wind Tunnel.

Figure 2 shows the variation with yaw angle of the $\Delta\bar{C}_{\mathrm{p}}^{FB}$, $\Delta\bar{C}_{\mathrm{p}}^{LR}$, and $\Delta\bar{C}_{\mathrm{p}}^{FLR}$ parameters, using the wind-speed-based $\Delta\bar{C}_P$ values from the wind-tunnel measurements. Although base pressure generally decreases with increasing yaw angle, the corresponding lateral shift of the front stagnation point away from the centreline causes a decrease at the front-centre position, which is approximately equal to the change in base pressure. This results in an insensitivity of the $\Delta\bar{C}_{\mathrm{p}}^{FB}$parameter to yaw angle for this DrivAer shape. This behaviour suggests that $\Delta\bar{C}_{\mathrm{p}}^{FB}$ may be a good indicator of dynamic pressure experienced by the vehicle. The lateral pressure differences, at the front of the body ($\Delta\bar{C}_{\mathrm{p}}^{LR}$) or from door to door ($\Delta\bar{C}_{\mathrm{p}}^{FLR}$), show near-linear changes with yaw angle, which suggest that either of these parameters may be a good indicator of the yaw angle experienced by the vehicle. The main difference between $\Delta\bar{C}_{\mathrm{p}}^{FLR}$ and $\Delta\bar{C}_{\mathrm{p}}^{LR}$ is the slope, with the former having five times the sensitivity of the latter.

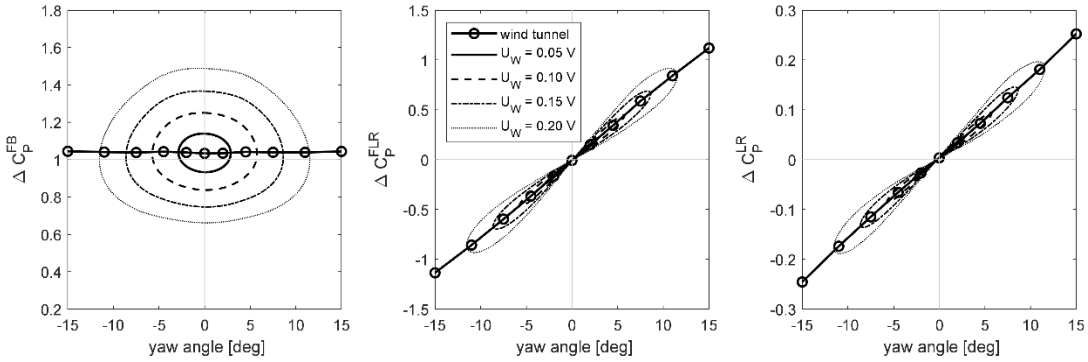

Figure 2: $\Delta\bar{C}_P$ metrics from wind-tunnel tests of the isolated DrivAer model.

Figure 2 estimates the variation of the three $\Delta\bar{C}_P$ parameters that would arise when encountering different terrestrial wind speeds (increments of 5% of vehicle speed, up to 20%). These $\Delta\bar{C}_P$ variations were calculated using a dynamic pressure based on the vehicle speed, not the apparent wind speed. For each of the wind-speed increments, the data show a path representing a 360° change in the direction of the wind relative to the direction of motion of the vehicle. Head- and tail-wind conditions scale the near-zero-yaw-angle values to greater or lesser magnitudes, while cross-wind conditions increase the yaw angle. This is particularly apparent for the front-to-back $\Delta\bar{C}_\mathrm{p}^{FB}$ parameter which shows up to a ±40% change at 0° yaw angle associated with the 20% wind-speed increment, again suggesting that it may be a good indicator of the dynamic-pressure of the wind. In a cross-wind orientation, the 20% wind speed generates yaw angles that reach about 11°. The incremental $\Delta\bar{C}_\mathrm{p}^{LR}$ and $\Delta\bar{C}_\mathrm{p}^{FLR}$ values, when terrestrial wind effects are estimated, show small changes at low wind speeds, and extend reasonably proportionally with yaw angle as cross winds increases. If measured on a vehicle, the $\Delta\bar{C}_P$ characteristics shown in Figure 2 suggest that these parameters can be used to estimate the wind conditions (speed and yaw angle) while driving. Either $\Delta\bar{C}_\mathrm{p}^{LR}$ or $\Delta\bar{C}_\mathrm{p}^{FLR}$ could be used to first estimate the yaw angle, while the estimated yaw angle and the $\Delta\bar{C}_\mathrm{p}^{FB}$ parameter could be used to infer the dynamic pressure, and correspondingly the wind speed. With appropriate characterization, this boundary-condition estimation can be related to performance metrics, like the drag coefficient, to estimate the "aerodynamic state" of the vehicle.

When travelling in traffic, significant challenges can arise that invalidate the relationships of $\Delta\bar{C}_\mathrm{p}^{FB}$, $\Delta\bar{C}_\mathrm{p}^{LR}$, and $\Delta\bar{C}_\mathrm{p}^{FLR}$ as direct indicators of local aerodynamic boundary conditions. Some of these challenges are highlighted in Figure 3 that compares the variability of these $\Delta\bar{C}_P$ parameters in different wind conditions for specific traffic-interaction conditions. The isolated vehicle case is contrasted against the "side by side SUV" case, the "following an SUV" case, and the "side by side HDV" case, based on the wind-tunnel measurements. For each case, the symbol represents the 0°-yaw-angle value that represents no-wind conditions, and the lines represent the same terrestrial-wind magnitudes of Figure 2. There is no general consistency in the magnitudes and trends of the $\Delta\bar{C}_P$ characteristics amongst the

various cases. The "side by side SUV" is similar to the "isolated" case for the $\Delta\bar{C}_{\mathrm{p}}^{FB}$ parameter, but has distinct and opposite offsets for the $\Delta\bar{C}_{\mathrm{p}}^{LR}$ and $\Delta\bar{C}_{\mathrm{p}}^{FLR}$ parameters with some reduction in linearity. When "following an SUV", a distinct downward shift is observed for $\Delta\bar{C}_{\mathrm{p}}^{FB}$, and reductions in slope and linearity are observed for $\Delta\bar{C}_{\mathrm{p}}^{LR}$ and $\Delta\bar{C}_{\mathrm{p}}^{FLR}$. The "side by side HDV" case differs in that it demonstrates significant yaw asymmetry in all three parameters, the largest spread of $\Delta\bar{C}_{\mathrm{p}}^{FB}$ values, and non-monotonic variability with yaw angle.

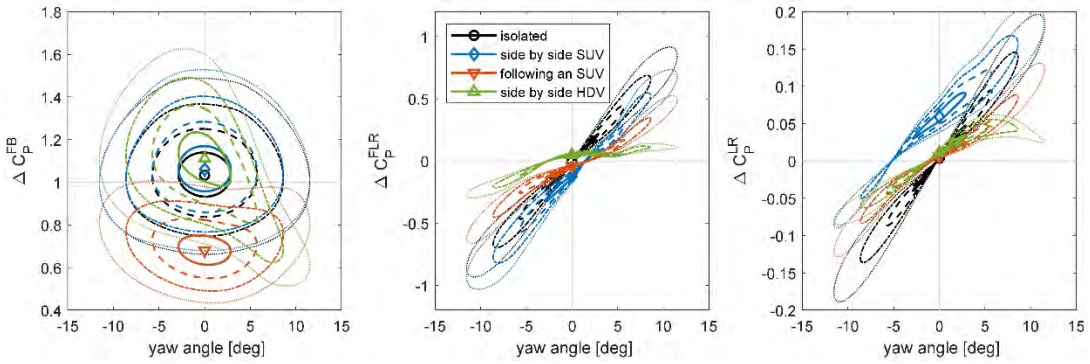

Figure 3: $\Delta\bar{C}_P$ metrics in various on-road scenarios relative to yaw angle.

These varying characteristics in the $\Delta\bar{C}_P$ plots of Figure 3 make prediction of local boundary conditions much more complicated than isolated-vehicle results would suggest. For example, if a yaw angle is inferred from $\Delta\bar{C}_{\mathrm{p}}^{LR}$ and $\Delta\bar{C}_{\mathrm{p}}^{FLR}$, the variability of the $\Delta\bar{C}_{\mathrm{p}}^{FB}$ parameter amongst different conditions will make an accurate estimation of the local wind speed nearly impossible. However, the manner in which the scenarios differ from each other suggests that multi-variable or multi-state approaches may provide a solution to estimate the "aerodynamic state" of the vehicle. Figure 4 shows these types of multi-state relationships for the data of Figure 3, but with the $\Delta\bar{C}_P$ parameters plotted against each other instead of against yaw angle. Significant variation is again seen for the $\Delta\bar{C}_{\mathrm{p}}^{FB}$ plots (left and middle), while the $\Delta\bar{C}_{\mathrm{p}}^{LR}$ vs. $\Delta\bar{C}_{\mathrm{p}}^{FLR}$ plot shows some collapsing of data along distinct characteristics for some of the traffic-interaction scenarios. Combined with transition-network concepts [5], a suitable approach to aerodynamic-state estimation may be feasible. This concept of this project intends to use sparse sensor data captured on the test vehicle and combined with a pre-trained algorithm to provide an estimate of the present aerodynamic state. By embedding these measurements into a reduced-order phase-space model, the system can then characterize distinct aerodynamic regimes and quantify the likelihood of transitions between them. Transition-network concepts, coupled with Bayesian statistics, will provide the framework for eventually estimating the current aerodynamic state in real time. The final result will provide a low-order representation of the inherently non-linear vehicle-flow interactions, which should remain robust to the elevated noise levels typical of experimental on-road pressure measurements. The remainder of this paper describes preliminary results from an on-road demonstrator

being developed that will make use of these concepts, amongst other sensor-fusion approaches, to adopt aerodynamic-state estimation as a control metric for minimizing energy use of automated multi-vehicle-traffic systems. Preliminary measurements of the $\Delta\bar{C}_{\mathrm{p}}^{FB}$, $\Delta\bar{C}_{\mathrm{p}}^{LR}$, and $\Delta\bar{C}_{\mathrm{p}}^{FLR}$ metrics are shown to demonstrate the potential feasibility of boundary-condition estimation from on-road measurements.

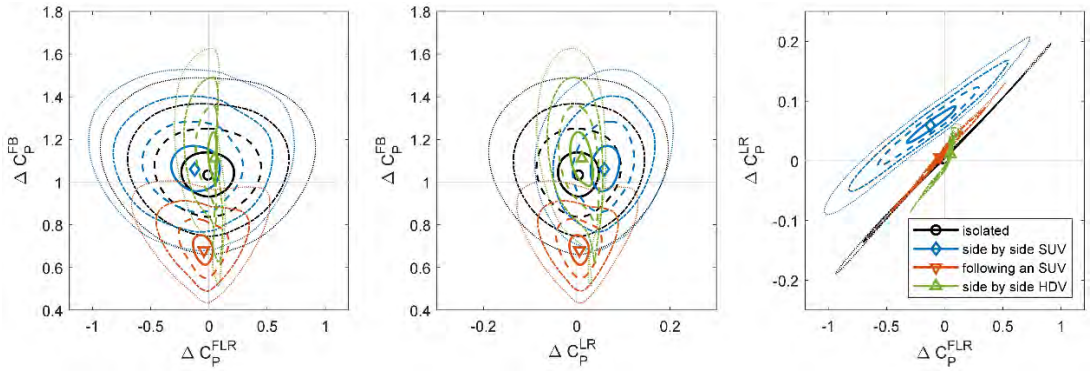

Figure 4: $\Delta\bar{C}_P$ metrics in various on-road scenarios relative to each other.

3 On-Road Tests

An on-road demonstrator is being developed for the AeroCAV project with its end-use goal to provide a platform to demonstrate the potential for energy savings from controlled aerodynamic optimization with respect to wind and traffic conditions. The system will be interchangeable on a number of vehicles. For initial concept evaluation, the first use is with a compact battery-electric SUV. This section documents the vehicle system, the initial test conditions, and the data processing methods.

3.1 Vehicle Systems

The experimental platform consisted of a 2022 Hyundai Ioniq 5 instrumented with a Robotic Operating System (ROS)-based multimodal data acquisition system developed in-house (Figure 5). The platform integrates multiple temporally synchronized perception and vehicle-state sensing nodes. Two RGB cameras were mounted at the front and rear of the vehicle to capture forward- and backward-facing video. An Ouster OS1 LiDAR was installed to provide 3D point cloud data for depth perception and object detection. Vehicle dynamics and reference pressure measurements were recorded using an Xsens MTi-710 Inertial Measurement Unit (IMU) sensor, installed inside the cabin. Eight Bluetooth Low Energy (BLE)-enabled pressure sensors (Arduino Nano 33 BLE Sense Rev2) were mounted around the vehicle—three on the front bumper, one on the roof, one on the driver's side door, one on the passenger's side door, and one on the rear door. An additional sensor was

deployed to measure ambient temperature outside the vehicle. All BLE nodes streamed pressure or temperature readings to the ROS ecosystem. Vendor supplied drivers along with custom microcontroller firmware and ROS drivers were developed to interface the BLE-enabled pressure and temperature sensors, enabling time synchronized acquisition and storage of camera images, LiDAR scans, IMU readings, and pressure/temperature values within a unified ROS bag-based data collection framework.

Figure 5: Instrumented test vehicle.

3.2 Test Conditions

On-road test data for this initial study were acquired between July 14 and 16, 2025, in the province of Ontario, Canada, on roadways between the cities of London and Sarnia. Most data were acquired on Highway 402, which is a four-lane divided highway oriented east-west, with combinations of open terrain and tree-lined segments, and a speed limit of 110 km/h. The target test conditions were constant-speed driving with various boundary conditions. Early-day testing was conducted, in lower-wind conditions, to target isolated constant-speed conditions with as little traffic as possible. Only data for which forward vehicles were estimated to be at a distance of at least 200 m, or more, were used for these “isolated” conditions, and larger distances for heavy trucks. Test runs of particular interest for this manuscript, and descriptions of the pertinent data segments, are:

- July 15, 2025, Run 01: Travelling westbound on Hwy 402, low traffic, relatively-low southerly winds (around 5 km/h or lower, from left to right).
- July 15, 2025, Run 02: Travelling eastbound on Hwy 402, low traffic, relatively-low southerly winds (around 5 km/h or lower, from right to left).

- July 15, 2025, Run 03: Travelling westbound on Hwy 402 in the wake of heavy trucks, relatively-low southerly winds (around 5 km/h or lower, from right to left).
- July 16, 2025, Run 01: Travelling westbound on Hwy 22 and Hwy 402 in the wake of light duty vehicles, moderate southerly winds (around 10 km/h or lower, from right to left).

3.3 Data Methods

Converting data from the BLE pressure sensors to useful pressure-coefficient-difference ($\Delta\bar{C}_P$) values required a number of data processing steps. A sample set of time-series data are provided in Figure 6 demonstrating measured data (speed, altitude, pressures) and processed data (pressure coefficients).

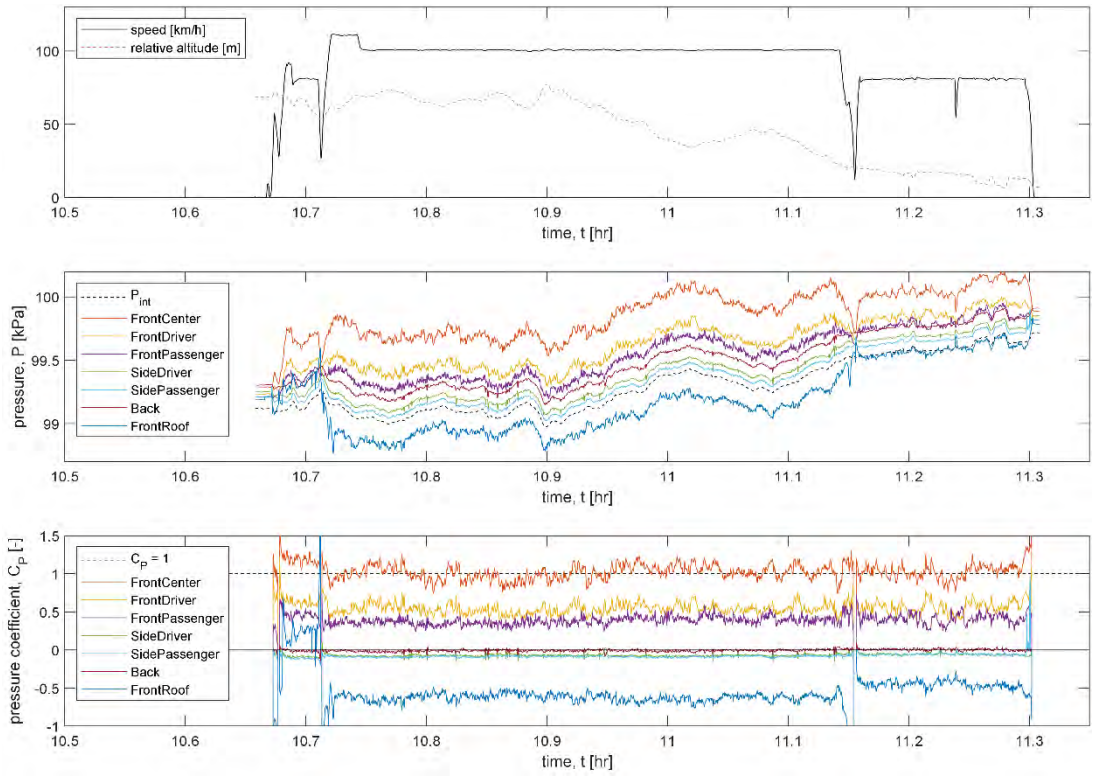

Figure 6: Subset of test data for Run 01 on July 15, 2025.

The top plot in Figure 6 shows the vehicle speed and its altitude profile for this test segment. The BLE pressure sensors measure absolute pressure (middle plot), and each has a small but quantifiable bias error, relative to the others, that drifts slightly over time. Furthermore, elevation changes and temporal changes due to the local climate generate variations in the pressure that can exceed the dynamic pressure of

the apparent wind during testing. The hydrostatic pressure change associated with the 55 m altitude change (approx. 650 Pa) is equivalent to the dynamic pressure of a 120 km/h wind. To compensate for these various factors, to permit a reasonably-accurate calculation of the pressure coefficient for each sensor, a method to correct the measurements based on a reference pressure acquired internal to the cabin (P_{int} value in the middle plot, from the Xsens IMU sensor) was developed. The method is still under development, but its preliminary results provide a reasonable adjustment for each sensor. The C_P time-series data for each sensor are shown in the bottom plot of Figure 6. The Front Centre sensor, which resides near the stagnation point, provides a value near one, while the sides and base provide values near or slightly-below zero, providing reasonable validation of the approach. The Front Roof sensor shows the strongest sensitivity/uncertainty, with distinct offsets observed between the different-speed segments of the run. Although the metrics of interest for the transition-network methods are the pressure differences amongst the front, back, and side sensors ($\Delta\bar{C}_P$), and an accurate reference offset is not strictly necessary, these corrected C_P traces provide a means to interpret the aerodynamic behaviour of the vehicle based on conventional approaches, and permit spectral analysis of C_P signals for individual sensors.

4 On-Road Measurements

4.1 No-Traffic Conditions

To begin to understand the complex aerodynamic boundary conditions in the on-road data encountered by the test vehicle, the most basic case is analyzed. Isolated conditions for the on-road test can be assumed to have minimal cross/head wind, minimal interactions with other vehicles, and steady velocity. In Figure 7, on-road $\Delta\bar{C}_\mathrm{p}$ are plotted for steady-velocity data segments of low-wind test runs. The data are sorted by environmental conditions including estimated roadside tree density (colour) and vehicle direction (marker shape). Assuming that the low-wind conditions average to a no-wind result, 10 km/h wind limits on $\Delta\bar{C}_\mathrm{p}^{FB}$ are denoted about its mean and suggest that reasonably-low winds were encountered during these tests. The small range of $\Delta\bar{C}_\mathrm{p}^{FLR}$ and $\Delta\bar{C}_\mathrm{p}^{LR}$ values suggests low yaw angles, resulting from low winds, but the sensitivity of these parameters to yaw angle is unknown for this particular vehicle. Comparing these results to the DrivAer estimates in Figure 4, these results generally cluster within a range of $\Delta\bar{C}_\mathrm{p}$ values that indicate low winds. The general offset of the $\Delta\bar{C}_\mathrm{p}^{FLR}$ data towards positive values (about 0.1) is due to slight lateral asymmetries in the surface position and casing shape of the BLE sensors. Moderate linearity is observed between $\Delta\bar{C}_\mathrm{p}^{FLR}$ and $\Delta\bar{C}_\mathrm{p}^{LR}$, providing additional evidence that these state-space metrics may be suitable for transition-network analysis.

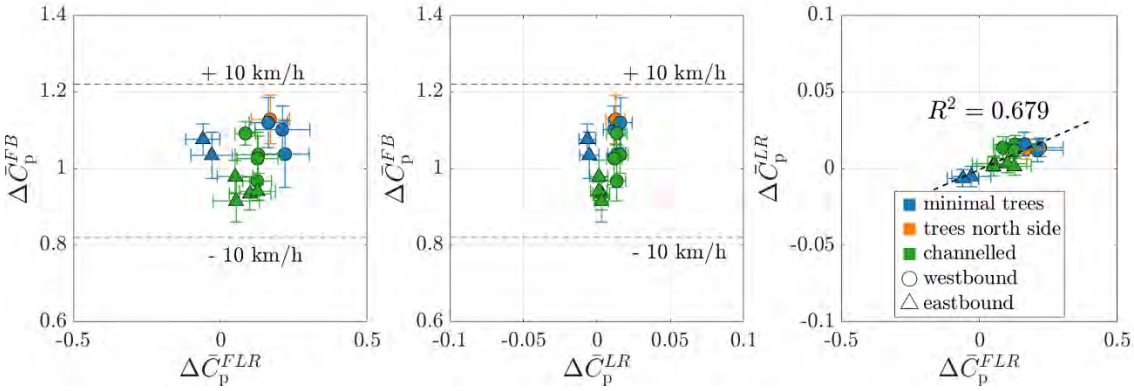

Figure 7: On-road $\Delta\bar{C}_p$ plotted for isolated steady velocity data segments of Runs 01 and 02 July 15, 2025. Error bars represent one standard deviation.

4.2 Wake-Effects Conditions

To differentiate between close-proximity pressure-field influences and wake effects from leading vehicles such as an HDV or LDV, on-road $\Delta\bar{C}_p$ parameters are plotted in Figure 8 for steady-velocity data segments for various following distances, all acquired on Hwy 402. On-road data are sorted by environmental conditions, with estimated roadside tree density encoded by marker colour, mean vehicle direction indicated by marker shape, and estimated following distance d represented by marker transparency. Error bars denote one standard deviation, reflecting the variability within each condition. Results show some clustering around the wind tunnel baseline $\Delta\bar{C}_p$, as illustrated in Figure 4. Again, the dashed lines plotted in Figure 8 demonstrate expected $\Delta\bar{C}_p^{FB}$ values under an assumption (±10 km/h wind speed) that this parameter behaves the same way for this test vehicle as it does for the wind-tunnel DrivAer model. The low $\Delta\bar{C}_p^{FB}$ values suggest that wind-speed deficits in the LDV wakes reach about 10% of the driving speed, while in the HDV wakes they reach up to about 20%. The westbound LDV-wake data in regions with minimal trees show increased $\Delta\bar{C}_p^{FLR}$ values with low $\Delta\bar{C}_p^{FB}$ values, suggesting wake interactions with cross winds, but the $\Delta\bar{C}_p^{LR}$ values do not show an increase as would be expected with cross winds based on its isolated-condition relationship to $\Delta\bar{C}_p^{FLR}$ (right-side plot in Figure 6). Lateral shear in the wake, at small cross winds or small lateral offsets, may induce $\Delta\bar{C}_p^{FLR}$ values indicative of cross winds when none are present. These results highlight the complexities of multi-condition interactions, and provide evidence that the three indicators selected ($\Delta\bar{C}_p^{FB}$, $\Delta\bar{C}_p^{FLR}$, and $\Delta\bar{C}_p^{LR}$) may be insufficient to characterize adequately the aerodynamic state of the vehicle.

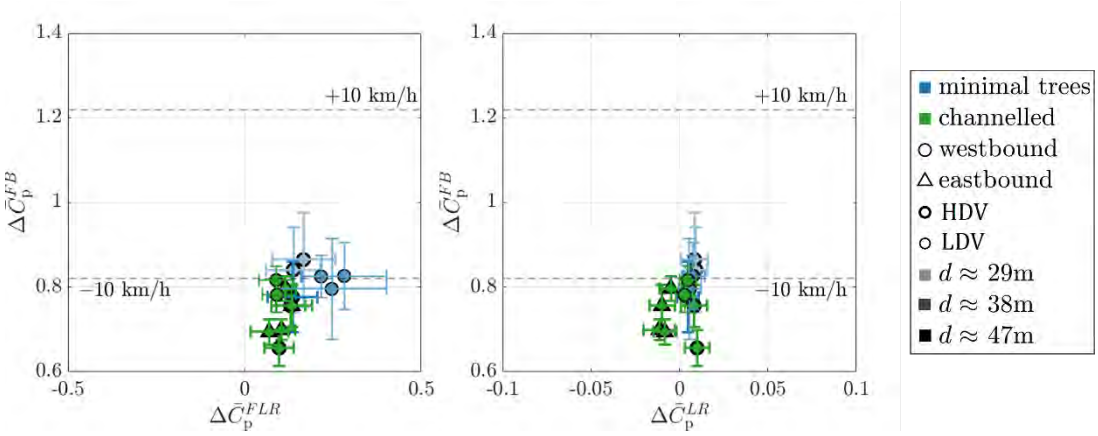

Figure 8: On-road $\Delta\bar{C}_p$ parameters plotted for steady velocity data segments for following a LDV and HDVs. Test speeds between 100 km/h and 110 km/h.

As a secondary diagnostic of wake–proximity effects, power spectral densities (PSDs) of the pressure-differential metrics were computed. Welch's method was used with a Hanning window and 75% overlap. This combination reduces noise but preserves resolution. The spectra are plotted in Figure 9 against reduced frequency, $f_r = fL/U$, where L corresponds to the width of vehicle being followed (estimates of 1.9 m used for LDVs and 2.6 m for HDVs) and U represents the steady vehicle speed. Significantly greater spectral energy is observed in the *FLR* metric (right plot) than for *FB* metric (left plot), due to the greater lateral coherence of wake turbulence across the front of the test vehicle than longitudinal coherence over its length. For the 'following HDV' cases, the spectra exhibit pronounced peaks at $\mathrm{St} = 0.076, 0.216, 0.260$ and 0.357. The energy clustering near $f_r = 0.2{\sim}0.24$ matches a previously derived band for HDV wakes [11].

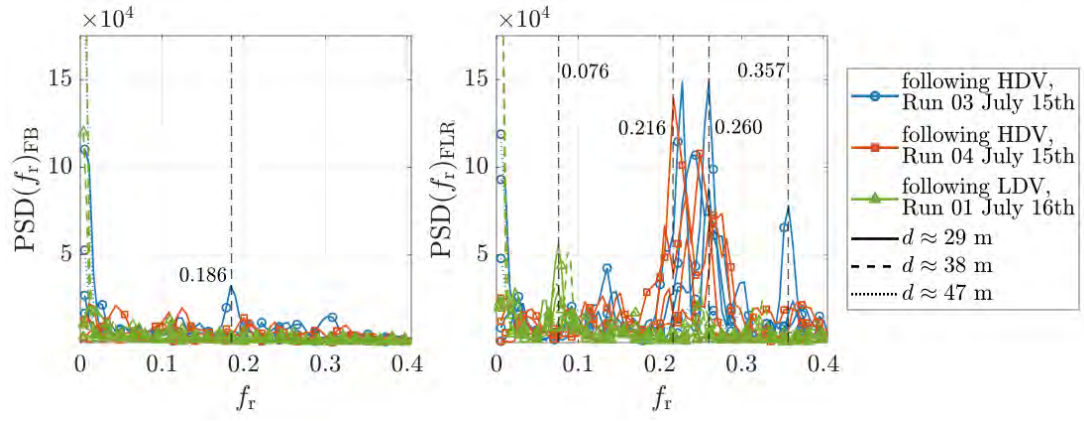

Figure 9: On-road pressure differential spectral analysis is plotted for steady velocity data segments for following an HDV and an LDV.

In contrast, for the 'following LDV' case (Run 01, July 16), peaks within the HDV band are absent or markedly weaker with only one pronounced peak at $\mathrm{St} = 0.186$, and the spectrum is more broadband. These differences are consistent with the smaller, less coherent wake of an LDV at the same streamwise spacing, possibly indicating stronger cross-flow fluctuations experienced by the test car due to wind.

4.3 Proximity-Effects Results

The proximity and relative position of other vehicles with respect to the test vehicle can impact greatly the measured $\Delta\bar{C}_\mathrm{p}$ parameters, as was shown for the DrivAer wind-tunnel data in Figure 4. A sample of proximity effects in on-road conditions are presented by looking at a segment of the July 15 tests (Run 01) where the test vehicle was in relatively-low wind conditions in a channeled-flow environment and was passed by an HDV. In Figure 10, $\Delta\bar{C}_\mathrm{p}$ time-series measurements are plotted to demonstrate the effect of the HDV position with respect to the test vehicle. The black dot with error bars represents the mean $\Delta\bar{C}_\mathrm{p}$ values and one standard deviation for this 45 s segment. The 0.1 offset in $\Delta\bar{C}_\mathrm{p}^{FLR}$ corresponds roughly with the sensor-position/shape bias noted in Section 4.1.

Figure 10: On-road $\Delta\bar{C}_\mathrm{p}$ parameters and respective mean values plotted for a steady velocity data segment where an HDV passed the test vehicle. Images show the progression of the passing maneuver and the effect the HDV position has on $\Delta\bar{C}_\mathrm{p}$ parameters over time.

With reference to published studies examining LDVs overtaking larger vehicles [12,13], and some of the author's yet-to-be-published wind-tunnel work on LDV-HDV-proximity effects introduced in Section 2, the overtaking scenario in Figure 10 is explained. Each of the four highlighted positions correspond to an extreme in the $\Delta\bar{C}_\mathrm{p}$ parameters, identified by the timestamped images:

- t = 0 s, HDV behind test vehicle: The high-pressure field forward of the HDV increases the base pressure of the test vehicle, leading to $\Delta\bar{C}_{\mathrm{p}}^{FB}$ lower than 1, and displaces the airflow laterally causing an effective yaw angle for the vehicle, resulting in the positive $\Delta\bar{C}_{\mathrm{p}}^{FLR}$ values.
- t = 14 s, HDV approximately nose-to-nose with test vehicle: As the HDV begins to overtake the test vehicle, the combined blockage of the two-body system reduces the base pressure, increasing $\Delta\bar{C}_{\mathrm{p}}^{FB}$, and the flow-displacement effect of the HDV causes stronger local yaw angles, further increasing $\Delta\bar{C}_{\mathrm{p}}^{FLR}$.
- t = 35 s, test vehicle approximately nose-to-tail with the HDV: Localized blockage interactions between the vehicles generate reduced pressure over the front of the test vehicle, causing a decrease in $\Delta\bar{C}_{\mathrm{p}}^{FB}$, and concentrated more strongly on the left side, causing the change to negative $\Delta\bar{C}_{\mathrm{p}}^{FLR}$.
- t = 45 s: test vehicle behind HDV after it completes a lane change: Wake effects are introduced, lowering $\Delta\bar{C}_{\mathrm{p}}^{FB}$, and the lateral shear during the HDV-lane-change process is suspected to be the cause of the increasingly-negative $\Delta\bar{C}_{\mathrm{p}}^{FLR}$.

These individual $\Delta\bar{C}_P$ states may be interpreted differently if examined in isolation. For example, t = 0 s and 35 s states may be interpreted as wake-effect states with cross winds. However, the temporal transition between states provides additional context to the aerodynamic state of the vehicle, which is where transition-network concepts are expected to be beneficial for automated-vehicle control strategies.

5 Conclusions

This paper presented preliminary work towards a general concept for estimating the on-road aerodynamic state of a road vehicle, with anticipated uses for vehicle-automation technologies. On-road measurements were presented for three specific scenarios in relatively-low wind conditions, representing an isolated vehicle, following in the wakes of LDVs and HDVs, and being overtaken by an HDV. The measurements highlight that a combination of multiple metrics will be necessary to infer adequately the aerodynamic state of a vehicle. Complex conditions and varied positions of other vehicles in traffic highlight the need to track temporal changes in states, for which the use of transition networks will be applied to understand better, and to predict, aerodynamic states.

6 Reference list

[1] McTavish, S, Barber, H., Wall, A., “Field Measurements of the Airflow in the Urban Environment: An RPAS Use-Case in Montréal, Canada.”, Vertical Flight Society 80th Annual Form Proceedings, Montreal, Canada, May 2024, Paper 1133.

[2] Wang, Z., Bian, Y., Shladover, S.E., Wu, G., Li, S.E., Barth, M.J., 2019. “A survey on cooperative longitudinal motion control of multiple connected and automated vehicles.” IEEE Intelligent Transportation Systems Magazine,” doi:10.1109/MITS.2019.2953562.

[3] Bleckmann H, Zelick R. Lateral line system of fish. Integr Zool. 2009 Mar;4(1):13-25. doi: 10.1111/j.1749-4877.2008.00131.x. PMID: 21392273.

[4] Jessing, C., Wilhelmi, H., Wittmeier, F., Wagner, A. et al., “Investigation of Transient Aerodynamic Effects on Public Roads in Comparison to Individual Driving Situations on a Test Site,” SAE Technical Paper 2020-01-0670, 2020, doi:10.4271/2020-01-0670.

[5] Kaiser, F., Iacobello, G., and Rival, D.E., “Cluster-based Bayesian approach for noisy and sparse data: Application to flow-state estimation” Proc. R. Soc. A. , 48020230608 doi:10.1098/rspa.2023.0608.

[6] McAuliffe, B. and Barber, H., “Aerodynamic Drag of Road Vehicles in Close Lateral Proximity,” SAE Int. J. Advances & Curr. Prac. in Mobility 5(6):2004-2020, 2023, doi:10.4271/2023-01-0952.

[7] Le Good, G., Resnick, M., Boardman, P., Clough, B. et al., “Effects on the Aerodynamic Characteristics of Vehicles in Longitudinal Proximity Due to Changes in Style,” SAE Technical Paper 2018-37-0018, 2018, doi:10.4271/2018-37-0018.

[8] Chan, R., “On-road Aerodynamic State Estimation Using Sparse Pressure Sensors with Application to Truck Platooning,” M.A.Sc. Thesis, Queen’s University, Kingston, Ontario, Canada, 2023.

[9] McAuliffe, B. and Barber, H., “Simulating Traffic-wake Effects in a Wind Tunnel,” SAE Int. J. Advances & Curr. Prac. in Mobility 5(6):1969-1987, 2023, doi:10.4271/2023-01-0950.

[10] Ghorbanishohrat, F., McAuliffe, B., and O'Reilly, H., “Design and Evaluation of a Conceptual Zero-Emission Truck Model Considering Aerodynamic Efficiency,” SAE Technical Paper 2025-01-8784, 2025, doi:10.4271/2025-01-8784.

[11] Ficenec, K., McAuliffe, B., Lammert, M., and Holden, J., “Analysis of the Unsteady Wakes of Heavy Trucks in Platoon Formation and Their Potential Influence on Energy Savings,” SAE Technical Paper 2021-01-0953, 2021, doi:10.4271/2021-01-0953.

[12] Howell, J., Garry, K., and Holt, J., "The Aerodynamics of a Small Car Overtaking a Truck," SAE Int. J. Passeng. Cars - Mech. Syst. 7(2):2014, doi:10.4271/2014-01-0604.

[13] Shimizu, K., Nakashima, T., Hiraoka, T., Nakamura, Y. et al., “Investigation of Increase in Aerodynamic Drag Caused by a Passing Vehicle,” SAE Technical Paper 2018-01-0719, 2018, doi:10.4271/2018-01-0719.

Quasi-Steady and Unsteady Components of Aerodynamic Drag in Natural Wind Environments

Yasuyuki Onishi, Yasutaka Masumitsu*, Hiromu Shimiya

Honda R&D Co., Ltd.

Company 4630 Shimotakanezawa, Haga-machi, Hagagun, Tochigi 321-3393, Japan

*Honda Racing Corporation

1220-32 Shimokodo, Sakura-shi, Tochigi 329-1402, Japan

yasuyuki_onishi@jp.honda

yasutaka_masumitsu@jp.honda

hiromu_shimiya@jp.honda

Abstract:

This study evaluates the necessity of a turbulence generating system for assessing aerodynamic performance in natural wind environments. Various vehicle types were tested to classify the drag coefficient under turbulent flow into Quasi-steady and Unsteady components. The study revealed the limitations of current static pressure gradient correction methods and highlighted the potential for aerodynamic optimization through Quasi-steady weighting. The findings confirm that improving Quasi-steady components can reduce unsteady components, contributing to better aerodynamic performance in natural wind conditions.

Contribution: 2025 FKFS Conference on Vehicle Aerodynamics and Thermal Management
15 – 16 October 2025 | Leinfelden-Echterdingen

1 Introduction

In order to mitigate global warming, permitted CO2 emissions are being reduced in countries around the world. As a result, electric vehicles (BEVs), which do not emit CO2 while driving, are expected to become more widespread. BEVs are more energy-efficient than internal combustion engine vehicles, and most of the energy loss during driving is due to aerodynamic drag on highways. Therefore, reducing aerodynamic drag contributes to extending the range of electric vehicles [1].

Currently, the range and fuel efficiency on the label are calculated from road loads in mode drive cycles such as Worldwide-harmonized Light vehicles Test Cycle (WLTC) and The Environmental Protection Agency (EPA) drive cycles, which measure aerodynamic drag in a flow with an angle of attack of 0 degrees and very low turbulence intensity [2,3]. The road loads used for fuel efficiency dynamometer tests are measured by coasting down under ambient conditions with low wind or calculated by wind tunnel methods as in WLTC [4]. Consequently, in the aerodynamic development of vehicles, aerodynamic specifications are optimized under a flow with an angle of attack of 0 degrees and low turbulence in the wind tunnel. The road loads submitted for certification do not include the effects of natural wind because they assume no wind conditions [4]. Therefore, the difference between the drag coefficient (C_D) in the wind tunnel and the C_D with some turbulence due to natural wind may be one of the factors that cause the discrepancy between the label fuel economy and the actual fuel economy.

The characteristics of natural wind encountered by vehicles on public roads have much higher turbulence intensity and yaw angles larger than 0° compared to those in a wind tunnel [5,6,7,8,9,10]. To investigate the effect of turbulence on aerodynamic performance, several studies have been conducted to simulate turbulence using improved wind tunnel facilities, suggesting that turbulence increases aerodynamic drag in the real world [11,12]. The driving energy calculated from the aerodynamic C_D predicted from measured wind conditions was compared with the fuel consumption and the effect of natural wind on the fuel consumption was verified[13]. On the other hand, different vehicle models have different differences between the drag measured in turbulence and the weighted average drag value calculated by weighting the steady-state yaw sweep of C_D and the yaw angle probability distributions [14]. However, no studies have reported on the relationship and correlation between weighted-average drag and drag measured in turbulent flows.

The objective of this study is to determine whether a turbulence generating system (TGS) is necessary to evaluate aerodynamic performance in a natural wind environment. To the objective, several body types of vehicles were measured to classify C_D under turbulence flow conditions into Quasi-steady and Unsteady components and focused on the correlation between the Quasi-steady and Unsteady components. In the process, it was clarified the limitations of the current static pressure gradient correction method and also found it possible in proceeding with aerodynamic optimization with Quasi-steady weighting.

2 Evaluation definition

2.1 Natural Wind Parameters

Natural wind parameters are generally expressed as turbulence parameters, namely turbulence intensity (*TI*) and vortex scale length (*TL*). *TI* is expressed as the standard deviation of each velocity component relative to the mean velocity. Meanwhile, vortex scale length is expressed as the product of the inverse of the representative vortex frequency and the mean velocity as shown in Figure 1. These values change due to the influence of natural convection, the road environment, and surrounding vehicles, and various values are measured depending on the location. The wind has three components, u,v,w thus there are three *TI*, *TIu*, *TIv*, *TIw*. However, from the Aerodynamic Drag points of view, *TIv* is the domain parameter [11] and hereafter, The discussion focus on *TIv*.

①*TI* [%] $= \dfrac{\text{Standard deviation}}{\text{Mean Velocity}}$

②*TL*[m] = Representative Vortex length [m]
= 1/Representative Vortex frequency[s]
× Mean Velocity[m/s]

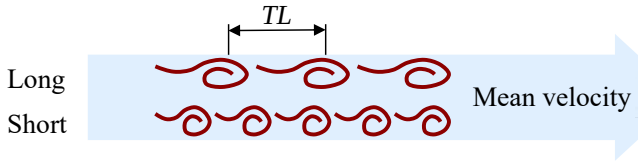

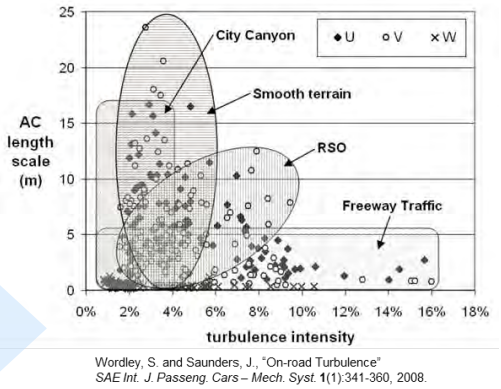

Wordley, S. and Saunders, J., "On-road Turbulence"
SAE Int. J. Passeng. Cars – Mech. Syst. **1**(1):341-360, 2008.

Figure 1 : Natural wind parameters [5]

In places with many structures and surrounding vehicles, turbulence intensity tends to be high and vortex scale length tends to be short. For example, on the highway road in the city. Conversely, in flat or open areas with few surrounding vehicles, turbulence intensity tends to be low and vortex scale length tends to be long. Past research has reported that turbulence intensity on roads is on the order of a few percent, and vortex scale length is often less than 10m. For example, on the smooth terrain [5].

2.2 Definition of Turbulence CD

It is assumed that the turbulent C_D can be divided into a Quasi-steady component and an Unsteady component. As shown in Figure 2, the C_D obtained from a turbulence flow with turbulence intensity and vortex scale length is defined as the turbulent C_D. The Quasi-steady component is the difference between C_D measured under low turbulence with Yaw 0degree and C_D calculated by weighting the steady state Yaw sweep of the C_D by the Yaw probability distributions of the turbulence flow, weighted C_D. It is calculated by multiplying the frequency of each angle by the C_D of that angle over all angles. The Unsteady component is the difference between the weighted C_D and the turbulent C_D. In other words, the delta C_D component that cannot be explained by the Quasi-steady component is defined as the Unsteady component. Hereafter, delta C_D is expressed as dC_D.

It is considered that the Quasi-steady component mainly depends on the turbulence intensity, while the Unsteady component depends on the vortex scale length.

Turbulence intensity is defined as the ratio of the standard deviation to the mean velocity. If the turbulence is isotropic, each velocity component is likely to have a normal distribution, and the standard deviation is equivalent to the Yaw probability distribution.

The weighted C_D that is the basis of the Quasi-steady component is calculated from the Quasi-steady state Yaw sweep of C_D and the Yaw probability distribution. The Quasi-steady component is determined by the turbulence intensity, which is the standard deviation.

Therefore, it can be said that the Unsteady component is caused by the vortex scale length, which is a parameter other than the turbulence intensity. Hereafter, C_D 0.001 is expressed as 1ct.

In order to evaluate the Unsteady components that cannot be explained by the Quasi-steady components, it is necessary to measure the turbulent C_D under turbulent conditions in a wind tunnel that can generate turbulence, and compare it with the weighted C_D under the turbulent conditions, that is, the Yaw probability distribution under the turbulent conditions and the C_D Yaw sweep integration under steady input. To do this, evaluation in a wind tunnel with a turbulence generator system is required, for example, FKFS side wind generator (FKFS ***swing***) [15].

.

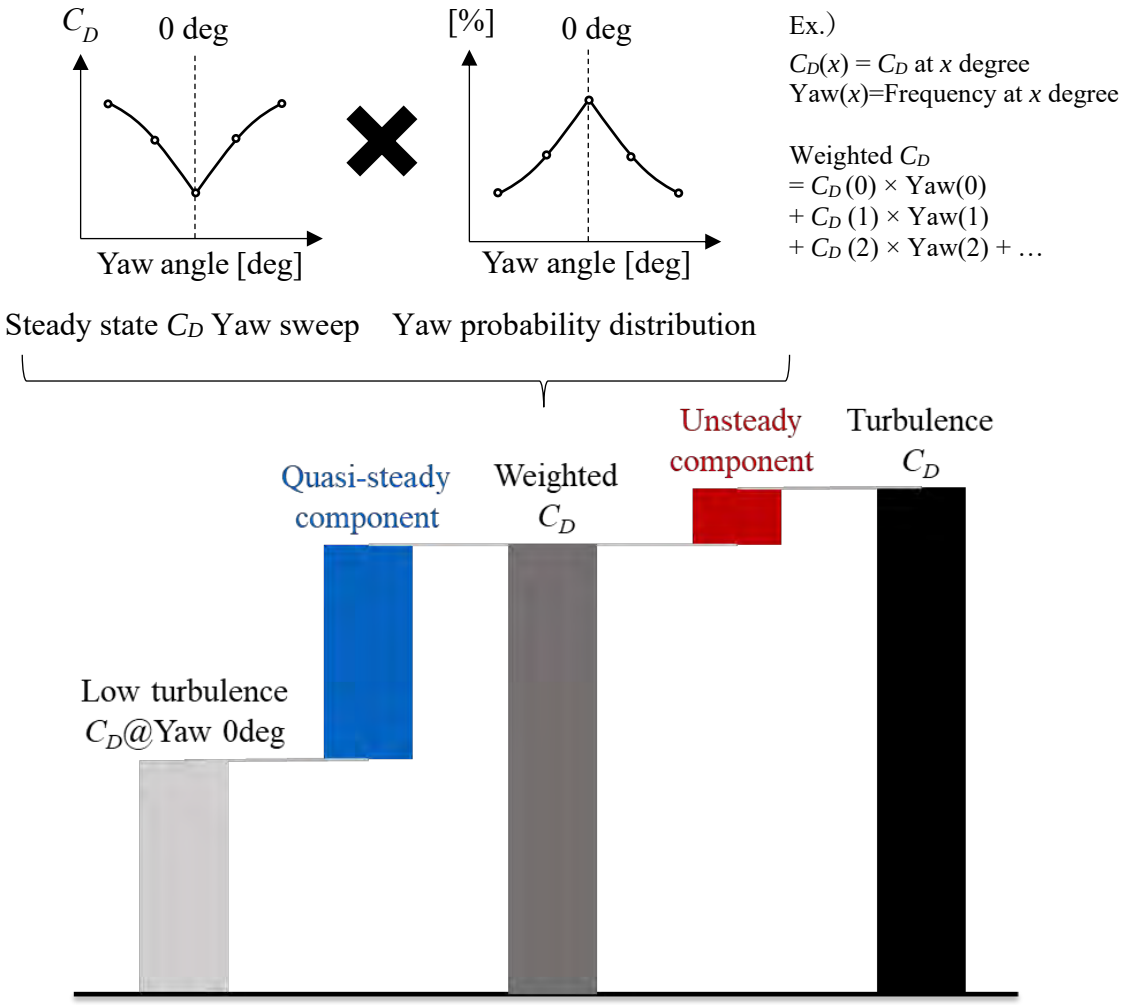

Figure 2 : Definition of Turbulence and Weighted C_D components

2.3 Static pressure gradient change and correction when using Turbulence Generation System

Generally, when the static pressure is different between the front and the end of the test vehicle, it is applied the correction for measured C_D in a wind tunnel to evaluate it without the effect from the horizontal buoyancy.

Figure 3 shows the static pressure gradient under several swing mode in FKFS scale wind tunnel. As Figure 3 shown, When the swing operates, the static pressure gradient in the X direction is changed by the movement of the turbulence generator, because the kinetic energy of the fluid added by the flap is converted into pressure for the mainstream velocity to be a constant value in the collector. Therefore, the change in the static pressure gradient becomes greater as the kinetic energy input into the mainstream becomes greater, for example, the higher the frequency with the flap operating of the same angle, the static pressure increases more near the corrector.

In this study, FKFS side wind generator (FKFS ***swing***) [14] consisting of flaps with a constant section shape in the Z direction is used. Even so, since the static pressure gradient differs depending on the turbulence mode as shown in Figure 3, it is necessary to measure the static pressure gradient and correct the impact on C_D for each turbulence condition.

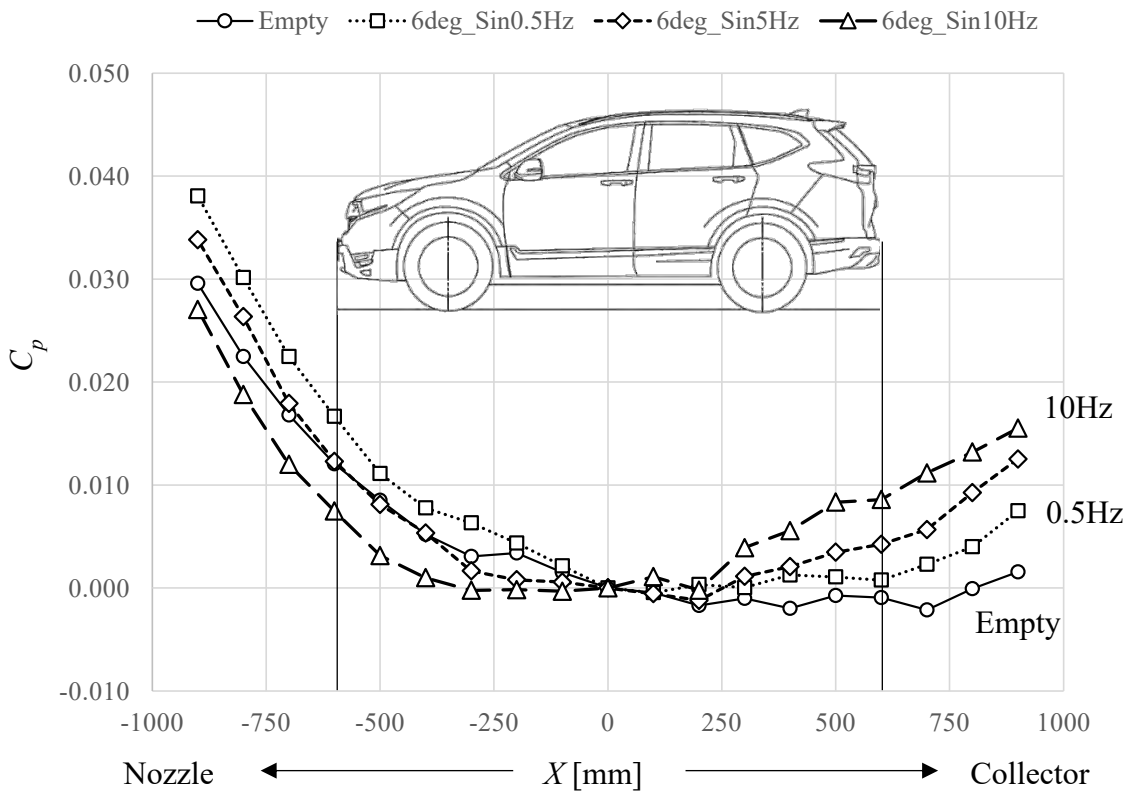

Figure 3 : Static pressure gradient at each ***swing*** mode

3 Methodology

3.1 Test vehicles

Three different body type vehicles, sedan, hatchback, and SUV were chosen to represent the flow structure from aerodynamic points of view. Sedan and hatchback have three aero options by combination of aerodynamic components to change the yaw characteristics. Figure 4 shows the C_D yaw sweep on these test vehicles with options. The absolute C_D and yaw trend are different from each other.

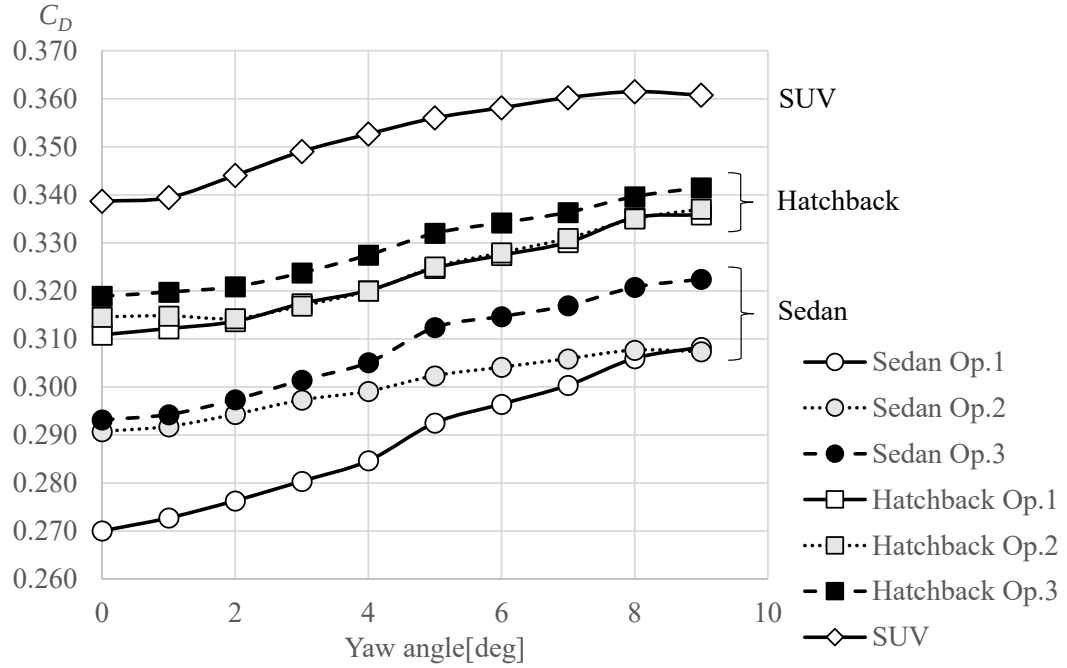

Figure 4 : C_D yaw sweep on these test vehicles with options

3.2 FKFS *swing* mode

In order to simulate as it is and simplify the natural wind condition measured on Japanese highway [11], 16 different modes were used to evaluate the relationship between Quasi-steady component and Unsteady component.

Two random modes are used to simulate the natural wind as it is in Japanese highway, which modes have *TIv* 2.6%, *TLv* 3m and *TIv* 2.2%, *TLv* 2m respectively. And Sin signal with flap angle 3 and 6 degrees from 0.4Hz to 1Hz. The flap angles were determined based on measurements, from 1σ at 3 degrees to 3σ at 6 degrees. The frequency range was also adjusted to the vortex scale length on the road. 0.4-1Hz corresponds to a vortex scale length of 5-13m, covering the range in which it mainly occurs in measured data.

4 Result

4.1 The relationship between Quasi-steady component and Unsteady component with static pressure gradient correction.

Figure 5 shows the relationship between Quasi-steady component and Unsteady component. These results were corrected for the effect of horizontal buoyancy caused by static pressure gradient. Although Two-measurement correction method was reported, here the simple correction method, which is calculated from the static pressure difference between the front and rear of the test vehicle as shown in Figure 4, is used. The correlation between the Quasi-steady and Unsteady components seems to be low and there seems to be little physical relationship between them. That means it is impossible to predict the Unsteady component impact from the Quasi-steady component.

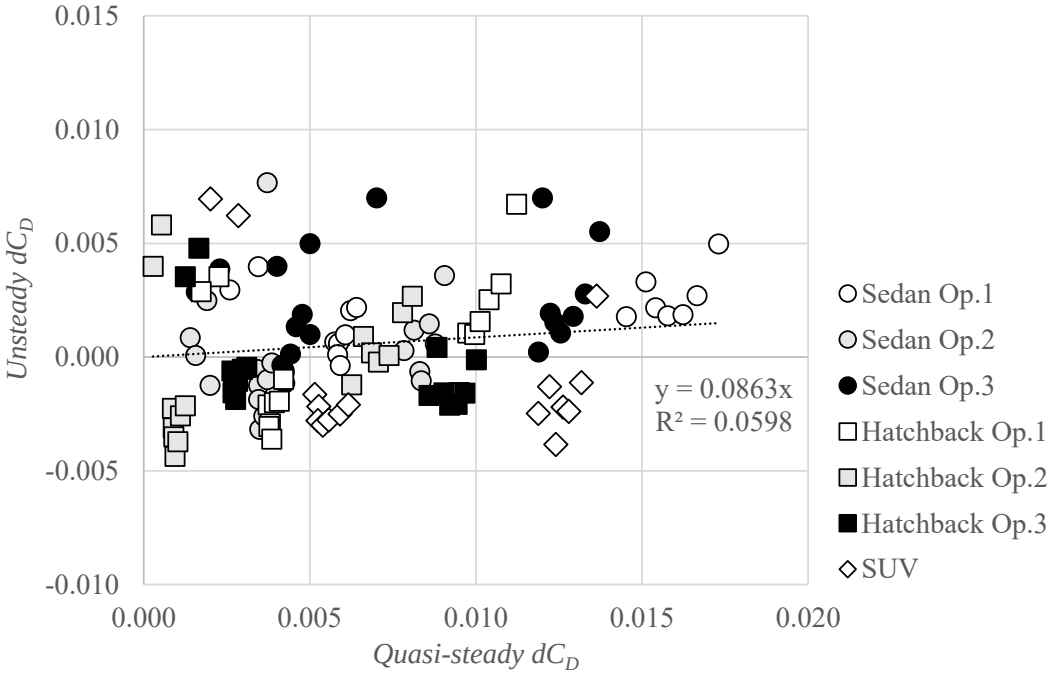

Figure 5 : The relationship between Quasi-steady component and Unsteady component measured at FKFS FSWT

4.2 Test results at Honda scale wind tunnel with Turbulence Generation System

4.2.1. Turbulence Generation System at Honda scale wind tunnel

In order to investigate the cause of Unsteady component, Honda installed Turbulence Generation System similar to FKFS ***swing*** to Honda scale wind tunnel as shown in Figure 6. Honda scale wind tunnel is designed to use 25% scale model with 5 belt rolling road system. The nozzle size is 2.3m width and 1.3 m height, and the test section length is 4.8m. The corrector size is 3.5m width and 1.9m height.

The turbulence generation system is installed at the exit of the nozzle and totally 12 flaps are installed inside the nozzle. The flap section keeps the constant section shape through the Z directions. Each flap is controlled by the motor mounted at the top of the nozzle individually. Therefore, as system, not only sin wave, but also random wave can be generated. Also, each flap can be operated individually. The flap is made of Carbon Fiber and designed the eigenfrequency over 20Hz. The weight is controlled within 2.5kg at each flap.

Maximum target averaged wind speed is limited up to 160kph. This is because the flow speed changes within 20km/h around the average wind speed, and depending on the time, the maximum wind speed approaches 190kph, which is the limit of the fan motor power. This system can generate not only v-component fluctuations, but also u-component fluctuations by changing the nozzle exit area using the two outer flaps at each. Maximum excitation frequency by this system is designed up to 10Hz and maximum flap angle is designed up to 12degrees.

The enough test section length and corrector size can achieve the flat static pressure gradient within *Cp* 0.002 from -800mm to +800mm in the X direction on the centreline at 250mm height from the ground at the balance centre as shown in Figure 7. The static pressure gradient in the Honda scale wind tunnel has been scaled up to full scale and aligned with the model.

Figure 6 : Turbulence Generation System at Honda Scale Wind Tunnel

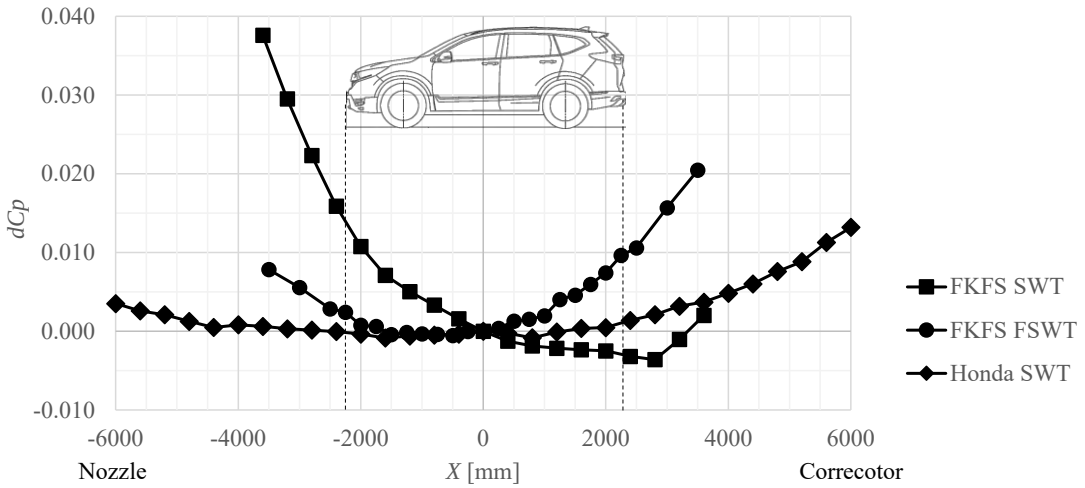

Figure 7 : Static pressure gradient comparison

4.2.2. Effect of static pressure gradient under TGS mode at each wind tunnel

Figure 8 shows the static pressure gradient results for the Honda scale wind tunnel, the FKFS scale wind tunnel, and the full-scale wind tunnel with ***swing***/TGS OFF and in a certain TGS mode (*TIv*6%, *TLv*10m). It shows that the static pressure gradient in FKFS WT decreases on the nozzle side and increases on the collector side when TGS is ON. On the other hand, in the Honda scale wind tunnel, the change in the static pressure gradient due to TGS operating is small.

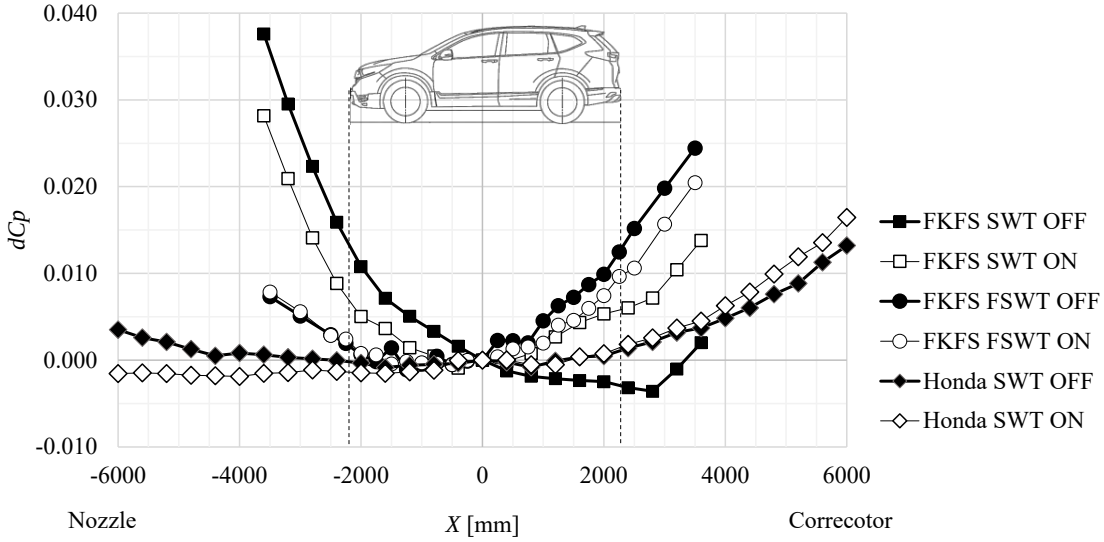

Figure 8 : Static pressure gradient under ***swing***/TGS operating mode

Figure 9 shows the value of the static pressure gradient correction with various *TIv* differences at each wind tunnel. *TLv* is about 1-2m. The horizontal axis shows *TIv*, and the vertical axis shows the static pressure gradient correction value. The static pressure gradient correction here is the static pressure difference at the front and rear positions of the vehicle.

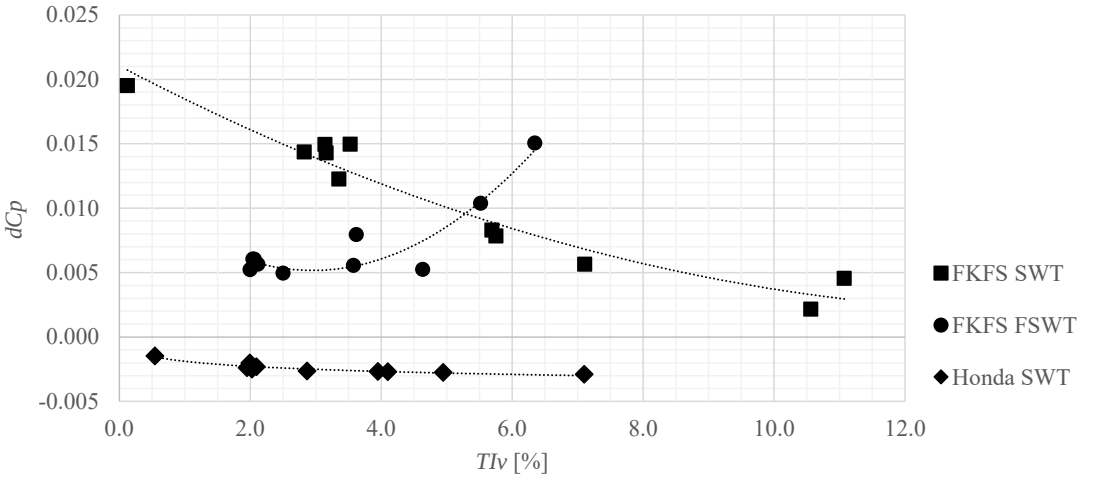

Figure 9 : The static pressure gradient correction on test vehicle Sedan through TIv differences

It can be seen that the static pressure gradient correction changes significantly depending on *TIv* in both the FKFS scale wind tunnel and the full scale wind tunnel. In addition, the tendency for the increase in *TIv* is opposite for scale wind tunnel and full scale wind tunnel. On the other hand, the static pressure gradient correction value of the Honda scale wind tunnel is almost constant regardless of the change in *TIv*, and the correction value is small at 1-3ct, which shows that the effect of the static pressure gradient due to TGS operation is small regardless of *TIv*. Although it is not possible to provide a physical basis for this difference, a hypothesis can be stated based on circumstantial evidence of the dimensions.

Table 1 shows a comparison of dimensions between the FKFS Full scale wind tunnel and scale wind tunnel, and the Honda scale wind tunnel. The scale wind tunnel dimensions are converted to full-scale dimension. It can be seen that the nozzle size, test section length, and collector size of the Honda scale wind tunnel are more than 50% larger than those of the FKFS. As mentioned earlier, the kinetic energy added by the TGS leads to an increase in pressure in the collector, so if the collector size is large and the distance to the model is long, there is less pressure propagation, and so it can be inferred from the comparison of dimensions that operating the TGS in the Honda scale wind tunnel has less impact on the static pressure gradient.

Table 1 : Comparison of dimensions between the FKFS Full scale wind tunnel and scale wind tunnel, and the Honda scale wind tunnel

Dimensions	FKFS		Honda
	SWT	FSWT	SWT
Nozzle width(m)	6.3	5.8	9.2
Nozzle Height(m)	4.2	3.9	5.2
Nozzle Area(m^2)	26.5	22.4	47.8
Nozzle to tunr table center(m)	4.7	4.6	8.8
Turn table center to Collector(m)	5.6	5.4	9.2
Test section(m)	10.3	10.0	19.2
Collector Area(m^2)	31.2	26.9	106.4

4.3 Relationship between Quasi-steady and Unsteady component

It is compared that the results measured in Honda scale wind tunnel and that in FKFS scale wind tunnel with and without static pressure gradient correction. The turbulence intensity conditions by TGS were set to be similar range for Honda scale wind tunnel and FKFS scale wind tunnel. And the turbulence scale length was about 2m for both. The wind speeds are 180kph for FKFS and 160kph for Honda. These data were measured by exactly the same Sendan model.

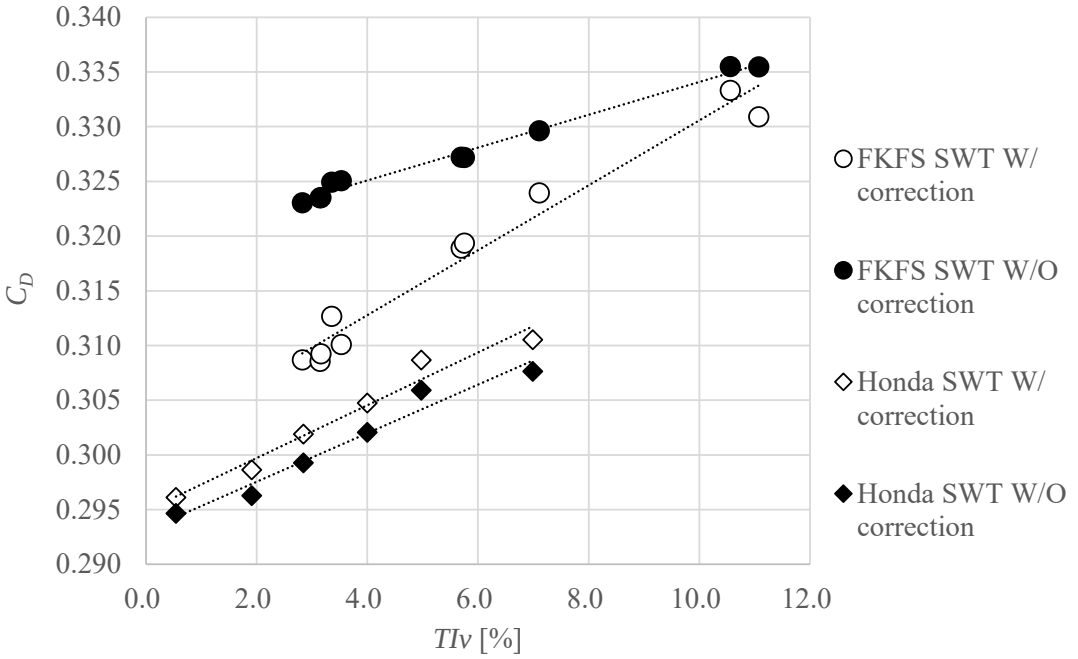

Figure 10 : The relationship between *TIv* and C_D with and without static pressure gradient correction

Figure 10 shows the relationship between *TIv* and C_D with and without static pressure gradient correction. Regardless of whether or not static pressure gradient correction is applied, C_D tends to increase as *TIv* increases. Also, the static pressure gradient correction is small due to the *TIv* difference in the Honda scale wind tunnel, so the slope is almost the same with and without correction. On the other hand, The FKFS scale wind tunnel results show that the increase in C_D versus *TIv* and the slope are different depending on whether or not correction is applied. Figure 11 shows the relationship between *TIv* and the Quasi-steady component with and without static pressure gradient correction. Honda scale wind tunnel results shows that the changes in the Quasi-steady component on TIv with and without correction are almost the same that they overlap. The FKFS scale wind tunnel results show the offset, but the changes in the influence of the Quasi-steady component on *TIv* follow the same trend. The Quasi-steady component is determined by the Yaw frequency (*TIv*), so the trend shall be the same. The offset is determined by the static pressure gradient correction value.

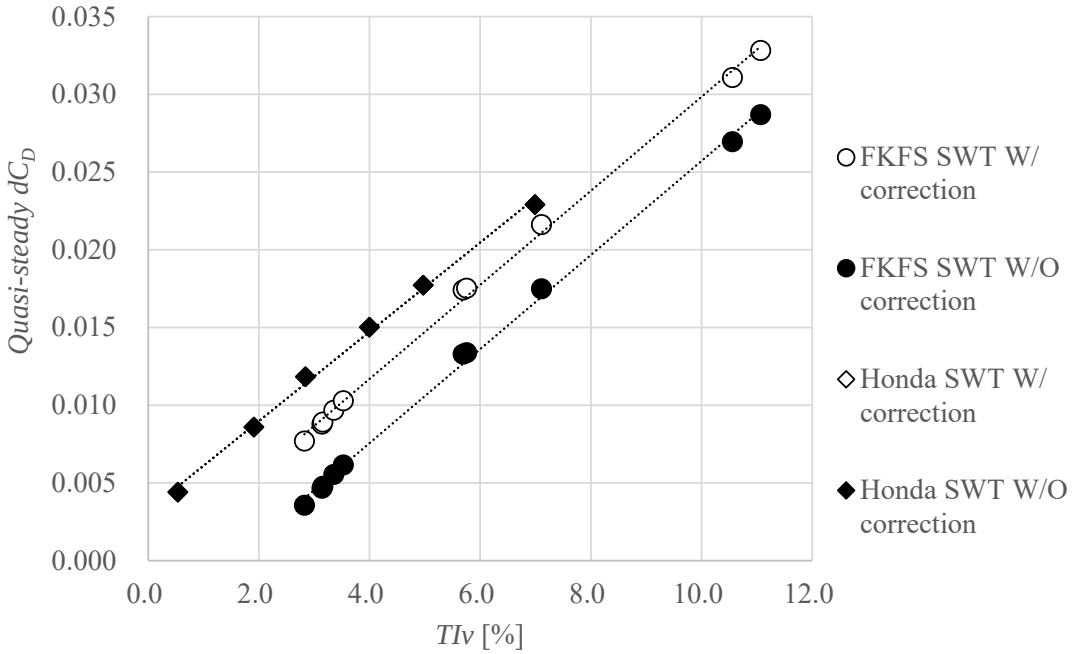

Figure 11 : The relationship between *TIv* and the Quasi-steady component with and without static pressure gradient correction

Figure 12 shows the relationship between *TIv* and Unsteady component with and without static pressure gradient correction. Honda scale wind tunnel results shows that the changes in the Unsteady component on *TIv* with and without correction are almost the same that they overlap. Because the correction value remains almost the same in the Honda wind tunnel. And also, the influence of the Unsteady component increasing in the negative direction as *TIv* increases. FKFS scale wind tunnel results show that the tendency of the Unsteady component is clearly different with and without the static pressure gradient correction value. With static pressure gradient correction, it becomes almost constant, but without static pressure gradient correction, the negative effect of the Unsteady component becomes larger as the *TIv* increases like with Honda.

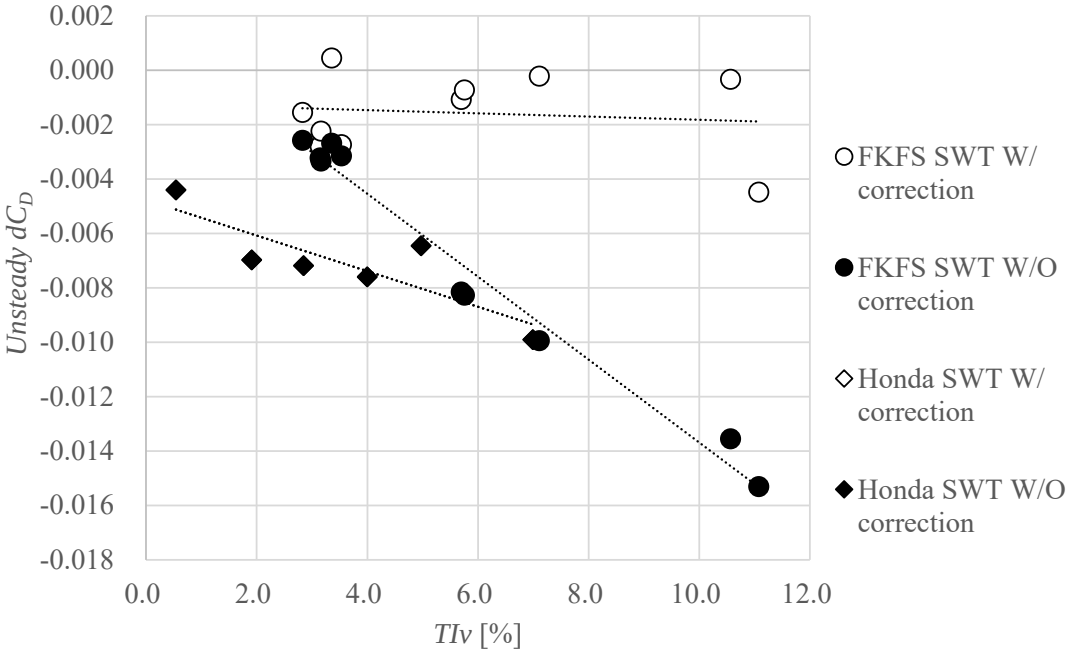

Figure 12 : The relationship between *TIv* and Unsteady component with and without static pressure gradient correction

Finally, Figure 13 shows the relationship between the Quasi-steady component and the Unsteady component. Regardless of whether a static pressure gradient correction is applied or not, Honda scale wind tunnel results show that as the Quasi-steady component decreases, the Unsteady component approaches zero. On the other hand, for the FKFS results, the results without static pressure gradient correction show that as the Quasi-steady component decreases, the Unsteady component approaches zero like the Honda scale wind tunnel results. From this, although it cannot be explained from a physical phenomenon, it is possible that the static pressure gradient correction in FKFS is not working as theoretically expected. The static pressure gradient was measured using a pitot probe while the TGS was in operation, with a measurement time of 60 seconds for each measurement point, but it is possible that the actual static pressure gradient was not captured correctly.

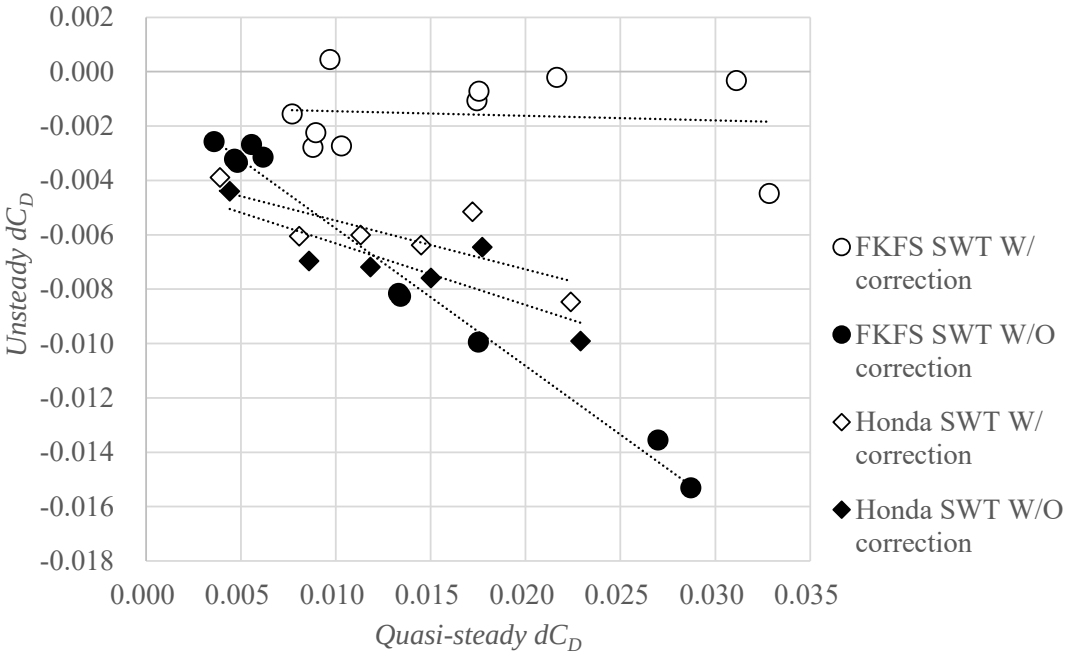

Figure 13 : The relationship between the Quasi-steady component and the Unsteady component

Assuming that static pressure gradient correction is not working properly with TGS ON, Figure 14 shows again the relationship between the Quasi-steady and Unsteady components for different vehicle types and models in the FKFS full scale wind tunnel without static pressure gradient correction. Without applying the static pressure gradient correction, it seems to be a linear relationship between the effects of the Quasi-steady and steady components. And also, it can be seen that as the Quasi-steady component becomes smaller, the Unsteady component also becomes smaller. In terms of general understanding of the phenomenon, it is natural to think that the less yaw sensitivity there is and the less likely separation will occur due to yaw changes, in other words, the smaller the influence of the Quasi-steady component, the less likely Unsteady separation phenomena will occur.

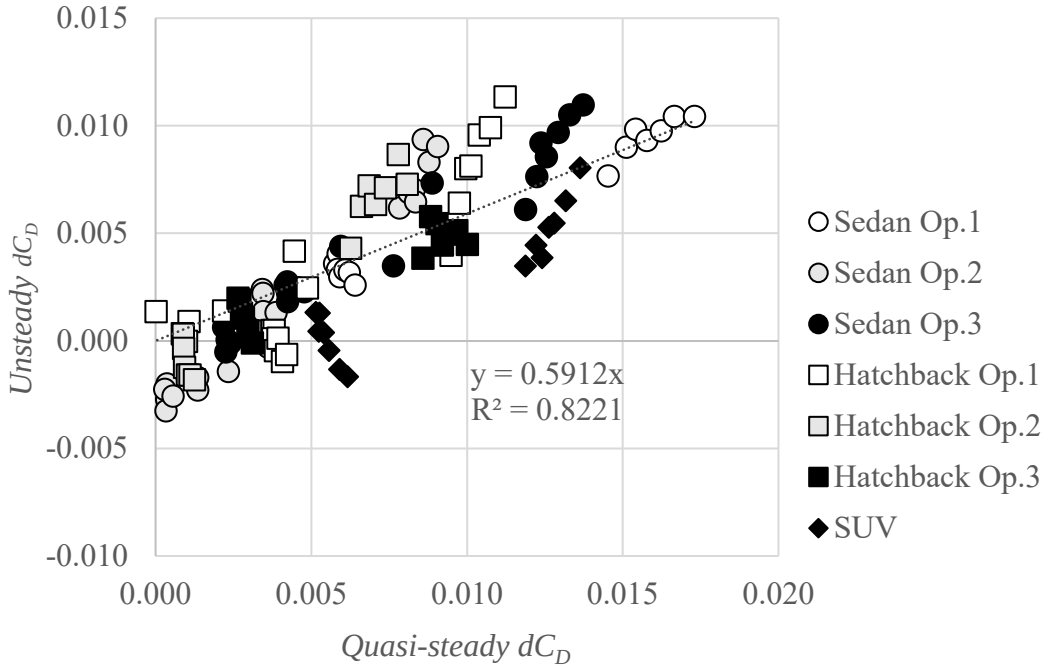

Figure 14 : The relationship between the Quasi-steady and Unsteady components in the FKFS full scale wind tunnel without static pressure gradient correction

In order to investigate where the Quasi-steady and Unsteady components appear in the flow around the vehicle, it was measured that the total pressure distribution in the WAKE behind the vehicle in the Honda model wind tunnel and identified the areas where the effects of each were apparent. The methodology how to isolate the Quasi-steady and Unsteady component from total pressure distribution is the same way of thinking as weighed C_D and Turbulence C_D. The measurements were conducted under the turbulence and steady flow at each yaw angle rotated by Turn table of the balance. Then Quasi-steady component of total pressure distribution is calculated from total pressure distribution in the WAKE behind the vehicle at each yaw angle and the yaw probability of the turbulence mode. Then, the Unsteady component is calculated by subtracting the Quasi-steady component from the pressure distribution under turbulent flow. The position of the total pressure measurement probe was calculated and adjusted to match the change in position of the model due to rotation on the turntable so that the position of the probe would be the same relative to the model.

Figure 15 shows the relationship between Quasi-steady component(dC_D) and Unsteady component(dC_D) of three test models measured at Honda scale wind tunnel under *TIv* 5% and *TLv* 1.5m. Two test models are different sedan with several aero options and One Hatchback model with several aero options. Similar to the results shown in Figure 14, there is a correlation between a reduction in the Quasi-steady component and a reduction of the Unsteady component. Op.1 and Op.2 were picked up to measure the total pressure in WAKE behind the vehicle in order to clarify the difference of both from the same vehicle model. Both Options are the same hatchback model, but with the different aerodynamic parts. Figure 16 shows C_D Yaw sweep on both options and the increase in C_D with increasing yaw angle in Op.2 is suppressed compared to Op.1. Therefore, in these test configurations Op.1 delta turbulence C_D is +6ct, Op.2 delta turbulence C_D is -1ct at each and there is clear difference between of both under turbulence.

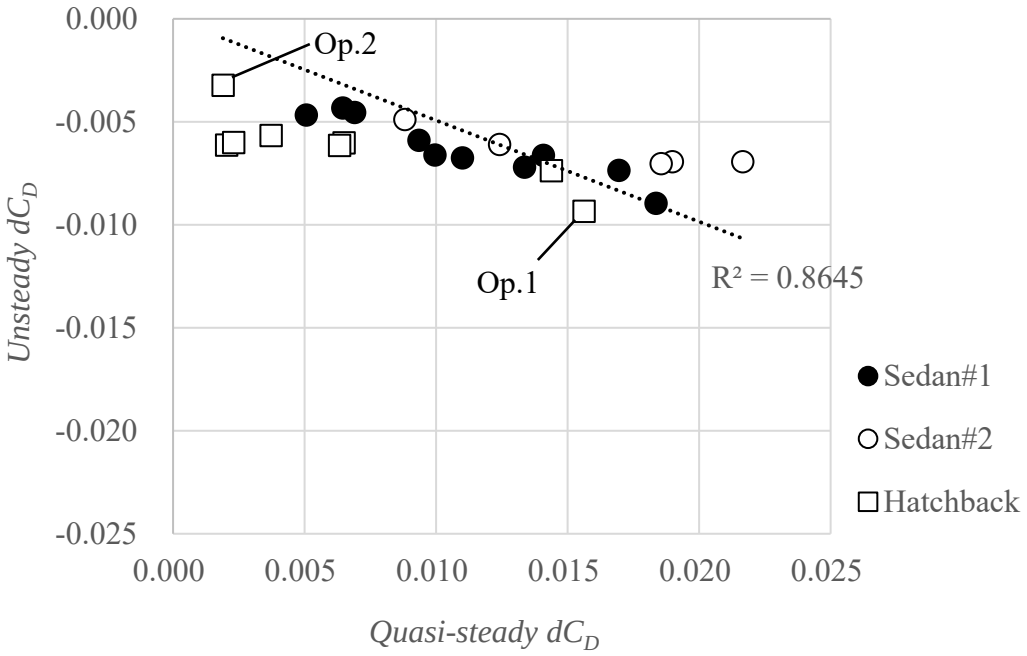

Figure 15 : The relationship between Quasi-steady component and Unsteady component of three test models measured at Honda scale wind tunnel.

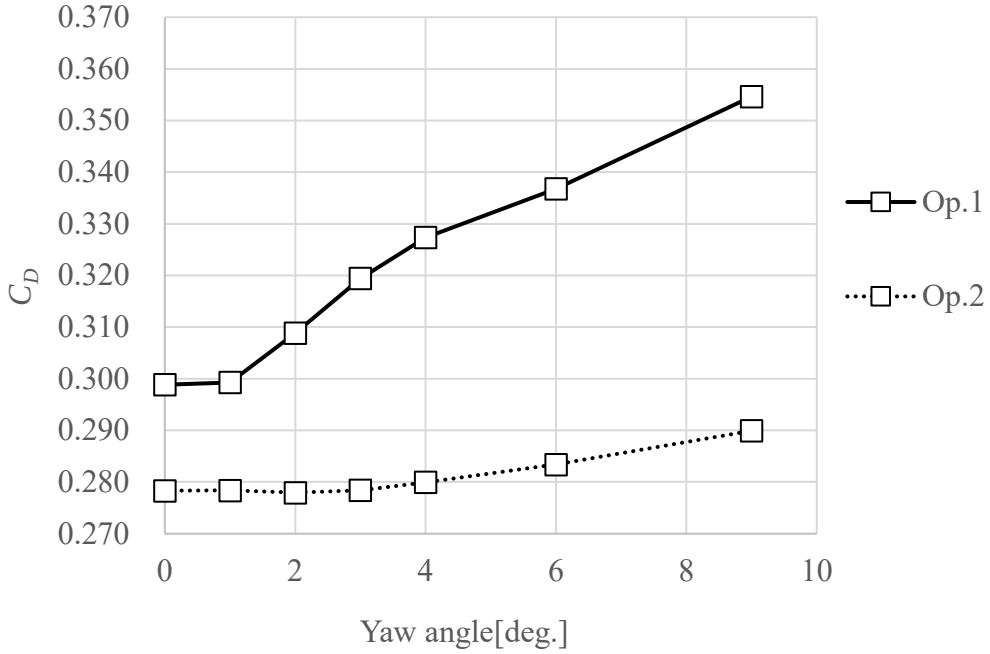

Figure 16 : C_D Yaw sweep on both options

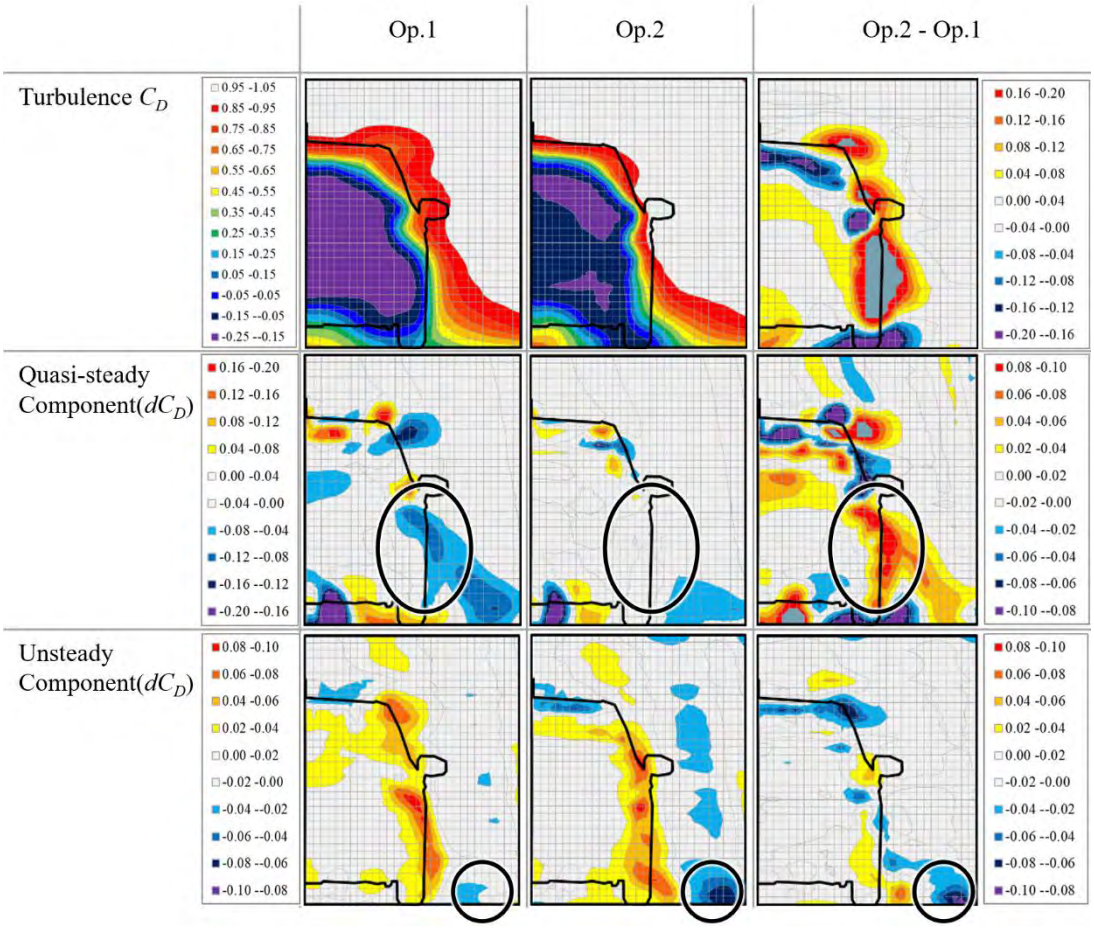

Figure 17 : the Quasi-steady component and the Unsteady component of total pressure in WAKE behind each option.

Figure 17 show the Quasi-steady component and the Unsteady component of total pressure in WAKE behind each option. At first, it is compared that the total pressures for the two options in turbulent. The result of Op.2, which is lower turbulence C_D than Op.1, the total pressure beside the vehicle is higher than that of Op.1. Next, it is compared that the Quasi-steady component of total pressures for the two options. Op.2 has not only lower C_D in turbulence, but also lower Quasi-steady C_D component than that of Op.1. The difference appears the Quasi-steady component of C_D total pressures beside the vehicle. This means that there is less separation of the Rear tire WAKE or side of Rear Bumper. On the other hand, Unsteady component of C_D at Op.1 works to reduce C_D 12ct and that at C_D at Op.2 works to reduce C_D 3ct. Therefore, the Unsteady component of total pressure of Op.2 is relatively lower than that of Op.1. According to this way of thinking, the Unsteady component of total pressure of Op.2 shows the lower total pressure. In specially, the difference beside the tire comes from Fr tire wake and it is predicted that the Fr tire separation point is different from both of options. The difference between both options is the Front strake, which acts to redirect the flow to the Front tire, thus affecting the separation location of the Front tire, thus matching the flow description.

These results suggest that reducing the Quasi-steady component also reduces the Unsteady component. In other words, in aerodynamic performance development that takes natural wind into account, improving the Yaw sensitivity of the C_D measured by the turn table sweep can also reduce the Unsteady component.

5 Conclusions

The static pressure gradient correction under TGS operating may not be appropriate, and it might not be necessary to apply it for C_D.

In order to reduce the effects of static pressure gradients that occur on the test vehicle due to various causes, it is best to make the length of the test section of the wind tunnel as long as possible, in line with the trend in state-of-the-art wind tunnels.

Improving the yaw sensitivity, Quasi-steady component, reduces Unsteady component.

6 Future work and limitations

This study suggested that reducing the Quasi-steady component also reduces the Unsteady component and improving the Yaw sensitivity of the C_D measured by the turn table sweep can also reduce the Unsteady component. However, there is a discrepancy between the scale wind tunnel results and the full scale wind tunnel results. The sign of the Unsteady component is opposite between the results in the scale wind tunnel and that in the full scale wind tunnel. The Unsteady component is negative in the scale wind tunnel, that is, it works in the direction of reducing C_D, whereas in the full scale wind tunnel it is positive, that is, it works in the direction of increasing C_D. The reason for this will be considered in the next study. On the other hand, the results of this study are focused on C_D effect from turbulence, and it is possible that TGS may be effective in terms of wind noise and stability.

7 Nomenclature and Abbreviations

WLTC	Worldwide-harmonized Light vehicles Test Cycle
EPA	The Environmental Protection Agency
C_D	the Drag Coefficient
TGS	Turbulence Generating System
TI	Turbulence Intensity
TL	Vortex scale length

FKFS ***swing***	FKFS side wind generator
CFD	Computational Fluid Dynamics
FSWT	Full Scale Wind Tunnel
SWT	Scale Wind Tunnel

8 Reference List

1. Where the Energy Goes: Gasoline Vehicles, https://www.fueleconomy.gov/feg/atv.shtml, 2023.

2. SAE International Light Duty Vehicle Performance &Economy Measure, “Road Load Measurement Using Onboard Anemometry and Coastdown Techniques,” SAE Standard J2263, Rev. Dec. 2008.

3. EPA Compliance Division. “Joint Technical Support Document: Final Rulemaking for 2017-2025 Light-Duty Vehicle Greenhouse Gas Emission Standards and Corporate Average Fuel Economy Standards,” EPA-420-R-12-901, August 2012.

4. UN Regulation No. 154 - Worldwide harmonized Light vehicles Test Procedure (WLTP)

5. Wordley, S. and Saunders, J., On-road Turbulence, SAE Technical Paper 2008-01-0475 (2008)

6. Wordley, S. and Saunders, J., On-road Turbulence: Part 2, SAE Technical Paper 2009-01-0002 (2009)

7. Schröck, D., Widdecke, N., and Wiedemann, J., “On-Road Wind Conditions Experienced by a Moving Vehicle,” in:Wiedemann, J. (ed.), Progress in Vehicle Aerodynamics and Thermal Management, Expert Verlag, Renningen, 2007.

8. McAuliffe, B. R., Belluz, L., & Belzile, M. (2014). Measurement of the On-Road Turbulence Environment Experienced by Heavy-duty Vehicles. SAE International Journal of Commercial Vehicles, 7(2), 685-702. doi:10.4271/2014-01-2451

9. Stoll, D., Schoenleber, C., Wittmeier, F., Kuthada, T. et al., "Investigation of Aerodynamic Drag in Turbulent Flow Conditions," SAE Int. J. Passeng. Cars - Mech. Syst. 9(2):2016, doi:10.4271/2016-01-1605.

10. Jessing, C., Wittmeier, F., Wiedemann, J., et al., “Characterization of the Transient Airflow Around a Vehicle on Public Highways” in:Wiedemann, J. (ed.), Progress in Vehicle Aerodynamics and Thermal Management, Expert Verlag, Renningen, 2019.

11. Cogotti, A., “Generation of a Controlled Level of Turbulence in the Pininfarina Wind Tunnel for the Measurement of Unsteady Aerodynamics and Aeroacoustics,” SAE Technical Paper 2003- 01-0430, 2003, doi:10.4271/2003-01-0430

12. Stoll, D., and Wiedemann, J., “Active Crosswind Generation and Its Effect on the Unsteady Aerodynamic Vehicle Properties Determined in an Open Jet Wind Tunnel”, SAE Technical Paper 2018-01-0722, 2018, doi:10.4271/2018-01-0722.

13. Onishi, Y., Ogawa, K., Sawada, J., Suwa, Y. et al., “On Road Fuel Economy Impact by the Aerodynamic Specifications under the Natural Wind,” SAE Technical Paper 2020-01-0678, 2020, doi:10.4271/2020-01-0678.

14. Fei, X., Kuthada, T., Wagner, A., and Wiedemann, J., “The Effect of Unsteady Incident Flow on Drag Measurements for Different Vehicle Geometries in an Open Jet Wind Tunnel,” SAE Int. J. Adv. Curr. Pract. Mobil. 4, no. 6 (2022):1999-2011, doi:10.4271/2022-01-0894.

15. Blumrich, R., Widdecke, N., Wiedemann, J., Michelbach, A. et al., "New FKFS Technology at the Full-Scale Aeroacoustic Wind Tunnel of University of Stuttgart," SAE Int. J. Passeng. Cars - Mech. Syst. 8(1):2015, doi:10.4271/2015-01-1557.

9 Acknowledgements

The authors would like to acknoledge the support from and collaboration with Dr.-Ing.Felix Wittmeier and Dr. Fei, X. at FKFS. The aouthors would like to thank FKFS for giving their permission to publish this papers.

On the Origin of Low Frequency Pressure Fluctuations in Passenger Compartments of Vehicles

Laura Breitenbücher, Dr.-Ing. Matthias Lang, Dr.-Ing. Maarten Brink, Dr.-Ing. Thomas Wiegand, Prof. Dr.-Ing. Andreas Wagner
Dr. Ing. h.c. F. Porsche AG
Porschestraße 911
71287 Weissach

laura.breitenbuecher1@porsche.de
andreas.wagner@ifs.uni-stuttgart.de

Abstract: Aeroacoustics have become increasingly important as they significantly determine comfort in passenger compartments.
Electric vehicles typically feature an underbody designed to minimize drag. The aerodynamic design also contributes to a reduction in acoustic interference. However, low frequency pressure fluctuations with significant amplitudes in the range of 30 Hz have been observed as a result of the optimization. Time-resolved Particle Image Velocimetry (PIV) measurements in the flow field beneath the car already showed periodical structures around the dominant frequency.
The aim of this study is to show the correlation between flow characteristics and low-frequency pressure fluctuations in the interior. A mobile measurement system was established to simultaneously acquire acoustic data and velocity fluctuations near the underbody using hot-wire anemometry. Direct online processing of both data streams enables a precise quantification of the mathematical correlation between acoustic and aerodynamic signals. Relevant flow phenomena were detected beneath the vehicle by pointwise traversing the hot-wire probe. Additionally, visualizations of the wall shear pattern along the underbody showed a strong correlation with measured results and provided further insights into the underlying flow physics.
It is demonstrated that a combined application of quantitative and qualitative experimental techniques, as well as simulations, provides a deeper insight into the underlying mechanisms, thereby enhancing the understanding of the complex flow field. Finally, this approach facilitated the development of countermeasures in the early stages of development, reducing the need for unplanned optimization loops.

Contribution: 2025 FKFS Conference on Vehicle Aerodynamics and Thermal Management
15 – 16 October 2025 | Leinfelden-Echterdingen

1 Introduction

Customers' expectations of the driving experience in the interior of a vehicle are becoming increasingly important. Battery electric vehicles (BEVs) generate almost no drive noise and there are no combustion masking effects either. As a result, flow noise becomes relevant at lower speeds. [1] Due to the absence of an exhaust system and advantages regarding drag coefficients, BEVs typically have a very streamlined underbody. This underbody shape is generally characterized by a low acoustic disturbance potential. However, low-frequency pulsations in the frequency range below 20 Hz have been observed in certain prototypes of battery electric vehicles. These strong pressure fluctuations excite the vehicle's interior through the air path of the ventilation exits in the rear area. As a result, uncomfortable pressure fluctuations occur in the vehicle interior, leading to a reduction in passenger comfort. In this study, this phenomenon is referred to as “underbody buffeting.”

Previous investigations have shown that the flow phenomenon is very sensitive to geometric modifications on the vehicle’s underbody. However, even small modifications can influence not only the aeroacoustics but also the aerodynamics of the vehicle. [2, 3, 4]

In [2], Weber identified high-energy separations at the front wheel spoilers and at the front wheels as the cause of the high-pressure fluctuations in the rear area of the vehicle. The underbody buffeting can be generated at a generic car reference model. This was demonstrated in [4], where investigations were conducted both in CFD-simulations and in the wind tunnel. In order to identify the exact formation mechanism of the underbody buffeting, time-resolved Particle Image Velocimetry (PIV) measurements were carried out in the model wind tunnel of the Research Institute for Automotive Engineering and Powertrain Systems Stuttgart (FKFS). [5]

In addition to analysing the mean and instantaneous velocity, the velocity fluctuations were subsequently investigated. The Ω-method was employed for the identification and visualization of vortices. [6] The Spectral Proper Orthogonal Decomposition (SPOD) method was applied to identify coherent structures. [7]

The dominant frequency that can be perceived in the interior could be detected by PIV measurements in the flow. [5] This paper presents supplementary hot-wire and microphone measurements as well as visualizations that offer deeper insight into the fundamental mechanism primarily responsible for underbody buffeting. It will be demonstrated that combining the strengths of these various quantitative and qualitative techniques yields results unattainable by applying any single method alone. A transient measurement system is being developed to detect acoustically relevant flow structures, utilizing real-time online evaluation. Through signal correlation, the system aims to establish a direct relationship between measured flow fluctuations and their effects on acoustics. The measurement system is intended to be relatively cost-effective, quick, and mobile. The critical areas identified through hot-wire and microphone coherence will subsequently be compared with the flow structures using flow visualization techniques. Finally, the findings from the investigations will be utilized to develop appropriate countermeasures.

2 Method

All investigations in this study were carried out in the model wind tunnel of the FKFS. The measurements were performed using a generic vehicle reference model based on the SAE-Body defined by the SAE committee, scaled at 1:4 [8]. This setup enables the isolation of flow phenomena by eliminating additional aeroacoustics noise sources and related interference effects. Unlike the original model with a smooth underbody, the current model includes wheel arches and wheels. Moreover, various wheel spoilers and add-on components can be attached to the vehicle's underbody. Figure 1 shows the model in the wind tunnel.

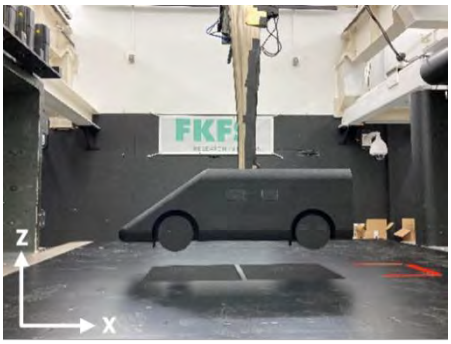

Figure 1: Geometry of the SAE-Body with wheels and wheel spoilers

It has been demonstrated that applying PIV enables the detection of flow structures associated with low-frequency phenomena within the flow field [5]. While PIV provides valuable imaging data, its setup and data postprocessing require a comparatively high time investment. Consequently, the relationship between velocity fluctuations and their acoustic feedback is not immediately accessible during the measurements.

To reduce measurement time and improve efficiency during the development of countermeasures in such measurement campaigns, a new measurement system has been set up. The schematic setup of this system is shown in Figure 2. It allows for the simultaneous acquisition of time-resolved signals with one microphone, two pressure transducers, and a single hot-wire probe. Additionally, a traverse system can be connected to acquire time series of pressure or velocity automatically within the flow field.

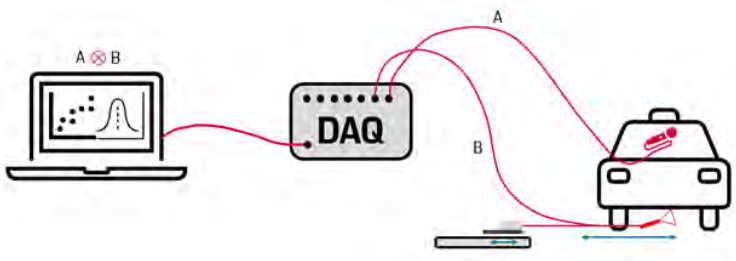

Figure 2: Schematic setup of the measurement system with hot-wire and microphone

A custom-developed software enables real-time processing of signals acquired from a continuous data stream. Frequency spectra and the coherence between two selected signals are computed and displayed immediately. The coherence function, calculated as described in [9], quantifies the correlation between two signals across different frequencies. In other words, it indicates the strength of the connection or any linear dependency between the signals in the frequency domain. This system allows for scanning of the flow field to identify regions where velocity fluctuations correlate strongly with acoustic frequencies, thereby pinpointing flow areas with coherent structures directly related to aeroacoustics phenomena. In the present study, signals from the microphone and hot-wire probe were analysed to precisely quantify the mathematical correlation between acoustic and aerodynamic phenomena while moving the hot-wire probe beneath the car model along the y-axis. The microphone was positioned inside the model, specifically within the passenger compartment. For direct comparison with PIV measurements [5], the z-position of the hot-wire probe was selected to match the height of the PIV light sheet.

Another classical method applied is the kerosene soot technique, which is used to visualize the direction of wall shear stress. In contrast to the traditional approach, a mixture of paraffin oil and coloured particles was employed. The components of this mixture were selected so that its viscosity, combined with the wall shear stress, permits a certain movement of the liquid, thereby revealing the resulting flow structures. The substance was applied to the underside of the SAE-Body, and the model was subjected to the same flow conditions as during the PIV and aeroacoustics measurements. While the direction of the shear stress indicates the orientation of the wall streamlines, the concentration of the liquid after the experiments serves as an indicator of the wall shear of the flow velocity.

3 Results

In this chapter, the results of three different configurations are presented. Figure 3 shows the frequency spectra of the considered variants. These spectra were derived from pressure fluctuations measured with surface microphones positioned in the rear area of the vehicle's underbody. The configuration *with_WS* features wheel spoilers in front of the wheels. The dominant peak around 90 Hz in the frequency spectrum clearly indicates a strong occurrence of underbody buffeting. In the configuration without wheel spoilers (*without_WS*), the wheel spoilers were removed, and underbody buffeting does not occur. For the configuration *with_VG*, a forward-facing vortex generator was installed at the inner edge of the wheel spoiler, which significantly reduces underbody buffeting.

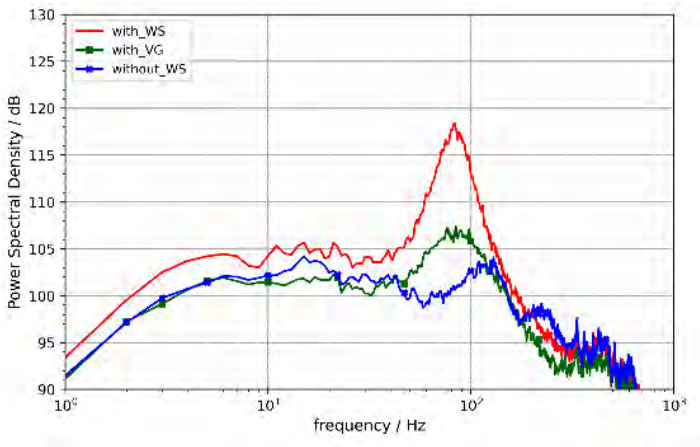

Figure 3: Frequency spectra of configurations *with_WS* (with front wheel spoiler), *with_VG* (with vortex generator) and *without_WS* (without front wheel spoiler) measured with a microphone in the diffusor area of the vehicle

3.1 Configuration with wheel spoiler

In the following, the configuration with front wheel spoilers *with_WS*, where underbody buffeting occurs, will be discussed.

Previous studies using PIV measurements have provided detailed insights into the underlying flow. In this context, SPOD analysis was employed to identify coherent structures within the flow. Figure 4 presents the SPOD spectrum and the first SPOD mode at 78 Hz.

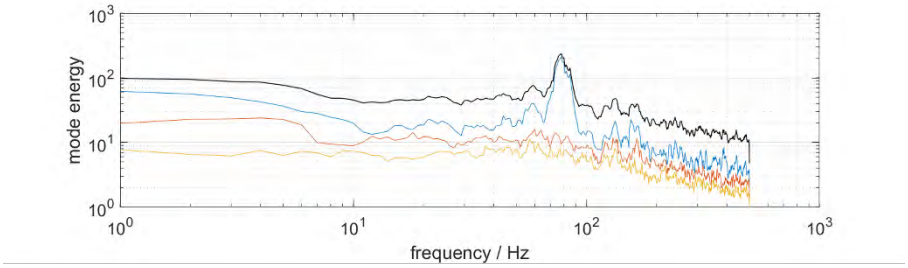

a)

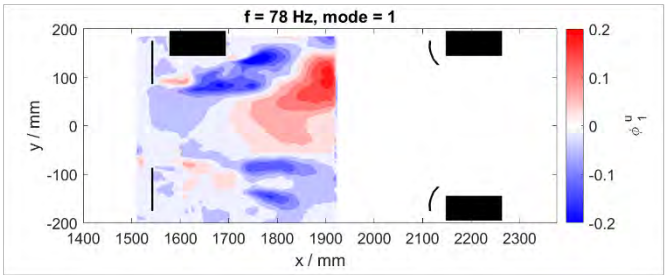

b)

Figure 4: a) SPOD spectra and b) first SPOD mode of configuration *with_WS*

The investigation reveals that the coherent structures primarily originate at the inner edge of the wheel spoiler. Furthermore, it is evident that fluctuations in flow parameters occur within the shear layer behind the wake of the wheel spoiler.

Hot-wire measurements were performed at selected positions along the x-direction (wind direction) to capture velocity fluctuations beneath the model. The hot-wire probe was traversed along the y-direction. Figure 5 shows profiles of the mean velocity and standard deviation derived from the hot-wire signals across the vehicle width in the y-direction for all three configurations. In this section, configuration *with_WS* (red lines) is considered. The shear layer is located within the range of - 100 mm < y < - 60 mm, indicated by the strong velocity gradient. A high standard deviation level indicates significant flow fluctuations, with the maximum standard deviation occurring at approximately y ≈ -100 mm, as shown in Figure 5b).

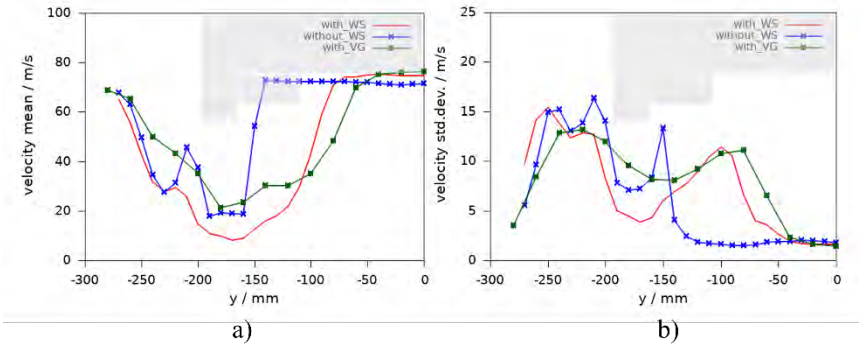

Figure 5: a) Mean velocity and b) standard deviation of measured velocity profiles across the vehicle width of configurations *with_WS*, *without_WS* and *with_VG*

Shear layers are regions characterized by a strong velocity gradient between two fluid layers. They exhibit high instability with significant disturbance growth, resulting in pronounced velocity fluctuations. Figure 6a) shows the 1/3 octave sound pressure level frequency spectra. The solid lines represent the measurement from the microphone inside the vehicle cabin, while the dashed lines correspond to the hot-wire signal at y = -80 mm within the shear layer. Although expressing velocities in decibels is not strictly physically accurate, we use this approach to enable a direct comparison with acoustic quantities. The coherence functions between these two signals are presented in Figure 6b).

For configuration *with_WS* in the region of strong disturbance growth, prior to saturation, the fluctuations are confined to a dominant frequency range (here 55 Hz < f < 110 Hz). As shown in Figure 6b), the coherence between the hot-wire and microphone signals exhibits a pronounced peak within this frequency range, corresponding to the underbody buffeting. This peak indicates a strong correlation between the velocity fluctuations within the shear layer beneath the model and the acoustic phenomena measured in the passenger compartment. These findings suggest that the flow structures developing in this shear layer are acoustically significant.

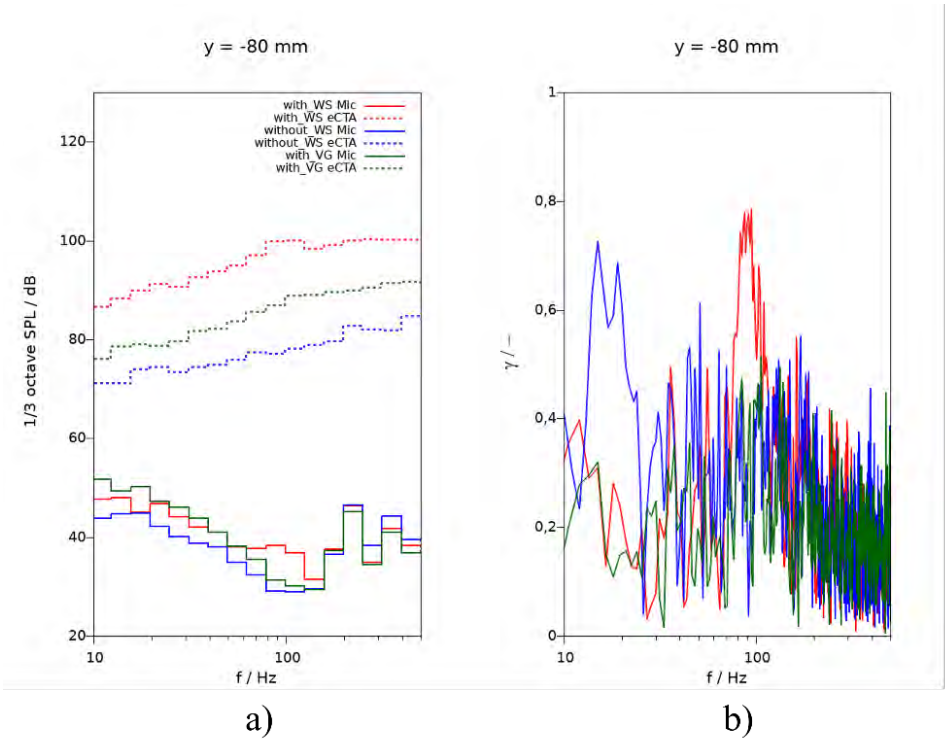

Figure 6: a) 1/3 octave sound pressure level frequency spectra and b) coherence function between hot-wire signal and microphone at y = - 80 mm of configurations *with_WS*, *without_WS* and *with_VG*

Figure 7 illustrates the distributions of the maximum sound pressure levels and coherence along the y-direction for the dominant frequency band associated with underbody buffeting (55 Hz < f < 110 Hz). It is important to note that high coherence does not necessarily correspond to large velocity fluctuation amplitudes, as coherence is derived from the cross-correlation function normalized by the autocorrelation functions of the two signals [9]. Rather, high coherence indicates a strong linear relationship between the two signals. This is evident when comparing Figures 7a) and 7b) of configuration *with_WS*. While coherence reaches its maximum in the fast main flow between the wheel spoilers, velocity fluctuations peak within the shear layer and decrease slightly towards the centre region. Figure 7b) further reveals a pronounced increase in coherence along the y-direction within the shear layer region, associated with dominant disturbance modes in the considered frequency range. These results highlight the crucial role of the shear layer in the development of buffeting.

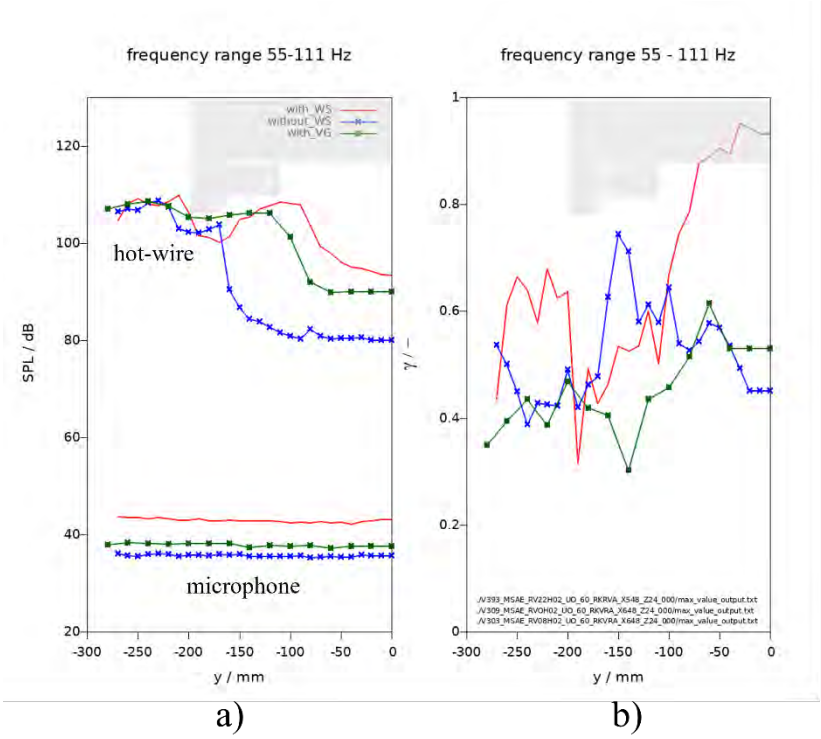

Figure 7: a) Maximum sound pressure levels and b) coherence functions for frequency range 55 Hz < f < 110 Hz across the vehicle width of configurations *with_WS*, *without_WS* and *with_VG*

3.2 Configuration without wheel spoiler

This section discusses the configuration without wheel spoilers (*without_WS*), where no underbody buffeting occurs. The curves for this configuration are shown in blue in the diagrams.

First, the mean velocity profiles and standard deviation profiles of configurations *with_WS* and *without_WS* are compared (Figure 5). The position of the front wheel is indicated in the diagram between -200 mm < y < -150 mm. Downstream of the wheel, in the wake region, the flow velocity is significantly reduced in both cases, while between the wheels, the flow velocity approximately matches the free-stream velocity. Although both configurations exhibit a shear layer, buffeting occurs only in the *with_WS* case, as will be demonstrated. The configuration *without_WS* shows a strong velocity gradient around y ≈ -150 mm, whereas in the *with_WS* case, the shear layer is located further towards the vehicle centre at approximately y ≈ -100 mm. This shift is due to the wheel spoilers extending further towards the centerline. The thickness of a shear layer increases with its downstream length; since the hot-wire probe is positioned relatively close behind the front wheel, the shear layer behind the configuration *without_WS* is significantly narrower than that of the configuration *with_WS*.

Next, the 1/3 octave sound pressure level frequency spectra and the coherence function are examined (Figure 6). Comparing the hot-wire signals reveals that velocity fluctuations across the depicted frequency range are significantly lower in the configuration *without_WS* than in the configuration *with_WS*. Additionally, the differences in pressure fluctuations between the two configurations within the buffeting frequency range are considerably higher compared to other frequency ranges. Figure 6b) presents the coherence function calculated from the spectra shown on the left. A broad coherence peak is clearly visible within the buffeting frequency range of 55 Hz < f < 110 Hz. This peak is absent in the *without_WS* case (blue line). A peak observed in the 10 Hz < f < 25 Hz range is considered irrelevant due to the low amplitude levels in the signal. These results suggest that, without wheel spoilers, no acoustically significant flow structures occur in the considered case. When wheel spoilers are installed, a shear layer is formed where disturbance modes are amplified, causing underbody buffeting.

The frequency spectrum in Figure 7 clearly shows that velocity fluctuations, especially in the region between the wheels, are significantly lower for the configuration *without_WS* compared to the configuration *with_WS*. Similar amplitude levels in both hot-wire signals are observed only in the wake region of the wheels. This is because the fluctuating wake exhibits high levels across a wide frequency range, not limited to the shown bandwidth of 55 Hz < f < 110 Hz. Additionally, there is almost no correlation between the acoustic signals and the flow fluctuations measured by the hot-wire in the configuration *without_WS* (blue lines).

With installed wheel spoilers (*with_WS*, red), the amplitude measured by the microphone is significantly increased within the shown frequency range. The same applies to the fluctuations in the underbody flow field between the wheels. In this case, a strong coherence is observed. These two measurements clearly and quantitatively demonstrate that underbody buffeting occurs only when wheel spoilers are installed. The strongest correlations between sound signals measured inside the model and flow fluctuations beneath the vehicle are found in the region between the wheels. Disturbance modes within the shear layer separating the wake are strongly amplified, ultimately causing buffeting.

To gain additional insight into the flow field, the so-called kerosene soot technique was applied to visualize wall streamlines beneath the model. Figure 8 compares the flow patterns of the configurations *without_WS* and *with_WS*. Regions with high color density indicate areas where the oil accumulates due to low wall shear stress, whereas regions with less colour correspond to high wall shear stress caused by elevated flow velocities or strong velocity fluctuations resulting from intense turbulence. The shear layer regions exhibit high wall shear stress due to increased momentum exchange in the highly turbulent flow.

The baseline configuration *without_WS* (Figure 8a)) exhibits an almost homogeneous distribution of wall shear stress. In the configuration with wheel spoilers (Figure 8b)), two streaks of fluid accumulation form around the inner edge of the front wheel spoilers, separating the centre flow from the shear layer. The wake regions, which also contain the shear layers caused by the wheel spoilers, are identifiable by brighter areas where the oil paint has been strongly sheared off due to high skin friction. Within the shear layer separating the wakes from the mean flow between the wheels, disturbance modes are amplified, leading to low-frequency buffeting, as demonstrated by the quantitative measurements presented above. The shear layer position along the y-axis is further confirmed by the maximum standard deviation shown in Figure 5a).

a) b)

Figure 8: Wall shear patterns for the configurations a) *without_WS* and b) *with_WS*. Flow goes from left to right.

3.3 Configuration with vortex generator

From an aerodynamic perspective, wheel spoilers are essential components on the vehicle underbody to optimize the balance between drag and lift. The previous section demonstrated that wheel spoilers can induce buffeting, which is clearly perceptible in the passenger compartments of vehicles with flat underbodies (BEVs). The next step is to retain the spoilers while eliminating the buffeting.

By applying the various qualitative and quantitative methods presented above, the mechanism leading to underbody buffeting was identified. The disturbance modes originate from the shear layer developing around the inner edge of the wheel spoilers. Based on these findings, the goal was to modify the flow around the spoilers to prevent the formation of the unstable shear layer. The most straightforward approach is to generate a moderate vortex that suppresses the formation of an extensive wake (see Figure 8b)). This was achieved by a delta-shaped vortex generator adapted to the inner edge of the wheel spoiler. The longitudinal vortex prevents the formation of a large wake and its shear layer by enhancing momentum exchange along the model's underbody. As a result, pressure fluctuations caused by the shear layer are suppressed. The next section compares hot-wire measurement results and their correlation with those of the previously presented configurations *without_WS* and *with_WS*.

First, the mean velocity profiles and standard deviation profiles are considered. Figure 5 shows that the overall curve pattern for the configuration *with_VG* (green) is similar to that of the configuration *with_WS* (red). However, mean velocities in the wake region behind the wheel spoiler and wheel area have increased for the configuration *with_VG*, approaching values comparable to those in the *without_WS* case. The similarity between the configurations *with_WS* and *with_VG* arises because the mean values and standard deviations in Figure 5 encompass the entire frequency spectrum. To distinguish the different flow regimes of the *with_WS* and *with_VG* cases, it is essential to analyse the amplitude distributions in the frequency domain. Again, hot-wire results, their correlation with the microphone signal, and flow visualizations will demonstrate that the wake region behind the wheel spoilers behaves and appears significantly differently when combined with vortex generators compared to the original case with only wheel spoilers installed.

Next, the 1/3 octave frequency spectra and the coherence function between the acoustic and hot-wire signals are analyzed (Figure 6). Within the low-frequency range shown (0 Hz < f < 500 Hz), the amplitudes of the hot-wire signal are significantly reduced compared to configuration *with_WS*. Notably, underbody buffeting is completely suppressed, with amplitude levels comparable to the case *without_WS* and no buffeting. This suggests that the shear layer has been nearly eliminated, which may explain why the mean velocities in the wake of the configuration *with_VG* are approximately twice as high as those for configuration *with_WS*, as shown in Figure 5a).

Figure 5b) shows that in certain regions across the vehicle width, the standard deviation for configuration *with_VG* is significantly higher than for the case *without_WS*. Figure 6 reveals that these increased fluctuations are broadband, distributed across the entire frequency spectrum. The cause of the increased fluctuations is the vortex generator, which enhances momentum exchange. However, the interior microphone indicates that the relevant pressure fluctuations, especially within the underbody buffeting frequency range, are nearly as low as in the case *without_WS*. Consequently, the vortex generator reduces acoustically relevant velocity fluctuations and thus pressure fluctuations in the critical low-frequency range. This observation aligns with the coherence spectrum, where no significant correlations between velocity and pressure signals are detected across the relevant low-frequency range.

The hot-wire signal amplitudes in Figure 7 show a reduced level in the area between the wheels for the case *with_VG* (green) compared to the buffeting case (*with_WS*, red). Similarly, the pressure fluctuations inside the model are reduced to nearly the levels observed without underbody buffeting (*without_WS*, blue). Furthermore, the low maximum coherence values indicate no correlation between velocity fluctuations and the acoustic signal, confirming that the vortex generators effectively suppress underbody buffeting.

Figure 9 compares the visualized flow patterns for the configurations *with_WS* and *with_VG*. The formation of the unstable shear layer is clearly visible. In the *with_VG* case, the shear layer is significantly weakened by the longitudinal vortex generated by the vortex generator.

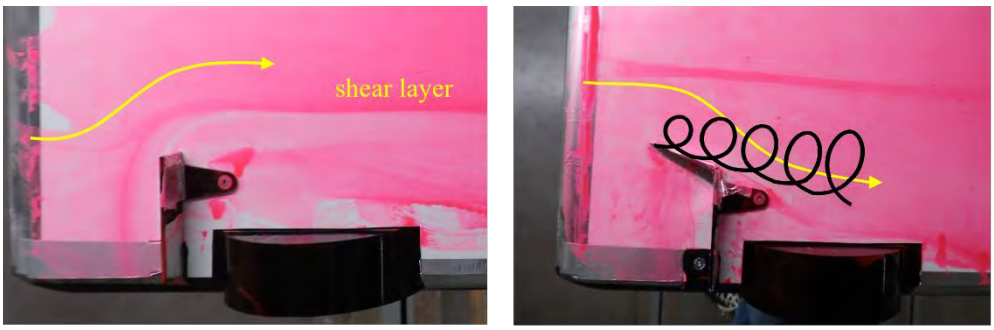

Figure 9: Soot visualizations of configuration a) *with_WS* and b) *with_VG*. Flow goes from left to right.

4 Conclusion

This paper investigates the underlying mechanism of the flow phenomenon "underbody buffeting." While previous studies employed extensive PIV measurements, this study utilizes a combined approach of hot-wire anemometry and microphones, integrated with real-time online evaluation, to demonstrate the direct relationship between measured flow fluctuations and their acoustic effects. The findings indicate that a strategic combination of various measurement methods provides deeper insights into the underlying mechanisms.

The measurements confirm that the disturbance modes, and thus the underbody buffeting, originate from the shear layer developing around the inner edge of the wheel spoilers. Subsequently, the measurement system was employed to develop a countermeasure against the buffeting by adapting a delta-shaped vortex generator to the inner edge of the wheel spoiler. The results show that this approach effectively reduces the high-pressure fluctuations. Additionally, the effectiveness and functioning of the vortex generators were visualized through the kerosene soot technique.

5 Acknowledgement

We gratefully acknowledge the Research Institute for Automotive Engineering and Powertrain Systems Stuttgart (FKFS) for the execution of the wind tunnel experiments. Furthermore, we would also like to acknowledge all our aerodynamics and aeroacoustics colleagues as well as the concept building team.

6 Bibliography

1. Helfer, M. “Umströmungsgeräusche“ from Hucho Aerodynamik des Automobils: Strömungsmechanik, Wärmetechnik, Fahrdynamik, Komfort,“ (München, Springer Vieweg, 2013), doi:10.1007/978-3-8348-2316-8.
2. Weber, C. “Aufbau einer aeroakustischen Simulationsmethode zur Bewertung der Fahrzeug-Unterbodenströmung,“ Master's thesis, Institute of Automotive Engineering, Stuttgart, 2018.
3. Staudenmayer, B. “Analyse der tieffrequenten Strömungsphänomene bei Fahrzeugen mit geschlossenem Unterboden,“ Master's thesis, Institute of Automotive Engineering, Stuttgart, 2021.
4. Breitenbücher, L., Wagner, A., Wiegand, T. and Brink, M., “Low Frequency Aerodynamic and Aeroacoustics Phenomena of Vehicles with Flat Underbody,“ presented at 13th FKFS Conference, Stuttgart, October 11-12, 2023.
5. Breitenbücher, L., Wagner, A., Wiegand, T., and Brink, M., “Experimental Investigation of Low-Frequency Flow Phenomena on the Vehicle Underbody Using Particle Image Velocimetry,” Tech. rep., SAE Technical Paper, 2024.
6. Breitenbücher, L., Wagner, A., Buderer, B., Wiegand, T., and Brink, M., “Identification of the Mechanism of Low Frequency Pressure Fluctuations Using Vortex Identification Methods,” AIAA/CEAS Aeroacoustics Conference 2024
7. Breitenbücher, L., Wagner, A., Wiegand, T., Brink, M., and Buderer, B., “Development of an Evaluation Methodology for PIV Measurements of Low-Frequency Flow Phenomena on the Vehicle Underbody,” Tech. rep., SAE Technical Paper, 2024.
8. AE Road Vehicle Aerodynamics Committee, “Aerodynamic Testing of Road Vehicles in Open Jet Wind Tunnel”, SAE Report J2071 (Open Throat Wind Tunnel Adjustments), Detroit, 2004
9. Bendat, J. S., & Piersol, A. G. (2010). Random Data: Analysis and Measurement Procedures (4th Edition). Wiley-Interscience.

Comparative Analysis and Integration of MPC and RL-Control for Cabin Comfort in Heavy-Duty BEVs

Daniel Linse[1], Kai Franke[1], Prof. Dr.-Ing Stefan Pischinger[1], Dr.-Ing. David Hemkemeyer[2], Dr.-Ing. Tobias Voßhall[3], Dr.-Ing. Christoph Müller[2], Patrick Schutzeich[2]

[1] Chair of Thermodynamics of Mobile Energy Conversion Systems, RWTH Aachen University, Forckenbeckstraße 4, 52074 Aachen, Germany

[2] FEV Vehicle GmbH, Neuenhofstraße 181, 52078 Aachen, Germany

[3] FEV Europe GmbH, Neuenhofstraße 181, 52078 Aachen, Germany

linse@tme.rwth-aachen.de

Abstract: Cabin climate control in battery electric trucks is particularly challenging due to prolonged occupancy periods and the high energy demand of HVAC systems, which can significantly reduce driving range. This work investigates advanced control strategies for cabin thermal management using a model-in-the-loop simulation environment representative of long-haul operations. A model predictive controller (MPC) and a reinforcement learning (RL) framework were developed and benchmarked against a rule-based strategy over a 22-hour driving cycle for a cabin cooling scenario. The MPC improved thermal comfort by maintaining temperature, CO_2 concentration, and humidity within defined limits, while achieving energy usage comparable to the rule-based strategy, thereby demonstrating its capability for multi-objective control under realistic boundary conditions. The initial application of RL as a complementary data-driven approach indicates that comfort targets can be achieved through a direct trade-off between energy use and comfort. However, RL must be extended to true multi-target control to be properly evaluated against the RB approach. In conclusion, the integration effort of both control strategies was assessed, providing an understanding of their respective advantages and limitations for future thermal management applications.

Keywords: Model Predictive Control (MPC), Battery Electric Vehicle (BEV), Reinforcement Learning (RL), Cabin comfort

1 Introduction

The rapid expansion of electromobility is a cornerstone of Europe's climate strategy on the path to carbon neutrality. Policy packages such as the EU Green Deal and "Fit for 55" aim to accelerate the transition by tightening CO_2 limits and incentivizing zero-emission road transport [1]. In Germany, registrations of fully electric trucks increased from 24,380 in 2020 to 92,312 in 2025 [2], yet they still represent only a small fraction of the 3.83 million trucks registered overall in 2025 [3]. Despite growing adoption, there remains a significant gap. Enhancing the real-world performance and appeal of electric heavy-duty trucks continues to be crucial, as range limitations remain a key concern for fleet owners [4].

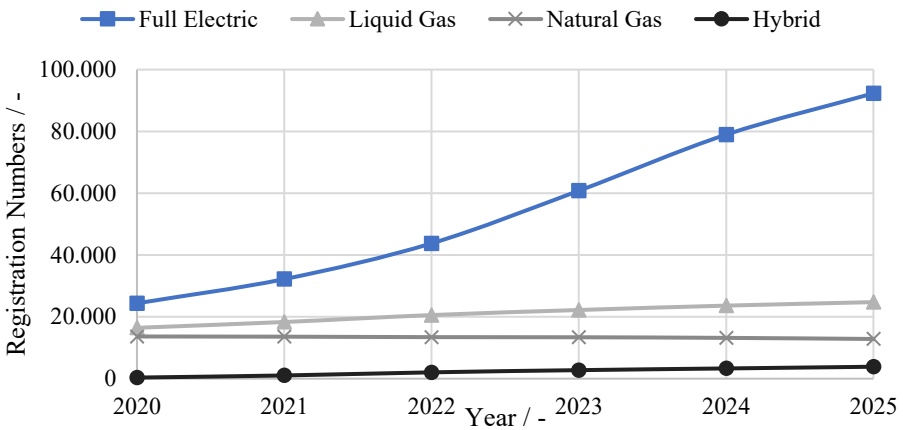

Figure 1: Number of trucks with alternative drivetrains, Germany (2020 - 2025) [2].

For battery electric vehicles (BEVs), cabin air conditioning is a major auxiliary load that can reduce usable driving range under real operating conditions. Especially in cold weather, the absence of powertrain waste heat means the cabin heating demand must be supplied electrically from the traction battery. This has a significant impact on the range [5]. In heavy-duty applications such as battery electric trucks, this challenge is intensified by prolonged cabin occupancy and overnight stays ("hotel function"), which increase HVAC energy demand [6]. Maintaining target temperature, humidity and CO_2 levels while minimizing energy consumption requires advanced, adaptable control strategies [7] [8].

This work investigates intelligent control strategies to improve the energy efficiency and comfort of cabin climate systems in heavy-duty BEVs, focusing on model predictive control (MPC). The MPC leverages accurate thermal models and external data sources, such as ambient forecasts, to manage the cabin climate dynamically under extended-occupancy conditions. It is implemented within a detailed MATLAB/Simulink simulation environment developed as part of the EU research project ESCALATE, which focuses on developing modular, cost-effective heavy-duty vehicles, leveraging the realistic digital twin presented in this study. Furthermore, a preliminary reinforcement learning (RL) framework is introduced as a complementary, data-driven control approach. The method is developed with a focus on general applicability to cabin climatization problems, emphasizing key design aspects such as state representation, reward shaping, and environment interaction. This framework forms the basis for future integration into thermal management systems and enables the development of hybrid control strategies that combine the strengths of RL and MPC.

2 Methodology

This section outlines the two control approaches of MPC and RL, which are integrated and investigated in this work. Both are implemented in a model-in-the-loop (MiL) simulation environment developed in MATLAB/Simulink.

These approaches both offer the ability to develop controllers which are able to do multi-objective control based on optimization methods. The simulation environment features a detailed full thermal system model and a reduced-order model (ROM) of the cabin and HVAC system. The latter enables efficient and realistic closed-loop control development and is described in chapter 2.3. The objective for both controllers in this work builds on the initial development of a cooling controller. It focuses on regulating air temperature, cabin CO_2 concentration, and relative humidity by controlling the compressor rate, blower rate, and recirculation rate.

2.1 Model Predictive Controller

Cabin air conditioning in electric vehicles presents a nonlinear, multivariable control problem (NLP), influenced by ambient conditions, driver demands, and internal system dynamics. Model Predictive Control (MPC) is well-suited for this task due to its ability to predict future states, enforce system constraints, and optimize control actions over a defined prediction horizon [9] [10]. In this work, MPC is implemented using the acados framework, which supports real-time optimization [11]. The user defines the system dynamics, control variables, and the cost function, while the framework handles formulation of the optimization problem and solver execution. The problem is automatically discretized in discrete timesteps k over the prediction horizon on which the cost function J is minimized via direct multiple shooting. Afterwards it is solved with a sequential quadratic programming method (SQP). For a comprehensive treatment of NLP solution methods, the reader is referred to in-depth literature [10] [11].

The main objectives of the controller are contained within a compact representation of the system boundaries (eq. 1) and the cost function (eq. 2) and include maintaining passenger comfort while minimizing energy consumption. The comfort terms are modelled as the system states x and are bound to a lower boundary x_{lb} and an upper boundary x_{ub}. The slack variable x_{slack} allows for constraint relaxation, thereby converting the hard boundary into a soft boundary. The cost function is defined as the sum of the state-related term J_{x} and the cost term J_{u}, which are both evaluated and accumulated over the prediction horizon.

$$x_{\mathrm{lb(k)}} \leq x(k) + x_{\mathrm{slack(k)}} \leq x_{\mathrm{ub(k)}} \qquad (1)$$

$$J = \sum_{k=1}^{N} J_{\mathrm{x(k)}} + \sum_{k=0}^{N-1} J_{\mathrm{u(k)}} \qquad (2)$$

Minimization of the cost function inherently enforces the state constraints. Equation 3 defines the state-related term as the weighted sum of all quadratic slack variables of the MPC. The weighting is determined by the tunable matrix Q. The central slack variables consist of the cabin air temperature T_{slack}, the CO_2 concentration $X_{\mathrm{CO2,\,slack}}$ and the relative humidity $X_{\mathrm{hum,\,slack}}$.

$$J_{\mathrm{x(k)}} = Q_{\mathrm{T_{slack}}} T_{\mathrm{slack}}(k)^2 + Q_{\mathrm{X_{CO2,\,slack}}} X_{\mathrm{CO2,\,slack}}(k)^2 + Q_{\mathrm{X_{hum,\,slack}}} X_{\mathrm{hum,\,slack}}(k)^2 \qquad (3)$$

Finally, the cost term in eq. (4) contains the weighted quadratic energy consumption of the compressor E_{Cpr} and the cabin blower E_{Blower}. The power consumption of the recirculation flap is assumed negligible.

$$J_{\mathrm{u(k)}} = Q_{\mathrm{Cpr}} E_{\mathrm{Cpr}}(k)^2 + Q_{\mathrm{Blower}} E_{\mathrm{Blower}}(k)^2 \qquad (4)$$

With the problem formulation established, the MPC is then integrated into a model-in-the-loop (MiL) environment in MATLAB/Simulink, which consists of three core components: the MPC controller, the plant model, and the prediction module. The controller operates with a fixed sampling interval of 10 s, selected to ensure both robust control performance and real-time feasibility. This interval reflects the slow thermal dynamics of the cabin environment and the response characteristics of the actuators. At each step, the controller computes the optimal control and state trajectories over a prediction horizon of 10 minutes. This horizon length is sufficient to capture the dominant cabin thermal dynamics and anticipated disturbances, while allowing the system states to be adjusted within this time frame. After the optimization is completed, only the first element of the control input vector is applied to the plant model. The plant, representing the HVAC and cabin thermal system, simulates the system response at each step, and the updated states are fed back to the MPC, thereby closing the control loop. The prediction module provides forecasted boundary conditions, including relevant ambient factors and comfort constraints derived from route and trip data (e.g., planned stops). By solving the optimization problem over the moving horizon, the controller can anticipate future disturbances and proactively adjust its control actions. Ultimately, the MPC is applied to the reduced-order model, enabling efficient testing and iteration without compromising the physical relevance of the results.

2.2 Reinforcement Learning Controller

RL is investigated in this research as a data-driven control strategy for cabin climate management. A Deep Deterministic Policy Gradient (DDPG) agent is employed, following an actor–critic structure (Fig. 2). DDPG agents can operate in a continuous action space and are therefore suitable for fully variable control [12] [13]. An RL agent interacts with its environment in a closed loop: it observes the current state s_{t}, selects an action a_{t}, and receives the next state $s_{(\mathrm{t+1})}$ together with a scalar reward r_{t}. By maximizing cumulative rewards through repeated interaction, the agent gradually learns strategies that optimize long-term performance. The DDPG architecture is based on the following three fundamental components:

- Actor (policy network θ^{μ}): maps states s_{t} to continuous actions $a_{\mathrm{t}} = \mu(s_{\mathrm{t}} \,|\theta^{\mu})$.
- Critic (Q-network θ^{Q}): evaluates these actions by estimating their long-term value $Q(s_{\mathrm{t}}, a_{\mathrm{t}})$.
- Training process: the Actor is updated via policy gradients, the Critic via minimization of a loss function. Soft target updates are applied to stabilize training.

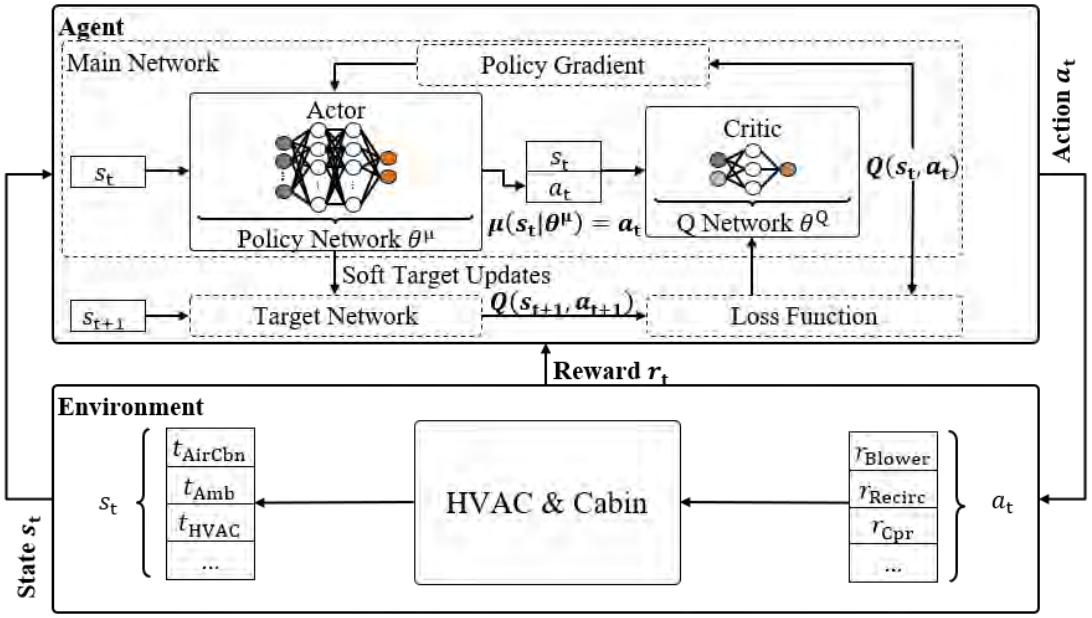

Figure 2: Integration of the RL agent framework inside the simulation environment.

Two complementary training approaches are pursued. In the first, the agent is trained directly on the high-fidelity digital twin, which avoids model reduction and ensures maximum physical fidelity, but at the cost of substantial computational resources. In the second, training is performed on the ROM, enabling faster iterations, direct benchmarking with MPC, and providing insight into potential hybrid MPC–RL strategies. The RL agent processes the system states cabin air temperature (t_{CbnAir}) and setpoint t_{CbnAirSP}, ambient temperature (t_{Amb}), HVAC outlet air temperature ($t_{\mathrm{HVACAirOut}}$), and action signals (current $r_{\mathrm{Comp,t}}$ and previous $r_{\mathrm{Comp,t-1}}$). Based on these inputs, it determines the control action of the compressor (r_{Comp}). The agent is trained using a composite reward that balances comfort, energy efficiency, and smoothness of control (see Figure 3). The temperature reward targets the passenger comfort by penalizing deviations from the cabin air temperature setpoint. The energy reward promotes efficient operation by discouraging high activation levels of HVAC components. Finally, the smoothness reward penalizes abrupt control changes, targeting stable and hardware-friendly operation.

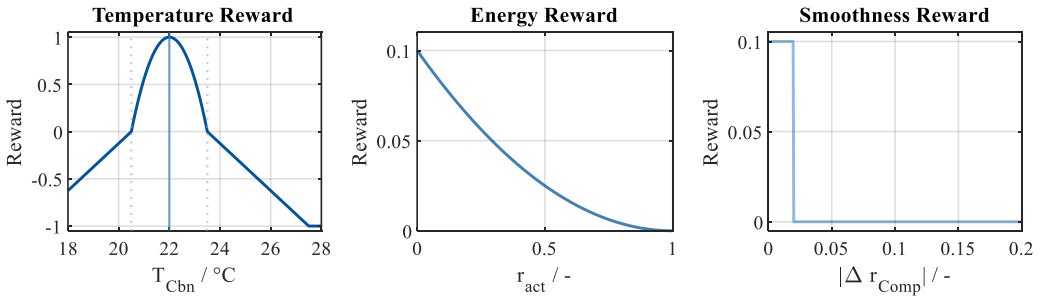

Figure 3: Sub-reward functions for temperature, energy, and smoothness.

2.3 Reduced-Order-Model of Cabin and HVAC

To enable efficient development of the controllers, a reduced-order-model of the vehicle cabin and HVAC system was created. The ROM captures the essential thermal dynamics while ensuring low computational load and enabling rapid simulation. Validation was conducted using the full thermal system model. This model was previously plausibilized to represent the thermal behavior of a generic truck, ensuring physical consistency.

The cabin is modeled as a single-zone thermal system, assuming spatially uniform air temperature. The core of the model is an energy balance over the enclosed air volume:

$$\frac{dE_{Cabin}}{dt} = \sum \dot{Q}_i + \sum \dot{m}_{in}\, h_{in} - \sum \dot{m}_{out}\, h_{out} \qquad (5)$$

This equation accounts for internal energy changes due to air temperature variation, enthalpy flows from ventilation, and additional heat sources or sinks $\dot{Q}_i$, such as solar radiation or internal gains. To represent the thermal inertia of the cabin interior, a lumped thermal mass is included in equation 6. This mass represents components like seats, dashboard and other internal masses and is thermally coupled to the cabin air via a resistance $R_{th,\,Interior}$.

$$\dot{Q}_{Interior} = \frac{T_{Air,Cabin} - T_{Interior}}{R_{th,\,Interior}} \qquad (6)$$

This formulation allows the model to replicate realistic heating and cooling dynamics, including the effect of delayed thermal response. The resistance $R_{th,\,Interior}$ and other parameters were validated within the Simulink full vehicle model. The HVAC system is modeled with key functionalities such as air mixing, heating, and cooling via heat exchangers, as well as flap positions to switch between fresh air and recirculation modes. The blower fan modulates the air mass flow supplied to the cabin.

In addition to thermal comfort, the model also considers air quality, specifically the accumulation of CO_2 in recirculation mode. The mass balance for CO_2 includes both external input and occupant respiration as source terms:

$$\dot{m}_{Air} X_{Inlet} + \dot{m}_{CO_2,\,Passengers} = M \frac{dX_{Cabin}}{dt} + \dot{m}_{Air}\, X_{Cabin} \qquad (7)$$

Here, x_{Inlet} and x_{Cabin} are the CO_2 concentrations of incoming air and cabin air, and M is the total cabin air mass. Leakages are neglected in this reduced order model. Under full recirculation, CO_2 concentration increases steadily, making the model suitable for studying the trade-off between energy efficiency and air quality. As a second metric for air quality the cabin air humidity is modelled by a control volume mass balance of the water vapor. The rate of change of the cabin humidity ratio $\dot{w}_{Air}$ is expressed as:

$$\dot{w}_{Air} = \frac{1}{m_{Air}} \left[\dot{m}_{Air}(w_{mix} - w_{Cabin}) + \dot{m}_{gen} + \dot{m}_{deh}\right] \qquad (8)$$

Here, m_{Air} denotes the total air mass inside the cabin. The first term accounts for the humidity change due to exchange with the supply airflow, with $\dot{m}_{Air}$ representing the air mass flow into the cabin and w_{mix} the humidity ratio of the mixed ambient and recirculated air. The second term $\dot{m}_{gen}$, describes the generation of water vapor by passengers (e.g., through breathing and perspiration). The third term $\dot{m}_{deh}$, represents the removal of moisture through condensation at the evaporator coil surface whenever the incoming air exceeds the saturation limit at coil temperature. Overall, this ROM provides the necessary balance between physical fidelity and computational efficiency, enabling its use in the computational expensive MPC and RL control development.

3 Results & Discussion

Using the MiL environment described previously, the performance of the MPC and the RL controller was evaluated under varying ambient conditions based on real-world measurement data. To assess robustness, stochastic disturbances were added to the ambient temperature, humidity, and solar radiation, introducing controlled misalignment between the plant model and the controller's internal prediction model.

The evaluation covered a 22 h 15 min cycle representative of long-haul truck operation. The cycle consisted of two driving phases of 3 h 45 min and 5 h, a 12 h overnight stay, and 45 min rest periods in between. Driver presence is assumed according to an expected occupancy schedule. During the overnight stay, the sleep mode is activated in which the cabin temperature setpoints are lowered to enhance comfort during rest. During the day, these values are set at 22 °C for the upper boundary and at 20 °C for the lower boundary. The relative humidity setpoints during the day are defined between 30 - 60% and are bound to a stricter window of 35 - 55% during sleep mode. For the CO_2 concentration an upper boundary of 1200 ppm is defined throughout occupancy of the cabin. This setup provides a comprehensive framework for evaluating the controllers under realistic, time-varying thermal boundary conditions, including heat soak, idle periods, and extended occupancy.

To establish a baseline, a rule-based strategy with fixed recirculation rates was applied across the cycle to control the cabin air temperature. Figure 3 illustrates the effect of increasing the recirculation rate on total HVAC energy consumption.

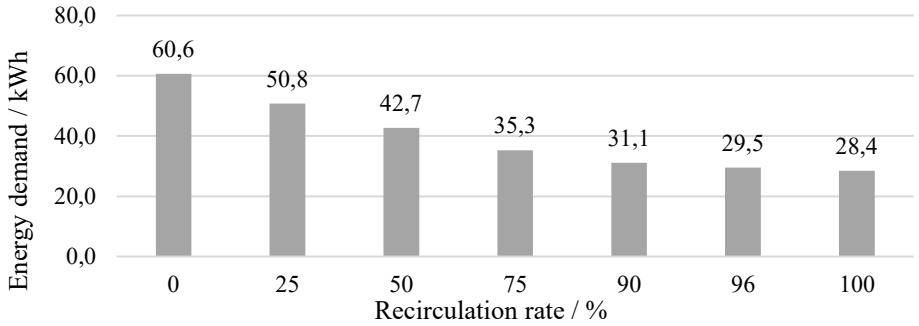

Figure 3: Energy consumption of the rule-based HVAC control at average ambient temperature of 32 °C with varying recirculation rates.

A clear trend is visible: as the recirculation rate increases from 0% to 100%, the energy demand steadily decreases from 60.6 kWh to 28.4 kWh, corresponding to a total reduction of approximately 53.1%. However, high recirculation rates also impact the performance in terms of cabin comfort such as temperature targets, relative humidity, and CO_2 concentration. Simulation results show that the CO_2 concentration threshold of 1200 ppm is only exceeded at recirculation rates above 96 percent, indicating that high recirculation levels can maintain acceptable air quality while still offering energy savings. These findings highlight the need for dynamic control strategies, which can continuously balance energy efficiency and air quality, rather than relying on static setpoints.

Consequently, the performance of the MPC, RL and RB strategy are compared in the following section. As initially stated, to complement the comparison a preliminary RL framework was developed and applied. Similar to the RB approach, only the cabin temperature was controlled using compressor actuation alone, while maintaining a fixed recirculation rate and blower speed. To ensure comparability, the recirculation rate of the RB approach was selected to align its energy usage with that of the MPC approach and ensure a sufficient rate of fresh air. To quantify the control quality of the strategies, the target deviation $|\Delta x(t)|$ is time-averaged over the periods in which the boundaries are exceeded, resulting in three comfort metrics for temperature, CO_2 and humidity. The first metric is the temperature comfort, which is displayed in figure 4.a. The air quality is evaluated for CO_2 levels in figure 4.b and for the relative humidity in figure 4.c.

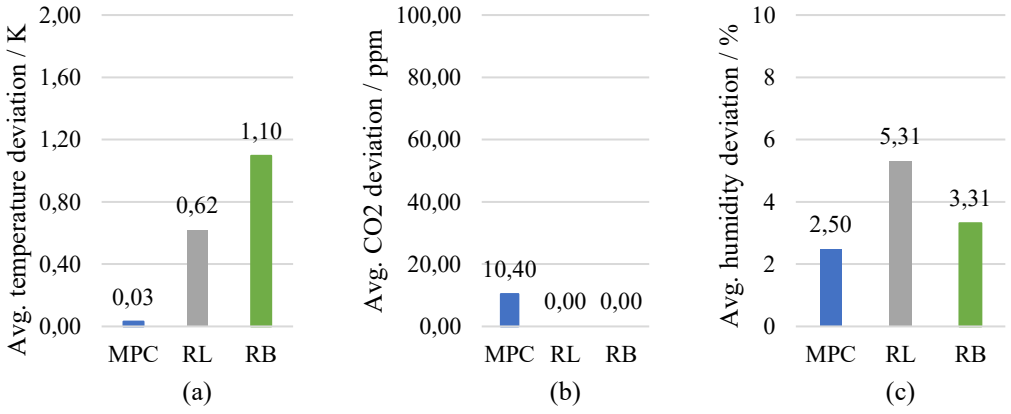

Figure 4: Comparison of comfort metrics for the MPC, RL, and RB strategy

The MPC strategy achieves the lowest average deviation of 0.03 K compared to 1.1 K with the RB strategy. This is also reflected in the resulting maximum deviations. The MPC maximum deviation from the control target of 6.21 K is present at the beginning of cabin conditioning, while the RB strategy reaches an even higher value of 16.11 K but at a later stage due to hot soak during the idle phase. During this idle phase the MPC achieves a much lower deviation of 2.15 K by pre-conditioning the cabin according to the predicted change in the temperature boundaries.

The RL strategy achieves an average deviation of 0.62 K but, lacking the predictive capability, does not pre-condition the cabin and therefore reaches maximum deviation of 16.45 K, similar to the RB strategy. These comfort gains of MPC and RL come at only a minor increase in energy consumption, with 30.18 kWh and 30.13 kWh respectively, compared to 29.48 kWh for the RB strategy.

Consequently, air quality discomfort is also evaluated. The MPC targets to maintain CO_2 levels below a soft-constrained upper bound. This bound is exceeded in some cases due to the balancing of the multi-target optimization and the improved convergence of the optimization. This results in a recorded average deviation of 10.4 ppm, which is negligible compared to typical indoor CO_2 concentration fluctuations and has no perceptible impact on passenger comfort. In contrast, the RB and RL strategies do not enforce any explicit CO_2 limit since CO_2 is not directly controlled. As the setpoint was defined to ensure sufficient fresh air, both strategies show no violation of the CO_2 discomfort metric

Lastly, humidity deviation is evaluated. The MPC strategy achieves the lowest average deviation at 2.5% compared to 3.31% for the RB approach, as the MPC explicitly enforces the humidity boundary. The RL strategy exhibits a considerably higher deviation of 5.31% since humidity is not actively controlled, leading to excessive dehumidification at the evaporator caused by increased compressor actuation. Given the average outdoor humidity of 31%, these deviations remain non-critical under the tested conditions due to overall system stability, though they may become more relevant in high-humidity heating scenarios.

Overall, MPC achieves the best balance between comfort and energy consumption by minimizing temperature and humidity deviations while maintaining CO_2 within acceptable limits. The preliminary RL controller shows intermediate performance by improving temperature target deviation, but lacks predictive capabilities and an extended actuator control. Nevertheless, it offers a promising foundation for further development toward a highly automatable controller design.

In the following the findings regarding the integration of both MPC and the initial RL approach are summarized in figure 5.

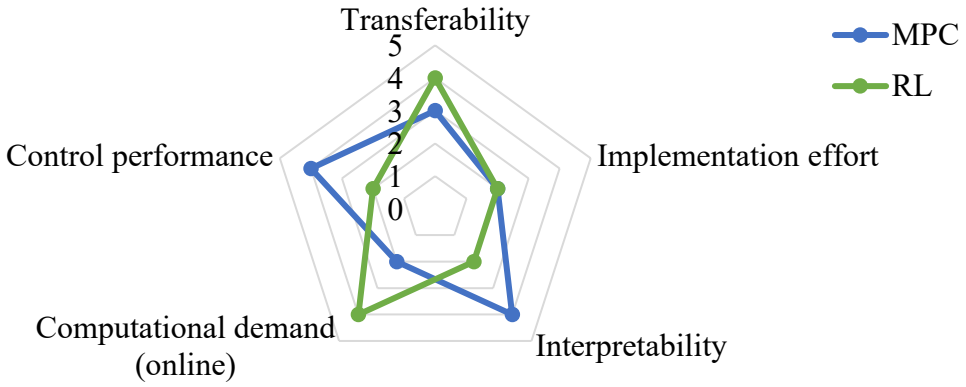

Figure 5: Comparison of evaluated performance metrics for MPC and RL approach for the MiL application in this work.

Here, various performance metrics that were evaluated during the development are rated according to the following scale:

1: Very poor (significant drawbacks), **2**: Poor (limited suitability),
3: Moderate (meets minimum requirements), **4**: Good (only minor limitations),
5: Excellent (highly suitable)

The transferability of the MPC is rated as moderate. A major challenge in this work was the application of the MPC framework to the full thermal system model. The higher complexity of the digital twin caused a divergence between the internal system dynamics of the MPC and the actual plant behavior, which prevented direct application and led to high deviations to the control targets in the cabin control case. This highlights a well-known limitation of MPC, namely the need for model reduction to embed an equation-based system model while ensuring real-time feasibility, which inevitably leads to a model-plant mismatch [14] [15]. Within digital twins such model reduction is often not straightforward.

One possible mitigation strategy is the use of data-driven surrogate models, although this requires additional efforts for system identification and validation [16]. In contrast, the RL agent could also be trained directly in the full model environment and achieved comparable control performance to the reduced-order model for the cabin conditioning task. This potentially eliminates the need for model reduction and represents a clear advantage in the digital twin environment. However, this advantage is specific to simulations, since the training of RL on real systems would require considerably more time and resources. For this reason, RL received a higher transferability rating of four.

The implementation effort of MPC is rated at two, as is the case for RL. For MPC, the main effort lies in the development and validation of an internal prediction model tailored to the cabin thermal dynamics. The model must be suitable for optimization and verified against various measurements or simulation data, which is an obstacle to fast integration. RL requires less manual modelling effort since the framework only needs to be provided with selected observations and actions. The training of the neural networks is then conducted automatically. Due to the inherent flexibility of the RL framework, it can be implemented in a wide range of environments and therefore offers broad applicability without requiring the detailed modelling knowledge that is essential for a grey-box MPC. However, in this work only a simplified control objective was investigated. The implementation effort and training requirements are expected to increase once additional control variables are incorporated.

Interpretability plays a decisive role in improving control performance. MPC scores higher in this category with a rating of four, whereas RL is rated at two. MPC benefits from the possibility of incorporating grey-box models, which supports verification of predictions and thereby improves understanding of controller behavior. Furthermore, the tuning of the cost function can be conducted in an intuitive manner.

RL, on the other hand, operates as a black box and lacks direct interpretability, which results in an iterative and often time-consuming process of reward shaping, network architecture selection, and hyperparameter tuning. Automating this process through optimization-based hyperparameter tuning can resolve this issue as shown in [12]. However, the DDPG algorithm used in this study is deterministic, which means that it provides consistent outputs when presented with the same observations. This property allows the user to draw limited conclusions from the observed controller behavior [13]. In line with these limitations, the RL strategy received a lower rating of two.

With respect to computational demand, RL performs better than MPC. RL is rated at four, while MPC is rated at two. In this work the MPC used an SQP solver with average solution times below 0.5 seconds for a 2.3 GHz CPU, which is sufficient for real-time operation in the cabin conditioning task. Nevertheless, execution times are expected to increase if the controller is implemented on an embedded microcontroller with limited processing power. RL execution times are negligible once the training is complete, which represents a clear advantage. The drawback lies in the training phase, which is computationally intensive. For the compressor control task, a total of 500 episodes were run in parallel with 4 CPU cores, resulting in more than 10 hours of training. This effort, however, occurs entirely offline and does not affect embedded system performance.

Overall, MPC is better suited to the problem under consideration, as its interpretability enables more targeted and reliable implementation, while RL should be regarded as a preliminary approach at this stage.

4 Conclusion

Model-predictive-control demonstrated its capability to enforce operational boundaries and balance energy efficiency for multi-objective control. Reinforcement learning was introduced as a framework for cabin climatization, and an initial controller was evaluated to determine the requirements for control design. Open challenges remain in managing multi-objective control, along with the need for further investigation into hyperparameter tuning and reward shaping. Both strategies provide distinct advantages, with MPC excelling in interpretability and offering a more transparent design process, while RL shows superior transferability to detailed thermal system models. Future work will extend the MPC with active heating and advanced humidity control, explore data-driven models as internal predictors, and expand RL to additional control variables. Furthermore, synergies between RL and MPC will be evaluated, with the aim of combining the interpretability and constraint-handling of MPC with the adaptability and transferability of RL to enable more efficient cabin climatization strategies.

Acknowledgements

This project has received funding from the European Union's Horizon Europe research and innovation programme under the Grant Agreement No. 101096598

5 References

[1] Europäische Kommision, "Verordnung (EU) 2023/85 zur Änderung der Verordnung (EU) 2019/631 im Hinblick auf eine Verschärfung der CO2-Emissionsnormen für neue Personenkraftwagen und für neue leichte Nutzfahrzeuge im Einklang mit den ehrgeizigeren Klimazielen der Union," 2023.

[2] KBA, "Anzahl der Lastkraftwagen mit alternativen Antrieben in Deutschland in den Jahren 2020 bis 2025," [Online]. Available: https://de.statista.com/statistik/daten/studie/259803/umfrage/lkw-bestand-mit-alternativen-antrieben-in-deutschland/. [Accessed 08 09 2025].

[3] KBA, "Fahrzeugbestand von Straßenfahrzeugen in Deutschland 2025," [Online]. Available: https://www.bmv.de/SharedDocs/DE/Artikel/G/fahrzeugbestand.html. [Accessed 11 09 2025].

[4] C. Sugihara, S. Hardman and K. Kurani, "Social, technological, and economic barriers to heavy-duty truck electrification," *Research in Transportation Business & Management,* no. 51, p. 101064, 2023.

[5] Daimler Truck, "Cold, ice and snow successfully defied," 2023. [Online]. Available: https://www.daimlertruck.com/en/newsroom/pressrelease/cold-ice-and-snow-successfully-defied-mercedes-benz-trucks-tests-electric-trucks-in-finland-52179205. [Accessed 12 09 2025].

[6] K. Sheth, D. Patel and G. Swami, "Reducing Electrical Consumption in Stationary Long-Haul Trucks," *Open Journal of Energy Efficiency,* no. 13, pp. 88-99, 2024.

[7] S. H. Kim and H. J. Moon, "Case study of an advanced integrated comfort control algorithm with cooling, ventilation, and humidification systems based on occupancy status," *Building and Environment,* no. 133, pp. 246-264, 2018.

[8] Q. Wu, B. Ma and L. Guo, "Cabin Temperature and Humidity Comfort Control for Electric Vehicles in High Temperature and Humidity Environment," in *China Automation Congress (CAC)*, Qingdao, 2024.

[9] M. Auer, Ein Beitrag zur Erhöhung der Reichweite eines batterieelektrischen Fahrzeugs durch prädiktives Thermomanagement, Wiesbaden: Springer Vieweg, 2016.

[10] M. Papageorgiou, M. Leibold and M. Buss, "Optimierung: Statische, dynamische, stochastische Verfahren für die Anwendung," Springer Vieweg Berlin, Heidelberg, 2015.

[11] R. Verschueren, G. Frison, D. Kouzoupis, J. Frey, N. Van Duijkeren, A. Zanelli, B. Novoselnik, T. Albin, R. Quirynen and M. Diehl, "acados—a modular open-source framework for fast embedded optimal control," *Mathematical Programming Computation 14,* vol. Nr. 1, p. 147–183, 2022.

[12] J. Wang, C. Du, F. Yan, M. Hua, X. Gongye, Q. Yuan, H. Xu and Q. Zhou, "Bayesian optimization for hyper-parameter tuning of an improved twin delayed deep deterministic policy gradients based energy management strategy for plug-in hybrid electric vehicles," *Applied Energy,* no. 381, p. 125171, 2025,.

[13] E. H. Sumiea, S. J. Abdulkadir, H. S. Alhussian, S. M. Al-Selwi, A. Alqushaibi, M. G. Ragab and S. M. Fati, "Deep deterministic policy gradient algorithm: A systematic review," *Heliyon,* no. 10, p. 30697, 2024.

[14] A. S. Badwe, S. L. Shah, S. C. Patwardhan and R. S. Patwardhan, "Model-Plant Mismatch Detection in MPC Applications using Partial Correlation Analysis," in *Proceedings of the 17th World Congress*, Seoul, 2008.

[15] S. J. Kuntz and J. B. Rawlings, "Beyond inherent robustness: strong stability of MPC despite plant-model mismatch," *IEEE Transactions On Automatic Control,* pp. 1-13, 2025.

[16] K. Prag, M. Woolway and T. Celik, "Toward Data-Driven Optimal Control: A Systematic Review of the Landscape," *IEEE Access,* no. 10, pp. 32190-32212, 2022.

User-Centric Comfort Optimization With AI-Supported Methods

Daniel Braun, Andreas Raab

DZS
AVL Deutschland GmbH
Peter-Sander-Str. 32

55252 Mainz-Kastel

Daniel.Braun@avl.com
Andreas.Raab@avl.com

Abstract: The EU-funded SmartCorners project explores user-centered comfort in vehicles through AI-driven climate control. A method is developed to train a climate control algorithm with the help of AI and is trained in a comprehensive vehicle simulation model. Beyond personalization, AI is leveraged to optimize energy efficiency. The project also addresses the application of the virtually developed algorithm in a real-world vehicle. Initial simulation results are discussed in this paper with an outlook of the upcoming vehicle studies to validate the simulation results.

1 Introduction

Vehicle cabin comfort is a multifaceted concept influenced by thermal conditions, noise, vibration and harshness (NVH) levels, as well as air quality. Importantly, comfort is highly subjective – conditions that are acceptable for one occupant may be uncomfortable for another. Thermal comfort is typically managed through parameters such as zonal temperature settings, blower speed, air distribution, and the position of the recirculation flap. Zonal climate control systems have enabled personalized thermal environments for different seating areas, allowing occupants to tailor conditions to their preferences. However, accommodating these varying and dynamic preferences presents significant challenges for both the HVAC system and its control strategies.

Contribution: 2025 FKFS Conference on Vehicle Aerodynamics and Thermal Management
15 – 16 October 2025 | Leinfelden-Echterdingen

Traditional control strategies are often not optimized to balance user comfort with energy efficiency. By integrating artificial intelligence (AI) into simulation models and training it across diverse virtual scenarios, it is possible to develop adaptive solutions that significantly reduce the effort required for software development and calibration. Furthermore, AI systems can continue to learn post-deployment in real-world vehicles, enhancing their decision-making capabilities over time. This continuous learning approach simplifies the development of intelligent controllers, eliminating the need for multiples specialized control algorithms tailored to specific objectives such as individual comfort, overall cabin comfort, or energy efficiency (e.g., maximizing driving range).

2 Methodology

The development of AI-based control systems necessitates training with high-quality data to enable reliable decision-making. Acquiring such data using physical test benches or vehicles is time-consuming and costly. This challenge can be effectively addressed by using high-fidelity simulation models. By leveraging virtual environments, it becomes possible to generate large volumes of representative data for training AI algorithms, significantly reducing the need for physical testing.

This section provides a detailed overview of the proposed methodology, including the simulation setup, data generation process, and training pipeline for the AI controller.

2.1 Plant model

The plant model represents a comprehensive simulation model of the physical system under study. A highly accurate plant model ensures that the behavior of the simulated system closely mirrors real-world dynamics, thereby enhancing the reliability of AI training and control development. Any discrepancies in model accuracy can directly impact the performance and robustness of the resulting control strategies. Therefore, special emphasis is placed on the validation and calibration of the plant model to ensure it serves as a trustworthy foundation for virtual experimentation and AI-based control design.

The simulation environment incorporates detailed models of the vehicle, HVAC system, cabin, controller, driver and passenger comfort. Each model is designed with the necessary inputs and outputs to enable seamless interaction with the AI-based control system. Figure 1 provides a comprehensive illustration of plant model and the according interfaces. This section provides an in-depth description of the thermal and HVAC systems, as well as the cabin and comfort models, as the primary focus is on optimizing energy consumption of these systems while maximizing passenger comfort.

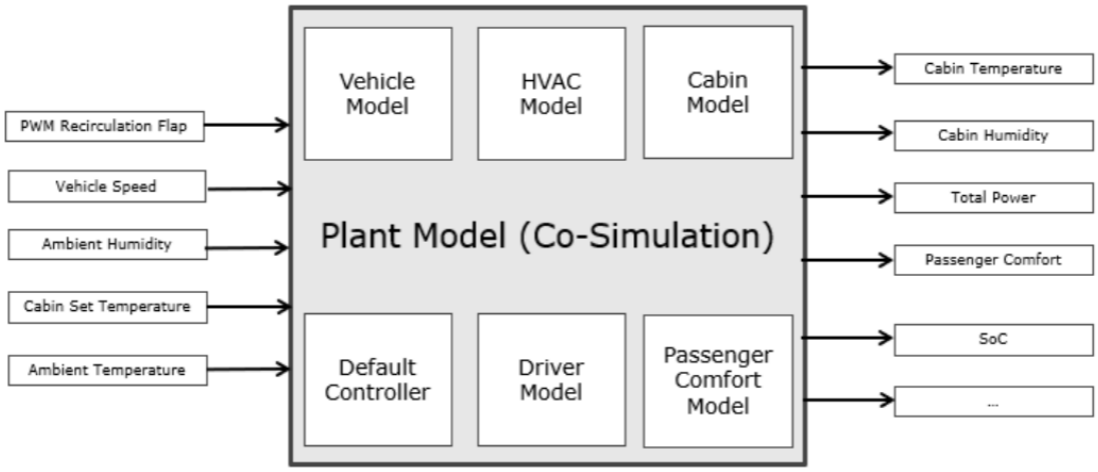

Figure 1: Overview plant model

Vehicle Thermal Management System (VTMS)

The thermal and HVAC system of the demo vehicle has a R290 and a R1234YF based refrigerant circuit and a coolant circuit. The vehicle can operate with both refrigerant circuits but in SmartCorners only R1234YF refrigerant circuit is used. Figure 2 shows the thermal management architecture consisting of the refrigerant circuit indicated in green color, the low-temperature circuit (LT-Circuit) indicated in blue color, the medium-temperature circuit (MT-Circuit) indicated in yellow color, the high-temperature circuit (HT-Circuit) indicated in red color, and the battery circuit (Bat-Circuit) indicated in grey color. The different operating temperatures of the circuit are determined based on the components placed in the circuits and their thermal requirements.

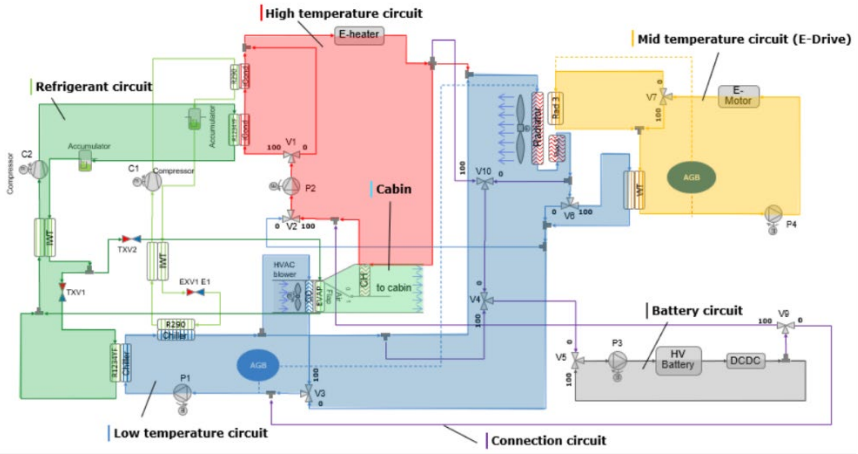

Figure 2: Layout coolant and refrigerant circuit

The plant model of the system is developed in AVL CRUISE^{TM}M, a system development software from AVL. The components are calibrated with the help of the measurement data gathered from the demo vehicle. The whole model is then validated with measurements from different operating conditions of the complete system.

Vehicle Cabin and Comfort Model

To accurately represent passenger comfort and cabin thermal dynamics, two complementary cabin models are developed:

Thermal cabin model:

A high-fidelity computational fluid dynamics (CFD) model is used to simulate airflow, heat transfer, and passenger comfort within the cabin. The model incorporates detailed geometry of the demonstrator vehicle (Mercedes-Benz B-Class), material properties of interior laminates, and additional heating devices such as seat heaters, steering wheel heating, and infrared panels. Environmental factors such as solar load and ambient conditions are also included. This model is primarily used for generating a 1D Matlab/Simulink model.

The 1D cabin model is a reduced-order representation derived from the high-fidelity 3D CFD cabin model. Its primary purpose is to provide a computationally efficient simulation environment for control development and real-time applications. The model uses aggregated thermal properties and response characteristics obtained from the 3D model. These derived parameters include heat transfer coefficients, thermal capacities, and airflow distribution characteristics.

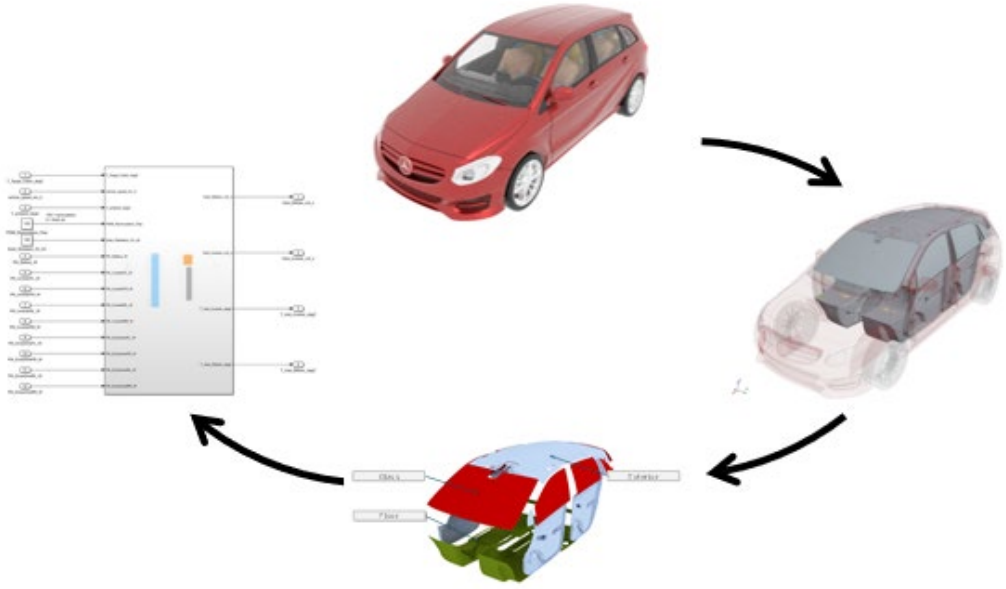

Figure 3: Body and clothing segments for EHT model

Cabin Comfort Modeling and Surrogate Model Development

To model thermal comfort in the cabin, the previously developed 3D CFD cabin model is utilized. This high-fidelity model includes detailed geometry of the demonstrator vehicle and incorporates thermal manikins to represent passengers. Each manikin is segmented into 17 body parts, enabling the calculation of local surface temperatures and heat fluxes under various operating conditions. The exact body parts and clothing segments are shown in Figure 4.

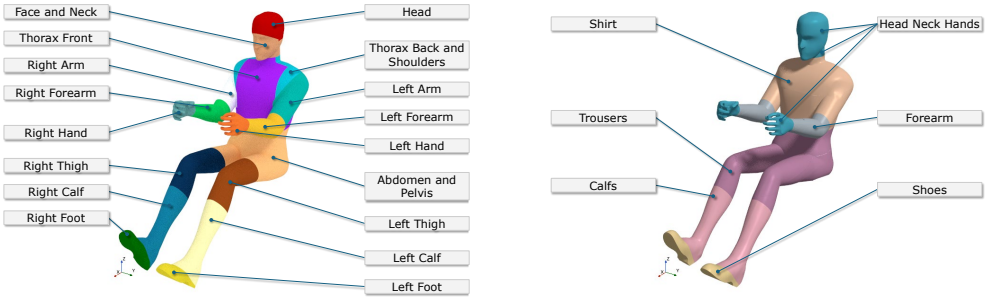

Figure 4: Body and clothing segments for EHT model

For comfort evaluation, the Equivalent Homogeneous Temperature (EHT) metric is applied. The EHT combines air temperature, mean radiant temperature, and air velocity into a single value, providing a comprehensive measure of thermal comfort in non-uniform environments such as vehicle cabins. Conceptually, EHT represents the wall temperature of a uniformly conditioned space under calibrated conditions, assuming negligible air velocity and equal mean radiant and air temperatures. Higher EHT values indicate reduced heat loss, while lower values correspond to increased heat loss. The EHT is computed from the manikin heat flux using the following relationships:

$$T_{eq} = T_S + \frac{x_0}{2x_1} - \frac{\sqrt{x_0^2 + 4x_1\dot{Q}}}{2x_1} \qquad \text{if } \dot{Q} > 0$$

$$T_{eq} = T_S - \frac{x_0}{2x_1} + \frac{\sqrt{x_0^2 + 4x_1\dot{Q}}}{2x_1} \qquad \text{if } \dot{Q} < 0$$

where $\dot{Q}$ is the heat flux on the manikin surface, T_s is the skin temperature, and x_0 and x_1 are calibration constants derived from regression analysis. Although the 3D CFD model provides high accuracy, its computational cost makes it unsuitable for real-time control development. To overcome this limitation, a fast-running surrogate model (FRM) is derived. A Design of Experiments (DoE) study is conducted to systematically vary key parameters such as HVAC settings, ambient conditions, and solar load. The resulting dataset is processed using AVL CAMEO, which generates mathematical response models for comfort indices and thermal states.

In Figure 5 plots of the model qualities are shown. The green point in the graphs represent the validation experiments which were not used for the mathematical model training. The shaded areas indicate the accuracy of the 3D model, ±2K.

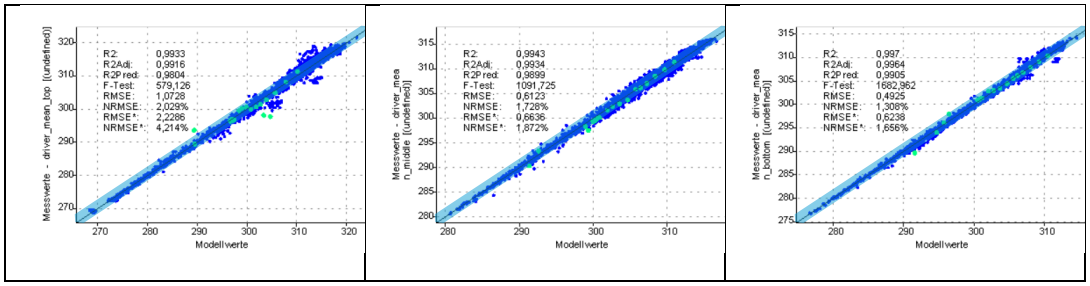

Figure 5: Example results for FRM

These models are packaged as a Functional Mock-up Unit (FMU) and integrated into the plant model, enabling real-time simulation for reinforcement learning (RL) training and hardware-in-the-loop (HiL) applications.

Virtual Driver Model

A virtual driver model is integrated to emulate human interactions with the climate control system. It adjusts parameters such as target cabin temperature, blower speed, and air distribution modes based on comfort feedback. This enables realistic training scenarios for the AI controller and facilitates user-specific adaptation.

2.2 RL Framework

This section gives a brief introduction to the most important concepts of RL and provides the context under which RL can provide solutions for the problem of optimal thermal control of the SmartCorners project.

Introduction to RL

An RL agent is the entity that interacts with an environment to learn how to achieve a goal by maximizing a reward it receives from the interaction. The training environment is the simulated context under which the agent learns how to act in the real world. The schema is shown in Figure 6. The training environment contains states, as well as a set of rules or transition dynamics under which the states transition from one to another. The agent interacts with the environment by

- observing certain states exposed by the environment
- setting actions within the environment, and
- receiving rewards for its actions.

The agent designs a control policy, which is a set of rules that predict the optimal actions an agent should apply given a set of observations. RL training refers to the process of continuous interaction between the agent and the environment during which the agent optimizes the control policy by maximizing the reward it receives after applying an action.

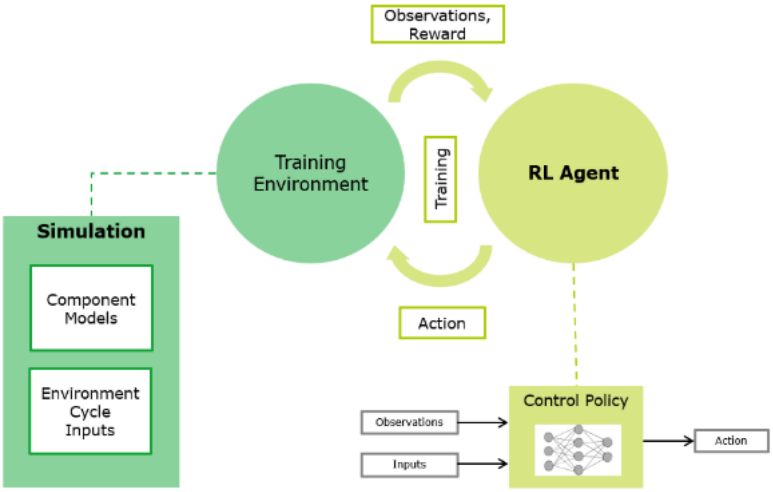

Figure 667: Scheme of the RL training process. The agent trains a control policy to optimally interact with the training environment. It receives an observation and a reward after each action. The optimal policy maximizes the agent's expected reward.

In the context of SmartCorners, the training environment contains all information relevant to the optimization of the thermal controls of the thermal control unit. Specifically, this includes

- an interface to the high-fidelity plant model described in Section 2.1
- a model for all relevant ambient conditions
- a model for driving cycles

The agent interacts in a stepwise and discrete fashion with the environment. That is, at each given point in time, the agent observes some states at a discrete time, determines an appropriate action based on its observations, and applies the action before the environment transitions to the next discrete time step with a new state. During the project we used the interface described in OpenAI's Gym library *Gymnasium*. This interface is simple to use as it only consists of two methods, the initialize method and the step method, which transitions the environment to the next state given an action and returns the current observation and reward.

Ambient Model & Driving Cycles

The training process must contain a model of the ambient environment under which the electric vehicle (EV) is operated. In the RL framework, the ambient model is intrinsically embedded in the training environment. The ambient model must reflect the real-world conditions under which the EV is operated. Moreover, for the sake of robust calibration, the model should contain as many so-called corner cases as possible, i.e. special cases under which either the simulation model or the control policy will respond in extreme ways.

The ambient model contains all necessary information for all model inputs and parameters that are not under direct control of the agent. This information may be given in the form of input distributions, e.g. for ambient weather conditions, or specific driving cycles, such as Worldwide Harmonized Light-duty vehicles Test Cycle (WLTC) for vehicle speed.

In the context of RL, the combination of a single driving cycle with a set of ambient conditions constitutes a so-called episode. During training the agent should be trained on as many representative episodes as possible. For this reason, the training environment was implemented in such a way that random episodes could be generated during training, i.e. the agent can be trained on a theoretically infinite number of realistic episodes.

RL Reward, Targets & Constraints

In RL, the agent will tune its control policy in such a way to maximize the reward it receives from the environment for its actions. In this sense, the reward represents the target of the underlying optimization problem, and it must be carefully designed to respect and trade-off several conflicting goals with each other.

For the SmartCorners project, the reward must therefore reflect all goals of thermal control as well as measures for user comfort based on individual preferences.

For this reason, the RL framework allows the definition of multiple types of control targets, and it allows the definition of multiple targets at the same time. These following types of control targets have been implemented so far:

- **Optimization Target**: allows to minimize/maximize a system output channel.
- **Control Target**: allows to control a system output channel towards a given demand channel. The demand channel must be contained in the ambient data model.
- **Constraints**: allows to force a system output within a specified range of values.

The agents' reward is a combination of all defined target functions. For the SmartCorners project, the following targets have been considered:

- Cabin humidity must be controlled towards a target of 40%
- User comfort must be maximized.

Boundary Conditions / Trainings Setup

The training setup defines the temporal resolution of the simulation, the initialization of each episode, and the physical and operational constraints that ensure safe and meaningful learning.

Each training episode represents a two-hour driving scenario with a total duration of 7200 seconds, with simulation steps of 1 second. The action is updated every 5 seconds.

At the start of every episode, the ambient temperature and humidity are sampled randomly to promote generalization. The ambient parameters continue to vary during the episode to reflect changing driving conditions.

- Ambient temperature: uniformly sampled from 10 °C to 30 °C
- **Relative ambient humidity**: uniformly sampled from 0% to 100%

To maintain physical plausibility and passenger safety, multiple constraint mechanisms are applied:

- **Hard and soft clipping**: Cabin temperature and humidity are subject to both hard limits (enforced at every step) and soft limits that introduce penalties when approached
- **Actuator normalization**: The controllable actuators are scaled to a normalized action range [-1, 1] and then rescaled to their allowed range. This ensures that the actuators stay inside their allowed ranges

The reward function combines two competing objectives:

- Thermal comfort (primary objective)
- Humidity regulation

Additional penalties are introduced when the observations reach a soft limit. The rewards are not scaled.

The training is carried out on GPU hardware when beneficial for algorithm speed, but may fall back to CPU execution if faster for specific algorithms (e.g. PPO). The training time is approximately 5 hours.

3 Results & Conclusion

After training several different RL algorithms, the best candidate is chosen. The chosen agent is based on the AWAC algorithm. This type of algorithm allows training on both offline and online data. Offline data is used to direct the agent in a good starting direction for online training in the real environment.

The final agent uses four environment observations: Ambient temperature, Relative ambient humidity, Cabin temperature, Relative cabin humidity

To demonstrate the agent in action, Figure 7 shows the agent's actions in a driving simulation. The first column of plots shows the observations of the algorithm, the second column shows the actions and the third column shows the resulting reward and comfort.

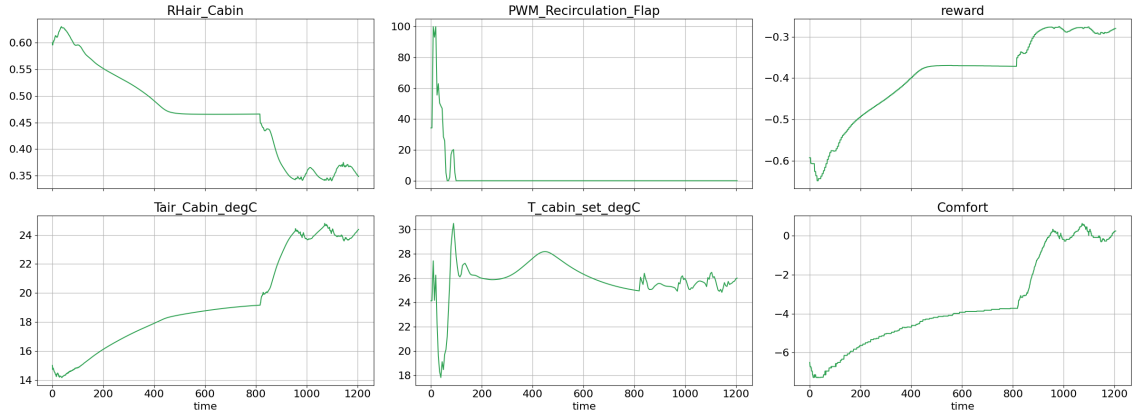

Figure 7: Driving simulation

It can be observed that the trained algorithm selects a cabin set temperature that results in a comfortable thermal sensation at the end of the driving cycle. Moreover, the cabin humidity is close to its target value of 40%. However, greater air recirculation would have been possible in this case.

Nevertheless, this example demonstrates that the training of the algorithm was successful and can be extended to include additional influencing factors such as solar radiation and vehicle speed. The results also indicate that it is particularly challenging for the AI to learn an appropriate set temperature during the heat-up phase. Especially within the first 200 seconds, the set temperature fluctuates

significantly over short time intervals. This behavior is likely due to the limited influence of the set temperature during this phase, as the actual cabin temperature is still far from the target value. Such conditions may encourage random set temperature selections during training, leading to these pronounced variations.

4 Outlook

The subsequent steps in the reinforcement learning (RL) training process involve extending both the observation space and the action space of the RL agent. Regarding observations, the model will be augmented to incorporate indicators of user comfort, such as perceived air quality based on CO_2 concentration, and the likelihood of windshield misting due to humidity levels. These parameters must be maintained within predefined thresholds while minimizing electrical energy consumption.

Furthermore, the learning process will be expanded beyond a generic user profile to include adaptation to individual user preferences. This personalization will be achieved by analyzing user interactions and manual adjustments to system settings, which will serve as feedback signals for the learning algorithm.

Following successful demonstration of user-specific learning behavior in a simulation environment, the approach will be validated in a real-world test vehicle. Initially, the baseline algorithm trained on the standard user profile will be deployed. As the vehicle is operated by individual users over time, it is expected that the frequency of manual interventions will decrease, thereby enhancing the overall user experience through a more intuitive and personalized system response.

Use of Low-order Simulations to Predict Proximity Interactions in Traffic

Faegheh Ghorbanishohrat, Brian R. McAuliffe

National Research Council Canada
1200 Montreal Rd., Ottawa, Ontario, Canada, K1A 0R6

Faegheh.Ghorbanishohrat@nrc-cnrc.gc.ca
Brian.McAuliffe@ nrc-cnrc.gc.ca

Abstract: The aerodynamic performance of road vehicles is quantified conventionally via isolated-vehicle assumptions, while recent research has shown that aerodynamic forces and moments can vary by +/-50% in traffic, associated with proximity to vehicles in adjacent lanes. Mapping the aerodynamic performance for common traffic scenarios requires hours of wind tunnel testing or time-consuming road measurements. These interactions are caused predominantly by pressure field interactions and blockage effects, which can be replicated reasonably well using low-order CFD modelling. This paper examines various levels of simplification, including coarse-mesh simulations using a commercial CFD solver and a potential-flow method, to predict the proximity interactions observed in experimental wind-tunnel results.

1 Background and Objectives

Aerodynamic interactions between road vehicles in traffic has emerged in recent years as a topic of interest, related to energy-use and emissions from transportation systems and to vehicle autonomy via platooning concepts [1,2]. Two distinct phenomena dominate these interactions.

Wakes from surrounding vehicles introduce flow-field variations that can reduce the aerodynamic drag of a following vehicle, due to the lower effective wind speed [3], or can momentarily increase the drag when impinging from vehicles in opposing traffic [4]. These wake effects can persist for large distances from the wake-source vehicle, up to hundreds of meters [5].

In close proximity (within a vehicle dimension), pressure fields interact to generate significant increases or decreases in aerodynamic forces and moments, relative to isolated-vehicle conditions [6]. Most notably, in a close-longitudinal-following configuration (i.e. platoon configuration), the pressure field forward of a trailing vehicle interacts with the body and wake region of a leading vehicle to increase the

Contribution: 2025 FKFS Conference on Vehicle Aerodynamics and Thermal Management
15 – 16 October 2025 | Leinfelden-Echterdingen

base pressure of the leading vehicle and reduce its drag. Interactions amongst vehicles in adjacent lanes also lead to significant increases or decreases in aerodynamic forces and moments [7]. Based on the authors' previous work [8], these proximity effects appear to be dominated by interacting blockage effects on the surrounding flow field, leading to a hypothesis that these influences can be predicted by low-order computational methods. Blockage corrections for wind tunnels have been successfully developed based on potential-flow theory [9], suggesting similar methods may be suitable for proximity interactions. Low-order computational-fluid-dynamics (CFD) methods, such as panel methods or coarse-grid Reynolds-averaged Navier-Stokes (RANS) methods, may also provide efficient techniques to predict these influences.

The objective of this paper is to examine two simulation approaches to predicting proximity interactions for vehicles travelling in adjacent lanes. One approach uses a coarse-grid RANS method for a two-vehicle system, described in Section 2. The other approach uses a simple potential-flow method that combines source and sink models with a uniform flow to represent a multi-vehicle system, described in Section 3. Wind conditions for this preliminary study are limited to 0° yaw angle.

Results from the two methods are contrasted with wind-tunnel measurements of a two-vehicle combination (sedan + SUV), using incremental drag-coefficient and surface-pressure-coefficient values as indicators of their suitability. The measurements were conducted at 15% scale in the NRC 2 m x 3 m Wind Tunnel using a DrivAer Notchback model and an AeroSUV Estateback model [8]. The data provide measurements for a range of longitudinal distances (±2 vehicle lengths) for a lateral separation representing a typical North American highway lane width (3.7 m full scale, providing approximately one vehicle-width separation). Measurements demonstrated drag-coefficient reductions for the individual vehicles up to about 10% and increases that exceeded 20%.

2 Reynolds-Averaged Navier-Stokes Method

2.1 Geometric Model and Computational Domain

For this study, CFD analysis was performed on a full-scale, simplified mid-sized SUV model (L×W×H: 4764 mm ×1936 mm ×1700 mm). The simulations were designed to analyze the aerodynamic interaction between two identical SUV models traveling in adjacent lanes. The vehicles were configured with a constant lateral, centre to centre separation of 3.7 m, a value corresponding to the average width of a common road lane. The primary variable was the longitudinal spacing between the vehicles, defined relative to the vehicle length (L). A matrix of five test cases was studied corresponding to longitudinal separation distances (x) of x/L=0, 0.5, 1.0, 1.5, and 2.0.

The domain is illustrated in Figure 1, which extends approximately 5.5 vehicle lengths (L) upstream, 10.5 lengths downstream, 16 vehicle widths (W) across, and 12 vehicle

heights (H) vertically from the primary vehicle. This configuration yields frontal area blockage ratios of 0.5% for the isolated vehicle case and 1% for the proximity configurations, both of which are well within the acceptable limits for bluff body aerodynamic simulations.

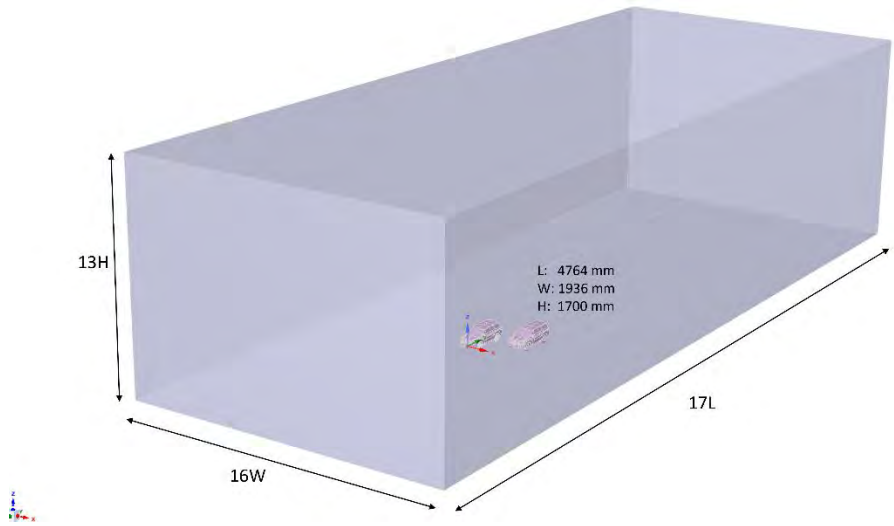

Figure 1: Schematic of the full-scale computational domain and vehicle models.

2.2 Numerical Simulation Setup

All simulations were performed using the commercial software package ANSYS Fluent. The analysis employed a steady-state Reynolds-Averaged Navier-Stokes (RANS) approach to solve the governing equations of fluid flow. Turbulence effects were modeled using the k-ω Shear Stress Transport (SST) model [10]. The simulation was configured with an inlet velocity of 29 m/s (~105 km/h) at a 0° yaw angle. To model the road interface, a moving ground boundary condition was applied at the same velocity as the inlet flow. For computational simplification, the wheels were modeled as stationary.

2.3 Meshing and Grid Independence

The domain was discretized using a poly-hexcore mesh, which employs a combination of polyhedral and hexagonal cells to efficiently capture complex geometry. To ensure computational accuracy, multiple bodies of influence were implemented to selectively refine the mesh density in regions with significant flow gradients.

A grid sensitivity analysis was performed to ensure the numerical results of interest were independent of mesh resolution. Four distinct mesh densities were evaluated for an isolated vehicle and a two-vehicle proximity configuration, with the convergence of the drag coefficient (C_D) Presented in Table 1. The primary objective of this study is to predict the change in aerodynamic drag resulting from vehicle proximity in traffic situations. Consequently, the key metric is the delta drag coefficient (ΔC_D), rather than the absolute C_D value. Table 2 summarizes this metric, showing the change in drag for each vehicle in a specific proximity case relative to its isolated baseline. This configuration—with the proximity vehicle positioned one lane-width away laterally and half a vehicle length behind the primary model—was selected for detailed analysis as it has been identified in previous research [8] to produce the maximum changes in drag for the individual vehicles (increase for lead vehicle, decrease for trailing vehicle).

To ensure a margin of safety for numerical accuracy, the mesh selected for the rest of simulations was the second coarsest. The final mesh consists of approximately 10.8 million cells for the isolated vehicle simulation and 19 million cells for the two-vehicle proximity case. Fine-scale refinement was applied in high-curvature regions of the vehicle model, achieving a minimum face area of 3.5×10^{-3} mm² and a minimum cell volume of 3.9×10^{-3} mm³.

The grid sensitivity analysis (Table 1) showed a total variation of 2-3% in the drag coefficient (C_D) across all tested meshes. Critically, the variation between the 8 million cell and 18 million cell grids was less than 1%. This demonstrated that a grid-independent solution was reasonably achieved. The 10.8 million cell mesh was deemed sufficient for the study's primary objective of estimating the delta drag coefficient relative to isolated vehicle (ΔC_D), which is in range of 4%-20%.

Table1: Drag coefficient (C_D) of a simplified mid-sized SUV model for the isolated and proximity vehicle cases for various meshes.

Isolated vehicle Mesh	Proximity Model Mesh	C_D Isolated	C_D Leading vehicle	C_D Following Vehicle
57,519,272	98,535,909	0.301	0.354	0.272
17,535,439	29,514,219	0.306	0.359	0.279
10,775,254	19,215,304	0.305	0.358	0.28
7,973,372	13,802,265	0.306	0.362	0.28

Table2: ΔC_D for the isolated and proximity vehicle cases for various meshes.

Proximity Model Mesh	C_D System	ΔC_D Lead-Follow	ΔC_D Isolated-Lead	ΔC_D Isolated-Follow	ΔC_D Isolated-System
98,535,909	0.313	0.082	0.053	-0.029	0.012
29,514,219	0.319	0.080	0.053	-0.027	0.013
19,215,304	0.319	0.078	0.053	-0.025	0.014
13,802,265	0.321	0.082	0.056	-0.026	0.015

2.4 Results of Proximity Influence

Figure 2 illustrates the drag coefficient (C_D) and delta drag coefficient (ΔC_D) for all tested configurations from x/L=0 to 2.0. The most significant aerodynamic interaction occurs at a longitudinal separation of x/L=0.5. At this critical spacing, the primary model experiences an 18% drag increase, while the proximity model benefits from an 8% drag reduction. Although the experimental data of [8] uses vehicles of different shapes and sizes, these ΔC_D values align well with the magnitudes observed in the wind-tunnel study, on the order of 20% increase for the leading vehicle and 10% decrease for the trailing vehicle. The net effect on the two-vehicle system is a drag penalty of approximately 5%. The analysis further reveals the sensitivity of these interactions, with the lead model's performance ranging from the 18% drag increase at x/L=0.5 to 4% drag decrease at x/L=2.0.

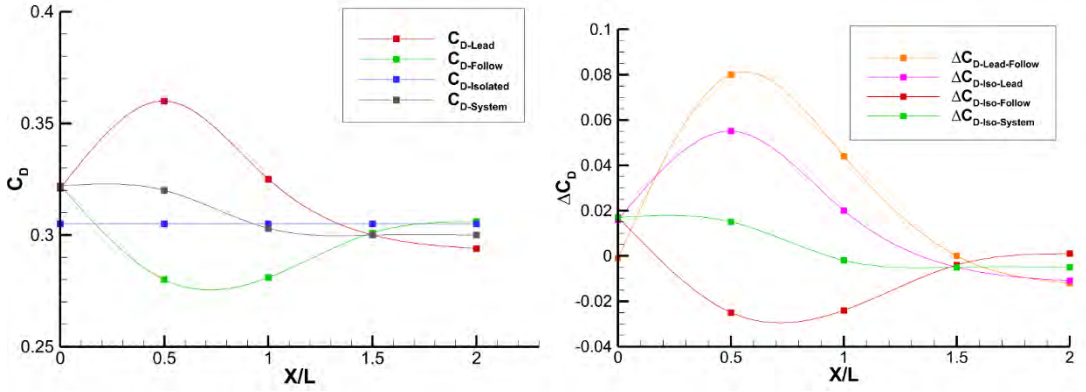

Figure 2: CD and ΔCD for the isolated and proximity vehicle cases at various longitudinal separations (x/L=0,0.5,1.0,1.5, and 2.0).

Figure 3 presents the static pressure contours on the vehicle surfaces and on a horizontal plane 0.25 m above the ground, comparing the isolated vehicle against the x/L=0.5 and x/L=2.0 proximity configurations. The figure visually confirms the aerodynamic coupling between the vehicles, with a lower C_P between the vehicle in the middle plot identifying the mutual blockage influence between the two bodies.

It is important, however, to contextualize these findings within the known limitations of the steady-state RANS methodology. A recent study by Aultman et al. [11] investigated various simulation methods (RANS, URANS, DDES) for automotive aerodynamics. Their findings showed that while RANS can provide fairly accurate predictions of the overall drag coefficient, it often fails to accurately capture detailed flow features. Specifically, they noted that RANS modeled the flow poorly in the vehicle's wake, yielding a structure inconsistent with unsteady simulations and experiments. Aultman et al. attribute this discrepancy to the RANS model's tendency to predict larger regions of flow separation, leading to an over-prediction of base drag.

The primary objective of this study is to quantify the aerodynamic proximity effect, rather than to obtain a perfectly resolved flow field. If the presence of a second vehicle primarily alters existing flow parameters without inducing new, large-scale phenomena like flow separation, then analyzing the difference between isolated and proximity cases with RANS may provide an estimation of system drag. This assumption is supported by the cumulative drag coefficient data versus the distance along the vehicle length (x_v) in Figure 4, which shows similar trends between the multi-vehicle cases and the isolated-vehicle case. These drag-accumulation plots show that, for x/L=0.5, the lead vehicle experiences drag increase from a mid-length position (around x_v/L=0.3) and a significant increase at its base, while the trailing vehicle experiences its drag reduction over its forward section (forward of about x_v/L=0.4).

The results provide evidence for this approach. At the largest tested separation of x/L=2.0, the pressure distribution on the trailing vehicle closely mirrors that of the isolated case, consistent with their nearly identical C_D values. Despite this large separation between the vehicles, a discernible interference effect persists: the presence of the trailing vehicle modifies the pressure field in the wake of the lead vehicle, resulting in a drag reduction of approximately 3% for the leading vehicle.

It is acknowledged that the RANS model does not replicate perfectly the true physical flow, particularly in regions of complex turbulence and separation. However, if the RANS method can accurately capture the relative change in the pressure field induced by vehicle proximity, it serves as a highly efficient tool for estimating these effects, offering substantial savings in computational time. Further investigation, with mesh densities for different vehicle-size and vehicle-shape combinations, and comparison against corresponding experimental data, is required to validate this hypothesis.

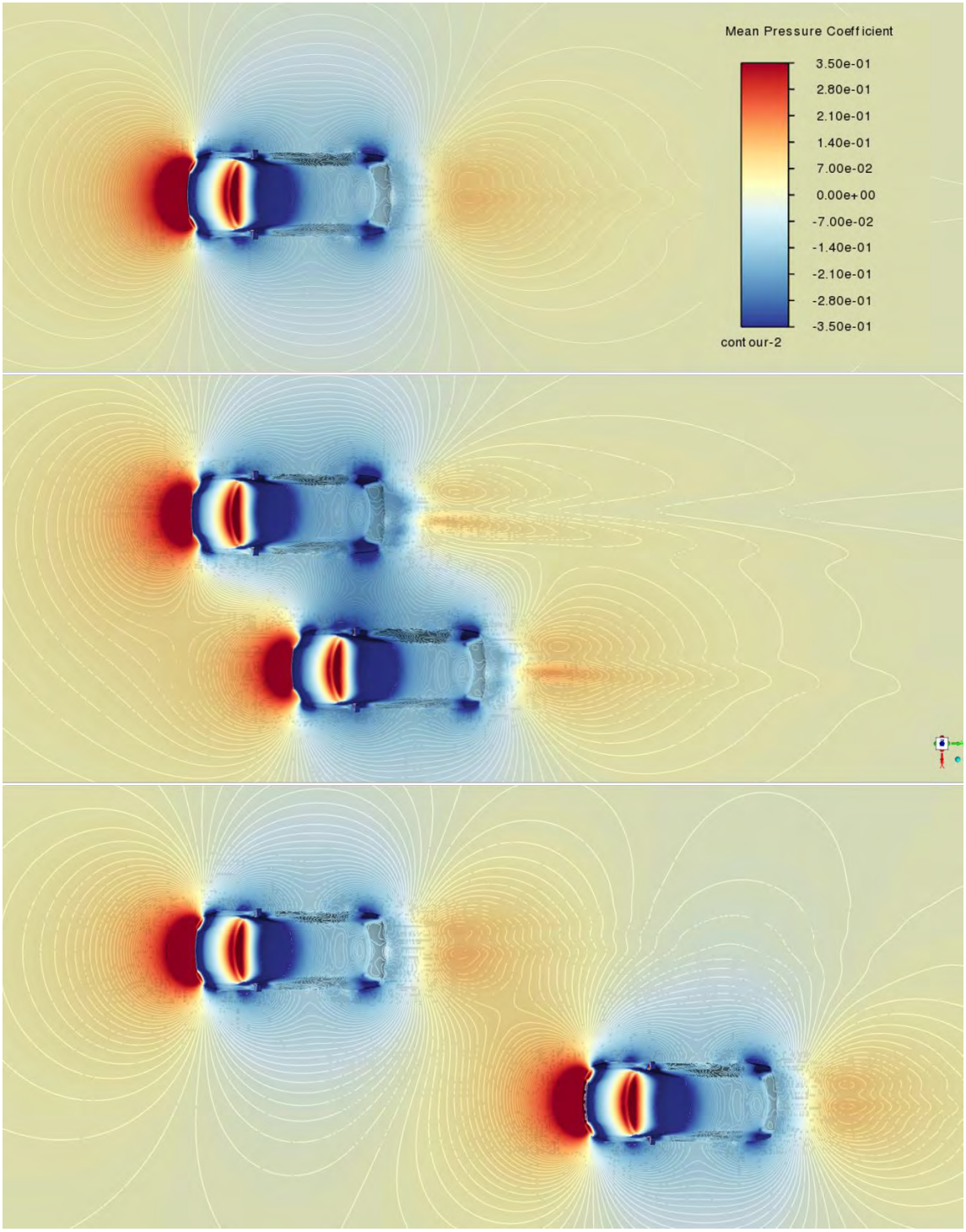

Figure 3: Mean pressure coefficient for Isolated, x/L=0.5 and x/L=2 simulations (from top to bottom) on vehicle's surface and a surface of the plane located at 0.25 m above the ground.

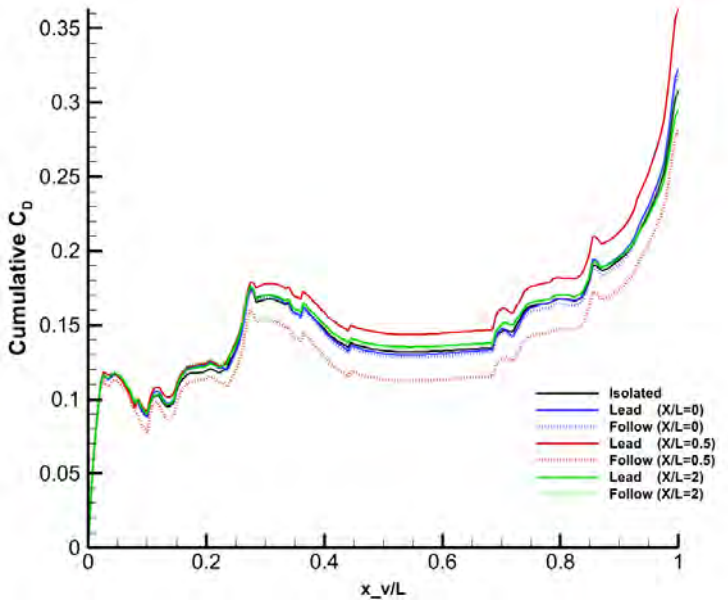

Figure 4: Drag accumulation graph for Isolated, and two proximity models simulations.

3 Potential Flow Method

A three-dimensional potential-flow method has been adopted for this investigation. This method is based on the superposition of potential flows associated with sources/sinks pairs placed strategically to represent solid-body disturbances associated with each vehicle, and sources placed appropriately to generate a wake disturbance for each vehicle. The sources and sinks are placed on the ground plane such that the symmetry about this plane represents the solid ground. This follows the approaches used for wind-tunnel blockage corrections [9], whereby a three-dimensional doublet is generally used to represent the solid blockage of a body in a duplex-tunnel arrangement. Here, the use of a source/sink pair, instead of a doublet, provides a disturbance representative of an ellipsoid rather than a sphere, mimicking better the longitudinal spatial extent of a road vehicle.

The induced velocity of a source is defined as

$$u_i = \frac{S}{4\pi}\left(\frac{x_i}{(x_1^2 + x_2^2 + x_3^2)^{3/2}}\right) \tag{1}$$

where *i* represents the coordinate direction (1,2,3 representing x,y,z directions), and S is the strength of the source (+ for sources, - for sinks). These induced velocities, for N sources and/or sinks, are superimposed on the freestream flow, $U = [U_{fs},0,0]$, to define the flow field:

$$u_i = U_i + \sum_{n=0}^{N} u_{i,n} \tag{2}$$

The source/sink strengths are modelled after the formulation often used for the wake source [9], related to the drag of the vehicle:

$$S_{wake} = \frac{1}{2} C_D A_F U_{fs} \tag{3}$$

Here, this formulation is applied to the source/sink pairs for each vehicle body, with a scaling factor, Θ_{body}, to provide the large disturbances of the body while providing an approximate way to scale for different vehicle sizes. The magnitude of S_{wake} from Equation 3, although adequate for blockage correction methods that represent effects on the bulk flow in a test section, may be inadequate to provide the localized effect of wake displacement in close proximity to another vehicle. As such, a scaling factor Θ_{wake} is also applied to the wake source strength.

The relative positions of the source-sink pairs for the body displacement and the sources for the wake displacement are an important consideration for the proximity-effects analysis. Comparisons of CFD velocity flow fields to those produced by a potential-flow method permitted reasonable estimation of the source/sink locations to simulate the flow displacement around a road-vehicle shape.

The incremental changes to the drag of each vehicle were evaluated based on changes to the pressure field around each body. Based on the calculated velocity field, the pressure-coefficient field is calculated as:

$$C_P = 1 - \left(\frac{U}{U_{fs}}\right)^2 = 1 - \frac{u_1^2 + u_2^2 + u_3^2}{U_{fs}^2} \tag{4}$$

For each vehicle of the multi-body simulation, changes to the pressure-coefficient field are then calculated as:

$$\Delta C_{P,v} = C_P - C_{P,v,iso} \tag{5}$$

where v represents each individual vehicle and *iso* refers to the calculated isolated-vehicle pressure field. The non-linear nature of the pressure, compared to the linearly-superimposed velocity field, results in a non-zero ΔC_P field for each vehicle that represents localized changes to the static pressure associated with proximity to another vehicle.

A validation of this potential-flow approach is provided in Figure 5, comparing an estimate of the potential-flow solution for ΔC_P with experimental measurements for the two vehicles on which the calculations are based, those being a DrivAer Notchback (DN) and AeroSUV Estateback (SE) [8]. The results for the potential-flow solution are based on an interpolation of the ΔC_P fields for each assumed vehicle to the spatial locations of the pressure taps on the wind-tunnel models. The general ΔC_P patterns and magnitudes match well and highlight, for this case with a half-vehicle-length offset, the concentration of significant negative incremental pressure near the physical centre of the two-body system, resulting from the mutually-combined blockage effect. Additionally, the potential method captures well the pressure increase on the forward right side (from a driver perspective) of the lead AeroSUV body, and captures the greater incremental negative ΔC_P on the left side of the DrivAer body, due to the influence of the larger AeroSUV model.

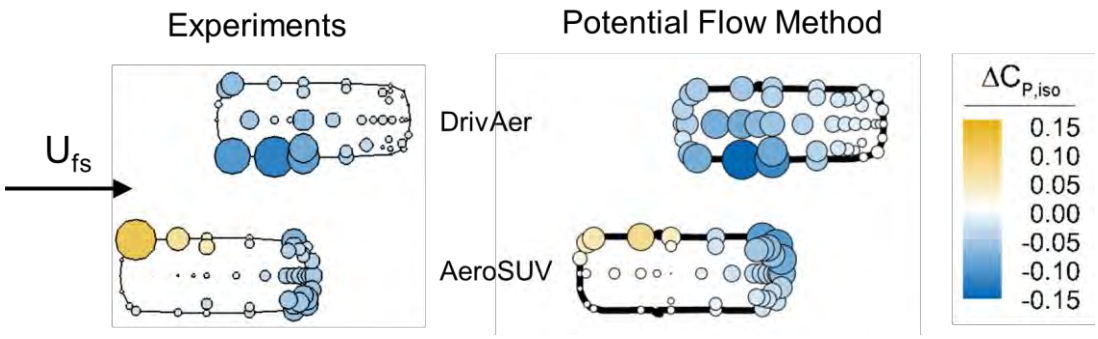

Figure 5: Top-down view comparing the experimental and predicted $\Delta C_{P,iso}$ changes due to proximity with adjacent-lane vehicles, at a half-vehicle-length offset. The Potential Flow Method shows values calculated at the pressure-tap locations.

To estimate the change in drag coefficient for each vehicle, an assumption is made that the incremental drag (ΔC_D) is proportional to the difference in incremental pressure (ΔC_P) across the longitudinal length of the vehicle. To do this, the ΔC_P field is interpolated onto rectangular planes, perpendicular to the freestream flow and located at the leading and trailing edges of the assumed vehicle shape, with a width and a height equivalent to those dimensions of the assumed vehicle shapes. The ΔC_P values within each interpolated plane are then area averaged, and the difference between the leading- and trailing-edge-plane values is calculated ($\Delta C_{P,l\text{-}t}$). This value is then assumed to be proportional to the ΔC_D of the vehicle.

Figure 6 compares the estimated ΔC_D values for both vehicle models, and for the combined two-vehicle system, with the corresponding experimental measurements that were made over a range of ±2 vehicle-length offsets. Negative x/L values represent the AeroSUV forward of the DrivAer. The calculated $\Delta C_{P,l\text{-}t}$ values are scaled by a factor 0.7 to provide the ΔC_D estimates for the potential- flow method. Good agreement is found for the trends of ΔC_D for each vehicle and for the combined system. The larger influence of the AeroSUV on the DrivAer, due to the size difference, is replicated well, as are the distances over which each body experiences drag increases versus drag decreases. As with the experimental measurements, the combined incremental drag is highest when side by side (x/L = 0) and show minima in the x/L=±1 to ±2 range.

These results are preliminary, and the potential-flow approach has not yet been validated for larger or smaller lateral offsets, for different vehicle lengths, or for cross winds. However, the results presented here show that the use of a simple and efficient potential-flow method can provide a reasonable estimation of proximity effects, and may provide a means to estimate sensitivity geometric changes for multi-vehicle (2 or more) and multi-lane systems (2 or more).

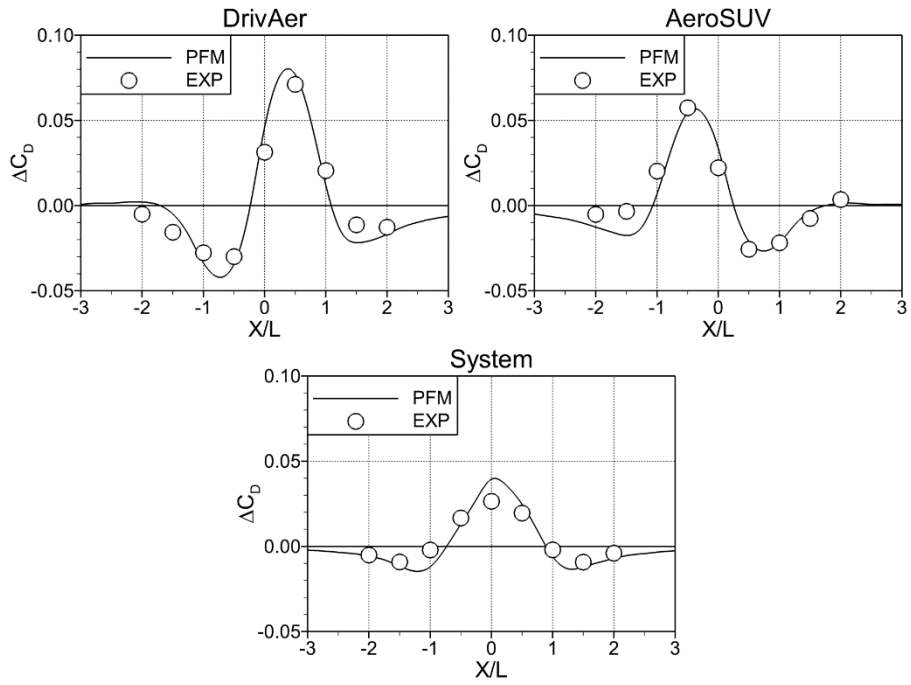

Figure 6: Comparison of drag-change-coefficient prediction using the potential-flow method (PFM) compared to experimental data (EXP) for the DrivAer Notchback and AeroSUV Estateback combination. Top plots show individual vehicles and bottom plot shows the two-vehicle system.

4 Conclusions

Mapping the aerodynamic performance of representative traffic scenarios typically requires extensive wind tunnel testing or prolonged on-road measurements. In this study, a low-order CFD simulation was employed to model interaction effects in proximity situations. In addition, a simplified and computationally efficient potential flow method was applied, producing results in alignment with experimental data. The findings demonstrate that these simplified and cost-effective methods can serve as effective tools for analyzing proximity interactions of traffic while reducing the expenses associated with purely experimental approaches. These methods show strong potential for the efficient estimation of proximity effects; however, further investigation is warranted, particularly to address crosswind conditions and variations in vehicle geometry.

5 Reference list

[1] Jessing, C., Wilhelmi, H., Wittmeier, F., Wagner, A. et al., “Investigation of Transient Aerodynamic Effects on Public Roads in Comparison to Individual

Driving Situations on a Test Site," SAE Technical Paper 2020-01-0670, 2020, doi:10.4271/2020-01-0670.

[2] Wang, Z., Bian, Y., Shladover, S.E., Wu, G., Li, S.E., Barth, M.J., 2019. "A survey on cooperative longitudinal motion control of multiple connected and automated vehicles." IEEE Intelligent Transportation Systems Magazine," doi:10.1109/MITS.2019.2953562.

[3] McAuliffe, B. and Barber, H., "Simulating Traffic-wake Effects in a Wind Tunnel," SAE Int. J. Advances & Curr. Prac. in Mobility 5(6):1969-1987, 2023, doi:10.4271/2023-01-0950.

[4] Dasarathan, D., He, W., Spencer, S., and Gargoloff, J., "Influence of Class-8 Truck Passing Oncoming Truck Using CFD Simulation," SAE Technical Paper 2022-01-1151, 2022, doi:10.4271/2022-01-1151.

[5] McAuliffe, B., Sowmianarayanan, B., and Barber, H., "Near-to-Far Wake Characteristics of Road Vehicles Part 1: Influence of Ground Motion and Vehicle Shape," SAE Int. J. Advances & Curr. Prac. in Mobility 3(4):2009-2024, 2021, doi:10.4271/2021-01-0957.

[6] Shimizu, K., Nakashima, T., Hiraoka, T., Nakamura, Y. et al., "Investigation of Increase in Aerodynamic Drag Caused by a Passing Vehicle," SAE Technical Paper 2018-01-0719, 2018, doi:10.4271/2018-01-0719.

[7] McAuliffe, B. and Barber, H., "Aerodynamic Drag of Road Vehicles in Close Lateral Proximity," SAE Int. J. Advances & Curr. Prac. in Mobility 5(6):2004-2020, 2023, doi:10.4271/2023-01-0952.

[8] McAuliffe, B. and Barber, H., "Wind-Load and Surface-Pressure Measurements of the Aerodynamic Interactions of a Passenger Vehicle with Adjacent-Lane Vehicles," SAE Technical Paper 2024-01-2549, 2024, doi:10.4271/2024-01-2549.

[9] Wickern, G., "On the Application of Classical Wind Tunnel Corrections for Automotive Bodies," SAE Technical Paper 2001-01-0633.

[10] Le Good, G., Self, M., Boardman, P., Resnick, M. "An Investigation of Aerodynamic Characteristics of Three Bluff Bodies in Close Longitudinal Proximity-Part 2," SAE Technical Paper 2021-01-0952, 2021, doi: 10.4271/2021-01-0952.

[11] Aultman, M., Wang, Z., Auza-Gutierrez, R., Duan, L., "Evaluation of CFD methodologies for prediction of flows around simplified and complex automotive models" Computers and Fluids, vol. 236, 2022, doi: 10.1016/j.compfluid.2021.105297.

Transformer-based Prediction of Vehicle Aerodynamics

John Higgins, Cyril Ngo Ngoc, Nicolas Fougère, Faron Hesse, Victor Oancea, David Sondak

Dassault Systèmes SIMULIA Corp.
175 Wyman Street, Waltham MA (USA)

John.HIGGINS@3ds.com
Cyril.NGONGOC@3ds.com
Nicolas.FOUGERE@3ds.com
Faron.HESSE@3ds.com
Victor.OANCEA@3ds.com
David.SONDAK@3ds.com

Abstract: The vehicle market is evolving rapidly. New players are entering the market, many variants of a vehicle are investigated prior to freezing the design, and more. In this context, vehicle aerodynamics is ever more crucial. It directly impacts the vehicle range and plays a major role in meeting regulation targets. Vehicle manufacturers must also keep in mind the need for a shorter time-to-market, where one must design faster and not permit late-stage redesign. Therefore, faster and earlier assessment of vehicle aerodynamics is imperative. Computational Fluid Dynamics (CFD) has opened the door to virtual aerodynamic testing, allowing manufacturers to test their vehicle shapes before developing a costly and time-intensive prototype that then needs to be experimented on using a wind tunnel. While high-fidelity CFD, such as the PowerFLOW® software from Dassault Systèmes, will remain an integral part of the aerodynamic development process of major OEMs, the growth of machine learning (ML) and continual improvement of its algorithms has opened doors to speed-up computational aerodynamics, allowing automotive manufacturers to get feedback on their vehicle design in a matter of minutes. The current work illustrates how aerodynamic data obtained using the Lattice Boltzmann Method with PowerFLOW® combined with transformer-based ML can enable car manufacturers to obtain clean 3D contour plots of the vehicle's surface X-force (or any other simulated quantity) distribution and the associated integrated vehicle drag force within several minutes on a single GPU (after training of the ML model). This represents a significant reduction in computational cost and time.

Contribution: 2025 FKFS Conference on Vehicle Aerodynamics and Thermal Management
15 – 16 October 2025 | Leinfelden-Echterdingen

1 Introduction

The ground vehicle market continues to shift its focus to more energy-efficient designs. As a result, aerodynamic performance of the vehicle is more critical than ever in achieving range and regulatory goals. In order for a vehicle platform to reach its aerodynamic performance targets, vehicle manufacturers must evaluate more designs virtually. In order to meet time-to-market deadlines, there is a need to evaluate more designs earlier in the design phase (such as the concept design phase). This is sometimes referred to as “left-shifting” of simulation within the design cycle.

Historically, high-fidelity Computational Fluid Dynamics (CFD) tools using the Lattice Boltzmann Method (LBM) such as the PowerFLOW® software from Dassault Systèmes have been used to virtually evaluate vehicle aerodynamics. This will remain an integral tool in both early and late stages of the design process. In early stages of the design process, high-fidelity CFD will be used to generate datasets with which to train machine learning (ML) models. In later stages of the design process where the highest level of simulation accuracy is required, high-fidelity CFD will continue to be used to verify final designs and validate physical tests. With the growth of machine learning surrogate models, it is possible to evaluate the aerodynamics of a vehicle virtually in a matter of minutes [1]. This will accelerate the aforementioned “left-shifting” of simulation within the design cycle by allowing design studios to quickly and easily evaluate the aerodynamic performance. This will ultimately allow vehicle OEMs to evaluate significantly more designs than they would have using traditional CFD methods, leading to more innovative and efficient vehicles.

Vehicle OEMs have been using CFD to predict their vehicle aerodynamics performance at different stages within the design process for decades. As a result, they have acquired a large database of simulation results. These existing datasets can be leveraged as a promising starting point for training ML models. Integrating new high fidelity simulation datasets into these trained models will further enhance their prediction capabilities.

There has been a surge of effort in scientific machine learning for CFD in recent years covering most aspects of CFD with varying degrees of success [2] [3] [4]. Early work focused on the development of novel RANS turbulence model closures with more recent extensions being developed for LES closures [5] [6] [7]. A large amount of effort has centered on physics-informed neural networks (PINNs) [8] [9] [10] as a way of solving conservation equations using neural networks. PINNs have some appealing qualities including straightforward blending of data with conservations laws, being fully differentiable, easy adaptation to complex geometries, and the ability to easily incorporate a variety of boundary conditions. In spite of these apparent advantages, PINNs are not competitive with traditional solvers and remain an active area of research. Machine learning algorithms have also been developed to discover new discretization strategies [11], accelerate traditional solvers [12], improve mesh generation [13] [14], discover equations from data [15], generate super-resolved flow fields from under-resolved data [16] [17] [18] [19], and most relevant to this manuscript, develop surrogate models [20] [21] [22] [23] [24] [25]. The majority of the work on ML has focused on data generated from Navier-Stokes simulations including RANS, LES, and DNS datasets. However, some recent work has emerged on fully-differentiable Lattice Boltzmann solvers [26], learning Lattice Boltzmann collision operators [27], and learning collision operators for the Bolztmann equation [28]. Regardless of the algorithm used, any scientific machine learning approach is strongly influenced by the quality of the training data. The present work uses PowerFLOW® CFD to generate state of the art training datasets for the development of surrogate models.

In this study, we apply a transformer-based machine learning surrogate model [25] [29] to the design of a vehicle external surface. The input to the neural network is a set of PowerFLOW® LBM CFD simulations applied to a sedan vehicle with varying design changes made to the A-surface. It is important to note that this ML methodology uses history-based data as input, meaning that geometric parameters are not required as input to the neural network. The reference vehicle model used in the present study is the DrivAer model from TU Munich [30]. PowerFLOW® CFD was previously validated on this particular vehicle model [31]. The trained neural network was used to predict the X-component of the surface force contours. This result was then used to calculate the overall vehicle drag coefficient (C_D) via integration over the entire vehicle surface. Both the surface X-force contours and C_D were found to be in excellent agreement with the PowerFLOW® results, even for vehicle designs outside of the training set. To the best of our knowledge, this is the first time an ML model has been trained using data generated with the Lattice Boltzmann Method in the context of vehicle aerodynamics.

2 CFD Numerical Approach to Generate the Dataset

The design set used for training contained large changes to the vehicle A-surface, including shape changes to the front bumper, windshield, and rear glass as well as ride height and front wheel deflectors on/off. These shape changes were applied through a mesh morphing technique. Figure 1 shows a subset of the designs that were used to train the neural network. A total of 50 DrivAer designs were included in this study.

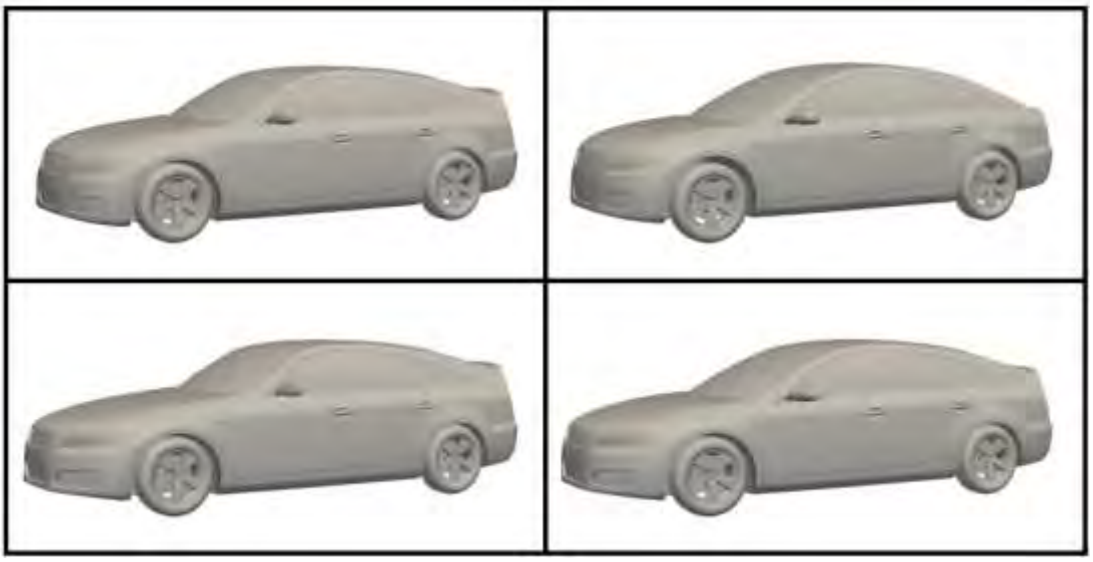

Figure 1: Subset of DrivAer designs used in study

All 50 of the DrivAer designs used in the present study were simulated using the PowerFLOW® LBM CFD solver. A full numerical description along with information regarding the Very Large Eddy Simulation (VLES) turbulence model can be found within the following references [32] [33] [34] [35] [36] [37] [38] [39] .

Such a CFD approach has been extensively validated by comparison to physical test from wind tunnel data [40] [41] [42] [43]. This gives confidence into the accuracy of the database.

The results of these CFD simulations were used as the input dataset to the neural network. The external aerodynamics simulation setup utilized an open-road scenario, consisting of a large domain with a velocity inlet far upstream of the vehicle and a pressure outlet far downstream. The walls and ceiling of the domain were modeled as frictionless walls. The floor was modeled with a moving wall condition to match the freestream velocity. Incompressible flow was assumed, with a freestream of $U_\infty = 140\ kph$ and an ambient temperature of $T = 20°C$. The reference area used for drag coefficient calculation was $A = 2.156\ m^2$. For added realism, the wheels of the vehicle were encased in a local rotating reference frame in order to simulate the effects of rotating wheel geometry with a sliding mesh technique.

The fluid volume was setup using a variable resolution scheme. The finest fluid cell size was 2.5mm, applied on regions containing highly unsteady flow and/or large velocity gradients such as mirrors, a-pillars, and wheels. The fluid and surface grid used for simulation was generated automatically by the PowerFLOW® discretizer. This resulted in 97M elements in the fluid domain and 7M elements on the vehicle surface.

All of the transient CFD simulations were run for 2 seconds of physical time. The end of the initial transient was identified using the approach described in [44]. The time-averaged drag force for all of the simulations converged within 1 count (0.001 C_D) accuracy with a 95% confidence interval. Figure 2 shows an example of the drag time history plot for one of the simulations. This 50-simulation set resulted in a broad range of time-averaged overall C_D values, ranging from 0.247 to 0.308.

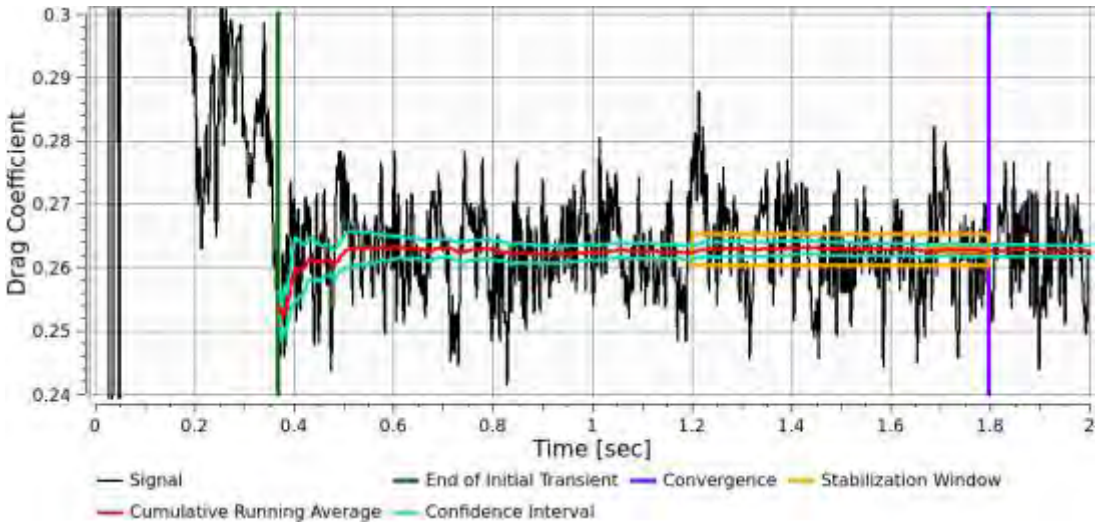

Figure 2: Transient drag history plot for Run 1

Before inputting the CFD dataset into the neural network, some post-processing was performed. The data on the surface of the vehicle directly from CFD contained around 3M points. This was too large for the neural network to run on a single-GPU card due to memory limitations. Therefore, the per-simulation dataset size was reduced from ≈3M points to 130k points via Voronoi kernel spatial interpolation [45]. Doing so introduced a mean error of 1.73% into the interpolated dataset. All of the results forthcoming neglect this error and compare the interpolated data (ground truth) to the ML prediction.

3 Machine Learning Training and Predictions

A transformer-based machine learning technique [25] [29] was used to train on the entire vehicle surface X-force contours from the PowerFLOW® simulations. A 90-10 training-test split of the 50-simulation dataset was used, resulting in 45 training points and 5 blind test points. Figure 3 shows the training and test loss curves where we track the evolution of the mean squared error for the training and test sets as a function of epoch. The training had completed after 700 epochs.

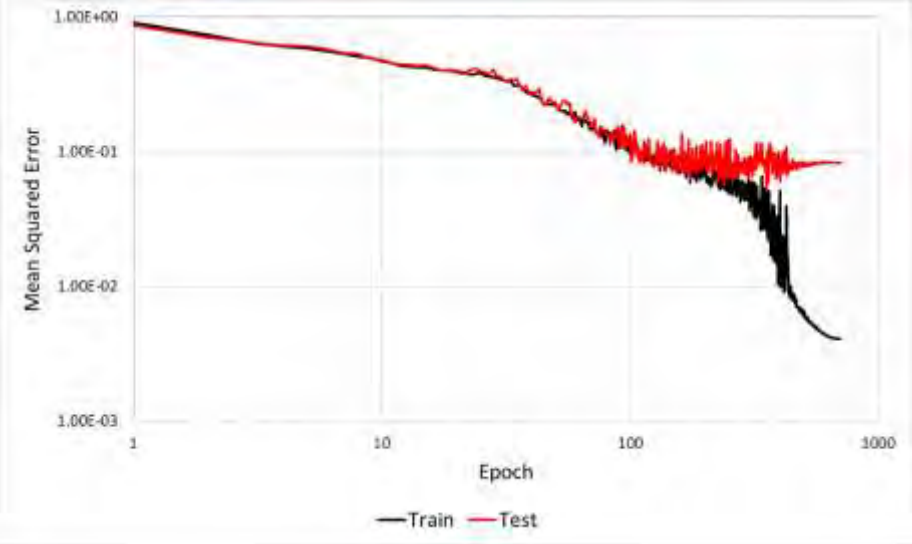

Figure 3: Training and test loss curves

The total vehicle drag force is calculated by integrating over the vehicle surface the X-component of the force per unit area surface predictions from the machine learning model. Analyzing both of these metrics is key to evaluating the accuracy of the model. Figure 4 shows a comparison of the X-component of the surface force contours for the test run that had the best C_D ML prediction. The top image shows the ground truth result, the middle image shows the ML prediction, and the bottom image shows their difference. The C_D error for this design point is 0.18%, indicating very good agreement. Qualitatively, the surface X-Force contour predictions correlate well with the ground truth. There are some minor discrepancies seen between the ground truth and ML prediction. These differences are primarily present at regions of high curvature, such as the front bumper, mirrors, and wheels.

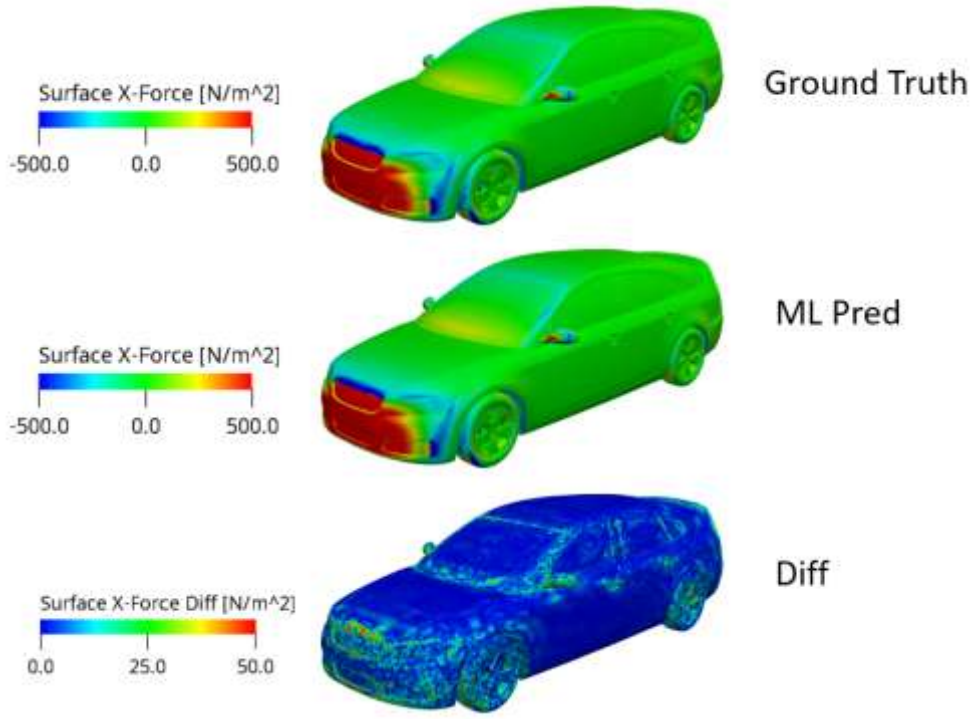

Figure 4: Surface X-Force for Run 18. This is the best prediction among all of the test points. top: Ground truth, middle: ML prediction, bottom: difference

Figure 5 shows a comparison of the surface X-force contours for the test run that had the worst C_D ML prediction. Even here, the ML prediction is in quite good agreement. The C_D error for this design point is 1.00%. The discrepancies between ground truth and ML prediction are in similar regions as the “best” run.

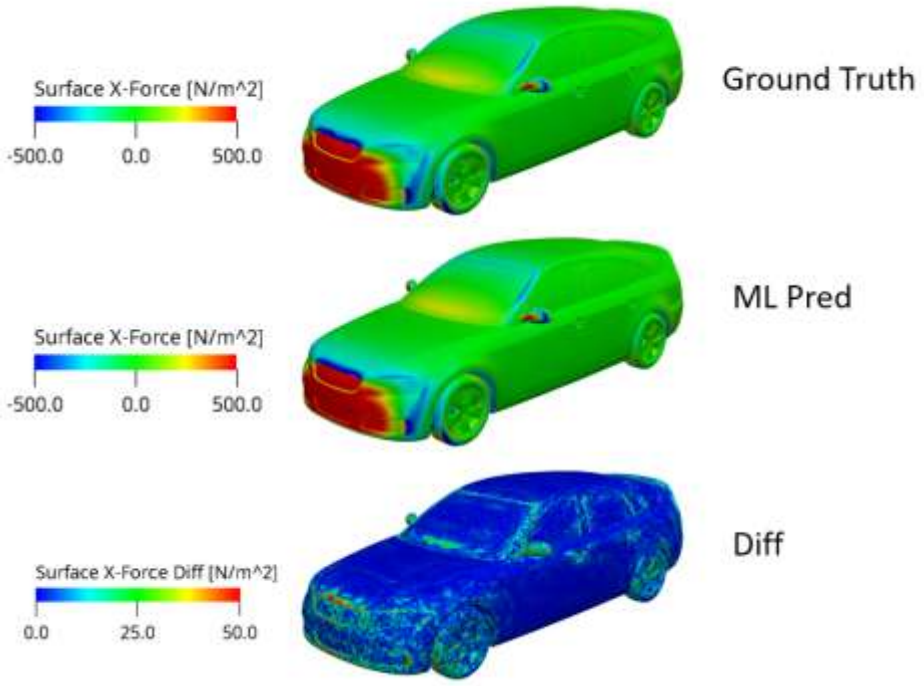

Figure 5: Surface X-Force for Run 42. This is the worst prediction among all of the test points. top: Ground truth, middle: ML prediction, bottom: difference

The overall performance of the ML model is shown in Figure 6. Here, the overall C_D derived from the predicted X-component of surface force contours is plotted against the C_D computed from the ground truth data. A perfect prediction would result in all of the data points falling on the 45-degree line. The mean error for the entire dataset (training points included) is 0.37% and the mean error for the test points only is 0.59%. As shown in Figure 6, all of the test points land on or within the 1% error bars.

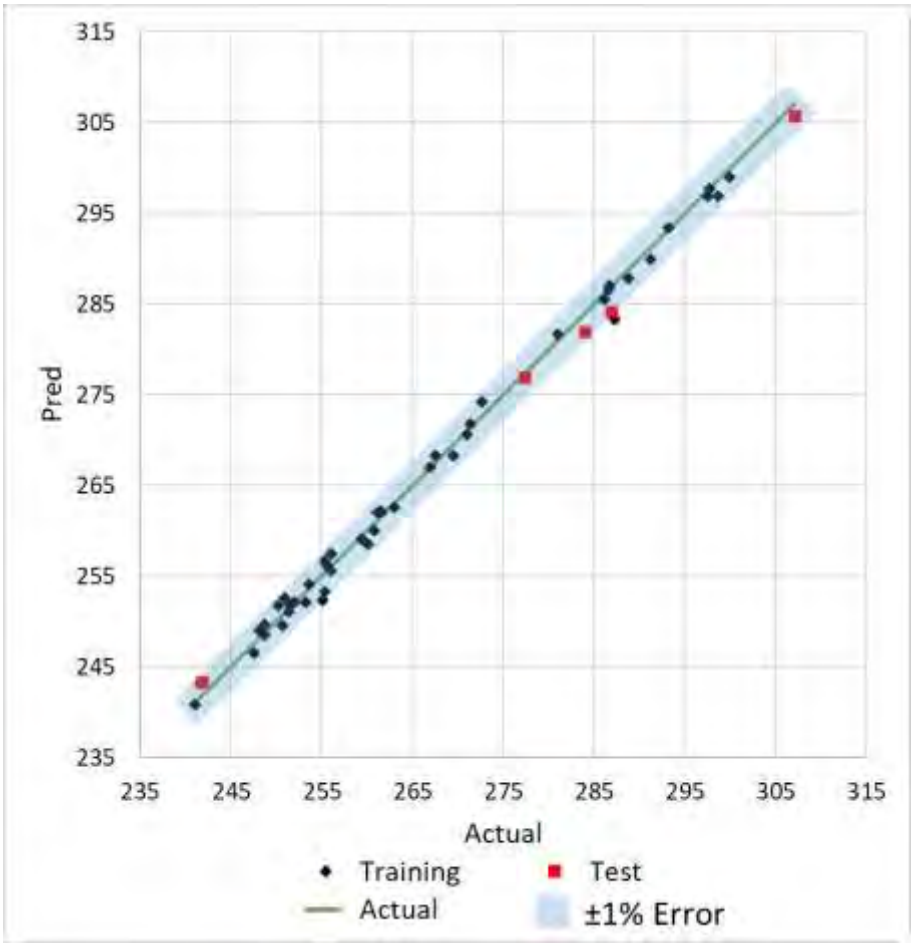

Figure 6: ML predictions (Pred) vs. ground truth (Actual) for overall vehicle drag (C_D) in counts. 1% error bars

It is also important to consider the ranking of designs based on an important metric (C_D in this case). This ensures that the neural network is able to predict trends accurately, which is key during the vehicle design phase. Figure 7 shows a ranking of the C_D for all of the test datasets, ordered from lowest to highest. Here, the ranking remains consistent between ground truth result and ML prediction for all of the test points. This indicates that the trained model can predict trends accurately, even between closely ranked designs like test points 2, 3, and 4.

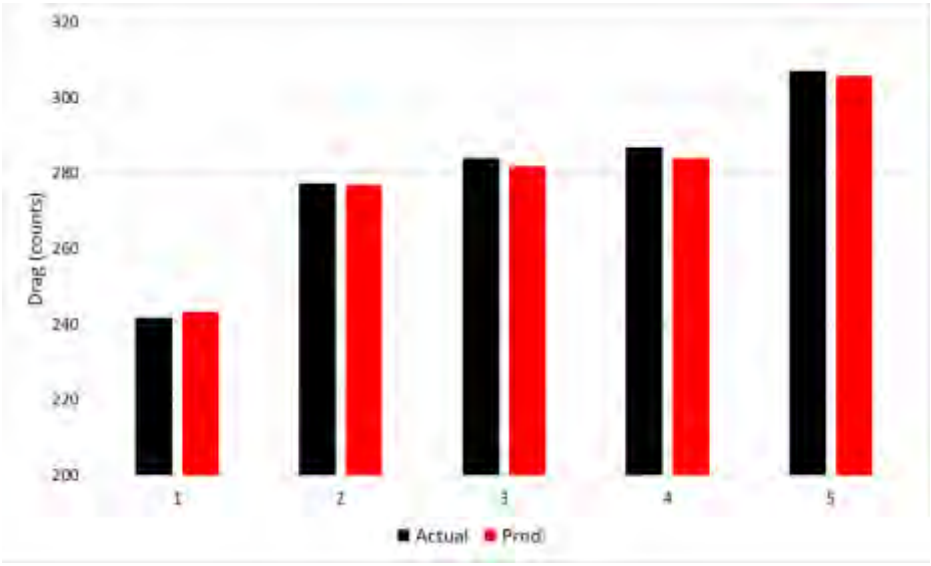

Figure 7: Overall vehicle drag for test runs. Ranked in ascending order based on the ground truth result.

4 Conclusion

Through this study, we have shown the ability for transformer-based neural networks to successfully create surrogate models from high-fidelity LBM CFD simulations. When applied to concept aerodynamics simulations, the key performance indicators of overall drag and surface X-Force contours were predicted by the neural network with a high level of accuracy. Specifically, in this study we utilized a 50-simulation dataset with a 90-10 training-test split, resulting in 45 training points and 5 test points. Training the model on the 3D contours of surface X-force resulted in an integrated drag force mean error of 0.59% for the test points. Moreover, the ranking of the different vehicle designs was accurately predicted by the ML model, ensuring that the methodology presented in this paper offers reliable design direction.

The 3D contour predictions are made in a matter of minutes, instead of the hours required to simulate high-fidelity CFD, providing almost instantaneous design guidance based on vehicle drag performance. This approach will enable designers to explore the aerodynamic impact on a wider variety of vehicle shapes in the early stages of the design process. This was previously not possible with traditional CFD simulation techniques.

Moving forward, the next steps are to evaluate the impact of expanding the training set, which would potentially improve the error even further. We also plan on applying this technique to other vehicles to ensure robustness. Finally, we would like to explore applying this history-based neural network technique to other CFD application areas such as acoustics and thermal applications.

5 References List

[1] X. Du, P. He und J. R. R. A. Martins, “Rapid airfloil design optimization via neural networks-based parameterization and surrogate modeling,” Bd. 113, p. 106701, June 2021.

[2] S. L. Brunton, B. R. Noack und P. Koumoutsakos, “Machine Learning for Fluid Mechanics,” *Annu. Rev. Fluid Mech.,* Bd. 52, Nr. 1, pp. 477-508, Jan. 2020.

[3] O. Obiols-Sales, A. Vishnu, N. Malaya und A. Chandramowliswharan, “CFDNet: a deep learning-based accelerator for fluid simulations,” in *Proceedings of the 34th ACM International Conference on Supercomputing*, Barcelona Spain, 2020.

[4] R. Vinuesa und S. L. Brunton, “Enhancing computational fluid dynamics with machine learning,” *Nat. Comput. Sci.,* Bd. 2, Nr. 6, p. 358–366, Jun. 2022.

[5] J. Ling, A. Kurzawski und J. Templeton, “Reynolds averaged turbulence modelling using deep neural networks with embedded invariance,” *J. Fluid Mech.,* Bd. 807, pp. 155-166, 2016.

[6] A. Beck und M. Kurz, “A perspective on machine learning methods in turbulence modeling,” *GAMM-Mitteilungen,* Bd. 44, Nr. 1, p. e202100002, Mar. 2021.

[7] M. Milano und P. Koumoutsakos, “Neural Network Modeling for Near Wall Turbulent Flow,” *J. Comput. Phys.,* Bd. 182, Nr. 1, pp. 1-26, 2002.

[8] I. E. Lagaris, A. Likas und D. I. Fotiadis, “Artificial neural networks for solving ordinary and partial differential equations,” *IEEE Trans. Neural Netw.,* Bd. 9, Nr. 5, pp. 987-1000, Sep. 1998.

[9] I. E. Lagaris, A. C. Likas und D. G. Papageorgiou, “Neural-network methods for boundary value problems with irregular boundaries,” *IEEE Trans. Neural Netw.,* Bd. 11, Nr. 5, pp. 1041-1049, Sep. 2000.

[10] M. Raissi, P. Perdikaris und G. E. Karniadakis, “Physics-informed neural networks: A deep learning framework for solving forward and inverse problems involving nonlinear partial differential equations,” *J. Comput. Phys.,* Bd. 378, pp. 686-707, Feb. 2019.

[11] Y. Bar-Sinai, S. Hoyer, J. Hickey und M. P. Brenner, “Learning data-driven discretizations for partial differential equations,” *Proc. Natl. Acad. Sci.,* Bd. 116, Nr. 31, pp. 15344-15349, Jul. 2019.

[12] D. Kochkov, J. A. Smith, A. Alieva, Q. Wang, M. P. Brenner und S. Hoyer, “Machine learning–accelerated computational fluid dynamics,” *Proc. Natl. Acad. Sci.,* Bd. 118, Nr. 21, p. e2101784118, May 2021.

[13] K. Huang, M. Krügener, A. Brown, F. Menhorn, H. J. Bungartz und D. Hartmann, “Machine Learning-Based Optimal Mesh Generation in Computational Fluid Dynamics,” *arXiv: arXiv:2102.12923,* 25 Feb. 2021.

[14] S. Sanchez-Gamero, O. Hassan und R. Sevilla, “A Machine Learning Approach to Predict Near-optimal Meshes for Turbulent Compressible Flow Simulations,” *Int. J. Comput. Fluid Dyn.,* Bd. 38, Nr. 2-3, pp. 221-245, Mar. 2024.

[15] S. L. Brunton, J. L. Proctor und J. N. Kutz, “Discovering governing equations from data by sparse identification of nonlinear dynamical systems,” *Proc. Natl. Acad. Sci.,* Bd. 113, Nr. 15, pp. 3932-3937, Apr. 2016.

[16] K. Fukami, K. Fukagata und K. Taira, “Super-resolution reconstruction of turbulent flows with machine learning,” *J. Fluid Mech.,* Bd. 870, pp. 106-120, Jul. 2019.

[17] K. Fukami, K. Fukagata und K. Taira, “Machine-learning-based spatio-temporal super resolution reconstruction of turbulent flows,” *J. Fluid Mech.,* Bd. 909, p. A9, Feb. 2021.

[18] K. Fukami und K. Taira, “Single-snapshot machine learning for super-resolution of turbulence,” *J. Fluid Mech.,* Bd. 1001, p. A32, Dec. 2024.

[19] J. Page, “Super-resolution of turbulence with dynamics in the loss,” *J. Fluid Mech.,* Bd. 1002, p. R3, Jan. 2025.

[20] K. Azizzadenesheli, N. Kovachki, Z. Li, M. Liu-Schiaffini, J. Kossaifi und A. Anandkumar, “Neural operators for accelerating scientific simulations and design,” *Nat. Rev. Phys.,* Bd. 6, Nr. 5, pp. 320-328, Apr. 2024.

[21] Z. Li, N. Kovachki, K. Azizzadenesheli, B. Liu, K. Bhattacharya, A. Stuart und A. Anandkumar, “Fourier Neural Operator for Parametric Partial Differential Equations,” *arXiv: arXiv:2010.08895,* 17 May 2021.

[22] L. Lu, P. Jin und G. E. Karniadakis, ““DeepONet: Learning nonlinear operators for identifying differential equations based on the universal approximation theorem of operators,” *Nat. Mach. Intell.,* Bd. 3, Nr. 3, pp. 218-229, Mar. 2021.

[23] J. Bi, C. Ngo Ngoc, J. Yao und V. Oancea, “Towards 3d interactive design exploration via neural networks,” in *presented at the NAFEMS World Congress 2023*, Tampa, FL, 2023.

[24] Y. Chen, J. Bi, C. Ngo Ngoc, V. Oancea, J. Cagan und L. B. Kara, “Attention to Detail: Fine-Scale Feature Preservation-Oriented Geometric Pre-training for AI-Driven Surrogate Modeling,” *arXiv preprint arXiv:2504.20110,* 3 May 2023.

[25] H. Wu, H. Luo, H. Wang, J. Wang und M. Long, “Transolver: A Fast Transformer Solver for PDEs on General Geometries,” *arXiv: arXiv:2402.02366,* 01 Jun. 2024.

[26] M. Ataei und H. Salehipour, “XLB: A differentiable massively parallel lattice Boltzmann library in Python,” *Comput. Phys. Commun.,* Bd. 300, p. 109187, Jul. 2024.

[27] A. Corbetta, A. Gabbana, V. Gyrya, D. Livescu, J. Prins und F. Toschi, “Toward learning Lattice Boltzmann collision operators,” *Eur. Phys. J. E,* Bd. 46, Nr. 3, p. 10, Mar. 2023.

[28] S. T. Miller, N. V. Roberts, S. D. Bond und E. C. Cyr, “Neural-network based collision operators for the Boltzmann equation,” *J. Comput. Phys.,* Bd. 470, p. 111541, Dec. 2022.

[29] Z. Hao, Z. Wang, H. Su, C. Ying, Y. Dong, S. Liu, Z. Cheng, J. Song und J. Zhu, “GNOT: A General Neural Operator Transformer for Operator Learning,” *arXiv: arXiv:2302.14376,* Feb. 2023.

[30] A. Heft, T. Indinger und N. Adams, “Introduction of a New Realistic Generic Car Model for Aerodynamic Investigations,” SAE Technical Paper 2012-01-0168, 2012.

[31] G. Parenti, G. Martins, A. Martinez und T. Linden, “PowerFLOW© Uncertainty Quantification using a DrivAer model,” in *4th Automotive CFD Prediction Workshop*, Belfast, 2024.

[32] S. Chapman und T. Cowling, “The Mathematical Theory of Non-Uniform Gases,” Cambridge Univerity Press, 1990.

[33] P. L. Bhatnagar, E. P. Gross und M. Krook, “A Model for Collision Processes in Charged and Neutral One-Component System,” *Phys. Rev,* Bd. 94, pp. 511-525, 1954.

[34] H. Chen, “Volumetric Formulation of the Lattice Boltzmann Method for Fluid Dynamics: Basic Concept,” *Phys. Rev. E,* Bd. 58, pp. 3955-3963, 1998.

[35] Y. Zhou, R. Zhang, I. Staroselsky und H. Chen, “Numerical Simulation of Laminar and Turbulent Buoyancy-Driven Flows using a Lattice-Boltzmann based Algorithm,” *Int. J. of Heat and Mass Transfer, 47,* pp. 4869-4879, 2004.

[36] Y. Li, R. Shock, R. Zhang und H. Chen, “Numerical Study of Flow Past an Impulsively Started Cylinder by Lattice Boltzmann Method,” *J. Fluid Mech,* Bd. 519, pp. 273-300, 2004.

[37] H. Chen, S. Orszag, I. Staroselsky und S. Succi, “Expanded Analogy between Boltzmann Kinetic Theory of Fluid and Turbulence,,” *J. Fluid Mech.,* Bd. 519, pp. 301-314, 2004.

[38] H. Chen, S. Kandasamy, S. Orszag und Shock et al., “Extended Boltzmann Kinetic Method For Turbulent Flows,” *Science,* Bd. 301, pp. 633-636, 2003.

[39] H. Chen, C. Teixeira und K. Molvig, “Realization of Fluid Boundary Conditions via Discrete Boltzmann Dynamics,” *Intl. J. Mod. Phys. C,* Bd. 9, Nr. 8, pp. 1281-1292, 1998.

[40] M. Gleason, B. Duncan, J. Walter und et al., “Comparison of Computational Simulation of Automotive Spinning Wheel Flow Field with Full Width Moving Belt Wind Tunnel Results,” *SAE Int. J. Passeng. Cars - Mech. Syst. 8(1),* 2015.

[41] A. Guzman, Y. Cho, J. Tripp und K. Srinivasan, “Further Analyses on Prediction of Automotive Spinning Wheel Flowfield with Full Width Moving Belt Wind Tunnel Results,” *SAE Int. J. Passeng. Cars - Mech. Syst. 10(2),* pp. 600-618, 2017.

[42] K. Sbeih, A. Guzman, D. Barrera Garcia, N. Fougere und et al., “Accurate Automotive Spinning Wheel Predictions Via Deformed Treaded Tire on a Full Vehicle Compared to Full Width Moving Belt Wind Tunnel Results,” SAE Technical Paper 2023-01-0843, 2023.

[43] N. Fougere, M. Demeo, H. Tuit Farquhar, D. Oliveira und et al., “Transient Aerodynamics Simulations of a Passenger Vehicle during Deployment of Rear Spoiler,” SAE Technical Paper 2024-01-2536, 2024.

[44] C. Mockett, T. Knacke und F. Thiele, “Detection of initial transient and estimation of statistical error in time-resolved turbulent flow data,” in *Proceedings of the 8th International Symposium on Engineering Turbulence Modelling and Measurements*, 2010.

[45] W. Schroeder, K. Martin und W. Lorensen, “The Visualization Toolkit, An Object-Oriented Approach To 3D Graphics,” 2006, pp. 359-362.

Simulation-Based Investigation and its Experimental Validation of the Thermal Behavior of a BEV Bus

Henrik Schäfer, Tobias Hellberg, Martin Meywerk

Automotive and Powertrain Engineering
Helmut Schmidt University / University of the Federal Armed Forces Hamburg
Holstenhofweg 85
22043 Hamburg

henrik.schaefer@hsu-hh.de
tobias.hellberg@hsu-hh.de
martin.meywerk@hsu-hh.de

Abstract: Electrification of the public transport sector has a high potential to reduce emissions, especially in metropolitan areas. Due to its strictly scheduled routes and regular idle times, the public transport sector is ideal for the use of battery electric vehicles (BEV). The energy efficiency of a BEV can be increased by the implementation of a thermal management system that is able to decrease the overall energy demand of the system. The thermal management of an electric city bus controls the thermal behavior of the components of the powertrain, such as motor and inverters (drive and auxiliary), as well as the conditioning of the battery system. Moreover, the heating, ventilation, and air conditioning (HVAC) of the drivers' front box and the passenger room play an important role for the energy demand. In this research, the thermal behavior of the important components of an electric city bus is modelled in MATLAB/Simscape in co-simulation with Dymola under the influence of a driving cycle. The heating of the components, geometry and behavior of the cooling circuits as well as the different mechanisms of heat transfer are modelled close to the real system. Moreover, a test setup is developed for the validation of the simulation results. Results are presented, which show that the thermal behavior can be modelled with high accuracy in comparison to the real system. Moreover, potentials to reduce the overall energy demand by improving the thermal energy flows are identified.

Contribution: 2025 FKFS Conference on Vehicle Aerodynamics and Thermal Management
15 – 16 October 2025 | Leinfelden-Echterdingen

1 Introduction

Road transportation is responsible for nearly 75 % of the carbon dioxide (CO_2) emissions in the transportation sector [1]. Besides passenger cars or heavy-duty trucks, which are the largest groups, the public transport sector has an influence on the global emissions, which must not be neglected. Therefore, decarbonization of the public transport sector has the potential to reduce global greenhouse gas emissions and limit the effects of climate change. With its highly scheduled routes and plannable parking times at the depository, the operation profile of urban bus transport is beneficial for electromobility. Therefore, numbers of newly registered electric city buses increase in most German cities [2]. Energy efficiency is even more important for electric city buses than for conventionally powered buses with an internal combustion engine (ICE) with respect to the maximum range. Besides other aspects the thermal management, namely the integration of all thermal systems has a high influence on the energy efficiency of battery electric vehicles (BEV) [3]. The difference with regard to conventional vehicles, where cooling of the ICE is the main task of the thermal system, is the thermal management of the battery systems' temperature. Depending on the ambient conditions, the battery system must be cooled or heated [4]. Very low battery temperatures follow the decrease of the maximum discharge power to avoid increased degradation of the battery cells. Therefore, external heating is necessary at low ambient temperatures which causes an increase in the overall energy demand and a decrease in the maximum vehicle range [5]. On the other hand, lithium-ion batteries generate heat depending on the load cycle [6]. Therefore, the battery cell temperature must be limited to a temperature level of roughly $T_{Cell} = 298.15\,K \pm 10\,K$, especially at high ambient temperatures, which causes an additional energy demand due to a complex cooling demand [7][8][9]. Numerous articles give an overview on the effects of inconvenient temperatures on the battery cells as well as a review on different designs of thermal management systems, for example Ma et al. [10]. Different approaches describe a simulative approach for modelling thermal management of electric vehicles. Most of them focus on passenger cars, like Kiss et al. [11], Reiter et al. [12] or Shelly et al. [13]. Otherwise, the investigation focuses on specific parts of the overall thermal system, like the battery management system [14]. This research considers all thermal components of the electric city bus and their thermal integration. In previous research, the modelling of the thermal behavior of a battery electric city bus in MATLAB/Simscape and Dymola is described [15]; the results show high accuracy with respect to experimental results. Based on a powertrain system consisting of a Voith electrical drive system (VEDS), a Webasto CV Standard Battery system including battery management system (BMS) and an electrical Battery Thermal Management (eBTM) and an Eberspächer heating, ventilation and air conditioning system (HVAC) the simulative results have been experimentally validated. Nevertheless, the described simulation model has to be validated by further experimental results, especially regarding the thermal behavior of the battery system at inconvenient ambient conditions. This is the key aspect of the following research. Adjustments to the former investigations are explained, mentioning changes in the simulation model as well as modifications of the test setup for the experimental

validation. Changes in the simulation model focus on the implementation of the eBTM and its activation and deactivation control mechanisms at cold or hot temperatures whereas the modification of the test setup deals with the pre-conditioning of the battery system to reach the necessary ambient conditions. The presented results show that the eBTM and the thermal behavior of the battery system under influence of external heating or cooling by the eBTM can be modelled accurately with the expanded simulation model. The summary gives an outlook on further research on this topic.

2 Simulation Model

The simulation model is based on MATLAB/Simulink in combination with the MATLAB/Simscape toolbox of physical systems and uses a Co-Simulation with Dymola in combination with elements of the TIL library to implement the HVAC system under usage of the Functional Mock-up Interface (FMI) exchange format. The detailed description of the simulation model of the system containing the VEDS, the Webasto battery system and the HVAC system can be seen in Schäfer et al. [15]. A schematic overview of the system and the simulation model including the interaction with the input signals can be seen in Figure 1.The model uses inputs as mentioned below and calculates the mechanical, electrical and thermodynamic values of the components.

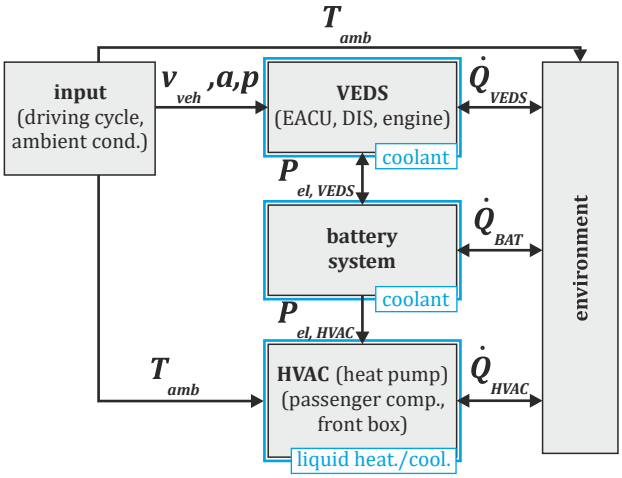

Figure 1: Schematic overview of the system and the simulation model in MATLAB/Simulink and MATLAB/Simscape in combination with Dymola/TIL library [15].

The simulation model contains a mechanical subsystem to calculate the tractive energy demand out of a longitudinal dynamics model. Adding the auxiliaries' power demand, the overall energy demand can be calculated. An electrical subsystem models the electrical behavior of the battery system, for example the calculation of the current state of charge (SoC) or the system voltage depending on SoC and cell temperature. A thermodynamic subsystem models the thermal behavior of each component and provides the components' temperatures as well as cooling or heating behavior of the coolant. The model is tested and validated adequately for medium ambient temperatures in which an external thermal management system for the battery system is not necessary. Further descriptions should explain the relevant modifications for modelling the thermal behavior and the impact on the overall energy demand of the eBTM.

2.1 Electrical Battery Thermal Management (eBTM)

The eBTM is a thermal management module provided by Webasto for conditioning the battery system by a liquid coolant circuit [16]. It consists of three circuits that are modelled in the simulation model as single subsystems connected to each other by exchange of the necessary physical variables. A schematic overview of the simulation model of the eBTM can be seen in Figure 2. The external coolant loop connects the coolant channels of the battery system with the eBTM and especially the heat exchangers of the refrigerant circuit. Moreover, a pump and a high voltage heater (HV heater) are implemented in the liquid circuit. The pump is activated when a cooling or a heating request is sent by the battery management system, the HV heater is only activated when a heating request is active. The HV heater provides a heating power of $P_{HVheater} = 10\,kW$. In the simulation model the external coolant loop is connected with the battery system by an input and an output connection. The physical values of liquid temperature, liquid pressure and volume flow are exchanged between the subsystems. On the other side, the external coolant loop is connected with the refrigerant loop and the heat exchangers. The refrigerant loop consists of two plate heat exchangers operating as evaporators, a climate compressor, one plate heat exchanger operating as condenser and a valve. In the simulation model the cooling power is controlled by defining the compressors' mass flow. The condenser of the refrigerant loop is connected with an internal coolant circuit that contains a second pump, an air-water heat exchanger and a fan.

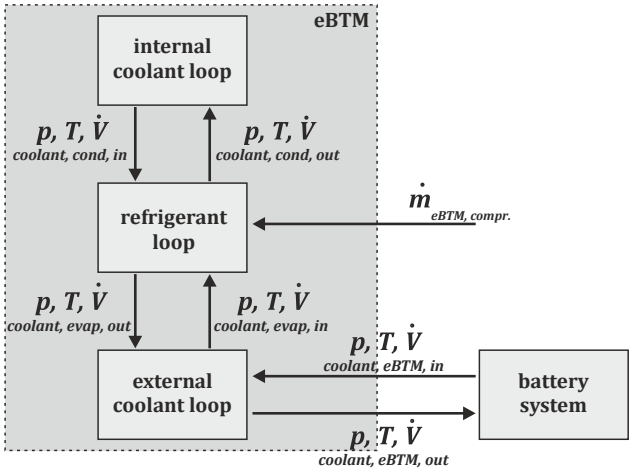

Figure 2: Schematic overview of the eBTM including the interfaces of the circuits in the simulation model.

Battery heating

Battery heating is realized by an HV heater implemented in the external coolant liquid cycle of the eBTM. In the simulation model, an external heat source is added to heat the coolant within the external coolant loop subsystem. The parameterization enables the accurate reproduction of the real system's thermal response. A subsystem named 'control eBTM' includes the logic to activate and deactivate heating based on simple MATLAB/Simulink paths. Heating is activated if the condition (lowest cell temperature $T_{Cell,min} < T_{Cell,min.limit,1}$, activation temperature heating) is active and deactivated if the condition (lowest cell temperature $T_{Cell,min} > T_{Cell,min.limit,2}$, deactivation temperature heating) is fulfilled. Moreover, the power demand of the HV heater is added to the overall power demand of the system and influences the battery capacity and the SoC.

Battery cooling

The cooling behavior of the eBTM is controlled by adjustment of the cooling power of the refrigerant compressor. Cooling is activated if the maximum cell temperature is above the limit ($T_{Cell,max} > T_{Cell,max.limit,1}$, activation temperature cooling). A defined target temperature for the coolant outlet temperature $T_{C,eBTM,out,SetPoint}$ is implemented and must be reached. In the simulation model the control behavior is reached by adjustment of the mass flow of the refrigerant compressor. The necessary mass flow is calculated in the 'control eBTM' subsystem and is proportional to a certain cooling power and a power demand of the refrigerant compressor $P_{compr.,eBTM}$. The cooling mode is deactivated if the maximum cell temperature decreases below a certain value ($T_{Cell,max} < T_{Cell,max.limit,2}$, deactivation temperature cooling). The control loop of the battery cooling can be seen in Figure 3.

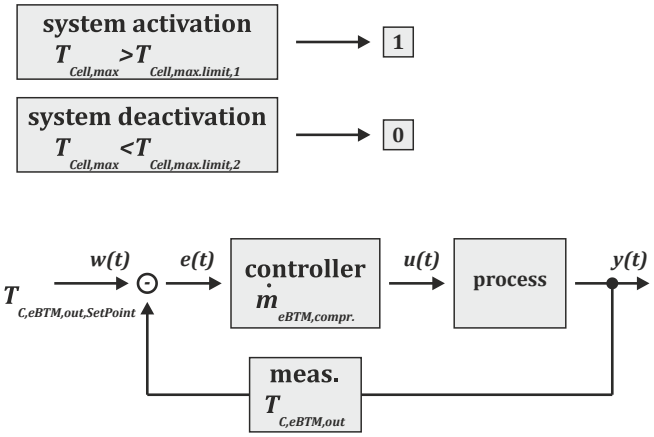

Figure 3: Structure of the control loop of the simulation model of eBTM cooling depending on activation due to high cell temperatures.

Both operating modes of the eBTM depend on basic criteria that must be fulfilled and are defined in the 'control eBTM' subsystem such as activation of the electric connection with the battery system and a minimum available energy in the battery system.

3 Model Validation

The experimental validation of the simulation model is done at the powertrain test rig of the Institute of Automotive and Powertrain Engineering at Helmut Schmidt University in Hamburg (HSU). A detailed description of the test rig and the test setup can be seen in Schäfer et al. [15]. The necessary modifications done in this research focus on the battery system. The battery system platforms' dimensions are $V = 3.20\ m * 2.40\ m * 0.60\ m = 4.61\ m^3$. The platform is enclosed in a construction of sandwich profiles manufactured of 40 mm of Polyisocyanurat foam with a thermal conductivity of $\lambda = 0.55\ \frac{W}{m^2 K}$. Figure 4 shows an overview of the test setup at the institutes' power and inertia test rig (PAISI) on the left side as well as the enclosed battery system in detail on the right side. The eBTM, due to its interaction with the environment, and the vehicle interface box (VIB), which establishes the connection between the battery system and the power electronics of the VEDS, are located outside of the housing.

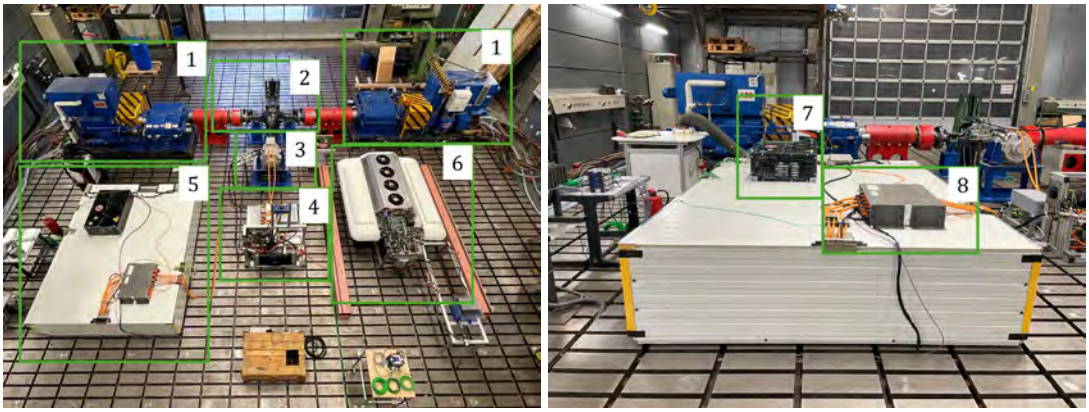

Figure 4: Modified test setup for the experimental validation of the modelled system on the PAISI of the Institute of Automotive and Powertrain Engineering (left). Components: (1) electric machines, (2) axle, (3) electric motor, (4) power electronics, (5) battery system, (6) HVAC system.
Detailed view on the thermal isolated battery system (right).
Components: (7) eBTM, (8) VIB.

The setup enables the preconditioning of the battery system at different ambient temperatures. The preconditioning is done before the test starts. During this time period the eBTM is deactivated by interrupting the power supply. Otherwise, the eBTM would be activated too early and prevent preconditioning. Two different procedures have to be established in order to cool down or heat up the ambient temperature within the housing. The different approaches can be seen in Figure 5.

Preconditioning: Cooling

In order to reduce the temperature of the battery system the cold-water circuit of the HVAC system of the test setup is used. It is connected detachable to the cooling circuit of the battery system by a lockable T-connection. Once the target temperature is reached, the connection is closed and the system's initial state is restored. The coolant temperature reaches values of $T_{HW,HP,out} = 277.15\ K$.

Preconditioning: Heating

To increase the ambient temperature of the battery system in the housing a heat blower is installed that supplies hot air. A target inlet temperature of $T_{amb,BAT,in} = 318.15\ K$ is adjusted and verified by a temperature sensor. Under this condition, a constant ambient air temperature inside the housing is reached and monitored by two additional temperature sensors at two different places in order to identify a homogenous temperature distribution. The increased ambient temperature follows an increase in the battery cell temperature. Once a certain value is reached the test can be started. The blower stays operational in order to maintain the ambient temperature at a constant level.

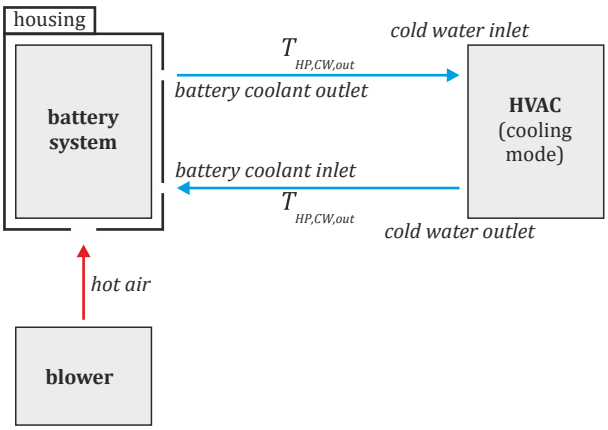

Figure 5: Implementation of the preconditioning at the test setup (heating and cooling of the battery system).

4 Simulation results

The high accuracy of the mechanical, electrical and thermal subsystem under neutral ambient conditions ($T_{amb} = \sim 293.15\ K$) is already described in detail in Schäfer et al [15]. The following evaluation is focused on the thermal effects affecting the battery system at low or high ambient temperatures with focus on the additional energy demand due to the activation of the battery thermal management system.

4.1 Low ambient temperatures

The simulation of the battery system at low ambient temperatures uses the initial temperature values of the system validation for battery cell temperature as well as the coolant temperature in the battery system that are reached under influence of the described cooling procedure. The ‘control eBTM’ subsystem acts similar to the real system and reacts to the heating request of the BMS because of the low battery cell temperature. Figure 6 shows the key figures of the thermal behavior of the battery system based on the defined driving cycle $v_{veh}(t)$ in comparison of simulation values and measurement data of the experimental validation. The external high voltage heater is activated due to the low initial battery cell temperature with a delay caused by the timespan to start and connect the system. The energy demand is $P_{HVheater} \approx 10\ kW$. When reaching the defined cell temperature, it is deactivated and the energy demand is zero again.

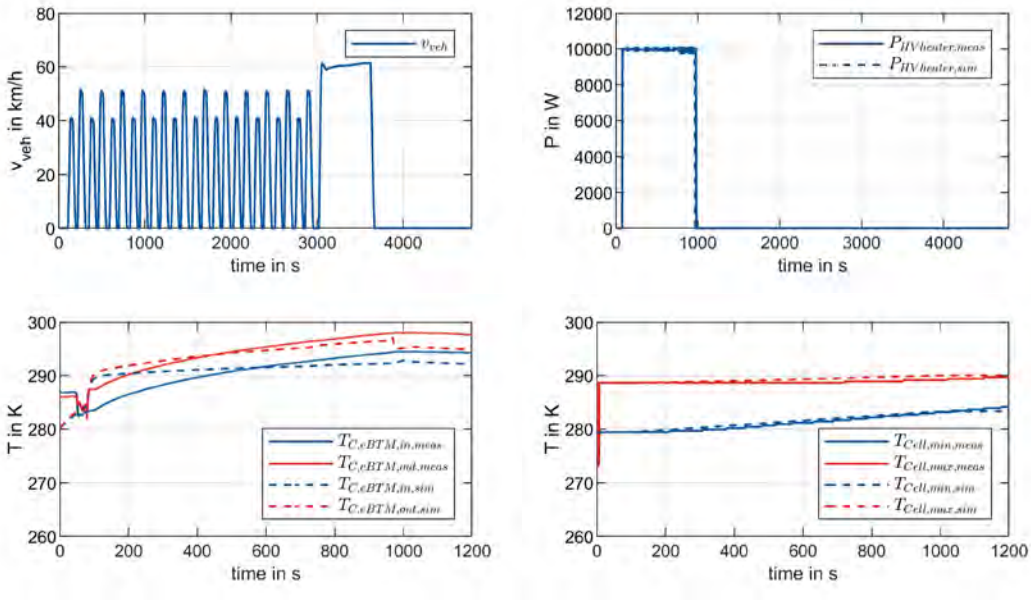

Figure 6: Simulation results in comparison to measurement data of the experimental validation at low ambient temperatures. Driving cycle $v_{veh}(t)$, power demand of HV heater $P_{HVheater}(t)$, battery coolant temperatures $T_{C,eBTM}(t)$ and battery cell temperatures $T_{Cell}(t)$ during heating period.

The comparison of the simulation results and the experimental values show a high accuracy regarding the thermal key figures. Considering the additional energy demand of the HV heater $W_{el,HVheater}$ (calculation in (4.1) and (4.2)) a deviation between the measured and the simulative results of < 2 % can be seen.

$$W_{el,HVheater,sim} = \int P_{HVheater,sim} = 2.46\ kWh \tag{4.1}$$

$$W_{el,HVheater,meas} = \int P_{HVheater,meas} = 2.50\ kWh \tag{4.2}$$

Moreover, the temperature curve of the coolant temperature shows a similar heating trend, where it should be noted that the gradient of the simulative coolant temperature increase at the beginning is higher than the measured result. A need for further refinement in the parameterization of the heat transfer between the HV heater and the coolant has been identified. Nevertheless, the increase in battery cell temperature can be represented with high accuracy.

4.2 High ambient temperatures

For simulating the thermal behavior under high ambient conditions, the initial state is defined by the high-temperature measurement obtained from the specified heating procedure. The BMS sends a cooling request that activates the eBTM in cooling mode. The eBTM control acts to reach a defined target liquid temperature at its outlet of $T_{C,eBTM,out} = 298.15\ K$ in order to limit the battery cell temperature. Undercooling is not targeted to avoid efficiency losses of the battery system or even its damage. The control structure is discrete and results in a stepped power demand of the refrigerant compressor of the eBTM which is shown in Figure 7. Moreover, an oscillating coolant temperature $T_{C,eBTM}$ can be seen because of the dynamic cooling behavior of the eBTM.

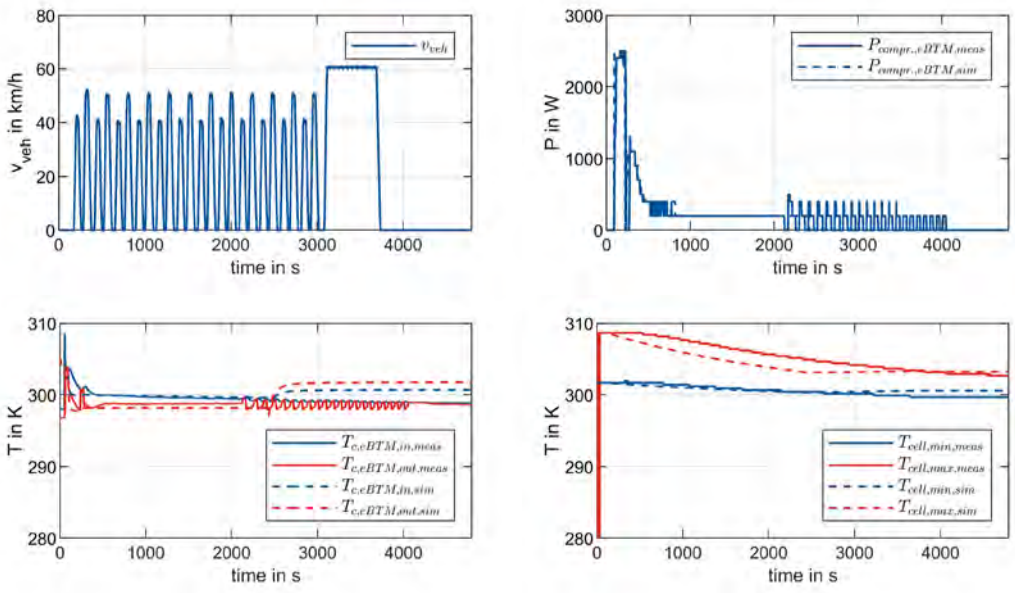

Figure 7: Simulation results in comparison to measurement data of the experimental validation at high ambient temperatures. Driving cycle $v_{veh}(t)$, power demand of eBTM compressor $P_{compr.,eBTM}(t)$, battery coolant temperatures $T_{C,eBTM}(t)$ and battery cell temperatures $T_{Cell}(t)$.

The comparison of the temperature values shows a high accuracy in the trend of the temperature decrease. The decrease of the simulated battery cell temperature shows a premature behavior that must be investigated. That follows a premature deactivation of the cooling system by reaching the target temperature of the battery cells. The additional energy demand $W_{el,compr.,eBTM}$ is calculated in (4.3) and (4.4) and therefore varies by values of roughly 10 %.

$$W_{el,compr.,eBTM,sim} = \int P_{compr.,eBTM,sim} = 0.27\ kWh \tag{4.3}$$

$$W_{el,compr.,eBTM,meas} = \int P_{compr.,eBTM,meas} = 0.30\ kWh \tag{4.4}$$

5 Summary / Conclusion

The results show that the thermal behavior of the components of a battery electric city bus, especially the calculation of the thermal key values of the battery system and its thermal management, can be modelled in MATLAB/Simscape. In addition to the results presented in the previous work by Schäfer et al. [15], the thermal behavior of the battery system at inconvenient ambient temperatures is validated by experiments on the test rig under usage of a modified test setup. In previous research, potentials have been identified to decrease the overall energy demand by combining the thermal liquid circuits and using synergy effects. The next step is the implementation of a thermal management module developed by Eberspächer to exploit the potentials and the implementation of this thermal management system in the simulation model including the experimental validation. Exemplary potentials to reduce the overall energy demand are the utilization of the engines' waste heat or the conditioning of the battery system under usage of the hot and cold liquid circuit of the HVAC. Factors such as passenger comfort and energy efficiency must be brought to harmony. The simulation model should identify an optimized operating strategy using the available heat flows to minimize the energy demand. The superior goal of the research is to increase the efficiency of the system and the busses range by decreasing the overall energy demand under influence of a certain driving cycle and certain ambient conditions.

6 Reference list

[1] Climate TRACE. (July 16, 2025). Distribution of carbon dioxide emissions produced by the transportation sector worldwide in 2024, by sub sector [Graph]. In Statista. Retrieved August 18, 2025, from https://www.statista.com/statistics/1185535/transport-carbon-dioxide-emissions-breakdown/

[2] PricewaterhouseCoopers GmbH, "E-Bus Radar," 2025

[3] Li, B., Kuo, H., Wang, X. et al. Thermal Management of Electrified Propulsion System for Low-Carbon Vehicles. Automot. Innov. 3, 299–316 (2020). https://doi.org/10.1007/s42154-020-00124-y

[4] A. Lajunen, Y. Yang and A. Emadi, "Recent Developments in Thermal Management of Electrified Powertrains," in IEEE Transactions on Vehicular Technology, vol. 67, no. 12, pp. 11486-11499, Dec. 2018, https://doi.org/10.1109/TVT.2018.2876315.

[5] Steinstraeter, M.; Heinrich, T.; Lienkamp, M. Effect of Low Temperature on Electric Vehicle Range. World Electr. Veh. J. 2021, 12, 115. https://doi.org/10.3390/wevj12030115

[6] Liu, G., Ouyang, M., Lu, L. et al. Analysis of the heat generation of lithium-ion battery during charging and discharging considering different influencing factors. J Therm Anal Calorim 116, 1001–1010 (2014). https://doi.org/10.1007/s10973-013-3599-9

[7] Pesaran, A.A., "Battery Thermal Management in EVs and HEVs: Issues and Solutions," in Advanced Automotive Battery Conference, 2001.

[8] Ianiciello, L., Biwolé, P.H., and Achard, P., "Electric Vehicles Batteries Thermal Management Systems Employing Phase Change Materials," Journal of Power Sources 383 (2018): 03787753, https://doi.org/10.1016/j.jpowsour.2017.12.071.

[9] Park, I., Kim, C., Lee, H. et al. Comprehensive Analysis of Battery Thermal Management and Energy Consumption in an Electric Vehicle: Impact of Driving Modes and Ambient Temperatures. Int.J Automot. Technol. 26, 621–636 (2025). https://doi.org/10.1007/s12239-024-00202-8

[10] Ma, S., Jiang, M., Tao, P. et al. Temperature effect and thermal impact in lithium-ion batteries: A review. Progress in Natural Science: Materials International, Volume 28, Issue 6 (2018), https://doi.org/10.1016/j.pnsc.2018.11.002

[11] Kiss, T., Lustbader, J., and Leighton, D., "Modeling of an Electric Vehicle Thermal Management System in MATLAB/Simulink," SAE Technical Paper 2015-01-1708, 2015, https://doi.org/10.4271/2015-01-1708.

[12] C. Reiter, J. Dirnecker and M. Lienkamp, "Efficient Simulation of Thermal Management Systems for BEV," 2019 Fourteenth International Conference on Ecological Vehicles and Renewable Energies (EVER), Monte-Carlo, Monaco, 2019, pp. 1-8, https://doi.org/10.1109/EVER.2019.8813683.

[13] T. Shelly, J. A. Weibel, D. Ziviani and E. A. Groll, "A Dynamic Co-Simulation Framework for the Analysis of Battery Electric Vehicle Thermal Management Systems," 2022 21st IEEE Intersociety Conference on Thermal and Thermomechanical Phenomena in Electronic Systems (iTherm), San Diego, CA, USA, 2022, pp. 1-8, https://doi.org/10.1109/iTherm54085.2022.9899690.

[14] Pesaran, A., “Battery thermal models for hybrid vehicle simulations," 2002 Journal of Power Sources, https://doi.org/10.1016/S0378-7753(02)00200-8.

[15] Schäfer, H., Meywerk, M., and Hellberg, T., “Simulation-Based Investigation and its Experimental Validation of the Thermal Behaviour of a Battery Electric City Bus,” SAE Technical Paper 2025-01-0266, 2025, https://doi.org/10.4271/2025-01-0266

[16] Webasto, “electrical Battery Thermal Management (eBTM)”, accessed August 2025, https://www.webasto.com/de-de/batterie/standardisierte-batterie-und-thermomanagement/electrical-battery-thermal-management.html

Numerical Investigation of Whistling Noise from Vehicle Side Mirrors

Xing Peng[1], Jiang Zuxiao[1,2,3], Chen Shengxian[2]

1. Shanghai Ground Vehicle Wind Tunnel Center, Tongji University, No. 4800, Caoan Highway, Jiading District, Shanghai;

2. Product Development Department, SAIC Volkswagen Automotive Co., Ltd., No. 63, Luopu Road, Jiading District, Shanghai;

3. Tongji University School of Automotive Studies, Tongji University, No. 4800, Caoan Highway, Jiading District, Shanghai

xingpeng@tongji.edu.cn

jiangzuxiao@csvw.com

chenshengxian@csvw.com

Abstract: Under specific driving conditions, the airflow passing through the vehicle's side mirrors can generate high-frequency noise with narrowband frequency characteristics, commonly referred to as whistling. The causes of whistling are multifaceted and include factors such as gaps, shape, and periodic airflow motion. Different mechanisms of whistling generation necessitate distinct solutions. In this paper, whistling was detected during subjective evaluation in the wind tunnel. Through wind tunnel testing and acoustic array analysis, the frequency of the whistling was identified, and the airflow velocity and yaw angle were determined. Subsequently, numerical analysis of the wall-bounded airflow near the side mirrors was conducted using a transitional transport function incorporating intermittency and momentum thickness Reynolds number corrections. The analysis revealed that the separation and reattachment of the laminar boundary layer led to localized turbulence enhancement, which was identified as the cause of whistling. Based on these findings, two optimization schemes for promoting early transition of the laminar flow were proposed and validated through simulations. The simulation results demonstrated that designs incorporating steps or modifications to surface roughness could effectively

Contribution: 2025 FKFS Conference on Vehicle Aerodynamics and Thermal Management
15 – 16 October 2025 | Leinfelden-Echterdingen

prevent the separation of the laminar boundary layer, thereby eliminating the generation of whistling. Moreover, the simulation results were found to be consistent with the experimental findings. This study not only elucidated the mechanism of whistling generation due to the shape of the side mirrors but also provided a theoretical basis and technical support for the design optimization of vehicle side mirrors.

1 Intruduction

As a complex mechanical system, a vehicle generates noise from multiple sources. While traditional automotive noise arises from the powertrain, tires, and aerodynamic effects, wind noise has become increasingly dominant, particularly with the growing use of high-speed urban roads and electric vehicles. The absence of engine noise in electric vehicles further amplifies the perception of wind-induced sound, making aerodynamic noise control a critical factor in enhancing in-cabin sound quality. Wind noise control typically involves three main strategies: leakage sealing, acoustic package design, and aerodynamic shape optimization. Leakage control focuses on sealing elements like glass and door seals; acoustic packages address broadband insulation, especially across firewall and floor panels. In contrast, aerodynamic shape design targets unsteady flow phenomena around exterior features-most notably the A-pillar and rearview mirror, which are known contributors to wind noise. Among these, the rearview mirror is particularly sensitive due to its protruding geometry. Unlike sealing and acoustic strategies, mirror-induced whistling noise lacks a well-established theoretical framework. Whistling is often triggered by shear flow instabilities when the flow reaches a critical velocity. Chanaud[1] classified flow-induced feedback mechanisms into three types: Type I involves purely hydrodynamic feedback from vortex shedding; Type II includes near-field acoustic feedback; and Type III covers far-field acoustic feedback, such as cavity resonance. Rearview mirror whistling is generally associated with Type II or III, due to its coupling of flow and sound. Although aerodynamic noise has been widely studied, mirror-specific whistling research remains limited. Prior works have examined general flow instabilities. Hucho[2] discussed some fundamental mechanisms of fluid, but this is usually limited to the development of laminar and turbulent boundary layers on flat plates or general shapes (airfoils or cylinders). Lucas[3] believes that the basic excitation mechanisms of whistling are mainly divided into mixing layers, jets, wakes, vortices, and cavities. Yang[4] analyzed the feedback mechanism and considered that the characteristic steps of feedback are the process of vortex generation, vortex shedding, aerodynamic noise generation, vortex regeneration, re-shedding, and aerodynamic noise regeneration. Vaik[5-6] studied an edge-tone configuration, which consists of a planar free jet impinging on a wedge-shaped object. They conducted a

parametric study on the velocity profiles of different types of jets by changing the average exit velocity of the jet and the distance from the nozzle to the wedge configuration, and proposed a set of formulas for predicting the frequency of edge tones. Sun[7] investigated the flow instability of a two-dimensional open cavity by varying the free-stream Mach number from 0.1 to 1.6 and provided stability curves over a wide range of Mach and Reynolds numbers. Yamouni[8] conducted a global stability analysis of open cavities, explaining that under incompressible conditions (Ma<0.3), the flow is affected by global instabilities due to the Kelvin-Helmholtz effect in the shear layer and, this instability is intensified by fluid dynamic pressure feedback. Under compressible conditions, as the Mach number decreases, all unstable global modes gradually transition to incompressible (Ma>0.3) shear layer modes. Lounsberry[9] experimentally studied the fluid changes in the laminar separation region on the rearview mirror housing. The boundary layer starts as laminar and then transitions to turbulent, and attempts were made to induce turbulence in the boundary layer early to eliminate whistling. Huang Lina[10] used the oil flow method in wind tunnel tests to observe the flow state on the vehicle's longitudinal symmetry plane and the side window position of the rearview mirror, but did not observe and analyze the flow phenomena on the surface of the rearview mirror. Guan Peng et al.[11] analyzed and optimized whistling and broadband noise through a combination of simulation and experiments, but did not find a specific method for analyzing rearview mirror whistling. Jiang Zuxiao et al.[12] measured the aerodynamic noise characteristics in the rearview mirror wake region through wind tunnel tests, analyzed the noise performance of the rearview mirror at different vehicle speeds, and solved the rearview mirror whistling problem through experimental research. Wu Haibo et al.[13] used a new transition model to simulate the fluid changes in the laminar boundary layer on the rearview mirror surface and validated the effectiveness of the method through wind tunnel tests. However, none of the above studies have provided a comprehensive explanation of the rearview mirror shape whistling problem.

In this study, wind tunnel experiments on a clay prototype vehicle revealed a whistling phenomenon at specific flow speeds and yaw angles. Acoustic arrays were used to localize the sound source and identify its narrowband frequency. The cause was traced to geometric features of the rearview mirror. A numerical simulation using the Local Correlation-based Transition Model (LCTM) was conducted to analyze shear stress, momentum thickness, and turbulent kinetic energy near the mirror surface. The results showed that laminar boundary layer separation and reattachment led to localized turbulence amplification, which triggered the whistling. Based on the findings, two design strategies-introducing a step and modifying surface roughness-were proposed to promote early transition and prevent separation. Wind tunnel validation confirmed the effectiveness of these solutions, providing practical guidance for the aerodynamic design of noise-optimized rearview mirror.

2 Problem identification and diagnosis

2.1 Problem identification

2.1.1 Test facility

The experimental tests were conducted at the Full-Scale Aeroacoustic Wind Tunnel of the Shanghai Ground Transportation Wind Tunnel Center, Tongji University. This facility is a 3/4 open-return wind tunnel with three open sides at the nozzle and one side connected to the ground. During testing, the prototype vehicle was fixed at the center of the turntable located on the wind tunnel balance platform. For this study, both the boundary layer suction system and the moving ground belt were deactivated during operation, as per standard acoustic testing protocols[14].

2.1.2 Subjective and Objective Evaluation

The evaluation was divided into two parts: subjective assessment and objective testing. Subjective evaluation focused on the overall perception of the external acoustic field in the wind tunnel under different speeds and yaw angles. Objective testing included external field measurements and acoustic imaging to verify the presence and characteristics of aerodynamic noise.

Based on the known generation and propagation mechanisms of aerodynamic noise, the tests considered the following key factors:

(1) Aerodynamic noise becomes dominant at high speeds, typically above 100 km/h.

(2) Crosswind conditions not only affect driving stability but also significantly influence wind noise characteristics. Therefore, yaw angles were introduced during the tests.

Accordingly, the subjective evaluation was conducted at speeds between 100 km/h and 140 km/h and yaw angles of ±5° and ±10°. During evaluation, a distinct whistling noise was audibly detected on the right-hand side of the vehicle exterior when the yaw angle was -5° and the wind speed approached 125 km/h.

To confirm the existence of the whistling noise, objective testing was conducted. The center of the balance turntable was defined as the origin (0, 0, 0), with a diameter of 11 m. The X-axis pointed from the nozzle toward the collector, while the Y-axis was perpendicular to it. Two free-field microphones were placed symmetrically at a height of 1.2 m from the ground, located at coordinates (0, ±6 m, 1.2 m), as illustrated in Figure 1.

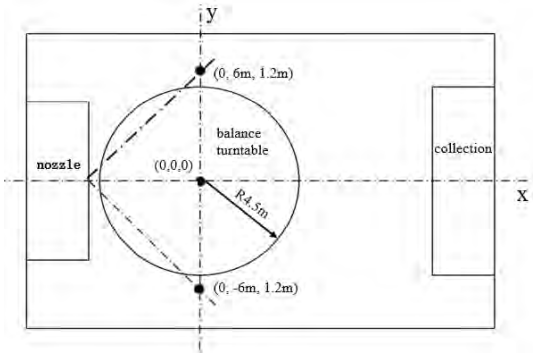

Figure 1: Schematic diagram of the test setup

The data acquisition period was 10 seconds, and the frequency range for noise analysis was 500–10,000 Hz. The FFT results are shown in Figure2.

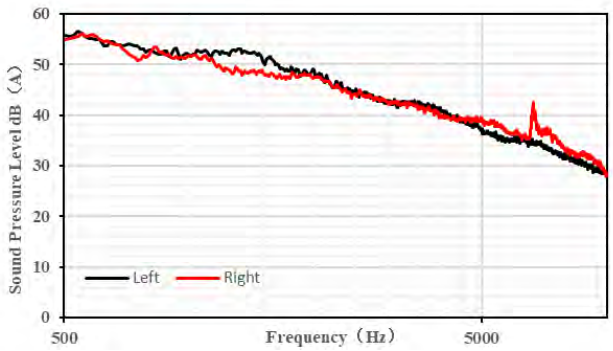

Figure 2: SPL results from external flow-field microphones

As shown in Figure 2, the sound pressure level (SPL) on the vehicle's right-hand side generally decreases with increasing frequency. However, a narrowband peak is observed at 6668 Hz, where the right-side SPL is 8.3 dB(A) higher than the left side. This result aligns with the subjective evaluation, confirming the presence of a whistling noise originating from the vehicle's right-side exterior flow field.

2.2 Diagnostic Process

Whistling noise can originate from various aerodynamic sources, including gap-induced whistling, geometry-induced resonance, and periodic flow instabilities. To identify the precise source and location of the noise, multiple experimental techniques were employed within the wind tunnel.

2.2.1 Acoustic Array Testing

An acoustic array is a visual-acoustic measurement system composed of multiple synchronized microphones, as illustrated in Figure 3. It can generate acoustic images or animations to help localize and characterize noise sources. In this study, a 120-channel spiral microphone array was positioned on the right-hand side of the test vehicle, carefully placed outside the influence of high-speed airflow.

Targeted acoustic imaging and scanning were performed for key regions including the front grille, front wheels, and rearview mirror. The objective was to identify the spatial distribution of aerodynamic noise across these areas.

Figure 3: Acoustic array test setup

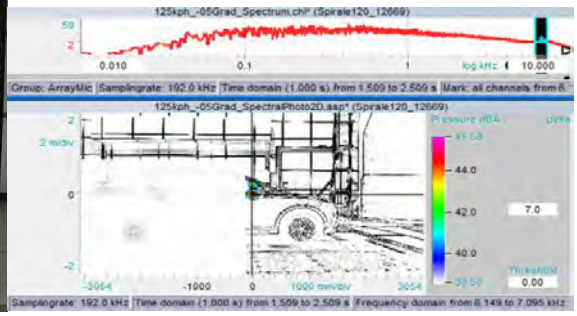

Figure 4: Acoustic imaging result from microphone array

The measurement results from the acoustic array are shown in Figure 4. A clear tonal peak was observed in the frequency band between 6149 Hz and 7095 Hz, consistent with the previously identified peak at 6668 Hz from the external field SPL measurements. These findings strongly confirm that the whistling noise originates from the rearview mirror region.

2.2.2 Source Confirmation of Whistling Noise

Following the acoustic array localization, the rearview mirror was confirmed as the origin of the whistling noise. However, the exact noise generation mechanism remained unclear. Based on structural analysis, two possible mechanisms were hypothesized: gap-induced whistling and geometry-induced resonance. To eliminate the first possibility, all gaps on the mirror surface were sealed with adhesive tape to block airflow entering internal cavities. After sealing, the whistling noise persisted during testing. Therefore, the source was attributed to an unfavorable surface geometry, suggesting that the noise was primarily caused by geometry-induced whistling.

3 Analysis of Underlying Mechanism

3.1 Linear Stability Theory

Boundary layer disturbances are inherently complex, and the transition from laminar to turbulent flow remains a key topic in fluid dynamics. Among various predictive models, linear stability theory (LST) is one of the most widely used. LST assumes that disturbances superimpose linearly on a steady base flow and that their amplitudes are sufficiently small not to affect the mean flow. Under this framework, the flow can be decomposed into a base state and small-amplitude perturbations, often expressed as temporal or spatial waves. By examining the growth rate of these disturbances, LST provides a theoretical means to predict flow instability onset conditions[15].

Although LST cannot fully describe the physical mechanisms of transition or predict nonlinear developments, it remains a powerful tool in understanding early-stage instability and guiding flow control strategies. It has also helped researchers analyze natural and bypass transition processes by capturing the evolution of Tollmien–Schlichting (T-S) waves and their interaction with vortical structures[16].

3.2 Tollmien–Schlichting (T-S) Waves

According to Chanaud's classification of whistling mechanisms, the rearview mirror noise can be attributed to a Type II feedback loop. This involves laminar boundary layer instabilities triggered by external disturbances, which manifest initially as two-dimensional T-S waves. These waves propagate along the surface, gradually evolving into three-dimensional structures, inducing low-amplitude pressure fluctuations while the flow remains nominally laminar.

As disturbances amplify, secondary instabilities emerge, generating turbulent patches and localized noise radiation. Part of the acoustic energy feeds back into the upstream flow, promoting earlier transition to turbulence near the mirror front. The resulting turbulence further energizes the feedback loop, forming a self-sustained T-S cycle that leads to discrete tonal peaks in the sound spectrum—characteristic of aerodynamic whistling consistent with Type II resonance.

This phenomenon, first hypothesized by Prandtl and later formalized by Tollmien and Schlichting[17], forms a natural instability pathway in low-turbulence environments. In particular, laminar separation bubbles provide a fertile ground for T-S wave amplification, with separation and reattachment enhancing the flow's receptivity to acoustic excitation. Such feedback between unstable shear layers and surface

geometry drives the sustained tonal noise observed in this study.

The interaction between weak acoustic perturbations and transitional shear layers not only underscores the sensitivity of the boundary layer to external forcing but also demonstrates how seemingly minor acoustic energy can reinforce turbulence. This feedback loop offers critical insight into the physical mechanism behind mirror-induced whistling and supports the use of T-S wave theory in aerodynamic noise diagnostics.

4 Numerical Analysis

In aerodynamics, transition is typically the result of flow instability, where small disturbances grow exponentially and ultimately trigger nonlinear breakdown into turbulence. One key mechanism is separation-induced transition, in which a laminar boundary layer separates under an adverse pressure gradient. Transition then develops within the detached shear layer, and the now-turbulent boundary layer may reattach under a strong favorable pressure gradient.

In this study, a transition model based on turbulence modeling was applied—specifically, the Local Correlation-based Transition Model (LCTM). The LCTM is a transport-equation-based model that relies exclusively on local flow variables, enabling efficient and practical integration into Reynolds-Averaged Navier–Stokes (RANS) simulations. It is particularly well-suited for predicting transitional flows where laminar regions exist within a predominantly turbulent boundary layer, as is common in aerodynamic whistling problems.

4.1 $\gamma - Re_\theta$ Transition Model

The LCTM adopted in this study is based on the two-equation correlation-based transition model developed by Menter et al[18-19]. This hybrid model retains the original turbulence model formulation near the wall and modifies it in the outer boundary layer to account for transition onset and progression. The governing transport equations for intermittency (γ) are expressed as:

$$\frac{\partial(\rho\kappa)}{\partial t} + \nabla\cdot(\rho U\kappa) = \nabla\cdot\left(\left(\mu + \frac{\mu_t}{\sigma_\kappa}\right)\nabla\kappa\right) + P_\kappa - D_\kappa \qquad (1)$$

$$\frac{\partial(\rho\omega)}{\partial t} + \nabla\cdot(\rho U\omega) = \nabla\cdot\left(\left(\mu + \frac{\mu_t}{\sigma_\kappa}\right)\nabla\omega\right) + \frac{\gamma}{v_t}P_\kappa - \beta\rho\omega^2 + \ldots$$

$$+2(1-F_1)\frac{\rho\sigma\omega_2}{\omega}\nabla\kappa:\nabla\omega \quad (2)$$

The terms, P_κ and D_κ in the model represent the production and dissipation of turbulent kinetic energy. ρ denotes the fluid density. U is the velocity field. μ_t is the turbulent viscosity. ω is the specific dissipation rate of turbulence.

The baseline turbulence model is inherently suitable for fully turbulent boundary layers. However, to accurately simulate laminar boundary layers and transitional regions, modifications to the production and dissipation terms of turbulent kinetic energy are required. For this purpose, a variable known as turbulence intermittency (γ) is introduced, which represents the time-averaged fraction of turbulent fluctuations within the boundary layer.

$$\frac{\partial(\rho\gamma)}{\partial t}+\nabla\cdot(\rho U\gamma)=\nabla\cdot\left(\left(\mu+\frac{\mu_t}{\sigma_\gamma}\right)\nabla\gamma\right)+P_\gamma-D_\gamma \quad (3)$$

$$\frac{\partial(\rho\omega)}{\partial t}+\nabla\cdot(\rho U\omega)=\nabla\cdot\left(\left(\mu+\frac{\mu_t}{\sigma_\kappa}\right)\nabla\omega\right)+\frac{\gamma}{v_t}P_\kappa-\beta\rho\omega^2+2(1-F_1)\frac{\rho\sigma\omega_2}{\omega}\nabla\kappa:\nabla\omega(2)$$

The terms , P_κ and D_κ in the model represent the production and dissipation of turbulent kinetic energy. ρ denotes the fluid density. U is the velocity field. μ_t is the turbulent viscosity. ω is the specific dissipation rate of turbulence.

The baseline turbulence model is inherently suitable for fully turbulent boundary layers. However, to accurately simulate laminar boundary layers and transitional regions, modifications tu the production and dissipation terms of turbulent kinetic energy are required. For this purpose, a variable known as turbulence intermittency (γ) is introduced, which represents the time-averaged fraction of turbulent fluctuations within the boundary layer. Thr transport equation for intermittency is expressed as:

$$\frac{\partial(\rho\gamma)}{\partial t}+\nabla\cdot(\rho U\gamma)=\nabla\cdot\left(\left(\mu+\frac{\mu_t}{\sigma_\gamma}\right)\nabla\gamma\right)+P_\gamma-D_\gamma \quad (3)$$

The production term of turbulence intermittency γ governs the length and onset of the transition region P_γ. It is defined as:

$$P_\gamma=F_{length}c_{\alpha1}\rho S(\gamma F_{onset})^{0.5}(1-c_{e1}\gamma) \quad (4)$$

Here, S is the local strain rate magnitude. F_{length} is a non-dimensional function controlling the length of the transition region. F_{onset} is another non-dimensional function used to control the onset location of transition. Both of them are non-dimensional functions used to control the intermittency transport equation within the boundary layer. They modulate the growth and onset of intermittency based on local

flow conditions. The destruction or relaminarization source term in the intermittency equation is defined as:

$$D_\gamma = c_{\alpha 2}\rho\Omega\Upsilon F_{turb}(c_{e2}\gamma - 1) \quad (5)$$

Here, Ω represents the vorticity magnitude, which serves to prevent the destruction of intermittency in the freestream caused by high strain rates. The model constant: $c_{\alpha 1} = 2.0,\ c_{\alpha 2} = 0.06$, It controls the strength of the destruction term and ensures that the entire term remains less than the turbulent Prandtl number $c_{e1} = 1.0,\ c_{e2} = 50.0$. It sets the lower bound of intermittency, and a threshold value of 50 is sufficiently low to preserve laminar flow in the boundary layer. F_{turb}It is used to deactivate the destruction term in fully turbulent regions[18].

4.2 Numerical Simulation Model

To reproduce the whistling caused by the rearview mirror geometry, a simplified vehicle model was constructed. Non-critical features such as the front grille, underbody, and minor grooves were sealed to reduce computational cost. Key flow-affecting elements—such as the A-pillar, windshield, and detailed mirror geometry (gaps, steps)—were retained. A half-car model was used based on wind tunnel observations indicating whistling on the right side. The computational domain was defined with the inlet placed 4 car lengths ahead of the front, the outlet 8 car lengths downstream, lateral boundaries 5 car widths from the side, and the top boundary 8 car heights above the roof. The setup is shown in Figure 5, and boundary conditions are listed in Table 1. According to wind tunnel data, the inlet velocity was set to 125 km/h, and the outlet pressure was set to 0 Pa.

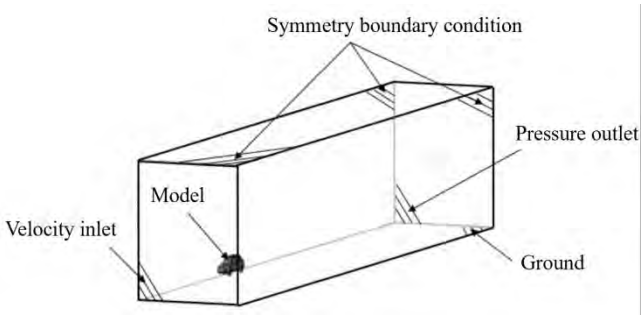

Figure 5. Computational domain of the numerical simulation model.

Table 1. Boundary conditions of the numerical simulation model.

Boundary	Type	Rematks

Inlet	Velocity inlet	145km/h，non-reflecting
Outlet	Pressure outlet	0 Pa, non-reflecting
Side	Symmetry boundary condition	slide

Table 2 summarizes the numerical discretization schemes used in the simulation.

Table 2. Discretization schemes employed in the CFD simulation.

Equations	Scheme
interpolationSchemes	linear
snGradSchmes	limited corrected 0.33
gradSchemes	cellLmited Gauss linear 1
divSchemes	div(phi, U):bounded Gauss linearUpwindV grad(U)
laplacianSchemes	bounded Gauss upwind Gauss linear limited corrected 0.33

To accurately capture the flow near the rearview mirror, local mesh refinement was applied to critical components including the mirror body, A-pillar, and windshield. Table 3 presents the mesh parameters used. The maximum surface mesh size in the computational domain was set to 512 mm. A total of 12 prism layers were generated near walls to resolve boundary layers, with the first-layer height of 0.01 mm and a growth rate of 1.2.

Table 3. Mesh parameters of the simulation model.

Main parameters			
Rearview mirror	Min_0.25mm Max_0.5mm	Front side window glass	1mm
A/B pillars & rain strips	1mm	Rear window glass	2mm
Windshield	8mm	Remaining areas	20mm

To better capture the whistle-generating flow near the side mirror, the mesh around the mirror was refined with 15 boundary layer layers, starting from a first-layer height of 5e-6 m and a growth rate of 1.3. A local refinement zone of 4 mm was also added near the mirror.

4.3 Flow Field Analysis

Using the LCTM transition model, simulations were conducted under a 125 km/h inlet velocity and a yaw angle of -5 degree, with 5000 steady-state iterations. Flow characteristics near the side mirror were evaluated via wall shear stress, momentum thickness, and turbulent kinetic energy (TKE) to assess the potential for tonal noise generation.

4.3.1 Wall Shear Stress

Figure 8 presents the surface velocity contour around the side mirror. As shown in the red-circled region, there is a notable reversal in wall shear stress direction (from negative to positive), indicating a progressive deceleration of near-wall airflow, potentially down to zero velocity- as further illustrated in the velocity field in Figure 7. This variation in velocity results in a local increase in wall shear stress, suggesting that intermittency in the laminar boundary layer is beginning to rise in this area.

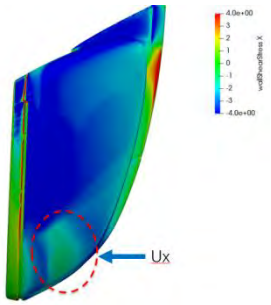

Figure 6. Wall Shear Stress

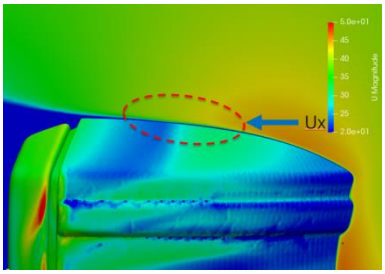

Figure 7. Surface Velocity

4.3.2 Momentum Thickness

As shown in Figure 8, the momentum thickness decreases after initially increasing, indicating a transition from laminar to turbulent boundary layer. The enhanced momentum mixing due to velocity fluctuations in the turbulent layer leads to an increase in momentum thickness. In other words, the variation in momentum thickness reflects the occurrence of boundary layer separation. Momentum thickness is closely related to surface drag. According to the von Kármán integral relation, its rate of change is directly linked to wall shear stress-consistent with the changes observed in shear stress in Figure 6. Furthermore, Figure 7 shows a sequence of thickening followed by thinning of the momentum thickness. This trend confirms that increased momentum loss within the boundary layer causes separation, which significantly raises drag and reduces flow efficiency. When flow velocity drops to zero, momentum thickness reaches its maximum. However, as turbulence intensity and momentum transfer improve, the flow reattaches to the mirror surface. This also suggests that the intermittency criterion within the governing function is no longer satisfied-intermittency gradually returns to zero, deactivating Equation (4), allowing the boundary layer to thin out and re-laminarization.

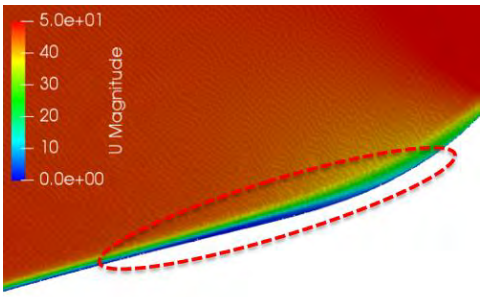

Figure 8. Momentum Thickness

4.3.3 Turbulent Kinetic Energy

TKE influences eddy viscosity and boundary layer stability, directly impacting transition onset and extent. According to Eq. (4), its distribution is critical for transition prediction. The adopted transition model incorporates separation-induced correction terms to better capture TKE evolution near the mirror.

TKE distribution indicates weak turbulence on the mirror surface, suggesting possible transition or laminar separation. The low TKE levels imply the boundary layer remains largely laminar, with instabilities likely triggered by T–S waves. Combined with the momentum thickness variations in Figure 7, the flow is inferred to separate and reattach, enhancing turbulence and pressure fluctuations. This behavior is consistent with the generation of tonal noise and potential acoustic feedback.

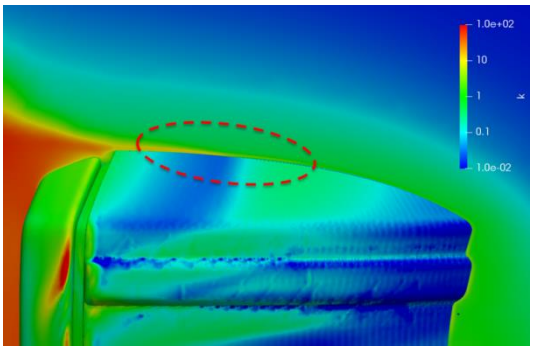

Figure 8. Turbulent Kinetic Energy

5 Optimization

Two mirror modification strategies were proposed to suppress tonal noise: (a) introducing a surface step to trigger early transition, preventing laminar separation; and (b) increasing surface roughness to promote flow attachment and reduce sensitivity to small disturbances. The modified areas are indicated by green lines in Figure 9.

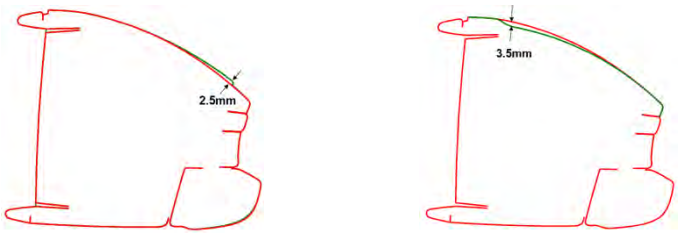

(a) Step Addition Design (b) Rough Surface Design

Figure 9 Modified Mirror Configurations

To verify the effectiveness of both designs, wind tunnel tests were conducted. As shown in Figure 10, neither modified mirror exhibited tonal noise, confirming the suppression of shape-induced whistling.

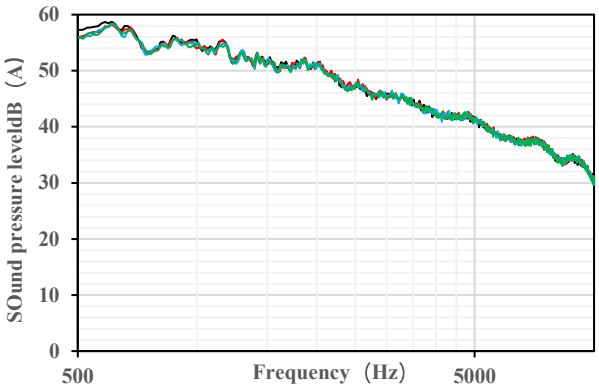

Figure 12 Wind Tunnel Test Results at 140 km/h and -5° Yaw

Based on the previous analysis, numerical simulations were conducted under the test condition of 140 km/h and -5 degree yaw. Flow field results confirmed the role and variation of key parameters during the laminar-to-turbulent transition, offering a predictive approach for early-stage design against tonal noise.

6 Conclusion

This study identified tonal noise issues around the vehicle's side mirror using wind tunnel experiments and investigated the underlying mechanisms via the LCTM transition model. The main conclusions are as follows:

(1) Whistling Identification:

Wind tunnel testing revealed that at 140 km/h and -5degree yaw, the SPL at 6668 Hz was significantly higher than adjacent frequencies, with a peak difference of 8.3 dB(A), confirming the presence of tonal noise on the right side-consistent with subjective evaluation.

(2) Mechanism Determination:

Simulations using the LCTM model analyzed wall shear stress, momentum thickness, and turbulent kinetic energy. Results indicated that the primary cause of mirror-induced tonal noise was laminar boundary layer separation and subsequent reattachment on the mirror surface.

(3) Design Optimization:

Two mirror design optimizations were proposed. Adding a step to promote early laminar-to-turbulent transition. Introducing surface roughness via an L-shaped feature to trigger transition. Both approaches were validated by wind tunnel tests to effectively eliminate tonal noise.

(4) Engineering Implications:

The combined use of simulation and experimental validation effectively resolved the mirror tonal noise issue. This approach is particularly suitable for early-stage vehicle development. Given the diversity of tonal noise types and mechanisms in vehicle design, future work can explore advanced simulation techniques and optimization algorithms to further refine prediction accuracy and coverage.

Reference

[1] Robert C. Chanaud. Aerodynamic whisltes [J]. Scientific American Inc., 1970, 222(1): 40-47.

[2] Thomas Christian Schuetz. Aerodynamics of Road Vehicles [M]. 5th Edition, London, England: SAE International, 2015.

[3] Michael J. Lucas, Robert A Noreen, Louis C Sutherland, et al. Handbook of the acoustic characteristics of turbomachinery cavities [M]. America: Newyork: American society of mechanical engineers, 1997.

[4] Dangguo Yang, Jianqiang Li, Jun Liu, et al. Analysis on physical mechanism of sound generation inside cavities based on acoustic analogy method [J]. Open journal of fluid dynamic, 2013, 3(1): 23-31.

[5] Vaik I, Varga R, Paál G. Frequency and phase characteristics of the edge tone [J]. Part I. Periodica Polytechnica Mechanical Engineering, 2014, 58(1): 55–67. DOI: 10.3311/PPme.7028

[6] Vaik I, Varga R, Paál G. Frequency and phase characteristics of the edge tone [J]. Part II. Periodica Polytechnica Mechanical Engineering, 2014;58(1):69–76. DOI: 10.3311/PPme.7031

[7] Yiyang Sun, Aditya G. Nair, Kunihiko Taira, Louis N. Cattafesta. Numerical simulations of subsonic and transonic open-cavity flows [C]. America: Atlanta: 7th AIAA theoretical fluid mechanics conference, 2014. DOI: http://doi.org/10.2514/6.2014-3092

[8] Sami Yamouni, Denis Sipp, Laurent Jacquin. Interaction between feedback aeroacoustic and acoustic resonance mechanisms in a cavity flow: a global stability analysis [J]. Journal od Fluid Mechanics, 2013, (717): 134-165. DOI: https://doi.org/10.1017/jfm.2012.563

[9] Peter G. Baines, Sharanya Majundar, Humio Mitsudera. The mechanics of the Tollmien-Schlichting wave [J]. Journal of Fluid Mechanics, 1996, (312): 107-124. DOI:10.1017/S0022112096001930

[10] Huang Lina. Research on Unsteady Pressure field and aerodynamic noise [D]. Jinlin University, 2014.

[11] Guan Peng, Pan Lei, Gu Yan. Research on the shape optimization of rear mirror wind noise performance [J]. Automobile applied technology, 2020(11): 113-116. DOI: CNKI:SUN:SXQC.0.2020-11-037

[12] Jiang Zuxiao, Xing Peng, Zhou Jiangbin. Experimental research on whistle characteristics of automobile side mirror [J]. Journal of machine design, 2020, 37(S02): 187-193. DOI: 10.13841/j.cnki.jxsj.2020.s2.047

[13] Wu Haibo, Xing Peng, Zhou Jiangbin. Theoretical study and test validation on vehicle rearview mirror whistling based on γ corrected transition model [J]. Automotive engineering, 2021, 6(43): 885-890. DOI: 10.19562/j.chinasae.qcgc.2021.06.012

[14] Wu Haibo, Xing Peng, Zhou Jiangbin. Theoretical study and test validation on vehicle rearview mirror whistling based on γ corrected transition model [J]. Automotive engineering, 2021, 6(43): 885-890.

[15] He Yingzhi, Yang Zhigang, Wang Yigang. The Mechanism and Experimental Study of the Effects of Car Body Sealings on Interior Aerodynamic Noise [J]. Automotive engineering, 2012, 8(34): 692-695. DOI: 10.3969/j.issn.1000-680X.2012.08.006

[16] Tao Zhi, Ma Yao, You Ruquan et al. A review of the research progress of boundary layer theory [J]. Scientia sinica technologica, 2024, 6(54): 979-1002. DOI: 10.1360/SST-2023-0316

[17] Zhang Feng, Cao Wei, Zhou Heng. Study of the Mechanism of Breakdown in Laminar-Turbulent Transition of a Supersonic Boundary Layer on a Flat Plate [J]. Applied Mathematics and Mechanics, 2006, 27(4): 379-386.

[18] Lounsberry T, Gleason M, Puskarz M. Laminar flow whistle on a vehicle side mirror [C]. America: Detroit, SAE Technical Papers, 2007. DOI: https://doi.org/10.4271/2007- 01-1549

Modulated Aeroacoustics Cabin Noise Under Controlled Unsteady Flow Conditions for Different Vehicle Geometries

Nur Syafiqah Jamaluddin, Nicholas Oettle

Vehicle Efficiency, Jaguar Land Rover
Abbey Road, Whitley, Coventry, CV3 4LF, UK

njamalud@jaguarlandrover.com
noettle@jaguarlandrover.com

Abstract: The unsteady wind conditions encountered by a vehicle whilst driving on the road are different from those typically experienced in the steady-flow wind tunnel development environment. This paper presents an experimental comparison using two large SUV-shaped vehicles to assess the effect of unsteady wind on modulated noise performance across different vehicle architectures. Both vehicles were also examined with a series of non-production geometric modifications to assess their contribution to modulated noise. The vehicle responses to unsteady wind conditions were assessed using a dynamic upstream unsteady flow generated by active side wind generator of the FKFS wind tunnel. The pressure distribution on the front side glass of both vehicles in the straight-ahead position was also examined to identify the differences in aerodynamic interactions with turbulent inflow between the two vehicle models. The results highlight the geometry-dependent factors that influence both sound levels and modulation characteristics perceived in the cabin under unsteady inflow condition. The tested vehicle with a steeper A-pillar and larger mirror exhibited stronger self-induced unsteadiness and broadband modulation. Conversely, the tested vehicle with a shallower A-pillar and smaller mirror, demonstrated greater sensitivity to upstream turbulence with narrower and low-frequency modulation.

Contribution: 2025 FKFS Conference on Vehicle Aerodynamics and Thermal Management
15 – 16 October 2025 | Leinfelden-Echterdingen

1 Introduction

The unsteady wind noise of a large SUV-shaped vehicle and its modulation characteristics has been examined in previous work by the authors [1]. The present study extends that investigation by including a second vehicle with a different geometry. The unsteady wind conditions experienced by a vehicle whilst driving on the road are different to those typically experienced in the steady-flow wind tunnel environment, due to turbulence in the natural wind, moving through the unsteady wakes of other road vehicles and travelling through the stationary wakes generated by roadside obstacles. Various studies have explored this phenomenon, as summarised comprehensively by [2].

The unsteadiness of the natural wind can create fluctuations in both speed and flow direction over the vehicle, which directly affects the separated flow structures around the side glass region [3]. These structures can generate strong aeroacoustic sources near the vehicle occupants, particularly in regions with greater flow separation [4]. The interaction of this unsteadiness with the vehicle surfaces results in temporal variation in the cabin noise, perceived as modulation or 'bluster' by the occupants. Previous studies comparing the impacts of the unsteady on-road environment on wind noise, using road tests, have been published by [5 - 7].

There has been increased interest in the development of controlled approaches to generate unsteadiness of the natural wind environment as experienced by a vehicle, providing improved reproducibility over on-road tests. Active lift-based devices have been shown to be the most capable of generating the levels of unsteadiness and the longer length scales observed on-road [8 - 10]. The FKFS *Swing* system [11] is an example of a full-scale active lift-based system, which is the basis of the present study. This has been shown to reproduce the levels of unsteady wind noise as experienced on-road through dynamic yaw variation up to 10 Hz.

The aeroacoustic response of a vehicle is also strongly influenced by the local geometry that influence the flow field disturbances around it [12]. The A-pillar flow separation region is known for producing a persistent and complex flow structure, generating strong surface pressure fluctuations and broadband noise, particularly under unsteady conditions [13, 14]. The side mirror, often treated as a bluff body, has geometry and placement that significantly affects vortex shedding and its interaction with the A-pillar wake. Modifications, including those such as inner ducts [15], have been shown to reduce sound pressure levels by stabilising flow and suppressing vortex formation near the mirror-pillar interface.

This work presents the use of an experimental approach, following the methodology described in [1], applied to two SUV-shaped vehicles with distinct A-pillar and side mirror geometries. Both interior sound and exterior surface pressure fluctuations were measured to examine the geometry-dependent influences at the receiver location and in the near field, respectively.

2 Experimental Setup

Two large SUVs were tested using the FKFS full-scale aeroacoustic wind tunnel at the University of Stuttgart in Germany. The experimental methodology followed [1] and included a second vehicle with geometric differences, particularly the A-pillar and side mirror. Interior cabin noise data were recorded using HEAD Acoustics HMS IV binaural heads, while surface pressure fluctuations were measured using HBK Type 4949 surface microphones. The surface microphones, mounted on the front-left side glass of both vehicles, a region where local flow structures are sensitive to flow direction.

Figure 1 shows the schematic diagram around the front side glass of both tested vehicles, highlighting key differences in the A-pillar angle and side mirror geometry as viewed from the side and top planes. SUV_a (Figure 1a), previously studied in [1] has a steeper A-pillar angle than SUV_b (Figure 1b), and features a relatively larger side mirror design. The positioning of the side mirrors relative to the side glass also differs between the two vehicles. In SUV_b (blue-shaded mirror in Figure 1c), the mirror forms a nearly parallel flow channel with a uniform throat gap along its length. In contrast, the mirror curvature of SUV_a (grey-shaded mirror in Figure 1c) creates a converging throat gap that narrows into a shorter parallel channel, guiding the airflow slightly inboard. In terms of vehicle glazing, SUV_a is equipped with toughened side glass, while SUV_b features acoustically laminated side glass of similar thickness.

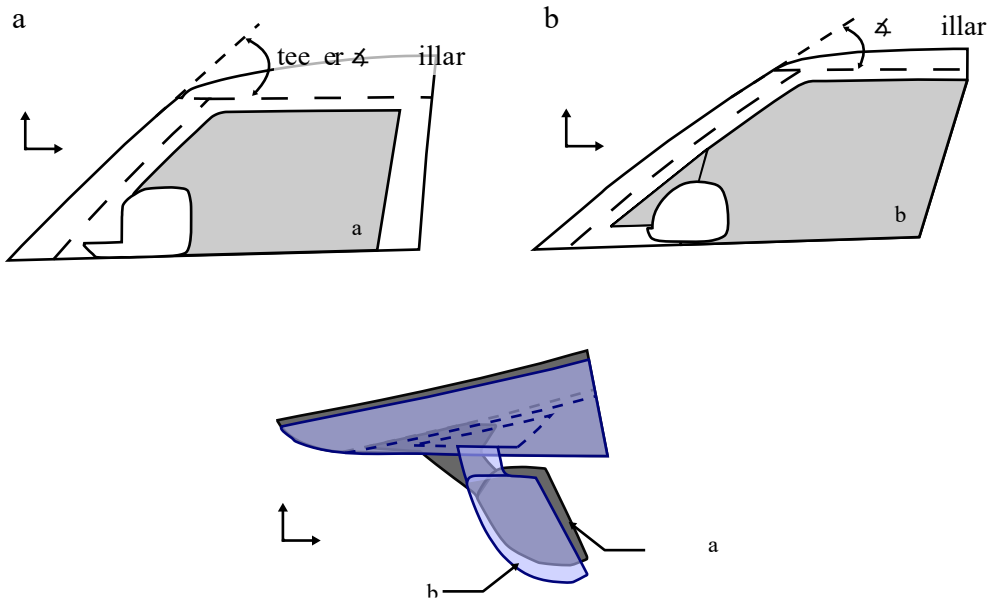

Figure 1: Schematic diagram comparing the front side glass region for (a) SUV_a, and (b) SUV_b, while (c) compares the side mirrors of both vehicles.

Non-production geometry modifications were also investigated by adding a small triangular profile trip along the A-pillar and removing the door mirrors. Tests were conducted at a flow speed of 140 km/h in both steady and unsteady freestream environments with the active side wind generator installed at the nozzle [16]. The unsteady environment is represented by von Kármán 2.5 m (VK) flow conditions, generated synthetically using the von Kármán wind turbulence model [17]. The turbulence characteristics generated are shown in Table 1.

Flow condition	von Kármán 2.5 *m* (VK)
Turbulence length scale	2.5 *m*
Turbulence intensity	6.5 %

Table 1: Turbulence properties of the unsteady flow in lateral direction in an empty test section at 140 km/h.

3 Results and Discussion

3.1 Sound Pressure Level Spectra

This section presents the time-averaged spectral characteristics of both tested vehicles, measured from the front left outer ear (FLOE) in-cabin microphone and surface-mounted microphones along the front-left side glass. Figure 2 presents the interior noise spectra of both vehicles in the fully taped configuration. Results are expressed as Δ P L_{inflow}, representing the difference in A-weighted sound pressure level (SPL) between steady (SS) and unsteady (VK) inflow conditions. For both vehicles, upstream turbulence increases the spectra within the mid-to-high frequency ranges (1 – 10 kHz).

In SUV_a (Figure 2a), the largest increase occurs above 3 kHz, while changes between 1 and 3 kHz are minimal, likely reflecting excitation from A-pillar and mirror-wake interactions that is less affected by upstream turbulence. For SUV_b (Figure 2b), SPL increases across the spectrum under VK inflow, indicating relatively weaker self-excitation and greater sensitivity to incoming turbulence.

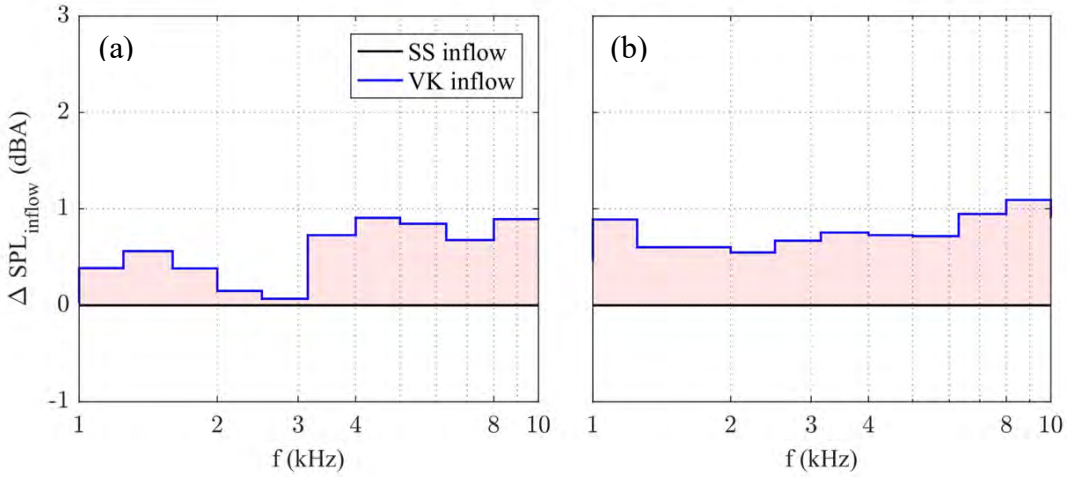

Figure 2: Comparison of interior sound spectra for fully taped (a) SUV_a and (b) SUV_b, shown as the difference in SPL to the steady inflow condition.

To illustrate the flow variation between both vehicles, Figure 3 shows the time-averaged flow topology from CFD simulation of the fully taped vehicles under steady inflow. The simulations were conducted using PowerFLOW and set up following the methodology described in [1, 18]. Results highlight baseline differences in the flow separation regions of the two vehicles. In SUV_a (Figure 3a), the A-pillar vortex appears longer and more developed than in SUV_b. A stronger recirculation is also evident at the mirror-pillar throat region. In addition, the mirror wake of SUV_a is more intense compared to SUV_b (Figure 3b). These flow features reflect the spectral results in Figure 2, where SUV_a indicates a dominant A-pillar and mirror wake interaction compared to SUV_b.

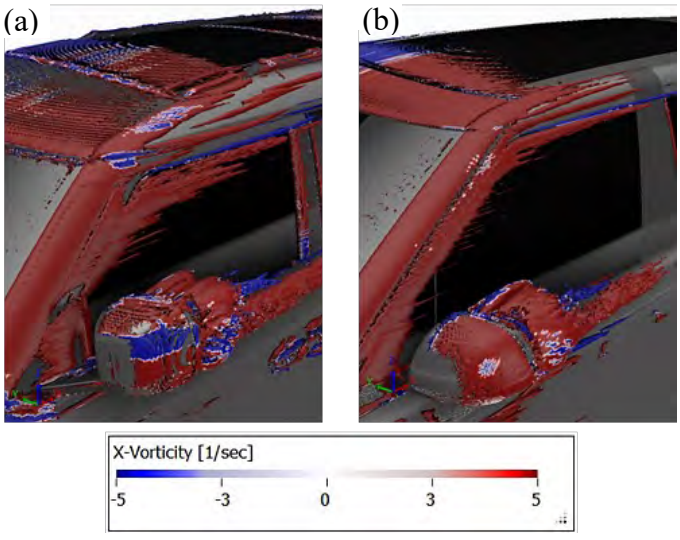

Figure 3: Flow visualisation of (a) SUVa and (b) SUVb in steady inflow conditions.

Figure 4 compares the third-octave spectra for both vehicles with tripped A-pillars and removed side mirrors in turn. Results are presented as the difference in A-weighted SPL between each modified configuration and the fully taped (Δ P L_{config}), under both inflows. The A-pillar trip cases are shown in red, while the mirror-removed cases are shown in blue. Solid lines denote steady inflow, and dotted lines denote unsteady VK inflow.

In SUV_a (Figure 4a), the tripped A-pillar of increases SPL across the spectra, which has been attributed to trip-induced flow separation that intensifies the A-pillar vortex [1]. Under VK inflow, SPL further increases, likely due to interactions between incoming turbulence and the A-pillar vortex structures. Upstream turbulence may re-energise the separated shear layer or amplify surface pressure fluctuations, increasing the transmitted noise in cabin.

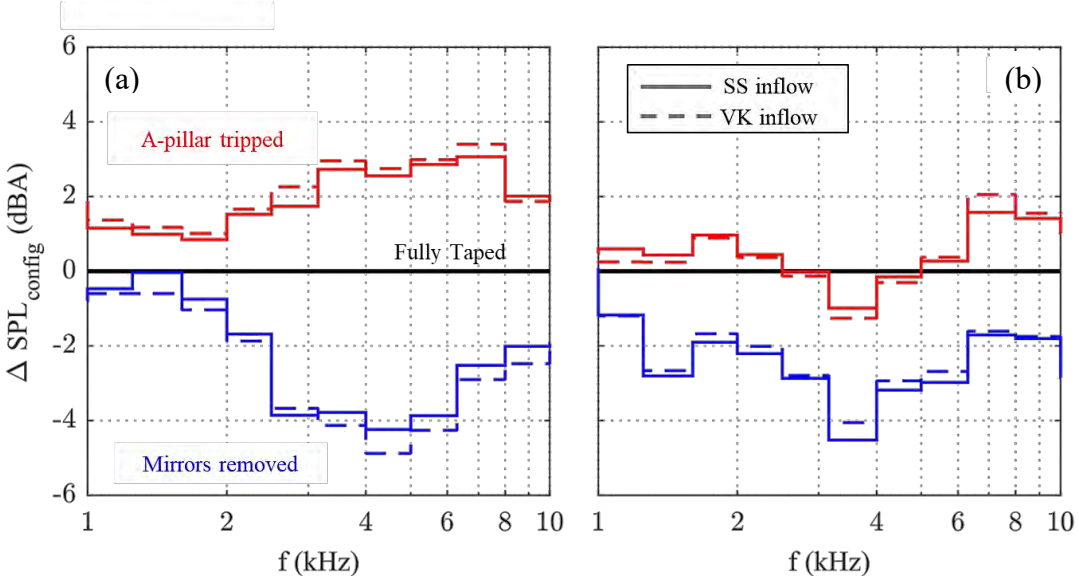

Figure 4: Comparison of interior sound spectra for (a) SUV_a and (b) SUV_b with geometric modifications, shown as the difference in SPL to the fully taped configuration.

For SUV_b (Figure 4b), the tripped A-pillar also increases SPL, albeit to a lesser extent. This is likely due to acoustic lamination of the side glass and a shallower A-pillar angle, which attenuates noise transmission and weakens the separated flow respectively. A local SPL reduction around 3 kHz is observed, possibly linked to modified local flow near front door quarter glass, which reduces excitation in that region.

Removing the side mirrors reduces SPL for both vehicles under all inflow conditions due to the elimination of mirror vortex shedding [1]. In SUV_b (Figure 4b), the mirrors-removed case shows a more broadband SPL reduction than SUV_a (Figure 4a), particularly within the 1 to 2 kHz range. This likely reflects the influence of its geometry and glazing specification. Under VK inflow, SUV_a shows a further SPL decrease, possibly due to breakdown of the remaining A-pillar flow structures without mirrors. In contrast, SUV_b shows a slight increase under VK inflow, suggesting that without mirrors its A-pillar wake is less responsive to upstream turbulence.

Figure 5 presents the surface SPL distribution ΔPL_{inflow}) on the front-left side glass of both vehicles for the fully taped, A-pillar tripped, and mirrors removed configurations. These pressure maps provide spatial insights into the nearfield pressure environment, capturing both hydrodynamic and acoustic contributions (albeit dominated by the hydrodynamic fluctuations), and help identify source regions that influencing the noise perceived in cabin.

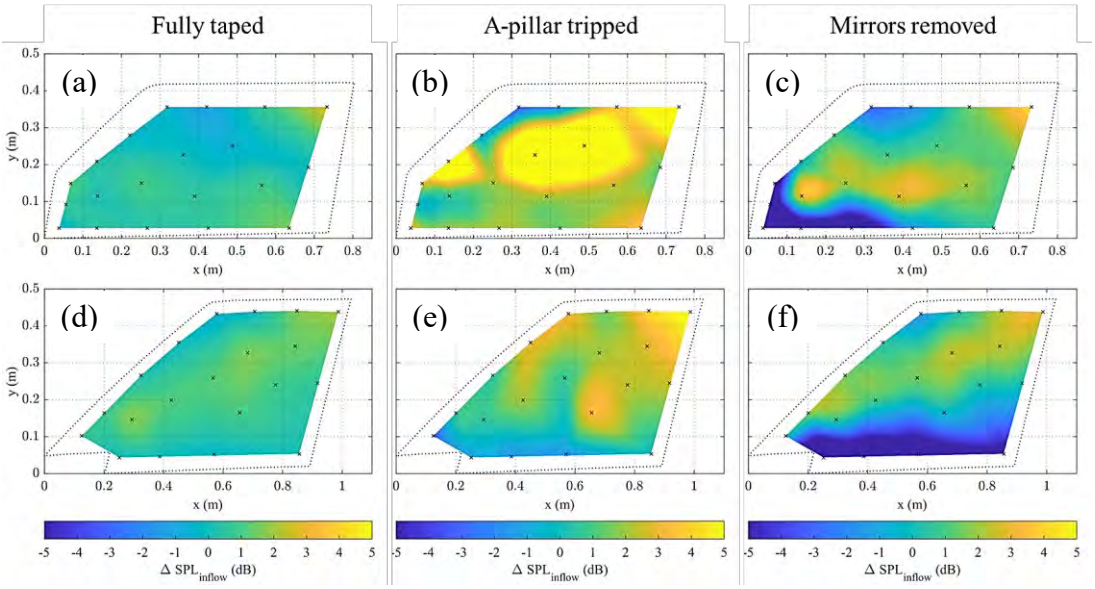

Figure 5: The distribution of surfa e PL, e re ssed in Δ PLinflow, on the front left side glass of SUVa (a) – (c) and SUVb (d) – (f) in different test conditions.

In the fully taped configuration, both vehicles show a slight increase in surface SPL under VK inflow, but with different distributions. SUV_a (Figure 5a) shows a localised increase downstream of the mirror with little change along the A-pillar, in line with the limited response to turbulence seen in Figure 2. SUV_b (Figure 5d), on the other hand, shows a broad surface SPL increase along the A-pillar wake, consistent with the broadband response seen in the interior sound spectra.

With the A-pillar tripped, SUV_a (Figure 5b) shows a significant increase in surface SPL, localised near the A-pillar and further downstream along the side glass. This trend reflects the interior spectra in Figure 4a, with a stronger vortex shedding at the tripped A-pillar interacting with the upstream turbulence. SUV_b (Figure 5e) also shows an increase in surface SPL, but at relatively lower levels, with a localised reduction near the front quarter glass region, in line with the 3 kHz dip observed in Figure 4b.

When the side mirrors are removed and under VK inflow, both vehicles show reduced surface SPL in the mirror wake region near the bottom of the A-pillar, approximately between 0.5 m < y < 0.15 m. This region represents the area subjected to the wake of the cowl vortex under upstream turbulence, which may interact and break the vehi le 's A-pillar vortex structures more effectively without the mirror. For SUV_a (Figure 5c), this surface SPL reduction is localised in the upstream half of the side glass, up to nearly x = 0.4 m. In contrast, this reduction is broader and spanned across the entire length of the side glass for SUV_b (Figure 5f), which is in-line to the broadband decrease in the interior spectra seen in Figure 4b.

3.2 Modulation Spectra

This section presents the modulation characteristics of the tested vehicles under the same test configurations and inflow conditions as previously analysed in Section 3.1. Modulation analysis was conducted using the Hilbert transform to extract the signal's envelope following the method described in [1]. This approach was then extended to isolate the fundamental modulation, as described in [19], and provides the wind-induced modulated noise in terms of its carrier frequency (F_c), degree of modulation (m) and frequency of modulation (F_m).

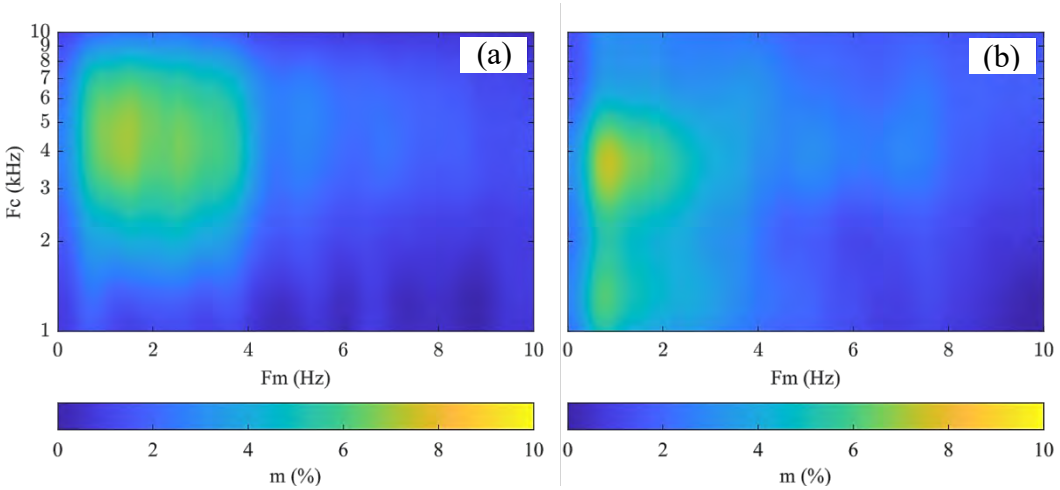

Figure 6: Comparison of wind-induced modulation spectrogram between (a) SUVa and (b) SUVb under unsteady inflow in the fully taped configuration.

Figure 6 compares the wind-induced modulation spectrograms for both tested vehicles in fully taped configuration under unsteady VK inflow. Steady inflow cases show near-zero modulation across all configurations and are not included for brevity. For SUV_a (Figure 6a), a broadband modulation over 5% is observed between 2 to 8 kHz at fluctuation rates of up to 4 Hz. In contrast, SUV_b (Figure 6b), shows a more band-limited response, with over 5% around 4 kHz and modulation frequencies limited to about 2 Hz. These differences are consistent with the geometric differences and flow characteristics described earlier, where SUV_a tends to generate stronger self-induced separation that interacts with upstream turbulence more than SUV_b.

These characteristics can be further examined from the two-dimensional modulation spectra in Figure 7, where the wind-induced modulation contributions of partial octave bands are presented. SUV_a (Figure 7a) shows a broader modulation spread, while SUV_b (Figure 7b) is more band-limited with a distinct peak. In both vehicles, the dominant modulation occurs at 4 kHz with similar levels of about 7%. At other octave bands, SUV_a is characterised by contributions at higher frequencies (i.e. 8 kHz), while SUV_b at lower frequencies (i.e. 1 and 2 kHz).

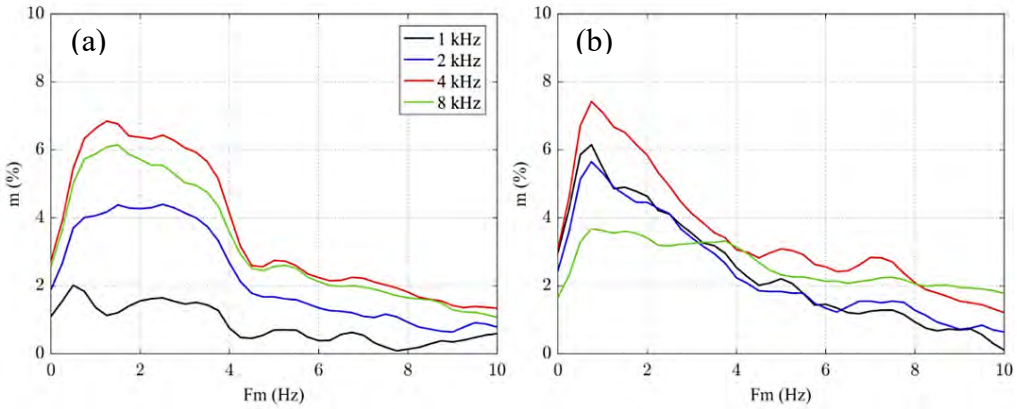

Figure 7: The wind-induced modulation spectra at varying octave band frequencies for (a) SUV_a and (b) SUV_b in the fully taped configuration.

Geometric modifications can further influence the modulation characteristics of both vehicles. This can be clearly demonstrated in Figure 8, where the wind-induced modulation spectrogram of both vehicles under VK inflow at varied test configurations are compared. When the A-pillar is tripped, the airflow is forced to separate earlier and more consistently, generating a stronger vortex compared to the weaker baseline structures without it.

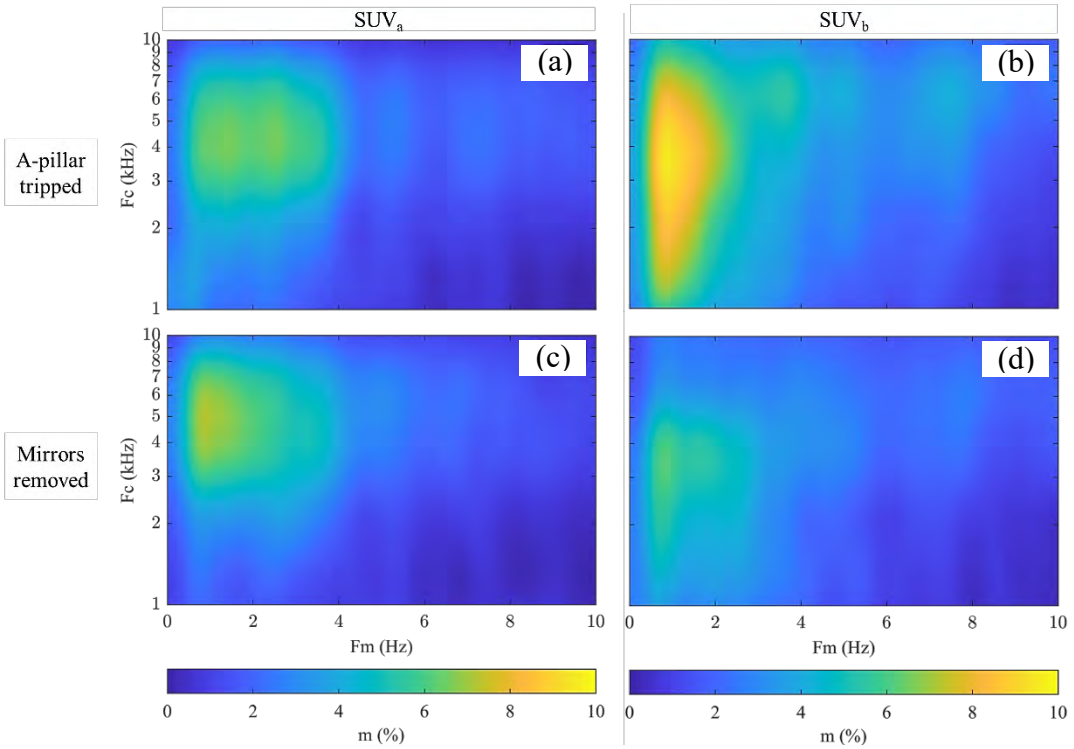

Figure 8: Comparison of wind induced modulation spectrograms for SUV$_a$ ((a) and (c)) and SUV$_b$ ((b) and (d)) for different test configurations.

For SUV$_a$ (Figure 8a), the modulation trends are similar to those seen in fully taped, but at slightly lower levels and band-limited. This can be attributed to its steeper A-pillar that already experience strong baseline A-pillar vortex, which lowers its sensitivity to upstream turbulence and the corresponding modulation characteristics. In contrast, the tripped A-pillar case of SUV$_b$ (Figure 8b) shows significantly higher modulation than untripped, with up to 10% modulation at a rate between 1 to 8 kHz. This may be due to its shallower A-pillar and weaker baseline vortex that gets stronger when tripped and becomes more sensitive to upstream turbulence. The modulation frequency, however, remains limited to about 2 Hz, similar to that observed in fully taped.

With the mirrors removed, the modulation characteristics of SUV$_a$ in Figure 8c remain comparable to the fully taped results, with a slight reduction at rates between 2 to 4 Hz. This trend is similar to Figure 5c, where localised SPL reductions on the side glass are observed together with regions that remain highly responsive to upstream turbulence. For SUV$_b$ (Figure 8d), a broader decrease in modulation is observed, consistent with the trend in Figure 5f, which shows a wider reduction of surface SPL along the side glass.

4 Conclusion

This study compares the aeroacoustic characteristics of two large SUV-shaped vehicles under unsteady inflow, focusing on how differences in geometry influence the perceived noise in cabin. SUV_a, that has steeper A-pillar, larger mirror and converging throat gap, generates stronger self-induced flow structure that dominates the response even under steady-state inflow. In contrast a SUV_b, with its shallower A-pillar, smaller mirror, and laminated side glass, produces quieter baseline noise and weaker flow separation with greater sensitivity to upstream turbulence. These characteristics were consistently observed across the interior spectra, surface pressure distribution and modulation analysis.

The CFD flow topology corroborate this trend with SUV_a showing longer and stronger A-pillar vortices and more intense mirror wakes than SUV_b. Geometric modifications further emphasise the role of baseline flow behaviour, where tripping the A-pillar had shown little effect on SUV_a with its larger vortex but increased SPL and modulation in SUV_b, while mirror removal reduced the mirror-wake contribution in both vehicles, more broadly for SUV_b.

The modulation results provided insight into how these flow features translate into perceived sound quality. SUV_a was characterised by a broadband modulation spread at higher carrier frequencies, which may be masked by the higher levels of overall SPL. SUV_b, on the other hand, showed narrower and more peaky modulation, concentrated at lower octave carrier bands with modulation rates up to 2 Hz, where human hearing is more sensitive. Overall, these findings highlight the geometry-dependent factors that influence both sound levels and modulation characteristics perceived in the cabin.

5 Acknowledgement

The authors wish to thank the staff of the FKFS full-scale aeroacoustic wind tunnel for their assistance during testing, instrumentation and discussion; Oliver Smith and Lucas Padial for supporting the CFD image generation; and to JLR for permission to publish.

6 Reference list

1. N.S. Jamaluddin, N. Oettle, and D. Staron. Experimental Investigation into Modulated Aeroacoustic Cabin Noise Arising from Unsteady Flow Conditions. SAE Technical Paper 2025-01-0029, 2025. doi:10.4271/2025-01-0029.
2. D. Sims-Williams. Cross Winds and Transients: Reality, Simulation and Effects. SAE Int. J. Passeng. Cars - Mech. Syst. 4(1):172–183, 2011. doi:10.4271/2011-01-0172.

3. N. Oettle, D. Sims-Williams, and R. Dominy. Assessing the Aeroacoustic Response of a Vehicle to Transient Flow Conditions from the Perspective of a Vehicle Occupant. SAE Int. J. Passeng. Cars - Mech. Syst. 7(2), 2014. doi:10.4271/2014-01-0591.
4. N. Oettle and D. Sims-Williams. Automotive Aeroacoustics: An Overview. Proc. Inst. Mech. Eng. D: J. Automob. Eng. 231(9):1177–1189, 2017. doi:10.1177/0954407017695147.
5. N. Lindener, H. Miehling, A. Cogotti, F. Cogotti et al. Aeroacoustic Measurements in Turbulent Flow on the Road and in the Wind Tunnel. SAE Technical Paper 2007-01-1551, 2007. doi:10.4271/2007-01-1551.
6. C. Peric, S. Watkins, E. Lindqvist, and J. Saunders. Effects of On-Road Turbulence on Automotive Wind Noise: Comparing Wind-Tunnel and On-Road Tests. SAE Technical Paper 970406, 1997. doi:10.4271/970406.
7. Oettle, N., Mankowski, O., Sims-Williams, D., Dominy, R. et al., "Evaluation of the Aerodynamic and Aeroacoustic Response of a Vehicle to Transient Flow Conditions," SAE Int. J. Passeng. Cars - Mech. Syst. 6(1):2013, doi:10.4271/2013-01-1250.
8. S. Terakado, T. Makihara, T. Sugiyama, K. Maeda et al. Experimental Investigation of Aeroacoustic Cabin Noise in Unsteady Flow by Means of a New Turbulence Generating Device. SAE Int. J. Passeng. Cars - Mech. Syst. 10(1):2017. doi:10.4271/2017-01-1545.
9. D. Staron, M. Riegel, R. Blumrich, and A. Wagner. Aeroacoustic Vehicle Development Method Considering Realistic Wind Conditions. SAE Technical Paper 2023-01-1123, 2023. doi:10.4271/2023-01-1123.
10. O. Mankowski, D. Sims-Williams, and R. Dominy. A Wind Tunnel Simulation Facility for On-Road Transients. SAE Int. J. Passeng. Cars - Mech. Syst. 7(3):2014. doi:10.4271/2014-01-0587.
11. M. Riegel, R. Blumrich, and M. Helfer. New Technology for Unsteady Wind Noise Measurements in an Aeroacoustic Full-Scale Wind Tunnel. Int. Conf. Vehicle Aerodynamics, Coventry, September 21–22, 2016.
12. D. Staron, M. Riegel, R. Blumrich, and J. Wiedemann. Vergleich von Methoden zur Bestimmung des instationären Windgeräuschs im Fahrzeug. Tagung Fahrzeug-Aerodynamik, Haus der Technik, München, 3–4 July 2018. Tagungsschrift Fahrzeugakustik und -schwingungen.
13. J. Howell, J.B. Fuller, and M. Passmore. The effect of free stream turbulence on a-pillar airflow. SAE Technical Paper 2009-01-0003, 2009. doi:10.4271/2009-01-0003.
14. J. Fischer, V. Valeau, L. E. Brizzi, and J. Laumonier. Joint acoustic and wall-pressure measurements on a model A-pillar vortex. Exp. Fluids 61(2):54, 2020. doi:10.1007/s00348-020-2880-5.
15. Y-J. Chu, Y-S. Shin, and S-Y. Lee. Aerodynamic Analysis and Noise-Reducing Design of an Outside Rear View Mirror. Appl. Sci. 8(4):519, 2018. doi:10.3390/app8040519.
16. R. Blumrich, N. Widdecke, J. Wiedemann, A. Michelbach et al. New FKFS Technology at the Full-Scale Aeroacoustic Wind Tunnel of University of Stuttgart. SAE Technical Paper 2015-01-1557, 2015. doi:10.4271/2015-01-1557.
17. F.W. Diederich and J.A. Drischler. Effect of spanwise variations in gust intensity on the lift due to atmospheric turbulence. NACA-TN-3920, 1957.
18. O. Smith and N. Oettle. Visualisation of Roof Bar Noise Sources through the Use of Acoustic Beamforming and Computational Aeroacoustics. SAE Technical Paper 2023-01-0840, 2023. doi:10.4271/2023-01-0840.
19. D. Staron. Entwicklung einer Methode zur Bestimmung und Bewertung des Windgeräuschs im Fahrzeug unter realistischen Strömungsbedingungen. Springer Vieweg, Wiesbaden, 2025.

How do thermal optimisations on the CCS charging inlet affect the charging time?

Dipl.-Ing. Jochen Krings, Daimler Truck AG
Department: Charging Components E-Mobility DTB
jochen.krings@daimlertruck.com

Daimler Truck AG
Fasanenweg 10
70771 Leinfelden-Echterdingen, Germany

Prof. Dr.-Ing. Hans-Christian Reuss, Universität Stuttgart / FKFS Stuttgart
Head of Board of Management for Vehicle Mechatronics
info@fkfs.de

FKFS (Forschungsinstitut für Kraftfahrwesen und Fahrzeugmotoren) Stuttgart
Pfaffenwaldring 12
70569 Stuttgart, Germany

Dipl.-Ing. Peter Ziegler, Daimler Truck AG
Department Leadership: Charging Components E-Mobility DTB
peter.z.ziegler@daimlertruck.com

B. Eng. Paul Steinmetz, Daimler Truck AG
Department: Charging Components E-Mobility DTB
paul.ps.steinmetz@daimlertruck.com

Daimler Truck AG
Fasanenweg 10
70771 Leinfelden-Echterdingen, Germany

Contribution: 2025 FKFS Conference on Vehicle Aerodynamics and Thermal Management
15 – 16 October 2025 | Leinfelden-Echterdingen

Abstract:

The CCS charging standard is the most widely used variant for charging electric vehicles in Europe. The further development of the charging components enables charging capacities to be achieved that reach the limits of the CCS standard. One way to increase the effective charging power is to reduce charging losses.

In this work, one approach to optimising the CCS charging inlet is presented using a specially developed thermal Matlab/Simscape simulation. Comparisons of the thermal results from the current CCS inlet and the version with optimisation approach show slower heating. This offers the possibility of charging with a higher current over a longer period of time before the permissible limit temperature is reached.

In addition, the time saving potential due to the increased charging performance of the CCS charging inlet is analysed and the reduction in charging time is derived.

Figure 1: left: Mercedes Benz eActros 600
right: detail view CCS inlet with charing gun
copyright: Daimler Truck AG

1 Introduction

In the course of the global electrification of the automotive sector, commercial vehicles with electric drives have also been increasingly developed in recent years [1].

Compared to cars for private transport, fast charging of large energy storage units is a major challenge in the commercial vehicle sector in particular [2]. A short downtime thanks to fast charging times enables faster availability of commercial vehicles. This is of great importance for the economic efficiency of logistics operations [3].

Due to the widespread use of CCS (Combined Charging System) throughout Europe, electrified commercial vehicles also use this charging standard.

Fast charging of the energy storage units via the CCS charging inlet requires correspondingly high charging capacities, which are accompanied by high charging currents. The commercial vehicle sector is pushing itself to the limits of the CCS standard [4].

Accompanied by charging currents of several hundred amps and the electrical resistance of the charging components, there are also losses in the form of heat. In order to increase charging efficiency, it is always desirable to keep the overall heat development as low as possible. In addition to saving energy costs, the cooling components can also be smaller on the vehicle side, which results in a lighter vehicle weight and thus lower energy consumption when driving [5].

At the same time, a lower and slower temperature rise in the charging components also leads to lower material stress due to temperature differences, which promotes the longevity of the charging components [6].

The aim when designing the charging path components is always to maintain the maximum permissible charging current for as long as possible and not to exceed the temperature limit value of touchable components in order to protect people.

Thermal simulation tests are suitable for checking thermal optimisation approaches at an early stage in charging component development. The simulation-based testing of the new design approaches for component optimisation allows the expected results to be quantified in advance and, in the best case, iteration loops in component development to be reduced.

In the following, a thermal optimisation approach of the CCS charging inlet is tested by means of software simulation and the results are presented.

2 Design of the CCS charging inlet

The design of a CCS charging inlet is shown in Figure 2.

Coming from the charging station via the charging gun, the current is led via the contact pins into the inside of the charging inlet to the connection plates. These are connected to the bus bars for the cable via a screw connection. The temperature is monitored separately for positive and negative via sensors located between the contact pins and the connection plates. The maximum temperature is 90°C, according to DIN EN IEC 62196-1, [7].

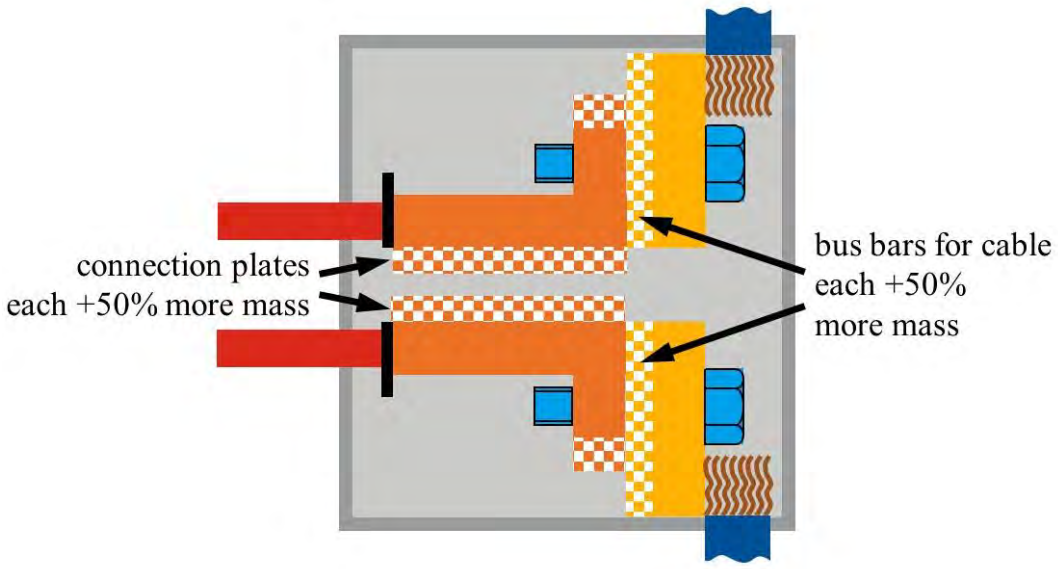

Figure 2: Schematic of internal design of CCS charging inlet
copyright: Daimler Truck AG

3 Modelling and simulation setup

Due to the electrical resistance of current-carrying components, internal losses occur, which lead to heating [8]. By means of Ohm's law Eq. (1), the electrical power Eq. (2) can be described with the voltage U, the current I and the electrical resistance $R_{electrical}$. Analogous to the electrical power, Joule's heating $P_{thermal}$, or the resulting heat flow $\dot{Q}$, can be described by Eq. (3):

Ohm's Law: $$U = I * R_{electrical} \quad (1)$$

Electrical Power: $$P_{electrical} = I * U = I^2 * R_{electrical} \quad (2)$$

Joule's Heathing: $$P_{thermal} = \dot{Q} = I^2 * R_{thermal} \quad (3)$$

The thermal resistance $R_{thermal}$ is described in Eq. (4) [9] by the length l of the component, the thermal conductivity λ as a material property and the component cross-sectional area A:

Thermal resistance: $$R_{thermal} = \frac{l}{\lambda * A} \quad (4)$$

Based on the "Technical Guideline for Thermosimulation Models" of the ZVEI (Zentralverband Elektrotechnik- und Elektroindustrie) the coupling of electrothermal simulations can be illustrated as follows [10]:

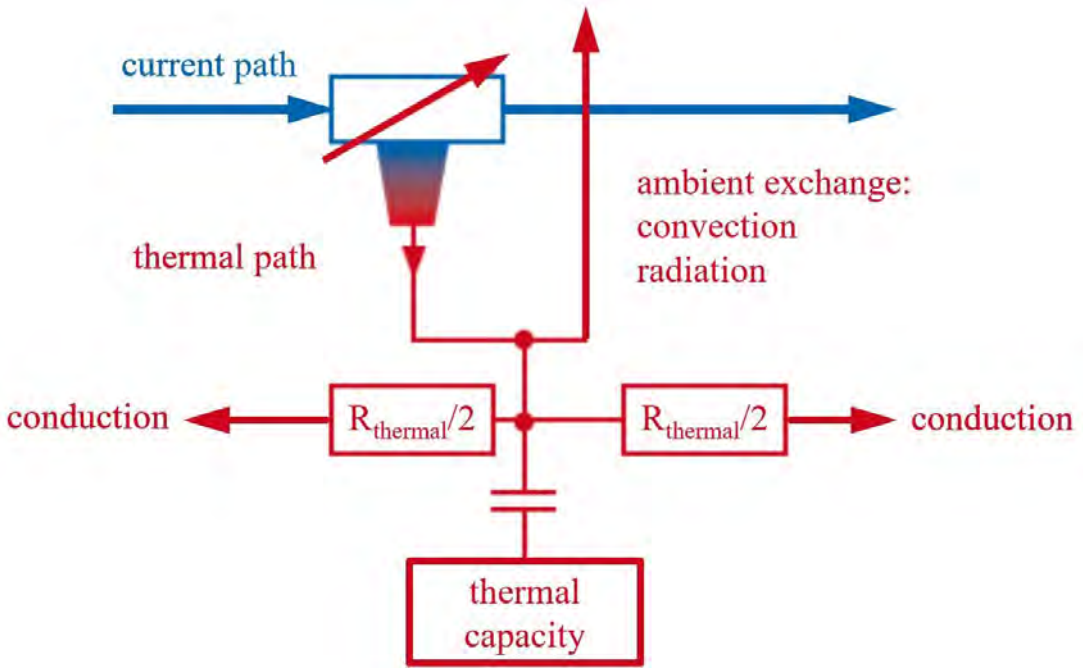

Figure 3: ZVEI Guideline Schematic for Electro-Thermal Coupling
copyright: ZVEI

An electrical component with its heat production is interpreted as a thermal source. Part of the heat can be absorbed by the component itself, which is called thermal capacity. Furthermore, heat can, for example, be exchanged with the ambient air by convection or radiated by radiation [11].

The heat conduction of the component is referred to as conduction. Since the heat input in the middle of the component is assumed in the modelling, the thermal resistance of the conduction is distributed in half in both directions.

For the structure of the thermal simulation in Matlab/Simscape, all current-carrying components can be represented as a series connection of electrical and thermal resistors, as shown in Figure 3. The components interact with each other through conduction, convection and radiation.

4 Design improvement potential: Increase in thermal mass connection

The conflicting goal of rapid charging of the energy storage unit results in increased heat development at high currents, which increases with the second power, see Eq. (3). One way to delay reaching the limiting temperature is to increase the thermal capacity C_{th} of the connection plate and the bus bar of the cable. The thermal capacity C_{th} describes the ability of a body to store and release thermal energy. It is proportional to the material property of the specific heat capacity c and the mass m of the component, see Eq. (5), [11]:

$$C_{th} = m * c \tag{5}$$

Multiplying the thermal capacity C_{th} with the temperature change dT as a derivation after the time dt, results in the heat flow $\dot{Q}$ that the body absorbs or emits, see Eq. (6), [12]:

$$\dot{Q} = C_{th} * \frac{dT}{dt} = m * c * \frac{dT}{dt} \tag{6}$$

The mass of the live parts can be easily increased by the material thickness and requires only minor adjustments in the given installation space without affecting the outer contour of the housing.

In addition to absorbing energy in the form of heat, the current-carrying parts can also transfer the heat within the component or to other components. This effect is called conduction. The heat flow $\dot{Q}_{conduction}$ can be determined with the thermal resistance $R_{thermal}$ Eq. (4) and the temperature difference ΔT, Eq. (7), [12]:

$$\dot{Q}_{conduction} = \frac{1}{R_{thermal}} * \Delta T = \frac{\lambda * A}{l} * \Delta T \tag{7}$$

The increase in the material thickness of the current-carrying parts results in a proportional increase in the cross-section A. This also results in a greater heat flow through conduction, which promotes the removal of heat.

5 Simulation-based test: increase in thermal mass

For the simulation-based test, the material thickness of the connection plates and the bus bars of the cables are increased by a factor of 1.5. This also increases the mass and the component cross-section by a factor of 1.5. In absolute terms, the mass of the components only increases by a few grammes. The temperature heating of the current design as the basis is compared with the results from the simulation for the variant with the increased thermal mass.

A start and ambient temperature of 25°C are assumed as boundary conditions. With a sufficient distance to the maximum permissible temperature of 90°C, an end temperature of 85°C is specified at the contact pins.

The charging current is initially constant 500A and is reduced after reaching 85°C until a constant temperature value is set at the contact pin.

The set cooling value per contact pin is 3.5W and is discharged via the charging station's charging gun [13].

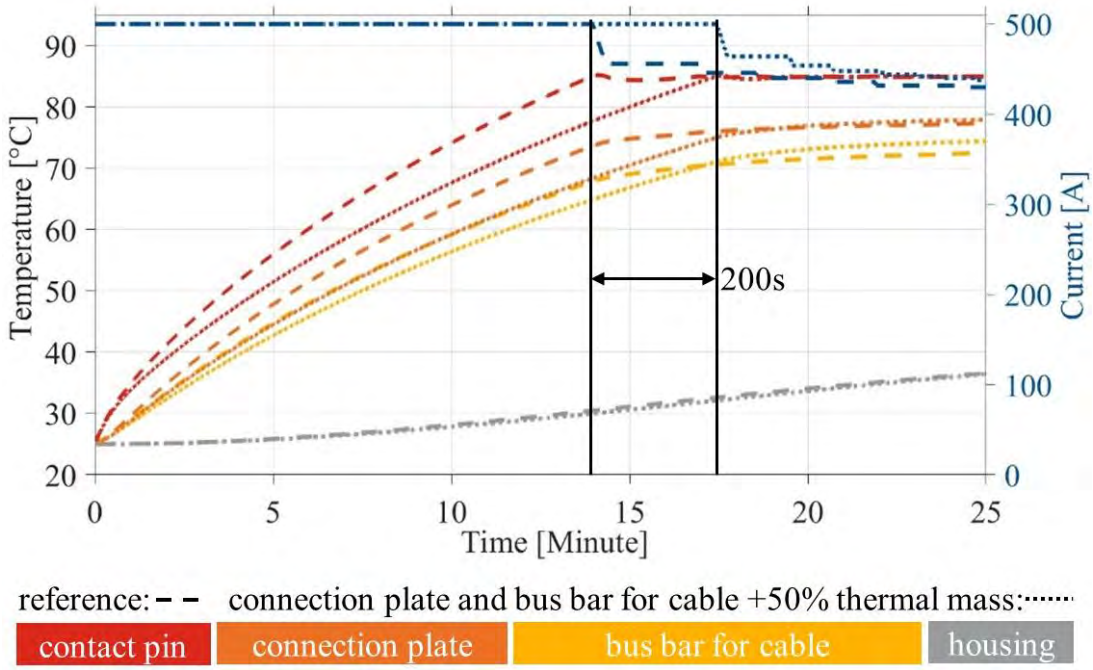

Figure 4: Comparison of basic version with adaptation of connection plate and bus bar of the cables with 1.5x thermal mass
copyright: Daimler Truck AG

6 Evaluation of the simulation test results

The start-up and ambient temperature is 25°C for both the basic version and the adapted version. With a constant charging current of 500A, blue graphs, the contact pin of the basic version, red dashed graph, reaches the final temperature of 85°C defined for the simulation within 837s. In the adapted version, the red dotted graph, the final temperature of 85°C is not reached until 209 seconds later. This means that the charging time at 500A can be maintained by 25% longer.

This is due to the increased thermal mass from the connection plate and bus bar of the cable. According to Eq. (5), the thermal capacity is increased by increasing the masses, which enables a higher heat flow $\dot{Q}$ Eq. (6) and thus serves as a larger heat sink. Due to the ability to absorb more heat, both the connecting plate, orange graph, and the bus bars of the cable, yellow graph, heat up more slowly. The reduction of the thermal resistance $R_{thermal}$ also increases the conductive heat flow $\dot{Q}_{conduction}$ Eq. (7). This allows the heat to be dissipated more quickly to adjacent components and the housing, grey graphs.

To counteract exceeding the end temperature, the charging current must be reduced after reaching a temperature at the contact pin of 85°C. In the basic version, the charging current is initially reduced to 456A for 170s until a constant temperature of 85°C is reached at the contact pin after a further reduction to 440A after 103s. In the adapted version, the charging current is initially reduced to 464A for 123s. After the subsequent reduction to 448A after 71s, a constant temperature of 85°C is also set at the contact pin. This means that the continuous charging current is 8A higher than in the basic version. Overall, this results in a greater amount of electrical energy being introduced into the system compared to the basic version. This is equivalent to a higher heat flow according to Eq. (3). The result can be seen in the two graphs of the connection plate, orange, and the busbar for the cable, yellow. Both dotted lines are above the temperature level of the respective basic version, shown in dashed lines. A similar process can also be seen in the heating of the housing, grey lines, even if the temperature difference is only slightly pronounced. The increased electrical energy input is also reflected here in the increased waste heat at a higher housing temperature. As the mass and conductive surface of the housing is large compared to the live parts, the small temperature differences can be explained.

7 Energy consumption CCS charging inlet

The simulation model of the CCS charging inlet is examined for the energy balance calculation. The amount of heat generated during the charging process in the initial situation serves as a reference value for comparing the optimisation approach of the CCS charging inlet. The system limit for the calculation extends up to the plug of the high-voltage cables of the CCS charging inlet. For this purpose, the heat flow through Joule's heating is calculated as an integral over time at all current conductors.

In order to compare the different optimisation approaches, the amount of electrical energy required to increase the vehicle's energy storage from a charge level of 20% to 80% is selected. In reality, this usually corresponds to the range of electrical energy storage units in which a constant charging power can be absorbed without having to be derated due to temperature or saturation. In the special case of this simulation, this corresponds to a charged energy quantity of 360kWh. This would result in a theoretical charging time of 56 minutes with a constant charge of 500A.

The simulation of the reference model of the CCS charging inlet including the high-voltage cables generates a heat quantity of 75.8Wh during the charging process. The temperature-related reduction of the charging current results in a total charging time of 63.7 minutes in the 360kWh transmitted.

CCS inlet	produced heat		charging time	
	[Wh]	[%]	[min]	[%]
reference	75,8	-	63,7	-
increase of thermal mass +50%	77,5	2,2	62,4	-2,0

Figure 5: CCS inlet: max. 500A, 360kWh, 25°C air temperature

The optimisation approach with the increased thermal mass of the connection plates and the bus bars of the cables of the CCS charging inlet by 50% leads to a time delay until the maximum temperature at the CCS charging inlet is reached. The charging current of 500A can thus be maintained for about 200 seconds longer. The permanently transferable charging current is 10A higher than that of the reference version. The higher charging power over a longer period of time leads to an increase in the amount of heat in the CCS charging inlet to 77.5Wh and thus an increase of 2.2%. The increased amount of heat is temporarily stored in the thermal mass of the current-conducting bus bars. The charging time, on the other hand, is reduced by 2%, which corresponds to a shorter charging time of just over one minute.

8 Conclusion

The expected results could be quantified in advance by means of thermal simulation-based testing of the new design approach for increasing the thermal mass of live conductors in the CCS charging inlet.

The comparison between the reference version and the design optimisation showed slower heating due to the higher thermal capacity. As a result, the constant charging current of 500A could be maintained for 209s or 25% longer until the defined limit temperature of 85°C was reached. This result is equivalent to a larger, charged amount of energy at the same time. Since the adjustments to the current conductors mean only a few grammes more material in absolute terms despite the enlargement by a factor of 1.5, the changes are minimal overall. This design approach can therefore be implemented in the existing housing.

Due to the modular design of the thermal test simulation, it is possible to carry out further comparisons and investigations of new solution approaches for thermal optimisation of the CCS charging inlet in special or comparable components from the charging path in general.

The test simulation can thus reduce the number of iteration loops of design approaches for component optimisation and thus reduce development time and costs.

In addition to the fact that the charging current can be kept at a higher level for longer due to the optimisation approach, the charging time is also reduced. This is important with regard to fast charging in order to promote fast vehicle availability. In addition, the improvement measures also result in energy saving potential if the charging current is reduced and the maximum permissible temperature of the CCS charging inlet is not exceeded.

9 Reference list

[1] Infineon Technologies AG, Neubiberg, Germany, https://community.infineon.com/t5/Blogs/Driving-the-Future-of-Electrified-Commercial-Vehicles/ba-p/916830#., online 15.09.2025

[2] Daimler Truck AG, Leinfelden-Echterdingen, Germany, https://hub.mercedes-benz-trucks.com/de/de/trucks/eactros-600.html, online 15.09.2025

[3] S. Schulze, “Ist Megawatt Laden die Zukunft? Potentiale, Herausforderungen und Risiken”, Daimler Truck AG, tme (Lehrstuhl für Thermodynamik mobiler Energiewandlungssysteme), RWTH Aachen University, Aachen, March 2024

[4] B. Horrmeyer, DKE (Deutsche Kommission Elektrotechnik Elektronik Informationstechnik), https://www.dke.de/de/arbeitsfelder/mobility/news/megawatt-charging-system-elektrifizierung-schwerlastverkehr, online 15.09.2025

[5] R. Collin, Y. Miao, A. Yokochi, P. Enjeti, A. v. Jouanne, “Advanced Electric Vehicle Fast-Charging Technologies“, MDPI: Energies, May 2019

[6] M. Thoben, F. Sauerland, K. Mainka, S. Edenharter, L. Beaurenaut, “Lifetime modeling and simulation of power modules for hybrid electrical/electrical vehicles”, Volume 54, Issues 9–10, 2014, pages 1806-1812, Science Direct, London, ISSN 0026-2714, https://doi.org/10.1016/j.microrel.2014.07.009, 2014

[7] DIN e.V., DIN EN IEC 62196-1:2022, german version: Stecker, Steckdosen, Fahrzeugkupplungen und Fahrzeugstecker - Konduktives Laden von Elektrofahrzeugen - Teil 1: Allgemeine Anforderungen, Berlin, Germany 2022

[8] M. Vidmar, Lectures on the scientific fundamentals of electrical engineering, University Ljubljana, Slowenien, Print ISBN 978-3-642-52572-8, 1928

[9] C. Gerthsen, D. Meschede, Gerthsen Physik, Die ganze Physik zum 21. Jahrhundert, Springer, Berlin, ISBN 978-3-540-02622-8, 2004

[10] ZVEI, Zentralverband Elektrotechnik- und Elektroindustrie, Technischer Leitfaden Thermosimulationsmodelle Version 1.1, Köln, Germany 2020

[11] J.P. Huang, Transformation Thermotics for Thermal Conduction, Convection and Radiation, Springer, Singapore, Online ISBN 978-981-15-2301-4, January 2020

[12] C. Borgnakke, R. E. Sonntag, Fundamentals of Thermodynamics, Weinheim, Wiley, 10th Edition, ISBN: 978-1-119-72365-3, July 2020

[13] P. Steinmetz, Thermische Simulation einer CCS (Combined Charging System) Ladedose für Schwerlastkraftwagen, Hochschule Bonn-Rhein-Sieg, unpublished, April 2024

Advances in Multiphase HVB Modelling: Coupling of Particle Depositions and Channel Blocking

David Koti, Dr. Enes Aksamija

Magna Vehicle Engineering
MAGNA STEYR Fahrzeugtechnik GmbH & Co KG
Liebenauer Hauptstrasse 317

david.koti@magna.com
enes.aksamija@magna.com

Abstract: Thermal runaway and venting of HV-Batteries are multi-physical fields which include many interconnected phenomena under extreme flow and heat transfer conditions (velocity, pressure, temperature and their respective gradients). Radiation, phase change (boiling, melting, solidification), housing deformation, combustion, arcing and particle/wall interactions play a significant role but only a few of these mayor contributors can be modelled in an effective manner.

So far, only thermal coupling was implemented in previous work which did not fully represent the modified flow behavior due to particle deposition. Mayor breakthrough was achieved in the current study by combining the heat transfer of particulate depositions with the effect of channel blocking (sudden closure of flow passages).

A combined multi-phase approach was used to account for these effects simultaneously. The framework was successfully implemented in the STAR-CCM+ environment and was tested from module to complete pack level.

Keywords: CFD, HVB, thermal runaway, venting, particle deposition, channel blocking

Contribution: 2025 FKFS Conference on Vehicle Aerodynamics and Thermal Management
15 – 16 October 2025 | Leinfelden-Echterdingen

1 Introduction

It has been observed by multiple research groups that large glowing particles, which manage to escape the pack after a venting event are one of the major sources for ignition of the highly flammable gas mixture (see Figure 1). It is a common strategy in the automotive industry to implement particle separation strategies into the venting channel design, by means of baffles, traps, mazes, grids or dedicated venting devices. CFD simulations can only contribute value to channel design if understanding of particle-wall interactions is further deepened and calibrated with measurements. Modelling workflows need to account for all the interconnected physical effects of which there are many: high Mach number flow, multiple reacting species, thermal radiation, particle deposition with phase change, gradual channel clogging, geometry deformation, etc. The present project aims at closing one of the largest and last missing links in the modelling chain, namely the thermal and gas dynamical impact of particle depositions on cell-to-cell propagation and therefore channel design.

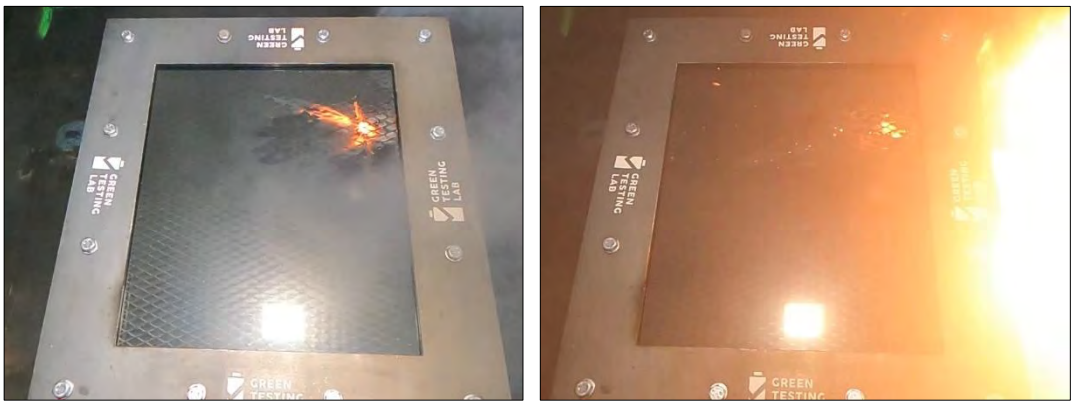

Figure 1: Glowing particles ejected during venting (left), ignition outside caused by the escaped large glowing particles (right), [1].

2 Modelling

Modelling of venting phenomena is a novel and lively field with many different approaches among research institutes and OEMs for tackling the complex multi-physical challenges. It is common practice to increase modelling complexity step-wise and add physical phenomena depending on the problem statement. Due to the increasing geometrical complexity of particle separation strategies in modern HVB venting channels, the particle-wall interactions (incl deposition and clogging) need to be modeled reliably in order to evaluate different design with CFD. As a modelling foundation, the multi-component turbulent gas phase was modeled together with solid walls (CHT) (Figure 2a). The first step-up of complexity is the addition of a lagrangian phase representing molten particles, including thermal radiation and temperature dependent probability for deposition (Figure 2b). As a third complexity step, the

deposition is modeled as a separate continuous phase, which can exchange mass and heat with walls and gas while blocking the flow locally for the gaseous phase (Figure 2c).

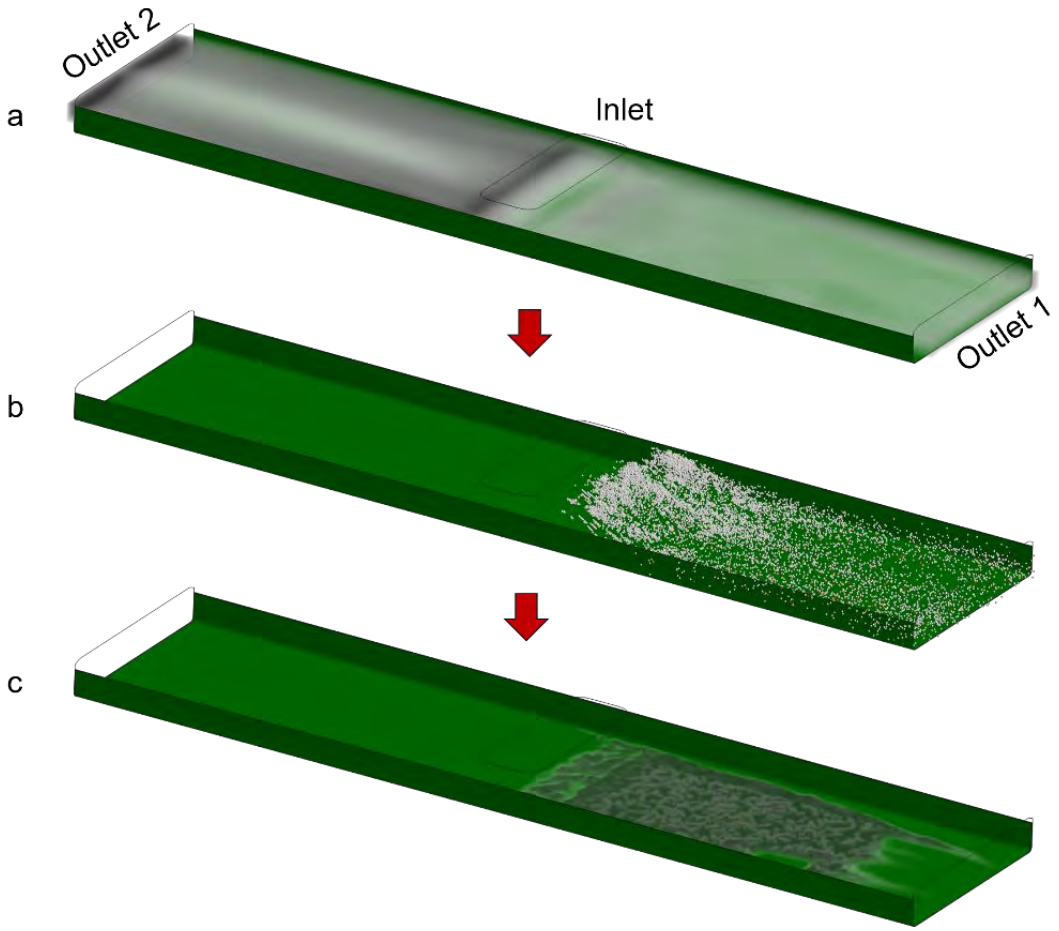

Figure 2: Schematic overview of different modelling level strategies for multi-physical problems.

2.1 Demonstration geometry

A generic T-junction was chosen as a demonstrator geometry as it represents many typical flow scenarios within battery packs and modules. Figure 3 shows an isometric view of the geometry with the respective in/outlets. The venting direction was chosen downwards with realistic distances between cells and solid walls which represent battery/cell housings. The injection angle of the particles was varied between three discrete injection angles relative to the main gas flow in order to demonstrate the increased deposition rate and clogging behaviour on one side.

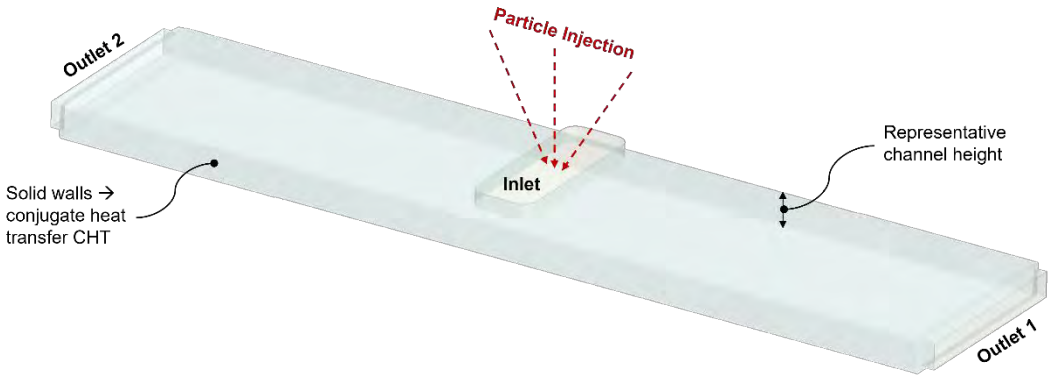

Figure 3: Schematic overview of the simulated geometry

3 Results

Figure 4 shows the velocity distribution on a cut plane in the middle of the channel comparing two modelling approaches. While modelling without particulate phase results in a perfectly symmetrical flow distribution between the two outlets (Figure 4a), inclusion of a lagrangian phase leads to accumulation of a deposition phase in the respective channel (Figure 4b-4d).

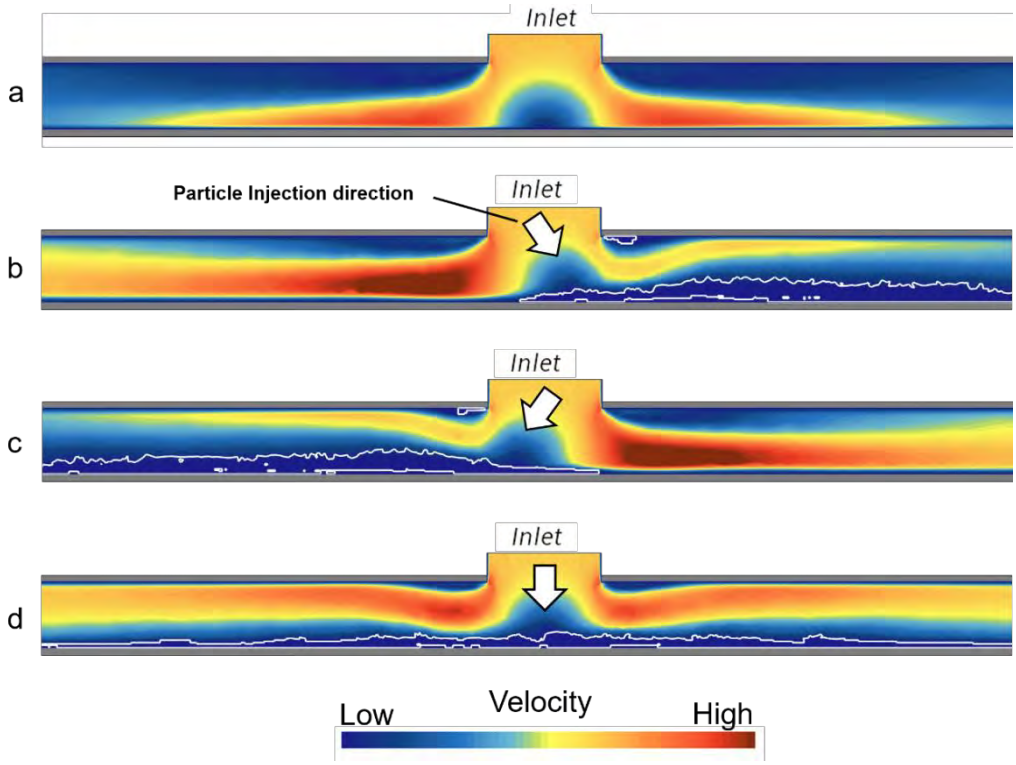

Figure 4: a: gas flow only, b: particle injection to the right, c: particle injection to the left, d: neutral particle injection direction; phase boundary to the deposit phase is indicated by the white line.

Depending on the particle injection direction, increased gas flow rate can be observed at the opposite side of the channel, proving the clogging behaviour of the deposited phase.

At the outlets, gas mass flow rates and average temperatures were recorded (see Figure 5). The simulation with only gas is represented by the black line for both outlet 1 (right) and outlet 2 (left). The case with inclined particle injection towards one outlet is represented by the blue line. Two main findings can be observed: the flow rate is lower at outlet 1 due to deposition towards this direction (Figure 5b) and respectively the flow rate is higher in the opposing channel where the cross section is free (Figure 5a). In contrast, the temperature profiles do not show the same symmetrical behaviour when channel blocking occurs. The shape and level of the gas outlet temperature strongly depends on the particle deposition probability (Figure 5d) as this parameter determines which portion of the enthalpy is removed from the gas stream during a particle-wall interaction.

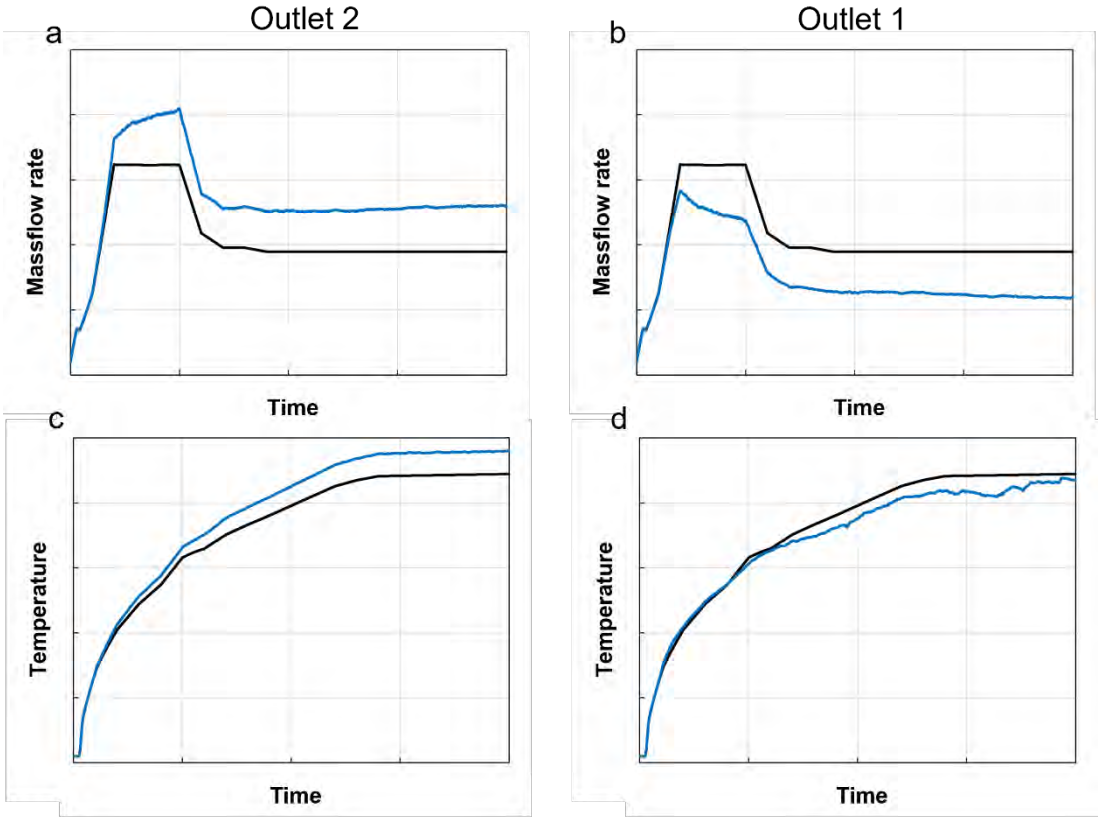

Figure 5: Mass flow- and temperature profiles at the channel outlets for two modelling approaches; gas only (black), deposition modelling with injection towards outlet 1 (blue).

The distinct differences of flow fields when changing modelling depth is also reflected in vastly intensified heat transfer and significantly higher local wall temperatures, as seen in Figure 6. Heat transfer from a pure gas stream is typically homogeneous (see Figure 6, top) and significantly less intense compared to conductive heat transfer from a sticking molten solid. Local wall temperatures at the deposition sites can be higher by several hundred degrees (see Figure 6, bottom) and therefor cause thermal propagation if located on a neighboring cell wall. This example shall demonstrate the importance of the correct modelling depth for the prediction of cell-to-cell propagation.

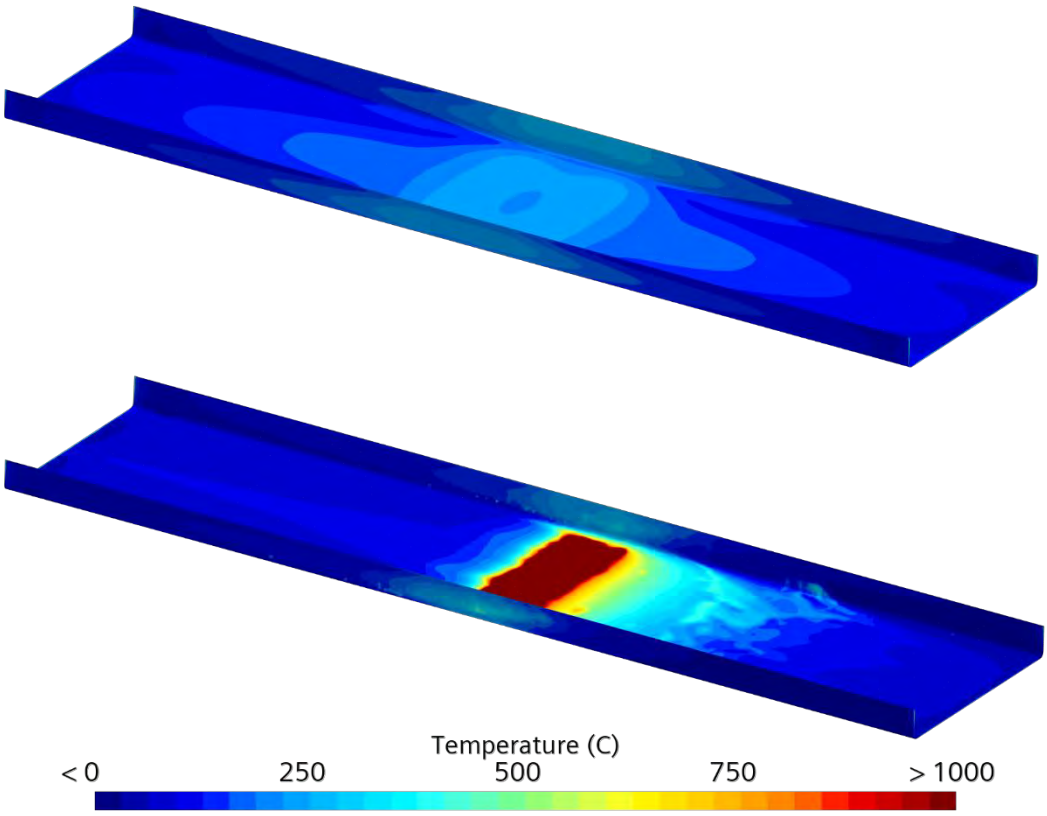

Figure 6: Comparison of wall temperatures depending on the modelling approach; smooth distribution with the gas-only approach (top) and increased temperature levels with heterogenous patches when particle deposition is modelled (bottom).

4 Validation

Validation of venting simulations is extremely challenging due to the multi-physical nature of the problem and the extremely harsh conditions which can damage equipment and falsify results. In general, CFD can be an indispensable tool in venting channel design if the adequate modelling depth is chosen and all relevant phenomena are captured. While generic flow field understanding can be obtained from straight-forward CHT simulations, where only the gas phase is considered, higher modelling depth is required for the evaluation of propagation risk. As shown in Figure 7, the measured outlet temperature of the glass battery matches the confidence band of the simulated values when the heat of the particles is considered (red band) using the above-mentioned approach.

Future focus will be put on validation of deposition probabilities. The model parameters need to be calibrated against recorded video data until matching deposition patterns are obtained in the simulation. As particle sizes and composition vary vastly between cell chemistries, accompanying validation will remain mandatory in the foreseeable future.

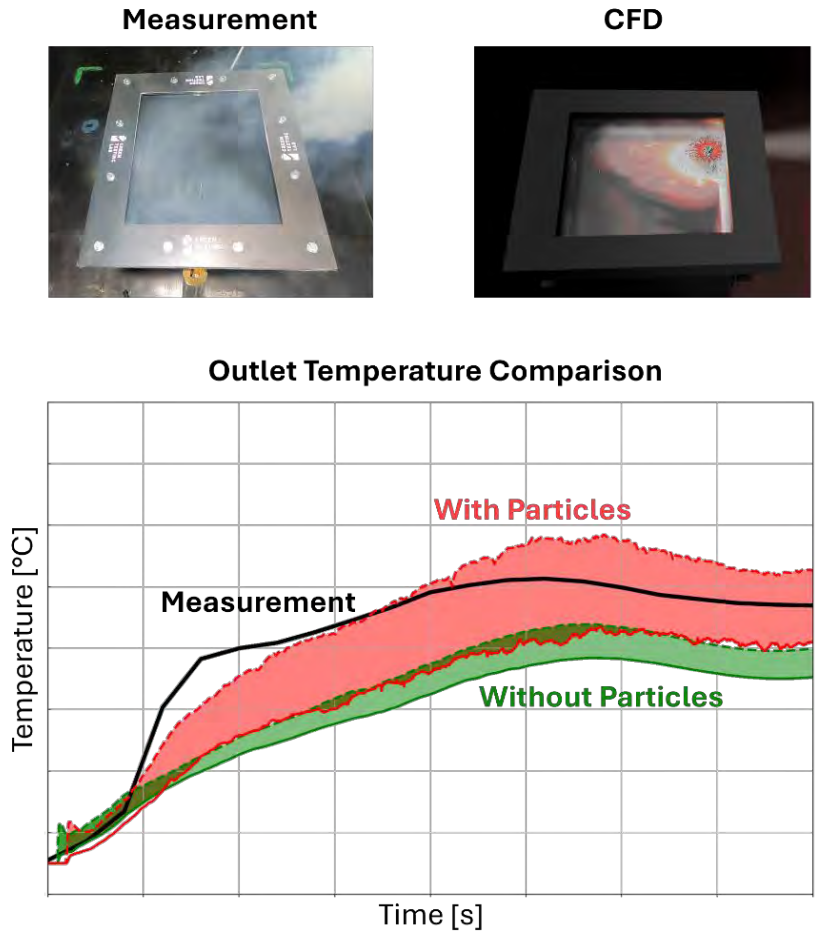

Figure 7: Experimental validation of two modelling approaches for temperature probes placed at the channel outlet.

5 Conclusion & Outlook

Due to the ongoing trends of stricter legislation for HVB pack design (no thermal propagation & no fire within increasing time frames), the requirements for CFD Simulations as a predictive and supportive tool are also increasing. The current work demonstrated the closure of one significant gap in the modelling chain of HVB venting modelling, namely the thermal coupling of local particle depositions as well as the subsequent local clogging of the channel. Only by taking into account the change of the velocity flow field due to the deposited phase, CFD becomes a viable tool for complex channel design with multiple possible gas paths, obstacles and particle traps.

The authors want to thank the partners from the FFG funded project *Prevent+* in which the results from present paper were elaborated: *Virtual Vehicle Research GmbH*, *Green Testing Lab*, *Kreisel Electric GmbH & Co KG*, *Technische Universität Graz* and *Magna Vehicle Engineering*.

In the upcoming follow-up project SafeSustain [2] deeper focus will be put on particle-wall interactions during venting as well as the implementation of ecofriendly materials for thermal protection.

6 Reference list

[1] PREVENT+, FFG funded project, “Understand PaRticlE VENTing and Arcing for Safer Batteries Plus”, 2022-2025.

[2] SafeSustain, FFG funded project, “Safety by Sustainability”, 2025-2028.

Efficient Pulsation Mitigation Modeling for Low Speed Open Jet Wind Tunnels with Helmholtz Resonator

Joseph C. Yen, Amir A. Kharazi, Edward G. Duell, and Joel Walter

Amentum Technology, Inc. (formerly Jacobs Technology, Inc.)
600 William Northern Blvd., Tullahoma, Tennessee, USA

Joseph.Yen@us.amentum.com
Amir.Kharazi@ us.amentum.com
Ed.Duell@us.amentum.com
Joel.Walter@us.amentum.com

Abstract: Recently the authors demonstrated a novel computational strategy for the simulation of the low frequency pressure pulsation phenomena that pertains to Göttingen style open jet wind tunnels (OJWT). The analysis strategy incurs very low computational cost and yet is predictive since the unsteady solution unequivocally reveals the airspeed dependence of the flow acoustics coupling physics. The work is now expanded to demonstrate the scope of mitigation control of the pressure pulsation using a Helmholtz resonator (HR) with the same OJWT geometry . The study begins with a simple benchmark acoustic problem to render a demonstration of the computational aeroacoustics (CAA) solver and an instructive review of a standing wave attenuation by HR on a looped straight waveguide. In the follow on wind tunnel study, the computer simulation reveals a strong effect by HR installation location on the effectiveness of pulsation attenuation. This effectiveness is demonstrated using a holistic presentation of the transient pressure response over the entire wind tunnel airline. The simulated antinodal HR installation is shown to significantly mitigate the pressure fluctuating amplitudes in the test section and along the rest of the airline duct. The current study renders an expanded understanding of the pressure pulsation phenomenon that is significant and valuable for continuous design improvement of OJWT. The tested computational strategy gives rise to a digital twin of an OJWT, particularly for pressure pulsation study. The computer model can provide accurate guidance and thus reduced costs for developing a subscale wind tunnel model experiment, which has been the most reliable but more expensive method for the development of pulsation mitigation design. With the predictive method of the OJWT digital twin, a significant reduction or eventual replacement of the laboratory effort in the future development of open jet wind tunnel airline may be possible.

1 Introduction

Helmholtz resonators (HR) have been used to mitigate the low frequency pressure pulsation phenomenon (Sellers et al., 1985) in Göttingen style low-speed open jet wind tunnels (OJWT). Several successful applications were reported (Waudby-Smith and

Contribution: 2025 FKFS Conference on Vehicle Aerodynamics and Thermal Management
15 – 16 October 2025 | Leinfelden-Echterdingen

Ramakrishnan, 2007; Duell et al., 2010; Kharazi et al., 2013; Best et al., 2023). The deployment design of HR usually depends on a subscale model of a wind tunnel under development. The experimental method is by far the most reliable and preferred approach, due to the lack of a predictive and computationally efficient tool for simulating the flow acoustics coupling phenomenon of pressure pulsation in a physical wind tunnel airline geometry.

Recently, an innovative computational strategy for the study of the pressure pulsation was proposed and demonstrated (Yen et al., 2025). The method was built on a non-conventional high resolution computational aeroacoustic (CAA) methodology and leveraged the low frequency nature of the physical problem in the computer model development. The computational strategy gave rise to a significant reduction in computational overheads while preserving the numerical resolution power for the unsteady flow field and companion acoustic field, both of which are necessary elements to the forming of the OJWT pressure pulsation phenomenon.

The previous study successfully revealed the conditional or staged intensification of the unsteady pressures when the airspeed was varied. In a most intensified pulsation condition, the same dominant frequency could be identified from both the preferred open jet vortex shedding mode and an excited longitudinal standing wave mode along the closed loop airline. This simulation result agrees very well with the long understood mechanism of the low frequency pressure pulsation phenomenon. In addition to showing frequency coincidence as explained by analytical methods (Arnette et al. 1999; Rennie, 2000), the computational method also predicts the fluctuating pressure amplitudes for quantitative assessments.

The same efficient, predictive computational strategy is expanded in this paper to the study of pulsation mitigation control with Helmholtz resonator (HR). Table 1 shows six cases that are included in the study whose solution will be discussed later in Section 4.1 through 4.6,

Table 1. Matrix of study

Case number	Computational model	Wind on/off
1	Baseline Closed-Return Open-Jet Wind Tunnel (OJWT)	On
2	Design Verification of 3.06 Hz Helmholtz Resonator	Off
3	Effect of HR on Acoustic Response with a Looped Long Straight Duct	Off
4	Installation of HR on Baseline OJWT at Pressure Node	On
5	Installation of HR on Baseline OJWT at Pressure Antinode #1	On
6	Installation of HR on Baseline OJWT at Pressure Antinode #2	On

respectively. The current study leverages the previous results to develop an HR of natural frequency that matches the dominant frequency in a most intensified pressure pulsation condition of the baseline OJWT (without HR). This HR design is then verified computationally using the same CAA solver with quiescent air. The effectiveness of the HR at attenuating a frequency matched standing wave is demonstrated next on a straight duct with the installation location at a pressure node and a pressure antinode, respectively. This case is a pure acoustic test condition with quiescent air, and the result provides a reference condition for comparison with the solution of the simulated OJWT airline with HR. The effect of the HR on the OJWT pressure pulsation is studied next with the resonator installed at each one of three locations that include one pressure node and two different pressure antinodes. These locations coincide spatially with the amplitude extremities of fluctuating pressure predicted by the baseline OJWT solution.

2 Open Jet Wind Tunnel Computer Model

Figure 1 shows a computer model of a modern design of Göttingen style automotive OJWT (Best et al., 2023). The wind tunnel is engineered for aeroacoustic testing purposes and includes several distinct noise control features. For example, the airline is shown to include elongated sound absorbing turning vanes in some corners and slanted wall design in the test chamber to prevent lateral standing waves. Aerodynamically the overall wind tunnel airline circuit is streamlined and generally produces a minimum overall pressure loss and therefore low power consumption. The overall centerline duct length of the full scale OJWT is about 224 m. This wind tunnel geometry is the basis of the baseline airline that was studied previously (Yen et al., 2025) for pulsation prediction demonstration. The same computer model will also be applied in the current study.

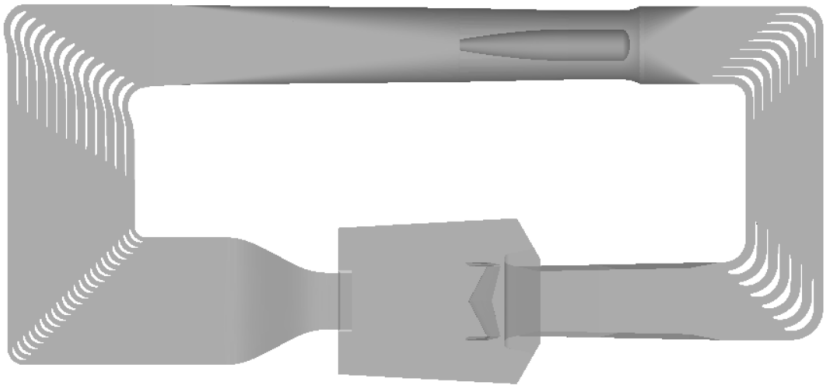

Figure 1. A modern closed return OJWT airline for aeroacoustic testing

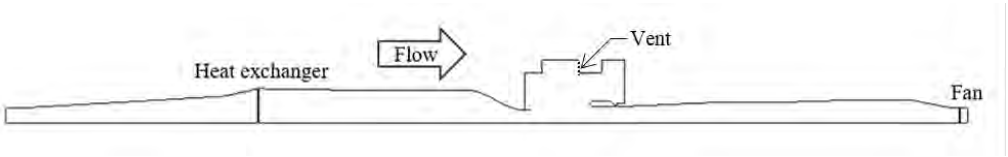

Figure 2. Axisymmetric representation of open jet wind tunnel

It is computationally very costly to undertake a CAA simulation of the pressure pulsation phenomenon with the physical 3-D wind tunnel airline geometry. As reasoned in detail in the previous work, the low frequency nature of the problem permits the use of a simplified axisymmetric representation of the OJWT airline as shown in Fig. 2. As demonstrated previously with the same simplified airline geometry, the flow acoustic coupling physics was unequivocally revealed to predict the conditional intensification of the fluctuating pressures over a range of airspeed setpoints. In the axisymmetric geometry, the nozzle exit diameter (D) is 5.64 m based on which the airline length is about 40 D. The axial range of the open jet test section starts from the nozzle exit plane that is X/D=0 to the beginning of the collector at about X/D=2.5. More detail of the simulated test section geometry can be referred to the previous work.

The axisymmetric OJWT airline retains the effect of closed loop circuitry of the physical wind tunnel by imposing a paired cyclic boundary condition for the two far end boundaries of the linearized airline geometry. The computer model also mimics the actual wind tunnel by including an atmospheric vent in the test chamber, a fan model, and a heat exchanger model. These models are shown in Fig. 2. The vent is designed to provide an invariable pressure reference regardless of the airspeed. The overall energy balance of the closed airflow

system during a steady state running condition is sustained with the fan and heat exchanger models. More detail of the rationale and setup of these modelling features are detailed in the previous work (Yen, et al, 2025).

3 Computational Aeroacoustics Solver and Meshing Strategy

The computer simulation of the unsteady wind tunnel flow will be performed using an in-house developed JUSTUS code (Yen et al. 2010). The methodology of the solver is based on the method of space-time conservation element and solution element (abbreviated as CESE by the methodology originator Chang, 1995). It is an explicit method with a solution formulation that fundamentally complies with the hyperbolic nature of flow physics. The high resolution solution methodology also incorporates a time-accurate local time stepping scheme (Chang, 2003; Yen, 2011) whose implementation also complies with the non-conventional space-time flux conservation methodology of the CESE method. The local time stepping scheme facilitates a uniform numerical quality for the flow and acoustic solution across a space domain that is spanned by solution cells of very large size disparity for various resolution requirements. This solution capability feature is important for ensuring consistent solution quality anywhere in the wind tunnel air space. It is also very advantageous computationally because the solution method permits the use of very coarse cells for the air space outside the test chamber where the resolution of sound propagation is much more important and requires much lower mesh density than the bulk flow motion of small turbulence length scales. The solution method permits bespoke spatial resolutions in different locations that renders significant solution efficiency for the challenging flow acoustics coupling problem. The open jet solution is acquired using a method of implicit large eddy simulation (ILES) (Yen et al. 2010).

a)

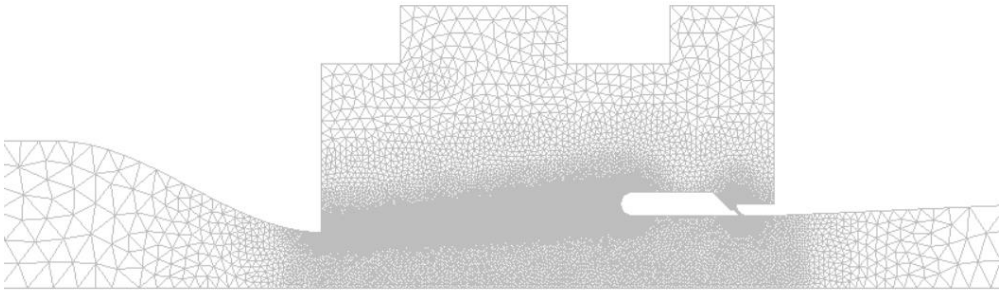

b)

Figure 3. a) Overall view and b) close-up view of unstructured triangular mesh

Figure 3 shows the computational mesh that was applied to study the baseline OJWT geometry (Yen, et al, 2025). The mesh includes all triangular cells with various levels of refinements where the finest mesh is designated for the open jet shear layer resolution and progressively coarser mesh is used elsewhere. As shown in Fig. 3, the coarsest mesh is present in the airline space outside the test chamber where the solution resolution requirement is set up to fully capture the passing sound waves that pertain to the pressure pulsation phenomenon. The coarse mesh also becomes a natural filter that damps off the flow and acoustic energy

that is associated with smaller length scales or wavelengths. The smaller mesh is also created near the proximity of HR connection to the airline duct. Figure 4 illustrates an example mesh refinement near the neck of HR. The detail of the mesh design can be referred to the previous work (Yen et al., 2025). The same meshing strategy for the axisymmetric wind tunnel geometry produces total cell count for different cases in the study ranging approximately from 52,000 to 57,000.

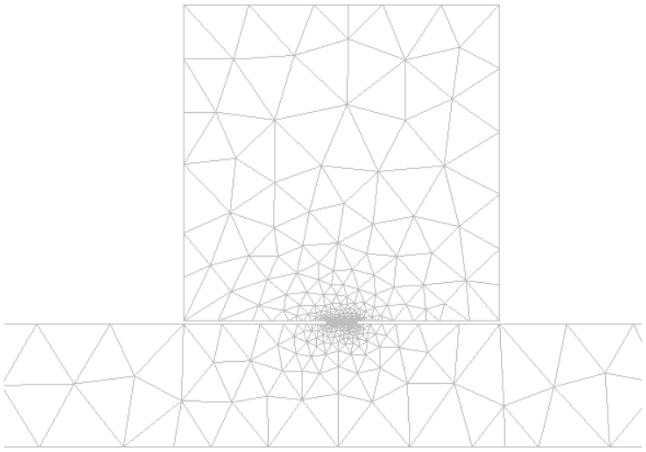

Figure 4. Example of mesh refinement near the neck of Helmholtz resonator on a duct

The previous work carefully examined the predicted time-averaged flow properties and statistical result of the turbulent open jet solution by comparing to applicable theories. Very good agreement was found, which verified the solution capability of the computational solver and meshing strategy. The current study applies the same computational strategy for the different demonstration cases of pulsation mitigation study using Helmholtz resonator. To provide a consistent quality of unsteady solution with the previous work, the same Courant–Friedrichs–Lewy (CFL) number of 0.75 is used here for the solution time integration. The minimum solution time step size for the different cases in the study ranges from approximately 1.2e-5 s and 1.5e-5 s based on the chosen CFL value and the design of the unstructured triangular mesh. The minimum time step size pertains to the smallest cell sizes and larger cells will naturally incur larger time step sizes during the solution time marching process, as defined in the applied local time stepping method (Yen, 2011).

The 2D axisymmetric wind tunnel model neglects several loss factors in the real wind tunnel such as wall boundary layers, flow conditioning and cornering devices, high loss elements in the heat exchanger. This condition represents a reduced damping factor to counter the intensification of flow acoustics coupling. That is to say that the simulated resonance condition is expectedly to produce pressure perturbation amplitudes that are higher than the real wind tunnel data. In addition, the 2D problem setting is also a compounding factor for higher perturbation amplitude prediction, due to the more coherent shedding vortices than in 3D and therefore a stronger forcing function to produce a more intensified result of pressure pulsations. Despite the expected higher amplitude prediction, the proposed solution strategy remains useful of providing efficient assessment of relative effects on pulsation tones and amplitudes for the study of changes in geometry and boundary conditions.

4 Results and Discussion

The airspeed setpoint in each case of the study is determined by the velocity solution inside the nozzle of the simulated wind tunnel airline. In a calculation, the setpoint is reached by

varying the pressure rise of the fan model (to replenish the momentum of the wind tunnel flow) until the transient solution reveals a stable oscillatory response about the target airspeed. The temperature setpoint at the same nozzle location is reached with removal of the increased flow internal energy by the heat exchanger model (to remove the dissipated heat from the turbulent open jet flow). The fan pressure rise cannot be known accurately a priori and therefore the arrival of an airspeed setpoint requires an iterative calculation process until the target airspeed is reached.

The previous work (Yen et al., 2025) showed that both the airspeed and temperature setpoints could be reached and became sustaining after the wind tunnel flow solution was developed for 60 s or about 180 cycles of the most intensified frequency of the flow perturbation. To report the transient solution after the initial 60 s of run time, the stable fluctuating solution is further developed for another 12 s or about 36 cycles to provide a sufficient population of transient data points. This extended solution time is important for statistical quality due to the nonstationary nature of turbulent wind tunnel flow. The nonstationary flow nature is commonly experienced in a real-world wind tunnel condition. The required two-stage solution development would be very costly computationally if a 3-D wind tunnel model were to be applied to tackle the problem. In contrast, the computational strategy proposed in the current study is quite affordable as an efficient design tool due to the capability of rendering a quick solution turnaround time.

The study examines the perturbation pressure based on root-mean-square (RMS) values to assess the magnitude of the pulsation phenomenon. The companion turbulent kinetic energy (TKE) inside the open jet shear layer will also be examined. The holistic map of the perturbation pressures will be presented. The perturbation pressure is calculated by subtracting the time-averaged pressure from the predicted pressure solution at each solution location of the entire wind tunnel domain. The TKE as presented is calculated based on the perturbation velocity by subtracting the time-averaged velocity from the predicted transient velocity solution. The reported perturbation pressures and TKE are nondimensionalized based on the dynamic pressure and kinetic energy at the setpoint airspeed value.

4.1 Baseline Closed-Return Open-Jet Wind Tunnel (OJWT)

The baseline condition was previously investigated using the same computational strategy reported in the current study. The predicted result showed a most intensified condition of pressure pulsation whose oscillating energy peaked sharply at 3.08 Hz frequency with a 50 m/s airspeed setpoint. This frequency coincides with the 3.06 Hz which is the fourth longitudinal eigenmode (Kinsler, et al, 1982) of the simulated wind tunnel airline. This baseline solution is a reference condition that does not include any pulsation mitigation applied to the simulated wind tunnel geometry. The baseline geometry applies a neutral horizontal position of the collector flap in the test section and the pressure shell effect of the airline duct is intact without inadvertent venting (such as air leaks through the perimeter of an access door). For comparison to the baseline solution, the simulation of the current study for mitigation control demonstration is performed at the same 50 m/s airspeed setpoint.

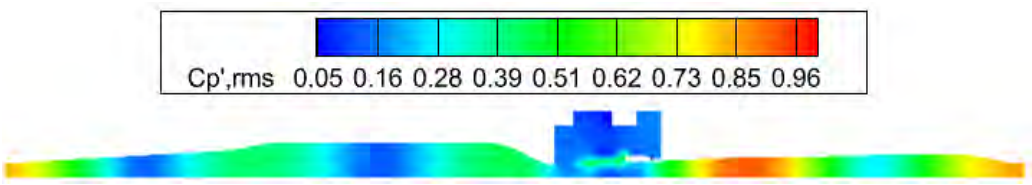

Figure 5. Perturbation pressures of baseline condition of open jet wind tunnel

Figure 5 shows the previously predicted solution whose perturbation pressures are now analyzed to present the root-mean-square (RMS) values. The $C_{p',rms}$ is calculated using the transient pressure solution collected after a steady response solution is reached. The statistical calculation is made where the pressure perturbations (in reference to the time averaged value) are nondimensionalized by the flow dynamic pressure at the airspeed setpoint. Figure 5 highlights important observation also reported previously (Yen et al., 2025). The pressure solution shows a clear pattern of standing wave along the simulated airline where repeated crests and troughs of perturbation pressure can be identified. The axial spacings between consecutive amplitude peaks are approximately 10 D in reference to the nozzle diameter (D) of the linearized axisymmetric airline. The predicted peak pressure amplitudes are higher in the airline duct downstream of the test section in comparison to the upstream.

The baseline pulsation result obtained from the previous work will be included for comparison in the following discussion. The predicted peak pulsation frequency will also be the basis for the Helmholtz resonator design to be used in the demonstration of pulsation mitigation simulation based on the advocated computational strategy.

4.2 Design Verification of 3.06 Hz Helmholtz Resonator (HR)

The use of Helmholtz resonator (HR) for pulsation attenuation is inspired by the postulated theory that the coupling between the unsteady open jet vortex shedding modes and frequency-matched longitudinal acoustic eigenmodes along the wind tunnel airline would give rise to more pronounced amplitudes of the unsteady pressures when compared to a neutral nonstimulated open jet condition. A successful working of HR is thought to weaken or break the coupling mechanism between the forcing function by the flow induced perturbation and the responses of the acoustic airline eigenmode. Based on this premise and the baseline solution, a 3.06 Hz Helmholtz resonator is developed and computationally verified. The verification simulation is made with the HR on a simple straight waveguide whose cross sectional area is four times the neck opening area of the resonator. The acoustic solution is acquired using the full (instead of linearized) Euler solver of the JUSTUS code.

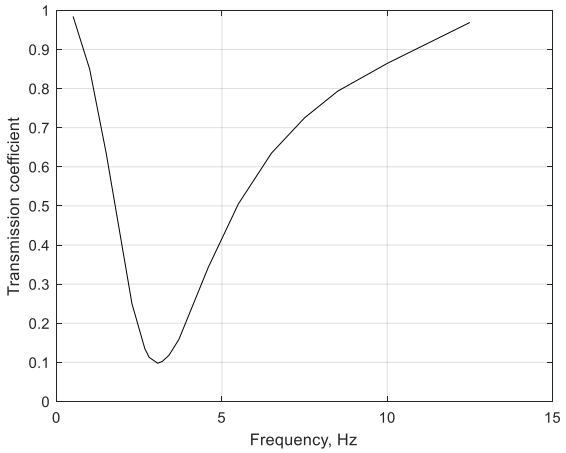

Figure 6. Predicted transmission curve of a 3.06 Hz Helmholtz resonator

Figure 6 shows the predicted transmission coefficient curve of the HR over a range of forcing frequencies. As shown, the result resembles the response of a bandpass filter (Kinsler et al., 1982) in which the design frequency is centered at 3.06 Hz where a transmission coefficient of 9.8% is shown in reference to the simulated sound source power. This 3.06 Hz Helmholtz resonator geometry will be applied thoughout this pulsation mitigation study

In this verification study, the HR is predicted to block and reject 90.2% of the incoming sound power back toward the source end. The 9.8% remaining sound power would pass over the HR location toward the opposite end of the sound source. The rejected sound wave and transmitted sound wave do not get to interact in the simulated condition with the open ended ductwork. When the ductwork becomes looped as in a closed return wind tunnel airline, such a wave interaction would occur and produce some form of standing wave. This condition will be studied next.

4.3 Effect of HR on Acoustic Response with a Looped Long Straight Duct

The acoustic attenuation effectiveness of the 3.06 Hz HR is first examined in a simple problem setting with a standing wave along a looped long duct with quiescent air. The looping of the long duct at the two far end boundaries is simulated based on a paired cyclic boundary condition as also applied in the baseline closed return OJWT model (Yen et al., 2025). Figure 7 shows the computer model of the long duct with HR installed separately at the pressure node and antinode. The location of the sound source is shown by a darkened line segment between two circular markers denoting the range of the sound source. The duct length is chosen to be the same as the 40 D long OJWT airline, which equals to two wavelengths of a 3.06 Hz sound wave at 20° C. The acoustic sound source is located on the duct wall over the axial range that coincides with the range of the flow collector in the simulated OJWT test section. The radius of the duct is set to equal to the axial range of the sound source such that the sound emitting surface area of the source equals to twice the duct cross sectional area. The sound source is assumed to emit a coherent pressure at 1.0 Pa peak amplitude ($\frac{1}{\sqrt{2}}$ Pa RMS), and the problem setting would produce a left running and a right running sound waves along the duct of the same 1.0 Pa peak amplitude ($\frac{1}{\sqrt{2}}$ Pa RMS). In an uncontrolled condition, a standing wave is expected to form with 2.0 Pa peak amplitude ($\sqrt{2}$ Pa RMS). This subset problem of the current study includes a baseline case and two controlled cases with the HR at a pressure node and at a pressure antinode, respectively. The locations of node and antinode are determined from the baseline standing wave solution. The problem setting would produce multiple nodes and antinodes, and without losing generality for attenuation discussion only those to the right hand side of the sound source are included in the acoustic study.

a) HR installed at a pressure node

b) HR installed at a pressure antinode

Figure 7. Installation of Helmholtz resonator on a long duct

Figure 8 shows the predicted root-mean-square (RMS) pressure contour map of the acoustic response of the three cases in the study. Figure 9 displays the same pressure response result as a function of axial displacement from a X=0 location. The X=0 reference location coincides with the nozzle exit of the OJWT, whose longitudinal length is 40 D. The baseline result shown in Fig. 8a reveals a clear pattern of standing wave where it shows equally spaced, alternate minimum and maximum amplitudes along the long duct. As detailed in Fig. 9, the peak RMS value is about 1.4 Pa and the peak-to-peak spacing is 10 D. This predicted standing waveform result agrees with the theory result, as discussed previously. Figure 8b shows the solution with the HR at the first pressure node to the right of the sound source. As shown in Fig. 9, the predicted standing wave pattern is nearly unchanged except for a slightly higher

peak amplitude than the baseline. Figure 8c shows the result with the HR installed at the first pressure antinode to the right hand side of the sound source. Compared to the other two cases, the result of the HR at the antinode shows a weakened standing waveform of lower peak amplitude. The original antinode location of the HR installation is turned into a node and the phase of the standing waveform is shifted by 5 D distance (one half of the 10 D peak-to-peak

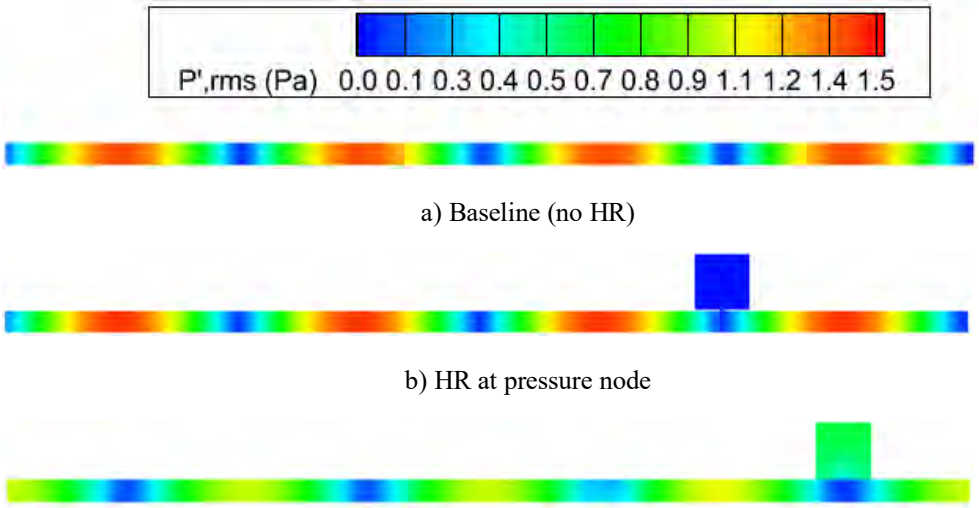

a) Baseline (no HR)

b) HR at pressure node

c) HR at pressure antinode

Figure 8. Acoustic pressure in root-mean-square values

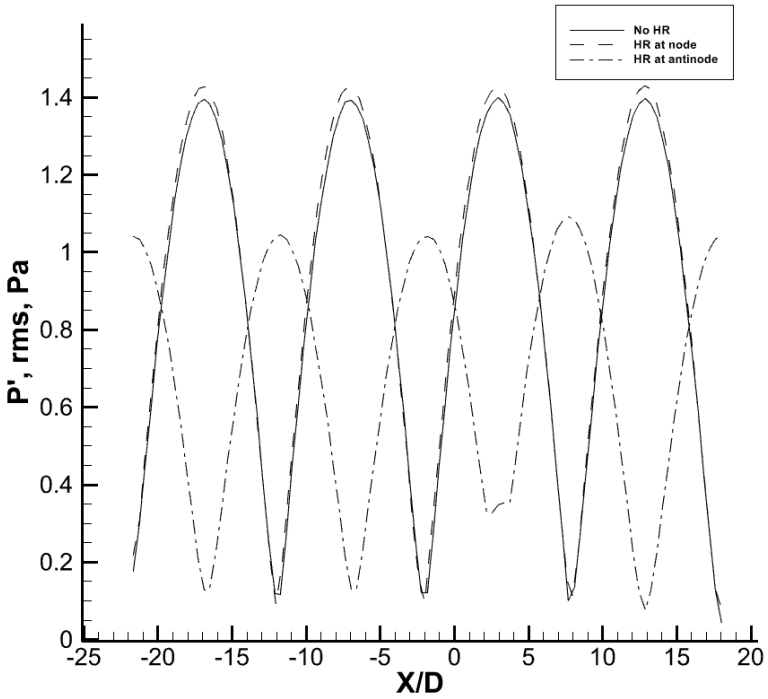

Figure 9. Variation of acoustic pressure along duct

spacing). The peak RMS amplitude is seen to reduce to about 1.05 Pa, which is 25% lower than the baseline condition.

The result of the antinode HR installation in Fig. 9 also represents a reduced standing wave ratio (SWR) (the ratio of the antinode to node amplitude) when compared to the baseline condition. This suggests the modified standing wave is now comprised of two opposite traveling waves of different amplitudes. This amplitude disparity may be understood from the result of the HR design verification in Fig. 6. The HR produces a reduced transmitted sound energy and therefore a lowered sound pressure. In the simulated standing wave condition, the reduced sound amplitude wave, after being looped to the other duct end, becomes a right running wave to interact with the left running wave of unattenuated sound pressure from the sound source. The wave interacting result would not be a strict standing wave but includes some left running wave component due to the higher amplitude of the constituent left running sound wave from the source. The amplitude disparity also gives rise to lower resultant wave amplitude in comparison to the unattenuated condition.

This simple problem demonstrates that when installed at a pressure node the Helmholtz resonator (HR) is not effective of attenuating the standing wave in the looped waveguide. In contrast, the attenuation becomes significant when the HR is at a pressure antinode. In the baseline wind tunnel geometry, there is no efficient energy dissipating mechanism for infrasound (lower than 20 Hz). The working of HR does not produce energy dissipation of the infrasound power. Instead, the capability of weakening a standing wave is hypothesized to come from mitigating the acoustic feedback excitation due to airline longitudinal eigenmodes that escalates the open jet unsteadiness.This would further fuel the standing wave energy into the otherwise uncontrolled increase of very intensified pressure pulsation in the flow acoustic coupling phenomenon. In this sense, the role of the HR is attributed to decoupling the infrasound excitation from the open jet unsteadiness.

4.4 Installation of HR on OJWT at Pressure Node

The effect of Helmholtz resonator on pulsation attenuation is first studied with the 3.06 Hz HR installed at X=11.8 D, which is the first pressure node in the downstream of the collector based on the baseline wind tunnel solution in Fig. 5. Figure 10 shows the predicted perturbation pressure solution over the entire wind tunnel airline. The holistic response map also reveals a clear pattern of standing waveform that is very similar to that of the baseline result in Fig. 5 except that the peak pressure amplitudes are reduced slightly. The nodal HR installation location remains essentially as a pressure node, where the response amplitude is a minimum locally.

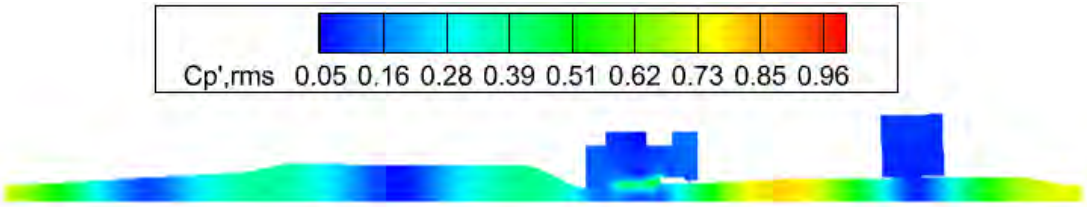

Figure 10. Perturbation pressures of open jet wind tunnel with HR at pressure node

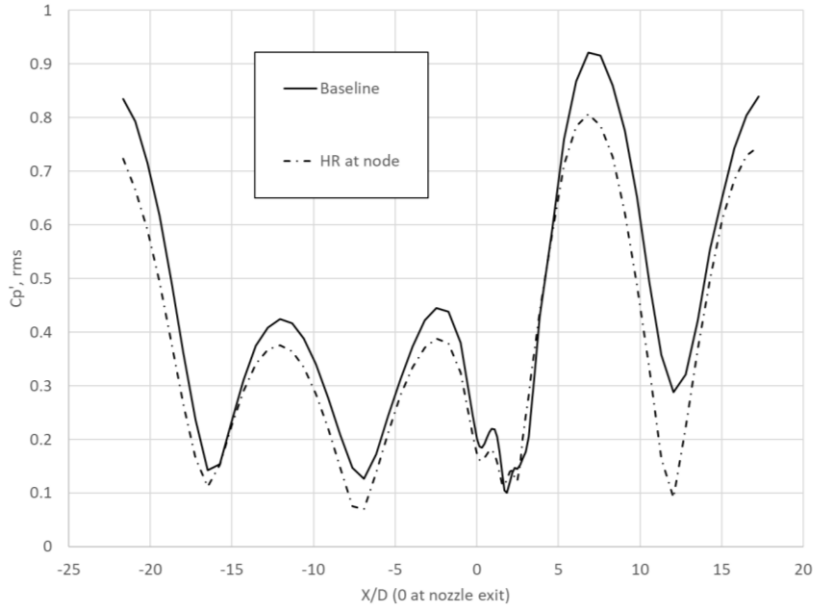

Figure 11. Perturbation pressures along airline

Figure 11 shows a comparison of perturbation pressures along the centerline of the linearized airline. As shown, the standing waveform retains the same amplitude peak-to-peak spacing while the nodal HR produces about 13% of peak amplitude reduction from the baseline condition. The result of no phase shift in the standing waveform is similar to that in the Figs 8b and 9 for the nodal HR on a straight duct. In that quiescent flow acoustic study (Sec. 4.3), the simulated sound source strength is kept unchanged. In the wind-on OJWT, the source of pressure perturbation is the flow unsteadiness of the test section open jet, which is susceptible for acoustic excitations, particularly the low frequency longitudinal eigenmodes of the wind tunnel circuit. Despite that the nodal HR is not expected to significantly alter the acoustic response to the source of perturbation, the predicted 13% reduction in the peak response pressure reiterates the acoustic susceptibility of the open jet unsteadiness and suggests a design that acoustically decouples the open jet perturbation and longitudinal circuit modes to be a potentially effective means to mitigate the pressure pulsation problem.

Figure 12 shows the companion frequency spectrum of the open jet turbulent kinetic energy (TKE) with comparison to the baseline solution. As shown, the overall shape of the TKE spectrum remains largely unchanged. The prediction shows compliance to the postulated -5/3 slope energy cascading law in frequency range that are higher than the interested low frequencies of pressure pulsations. The TKE reveals a steeper decay for frequencies higher than 50 Hz. This result shows a proof of sufficient spatial resolution of the applied numerical method for the transient open jet flow. As also shown in Fig. 12, the primary peak energy of the vortex shedding frequency stays sharply at about 3.06 Hz as seen in the baseline condition. The HR gives rise to a slight reduction in the peak energy of the flow unsteadiness and also some different secondary peaks. From the standpoint of unsteady flow energy over the entire frequency spectrum however, the effect of the nodal HR is insignificant to incur changes to the open jet flow unsteadiness.

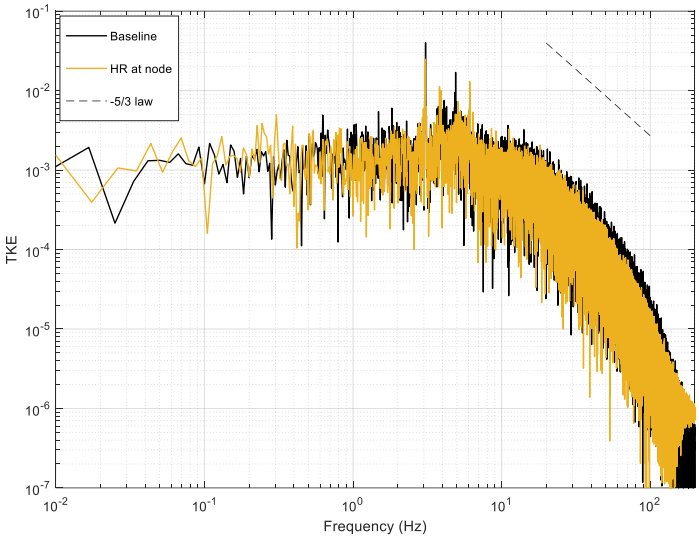

Figure 12. Frequency spectrum of turbulent kinetic energy (TKE) inside open jet shear layer

The turbulence property reported in Fig. 12 is surveyed inside the open jet shear layer that is located at X=1.75 D and on the nozzle lip line (0.5 D radial distance from centerline). In the baseline wind tunnel solution (Yen et al., 2025), this axial location revealed self-similar shear layer velocity profile where the TKE cascading in the frequency spectrum showed a decaying trend that complied with the -5/3 slope law as postulated to take place in the inertial subrange (Tennekes and Lumley, 1972; Wilcox, 1998). The same location will be used for the TKE reporting throughout the study.

4.5 Installation of HR on OJWT at Pressure Antinode #1

The baseline OJWT solution shows the first pressure antinode downstream of the test section is located at X=7.7 D. This is the first antinode location chosen to demonstrate the effectiveness of the 3.06 Hz HR for pulsation attenuation. Figure 13 shows the predicted perturbation pressures. In a stark difference from the strong pulsation condition in Figs. 5 and 10, the amplitudes of the perturbation pressure are significantly diminished along the entire airline. The strong standing waveform in the baseline wind tunnel and the nodal HR installation case no longer prevails. As presented in Fig. 13, the perturbation pressure amplitudes become so low that the only region of appreciable fluctuations is inside the open

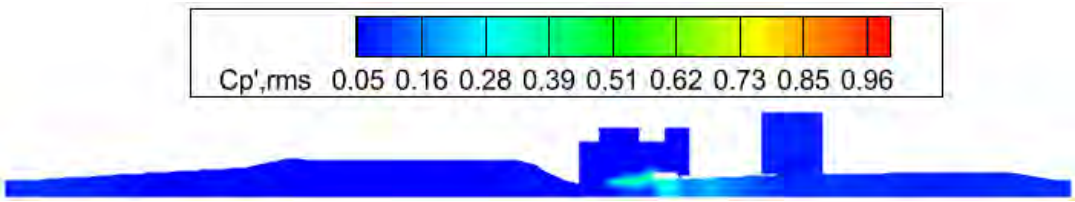

Figure 13. Perturbation pressures of open jet wind tunnel with HR at pressure antinode #1

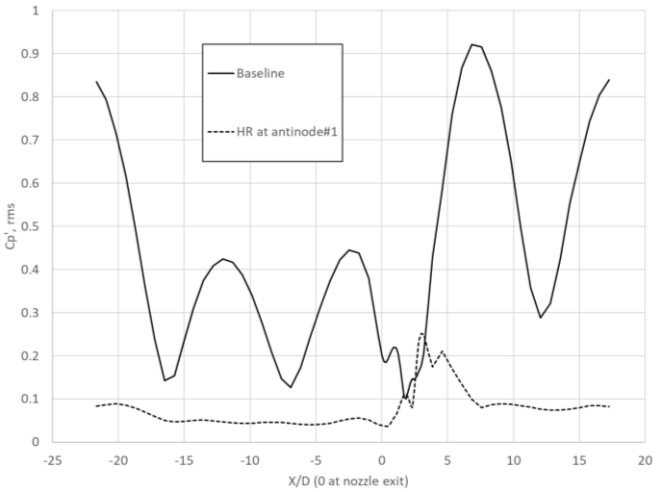

Figure 14. Perturbation pressures along airline

jet shear layer and the downstream airline duct until the resonator location. The perturbation amplitudes inside the shear layer are also reduced in comparison to the two much intensified conditions in Figs. 5 and 10.

Figure 14 shows the centerline Cp', rms as a function of the axial displacement from the nozzle exit. The result clearly echoes the result in Fig. 13 regarding the highly effective pulsation attenuation result with HR at the first antinode location. Outside the test chamber, the perturbation pressure along the airline is reduced to below 10% of the nozzle exit dynamic pressure. In contrast, the Cp', rms is higher than 92% with the baseline wind tunnel airline. The waveform of the pressure perturbations reveals a quicker variation (smaller wavelength) in a small axial range between X/D=0 and 5.0. This is related to the hydrodynamic signature imposed by the open jet vortex shedding. The attenuation effect of the HR can be seen in the test section range (bewteen X/D=0 and 2.0) to produce 5 to 6 times reduction from the peak perturbation pressure of the baseline condition.

Figure 15 shows the frequency spectrum of the TKE inside the open jet shear layer. The sharp peak of the turbulence energy at 3.06 Hz in the baseline condition is eliminated with the HR at the first antinode (denoted as AN#1 in Fig. 15). The controlled condition generates a few secondary frequency peaks and the overall broadband spectrum of the TKE resembles the baseline result except for slightly lower energy above 30 Hz. The computed turbulence solution retains the compliance with the -5/3 law of energy cascading rate in a frequency range that are higher than the interested perturbation infrasound. Steeper turbulence energy decay occurs at frequencies higher than 30 Hz.

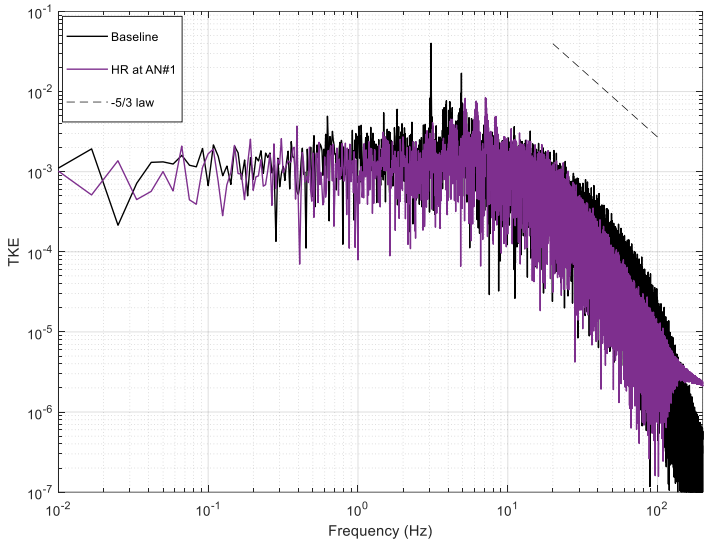

Figure 15. Frequency spectrum of turbulent kinetic energy (TKE) inside open jet shear layer

4.6 Installation of HR on OJWT at Pressure Antinode #2

The second pressure antinode in the test section downstream is located at about 15.7 D distance from the nozzle exit. The 3.06 Hz HR installed at this location is studied next. Figure 16 shows the contour map of the predicted perturbation pressure over the entire wind tunnel airline. Similar to the result of HR at the first antinode, the effect of pulsation attenuation is also significant. The standing wave in the baseline airline condition is largely diminished and the appreciable fluctuations are now only seen between the collector and the HR installation location. The magnitude of perturbation pressures inside the open jet shear layer remains high as was the case with the HR at the first antinode but much weaker in comparison to the baseline condition with more intensified pulsations.

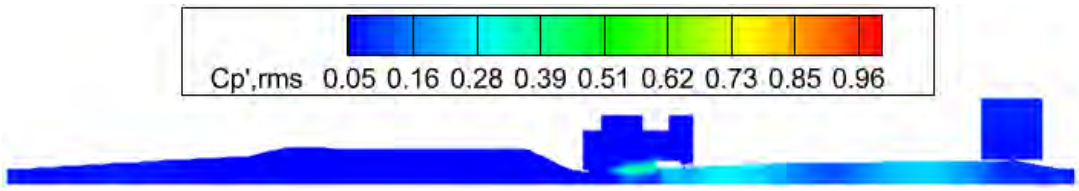

Figure 16. Perturbation pressures of open jet wind tunnel with HR at pressure antinode #2

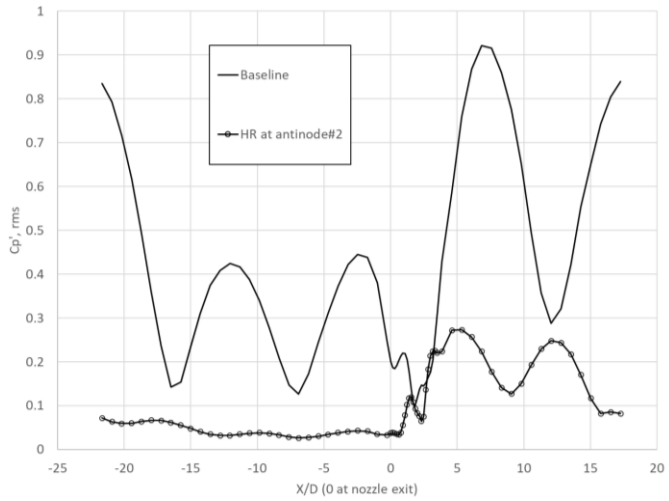

Figure 17. Perturbation pressures along airline

Figure 17 shows the Cp', rms distribution over the airline. The result confirms the effective pulsation attenuation result shown in Fig. 16. The amplitudes of the perturbation pressure remain below 10% of the nozzle dynamic pressure in the airline upstream of test section. In the downstream, a stronger standing wave pattern can be seen with 27.3% maximum peak amplitude until the second pressure antinode. Attenuation on the test section pulsation level is also quite similar to the result of the HR at the first antinode. Although not as visible in Figs.13 and 14, the HR at the second antinode in Figs. 16 and 17 produces a weakened standing wave remnant that is confined to the axial range between the test section and the HR location. The peak-to-peak distance of the standing wave also becomes shorter than that in the baseline wind tunnel condition. This suggests that the most intensified response frequency has been modified to a higher frequency.

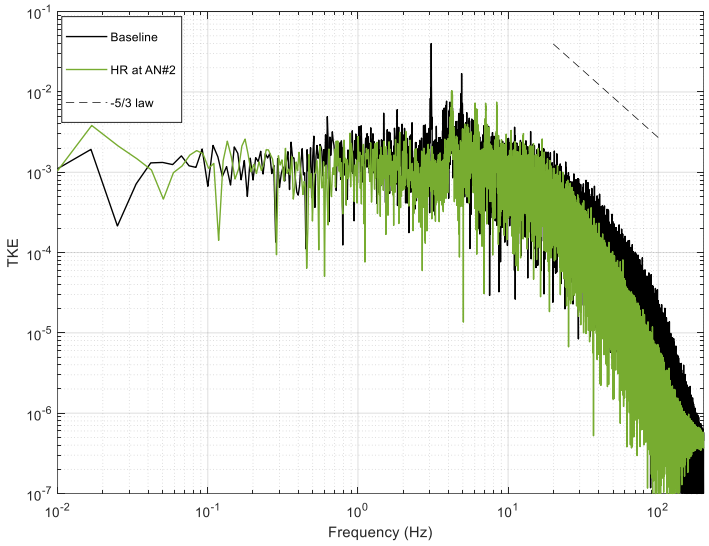

Figure 18. Frequency spectrum of turbulent kinetic energy (TKE) inside open jet shear layer

Figure 18 shows the frequency spectrum of the TKE inside the open jet shear layer for this antinal HR case (denoted as AN#2 in Fig.18). Figure 18 shows a very similar result to Fig.

15 that includes the elimination of the most dominant peak frequency, generation of secondary peaks and slightly lower turbulence energy in the broadband frequency range above 30 Hz. The predicted turbulence energy cascading again shows compliance with the -5/3 slope law over the frequency range between 10 Hz and 30 Hz, followed by a steeper decay rate in the higher frequencies.

5 Conclusion

An innovative and very efficient predictive computational strategy was successfully demonstrated in a previous study that pertained to the prediction of low frequency pressure pulsation phenomenon in a Göttingen style open jet wind tunnel. This study applied the same computational strategy and extended the work to demonstrate the predictive solution capability on pulsation mitigation using Helmholtz resonator (HR). It is anticipated that the new computational technique can supplement or eventually replace physical experiments at model scale whose objective is to identify and eliminate problematic pulsation in new full scale wind tunnel design. The demonstration again proved the computational efficiency and accurate nature of the computational aeroacoustic solver JUSTUS together with the applied analysis strategy. The computer simulation presented a holistic picture of the pressure pulsation over the entire wind tunnel airline. This solution capability provides detail of the formation of standing waves along the airline in different controlled scenarios with the HR. The study clearly demonstrated a strong dependence of pulsation attenuation on the HR installation location.

6 Reference list

Arnette, S., Buchanan, T., and Zabat, M., "On Low-Frequency Pressure Pulsations and Static Pressure Distribution in Open Jet Automotive Wind Tunnels," SAE Technical Paper 1999-01-0813, 1999

Best, S., Bari, G., Brooker, T., Flynt, G., Walter, J., and Duell, E., "The Honda Automotive Laboratories of Ohio Wind Tunnel," SAE Int. J. Adv. & Curr. Prac. in Mobility 5(6):2116-2137, 2023.

Chang, S. C., “The Method of Solution-Time Conservation Element and Solution Element – A New Approach for Solving the Navier-Stokes and Euler Equations,” Journal of Computational physics, 119, 295-324, 1995.

Duell, E. G., Kharazi, A. A., and Muller, S., Ebeling, W., and Mercker, E. “The BMW AVZ Wind Tunnel Center,” SAE Paper No. 2010-01-0118.

Kharazi, A., Duell, E., Walter, J. Application of Helmholtz Resonators in Open Jet Wind Tunnels. SAE Int. J. Passeng. Cars-Mech. Syst. 2013, 6, 436–447.

Kinsler, L. E. Frey, A. R., Coppens, A. B., and Sanders, J. V., “Fundamentals of Acoustics,” 3rd ed., 1982, John Wiley and Sons.

Rennie, M., “Effect of Jet Length on Pressure Fluctuations in ¾-Open Jets”, Motor Industry Research Association Vehicle Aerodynamics 2000 Symposium, October 2000.

Sellers, W.L.I.; Applin, Z.T.; Molloy, J.K. “Effect of Jet Exit Vanes on Flow Pulsations in an Open-Jet Wind Tunnel,” Technical Report NASA-TM-86299; Langley Research Center: Hampton, VA, USA, 1985.

Tennekes, H. and Lumley, J. L., “A First Course in Turbulence,” by The MIT Press, 1972.

Waudby-Smith, P. and Ramakrishnan, R., “Wind Tunnel Resonances and Helmholtz Resonators,” Canadian Acoustics/Acoustique Canadienne, Nov. 35, No.1, 2007

Wilcox, D. C., “Turbulence Modeling for CFD,” 2nd ed., by DCW Industries Inc., 1998.

Yen, J. C., Kimbrell, A. B., and Connor, C. H. "Study of WICS Data Using an Emerging Lower-Order CAA Method," AIAA 2010-1742

Yen, J. C., “Demonstration of a Multi-Dimensional Time-Accurate Local Time Stepping CESE Method,” AIAA-2011-2755.

Yen, J., Duell, E., Walter, J., Kharazi, A., “CAA Study of Helmholtz Resonator Application on Edge-Tone Noise Suppression”, AIAA-2012-2103.
Yen, J. C., Duell, E. G., Muller, S. A., “An Acoustic Resonance Study with an Open-Jet Wind Tunnel Geometry Using a Time-Accurate Local-Time-Stepping CESE Method,” AIAA 2019-2626.
Yen, J. C., Kharazi, A. A., Duell, E. G., Walter, J., “An Efficient CAA Strategy for Studying Flow-Acoustics Coupling Phenomenon in Low-Speed Closed-Return Open-Jet Wind Tunnels,” AIAA 2025-3689.

Numerical study on a boundary layer control system and vortex generator to alleviate a static pressure gradient

Seung Hun Lee, Ju Yeol You and Yongmin Park

Aerodynamics Development Team
Hyundai Motor Group
150, Hyundaiyeonguso-ro, Namyang-eup
Hwaseong-si, Gyeonggi-do, 18280, Korea

seunghun.lee@hyundai.com
aerodoctor@hyundai.com
parkie94@hyundai.com

Abstract: A primary distributed suction located at the close upstream of center-belt in HAWT (Hyundai Aero-acoustic Wind Tunnel) has been a major source of static pressure gradient inside a plenum. This gradient, however, is further augmented by a vortex generating (VG) system, which has been installed recently to mitigate aerodynamic data fluctuations. To alleviate the steep static pressure gradient, an optimal configuration of a boundary layer control system is investigated numerically regarding the static pressure gradient as well as the corresponding boundary layer thickness inside the plenum. Various configurations are investigated for the primary suction and scoop, secondary tangential blowing slot. With the combination of the primary suction (or scoop) and tangential blowing slot, a flatter static pressure gradient is obtained without sacrificing a boundary layer thickness compared to the current configuration. Secondly, a new VG configuration with less deviation in static pressure gradient is suggested by numerical investigations. In terms of reducing the aerodynamic data fluctuation, this new VG is experimentally proven to show comparable performance to the original VG.

1 Introduction

To have better simulation in open-jet automotive wind tunnels, flow qualities such as pressure fluctuation, boundary layer thickness and static pressure gradient in the plenum have been of great interest for aerodynamic engineers [1-6]. The Hyundai Aero-acoustic Wind Tunnel (HAWT) has been placed in operation since 1999 [2] and has been suffering from the flow quality problems. In 2000, for instance, unexpected pressure fluctuations were found at initial commissioning tests and a structural modification in a collector was followed [3]. Even though the pressure fluctuations were fairly mitigated after this corrective work, they still exist today. The second problem is the negative static pressure gradient inside the test section. In HAWT, the boundary layer is solely controlled by the primary and secondary distributed suctions at the close upstream of the moving ground system. This suction-dependent system has been a major source of the steep negative static pressure gradient in the test section, which has restricted any upgrade accompanying a side effect on the static pressure gradient.

For instance, a vortex generating system (VG) on a nozzle lip is experimentally proven to mitigate the low frequency data fluctuations, which halves the required data recording time (figure 1) [1]. However, the negative axial static pressure gradient within the plenum is increased by the VG, and a vehicle surface pressure is changed correspondingly (figure 1*c*). With the change in the axial static pressure gradient, the drag coefficient of a vehicle increases, and some aerodynamic parts show different effects on the drag coefficient. This is one of the reasons for an automotive wind tunnel to make the static pressure gradient as flat as possible. Therefore, the use of the VG in HAWT has been considered unacceptable.

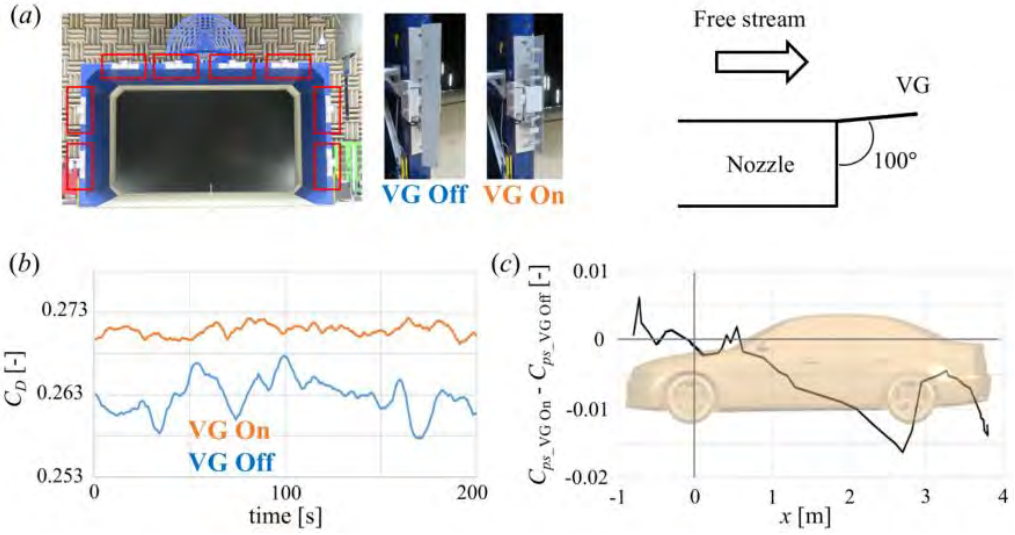

Figure 1. (a) Retractable vortex generators (VG) on the nozzle lip and its schematics. (*b*) Time histories of the drag coefficient and (*c*) deviation in the static pressure coefficient on the upper surface at y=0 of a DrivAer notchback model [1]

In this study, the vortex generating system (VG) is installed in a virtual HAWT model despite its negative impact on the steep static pressure gradient. After then, alternative boundary layer control layouts are numerically investigated to alleviate the steep static pressure gradient, without sacrificing the boundary layer thickness. The investigated alternative layouts are inspired by the novel designs of the state-of-the-art automotive wind tunnels [7-12]. Additionally, the static pressure gradients in the plenum are investigated for alternative VG configurations. A sophisticated virtual wind tunnel geometry and associated numerical schemes to assess wind tunnel interference effects such as the static pressure gradient and boundary layer thickness are introduced as well.

2 Numerical Setup

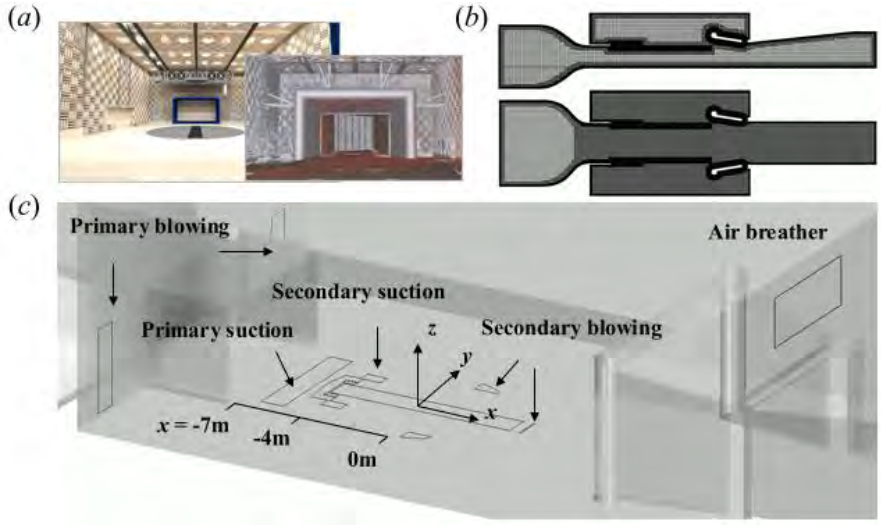

Figure 2. (*a*) Reconstruction of three-dimensional CAD geometries of HAWT. (*b,c*) Computational domain and grid systems. Note that secondary suction and blowing are not activated in this study

As a first step toward building the virtual wind tunnel, the three-dimensional CAD geometries of the entire circuit are reconstructed from the old blueprints written in the 90's. Missing parts and details are supplemented by the point cloud data measured from a state-of-the-art three-dimensional laser scanner (figure 2*a*).

For the investigation on the flow physics in the plenum, the computational domain can reasonably be reduced to the settling chamber with contraction, the first high-speed diffuser and the plenum with its appendages. In the plenum of computational domain, the center-belt of the moving ground system, the primary distributed suction, and the VG at the nozzle lip are considered (figures 2*b,c*). The air removed by the primary suction is reinjected to the plenum through blowing slots at the wall behind the nozzle. Even though HAWT has the secondary distributed suction and associated blowing slots, they are not activated in this study due to their minor impact on the negative axial static pressure gradient and the boundary layer thickness.

The governing equations for the 3-D incompressible turbulent flow in the virtual wind tunnel are solved numerically using a STAR-CCM+ with the built-in standard steady-state K-Omega SST turbulence model with all y^+ treatment. The so-called coupled implicit solver with the implicit spatial integration using a coupled algebraic multi-grid method is implemented, and the convective and diffusion terms are discretized by the second-order upwind scheme. At the boundaries, a boundary-normal mass flow condition is applied to the blowing slots, circuit inlet and outlet. A slip wall with prescribed boundary-normal velocity is imposed for the distributed suction, and a convective outflow boundary condition with gauge pressure of 0Pa is applied to the air breather above the collector flap. The no-slip condition is imposed on the rest of boundaries (figure 2*c*).

The trimmed cell type grids with 10 prism layers are imposed on all the surfaces except for the high-speed diffuser, the side walls and ceiling of the plenum. The first grid height is small enough to insure the y^+ value below unity at 140kph, and the longitudinal size of surface grid ranges from 3 to 30mm (figure 2*c*). The maximum volumetric grid size is 256mm. A grid convergence test is conducted to ensure less numerical errors, especially for the boundary layer and static pressure gradient.

For validation of the current numerical method, the calculated boundary layer profile and the axial static pressure gradient are compared with those of the experimental results (figure 3). Unless otherwise noted throughout the study, they are measured at the middle of center-belt (x=0m) and 0.6m above the ground (z=0.6m), respectively. Note that despite the secondary distributed suction with its associated blowing slots are excluded throughout this study, they are included in the present validation case because this is the test standard of HAWT. The calculated results are in excellent agreement with those of the experimental results, confirming the validity of the current model. The numerical model well captures the change in negative axial static pressure gradient by the VG (figures 3*b*,*c*).

Note that the δ_{99} value of the case without the secondary boundary layer treatment will be globally used in normalizing all the heights in the boundary layer profile throughout the paper. For instance, the boundary layer thickness of the standard experimental case with primary and secondary treatments is calculated to be $0.92\delta_{99}$. Likewise, the ΔC_{ps0} value along the center-belt (-4m to 4m) of the case with VG and without secondary boundary layer treatment is used to normalize the static pressure gradient.

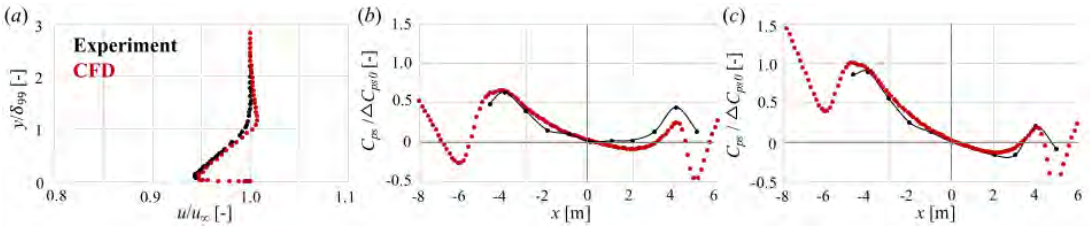

Figure 3. (*a*) Boundary layer profiles at x=0m without the VG. Axial static pressure gradients at z=0.6m without (*b*), and with (*c*) the VG

3 Investigation on Boundary Layer Control Systems

3.1 Primary suction

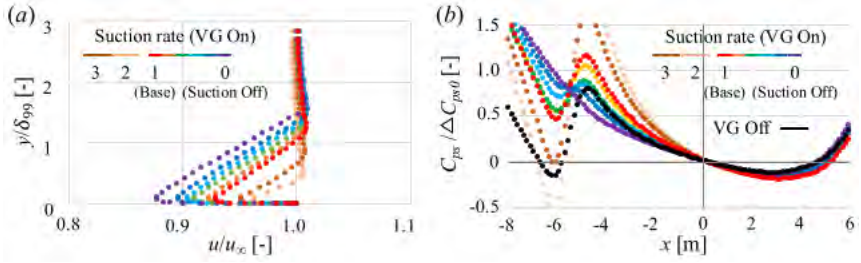

Figure 4. (a) Boundary layer profiles at x=0m and (b) axial static pressure gradients at z=0.6m for the different suction mass flow rates

As described in the introduction, the VG increases the negative static pressure gradient. With the existence of the current unmodified primary distributed suction, the VG increases ΔC_{ps} value along the center-belt (-4m to 4m) from -0.69 to -1.0ΔC_{ps0}. This chapter will show that the increased ΔC_{ps} value can be decreased by manipulating the total mass flow rate, location, and size of the primary suction [7-10].

The mass flow rate of the current unmodified position is investigated first, which can be the easiest test case in the real world. However, when the negative static pressure gradient becomes less steep, the boundary layer thickness becomes large, and vice versa (figure 4). For example, reducing the suction mass flow rate from 1 to 0.4~0.6 reduces the ΔC_{ps} value along the center-belt from -1.0 to -0.69ΔC_{ps0} (figure 4a). However, it increases the boundary layer thickness from 1.0 to 1.21δ_{99} (figure 4b). In a similar way, tripling the suction mass flow rate effectively reduces the boundary layer thickness from 1.0 to 0.35δ_{99}, while increasing the ΔC_{ps} value along the center-belt from -1.0 to -1.60ΔC_{ps0} (figures 4a,b). Therefore, adjusting the suction mass flow rate is not acceptable.

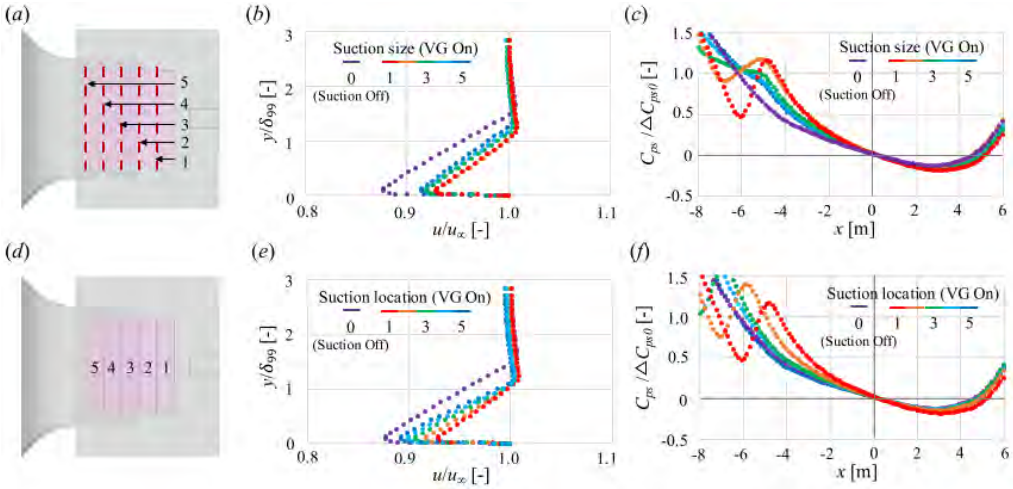

Figure 5. The (a) increase in size, and (b) change in location of the primary suction. (b,e) Boundary layer profiles at x=0m and (c,f) axial static pressure gradients at z=0.6m for (a) and (b), respectively

The recent automotive wind tunnels usually have large suction area to avoid strong suction velocity near the test section [7-10]. Here, the size of the primary distributed suction is extended toward the nozzle exit plane, and the total suction mass flow amount is not changed (figure 5*a*). The increase in primary distributed suction size does not decrease the boundary layer thickness (figure 5*b*) and has limited effect on the mitigation of the negative axial static pressure gradient (figure 5*c*). For example, with the increase in the size from 1 to 5, the ΔC_{ps} value along the center-belt (x=-4m to 4m) is reduced from -1.0 to -0.69ΔC_{ps0}. Note that the corresponding ΔC_{ps} value of the case with no suction is -0.50ΔC_{ps0}. Although the data are not presented here, increasing the suction mass flow rate for the extended suction size is not acceptable due to an excessive negative axial static pressure gradient.

The next step is to move the primary distributed suction toward the nozzle. In this case, the size of the suction plate and total suction mass amount are not changed. Interestingly, the boundary layer thickness remains nearly constant regardless of the suction plate position (figures 5*d*,*e*). Moving toward the upstream reduces the flow speed inside the boundary layer, which results in slight increase in the displacement thickness. Because the position 5 is far from the test section, the axial static pressure gradient is almost identical to that of the case with no suction (figure 5*f*).

Also, a reason for the upstream suction position can be found in the boundary layer profiles of the case without no suction. Here, the boundary layer thickness at the contraction exit (x=-10m) is already almost half of that at the leading edge of the center-belt (x=-4m) (figure 6). Therefore, the primary suction should be located inside the nozzle (i.e. position 5) exit plane to remove this already-grown local boundary layer. The regrowth of the boundary layer after the primary suction can be removed by secondary or tertiary boundary layer treatment [7-12].

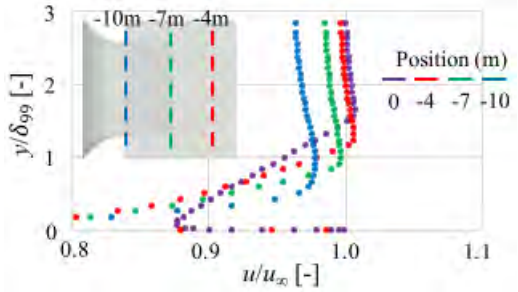

Figure 6. Boundary layer profiles of the case with no suction at x=-10, -7, -4 and 0m

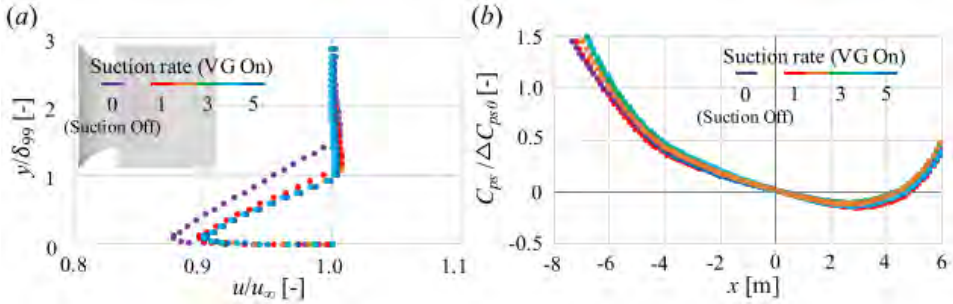

Figure 7. (*a*) Boundary layer profiles at *x*=0m and (*b*) axial static pressure gradients at *z*=0.6m for the primary suction in position 5 of figure 5*d*

Finally, the suction mass flow rate at the far upstream (i.e. position 5 of figure 5*d*) is investigated (figure 7). Note that the increase in the suction mass flow rate at the close upstream of the center-belt (position 1 of figure 5*d*) has proven to be unacceptable due to the excessive negative axial static pressure gradient (figure 4).

At position 1, the boundary layer thickness is effectively reduced by increasing the suction mass flow rate. For instance, tripling the suction mass flow rate reduces the boundary layer thickness from 1.0 to $0.35\delta_{99}$ (figure 4*a*). At position 5, however, the boundary layer thickness is not effectively reduced by the increase in the suction mass flow rate. For example, tripling the suction mass flow rate merely reduces the boundary layer thickness from 1.16 to $1.0\delta_{99}$ (figure 7*a*). These results indicate that the current suction mass flow rate is enough to remove all the local boundary layer at position 5. Without the boundary layer control, note that the boundary layer thickness at *x*=-10m is half of that at *x*=-4m (figure 6). Admittedly, the axial static pressure gradient at the test section is not affected by the increase in the suction mass flow rate (figure 7*b*).

3.2 Primary scoop

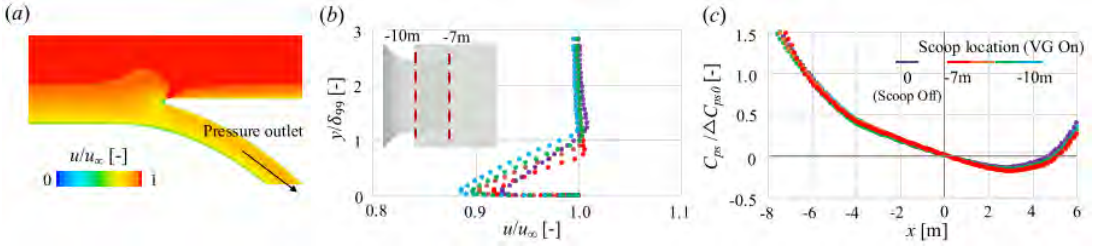

Figure 8. (*a*) Velocity contour around a primary scoop. (*b*) Boundary layer profiles at *x*=0m and (*c*) axial static pressure gradients at *z*=0.6m for the different scoop locations

In this chapter, a primary scoop with a passive convective outflow boundary condition with gauge pressure of 0Pa is employed (figure 8*a*). According to the previous studies [6,12], the scoop should be located inside the nozzle exit plane to avoid pressure interference from a vehicle. Because the boundary layer thickness at the nozzle exit plane (*x*=-7m) is approximately $0.92\delta_{99}$ (figure 6*a*), the scoop with width of $1.0\delta_{99}$ is representatively investigated for the various locations from *x*=-7m to -10m. It is obvious that the boundary layer removal becomes effective as the scoop moves close to the test section (figure 8*b*). The scoop itself, regardless of its location, does not affect the axial static pressure gradient within the test section (figure 8*c*). With the scoop at x=-7m, the boundary layer thickness is $0.75\delta_{99}$. This value is remarkably small since the boundary layer thickness with the primary suction at the similar location is greater than $1.0\delta_{99}$ (figure 5*e*).

Although the data are not presented here, the scoop with width of $0.5\delta_{99}$ is not enough to remove all the boundary layer at *x*=-7m. On the other hand, the scoop with width of $1.5\delta_{99}$ is redundant and has a similar boundary layer removal performance of the scoop with width of $1.0\delta_{99}$.

3.3 Tangential blowing

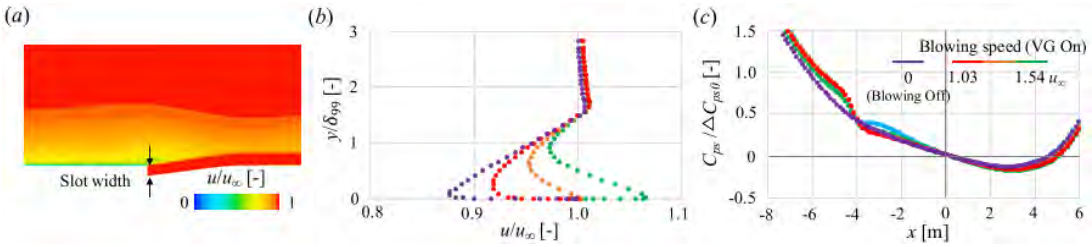

Figure 9. (*a*) Velocity contour around the tangential blowing slot. (*b*) Boundary layer profiles at x=0m and (*c*) axial static pressure gradients at z=0.6m for the slot width of $0.10\delta_{99}$

A lot of modern automotive wind tunnels employ a tangential blowing system as a supplementary boundary treatment [7-12]. As a preliminary study, a tangential blowing slot at the leading edge of the center-belt (x=-4m) is introduced without other boundary layer control systems. The slot span length in y-direction equals to the length of the nozzle. The x-directional length is one tenth of that in y-direction. The bottom surface within the slot asymptotically matches the test section ground (figure 9*a*). Considering the previous theoretical and experimental studies [4,5,13], the slot width of 0.05, 0.10, $0.20\delta_{99}$ and the blowing speed of 1.03, 1.29, $1.54u_\infty$ are considered.

The results for the slot width of $0.10\delta_{99}$ are representatively presented in figures 9*b*,*c*. With the tangential blowing, the boundary layer displacement thickness is decreased due to the increase in the velocity near the ground (figure 9*b*). However, the boundary layer thickness itself is rarely affected by the tangential blowing because the blowing jet is not fully mixed throughout the entire height of the boundary layer [4,13], which is why the tangential blowing should be used in conjunction with the primary boundary layer control system.

In this slot width, the proper blowing speed is around $1.29u_\infty$ to prevent velocity overshoot near the ground. As investigated previously [4,5], the associated static pressure gradient deviation is limited compared to that of the suction (figure 9*c*). For example, the ΔC_{ps} values along the center-belt (x=-4 to 4m) are $-0.46\Delta C_{ps0}$ and $-0.50\Delta C_{ps0}$ for with and without tangential blowing, respectively. Although the data are not presented here, the blowing speed needs to be higher for the smaller slot width. Further studies are needed to optimize the curvature within the slot, which is believed to affect the mixing behavior of the blowing jet within the boundary layer.

3.4 Combined boundary layer control system

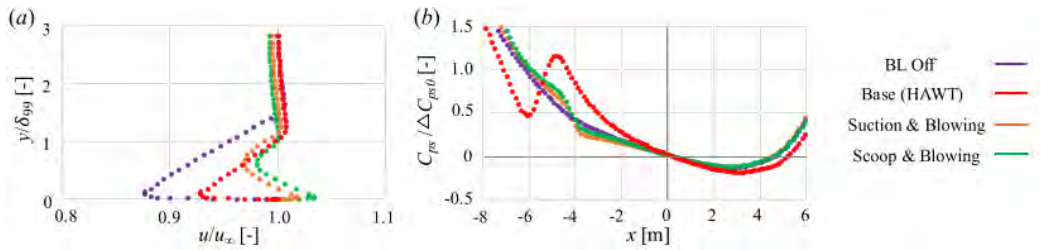

Figure 10. (*a*) Boundary layer profiles at x=0m and (*b*) axial static pressure gradients at z=0.6m

Finally, an optimal boundary layer control system in HAWT is realized by combining the primary suction or scoop with the secondary tangential blowing, which has already been demonstrated in the modern automotive wind tunnels [7-12]. From the conclusions above, the best options of each system are selected and representatively investigated. For instance, the upstream primary distributed suction (i.e. position 5 in figure 5*d*) with the current basic suction mass flow is considered. For the primary scoop, the width is $1.0\delta_{99}$ and the location is at the nozzle exit plane (x=-7m) (figure 8*b*). The width of tangential blowing slot is $0.10\delta_{99}$ and the blowing speed is $1.29u_{\infty}$.

The combined system of the primary suction or scoop with the tangential blowing shows the boundary layer thickness around $0.92\sim1.0\,\delta_{99}$ (figure 10*a*), which is comparable to the value of the current basic configuration ($1.0\delta_{99}$). Moreover, with the mass and momentum supplied from the tangential blowing, the boundary layer displacement thickness is significantly reduced. The displacement thicknesses are $0.042\,\delta_{99}$ and $0.016\,\delta_{99}$, respectively, for the current basic configuration and the primary suction with tangential blowing configuration. Even though the boundary layer (displacement) thickness is not sacrificed, the axial static pressure gradient becomes significantly flat. The ΔC_{ps} values along the center-belt (x=-4m to 4m) are $-0.46\Delta C_{ps0}$ and $-0.42\Delta C_{ps0}$ respectively for those with the primary scoop and suction, which are even lower than that from the case without the boundary layer control system (ΔC_{ps} = $-0.50\Delta C_{ps0}$).

4 Investigation on a new VG Design

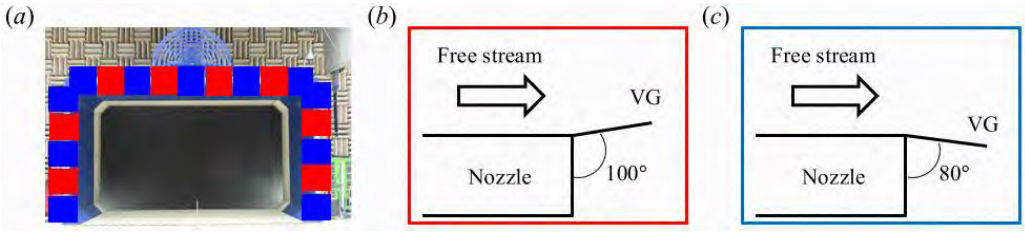

Figure 11. (*a*) The nozzle of HAWT. In red and blue regions, (*b*) inward and (*c*) outward vortex generating plates are respectively positioned

In addition to the investigation on the boundary layer control system, this chapter focuses on finding an alternative VG configuration whose associate negative static pressure deviation is less than the current VG. The current VG consists of flat plates, which are tilted 10˚ toward the free steam (figures 1*a*, 11*b*). This configuration squeezes the free stream and causes the augmentation of negative static pressure gradient in the test section. To the best of authors knowledge, the reason for the deviation in static pressure gradient under this configuration is not clear. After all, a new VG design is employed not to squeeze the free stream. Therefore, outward-tilting plates are additionally considered (figure 11*c*). Refer to the positions of inward- and outward-tilting plates at the nozzle lip in figure 11.

In this study, inward-only and outward-only VGs are respectively considered. The ($\Delta C_{ps}/\Delta C_{ps0}$, $\Delta u/u_\infty$) values along the center-belt (x=-4m to 4m) of inward and outward VGs are (-1.0, 0.013) and (-0.57, 0.003) respectively (figures 12*a*,*b*). Note that the corresponding (ΔC_{ps}, $\Delta u/u_\infty$) values of no-VG case are (-0.69, 0.007). These results indicate that the outward VG case shows a flatter static pressure and velocity gradient in the test section than those of inward VG and no-VG cases.

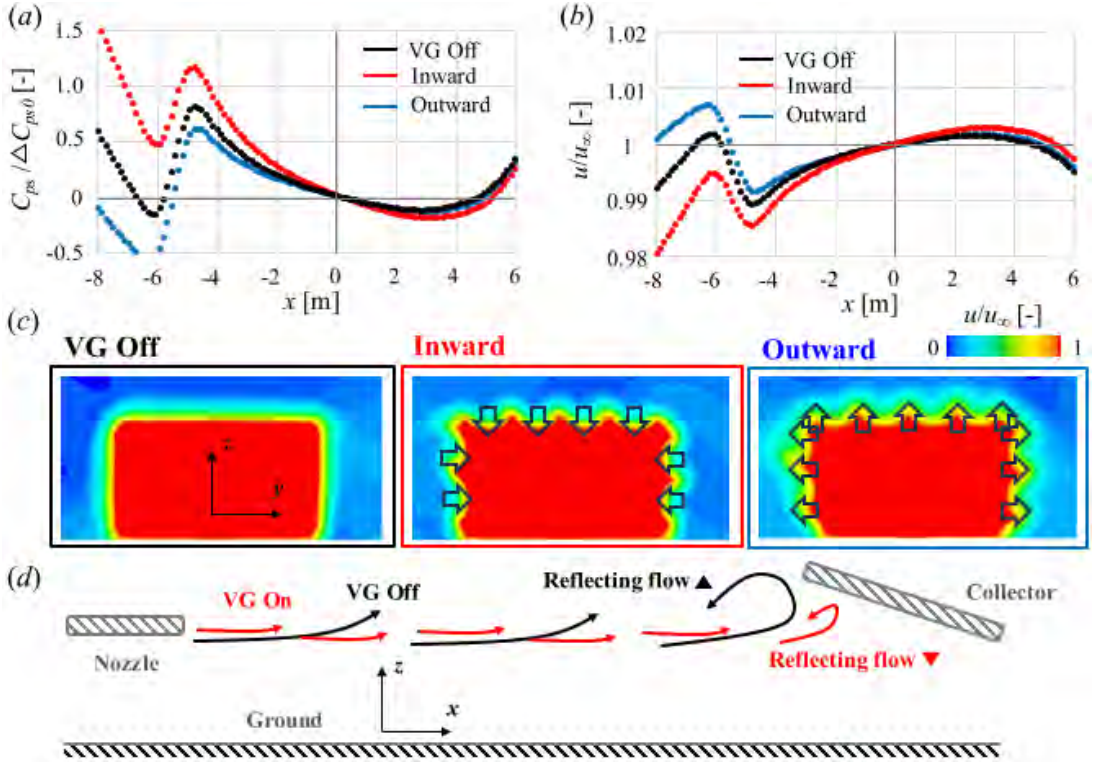

Figure 12. (*a*) Axial static pressure gradients and (*b*) velocity profiles at z=0.6m. (*c*) Velocity magnitude contours at x=0. The location and direction of arrows in (*c*) indicate the position and tilted direction of the vortex generating plates, respectively. (*d*) Schematic diagram of shear layer behaviors in open-jet test section

In no-VG case, large-scale coherent shear layer vortices are developed along the smooth perimeter of nozzle outlet. For instance, coherent z- and y-directional vortices are respectively observed for the lateral and upper sides of free stream jet boundary in no-VG case (figures 12*c*,*d*). These large-scale vortices are reflected by collector flaps and cause data fluctuation [1,2]. The primary purpose of VG is to dissipate these large-scale vortices into smaller pieces, thereby reducing the reflecting flow [1]. Interestingly, the coherent shear layer vortices disappear for both cases with inward and outward VGs (figure 12*c*). Small staggered vortical structures are presented along the free stream jet boundary, instead. Since the inward VG has experimentally been proven to mitigate data fluctuations, the outward VG is expected to show a similar effect.

However, the numerical investigation on unsteady data fluctuations with VG is limited since the current numerical scheme employes the steady-state solver. An unsteady numerical scheme needs to be developed and validated in the near future. In this study, experimental investigations on the unsteady characteristics of VG are presented alternatively.

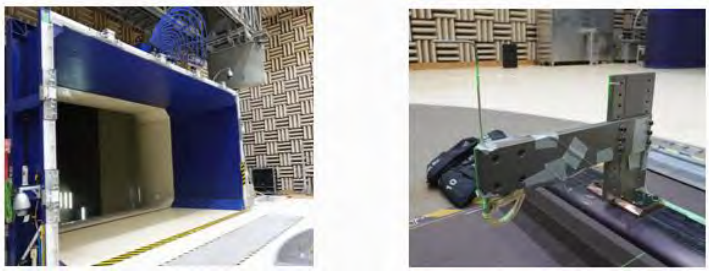

Figure 13. VG and pitot tude set-up in HAWT

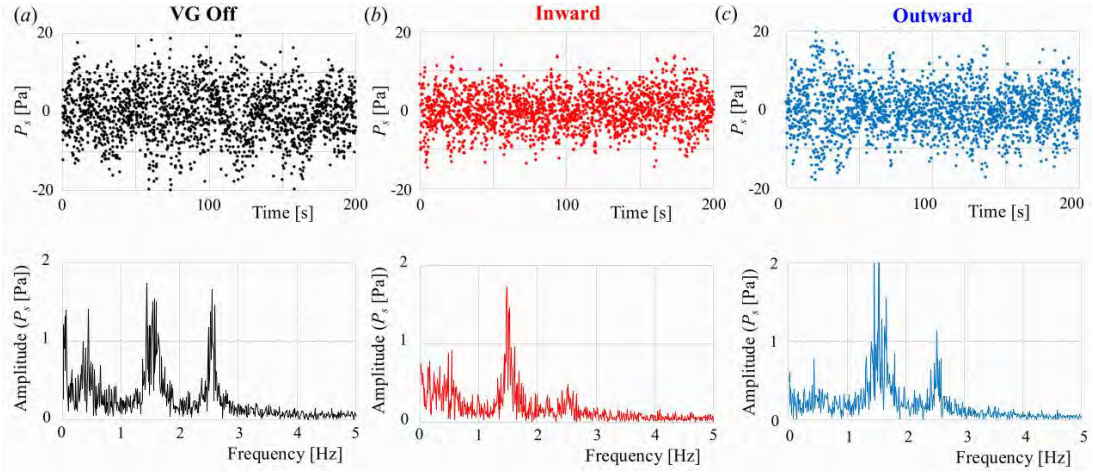

Figure 14. Time histories of static pressure at 0.6m above the middle of center-belt and their FFT results with (*a*) no-VG, (*b*) inward VG, (*c*) and outward VG

For the experiments, inward and outward VGs were installed on the nozzle lip of HAWT. With a pitot tube, time histories of static pressure at 0.6m above the middle of center-belt were measured for no-VG, inward VG, and outward VG cases (figures 13,14). In case of no-VG, the dominant frequencies of the static pressure fluctuation occur at around 0.5, 1.5 and 2.5Hz. On the other hand, the inward VG reduces the magnitude of dominant frequencies at 0.5 and 2.5Hz. The outward VG also reduces the dominant peaks at both 0.5 and 2.5Hz, but the magnitude at 2.5Hz is greater than the case with inward VG.

Especially, the reduction in the peak at 0.5Hz is an encouraging result since the required data acquisition time depends on the fluctuation in lowest frequency. As the inward VG halves the required data acquisition time, a similar effect is expected with the outward VG. To validate this assumption, drag fluctuations of DrivAer model with outward VG will soon be conducted.

5 Concluding remarks

A vortex generator (VG) on the nozzle lip was developed to reduce the fluctuation in aerodynamic data but the application of it has been limited because it increases the negative static pressure gradient. To alleviate the increased negative static pressure gradient by VG, alternative boundary layer control systems are numerically investigated. A far upstream primary distributed suction (or scoop) with secondary tangential blowing near the test section shows the most flatest static pressure gradient, without sacrificing the boundary layer thickness. Secondly, the new VG configuration is suggested by numerical simulation and is validated by experiment. This VG reduces the fluctuation in the aerodynamic data and shows the minimal deviation in the negative static pressure gradient. The combination of the new boundary layer control systems and new VG will help HAWT to have better flow quality.

Throughout the study, the current numerical scheme is validated to capture the various wind tunnel interference effects. The application of this invaluable method will not be limited to the current study and will be expanded to understand other flow physics. For instance, correlation study on the wind tunnel and open road conditions will be an interesting research topic. In addition to the current steady-state scheme for the wind tunnel, an unsteady scheme is under development.

6 Reference list

[1] You, J. Y., Kwon, H. & Jeon, S. et al., 2023 Reduction of flow fluctuation with vortex generating system. Proceedings of FKFS Conference on Vehicle Aerodynamics and Thermal Management. 2023

[2] Kim, M., Lee, J., Kee, J. & Chang, J. 2001 Hyundai full scale aero-acoustic wind tunnel. *SAE Tech. Pap.* 2001-01-0629

[3] Rennie, M., Kim, M., Lee, J. & Kee, J. 2004 Suppression of open-jet fluctuations in the Hyundai aeroacoustic wind tunnel. *SAE Tech. Pap.* 2004-01-0803

[4] Berndtsson, A., Eckert, W. T. & Mercker, E. 1988 The effect of groundplane boundary layer control on automotive testing in a wind tunnel. *SAE Int. J. Passeng. Cars* 94, 215-230

[5] Mercker, E. & Wiedemann, J. 1990 Comparison of different ground simulation techniques for use in automotive wind tunnels. *SAE Tech. Pap.* 900321

[6] Wickern, G., Dietz, S. & Luehrmann, L. 2003 Gradient effects on drag due to boundary-layer-suction in automotive wind tunnels. *SAE Tech. Pap.* 2003-01-0655

[7] Buckisch, R., Schwartekopp, B. & Pfisterer, J. 2018 Diamler aeroacoustic wind tunnel: 5 years of operational experience and recent improvements. *SAE Tech. Pap.* 2018-01-5038

[8] Xu, L., Zhu, X., Wang, Q. & Bu, H. et al., 2025 The new China automotive engineering research institute co., Ltd full-scale aero-acoustic wind tunnel. *SAE Tech. Pap.* 2025-01-8779

[9] Waudby-Smith, P., Bender, T. & Sooriyakumaran, C. et al., 2024 The new China automotive technology and research center aerodynamic-acoustic and climatic wind tunnels. *SAE Tech. Pap.* 2024-01-2541

[10] Blumrich, R., Widdecke, N. & Wiedemann, J. et al., 2015 The new FKFS technology at the full-scale aeroacoustic wind tunnel of university of Stuttgart. *SAE Int. J. Passeng. Cars* 2015-01-1557

[11] Nagle, P., Brooker, T. & Bari, G. et al., 2023 The Ford rolling road wind tunnel facility. *SAE Tech. Pap.* 2023-01-0654

[12] Best, S., Bari, G. & Brooker, T. et al., 2023 The Honda automotive laboratories of Ohio wind tunnel. *SAE Tech. Pap.* 2023-01-0656

[13] Launder, B. E. & Rodi, W. 1979 The turbulent wall jet. *Prog. Aerosp. Sci.* 19, 81-128

How Software keeps your Wind Tunnel up to date for Efficiency and new Use Cases

Dr. Jan Daniel Jacob

IT-Solutions for Testing
Werum Software & Systems AG
Anna-Vogeley-Strasse 20, 21337 Lueneburg, Germany

jan.jacob@werum.de

Abstract: Usually, wind tunnels have a supervisory control system originally installed. However, just like subsystems, the supervisory control system will "age" as new requirements come up. For some time, it might be possible to add functionality or to develop adjacent systems for certain tasks at rising cost. However, at some point it is just time to replace the system reaching its limits. Then, minimal downtime and minimal changes to subsystems to not involve all different (maybe even no longer available) suppliers is the goal. Thus, an ideal solution would be a modular and configurable system by a proven IT-integrator that can adapt to the present subsystem interfaces and their behaviors. Simultaneously, the new system shall avoid running into such obsolescence situations quickly again. Thus, it should offer a lot of configuration options and modularity to allow for future changes. We present a NoCode/LowCode-concept based on our platform WTCS, suitable for upgrades with minimal downtimes (actual parallel operation with the old system in many situations), and massive adaptability and future-readiness by modularity. From a self-installable base set, over customer-usable configuration editors for interfaces, test sequencer environment and ISO17025-compliant test management, to user-defined user interfaces, the system allows for various project situations from full-service projects to almost exclusive customer-executed implementation after corresponding training.

1 Introduction

When building a wind tunnel, the necessity of regular mechanical, electrical or hydraulic maintenance is accepted. Also, such components might have to be replaced over the wind tunnel's life cycle. But the Wind Tunnel Control System (WTCS) is software, and software does not age.

However, requirements evolve. New test scenarios come up. In compliance with regulatory guidelines requirements for documentation or traceability will change and become more challenging to keep up with. IT- and information security guidelines are evolving. Aspects of energy efficiency, increasing time and cost efficiency add to that.

Contribution: 2025 FKFS Conference on Vehicle Aerodynamics and Thermal Management
15 – 16 October 2025 | Leinfelden-Echterdingen

These changing requirements impose increasing requirements on the WTCS, which likely was well-suited to orchestrate the subsystems of the original wind tunnel setup. For some time, adding new functionality by attaching another tool, another script to the existing WTCS might work. But at some point, the requirements have changed dramatically. Thus, an outdated, pure SCADA system cannot keep up with the modern world of aerodynamic, aero-acoustic or thermal testing.

Then, it is time for a change. A modern, flexible, and adaptable IT-system, suited for control of all subsystems, for thorough data handling, process-safe information tracking, and efficient test-process automation is a major upgrade. It can significantly boost the facility's performance in efficiency, data and process quality, as well as test capabilities. However, such upgrades are major interruption of operation and may cause a ripple effect of remodeling interfaces or replacing hardware in all subsystems.

Thus, such upgrades are often avoided as long as possible, adding more extra tools, scripts, workarounds, operational procedures to keep the old world intact. However, this means investing more into obsolete systems and infrastructures, further losing ground to competitors, and increasing the effort when eventually deciding to upgrade.

Thus, it is important for wind tunnel centers to find ways to upgrade their control systems in a convenient way. Similarly important for system suppliers is to develop WTCSs with configuration and comfort features, to enable such upgrades with minimal downtime at minimal cost for the wind tunnel center.

The following sections describe the relevant aspects of WTCSs, reasons to upgrade to a more modern solution, the state of the field in terms of upgrade procedures as well as the common pitfalls. Then a novel approach is developed, the necessary improvements to WTCSs for such approach are described, and the benefits of this concept are highlighted.

2 Wind Tunnel Control Systems

The main task of a WTCS is interaction with the wind tunnel's subsystems. It sends setpoint commands controlling the test conditions. It reads status information and measurements and orchestrates the operation of all subsystems. Communication relies on industrial communication protocols like ProfiNET; OPC UA, etc., but also, proprietary Ethernet-based communication. Some subsystems are even controlled by analog and digital I/Os. Each subsystem exhibits a certain interface behavior, i.e. a certain way to react to commands, faults, etc. A well-defined architecture would standardize this behavior for all subsystems allowing easy modifications. However, each WTCS has different behavioral preferences. Thus, replacing the WTCS results in interface adaptation either within the new WTCS or in each connected subsystem.

Data obtained from subsystems is distributed to other subsystems for coupling and interlocking. Data is also presented in the user interface. Thus, data distribution is an important task. Often, hard links have been established, e.g. by (physically) wiring signals between subsystems. This might work while the architecture is constant, but it poses challenges when replacing subsystems. Thus, routing all data through the WTCS is advisable. Its subsystem interfaces act as hardware abstraction layer and ensure that changes to one subsystem don't affect the others. Also acting as "behavior abstraction layer" the interface drivers can provide a high degree of agnostics for each subsystem towards the WTCS and other subsystems.

All data shall be recorded. Continuous data recording in a ring-buffer database enables maintenance and fault-finding. Test-related, file-based recording in text or binary formats ensures all information about a test is stored in a dedicated place. Use of standard formats is advisable for easy access by all stakeholders. The formats should allow structured metainformation storage from test definition and documentation alongside the time-series data. Such metainformation is important for traceability and test documentation. Storage in text-files with minimal header information is no longer suitable. Instead, formats with extensible, indexed metadata are advantageous.

Recorded and live data commonly require processing. Derived quantities are calculated online from raw data, e.g. the wind speed from pressure differences in the plenum or nozzle. Statistics are calculated on recorded time series, data is checked for limit violations, etc. Thus, a configurable online calculation module computing derived quantities based on formulas is needed. Those math operations shall be adaptable to new situations, e.g. re-calibration, new entities, changes in parameters sets, etc. A suitable automated post-test analysis system should be included. To meet changing requirements, the analyses executed on test steps, test runs, or the test session must allow flexible modifications on processing and reporting.

The data obtained is visualized in standardized tables, graphs as well as specifically designed schematics of e.g. the cooling system, safety-related signals, etc. Also, historic data for trends as well as meta-information of the test are important to display.

Besides visual inspection of the data, automated monitoring is important. Failures or unexpected events should stop the test sequences. Notifications about violated test conditions help save time, otherwise wasted on unusable results. Further monitoring might be useful for process automation. The concept of monitoring parameterized rules, and on occurrence reacting with a certain sequence of steps is quite universal.

As results are only meaningful in context of the test description, thorough test management, describing the test is important. Also, integration with the department's test process is necessary. For uninterrupted operation, even without connection to central test planning, a local test management with reasonable capabilities including change tracking in compliance with ISO17025 [ISO17a] should be part of a WTCS.

Documentation of the tests starts with automated generation of reports without manual interaction to ensure no tampering with data can occur. But there are other aspects: photo documentation of the vehicle during a test run proves that test description and actual execution configuration match. Logging user comments and notes is also part of the ISO17025-compliant documentation.

All shall be in the context of the test description and results for a comprehensive and conclusive data set. Thus, data management is important. This includes archiving data to central test result management systems, removal of outdated data after archiving as well as separation of data belonging to different customers of the facility.

Automated test sequencing allows efficient test execution. Such sequences shall be easy to generate (e.g. from setpoint lists) and shall simultaneously be curated and quality assured for reproducibility and traceability by using templates. They should allow for a maximum of automation for a maximum of efficiency in test execution.

Collaboration between the operator and the test engineer is key for efficient and successful operation. Thus, both should have access to all relevant information. This includes viewing data, but is most powerful, when enabling the engineer to enter data defining upcoming test runs while the operator focuses on the execution.

Also, system administration is important. While overseeing daily operations, the wind tunnel engineer is responsible for first level support and maintenance. With an aerodynamics background, this person usually does not have in-depth IT knowledge. Thus, the administration, fault finding, etc. must be suitable for a trained user instead of a team of IT experts. In addition, recurring tasks should be encapsulated and automated to minimize the time effort required for routine maintenance.

The wind tunnel department is interested in process data and KPIs of the facility. While long-term storage and analysis of such data is not the primary scope, the systems should support necessary recording and processing to provide such data in a suitable way to department systems for further investigation.

3 Reasons for an Upgrade

There are various reasons to upgrade a WTCS. Most common is a major renovation of subsystems. Then, WTCSs with hard-wired or hard-coded interfaces require a significant redesign. Thus, it is a common time to decide on a completely new WTCS.

Also, the lack of test management or documentation in older systems leads to such decisions, especially with new norms and regulations. With stricter homologation requirements (e.g. in the context of WLTP [WLT21a]) thorough documentation of test conditions and results becomes mandatory [Jac24a]. ISO17025-compliant test processes require integration into department-wide test workflows, change tracking and data integrity measures. These are not easily achievable with legacy systems. Thus, upgrading to modern systems with integrated test management, photo documentation, change tracking, and quality assured data handling is advisable.

Lack of modularity and extensibility can lead to a deadlock where new features (e.g. support for active aerodynamic components [Jac25a]) cannot be added – or at extreme cost. Thus, the desire to enhance efficiency, capabilities or quality by new features can be another important reason for a new WTCS is necessary.

Old systems might not be compatible with new operating systems. Porting the existing system can be expensive if the software is not based on a platform with longevity in mind. Also, IT- and data security are increasingly important. Shared logins must be replaced with personalized accounts.IT infrastructure must enforce password rules and changes. Data security calls for separation of data of various customers, protection of personal data, etc. Achieving this requires significant reorganization and reprogramming for legacy systems. Such aspects can also lead to renewal.

4 Usual Upgrade Procedure

The usual upgrade procedure of a WTCS as outline in Figure 1 starts with gathering information about the interfaces of the subsystems. As the subsystems should be kept constant to avoid complexity and cost, full understanding of the data, the exchange mechanism as well as the subsystems' behavior is required. This involves extensive forensic work as old interfaces are often not well documented. Anything missed here has a significant impact on the commissioning of the new WTCS with unpleasant surprises later. Next, the features and capabilities of the new WTCS are specified.

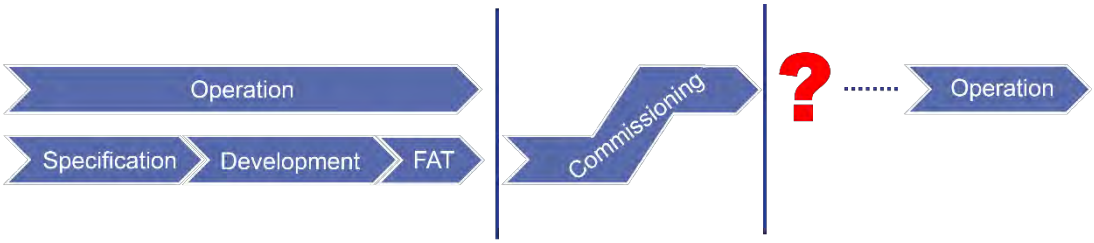

Figure 1: Common workflow of traditional wind tunnel control system upgrades

On this basis, the WTCS is implemented. If changes to subsystems are planned, this happens in parallel. After completion of software development, the operation of the facility is halted. Now there is no way back to the old system. The old WTCS is removed, physical interfaces are modified, and installation of new hardware begins.

Commissioning begins with subsystem interface tests. For a new wind tunnel, the subsystem supplier joins these tests. However, when upgrading, the subsystem supplier is usually not involved as their system was delivered long ago. They might even be no longer in business. The software supplier must test the interfaces alone, without support. Findings must be analyzed without insights into processes within the subsystems, and all solutions must be found within the new WTCS. There is a high risk of blocking issues, unexpected delays, and added cost for spontaneous changes.

The commissioning phase continues with complete tests of the new WTCS, the site acceptance test, and training for the operating and administering personnel. Finally, operations can be ramped up again. In the first weeks and months, the personnel will still have to acquaint themselves with the new system, its workflows and features. Thus, fully efficient operation will commence only after a certain time.

5 Downsides of a traditional Upgrade

The major downside of such an upgrade is the risk in identifying the exact behavior of the subsystem interfaces by complicated forensics. Any mistakes or missed information can result in massive issues later. It requires a traditional, lengthy specification as the supplier of the new WTCS must be familiarized with the wind tunnel center's detailed needs and wishes. The supplier needs a stable specification to have confidence in the tasks and work packages. However, the wind tunnel center might not have the time and resources for a full specification phase.

If old subsystem interfaces cannot be fully specified from available information or forensics, it might be necessary to involve many suppliers, and some might not be in business anymore. Thus, this can become a very complex project. The uncertainty in subsystem interfaces also bears a high risk of additional cost and delays, up to the point that the facility might not be operational due to blocking issues.

Shutting down operation on a certain date, then installing the new WTCS over several weeks, with the risk of delays in case of unexpected roadblocks, results in a long, unpredictable downtime of the facility. This queues up tests of important vehicle development projects, and results in significant revenue loss.

The steep learning curve when the new system becomes operational can lead to beginners' mistakes and decreased productivity in the first month of operations. This can be a prolonged period of unreliable, inefficient operation.

6 A novel Approach

Thus, a different approach as outline in Figure 2 is necessary. Instead of project-specific development, it requires a configurable, adaptable and easily integrated WTCS. Yet, the system must allow project-specific modules resolving roadblocks, which pure configuration cannot resolve.

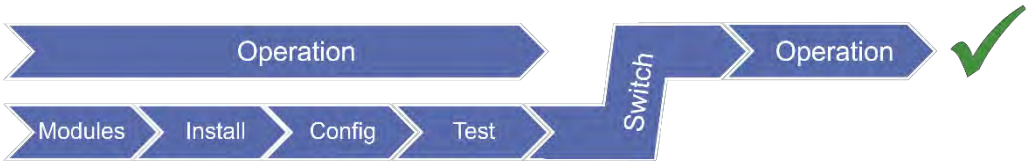

Figure 2: Workflow of novel wind tunnel control system upgrades

Ideally, the software is easy to install like office software. Thus, a downloadable installer, provided by the WTCS-supplier is the starting point. It can be installed and configured by IT-affine wind tunnel personnel on common hardware, and should contain necessary secondary installers to set up the WTCS on operator and customer workstations, etc.

Integral part of the concept is configuring the new WTCS in parallel while still using the old software. After basic installation, the subsystem interfaces can be configured one by one. Unused times (e.g. night shifts) can be used for communication tests with subsystems. Some communication settings of computers and subsystems might require changes to switch between systems. But, in general this allows further operation of the old WTCS without influence by and on the modernization project if the subsystem interfaces do not rely on hardwired signals. The new WTCS provider can support this with workshops and trainings, during which first configuration steps are taken together. Then the wind tunnel center can continue with further subsystems or additional settings saving cost of external personnel.

An important aspect is the ability to import and export the configuration in parts and in full. This allows frequent backups to keep the last viable state and is helpful for exchanging information between the WTCS supplier and the wind tunnel.

With such an approach, the facility can be operated with the old software until the very end. Then the new, fully configured and tested system is activated for a seamless transition. Defining test suites to validate the expected behavior and results and executing them with the old and the new system gives confidence in operational robustness and validity of results. As personnel is already working with the new solution for a while during the configuration and testing, the transition process is much smoother, and a higher operational efficiency from day one can be achieved.

7 Necessary Improvements of Wind Tunnel Control Systems

The provision of a configurable platform as shown in Figure 3 instead of project-specific solutions is a major paradigm-change. The approach is not new, but often not applied to niche-software like WTCSs. Such does not favor implementations of expensive configurable modules over static, but cheaper hard-coded one-off solutions. Thus, the approach is only suitable when having a significant client base with multiple installations.

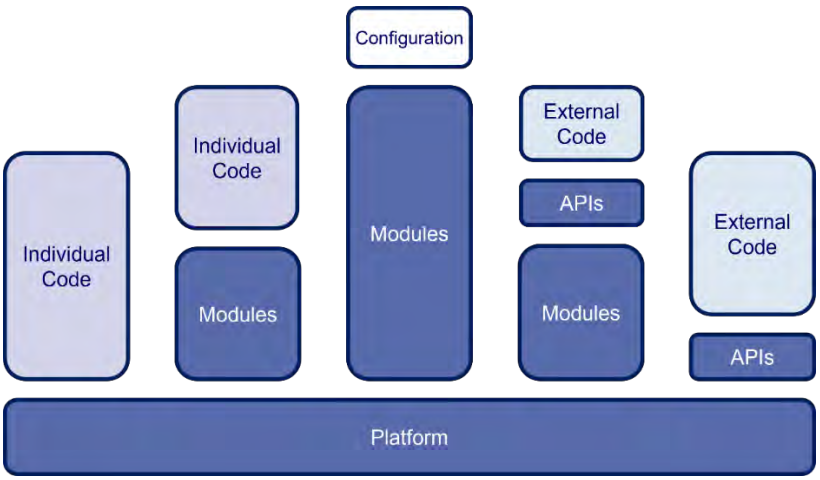

Figure 3: Platform concept

Meeting the specific requirements for a certain wind tunnel requires a modular approach. Distinct components should be separate platform modules, only included in a system, if required. This allows lean solutions to support a broad range of scenarios.

Tailoring the WTCS to a specific wind tunnel in a no-code approach requires convenient, end-user suitable configuration editors. These shall guide a domain expert with minimal system knowledge in configuring subsystem interfaces, control displays, data distribution, processing, and recording. Instead of technical aspects, logical domain components shall be the configured building blocks.

For aspects, requiring more than just configuration, where a no-code approach is not sufficient, a low-code approach should be followed. Scripting capabilities can tailor the behavior of the system, e.g. by integration of analysis scripts for tools like DIAdem, Excel or Matlab to process the result data automatically.

The concept is not limited to data analysis. It can be extended to most specific tasks going beyond configuration by utilizing scripting languages like Python. This can also include suitable APIs allowing development of specific code modules as outlined in Figure 4 or SDKs and plugins as exemplarily shown in Figure 5 for a subsystem interface driver. By providing such in various languages, including scripting languages, users can easily extend and customize the system to their specific needs. In addition, integration with external tools, which might provide valuable functionality already at hand in the department, can significantly improve the benefits of such solution.

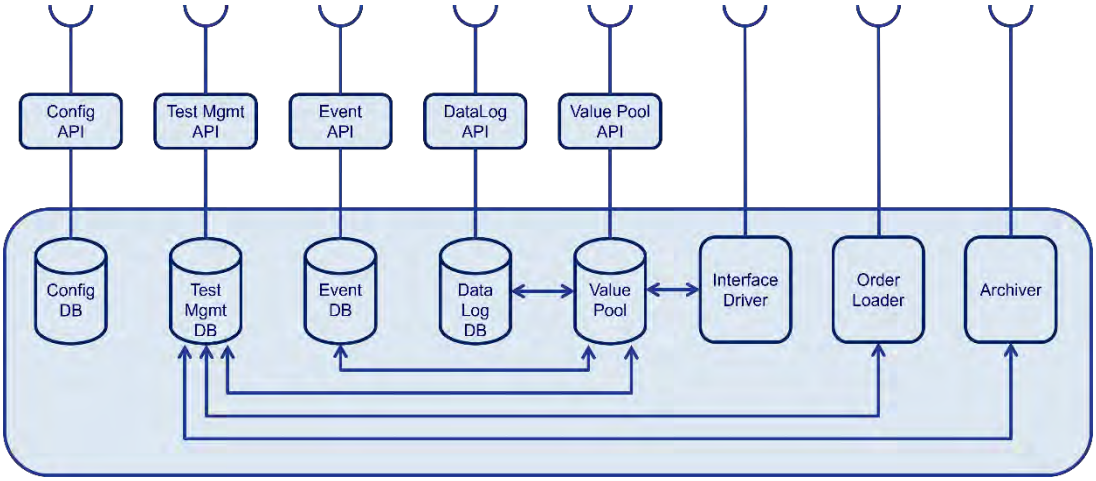

Figure 4: APIs and Interfaces

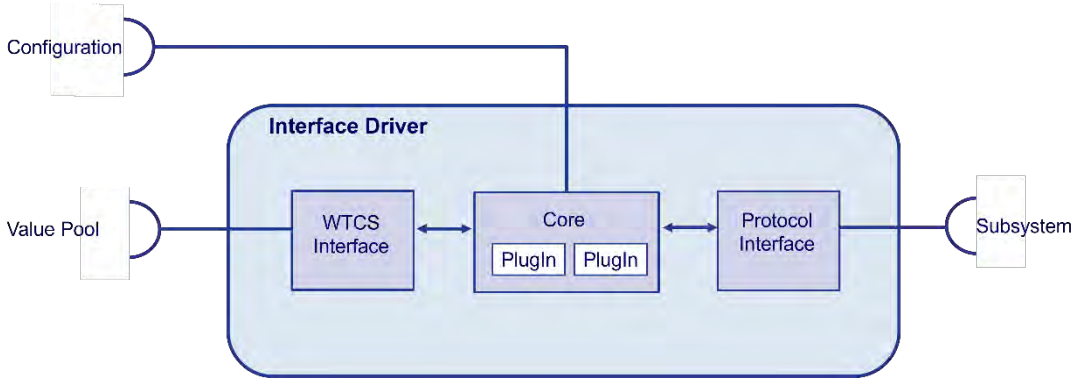

Figure 5: Architecture of interface drivers with modular interfaces and plugins

To keep track of the system configuration and allow for continuous support of such a modular solution with a lot of configuration options by the wind tunnel center, the software must allow for easy and reliable backups of the whole configuration as well as for distinct parts of that. Such saved configurations must be easily exchangeable between the supplier and the wind tunnel center to ensure both ends always have the same configuration at hand in case of updates, fault-finding support and consulting for modifications. Thus, thorough configuration management and tracking must be established as well as a reliable mechanism providing the wind tunnel with easy to install updates, setting up new software versions including the required configuration and without voiding the already made configuration settings on site. Such is also of importance in the context of IT- and information security standards like ISO27001 as well as for the traceability and reproducibility of tests as the software configuration is also part of the test setup. Figure 6 schematically shows such process for platform code, project configuration management, update generation, execution, and configuration feedback.

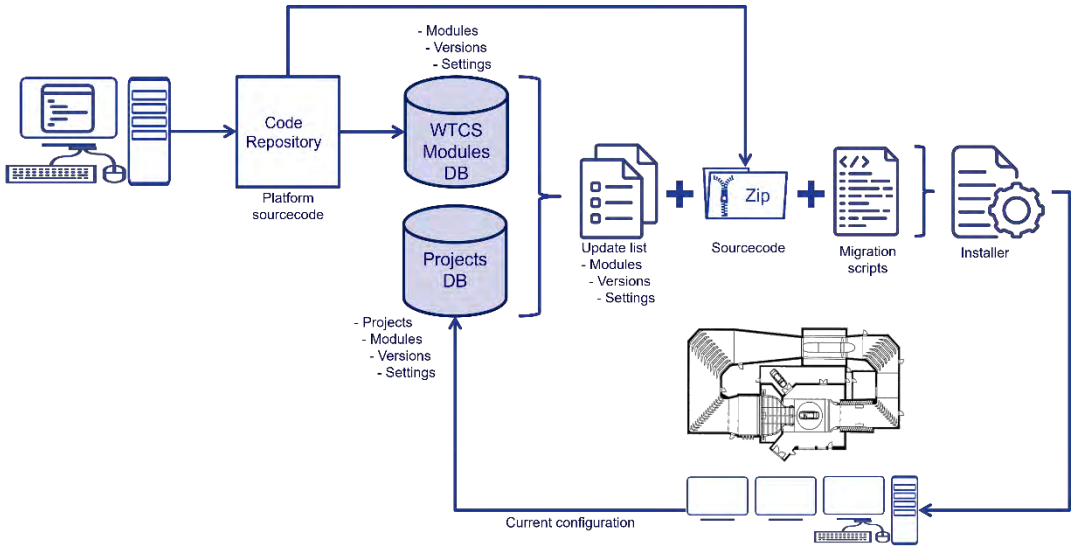

Figure 6: Concept of a version and configuration management cycle

In support of the wind tunnel personnel, the WTCS provider must have suitable domain-experts in operative and supervisory control aspects of aerodynamic and climatic wind tunnels, who at the same time have strong IT knowledge. For designing the system and for execution of successful workshops transferring knowledge from the provider to the owner such highly skilled and knowledgeable experts are of key importance to project success.

8 Benefits of the Approach

Such an approach offers benefits with respect to time, cost, and operations. By purchasing licenses of proven software, while installing and configuring it mostly on their own, wind tunnel centers can significantly reduce costs. Estimates from the first projects show a reduction by up to 50% of external cost.

The approach also offers a lower risk as the parallel operation allows most settings to be tested prior to the final system switch. The point of no return is only reached when new or changed subsystems are only integrated into the new system.

Simultaneously, this reduces downtime of the facility as full operation is possible for most of the time. Thus, the wind tunnel can still be operated, and be profitable, while the new system is commissioned in the background.

Using a platform ensures higher robustness than individualized coding while ensuring maximum functionality as it bundles features from the experience of many customers.

Tailoring the functionality by choosing the right modules and configuring them as needed gives a perfect fit. Each wind tunnel receives exactly the features it requires. Customization is easily done on-site by the wind tunnel center as many aspects are configurable for the user. APIs allow realizing own ideas independently. At the same time, a reliable partner also allows for such modifications done externally.

Always being operational, without deadlines or deadlocks, makes a painless transition possible. The upgrade is efficient. Administrators and operators learn to use the new software while configuring the system, giving them a head start with the new WTCS.

Such a WTCS is a perfect match by seamless integrating into various IT environments and test process workflows. Together with the modularity and configurability of the WTCS allows to easily interact with test resource planning, test definition, and results management systems for seamless, robust and certifiable processes.

9 Benefits beyond Upgrade Projects

The same advantageous features for such an upgrade project also provide benefits in other situations like setting up the WTCS for a new wind tunnel or during operation, when adapting to new requirements and new functionalities.

A strong user community and a supplier actively investing in the future of the platform ensures constant development to stay ahead of the curve as wind tunnel center. The easy expandability of a modular platform in combination with a domain-expert software supplier ensures wind tunnel centers can fulfil their constantly evolving ideas with such a solution in minimal time at reasonable cost. The common platform with a broad installation base allows to benefit from innovative new modules, which were developed by the supplier in response to market requests as such modules can be added to installations of all customers.

9.1 New Wind Tunnels

All benefits of a configurable solution apply here, too. Yet slightly more specification work and interface testing is needed as coordination with the subsystem suppliers is required, compared to a refurbishment project, where the interfaces are usually as is.

If the configuration dialogs allow for export of the configuration in a readable way, it is possible to minimize the additional workload by directly configuring the system and extracting the configuration as specification instead of first generating paper documents and then typing the same information into the configuration.

9.2 During operation

The modularity of a platform ensures easy integration of add-ons and new modules. A high degree of configurability ensures quick changes without significant cost or time needed. The widespread use of a platform always ensures reliable operation of the system, during normal operations as well as during upgrades. Even in case of failure, a platform-based solution has the advantage of well-established error handling and bug reporting allowing for easier recovery and faster fixing of issues.

10 Conclusion

Complex IT systems like a WTCS can be easy to install and configure, allowing cost-effective and hassle-free upgrades of existing facilities Individually hard-coded software development is replaced by a modular and configurable platform. In line with a no-code/low-code concept functionality and behavior are defined by configuration and scripting. Plug-in architectures and APIs seamlessly bridge any gaps in the few situations still requiring coding. This provides modern features for test management, documentation, and efficient operation to older facilities. Further, it ensures constant improvements over the life cycle minimizing the risk of another upgrade drastically. The self-paced and training-supported upgrade path ensures familiarization of the operating and administrating personnel for a smooth transition to a future-proof control system supporting the needs of modern wind tunnel facilities.

11 Reference list

[ISO17a] ISO/IEC 17025:2017 - General requirements for the competence of testing and calibration laboratories, https://www.iso.org/standard/66912.html

[WLT21a] UN Regulation No. 154 - Worldwide harmonized Light vehicles Test Procedure (WLTP), https://unece.org/transport/documents/2021/02/standards/un-regulation-no-154-worldwide-harmonized-light-vehicles-test

[Jac24a] Jan Jacob, “Software-Supported Processes for Aerodynamic Homologation of Vehicles“, SAE Technical Paper 2024-01-3004, 2024, doi: 10.4271/2024-01-3004.

[Jac25a] Jan Jacob, “Efficient Automation of Homologation Tests for Active Aerodynamic Components“, SAE Technical Paper 2025-01-0273, 2025, doi: 10.4271/2025-01-0273.

The New BMW Acoustic Wind Tunnel Centre

Peter Waudby-Smith and Christopher Sooriyakumaran, Aiolos Engineering
Christoph Gabriel and Martin Grabenstein, BMW AG

Aiolos Engineering Corporation
300-135 Queens Plate Drive
Toronto, Ontario, M9W 6V1, Canada

BMW AG
D-80788 München

Peter.Waudby-Smith@aiolos.com
Christopher.Sooriyakumaran@aiolos.com
Christoph.JO.Gabriel@bmw.de

Abstract: BMW has brought into service a new dedicated acoustic wind tunnel center (AWZ) at its Research and Innovation Centre in Munich. The AWZ represents an improvement in vehicle aero-acoustic testing capabilities. The background noise level of the wind tunnel is lower than in other automotive wind tunnels, and the hemi-anechoic performance extends lower in frequency, down to 30 Hz. The aerodynamic environment, both flow stability and flow uniformity, is uncompromised, with demanding requirements met across the full wind speed range. New testing capabilities include a large frontal acoustic array with 216 microphones and a multi-location laser vibrometry system for panel vibration measurements. An interchangeable floor module section allows for different floor conditions including one with a glass floor for underbody laser vibrometry measurements, one with wheel spinners for wind-roll noise simulation, as well as one equipped with a balance for motorcycle aerodynamics. This paper will describe the wind tunnel, its acoustic and aerodynamic capabilities, the features that have enabled these capabilities to be achieved, and its measurement systems.

Contribution: 2025 FKFS Conference on Vehicle Aerodynamics and Thermal Management
15 – 16 October 2025 | Leinfelden-Echterdingen

1 Introduction

Since 1987 BMW has used a dedicated acoustic wind tunnel on Hanauerstrasse for their aero-acoustic testing (HWK). This wind tunnel was highly productive but its capabilities have been eclipsed by more modern facilities and the need for a quieter testing environment for future vehicles. In addition, the HWK is located separate from BMW's other wind tunnels, which were built after the HWK and within the BMW Research and Innovation Centre (FIZ) in Munich. In 2019 BMW selected the group comprising Habau, MCE, ETS, and Aiolos Engineering for a new acoustic wind tunnel (AWZ) and a connected testing building (WPM), with Aiolos as the technical lead for the wind tunnel. The WPM provided space for the wind tunnel control room, offices, and vehicle preparation rooms, but was otherwise separate from the wind tunnel. Design of the AWZ and WPM started at the end of 2019 and the projects were completed by the end of 2024.

The available space for the new wind tunnel was limited, leading to a vertically oriented wind tunnel. Such a vertical orientation is often used for smaller wind tunnels but never previously for such a large wind tunnel as the AWZ. Local building height restrictions led to more than half of the wind tunnel being located below ground level.

Figure 1: Aerial view of the AWZ (green roof) and WPM (red roof) beside the climatic and aerodynamic wind tunnels (blue highlight) in the BMW Research and Innovation Centre (FIZ)

Aero-acoustics is particularly important for quiet electric vehicles. With the combustion engine no longer present to mask other noise sources, primarily wind and rolling noise, these noise sources become more apparent. The AWZ is designed to address both the wind and rolling noises.

The background noise requirements represent an improvement to the performance of existing acoustic wind tunnels. The plenum cut-off frequency requirement is 30 Hz, chosen to enhance the investigation of low-frequency phenomena on the vehicle. This cut-off frequency represents a step change improvement over the 50 Hz cut-off in recent wind tunnels (e.g. [1] to [5]), requiring a new design approach for the plenum acoustic treatment. The aerodynamic performance was required to be as good as the existing aerodynamic wind tunnels at BMW [6]. The only exception was the floor boundary layer thickness – the noise contribution from a boundary layer reduction system was not considered a worthwhile compromise. In contrast, rolling noise tests, with the complex interaction between the main airflow and tire induced airflows, were required as test capabilities for the AWZ. A wheel spinner system was therefore included with one of the interchangeable floor systems. Support for this approach can be found in [7].

The test section has a nozzle size of 25 m^2. The test section incorporates a ±70° rotating 9 m diameter turntable with its centre located 6.5 m downstream of the nozzle exit plane. The turntable incorporates a unique automated removable floor mechanism to switch amongst four surfaces: A solid floor for standard aero-acoustic tests; a solid floor with four wheel spinners; a large underbody 13.2 m^2 glass floor; and a motorcycle testing unit with balance and twin wheel spinners. The turntable also includes side-mounted vehicle lifts to allow for switching of the floors without removal of the vehicle.

The test section includes a full suite of noise and vibration measurement systems, of which the fixed frontal microphone array on top of the nozzle is the most prominent.

Figure 2: Test section showing vehicle operating with wheel spinners, and frontal array above the nozzle (left) and view looking downstream with the glass floor installed and the control room window visible (right)

2 Acoustic Design Features

With its emphasis on low background noise, the circuit design includes numerous acoustic design features. Fan noise attenuation in the circuit was achieved through a combination of acoustic turning vanes, annular acoustic treatment both upstream and downstream of the fan, and extensive duct acoustic treatment. The only duct sections not treated were between corner 4 and the nozzle, and the vertical and horizontal surfaces of the fan diffuser. Surface treatments (fabric and pile fabric) were used on the airflow side of selected areas with perforated plates to minimize the self-noise from the perforated plate. These treatments were used on the collector, plenum backwall, test section diffuser, and corner 1 vanes.

A relatively high contraction ratio of 6.8:1 was chosen to reduce the flow speed in the return circuit, reduce the fan power, and enhance the test section flow quality.

Structure-borne noise issues were a significant consideration in the design of the AWZ due to the vertical orientation of the wind tunnel. For the fan itself, structural decoupling was achieved using 12 spring-mass dampers, designed to attenuate the blade passing frequency impact, located between the concrete inertial mass supporting the fan and the circuit structure.

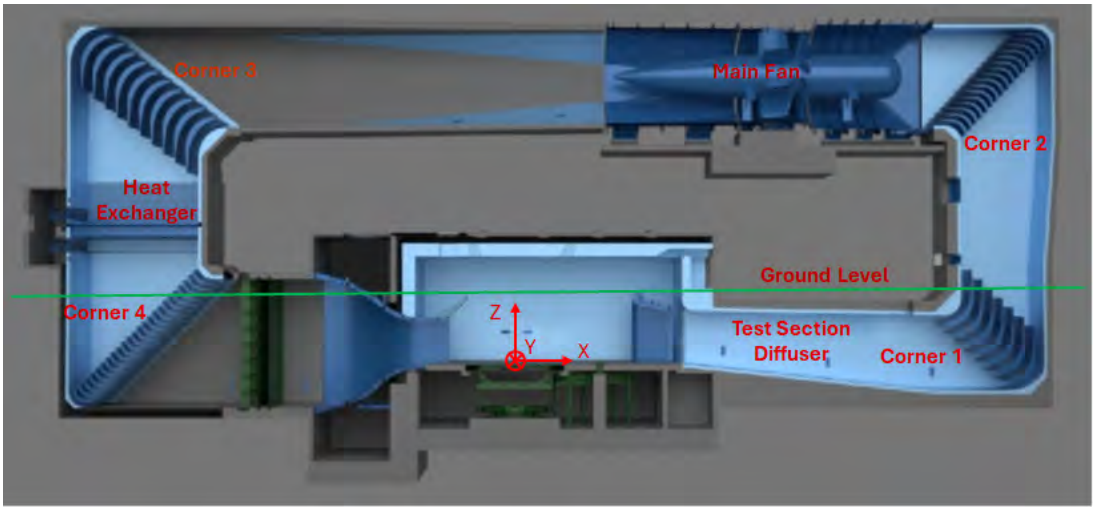

Figure 3: Layout of the AWZ Airline

The orientation of the AWZ circuit layout shown in Figure 3 is opposite to the exterior view shown in Figure 1.

2.1 Test Plenum Design

A unique feature of the AWZ is its capability for acoustic testing down to 30 Hz, achieved through the hemi-anechoic performance of the plenum. The acoustic panels of the AWZ were designed by Müller-BBM and manufactured by TAB to achieve a 30 Hz cut-off, but without the use of membrane absorbers. The depth of these panels is considerably greater than typical membrane absorber panels, but also considerably less than the 2.9 m required for a classical wedge design.

The plenum includes openings for an air exchange system, breather vents, and openings to the ceiling resonator. All of these openings feature silencers to prevent noise intrusion from outside. Flat reflective surfaces were minimized in the plenum walls and ceiling. The control room viewing window can be covered with a retractable acoustic cover.

The control of low-frequency pressure fluctuations and the axial static pressure gradient was achieved through appropriate collector and diffuser inlet sizing, and a set of four low-frequency resonators located in the circuit and above the plenum. The geometries for these components were developed in a $1/10^{th}$ scale model wind tunnel test program. The passive feedback connection developed in the model wind tunnel was not used [8].

Temperature control for the test section is set at a constant 22 °C operation regardless of the wind speed. An air exchange system is included to allow for idling of the test vehicle wind-on without requiring a closely-coupled exhaust extraction system. The air exchange system uses dry air to prevent condensation from the heat exchanger. Due to its location in the vertical cross-leg, a removeable bridge is incorporated at the heat exchanger to allow for inspection and maintenance of the heat exchanger.

3 Measurement Systems

Acoustic Measurement Systems: The wind tunnel includes a large set of acoustic measurements systems carried over from the previous HWK acoustic wind tunnel. These systems include a moveable GFaI 2.5 x 2.5 m^2 side acoustic array with 144 microphones and an interior spherical array with 48 microphones. A new fixed 4.5 m x 3 m acoustic array with 216 microphones was added to this system to allow for detailed noise investigations over the front of the test vehicle. There is provision for new side and top array units to be mounted on a large retractable open portal frame, with ceiling rails already installed and a room available behind the rear plenum wall to store the new equipment when not deployed.

Laser Vibrometry System: The wind tunnel integrates an innovative full-body laser vibrometry system. This system enables a 360° capture of vibrations on various vehicle components, setting new standards for vibro-acoustic measurement technology.

Laser Doppler Vibrometry (LDV) systems are considered the next step in vibro-acoustics as they overcome the many limitations of conventional sensors. Traditional accelerometers require glueing and wiring, which alters the investigated parameters due to mass, stiffness, and flow resistance. In contrast, LDV systems measure surface movements in a completely contactless and undistorted manner.

The system uses 10 scanning vibrometers from the Optomet SMART series, arranged to fully cover the surfaces of the vehicle. Three of these vibrometers are located below the vehicle and used with the glass floor. The other vibrometers are located on the side wall (2 each side), ceiling (2), and one behind the vehicle. All devices are synchronised via an Ethernet connection with sub-nanosecond accuracy, automatically capturing vibrations at several thousand points on the vehicle, including body, attachments, and underbody.

The measurement grid is created offline directly on the CAD model in advance to ensure efficient use of available wind tunnel time. During a test campaign, various configurations can be tested and the classic 'measure-modify-measure' cycle is reduced from days to hours. The associated software calculates phase-accurate animated 3D representations of the operational vibration modes based on reference channels such as the microphones inside the car cabin, LDVs on defined reference points, or accelerometers.

Operational modal analysis under wind load provides a precise understanding of all vibrational components involved and enables precise low-frequency measures to tackle the problem at its source rather than compensating measures such as stiff or tuned mass dampers. An example from a wind-on LDV measurement set is shown in Figure 4 below.

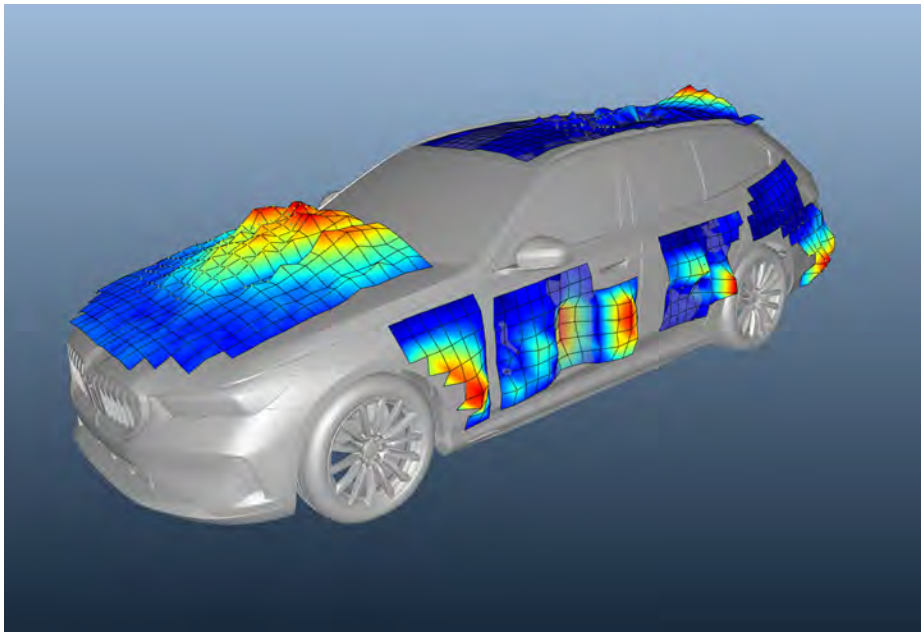

Figure 4: Example of LDV results from a BMW 5 series. The displacements shown for each section on the vehicle relate to unique frequencies relevant to that section

4 AWZ Acoustic Performance

The background noise in the AWZ was measured with a pair of GRAS 40AE freefield microphones positioned horizontally towards the turntable centre and located 6 m either side of the turntable centre at 1.2 m height. The control room window cover was in place. The overall sound pressure level (OASPL) is shown in Figure 5 and compared with published data from comparable aero-acoustic wind tunnels. The lower background noise of the AWZ is evident in this Figure. At 140 km/h the OASPL is 54.7 dB(A).

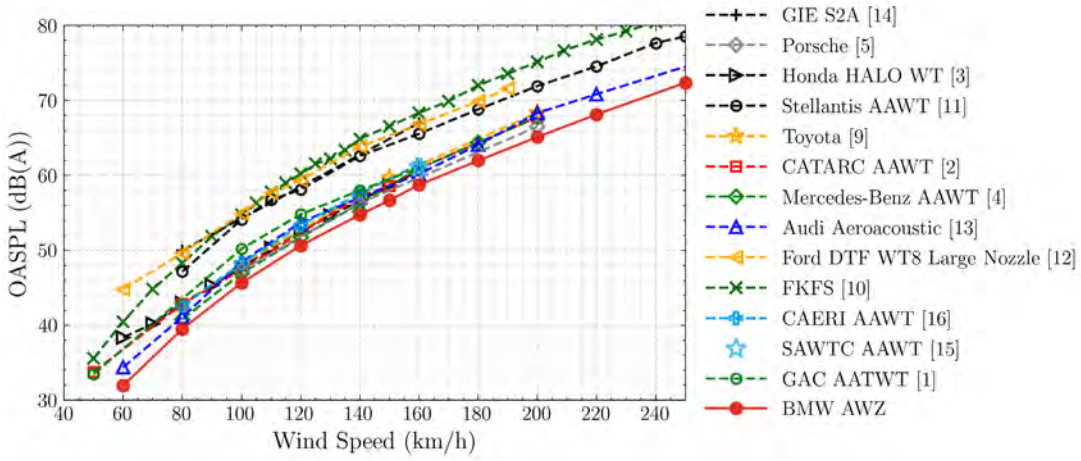

Figure 5: OASPL variation with wind speed at x, y, z = (0, 6, 1.2) m

Third-octave spectra for each wind speed are shown in Figure 6. These spectra show smoothly varying curves with increasing wind speeds without dominant noise features.

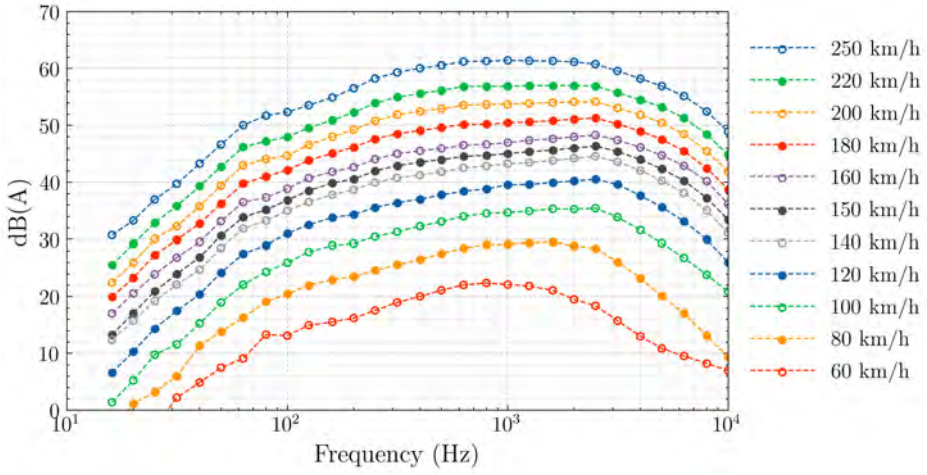

Figure 6: AWZ 1/3rd Octave Band Sound Pressure Spectra at x, y, z = (0, 6, 1.2) m

4.1 Low-Frequency Pressure Fluctuations

Low-frequency pressure fluctuation measurements were made out-of-flow 6 m either side of the turntable centreline at 0.7 m height, and in-flow at the turntable centre at a 1.2 m height. All of the measurements were made with GRAS 40AN microphones; the in-flow measurements used a GRAS RA0020 nosecone. The root-mean-square pressure fluctuations normalized by the freestream dynamic pressure are shown in Figure 7 along with data from other large automotive wind tunnels.

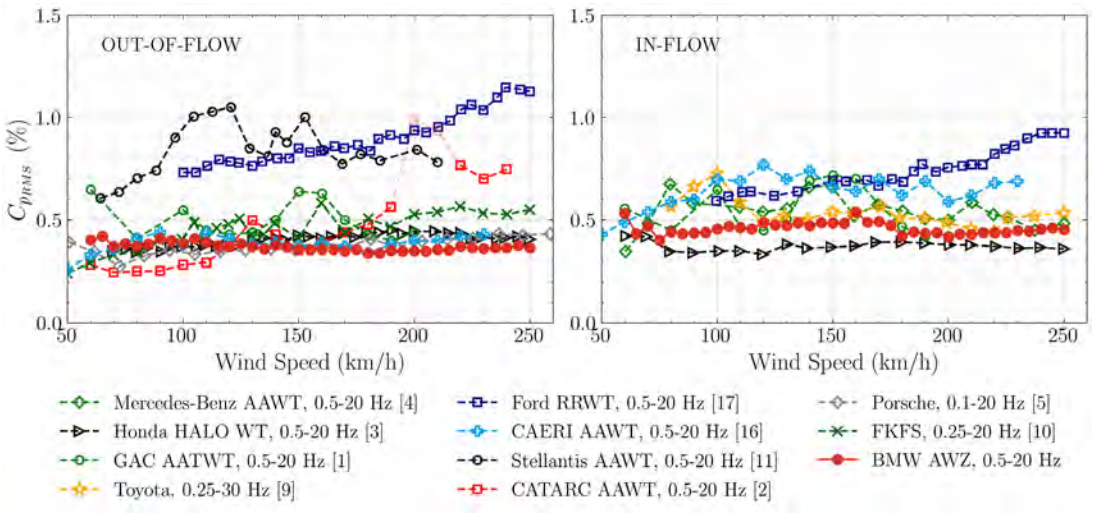

Figure 7: Out-Of-Flow (Left) and In-Flow (Right) Integrated Pressure Fluctuations

The spectral shape of the pressure fluctuations is also important. For BMW the narrowband pressure fluctuations for a frequency interval of $\Delta f = 0.1$ Hz over the range of 1-30 Hz should be less than 100 dB(Z) up to 120 km/h, and less than 105 dB(Z) up to 250 km/h. Examples of this spectral approach are shown in Figure 8 for measurements at the turntable centre axial position. Together with the Cp_{rms} data, the AWZ results show that the pressure fluctuations have been controlled and that there are no significant interactions with resonant modes of the circuit or the plenum.

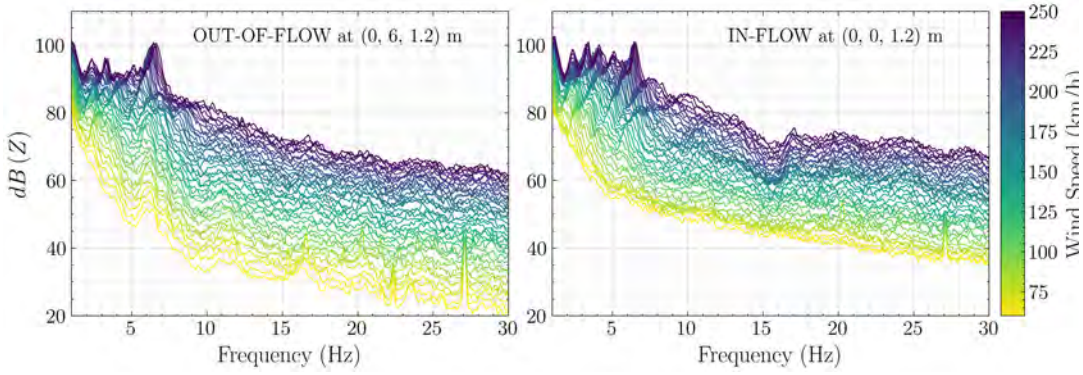

Figure 8: Narrowband low-frequency pressure fluctuation spectra, $\Delta f = 0.1$ Hz

5 Axial Static Pressure Variation

The AWZ did not include a wide-coverage in-flow traversing mechanism. A floor mounted traverser with a single pitot-static probe was used for the initial axial pressure measurements where adjustments to the collector were made. The final set of measurements were performed with a single probe mounted on a floor stand, manually moved wind-off for every 0.5 m increment. This procedure, though time-consuming, provided confidence in avoiding variable probe support interference over the length of the measurement region.

An adjustment to the static pressure variation near the nozzle exit was achieved with half-round surfaces applied to the nozzle exit, flush with the airflow surface. The half-round shape was also beneficial in terms of acoustic reflections.

Figure 9 shows the axial static pressure variation in the AWZ along with results from other wind tunnels for a similar wind speed (120 km/h to 150 km/h). The AWZ Cp variation is seen to stay within ±0.0021 over the measured range of -4.5 m to +6 m.

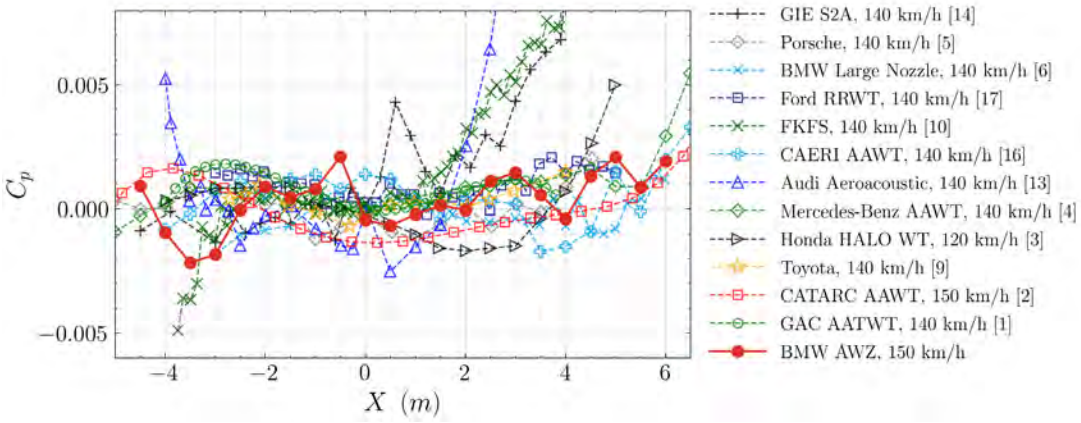

Figure 9: Axial static pressure coefficient distribution for several full-scale automotive wind tunnels. Results are relative to the turntable centre

Fourth-order curve fits were applied to the AWZ data to allow for a calculation of the pressure gradient. Plots of the resulting pressure gradient are shown in Figure 10. The pressure gradient remained within ±0.0009/m over the required axial length of -3.5 m to +5 m and for the full wind speed range of 80 km/h to 250 km/h.

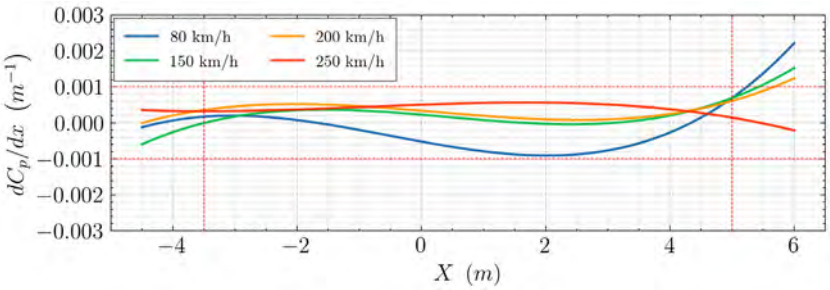

Figure 10: Axial static pressure gradient in the AWZ along Y=0 m, Z = 0.7 m

6 Flow Uniformity

The flow traversing mechanism selected for these measurements was a standalone floor-based unit with a vertical drive mechanism, shown in Figure 11. The horizontal and axial directions were manually driven. The concept, based on a traversing mechanism that was similar but with fixed probe positions on the strut [18], combined high stiffness, minimal variations in flow interference, and avoidance of fastening holes in the turntable.

Figure 11: Flow Uniformity Measurement Rig at the X = 4.5 m Test Plane

Measurements were obtained over YZ-planes extending into the jet shear layers at five discrete axial locations. Two measurement grids were used; a coarse grid with roughly 160 measurement points and a 400 mm spacing at axial locations of X = ±5.25 m, ±2.25 m, and 0 m; and an additional fine grid in the core of the jet with spacings of 200 mm at the turntable centre (X = 0). See Table 1 for further details.

The total pressure, static pressure, and flow angle uniformity measurements were made with an Aeroprobe 5+static multi-hole probe. An exposed thermally insulated 4-wire RTD sensor attached to the probe support, and a matching but fixed RTD in the flow, provided the temperature measurements (only recorded for the X = 0 m plane).

The dynamic pressure uniformity results are shown for all five planes in Figure 12. The contours use the measured dynamic pressure at each measurement location normalized by the reference freestream dynamic pressure. The progressive erosion of the uniform flow field by the shear layers is visually evident in this presentation. Although the total pressures are more uniform than the static pressure in the central region it is the erosion of the total pressure that contributes to most of the dynamic pressure fall-off in the shear layers.

Within the central region but over all five planes and all wind speeds tested the total pressure uniformity was less than 0.16% in each plane, while the static pressure uniformity was less than 0.23% (one standard deviation for both values). Further details are provided in the performance summary in Table 1.

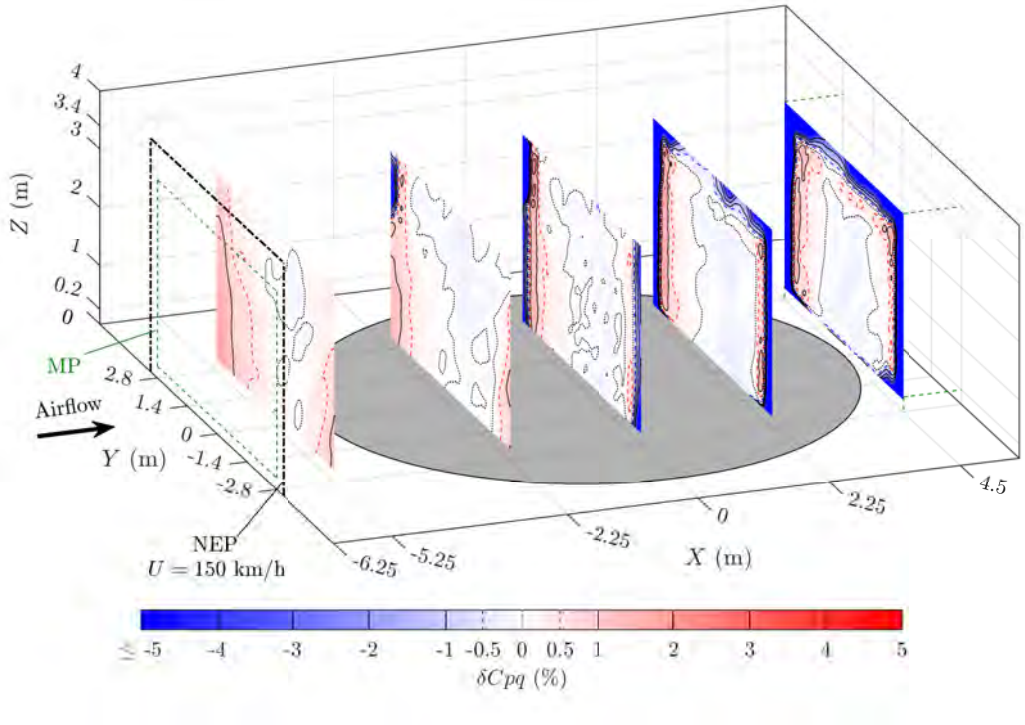

Figure 12: Dynamic Pressure Uniformity at 150 km/h
MP – Measurement Plane Boundary, NEP – Nozzle Exit Plane

The flow angle taps of the Aeroprobe probe were calibrated in-situ, with separate calibrations for each wind speed. A Leica Geosystems TS16 Total Station, located out of the flow in the plenum, was used to measure the pitch and yaw angles of the probe support for each probe position and for each wind speed at X = -5.25, 0, 4.5 m. The accuracy of these probe angle measurements was generally within ±0.02°. The flow angles are shown in a vector format in Figure 13. Within the specification planes at X =-5.25 m and 0 m the standard deviations of the flow angles were within 0.09° in pitch and 0.13° in yaw. At the X = 4.5 m plane the uniformity was only slightly degraded.

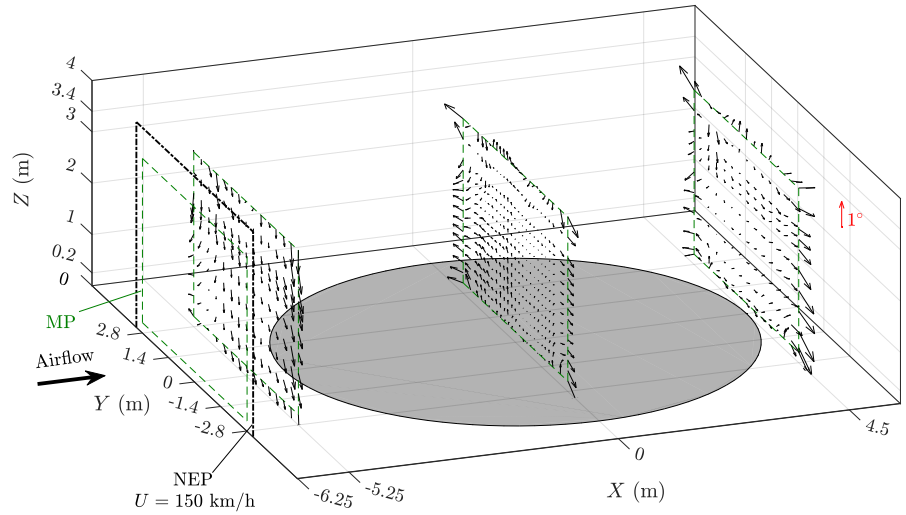

Figure 13: Flow Angle Distribution at 150 km/h

Turbulence was measured with a Dantec 55P11 single-wire hot-wire and a Dantec 54T42 miniCTA. The probe was calibrated in-situ with separate calibrations for each wind speed. The results across the full planes are shown in Figure 14. The X = 4.5 m plane could not be completed due to vibration of the probe support in the strong shear layers.

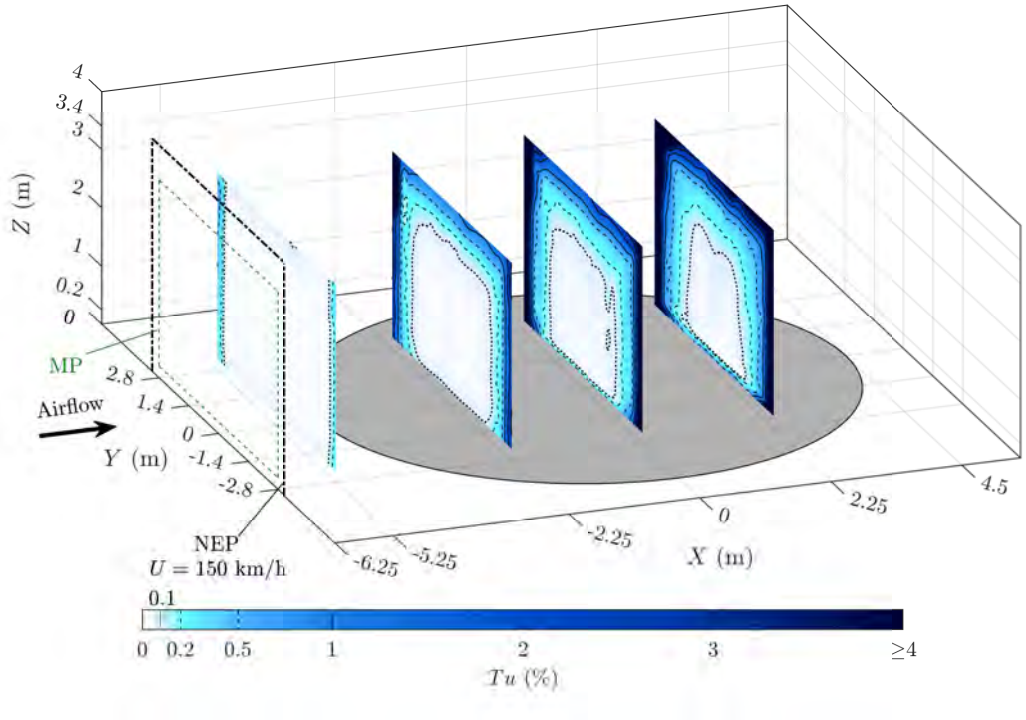

Figure 14: Turbulence intensity at 150 km/h for 10 Hz < f < 4 kHz

As is typical for an open jet, the low turbulence region is significantly eroded by the growth of the shear layers with increasing axial distance from the nozzle. The turbulence data from the four complete planes were interpolated to produce a 3-dimensional iso-contour for a single turbulence level. The iso-contour for 0.2% is shown in Figure 15. The plots show a consistent reduction in width and height with axial position for the 0.2% contour line. Also visible is the minimal but growing influence of the floor boundary layer on the turbulence. The different views of the iso-contour lines show that a typical vehicle will remain within the 0.2% turbulence lines.

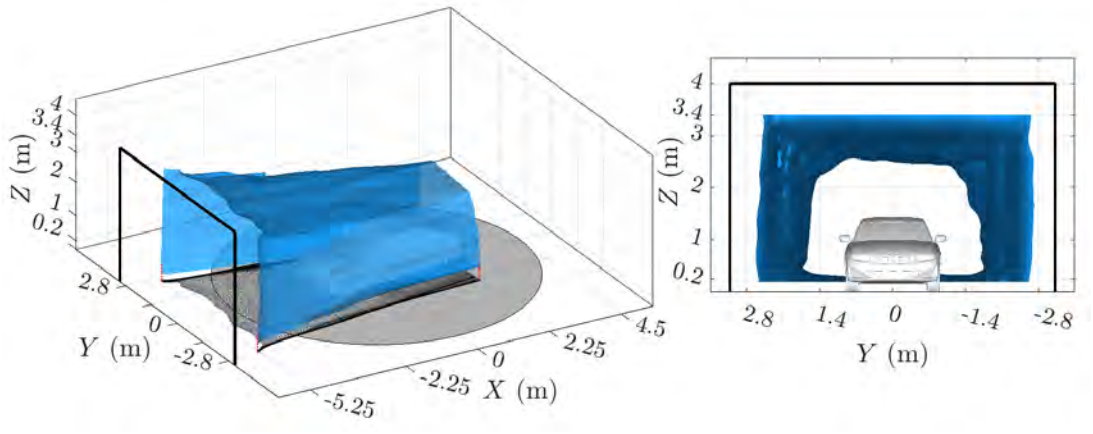

Figure 15: Iso-contour surface of Tu = 0.2% at 150 km/h

7 Summary and Conclusions

The new acoustic wind tunnel at BMW, the AWZ, brings together BMW's extensive wind tunnel testing capabilities, acoustic, aerodynamic, and climatic, into one central test centre. The AWZ represents a step improvement in the acoustic performance of automotive wind tunnels, exhibiting lower overall sound pressure levels and a lower plenum cut-off frequency. This performance was achieved while maintaining excellent flow quality. The AWZ includes a new large frontal microphone array, which when combined with the existing side and interior arrays allows for precise sound localization measurements. These acoustic systems are supplemented with a 10-camera 3D laser vibrometry system for detailed non-intrusive panel vibration measurements of the complete vehicle. Detailed underbody investigations are possible with a large glass floor. This glass floor can be switched, without removing the vehicle, to a solid floor with wheel spinners to include flow simulation at the rotating wheels. An additional floor module allows for motorcycle testing using an underfloor balance and twin wheel spinners. Taken together, the new AWZ and its testing systems expand BMW's acoustic testing capabilities to the next level within the integrated BMW research and innovation centre.

Table 1: Acoustic and Aerodynamic Performance of the AWZ

Parameter	Measurement Region	Wind Speeds	Measured Values
Background Noise OASPL	X=0, Y = ±6 m, Z = 0.7m 20 Hz - 10 kHz	60 km/h	32.0 dB(A)
		100 km/h	45.7 dB(A)
		140 km/h	54.7 dB(A)
		150 km/h	56.7 dB(A)
		200 km/h	65.1 dB(A)
		250 km/h	72.4 dB(A)
Low-frequency static pressure fluctuations, 0.5-20 Hz	X = 0, Y = ±6 m, Z=0.7m	60 – 250 km/h	$Cp_{rms} \leq 0.42\%$
	X = 0, Y = 0 m, Z=1.2 m	60 – 250 km/h	$Cp_{rms} \leq 0.55\%$
Axial static pressure variation	-3.5 m ≤ X ≤ 5 m Y = 0 m, Z = 0.7 m 4^{th} order curve fit	80, 150, 200, 250 km/h	|Cp| ≤ 0.002 |dCp/dX| ≤ 0.0009/m
Total Pressure Uniformity	Specification Plane at X = -5.25 m, -2.25 m, 0 m, 2.25 m, 4.5 m	100/150/250 km/h	$\sigma(P_t/q) \leq$ 0.16% / 0.10% / 0.08%
Static Pressure Uniformity		100/150/250 km/h	$\sigma(P_s/q) \leq$ 0.21% / 0.22% / 0.22%
Dynamic Pressure Uniformity		100/150/250 km/h	At X = -5.25 m, $\sigma(P_q/q) \leq$ 0.21% / 0.26% / 0.24% $\sigma(P_q/q) \leq$ 0.20% elsewhere
Flow Angle Uniformity	Specification Plane at X = -5.25 m, 0 m	100/150/250 km/h	$\sigma(\alpha) \leq$ 0.09°/ 0.08°/ 0.08° $\sigma(\beta) \leq$ 0.13° / 0.12°/ 0.11°
	Specification Plane at X = 4.5 m	100/150/250 km/h	$\sigma(\alpha) \leq$ 0.11°/ 0.10°/ 0.09° $\sigma(\beta) \leq$ 0.16° / 0.15°/ 0.14°
Turbulence Intensity 10 Hz ≤ f ≤ 4 kHz	Specification Plane at X = -5.25 m	100/150/250 km/h	Tu ≤ 0.09% / 0.06% / 0.07%
Temperature Uniformity	Specification Plane at X = 0 m	100/150/250 km/h	Max,min deviation = (°C) 0.1,-0.1 / 0.1,-0.1 / 0.2,-0.5
Boundary Layer	X = -2.5 m, Y = 0 m	100/150/250 km/h	$\delta \leq$ 117 / 112 / 105 mm
Fan Power	CdA = 1.0 m^2, T = 22 °C	250 km/h	3.5 MW
Acceleration Rate	X=0, Y=0, Z = 1.2 m	0-250 km/h: 40 s; 250-20 km/hr: 30 s	
Specification Plane	|Y| ≤ 1.6 m, $z_{min} \leq Z \leq$ 2.4 m z_{min} = 0.2 m, but larger of 0.2m and 1.5δ for total pressures, 2δ for Tu		
Measurement Planes	|Y| ≤ 2.8 m, 0.2 m ≤ Z ≤ 3.4 m X = -5.25 m, -2.25 m, 0 m, 2.25 m, 4.5 m; only 100, 150 km/h		

8 Bibliography

[1] T. Bendor, V. N. Esfahani, Z. Liu, H. Yang, S. Li, X. Song, M. Liu and Z. Ma, "The Guangzhou Automotive Group Co. Aerodynamic, Acoustic, and Thermal Wind Tunnel," *SAE Technical Paper 2025-01-8878,* 2025.

[2] P. Waudby-Smith, T. Bender, C. Sooriyakumaran, Z. Yilun, H. Wang, F. Zhao, G. Fan, J. Sun and X. Liu, "The New China Automotive Technology and Research Center Aerodynamic-Acoustic and Climatic Wind Tunnels," SAE Technical Paper 2024-01-2541, 2024.

[3] S. Best, G. Bari, T. Brooker, G. Flynt, J. Walter and E. Duell, "The Honda Automotive Laboratories of Ohio Wind Tunnel," SAE Technical Paper 2023-01-0656, 2023.

[4] R. Buckisch, B. Schwartekopp and J. Pfisterer, "Daimler Aeroacoustic Wind Tunnel: 5 Years of Operational Experience and Recent Improvements," SAE Technical Paper 2018-01-5038, 2018.

[5] H. Stumpf, P. Röser, T. Wiegand, B. Pfäfflin, J. Ocker, R. Müller, W. Eckert and H.-U. Kroß, "The New Aerodynamic and Aeroacoustic wind tunnel of the Porsche AG," in 15. Internationales Stuttgarter Symposium. Proceedings. Springer Vieweg, Wiesbaden, 2015.

[6] E. Duell, A. Kharazi, S. Muller, W. Ebeling, E. Mercker, "The BMW AVZ Wind Tunnel Center", SAE Technical Paper 2010-01-0118, 2010.

[7] E. Rajaratnam and D. Walker, " Experimental and Computational Study of the Flow around a Stationary and Rotating Isolated Wheel and the Influence of a Moving Ground Plane", 2019-01-0647, 2019.

[8] P. Waudby-Smith, A. Joshi, C. Sooriyakumaran, C. Gabriel, M. Grabenstein, “Using a Passive Feedback Connection to Control Low-Frequency Pressure Fluctuations in a Wind Tunnel,” Canadian Acoustics 50, no. 1 (2022): 11-17.

[9] K. Tadakuma, T. Sugiyama and K. Maeda, "Development of Full-Scale Wind Tunnel for Enhancement of Vehicle Aerodynamic and Aero-Acoustic Performance," SAE Technical Paper 2014-01-0598, 2014.

[10] R. Blumrich, N. Widdecke, J. Wiedemann, A. Michelbach, F. Wittmeier and O. Beland, "New FKFS Technology at the Full-Scale Aeroacoustic Wind Tunnel of University of Stuttgart," SAE Int. J. Passeng. Cars - Mech. Syst., vol. 8, no. 1, pp. 294-305, 2015.

[11] J. Walter, E. Duell, B. Martindale, S. Arnette, R. Geierman, M. Gleason and G. Romberg, "The DaimlerChrysler Full-Scale Aeroacoustic Wind Tunnel," SAE Technical Paper 2003-01-0252, 2002.

[12] J. Walter, E. Duell, B. Martindale, S. Arnette, P. Nagle, W. Gulker, S. Wallis and J. Williams, "The Driveability Test Facility Wind Tunnel No. 8," SAE Technical Paper 2002-01-0252, 2002.

[13] G. Wickern and N. Lindener, "The Audi Aeroacoustic Wind Tunnel: Final Design and First Operational Experience," SAE Technical Paper 2000-01-0868, 2000.

[14] P. Waudby-Smith, T. Bender and R. Vigneron, "The GIE S2A Full-Scale Aero-acoustic Wind Tunnel," SAE Technical Paper 2004-01-0808, 2004.

[15] He, Y., Yang, Z., and Wang, Y., “Wind Noise Testing at the Full Scale Aeroacoustic Wind Tunnel of Shanghai Automotive Wind Tunnel Center,” In: Bargende, M., Wiedemann, H.C., Reuss, J. (eds.), 14. Internationales Stuttgarter Symposium. Proceedings, Springer Fachmedien, Wiesbaden, 2014.

[16] L. Xu, X. Zhu, Q. Wang, et.al., “The New China Automotive Engineering Research Institute co., Ltd Full-Scale Aero-Acoustic Wind Tunnel”, SAE Technical Paper 2025-01-8779, 2025.

[17] P. Nagle, T. Brooker, G. Bari, J. Toth, et al., “The Ford Rolling Road Wind Tunnel,” SAE Technical Paper 2023-1-0654 (2023).

[18] E. Ljungskog, S. Sebben, and A. Broniewicz, "Uncertainty Quantification of Flow Uniformity Measurements in a Slotted Wall Wind Tunnel", SAE Technical Paper 2019-01-0656, 2019.

Numerical design and optimization of underhood cooling system based on coupled 1D and 3D flow modeling

Gowtham Chandrasekharan Parameswaran, Sagar Kulkarni, Dig Vijay

Gamma Technologies GmbH
Stuttgart, Germany

gc.parameswaran@gtisoft.com, sagar.kulkarni@gtisoft.com, d.vijay@gtisoft.com

Abstract: Underhood cooling systems are crucial for ensuring efficient thermal management leading to improved vehicle performance in terms of range and thermal derating of key powertrain components, while meeting packaging constraints. This work presents a synergetic 1D-3D solution by modeling external air flow with 3D computational fluid dynamics (CFD) and internal flow (coolant, refrigerant and gas) with 1D CFD in GT-SUITE. The presented methodology helps in achieving higher computational speed owing to 1D-2D spatial discretization of flow inside the heat exchangers and high accuracy due to detailed 3D CFD for external air flow. Moreover, the iterative exchange of boundary data between 1D and 3D domain ensures solution accuracy and stability while reducing computational efforts. Accordingly, a test case with inclined cooling module is presented, where the design optimization focuses on key parameters such as degree of inclination of different heat exchangers (HXs), HX dimensions, flow space geometry, fan characteristics and grill design. Optimization techniques like design of experiments and multi-objective Pareto optimization are deployed to balance cooling efficiency and energy consumption within given system constraints. In conclusion, this coupled 1D-3D modeling approach provides a unique numerical solution that is suitable for performing high number of design iterations desired for pre-design of vehicle cooling systems to make faster and accurate decisions.

Contribution: 2025 FKFS Conference on Vehicle Aerodynamics and Thermal Management
15 – 16 October 2025 | Leinfelden-Echterdingen

1 Introduction

The thermal management of electrified vehicles (xEV) presents unique engineering challenges that significantly impact vehicle performance, efficiency, and reliability. Underhood pre-design, a critical phase in xEV development, requires systematic consideration of multiple interacting thermal systems within stringent spatial constraints [1]. This paper examines the fundamental challenges of underhood thermal architecture and their implications for overall xEV performance. The complexity of xEV thermal management stems from the need to simultaneously address several competing requirements. Space constraints necessitate efficient packaging of cooling systems and battery thermal management components while maintaining adequate airflow pathways. Thermal interaction presents another significant challenge, as various components operate at different optimal temperature ranges, batteries typically prefer 20-40°C, while power electronics can function at higher temperatures, requiring careful thermal isolation or strategic integration. Airflow optimization represents a critical design consideration, demanding properly engineered ducting and flow paths to ensure sufficient cooling reaches all components while minimizing aerodynamic drag penalties. Furthermore, the integration of multiple cooling circuits operating at different temperature ranges (battery cooling, motor/electronics cooling, cabin HVAC) requires sophisticated control strategies to maintain system harmony and efficiency. The significance of effective underhood pre-design extends beyond basic thermal control, directly influencing vehicle range through cooling system efficiency, battery longevity through temperature management, fast-charging capabilities, passenger comfort, and overall vehicle reliability [2]. This paper explores these challenges and their implications for next generation xEV design methodologies.

The 3D computational fluid dynamics (CFD) with porous media approach to represent heat exchangers [3] is one of the detailed modeling methodologies for underhood thermal management in battery electric vehicles. This approach replaces detailed heat exchanger geometries with homogenized porous blocks defined by flow resistance and heat transfer characteristics. This enables efficient full-vehicle simulations while capturing key effects such as recirculation, flow maldistribution, and thermal interactions. Implementation involves defining heat exchanger volumes, assigning pressure drop and heat transfer data, and integrating them into the flow domain, with advanced models adding anisotropic resistance and non-equilibrium effects. While less computationally demanding than fully resolved CFD for internal flow inside heat exchangers, the method still requires complex setup, geometry preparation, meshing, solver tuning, and parameter calibration. Design changes often necessitate remeshing and re-simulation, limiting rapid design exploration despite efficiency gains.

In contrast, GT-SUITE, a multiphysics CAE software from Gamma Technologies, offers several methodologies for modeling underhood thermal systems. One of the two approaches is known as Quasi-3D approach. This approach provides a 3D environment to model heat exchangers, fans, shrouds, flow inlets/outlets, and

structural blockages. Unlike traditional full 3D CFD approaches, this methodology runs significantly faster by using a 2D discretization of control volumes representing heat exchangers, and fans, while utilizing quasi-3D airflow solution [4]. This makes it efficient in computational speed for analyzing multiple operating conditions and running design of experiments while producing results comparable to 3D CFD for overall system performance metrics. A key advantage of this approach is its ability to provide increased control over discretization (both tangential and axial) and specify spatially varying flow conditions at heat exchanger faces. The predictive capabilities eliminate the need for user-imposed flow distribution assumptions, as it can naturally predict flow redirection around structural elements. Thus, the quasi-3D approach can be naturally used to analyze how heat exchanger stacking affects the heat exchange and cooling system design. Despite its advantages, this approach provides low fidelity spatial resolution than full 3D CFD, making it less suitable for analyzing highly localized temperatures or complex flow patterns that involves flow turning and multiple recirculation regions.

GT-Auto-3DFlow, which is a detailed 3D CFD solution of GT-SUITE, combines the strengths of both the quasi-3D and traditional 3D CFD approaches to overcome their respective limitations while providing enhanced accuracy [5]. It integrates porous media heat exchanger modeling with 1D CFD modelling of heat exchanger, automating geometry handling, meshing, and solver settings. The workflow is designed for system focused engineering. It offers much faster turnaround, which is relatively faster than traditional porous media approach by using an optimized fan discretization scheme and automated parameter exchange between air flow domain and heat exchanger internal flow domain. The detailed 3D approach maintains the ability to capture key 3D flow phenomena such as recirculation, maldistribution, thermal interactions with high accuracy, but with far lower setup complexity and computational overhead than traditional porous media approach.

2 Material and method

This paper utilizes the detailed CFD framework, a high-fidelity computationally efficient 3D computational fluid dynamics (CFD) solution tailored for system focused analysis [6]. Developed through the integration of 3D CFD solver from Simerics Inc. with GT-SUITE, the framework enables accurate prediction of complex fluid flow and thermal phenomena within a system-level modeling context. The approach eliminates the need for extensive 3D CFD expertise, making it particularly well-suited for underhood thermal management, where multiple heat exchangers and intricate flow domains must be evaluated concurrently. In the following sections, a brief description of how different components of an underhood system are modeled is discussed.

2.1 Heat exchanger modeling

Heat exchangers are modeled using two fluid convection models and dedicated geometrical components. The heat exchanger is discretized, and correlations are utilized to create predictive models [4]. When measured performance data is available, it can be calibrated to preselected heat transfer and friction correlations. If measured data is not available, correlations can be chosen or custom correlations can be implemented with scaling multipliers to achieve desired performance. This correlation-based approach enables the heat exchanger model to predict performance both within and outside the entered data range under various conditions such as temperature, pressure, fluid properties, and geometry scaling.

2.2 Fan modeling

Fans are modeled using a non-dimensional theory that converts performance data into dimensionless coefficients for pressure (Ψ), flow (Φ), and power/torque [4]. This method enables predictive fan performance across all operating ranges (windmilling and positive pressure rise), including conditions outside the original test data. During simulation, instantaneous pressure rise governed by the system resistance and shaft speed/torque inputs are converted into non-dimensional coefficients to determine the flow rate and power consumption of the device. The performance of the fan at other temperatures is possible as density variations that significantly affect fan performance is accounted by correcting to reference conditions. The non-dimensional data also enables to scale the fan geometry to appropriately size the fan according to the system cooling performance needs.

2.3 Underhood Air Modeling

2.3.1 Numerical Approach

In this work, the airside is discretized using the finite volumes and the Darcy-Forchheimer formulation is utilized to model momentum source terms for porous media regions like heat exchangers. The equation is:

$$S = -\mu/\alpha \cdot v - \rho \cdot C \cdot |v| \cdot v$$

where:

- S is the momentum source term
- μ is fluid viscosity
- α is permeability
- ρ is density
- C is inertial resistance factor

- v is velocity

This formulation adds resistance terms to the standard momentum equations to represent pressure drop across heat exchangers without modeling their detailed internal geometry.

For the numerical solution, the finite volume scheme is deployed to discretize 3D Navier-Stocks equation with first and second order upwind and central differencing schemes for convective and diffusive terms. The solver applies relaxation factors (ranging from 0 to 0.8) to control solution stability during iterations for velocity, pressure, turbulent kinetic energy, turbulent energy dissipation rate, and energy variables. For turbulence modeling, users can select from standard K-Epsilon, RNG, or Realizable K-Epsilon models, with appropriate transport equations for each, in this paper K-Epsilon model is implemented.

2.3.2 Mesh Generation

Meshing is based on Cartesian (block-structured) base mesh and mesh generation is fully automated and controlled through resolution settings categorized as Coarse, Medium or Fine. Surface mesh export is also resolution-dependent, with configurable edge length parameters for accurate geometry representation in CFD domains.

2.3.3 Co-Simulation Strategy

A co-simulation methodology couples the 3D CFD air domain with the 1D CFD heat exchanger internal flow domain through iterative data exchanges as shown in Figure 1. The process operates as follows:

- The 1D CFD model in GT (referred for GT-SUITE) executes for a defined time interval.
- Boundary data is exchanged with the 3D CFD air domain.
- The 3D solver advances the solution for predefined number of iterations.
- The exchange repeats until user-defined convergence criteria are met or the maximum simulation time is reached.

This iterative scheme enables accurate prediction of key thermal-fluid performance metrics such as pressure drop, temperature distribution, heat transfer rates, and flow distribution, with a balance between accuracy and computational efficiency.

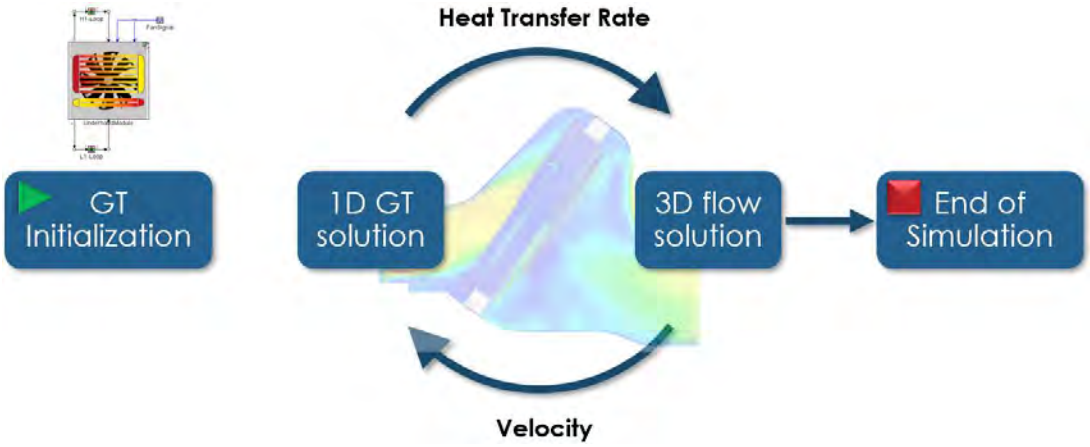

Figure 1: Co-simulation strategy between 1D flow domain (internal) and 3D flow domain (external).

3 Results

This paper employs the detailed 1D-3D approach to investigate the flow and thermal performance of an underhood system representative of a hybrid powertrain which is shown in Figure 2. The underhood system comprises of high and low temperature radiators, a condenser and dual electric fans that aid airflow management. The analysis focuses on the effects of cooling module orientation (0°, 15°, and 30°), grille flap angles (0°, 15°, 25°, 35°, 55°, and 75°), and variable vehicle velocity on overall air mass flow rate and coolant temperatures, which in turn influence the performance of powertrain components such as battery, e-motor, inverter and engine. Finally, it is also demonstrated how the scaling features can be leveraged to optimize the heat exchanger and fan sizes to obtain maximum air flow rate through the underhood to achieve lower coolant outlet temperatures.

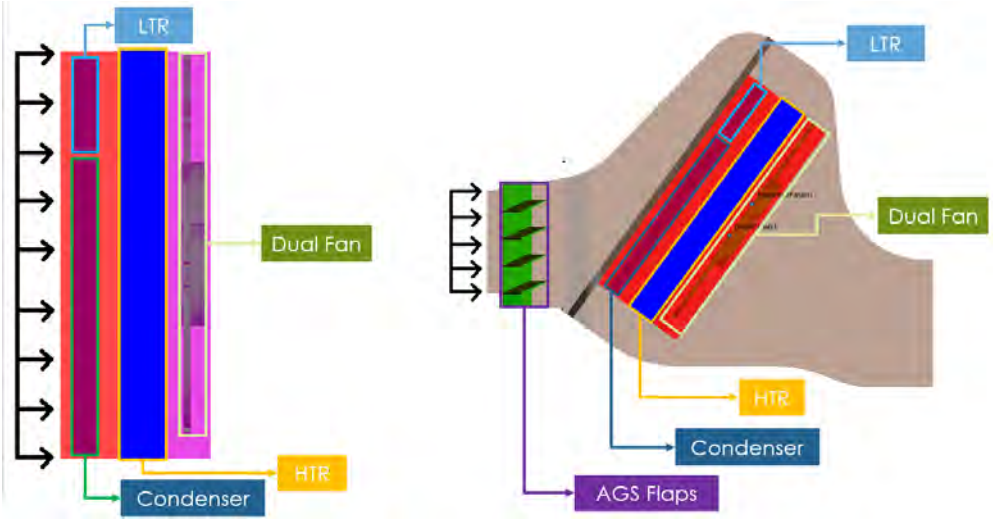

Figure 2: Typical underhood model for vehicle thermal management.

3.1 Impact of flap angle

Flap angle is one of the important parameters that controls the airflow rate and cooling efficiency as this determines how the heat exchangers interact with the incoming air. As a first study the flap angle varied from 5° (open) to 70° (close) for a fixed vehicle velocity to analyze the overall air mass flow rate through the underhood system, see Figure 3. While higher flap angles of 55° and 70° resulted in lower airflow and higher coolant temperatures, flap angle of 5° which represent almost a fully open configuration also resulted in high coolant outlet temperatures >100 °C, which may negatively impact the temperature sensitive components. From Table 1, it can be observed that flap angles of 15°, 25° and 35° facilitate higher airflow and lower coolant outlet temperatures (HTR Coolant Tout and LTR Coolant Tout), air outlet temperatures are listed under HTR Tout and LTR Tout.

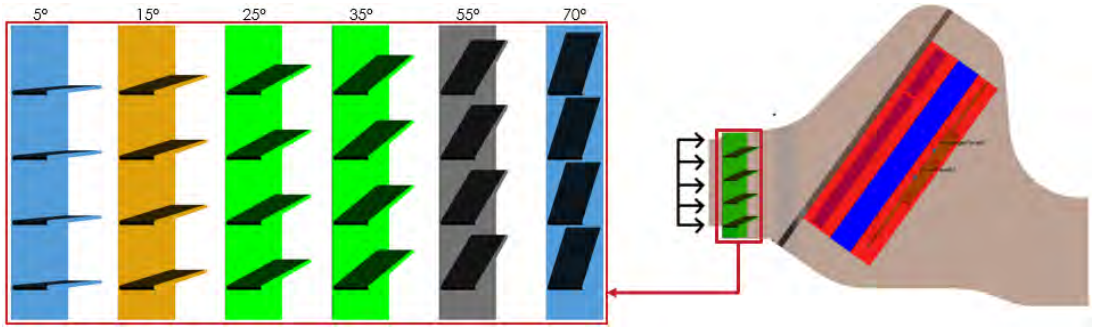

Figure 3: Different flap angles at the inlet of the underhood cooling module.

Table 1: Results of the various flap angles at the inlet

Flap Angle (°)	Vehicle Speed (km/h)	Flow In (kg/s)	HTR Tout (°C)	LTR Tout (°C)	HTR Coolant Tout (°C)	LTR Coolant Tout (°C)
5	50	1.463	76.368	83.49	91.409	108.262
15	50	1.445	75.599	81.328	90.627	105.961
25	50	1.390	77.479	80.38	92.414	104.971
35	50	1.308	80.891	79.265	95.684	103.715
55	50	0.979	98.041	86.707	112.417	111.406
70	50	0.643	131.839	104.856	145.083	127.923

3.2 Impact of vehicle velocity

The vehicle velocity affects the ram air pressure and creates higher pressure at the grille and controls the airflow and heat exchanger cooling performance. Subsequently, for the three best grille angles that resulted in higher airflow and lower coolant outlet temperatures, the effect of low and high vehicle velocity was studied as shown in Table 2, where it can be observed that 15° and 25° flag angle configurations results in overall higher airflow rate and relatively lower coolant outlet temperatures.

Table 2: Results of different vehicle speeds and flap angle

Flap Angle (°)	Vehicle Speed (km/h)	Flow In (kg/s)	HTR Tout (°C)	LTR Tout (°C)	HTR Coolant Tout (°C)	LTR Coolant Tout (°C)
15	0	1.123	85.359	84.907	100.103	109.498
	130	2.593	57.04	66.635	72.754	91.143
25	0	1.097	86.982	87.591	101.539	112.457
	130	2.542	57.403	64.777	73.068	89.133
35	0	1.045	89.876	82.202	104.267	106.548
	130	2.397	58.957	62.159	74.579	86.392

3.3 Impact of cooling module orientation

Though the flag angle and vehicle velocity affect the airflow, the cooling module (radiators, condensers, charged-air-cooler, fans) orientation also dictates the amount of surface area that is available for heat exchange and affects the pressure and flow distribution. During predesign analysis, cooling module orientation in an important

aspect that can be examined to determine the optimal layout and packaging constraints and choose appropriate heat exchanger sizes, see Figure 4. In this paper, it is demonstrated how the detailed 1D-3D approach can be leveraged to analyze the effect of different pack angles on the cooling performance.

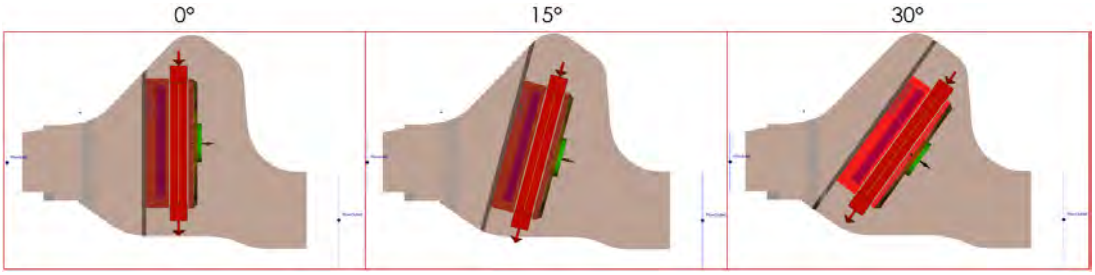

Figure 4: Orientation of cooling modules at different angles.

Table 3 shows the results of airflow rate and coolant outlet temperatures for three different cooling module orientation (0° (planar), 15° and 30°) and different flap angles and vehicle velocities. From the results presented below, the best performance is obtained from 30° cooling module orientation due to enhanced effective surface area that is available for heat exchange.

Table 3: Results of different orientation of the cooling module

Module Orientation (°)	Flap Angle (°)	Vehicle Speed (km/h)	Flow In (kg/s)	HTR Tout (°C)	LTR Tout (°C)	HTR Coolant Tout (°C)	LTR Coolant Tout (°C)
0	15	0	1.136	88.093	87.003	102.995	112.322
		130	2.239	55.966	58.12	71.97	82.56
	25	0	1.115	89.994	84.95	104.703	110.194
		130	2.182	56.735	56.523	72.531	80.807
	35	0	1.07	93.609	83.918	108.143	109.045
		130	2.084	58.09	54.996	73.689	79.017
15	15	0	0.94	100.95	141.911	117.964	167.349
		130	2.498	55.902	59.037	72.068	83.285
	25	0	0.9017	104.145	132.409	121.352	157.53
		130	2.402	57.18	58.161	73.308	82.29
	35	0	0.85	109.413	132.326	127.154	157.499
		130	2.257	59.682	55.907	75.535	79.87
30	15	0	1.123	85.359	84.907	100.103	109.498
		130	2.593	57.04	66.635	72.754	91.143
	25	0	1.097	86.982	87.591	101.539	112.457
		130	2.542	57.403	64.777	73.068	89.133
	35	0	1.045	89.876	82.202	104.267	106.548
		130	2.397	58.957	62.159	74.579	86.392

3.4 Sizing of heat exchanger for performance optimization

The coolant outlet temperatures for vehicle velocity of 0 km/h, representative of idling or charging case are still above the desired value of 100 °C for flap angle of 15°, heat exchanger design is scaled by 25% to achieve the desired performance. The baseline and scaled heat exchangers are shown in Figure 5.

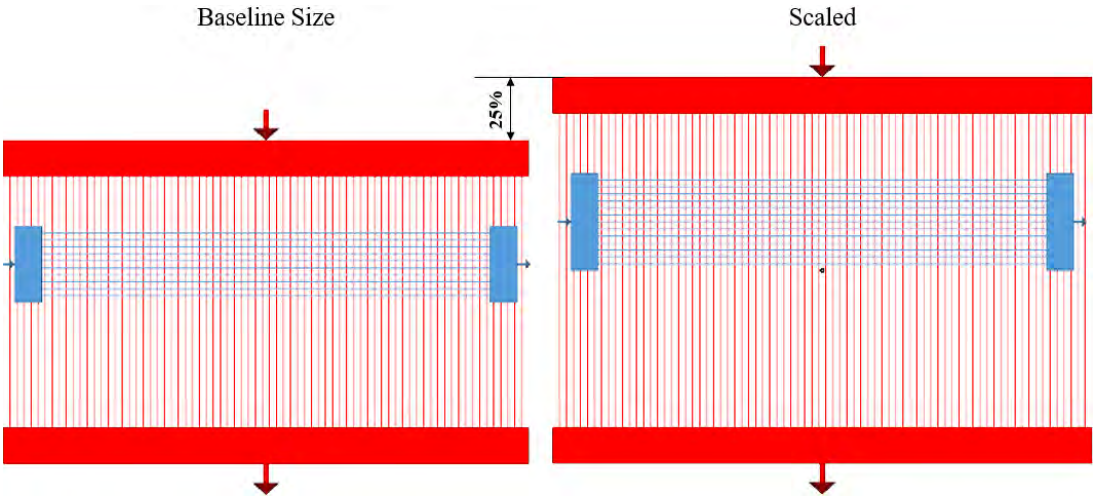

Figure 5: Comparison of baseline size of the heat exchangers with the scaled size.

Increasing the size of the heat exchanger results in lower coolant outlet temperatures as seen in **Error! Not a valid bookmark self-reference.** due to increased heat transfer area for coolant to air heat transfer, however, for some configurations the temperatures are still above 100 °C.

Table 4: Results of different heat exchanger

Size	Module Orientation (°)	Flap Angle (°)	Flow In (kg/s)	HTR Tout (°C)	LTR Tout (°C)	HTR Coolant Tout (°C)	LTR Coolant Tout (°C)
Base	30	15	1.123	85.359	84.907	100.103	109.498
		25	1.097	86.982	87.591	101.539	112.457
		35	1.045	89.876	82.202	104.267	106.548
Scaled	30	15	1.202	81.668	78.322	94.645	99.118
		25	1.162	83.877	77.937	96.930	98.722
		35	1.097	87.437	79.653	100.601	100.602

3.5 Selection of fan for performance optimization

The coolant outlet temperatures are still not in desired range, therefore, as a next step, the fan size is also scaled by 12 % to facilitate higher airflow rates, see Figure 6. The non-dimensional modeling of fans allows the performance to be extrapolated and can be predicted for scaled fan using the baseline performance data. As can be seen in Table 5, the scaled fan result in higher airflow rates and subsequently lower coolant outlet temperatures for both LTR and HTR that are below the desired limit of 100 °C. Velocity and temperature contour plots for this final design are shown in Figure 7 and Figure 8, which shows higher core airflow rates and regions where maximum air temperature is encountered. The detailed 3D methodology also helps in visualizing the streamlines (Figure 9) of the airflow which highlights the recirculation regions. Such information is crucial in airflow management and the cooling performance of the underhood.

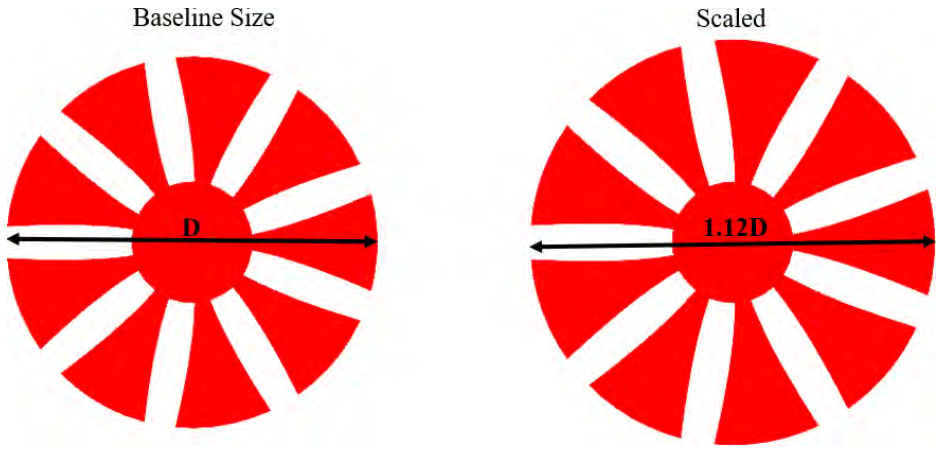

Figure 6: Comparison of baseline size of the fan with the scaled size

Table 5: Results of different fans

Size	Module Orientation (°)	Flap Angle (°)	Flow In (kg/s)	HTR Tout (°C)	LTR Tout (°C)	HTR Coolant Tout (°C)	LTR Coolant Tout (°C)
Base	30	15	1.202	81.668	78.322	94.645	99.118
		25	1.162	83.878	77.936	96.930	98.722
		35	1.097	87.437	79.653	100.604	100.602
Scaled	30	15	1.26596	79.004	78.134	91.256	98.871
		25	1.22083	81.012	74.658	93.272	95.457
		35	1.14412	84.418	74.572	96.620	95.257

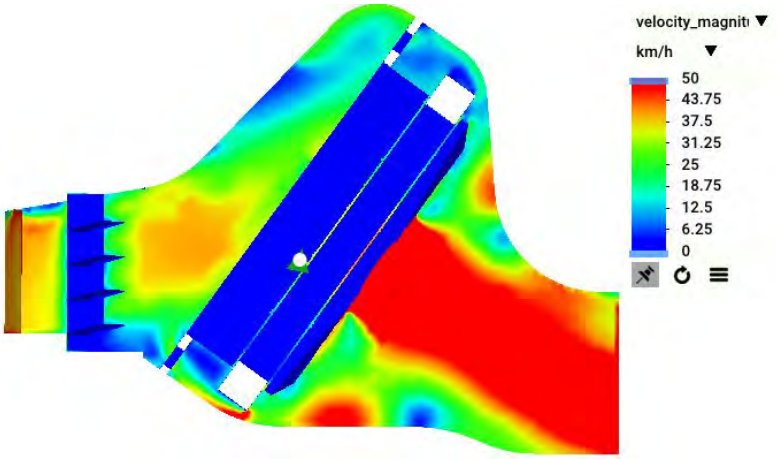

Figure 7: Velocity contour along the cross-section of the underhood flow space.

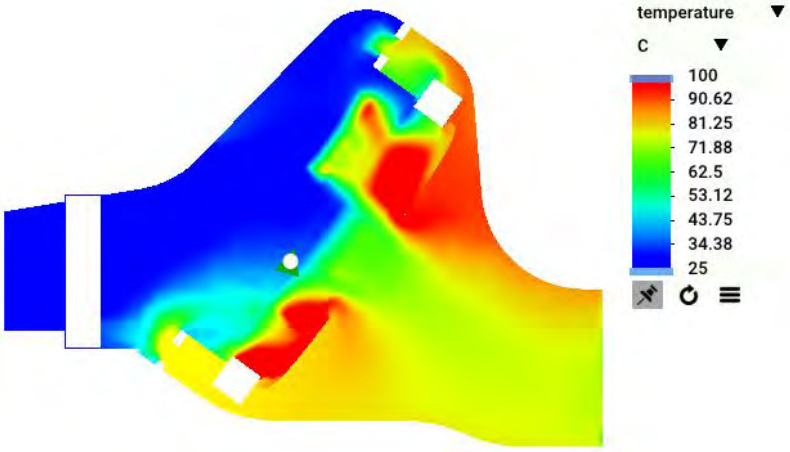

Figure 8: Temperature contour along the cross-section of the underhood flow space.

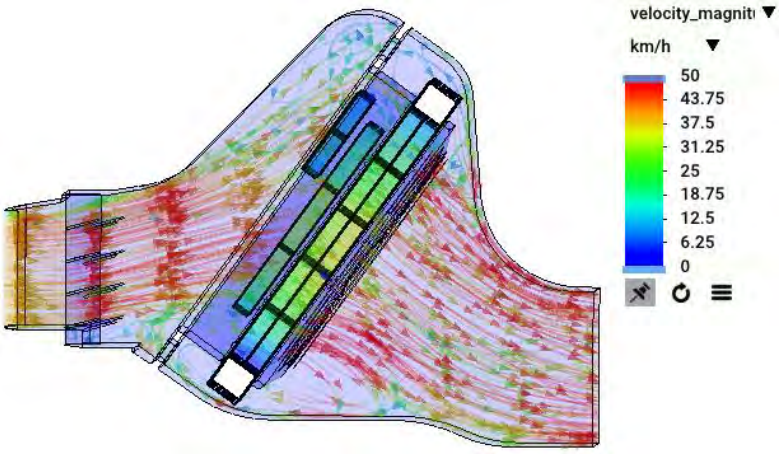

Figure 9: Streamlines along the cross-section of the underhood flow space.

4 Conclusion

This study introduced a coupled 1D–3D CFD methodology for underhood cooling system pre-design, combining detailed airflow modeling with predictive 1D heat exchanger representations. The case study showed that grille flap angle, cooling module orientation, and vehicle speed strongly affect airflow and coolant temperatures, with a 30° module orientation and moderate flap angles (15–25°) giving the best performance. Scaling of heat exchangers and fans further reduced coolant outlet temperatures below 100 °C, ensuring reliable operation even under idle conditions. The approach also provided valuable insight into airflow recirculation and thermal interactions. The results reported in this paper are the outcome of 3D numerical simulations performed on a standard PC with 8 CPU cores. The total number of cells per simulation is around 1.5 million elements, the computation time needed for each simulation was between 15 to 20 minutes. Overall, the 1D–3D co-simulation framework enables rapid design iterations, accurate performance prediction, and efficient optimization, supporting faster and more reliable vehicle thermal management development.

5 Bibliography

[1] A. Cappuccio, „BEV Thermal Management 1D Modeling for high performance system design," Politecnico di Torino, Torino, 2022.

[2] P. Dinakar, „Modelling and Simulation of Cooling Systems for BEV," Chalmers University of Technology, Göteborg, 2016.

[3] J. Nordin, „CFD Study of Optimal Under-hood Flow for Thermal Management of Electric Vehicles," Chalmers University of Technology, Göteborg, 2017.

[4] Gamma Technologies, „GT-SUITE Flow Theory Manual and Template Help," Gamma Technologies LLC, 2025.

[5] Shawn Harnish, Gamma Technologies LLC, „GT-Auto-3DFlow: New Underhood Fluid-Thermal Solution – Fast, Easy and Accurate," Gamma Technologies LLC, 2023.

[6] J. Varghese, Y. Wu, A.J. Juanos, R. Saha, S. Dhar, Simerics Inc., „Numerical Simulation of Class 8 Tractor Trailer Geometries and Comparison with Wind Tunnel Data," *SAE International,* Nr. 2024-01-2533, 2024.

[7] C. Boettcher, N. Framke, C. Altenhofen, T. Vevaud, Gamma Technologies GmbH, „Simulation based Development Methodology for the Thermal Security of Fuel Cell Powertrains," in *SIA Powertrain Conference*, Port-Marly, France, 2023.

[9] Sujan Dhar, Simerics Inc., „Numerical Analysis Using Fast RANS Simulations and Comparison with Experimental Measurements for Closed and Open Grille Realistic Car Models," *SAE International,* Nr. 2019-01-0655, 2019.

Introduction of a process to automatically translate a coupled aero-thermal simulation into a structural simulation with fatigue analysis

Gabor Matulik

SIMULIA
Dassault Systemes Deutschland GmbH
Meitnerstraße 8, 70563 Stuttgart-Vaihingen

gabor.matulik@3ds.com

Abstract: The author introduces a process, that is based on an in-house development, which enables CFD Simulation Engineers to automatically convert their PowerFLOW®-PowerTHERM® coupled aero-thermal simulation into an Abaqus® structural simulation including a fatigue analysis with fe-safe®. Structural simulation and fatigue analysis are using the results of the thermal simulation as their boundary conditions. With this automation process the time of creating the mesh and parametrizing the model for structural simulations are greatly reduced and the possibility of user errors is also lowered.

1 Introduction

Simulating the behavior of exhaust systems under extreme thermal and mechanical loads is essential for avoiding failures like cracking and fatigue. Traditional workflows require running aerothermal simulations and then manually preparing new meshes for structural analysis, which can be slow and error-prone. The Power-2-Abaqus tool addresses these challenges by integrating PowerTHERM® with Abaqus®, enabling seamless data transfer and automating structural simulations for efficient and accurate analysis.

The vision of the tool is to empower users conducting aerothermal simulations by enabling them to seamlessly reuse their geometry and results for structural simulations, fatigue analysis, and geometry optimization. Utilizing the same mesh for two different modeling fields reduces the overall preparation time. Connecting the members of the fluid and structural teams beyond simple boundary condition exchange helps for the colleagues to gain a deeper understanding of a complex system.

2 Power-2-Abaqus Workflow

2.1 Workflow concept

Aerothermal simulations alone are often insufficient for the design and optimization of many components, as they do not account for the critical structural and fatigue factors that influence performance and durability. It is essential to integrate structural simulations and fatigue analysis into the design process to ensure comprehensive evaluation and optimization.

Figure 1 highlights the conventional workflow for a typical company, with a fluids (CFD) and a structures (FE) team. The CFD user prepares the geometry, makes the mesh, creates the simulation model and performs aero-thermal simulation. Then exports the necessary boundary conditions, which the FE user needs to import into the structural simulation model, which took similar effort to create. However, it is easy to note the following inefficiencies in the conventional process:

1. Generating multiple meshes for Powerflow®/PowerTHERM® and for Abaqus®
2. Data transfer between teams and/or departments
3. Manual generation of input file for Abaqus®, which can be time consuming for complex cases

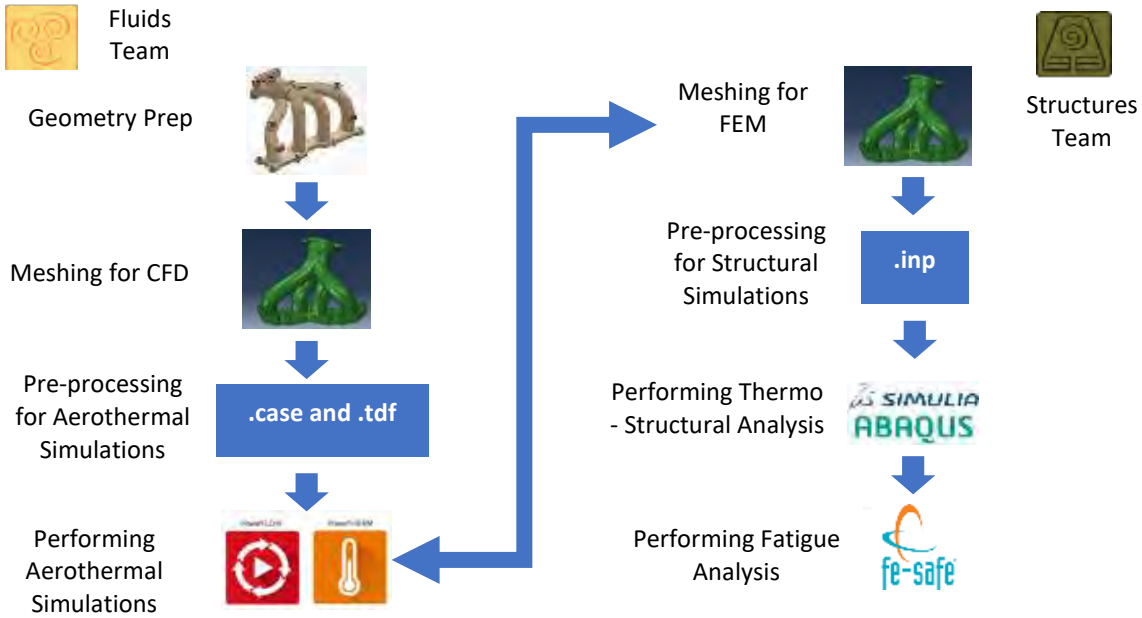

Figure 1: Conventional Workflow

The Power-2-Abaqus tool aims to improve the inefficiencies of the conventional workflow as shown in Figure 2. Utilizing the similar requirements for the structural mesh of the Abaqus® model and thermal mesh of the PowerFLOW®/PowerTHERM® simulation, the tool enables the reusability of the mesh with a conversion step to 2nd order elements in order to provide suitable structural results. It also allows for the automatic creation of input files for Abaqus® simulation, seamless data transfer and mapping of the temperature field from PowerTHERM® to Abaqus®. Moreover, lets the members of the fluids and structural teams to cooperate on a deeper level, shorten the iteration loops for the aero-thermal and fatigue analysis, contributing to an overall accelerated design process.

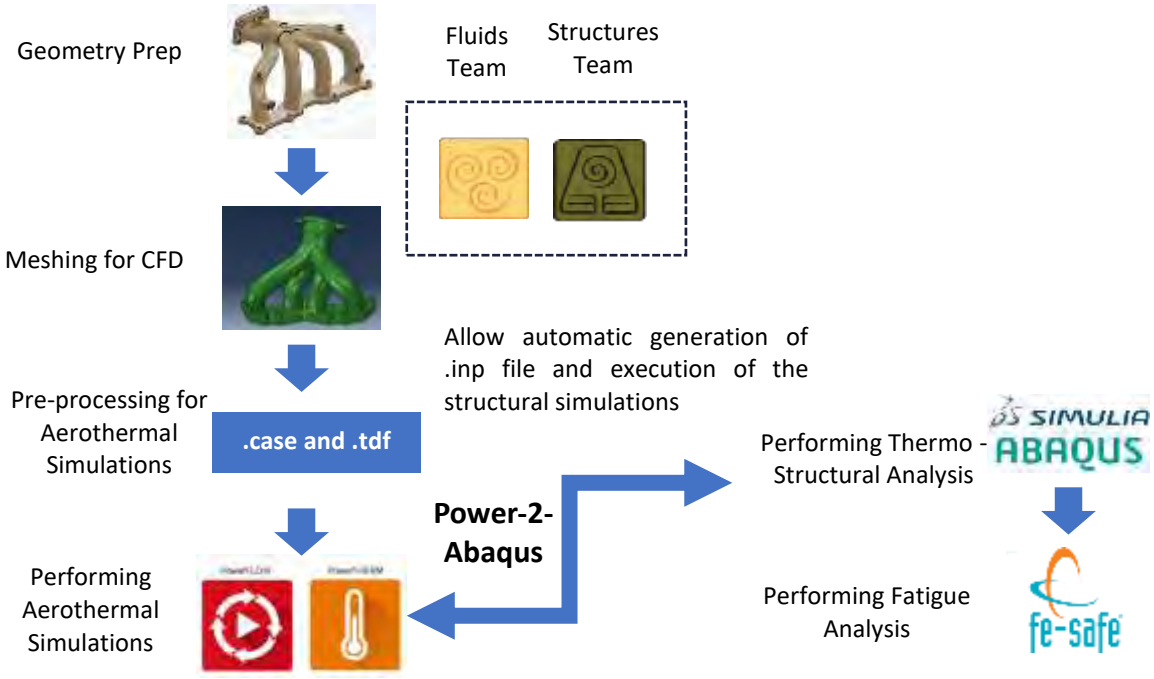

Figure 2: Workflow with Power-2Abaqus tool

2.2 Workflow steps

1. **Geometry export and analysis:** The tool extracts the mesh from the PowerTHERM® .tdf file and converts it into a NASTRAN format. It further processes the model and generates a geometry analysis report for the user.
2. **Geometry Processing:** After controlling the geometry analysis report from step 1, the users can modify the input file for the tool, which is then reprocessed during this second step.
3. **Temperature Export:** The tool exports the temperature fields from PowerTHERM® in .odb and .inp formats, ensuring compatibility with Abaqus®.

4. **Full Abaqus® Input File Creation:** The processed geometry and temperature data are used to generate the full Abaqus® input file, which is ready for simulation.
5. **Abaqus® Simulation Run:** The tool initiates the Abaqus® simulation, utilizing multiple CPU cores to accelerate the computation.

2.3 Capabilities and limitations of the tool

The process is controlled with an input file (JSON). This file contains all parameters for the simulation setup. The user has great control over the complete workflow: besides general settings like the path of SIMULIA® software executables or path to working directory, the configuration allows to setup assemblies or parts to be excluded, bodies to handle as rigid, surface-to-surface coupling, loads and pre-tensions and also to configure which steps to execute.

The current scope of the tool is limited to structural simulations of exhaust components, that can later be used for fatigue analysis. Therefore, the following analyses and capabilities are present:

- Elastic structural simulations accounting for thermal and mechanical loads using Abaqus® Standard Solver
- Capability to work with shell and solid elements
- Direct contact can be specified as surface-to-surface coupling, but the contact type is limited to simple friction
- Ability to automatically apply Pre-Tension values for bolts and screws

Despite these limitations, the tool is built on solid foundations and it is easy to extend the capabilities.

2.4 Material database

Abaqus® inherently does not have a predefined database. This is because it is a general-purpose tool, which can solve many types of complex problems, each requiring an individual and specialized set of material data.

However, to ease the user moving between PowerTHERM® and Abaqus®, a database is created which may be populated and used by the user to perform supported analysis types. The database stores the thermal properties such as density, specific heat and heat conductivity and the elastic properties, like Young’s modulus, Poisson’s ratio and expansion coefficient. This material database also contains a section for the friction coefficients between different materials.

In order to update and extend the material database a graphical interface was created, which lets the user to quickly put new materials, or change the existing ones.

2.5 Supported mesh elements

The Power-2-Abaqus tool only supports tetrahedral elements for solids and triangular elements for the surfaces. Those elements were chosen in order to minimize the numerical errors in mapping during the coupled PowerFLOW®/PowerTHERM® simulations and as the objective was to reuse the same mesh for aero-thermal and structural simulations, only support for these elements was programmed in the tool.

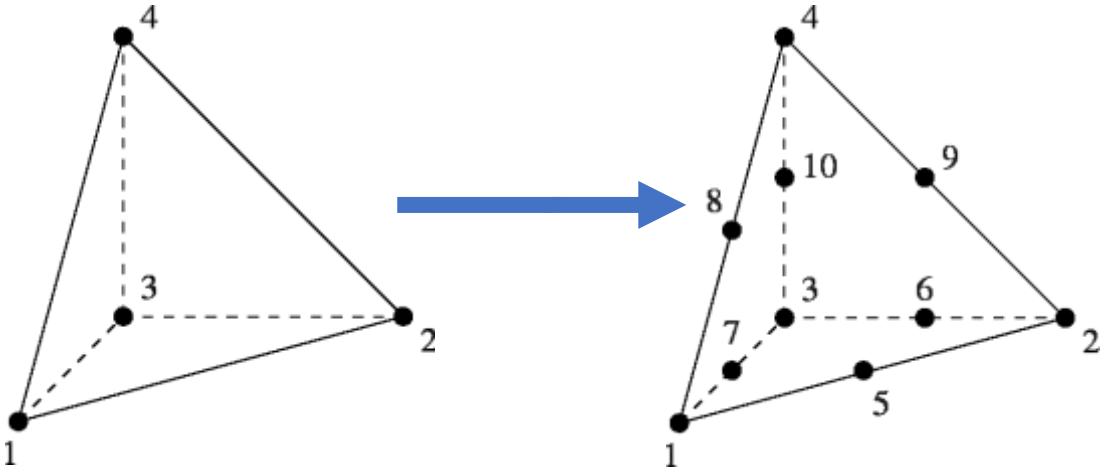

Figure 3: 1st Order tetrahedral volume elements converted to 2nd order elements

To improve the accuracy of structural simulations, the tool uses ANSA to convert the solid tetrahedral elements from 4 nodes to 10 nodes as seen in Figure 3, and the shell and surface elements from 3 node triangular elements to 6 node triangular elements as seen in Figure 4.

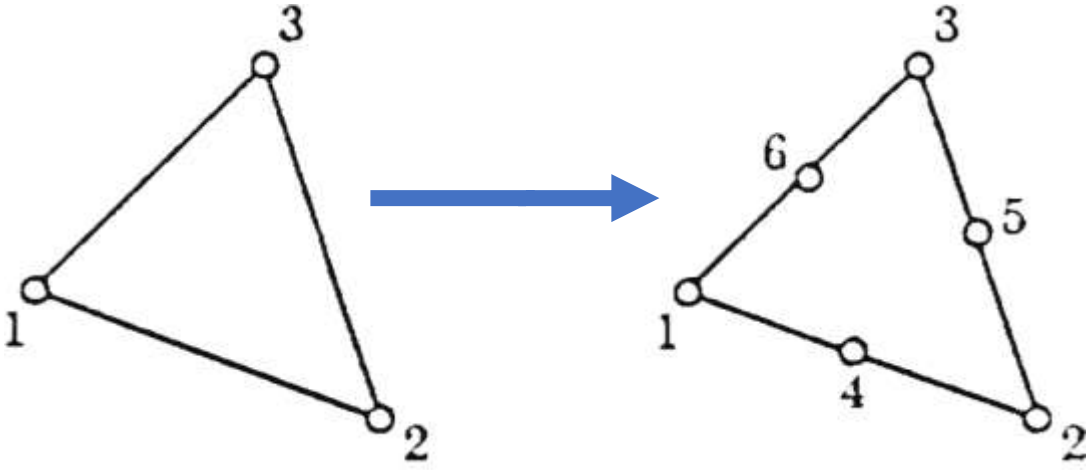

Figure 4: 1st Order triangle surface elements converted to 2nd order elements

3 Examples

In the following section two small IP-free examples will be presented from the tutorial section of the tool.

3.1 Exhaust manifold simulation

In this example the simulation of a simple exhaust manifold is shown. This part is subject to high thermal and mechanical loads. The boundary conditions are:

- Inlet Temperature: 900°C
- Flow rate 0.05 m^3/s

The tool automatically maps the temperature data from PowerTHERM® to Abaqus®, enabling accurate structural simulations without manual setup.

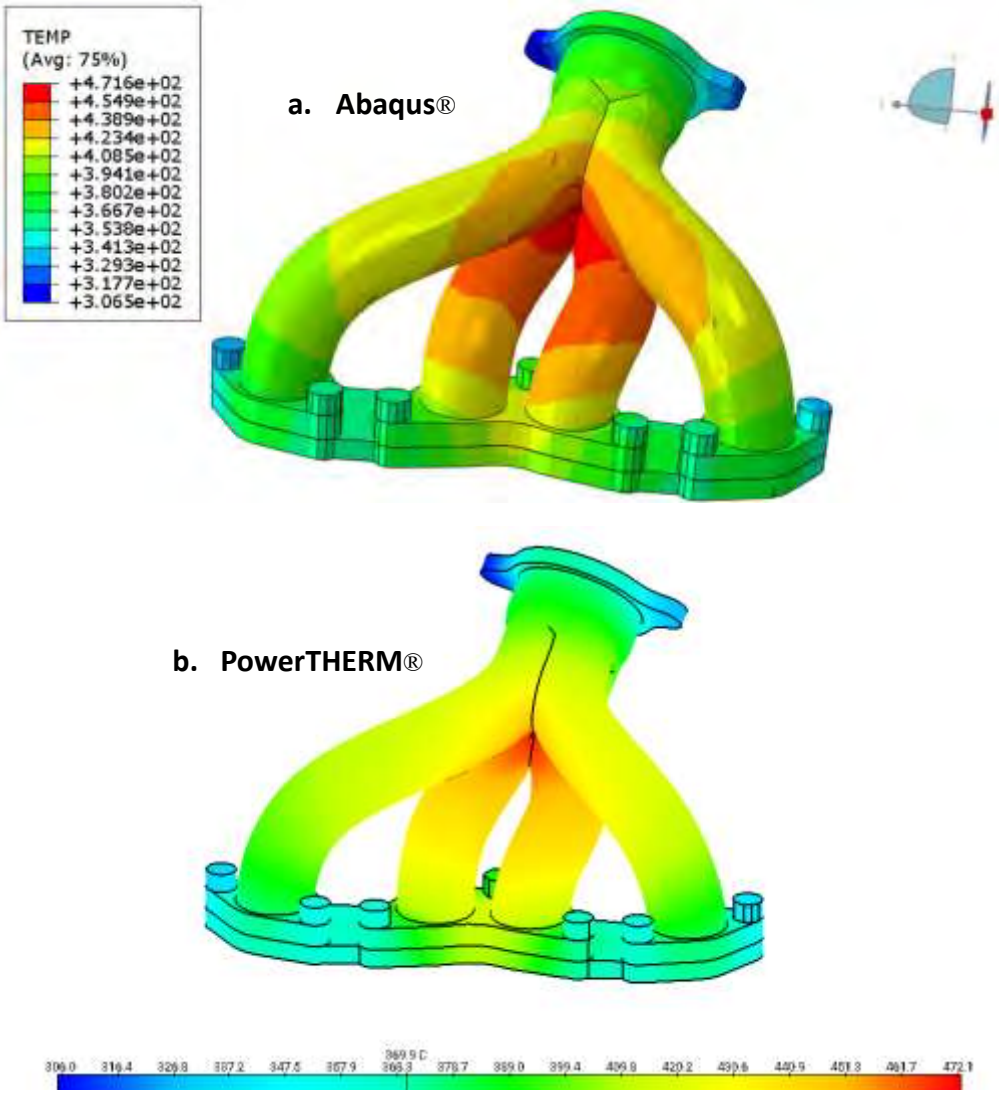

Figure 5: Mapping of the temperature field from PowerTHERM® to Abaqus®

This streamlined process allows engineers to quickly transition from thermal to structural analysis. The critical regions are (as expected) around the screws and the top part where the pipes are joined.

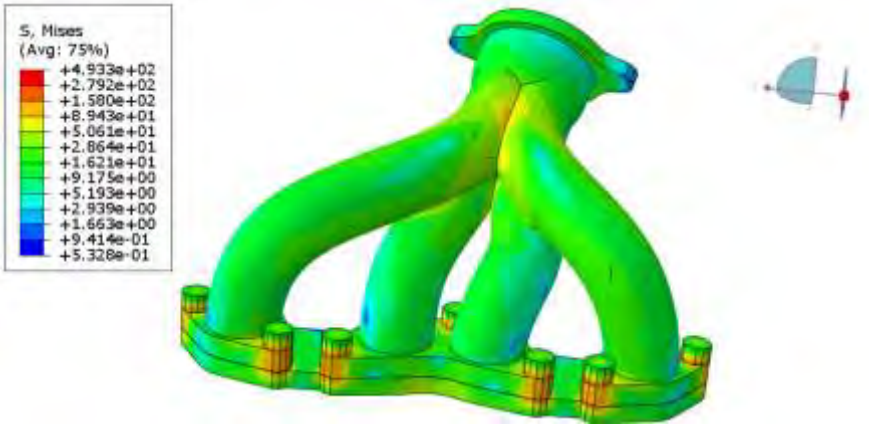

Figure 6: Von Mises stress distribution (Log scale) [MPa]

3.2 Motorcycle exhaust system

This example involves simulating a motorcycle exhaust system, which faces both thermal stress and mechanical impacts (such as the rider's foot). The exhaust system simulation includes:

- Inlet temperature: 900°C
- Foot impact load: 150N at the exhaust tip

By using shell elements for the simulation, Power-2-Abaqus allows the user to reduce model size while allowing them to model the complex interactions between thermal and mechanical forces. The mapping of the temperature is again perfect between PowerTHERM® and Abaqus® (as shown in Figure 7). The tool ensures accurate stress distribution across critical areas (as seen in Figure 8), enabling engineers to assess both thermal performance and structural durability.

This example highlights the tool’s versatility in handling different load conditions, component geometries and meshing strategies, allowing engineers to simulate real-world scenarios more effectively.

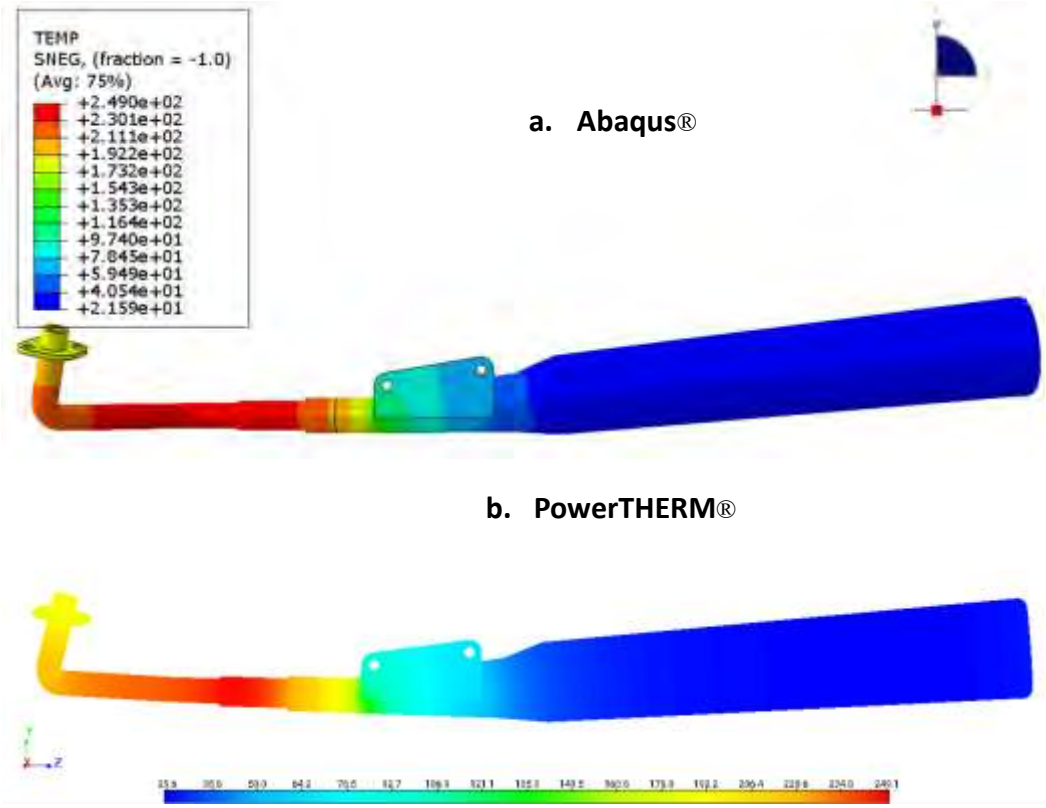

Figure 7: Mapping of the temperature field from PowerTHERM® to Abaqus®

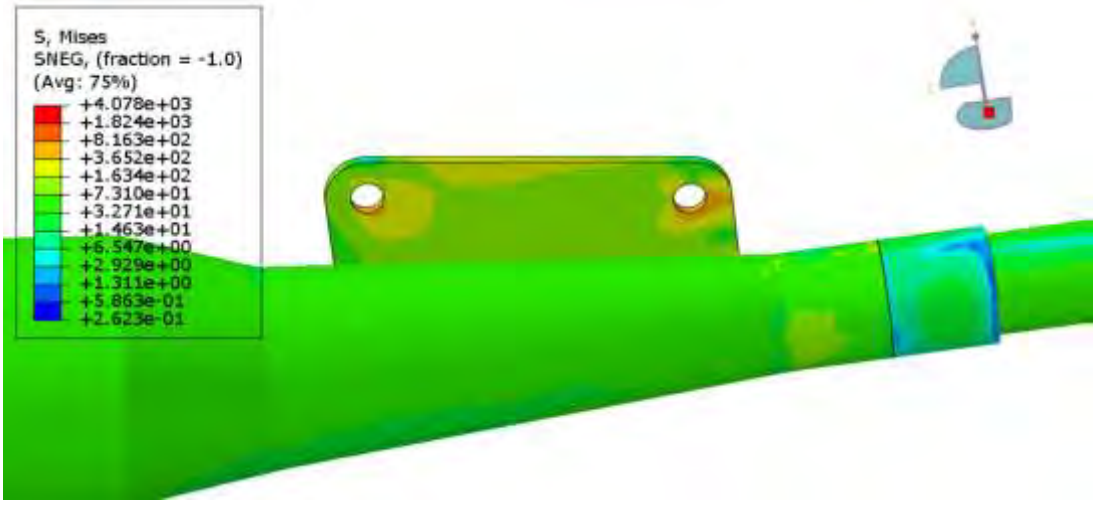

Figure 8: Von Mises stress distribution (Log scale) [MPa]

4 Future applications and Conclusion

Power-2-Abaqus is designed for flexibility. While it's optimized for exhaust system simulations, the tool can easily be expanded to other applications. With its modular architecture, it is possible to add new features like more complex boundary conditions or other advanced simulation capabilities of Abaqus®.

The tool's automated workflow and accurate data mapping lay the foundation for integrating aerothermal and structural simulations with fatigue analysis tool fe-safe® or with geometry optimization platforms like Tosca®, opening the door to even more comprehensive simulation capabilities.

Power-2-Abaqus transforms the simulation workflow for exhaust system design by bridging aerothermal and structural simulations, automating critical steps, and improving team collaboration. Its focus on mesh reusability, file automation, and precision makes it a valuable tool for engineers aiming to reduce time-to-market and optimize the performance of thermal-mechanical systems. Whether applied to the exhaust system or expanded to other application areas, Power-2-Abaqus ensures engineers can deliver durable, high-performing designs with greater efficiency.

Lumped Parameter Thermal Network Identification for Transient System Response Prediction of Automotive Components

Maximilian Kehe, Wolfram Enke, Hermann Rottengruber

EG-623
BMW AG
Knorrstraße 147, 80788 München

maximilian.kehe@bmw.de
wolfram.enke@bmw.de
hermann.rottengruber@ovgu.de

Abstract: This work presents a systematic approach to identify the thermal behavior of arbitrary automotive component systems. The proposed methodology leverages experimental temperature data and prior knowledge from Computational Fluid Dynamics (CFD) simulations to achieve a consistent system identification. The key aspects of the approach include thermal behavior identification through minimizing the least-squared error between the predicted thermal lumped parameter model and the experimentally measured temperature data, ensuring a robust and accurate representation of the system's thermal characteristics. The identified system model is then utilized to generate transient system responses for defined use-cases, enabling a comprehensive understanding of the thermal behavior under various operating conditions. The identification algorithm is based on the least-square programming algorithm from SciPy, providing a robust and efficient computational framework. Ensuring the reliability and durability of automotive components is crucial, as they must withstand the wide range of temperatures encountered during operation. To this end, the temperature-critical components are experimentally tested and simulated using CFD. The proposed methodology offers the capability to understand thermal interactions in experimental data and to generate transient responses based on stationary CFD simulations. Additionally, this work lays the groundwork for predicting temperatures in future vehicles with physics-informed neural networks. The method is tested with experimental temperature data and a numerical model of the component space of one control unit in the A-pillar of BMW's current 7 Series.

Contribution: 2025 FKFS Conference on Vehicle Aerodynamics and Thermal Management
15 – 16 October 2025 | Leinfelden-Echterdingen

1 Introduction

The thermal operating safety (TOS) of automotive vehicles is becoming increasingly challenging due to the rising complexity of the products. TOS focuses on ensuring that all components can withstand the thermal loads they encounter throughout their lifespan [FrER23]. Historically, the primary emphasis of TOS has been on components associated with or near combustion engines, such as engine rubber mounts [FrRE24]. The combination of extreme weather conditions, limited component space, cost pressures, and rising computational demands has added additional components to the scope of TOS, such as electronic control units (ECUs). This has compelled the automotive industry to take the lead in investing in thermal management for electronic devices [DhKA23].

The primary objective of TOS is to evaluate all critical components and implement cooling measures when necessary. To assess TOS, two main data sources are utilized: experimental testing and simulation. At BMW the experimental testing is conducted at the environmental test center in Munich [Bmwa25]. While experimental testing provides accurate and transient temperature data, it is both time-consuming and costly. It requires expensive prototypes and wind tunnel capacity, and testing must continue until a stationary state is reached. On the other hand, the capabilities of computational fluid dynamics (CFD) simulations have significantly improved in recent years, allowing for the assessment of TOS issues, such as heat transfer in exhaust systems [AhRF22, Enri15]. CFD simulations enable the evaluation of a wide range of boundary conditions and various TOS measures in a relatively short time frame. To determine the reliability of a component, it is essential to consider its cumulative thermal load over its lifetime, as components can experience fatigue not only from exceeding certain temperature thresholds [Elle17]. Consequently, TOS employs transient use cases to capture the complete temperature bandwidth. This approach has led to numerous publications on transient CFD simulations [Disc16, Gheb13]. However, for the TOS use-cases at BMW the experience shows, that transient CFD simulations are 4 to 10 times more expensive than stationary simulations.

To leverage the strengths of both methods, this paper proposes a combined approach that integrates the transient behavior derived from experimental data with the rapid calculations enabled by CFD simulations. Specifically, a zero-dimensional physical representation of thermal systems, known as the Lumped Parameter Thermal Network (LPTN), is utilized [MeRT91]. The parameters of the LPTN can be estimated with a minimization algorithm, allowing for the calculation of transient behavior [KeRE25]. In this study, the methodology is demonstrated using an E/E component from the G70 BMW, referred to as ‘IPBasis.’ The paper begins by explaining the mathematical modeling of the LPTN for this component space. Next, the transient behavior, represented by heat capacities, is fitted using multiple experimental data sets. The heat transfer parameters are then derived from the corresponding stationary CFD simulations. Finally, the combined LPTN is constructed using the fitted parameters, and the transient temperature curve is generated.

2 Mathematical Framework

To demonstrate the combined approach, first, the theory of the lumped parameter thermal network must be shortly introduced. A more detailed explanation is provided in [KeRE25]. First, the LPTN is introduced for the component space of the IPBasis, and the fundamental equations are derived. Secondly, the state-space approach to calculate the transient response of the LPTN is explained. Lastly, the minimization algorithm to derive the parameters of the LPTN from given data is tackled.

2.1 Modeling of Lumped Parameter Thermal Networks (LPTN)

Lumped parameter thermal networks are based on an energy formulation of lumped masses. Hence, this approach assumes that within these masses a homogeneous temperature is present. The energy approach results in a 0D formulation as there is no dependency on place. Two further simplifications are made in the current implementation of the LPTN. On the one hand, it is based on constants for heat capacities and heat transfer coefficients. Hence, temperature dependent effects like change of convection are averaged. On the other hand, radiation effects are not included, which simplifies the equations to a linear system.

In figure 1 the LPTN for the component space of the IPBasis is displayed. It consists of two bodies, the chassis and the IPBasis. The two bodies are connected by conduction. The chassis has a convection term to the outside temperature T_{ext}. The IPBasis is connected to the interior by convection which has the temperature T_{int}. The system is heated by the waste heat of the IPBasis $\dot{Q}_2^{\text{waste}}$.

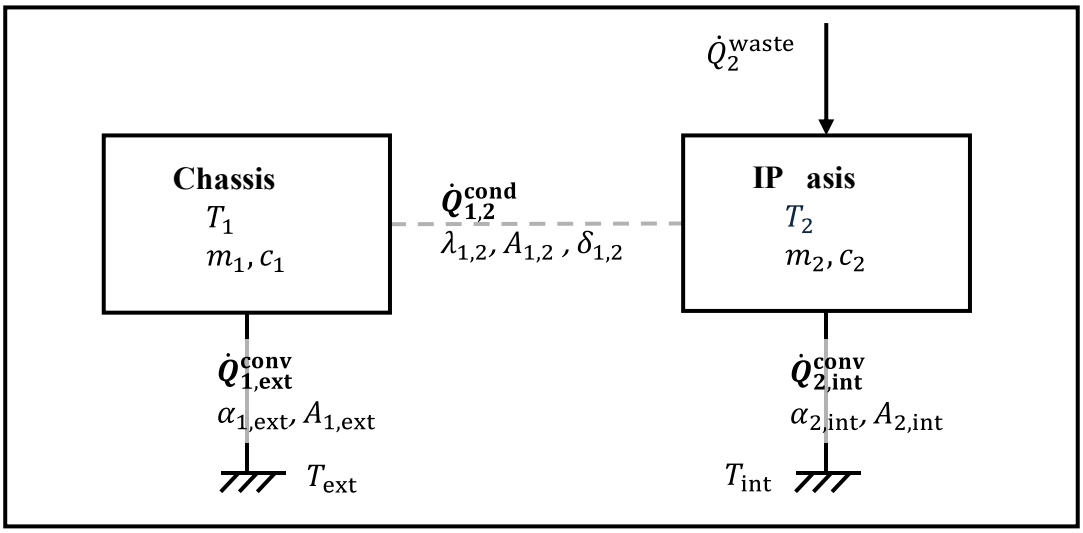

Figure 1: Lumped Parameter Thermal Network.

The lumped parameter thermal network can now be mathematically formulated by building the energy equilibrium of each body. The resulting two equations describing the time-dependent behavior of the system are displayed in equation 2.1.

$$
\begin{aligned}
m_1 c_1 \dot{T}_1 &= \frac{\lambda_{1,2} A_{1,2}}{\delta_{1,2}} (T_2 - T_1) + \alpha_{1,\mathrm{ext}} A_{1,\mathrm{ext}} (T_{\mathrm{ext}} - T_1) \\
m_2 c_2 \dot{T}_2 &= \frac{\lambda_{1,2} A_{1,2}}{\delta_{1,2}} (T_1 - T_2) + \alpha_{2,\mathrm{int}} A_{2,\mathrm{int}} (T_{\mathrm{ext}} - T_2) + \dot{Q}_2^{\mathrm{waste}}
\end{aligned}
\tag{2.1}
$$

2.2 Calculate Time-Response of LPTN

To calculate the time response of the LPTN, the state-space representation is leveraged. The general formulation in matrix form is displayed in equation 2.2.

$$
\dot{\boldsymbol{T}} = \boldsymbol{A}\boldsymbol{T} + \boldsymbol{B} \tag{2.2}
$$

In the next step, the energy equations from 2.1 can be reformulated in the A and B matrices. The resulting matrices are shown in the following equation:

$$
\begin{bmatrix} \dot{T}_1 \\ \dot{T}_2 \end{bmatrix} = \begin{bmatrix} -\frac{\lambda_{1,2} A_{1,2}}{m_1 c_1 \delta_{1,2}} - \frac{\alpha_{1,\mathrm{ext}} A_{1,\mathrm{ext}}}{m_1 c_1} & \frac{\lambda_{1,2} A_{1,2}}{m_1 c_1 \delta_{1,2}} \\ \frac{\lambda_{1,2} A_{1,2}}{m_2 c_2 \delta_{1,2}} & -\frac{\lambda_{1,2} A_{1,2}}{m_2 c_2 \delta_{1,2}} - \frac{\alpha_{2,\mathrm{int}} A_{2,\mathrm{int}}}{m_2 c_2} \end{bmatrix} \begin{bmatrix} T_1 \\ T_2 \end{bmatrix} + \begin{bmatrix} \frac{\alpha_{1,\mathrm{ext}} A_{1,\mathrm{ext}}}{m_1 c_1} T_0 \\ \frac{1}{m_2 c_2} \dot{Q}_2^{\mathrm{waste}} + \frac{\alpha_{2,\mathrm{int}} A_{2,\mathrm{int}}}{m_2 c_2} T_{\mathrm{int}} \end{bmatrix}
\tag{2.3}
$$

Finally, the time response of the LPTN in form of the temperatures $T(t)$ can be calculated by using the Runge-Kutta method of fourth order. The method is a standard solver for ordinary differential equations. Next to the matrices, the method needs initial temperatures $\boldsymbol{T}_0$, a simulation time step $\mathrm{d}t$, and the time interval $[t_0, t_{\mathrm{end}}]$. The calculation can be written as follows:

$$
\boldsymbol{T}(t) = \mathrm{RK4}(\boldsymbol{A}, \boldsymbol{B}, \boldsymbol{T}_0, \mathrm{d}t, [t_0, t_{\mathrm{end}}]) \tag{2.4}
$$

2.3 Calculate LPTN Parameters from Temperature Data

The idea is to find the parameters of the LPTN from only the temperature information. There are two concerns with this approach. First, there are unlimited combinations of the matrix A and B and therefore of the parameters that can show the same behavior as the data. Hence, this is considered an ill-posed problem. To tackle this issue, the parameters are fitted by a minimization algorithm to find the best fit. Secondly, multiplied values like $m_2 c_2$ cannot be distinguished, hence they need a surrogate parameter. These parameters are called identifiable, as they satisfy the necessary condition to be distinguishable. The list of identifiable parameters is provided in table 1.

Definition	Identifiable Parameter	Replaced Parameters	Unit
Heat Capacity	C^m	mc_p	J/K
Convection Term	C^α	αA	W/K
Conduction Term	C^λ	$\lambda A \,/\, \delta$	W/K
Boundary Heat Flux	$\dot{Q}$	$\dot{Q}$	W

Table 1: Table of the identifiable parameters.

The set of identifiable parameters is denoted with $\boldsymbol{\vartheta}$ and can be seen in the following equation:

$$\boldsymbol{\vartheta} = [\boldsymbol{C}_m, \boldsymbol{C}_\alpha, \boldsymbol{C}_\lambda, \dot{\boldsymbol{Q}}\,] \tag{2.5}$$

With the identifiable parameters the LPTN model is simplified. This is exemplary shown in equation 2.6 for the state-space representation.

$$\begin{bmatrix}\dot{T}_1\\ \dot{T}_2\end{bmatrix} = \begin{bmatrix} -\frac{C^\lambda_{1,2}}{C^m_1} - \frac{C^\alpha_{1,\mathrm{ext}}}{C^m_1} & \frac{C^\lambda_{1,2}}{C^m_1} \\ \frac{C^\lambda_{1,2}}{C^m_2} & -\frac{C^\lambda_{1,2}}{C^m_2} - \frac{C^\alpha_{2,\mathrm{int}}}{C^m_2} \end{bmatrix} \begin{bmatrix}T_1\\ T_2\end{bmatrix} + \begin{bmatrix} \frac{C^\alpha_{1,\mathrm{ext}}}{C^m_1} T_{ext} \\ \frac{1}{C^m_2}\dot{Q}_2^{\mathrm{waste}} + \frac{C^\alpha_{2,\mathrm{int}}}{C^m_2} T_{\mathrm{int}} \end{bmatrix} \tag{2.6}$$

Now, the minimization algorithm can be applied. The goal of the minimization is to find the parameter set $\boldsymbol{\vartheta}^{\min}$ that minimizes the error between the data $\boldsymbol{T}^{\mathrm{Data}}$ and the calculated system response of the LPTN $\boldsymbol{T}^{\min}$. The minimization term $\boldsymbol{\varepsilon}$ is calculated by the mean squared error:

$$\boldsymbol{\varepsilon} = \left(\boldsymbol{T}^{\mathrm{Data}} - \boldsymbol{T}^{\min}\right)^2$$
$$\text{With: } \boldsymbol{T}^{\min} = \mathrm{RK4}\left(\boldsymbol{A}(\boldsymbol{\vartheta}^{\min}), \boldsymbol{B}(\boldsymbol{\vartheta}^{\min}), \boldsymbol{T}_0^{\mathrm{Data}}, \mathrm{d}t, [t_0, t_{\mathrm{end}}]\right) \tag{2.6}$$

The calculated parameters provide a combination that fits the provided data the best. However, these parameters are not necessarily the correct physical parameters of the system. In the original paper it was proposed to fit over multiple files simultaneously to get a global and uniform estimation. This way, the heat coefficients can be compared between the files and the estimated heat capacities are representative of the system response as they describe multiple files. This approach is conducted in the next chapter for the experimental data.

3 Experimental Data

The goal of this chapter is to retrieve the global heat capacities ($C_1^{m,ED}, C_2^{m,ED}$) from the experimental data (ED). Figure 2 displays an overview of the LPTN that is minimized for this purpose. Every dataset contains the experimental temperatures (T_1^{ED}, T_2^{ED}) and the boundary conditions ($\dot{Q}_2^{\mathrm{waste}}, T_{\mathrm{ext}}, T_{\mathrm{int}}$). The global parameters (C_1^m, C_2^m) are used for all files. The local parameters ($C_{1,2}^{\lambda}, C_{1,\mathrm{ext}}^{\alpha}, C_{2,\mathrm{int}}^{\alpha}$) are fitted for each file. The hypothesis is that the masses and materials remain the same, but the heat transfer coefficients vary from file to file due to different boundary conditions.

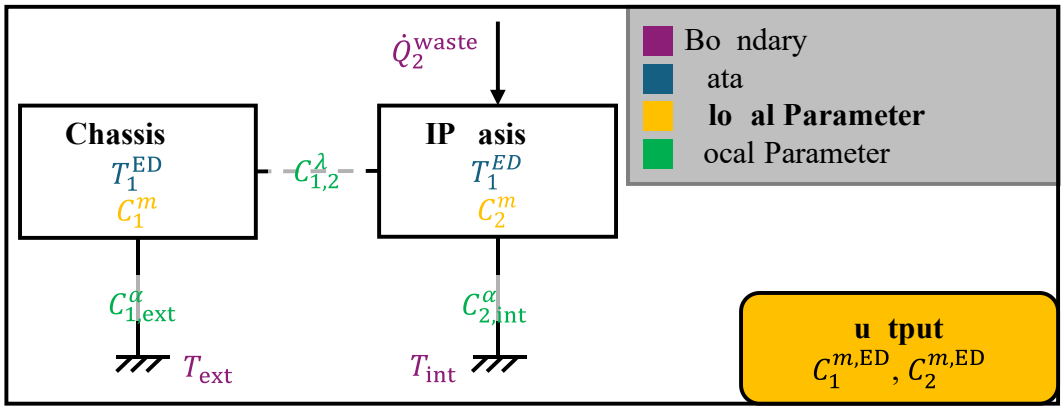

Figure 2: LPTN System to identify the global parameters in form of the heat capacities.

The data used for this approach is gained from windtunnel testing of the BMW G70 model. An overview of the test setup can be found in figure 3.

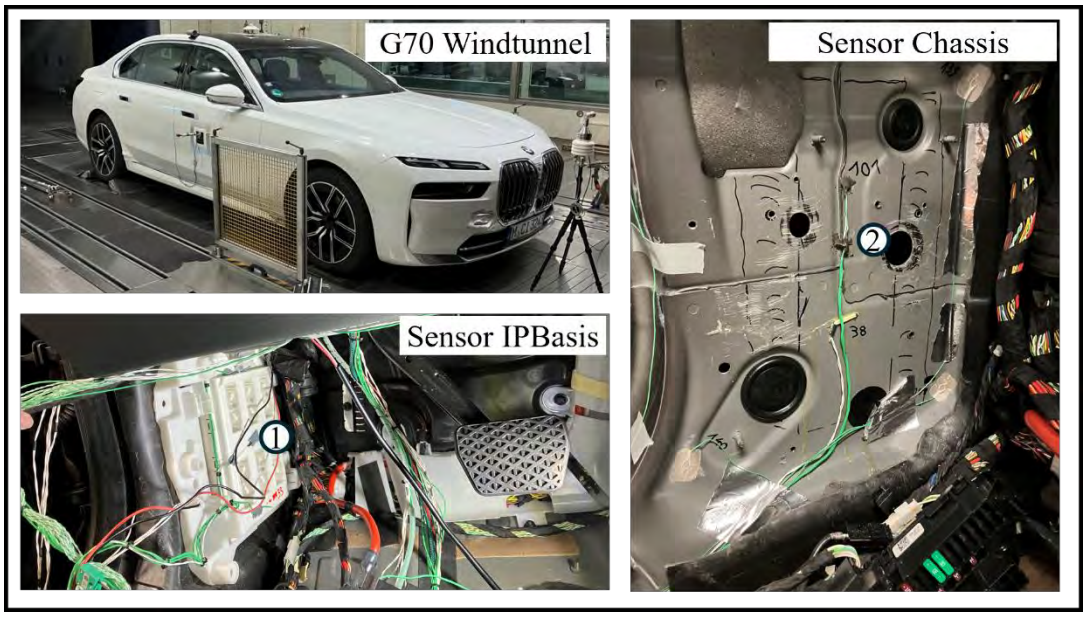

Figure 3: Measurement of the experimental data. The upper left corner is an exemplary picture of the G70 in the environmental testing center. In the lower left corner, the sensor placement at the IPBasis is shown. On the right the sensor placement at the chassis is displayed.

In the upper left of figure 3 an exemplary picture of a G70 in the environmental test center is displayed. The sensor placements inside of the IPBasis and at the surface of the chassis are displayed in the other two graphics.

In this setup multiply tests were conducted like Stop&Go, Soakbox heating, and Vmax. To get the most homogeneous data for the minimization, the initial heating phase during constant boundary conditions were segmented from the rest of the test periods. The representative LPTN for each file is build and the global heat capacities as well as the local heat transfer coefficients is found by fitting to the experimental data ($\boldsymbol{T}_1^{\mathrm{ED}}$, $\boldsymbol{T}_2^{\mathrm{ED}}$). The time responses of the fitted LPTN after the minimization ($\boldsymbol{T}_1^{\mathrm{min}}$, $\boldsymbol{T}_2^{\mathrm{min}}$) are shown in figure 4. Three measurements are displayed exemplarily.

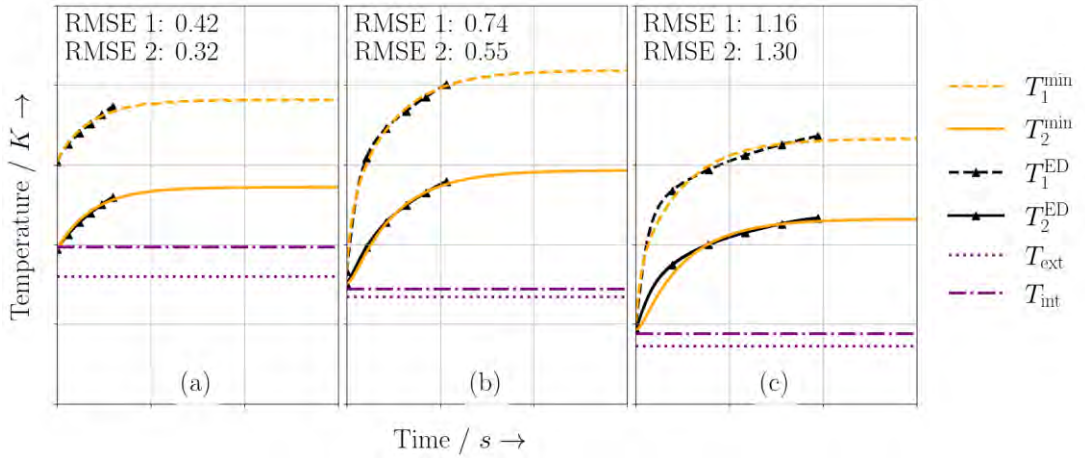

Figure 4: This graphic shows the global parameter estimation of three experimental measurements. Subfigure (a), (b), and (c) each show a different experimental setup with varying boundary conditions.

The fitting was able to capture the heating behavior of all files to an average root mean squared error (RMSE) of 0.91K. The RMSE of the IPBasis is slightly higher with 1.03°C compared to the chassis with 0.79°C, but the IPBasis is also generally significantly warmer. The results indicate that the global heat capacities $C_1^{m,\mathrm{ED}}$ and $C_2^{m,\mathrm{ED}}$ found are a good representative of the overall behavior of the system.

4 CFD Data

In the next step the heat transfer coefficients ($C_{1,2}^{\lambda,\mathrm{CFD}}, C_{1,\mathrm{ext}}^{\alpha,\mathrm{CFD}}, C_{2,\mathrm{int}}^{\alpha,\mathrm{CFD}}$) are found from the CFD-Simulation results. The CFD simulation is stationary, hence the temperatures ($T_1^{\mathrm{CFD,stat}}$, $T_2^{\mathrm{CFD,stat}}$) are of scalar nature. The CFD simulation can calculate the temperature results for arbitrary boundary conditions ($\dot{Q}_2^{\mathrm{waste}}, T_{\mathrm{ext}}, T_{\mathrm{int}}$). As only stationary information is available, the heat capacities ($C_1^{m,\mathrm{ED}}, C_2^{m,\mathrm{ED}}$) are not relevant for the calculation of the heat transfer coefficients. The overview of the LPTN for the fitting of the CFD parameters is provided in figure 5.

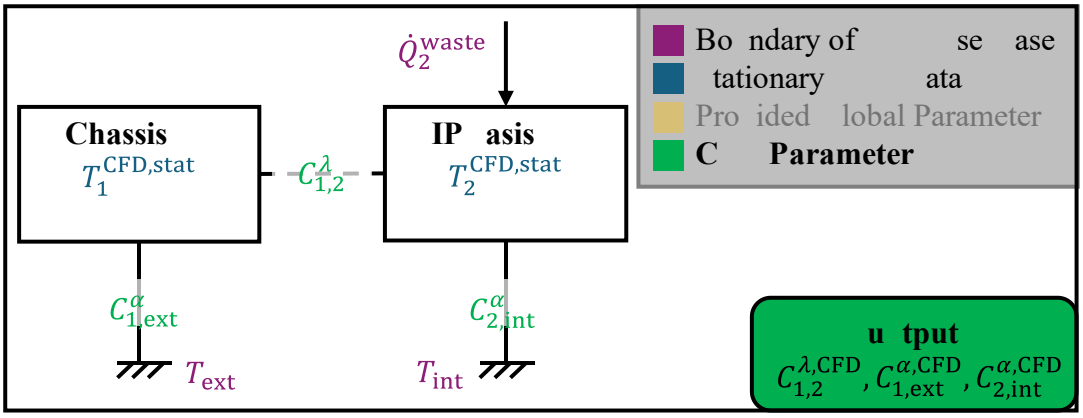

Figure 5: LPTN System to identify the conduction and convection parameter from the stationary CFD-Simulation.

In figure 6 an overview of the CFD simulation is provided. The boundary conditions are imprinted on the model by setting the external temperature at the bottom of the cassis and by setting a Dirichlet boundary condition in the air space of the IPBasis. The sensors are placed in the same locations as the experimental data, the IPBasis sensor is in the inside of the ECU and the Chassis temperature is taken at the surface of the chassis.

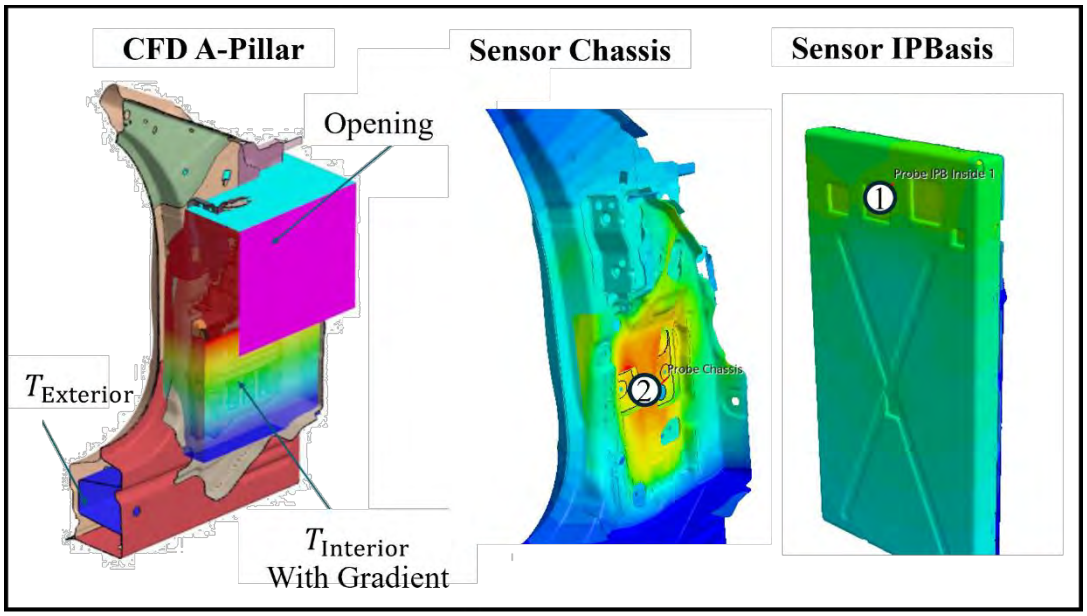

Figure 6: Overview of the CFD-Simulation.

As the temperature of the CFD is stationary, the state-space representation is simplified, and the heat capacities can be neglected. This is shown in equation 4.1.

$$\begin{bmatrix}0\\0\end{bmatrix} = \begin{bmatrix} -C_{1,2}^{\lambda,\text{CFD}} - C_{1,\text{ext}}^{\alpha,\text{CFD}} & C_{1,2}^{\lambda,\text{CFD}} \\ C_{1,2}^{\lambda,\text{CFD}} & -C_{1,2}^{\lambda,\text{CFD}} - C_{2,\text{int}}^{\alpha,\text{CFD}} \end{bmatrix} \begin{bmatrix} T_1^{\text{CFD,stat}} \\ T_2^{\text{CFD,stat}} \end{bmatrix} + \begin{bmatrix} C_{1,\text{ext}}^{\alpha,\text{CFD}} T_{\text{ext}} \\ \dot{Q}_2^{\text{waste}} + C_{2,\text{int}}^{\alpha,\text{CFD}} T_{\text{int}} \end{bmatrix} \tag{4.1}$$

This system has three unknowns ($C_{1,2}^{\lambda,\mathrm{CFD}}, C_{1,\mathrm{ext}}^{\alpha,\mathrm{CFD}}, C_{2,\mathrm{int}}^{\alpha,\mathrm{CFD}}$), but only two equations, hence it is underdetermined. The minimization algorithm is capable of still finding a set of parameters that will result in the correct stationary temperatures. However, to find a unique solution, an additional condition is necessary. Fortunately, it is comparably easy to retract additional information from a CFD simulation, like the heat flux over a defined area. Here, the heat flux to the exterior $\dot{Q}_{\mathrm{ext}}^{\mathrm{CFD}}$ is used as an additional condition. With this information, the system is determined. In this paper we reuse the minimization algorithm to calculate the parameters. The adjusted loss function can be seen in equation 4.2.

$$\boldsymbol{\varepsilon} = \left(T_1^{\mathrm{CFD,stat}} - \boldsymbol{T}^{\mathrm{min}}\right)^{\mathbf{2}} + \left(\dot{Q}_{\mathrm{ext}}^{\mathrm{CFD}} - \dot{Q}_{\mathrm{ext}}^{\mathrm{min}}\right)^{\mathbf{2}}$$

$$\text{With: } \boldsymbol{T}^{\mathrm{min}} = \boldsymbol{A}(\boldsymbol{\vartheta}^{\mathrm{min}}) \backslash \boldsymbol{B}(\boldsymbol{\vartheta}^{\mathrm{min}}) \tag{4.2}$$

$$\text{With: } \dot{Q}_{\mathrm{ext}}^{\mathrm{min}} = C_{1,\mathrm{ext}}^{\alpha,\mathrm{CFD}}(T_{\mathrm{ext}} - T_1^{\mathrm{min}})$$

As this is a determined problem, the calculated parameters ($C_{1,2}^{\lambda,\mathrm{CFD}}, C_{1,\mathrm{ext}}^{\alpha,\mathrm{CFD}}, C_{2,\mathrm{int}}^{\alpha,\mathrm{CFD}}$) are the correct description of the CFD simulation for the specific use-case. One issue is the fact that the heat transfer coefficients are found from the stationary point, here the hottest point of the use-case. Hence, the fitted parameters might overestimate the actual parameters over the complete heating period. This concern is especially relevant for the convection parameters, as they are usually temperature dependent. One solution for this problem could be to include a time-dependent nonlinearity in the convection parameters, for example linear interpolation from the initial state to the stationary state. However, this is not further investigated in this work. For the present use-case for the IPBasis the overestimation is assumed to be acceptable, as the overall temperature delta is not over 100K.

5 Combined LPTN

5.1 Proof of Concept

In a first step, the overall concept needs to be demonstrated. For this, a pragmatical approach is chosen which is displayed in figure 7. An artificial LPTN is designed, and for four use-cases artificial data (T_1^{AD}, T_2^{AD}) is generated. The heat capacities are found by minimizing three use-cases, one is shown exemplary in the (a). The fourth use-case is the ground truth (T_1^{Truth}, T_2^{Truth}). The heat transfer coefficients are calculated from the stationary data and one heat flux condition. This is displayed in (b). The parameters are then combined in a LPTN and simulated. The resulting temperatures (T_1^{combined}, T_2^{combined}) can be seen in (c). The figure shows that the combined temperatures exactly match the ground truth data. This proves that the concept to fit the masses from different use-cases and calculate the transient response of stationary data is viable.

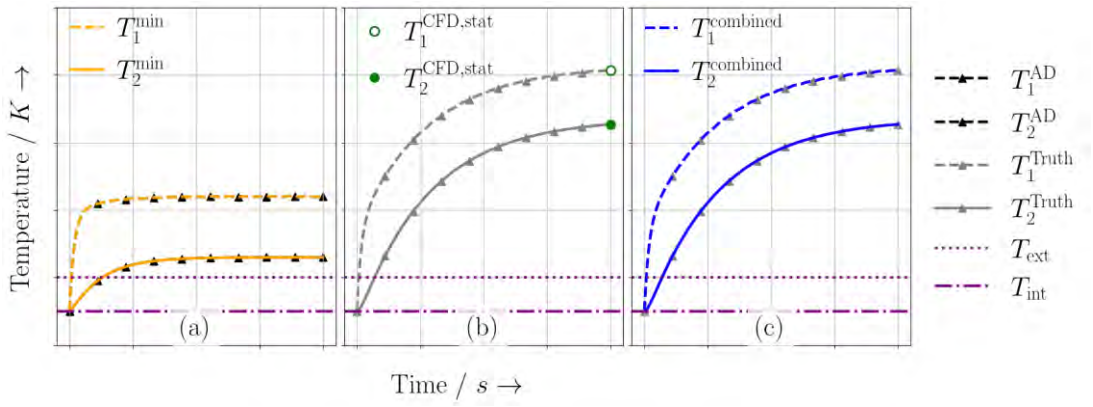

Figure 7: Proof of Concept for the correct calculation of the transient curves when the parameters are calculated from the stationary point. Subfigure (a) is the heat capacity minimization, (b) is the stationary CFD data, and (c) is the calculated LPTN response from the combined parameters.

5.2 Calculating the transient response for the IPBasis

At this point, all the necessary parameters to calculate the transient response for the CFD use-case are gained. The effective heat capacities ($C_1^{m,\text{ED}}, C_2^{m,\text{ED}}$) from the experimental data are fitted. The use-case specific heat transfer coefficients ($C_{1,2}^{\lambda,\text{CFD}}, C_{1,\text{ext}}^{\alpha,\text{CFD}}, C_{2,\text{int}}^{\alpha,\text{CFD}}$) from the CFD simulation are found for the LPTN. The goal is to calculate the transient temperatures (T_1^{Combined}, T_2^{Combined}). This can be achieved by building the LPTN from the known parameters. The LPTN system is displayed in figure 8.

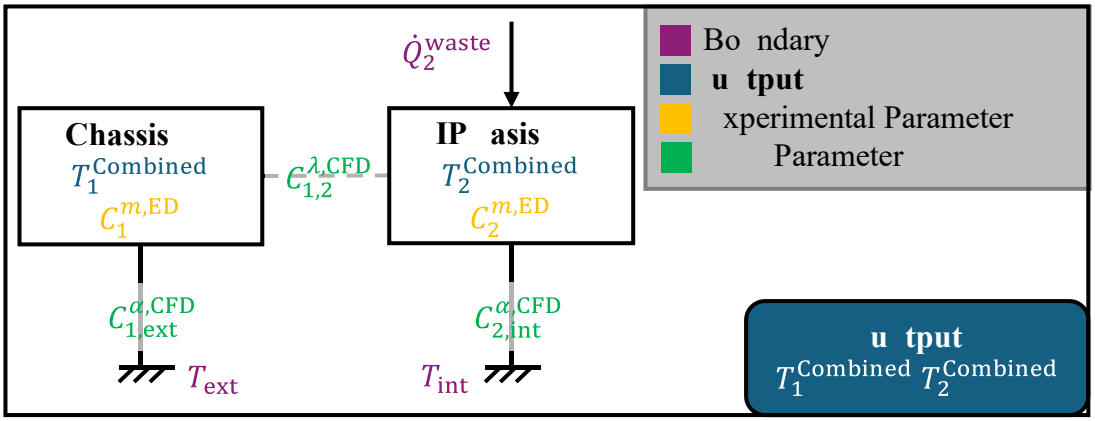

Figure 8: LPTN System Overview for combining the parameters from experiment and CFD-Simulation.

With this LPTN, the RK4 method can calculate the time response. The result is shown in figure 9. This calculation is the result this work was aiming for. The assessment of this result is not straightforward, as this combination of experimental and simulation data has created a new kind of information, which has no ground truth. This result is accurate if the masses and the heat capacities are identified correctly. The assessment of the fitting accuracy is not scope of this work.

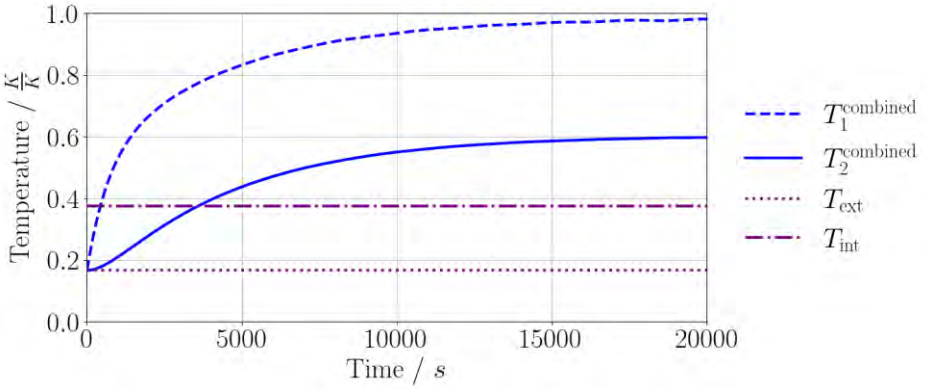

Figure 9: Resulting transient curves based on the heat capacity information from the experimental data and the stationary information from CFD-Simulation.

6 Conclusion

This paper achieved the calculation of a transient response for a stationary CFD simulation based on transient experimental measurements. The results were achieved for the component space of the IPBasis by leveraging a lumped parameter thermal network approach. The global parameter fitting of the experimental data represents a novel extension to the state-of-the-art minimization algorithm for estimating LPTN parameters from temperature data, achieving a RMSE of 0.91K. This work demonstrated the extraction of LPTN parameters from a CFD simulation. The assembly of the transient curve from the stationary data and the heat capacity information was demonstrated in section 5.1 as a proof of concept with 100% accuracy.

It is anticipated that utilizing multiple experimental files simultaneously will enhance the global fitting approach, allowing for more accurate determination of heat capacities. However, this assumption requires further investigation, and establishing a guideline for the optimal number of files necessary in an n-body LPTN would be advantageous. Additionally, the fitting of parameters derived from the CFD simulation is based on the stationary temperature point, specifically the highest temperature observed. Consequently, when fitting temperature-dependent parameters, such as the convection heat transfer coefficient, the estimated values are too high in the transient phases calculated. This tendency leads to an underestimation of temperatures, as too much energy is dissipated. To address this issue, introducing nonlinearity into the system could provide a viable solution. Future work should focus on developing and testing this approach using a transient CFD model.

7 Reference list

[AhRF22] Saad Ahmed, Hermann Rottengruber, Markus Full. Hybrid model for exhaust systems in vehicle thermal management simulations. In: *Automotive and Engine Technology* Bd. 7 (2022), Nr. 1–2, S. 115–136

[Bmwa25] BMW AG. *Das Energie- und umwelttechnische Versuchszentrum der BMW Group*. URL https://www.press.bmwgroup.com/deutschland/article/detail/T0080599DE/das-energie-und-umwelttechnische-versuchszentrum-der-bmw-group?language=de

[DhKA23] Amol R. Dhumal, Atul P. Kulkarni, Nitin H. Ambhore. A comprehensive review on thermal management of electronic devices. In: *Journal of Engineering and Applied Science* Bd. 70 (2023), Nr. 1, S. 140

[Disc16] Mario Disch. *Numerische und experimentelle Analyse von instationären Lastfällen im Rahmen der thermischen Absicherung im Gesamtfahrzeug*. Wiesbaden : Springer Fachmedien Wiesbaden, 2016

[Elle17] Jan Eller. *Stützpunktbasierter Ansatz zur Vorhersage von Bauteiltemperaturkollektiven im Thermomanagement des Gesamtfahrzeugs*. Wiesbaden : Springer Fachmedien Wiesbaden, 2017

[Enri15] Joshua Enriquez-Geppert. *Numerische und experimentelle Analyse der Wärmeübertragung einer Abgasanlage im Gesamtfahrzeug*. Stuttgart, University of Stuttgart, 2015

[FrER23] Lukas Freytag, Wolfram Enke, Hermann Rottengruber. Leveraging Historical Thermal Wind Tunnel Data for ML-Based Predictions of Component Temperatures for a New Vehicle Project. In: *SAE Technical Paper*. 2023-01-1216, 2023

[FrRE24] Lukas Freytag, Hermann Rottengruber, Wolfram Enke. Monitoring the Thermal Aging of Rubber Bearings Using Virtual Temperature Sensors. In: *SAE Technical Paper*. 2024-01-5099, 2024

[Gheb13] Daniel Ghebru. *Modellierung und Analyse des instationären thermischen Verhaltens von Verbrennungsmotor und Gesamtfahrzeug*. Berlin, Karlsruher Institut für Technologie (KIT), 2013

[KeRE25] Maximilian Kehe, Hermann Rottengruber, Wolfram Enke. Lumped Parameter Thermal Network (LPTN) for Automotive Components: Modeling, Simulation, System Identification, and Parameter Estimation. In: *SAE Technical Paper*. 25NETP-0072, 2025 (in review)

[MeRT91] P.H. Mellor, D. Roberts, D.R. Turner. Lumped parameter thermal model for electrical machines of TEFC design. In: *IEE Proceedings B Electric Power Applications* Bd. 138 (1991), Nr. 5, S. 205

Topology and Sizing Optimization of Thermal and Electric Energy Systems for Battery Electric Vehicle

Fakher Belkacem, Henrik Schäfer, Tobias Hellberg, Martin Meywerk
Helmut Schmidt University Hamburg / Professorship for Automotive Engineering
Holstenhofweg 85, 22043 Hamburg
fakher.belkacem@hsu-hh.de Henrik.schaefer@hsu-hh.de tobias.hellberg@hsu-hh.de
Martin.meywerk@hsu-hh.de

Abstract: The transition to battery electric vehicles requires electrification of power systems. The reliability and efficiency of electrical conversion systems are often compromised due to inadequate thermal management systems, leading to electronic failures and performance degradation. Addressing this challenge necessitates the optimization of thermal systems and the development of innovative vehicle architectures. The proposed study utilizes a novel design framework for topology and sizing optimization of electric vehicle energy systems using a graph-based modeling approach. To address the increasing complexity of electric vehicle systems, the model incorporates multi-physics modeling, integrating the interaction between the thermal, electrical, and mechanical domains. Additionally, the framework uses energy conservation laws to capture physical system dynamics, making optimization more structured and helping analyze design trade-offs effectively. To demonstrate its effectiveness, an electric bus powertrain design is investigated as a case study, with the goal of optimizing thermal and electrical component sizes and energy flow, as well as discrete choices in the topology of the system. The electric bus model incorporates experimentally validated empirical data obtained through advanced measurement techniques, ensuring credible optimization and realistic system behavior. This case study demonstrates how design optimization can influence the efficiency of thermal management systems.

1 Introduction

The rapid growth of electric mobility is creating new challenges for vehicle design. Engineers now face increasingly complex systems in which electrical, thermal, and mechanical domains strongly interact. To address this complexity, advanced frameworks are required that support system-level optimization. Several approaches have been developed for modeling the dynamics of such physical systems, including state-space models [1], partial differential equations [2, 3], bond graphs [4], and block diagram modeling techniques [5].

Contribution: 2025 FKFS Conference on Vehicle Aerodynamics and Thermal Management
15 – 16 October 2025 | Leinfelden-Echterdingen

These methods differ in their modularity, computational complexity, and ability to capture interactions between subsystems. A major difficulty in applying physics-based models to optimization lies in integration: because models from different disciplines often exchange information through incompatible signals, communication and simultaneous simulation across domains can become challenging [6].

To overcome these limitations, this paper applies a conservation-based optimization framework for dynamic systems of systems. The proposed approach builds on the graph-based modelling methodology developed by [7], which can be adapted to the generic formulation introduced by [8]. This procedure is further augmented by [9] to enable design optimization frameworks for systems governed by conservation laws. The modeling techniques are physics-based, modular, and designed to capture interactions across multiple domains [10].

The applicability of the graph-based methodology has already been demonstrated in several studies. For example, [8] shows its effectiveness in modeling a hybrid electric UAV powertrain and designing predictive control strategies, while other works validate its ability to capture the dynamics of thermal–fluid systems against experimental data [7]. Building on this foundation, another work of [9] applies the augmented graph-based framework to the optimization of battery-electric vehicles, investigating the influence of different configurations and component dimensions on energy efficiency and system mass. A hybrid electro-thermal energy storage system is also introduced as a representative design example, highlighting the benefits of employing the framework for system-level optimization of both plant and controller [11].

While system-level optimization of battery-electric vehicles has received attention in the literature, notably absent are results derived from real world data validating the capabilities of this framework as well as the realization of the impact of optimization frameworks on thermal management systems.To address this gap, the framework is instantiated here on a Battery Electric Vehicle (BEV) bus powertrain under realistic operating conditions. Here, electrical and thermal components are jointly optimized.

This leads to the following key contributions of the paper: → Formulation of a general graph-based framework for multi-domain, multi-objective optimization, enabling consistent representation and integration of several subsystems based on fundamental works of Alleyne e.g. [7-14] → Demonstration on a realistic BEV bus architecture**,** including strong electrical–thermal couplings, to illustrate the framework's workflow and applicability to real-world design problems→ Numerical case studies showcasing the potential of the proposed approach to improve thermal management systems, highlighting its capacity to handle coupled domains and system-level objectives.

2 Graph-Based Modeling Basics

This section introduces graph-based modeling [12, 13, 14] and outlines design optimization for these models [9].

2.1 Graph-Based Modeling

The graph-based models are derived by applying conservation equations to a component or system, inherently capturing the storage and transport of energy [15]. In such a representation, energy storing capacitive elements are modeled as vertices, while the paths for energy transport between storage elements (the vertices) are modeled as edges. An important feature that enhances the suitability of graph-based models is their capacity to incorporate orientation, which permits bidirectional power exchange between vertices. For example, in battery electric vehicle energy transfer occurs in both directions from the battery to drive the vehicle and back to the battery during braking (brake energy recuperation), which can be modelled by bidirectional graphs. The orientation of an edge defines only the reference direction for positive power flow. Each edge e_j is associated with a bidirectional power transfer p_j, which may depend nonlinearly on the states of the adjacent vertices and, if applicable, on an actuator input.

$$p_j = f_j\left(x_j^{\text{tail}}, x_j^{\text{head}}, u_j\right). \tag{1}$$

Here, $x_j^{\text{tail}}$and x_j^{head} denote the states of the tail and head vertices of edge j. Applying conservation of energy to a state x_i at vertex v_i gives the following dynamic equation:

$$C_i \dot{x}_\iota = p_i^{\text{in}} - p_i^{\text{out}}, \tag{2}$$

where $C_i \geq 0$ is the vertex capacitance, and p_i^{in} and p_i^{out} are the total incoming and outgoing power flows at vertex i. Appling the previous equation for all states, the full system dynamics can be rewritten as

$$\boldsymbol{C}\dot{\boldsymbol{x}} = -\bar{\boldsymbol{M}}\boldsymbol{p} + \bar{\boldsymbol{D}}\boldsymbol{p}^{\text{s}}, \tag{3}$$

where $\boldsymbol{x}$ ist the state vector, $\bar{\boldsymbol{M}}$ maps the edges to the vertices, $\bar{\boldsymbol{D}}$ describes the relationship between the sources and the vertices and $\boldsymbol{p}^s$ is a vector of external power flow and $\boldsymbol{C}$ is a matrix of vertex capacitances [7]. The states and the capacitances used for the case study are discussed in detail in Section 3.
However the graph based model described by Eq.(3) is not suitable for design optimization as it is. The next section is limited to the latter.

2.2 Design Optimization

To perform an optimization framework, the system must be expressed in terms of design variables, which serve as the fundamental degrees of freedom guiding the search for improved performance. Within a graph-based modeling approach, the influence of design variables manifests in two principal forms: modifications of component size and modifications of system topology. From a graph-theoretic perspective, the size of a component is encoded in the capacitance matrix, which governs the system's dynamic behaviour. Scaling the size of a vertex not only affects the vertex itself but also the connected edges, the resulting power flow, and ultimately the source contributions.

For example, increasing the battery capacity Q modifies its internal resistance R, which in turn changes the dissipated heat according to RI^2. This illustrates the principle of sizing optimization, where adjustments in design variables propagate through both local interactions and the global system response. In contrast, topology optimization focuses on exploring alternative system configurations through the addition or removal of edges. Such modifications affect the same three aspects as in sizing optimization—vertex properties, edge weights, and source-edge contributions—and therefore must be analyzed with equal care to preserve system consistency and physical feasibility.

The formal relationship between design variables and system dynamics is captured in the augmented graph-based model [9]. Its matrix form is expressed in Eq.(4):

$$\boldsymbol{\Psi_c \Phi_c C \dot{x}} = -\bar{\boldsymbol{M}} \boldsymbol{\Psi \Phi p} + \boldsymbol{D \Psi^s \Phi^s p^s}. \tag{4}$$

The six design matrices $\boldsymbol{\Psi_c}$, $\boldsymbol{\Phi_c}$, $\boldsymbol{\Psi}$, $\boldsymbol{\Phi}$, $\boldsymbol{\Psi^s}$and $\boldsymbol{\Phi^s}$ map the effects of component scaling and alternative architectures into the mathematical representation of the model. Specifically, $\boldsymbol{\Psi_c}$and $\boldsymbol{\Phi_c}$ capture the influence of sizing and topology decisions on vertex properties. The matrices $\boldsymbol{\Psi}$ and $\boldsymbol{\Phi}$ represent the corresponding effects on edge scaling and removal, while $\boldsymbol{\Psi^s}$ and $\boldsymbol{\Phi^s}$ account for these effects on the source edges of the graph-based model. These design matrices are diagonal and contain design functions that depend on the design variables. For further details cf. [9].

2.4 Formulating the Optimization Problem

The core of this framework lies in formulating and solving the optimization problem, which can be expressed as follow

$$\begin{aligned} &\min_{\boldsymbol{\theta}} \ \mathrm{J}_{\mathrm{total}}(\boldsymbol{\theta_c}, \boldsymbol{\theta_z}) \\ &\text{subj. to}: \quad \underline{\boldsymbol{\theta}} \ \leq \ \boldsymbol{\theta} \ \leq \ \overline{\boldsymbol{\theta}}, \\ &\qquad g(\boldsymbol{\theta}) \ \leq \ \mathbf{0} \end{aligned} \tag{5}$$

Here, $\mathrm{J}_{\mathrm{total}}(\boldsymbol{\theta_c}, \boldsymbol{\theta_z})$ denotes the objective function, which may serve various optimization purposes, such as minimizing mass, reducing energy losses, or enhancing overall performance. The design vector $\boldsymbol{\theta}$ comprises the sizing and topology-related design variables, $\boldsymbol{\theta_c}$ and $\boldsymbol{\theta_z}$, respectively and is defined as

$$\boldsymbol{\theta} \ = \begin{pmatrix} \boldsymbol{\theta_c} \\ \boldsymbol{\theta_z} \end{pmatrix}. \tag{6}$$

This vector is defined within specified bounds, such that each variable must remain between a given lower limit $\underline{\boldsymbol{\theta}}$ and upper limit $\overline{\boldsymbol{\theta}}$**.** The previously discussed augmented modelling approach is employed within the optimization problem, where the graph-based model is simulated for a given set of design variables and the objective function is evaluated from the resulting trajectories.

Eq. (5) presents also the set of nonlinear constraints with nonlinear function g for the design problem.
In the following section, this proposed optimization procedure is demonstrated through its application to a real-world battery electric bus.

3 Design of an Electric Vehicle Powertrain

This section applies the design optimization framework to a case study of a bus powertrain configuration, considering electrical, mechanical, and thermal power flows, with data experimentally validated in [16]. The baseline configuration, including sizing and architecture options, is outlined and represented as a graph based model. These configuration options are then formulated as an optimization problem within the framework, where different single- and multi-objective functions are defined. The results highlight the capability of the framework to identify designs that meet different requirements.

3.1 Configuration of the Bus Electric Powertrain

Fig 1 presents the baseline EV powertrain configuration, and Figs. 2–4 show the graphical models of the three parts of the powertrain.

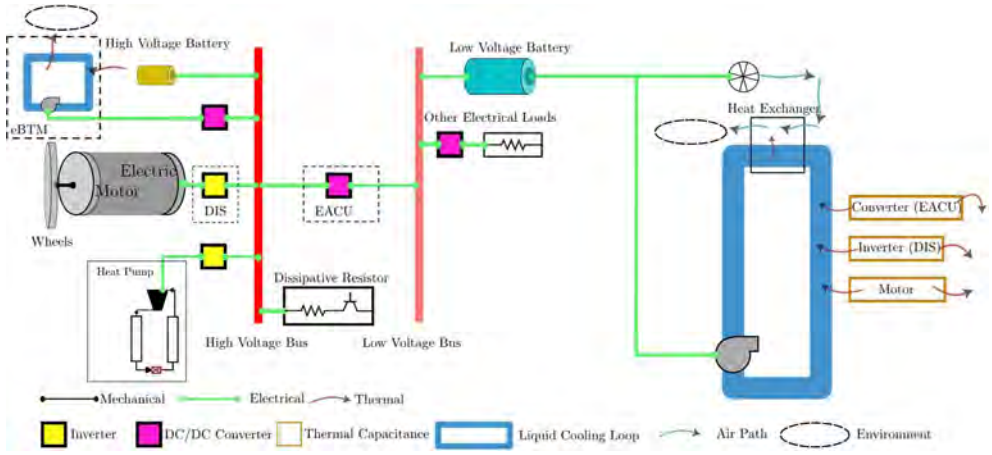

Figure 1: Electric vehicle baseline powertrain configuration.

The powertrain consists of a battery system as the main power source, connected in parallel to a high-voltage direct current (DC) bus. This bus distributes power to three subsystems: (i) the Drive Inverter System (DIS), which drives an AC motor responsible for vehicle propulsion; (ii) an inverter that supplies the HVAC system (heating, ventilation, and air conditioning); (iii) an Electronic Accessory Control Unit (EACU) and (iiii) an electric battery thermal management module (eBTM) to fulfil the conditional needs of the battery. Note that eBTM is not modeled in this case study.

In addition, the high-voltage bus is connected through a switch to a dissipative resistor that prevents overvoltage events.

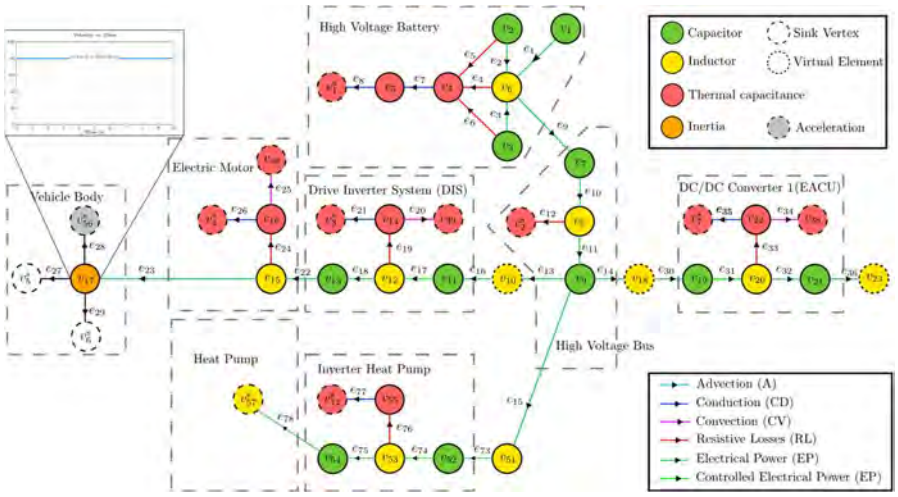

Figure 2: Graph-based model of high voltage bus (battery, motor and vehicle body).

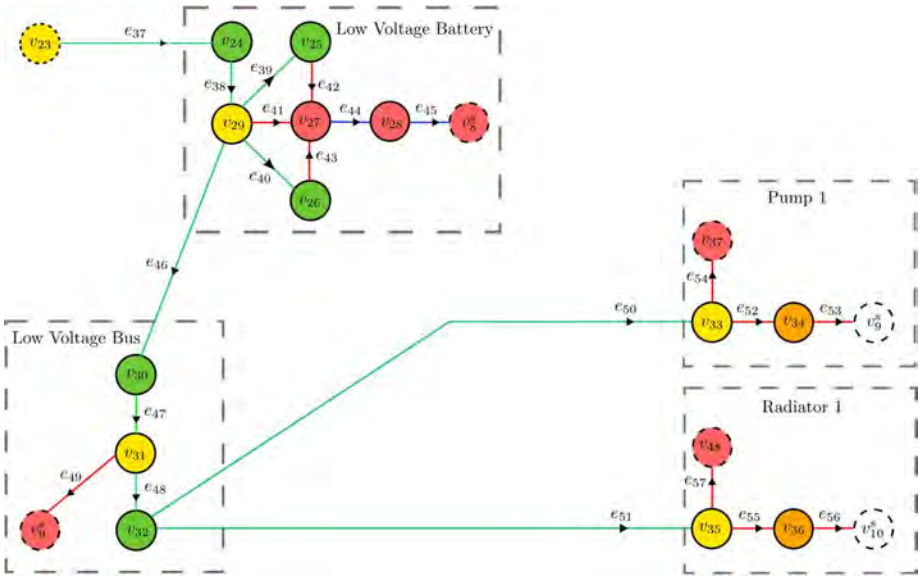

Figure 3: Graph-based model of the low voltage bus

The EACU, implemented as a bidirectional DC/DC converter, steps the voltage down to supply a low-voltage DC bus. This low-voltage bus both charges a 24 V auxiliary battery and powers additional electrical loads. The auxiliary battery in turn drives the cooling pump, which circulates coolant through the liquid cooling loop of the drive system, and the fan, which extracts heat from the coolant via a heat exchanger to the ambient environment.

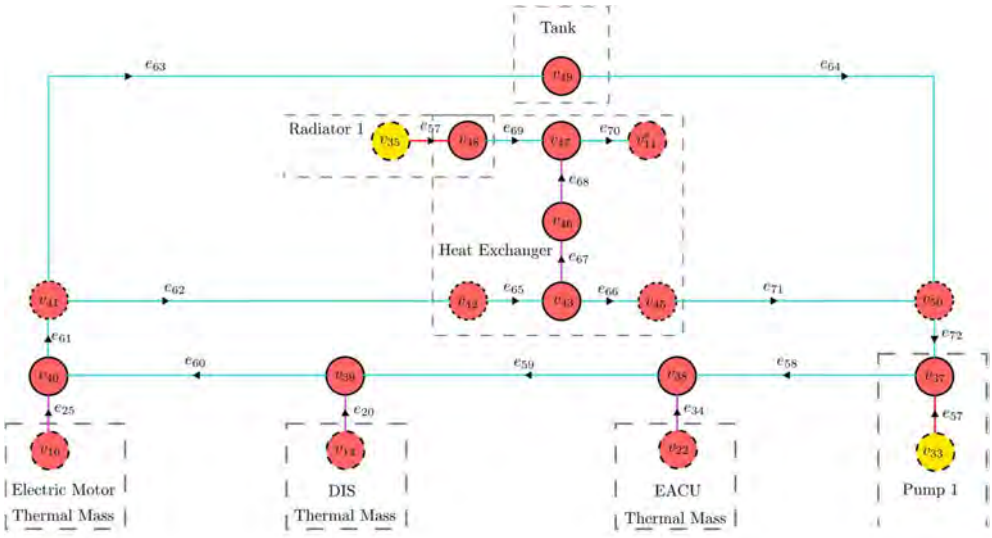

Figure 4: Graph-based of the Cooling System

Inputs to the system include the duty cycles of the three inverters/converters. The duty cycles of the DIS and the HVAC inverter are held constant to satisfy the required vehicle speed and the HVAC load demand, respectively. By contrast, the duty cycle of the EACU is controlled to ensure the auxiliary battery is charged with exactly the power required by the pump and the radiator.

In this study, the pump and radiator rotational speeds, as well as the vehicle velocity, are kept constant. This assumption allows the investigation of a single operating point. Switch input commands include (i) the buck/boost directionality for each of the three converters and (ii) the connection command for the dissipative resistor. For the considered case study, all converters are fixed in buck mode. Disturbances (sink states) include ambient air temperature, the current demand by the HVAC system, and the vehicle's velocity demand profile.

For clarity, the definitions of the state vector p and the connection matrix C (in Eq. (4)) varies depending on its type as specified in Table 1.

Table 1: Vertex types and capacitances.

Description	State	Capacitance
Voltage	V	$C_{\mathrm{v}}V$
Battery state of charge	q	$QV_{\mathrm{ocv}}(q)$
Current	I	LI
Temperature	T	C_{T}
Translating Mass	v	mv

The elements capacitance's are electrical capacitance C_{T}, inductance L, mass m, battery capacitance QV_{ocv} and thermal capacitance C_{v}. Note that, Q represents the battery capacity and V_{ocv} is the open circuit voltage of the battery. This graph contains vertices corresponding to battery state of charge (SOC), current, voltage, temperature and velocity. In Figures (2), (3) and (4), the voltage, temperature, and velocity states are indicated by green, yellow, and orange vertices, respectively.

The state battery state of charge (SOC) are given by the vertices v_1 and v_{24} in the Figures. (2) and (3), respectively. There are six types of edges in this graph representing different mechanisms of power transfer: electrical power, controlled electrical power, resistive losses, advection, conduction, and convection. Power flows of the same type follow similar governing equations, as specified by the corresponding edges in Table 2.

This case study explores three sizing design options. The next section relates these design options to the graph-based model within the proposed framework.

Table 2: Power flow edge equations by type.

Edge Type	Edge equation	Corresponding edge numbers
Electrical power	$P_j = x_j^{\mathrm{tail}} x_j^{\mathrm{head}}$	1-3, 9-11, 13-16, 18, 22, 23, 30, 32, 36, 73, 75, 78, 37-40, 46, 48, 50, 51
Controlled electrical power	$P_j = u_j x_j^{\mathrm{tail}} x_j^{\mathrm{head}}$	17, 31, 47
Resistive losses	$P_j = k_j \left(x_j^{\mathrm{tail}}\right)^2$	4, 5, 6, 12, 19, 24, 33, 42, 41, 43, 49, 52, 54, 55,
Advection	$P_j = k_j u_j x_j^{\mathrm{tail}}$	58–66, 69, 70
Conduction	$P_j = k_j \left(T_j^{\mathrm{tail}} - T_j^{\mathrm{head}}\right)$	7, 8, 21, 26, 35, 77
Convection	$P_j = k_j \left(x_j^{\mathrm{tail}} - x_j^{\mathrm{head}}\right)$	20, 25, 34, 67, 68

a For edge 1 and 24, $x_j^{\mathrm{tail}} = V_{\mathrm{ocv}}\left(x_j^{\mathrm{tail}}\right)$, where $\mathrm{V_{ocv}}$ is the corresponding battery open circuit voltage.

b. For edge 37: $x_j^{\mathrm{head}} = V_{\mathrm{ocv,l}}\left(x_j^{\mathrm{head}}\right)$, where $\mathrm{V_{ocv,l}}$ is the open circuit voltage of the low voltage battery.

b Example of controlled electrical power for edge 17: U *and* I represent voltage and current at two ends of the edge and u represents the duty cycle oft the Driving Inverter System (DIS).

3.2 Applying the Framework to the Battery Electric Vehicle Bus Powertrain

The discussed design optimization framework is applied to the case study system and requires at first step the definition of the design variables, which are described in Eq. (7). The used design function is

$$\mathfrak{f}\left(\theta_{\mathrm{c},\sigma}, \mu\right) = 1 + 4\,\mu\,\theta_{\mathrm{c},\sigma}, \tag{7}$$

and establishes a relationship between a design variable $\theta_{c,\sigma}$ and an output f. The first design option in this case study includes size of the battery ($\theta_{c,1}$). Sizing of the battery is considered analogous to adding fractions of cells in parallel n_{par}, which directly affects battery parameters such as capacity and mass. To reflect this, the first entry of $\boldsymbol{\Psi}_c$ in Eq.(4) is defined as:

$$f_{\psi_{c,1}}(\theta_{c,1}) = n_{\text{par}}(\theta_{c,1}) = n_{\text{par,nom}}\, \text{f}\left(\theta_{c,1}, \mu_{\text{n}_{\text{par}}}\right). \tag{8}$$

Here, $\mu_{\text{n}_{\text{par}}}$ is set to 0.47, ensuring that the number of parallel cells n_{par} varies between 6 and 18. The nominal number of parallel cells in the high-voltage battery, $n_{\text{par,nom}}$, is defined as 6. Important information is that the size of the series cells is kept constant during the optimization procedure to ensure the required voltage level for the driving motor. As the number of parallel cells in a battery pack increases, both the electrical capacity (vertices: v_2, v_3) and the thermal mass (vertices: v_4, v_5) scale proportionally. The internal resistance of the battery is also influenced by the overall pack size, which is modeled in edge e_4. The design functions applied in this study are described in detail in [9].

The parameters $\theta_{\text{c,2}}$ and $\theta_{\text{c,3}}$ are introduced to model the scaling of the motor and pump sizes, respectively. An increase in these parameters corresponds to an increase in the motor constant, which in turn leads to higher resistance in the associated components. Note that the motor constant defines the torque a motor can supply per unit of current. Using the design function in Eq.(7) captures this effect, as illustrated in Fig. (5).

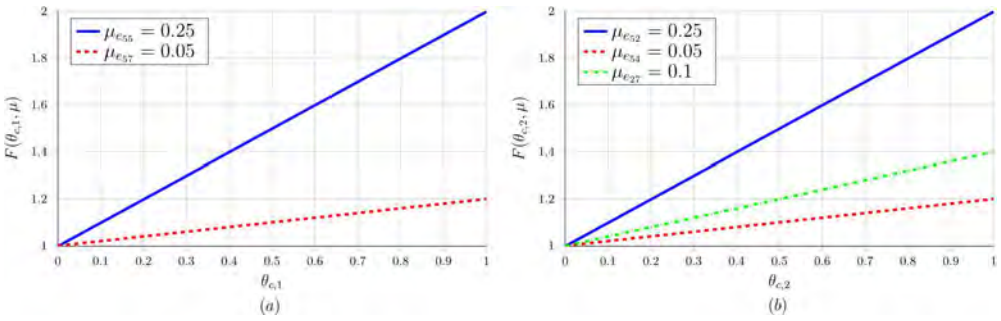

Figure 5: Design functions for component parameters. (a) Pump parameters and (b) motor parameters (blue: motor constant, red: resistance, green: mass).

Motor mass increases with scaling, thereby contributing to the total vehicle mass, which is used to compute the power flow from rolling and gradient resistances at edge e_{27}. The acceleration resistance is not considered in this study, as a constant driving velocity is assumed. As shown in Figure (5.a), the pump mass is considered negligible and has no impact on the model. The primary effects occur at edges e_{55} and e_{57}, where scaling the motor constant results in increased pump resistance.

In the next step of the framework is to define the total objective function, which is defined as

$$J_{\text{Total}} = w_1 J_{\text{EL,p}} + w_2 J_{\text{mass}} + w_3 J_{\text{Driving}} + w_4 J_{\text{EL,m}} + w_5 J_{\text{perf}}, \quad (9)$$

Here, $J_{EL,p} = R_{\text{pump}} f_{\psi_{54}}(\theta_{c,1}) I_{\text{pump}}^2$, minimizes the energy losses through the pump where R_{pump} and I_{pump} denotes the resistance of the pump and the current supplied to the pump, respectively. J_{mass} minimizes the mass of the vehicle and is defined as

$$J_{\text{mass}} = \frac{m_0 + m_{\text{motor}} \cdot \text{f}(\theta_{\text{c,2}}, \mu_{e_{27}}) + \text{n}_{\text{ser}} \cdot m_{\text{cell}} \cdot n_{\text{par,nom}} \cdot \text{f}(\theta_{\text{c,1}}, \mu_{n_{par}})}{m_{\text{ref}}}. \quad (10)$$

In this formulation, m_{ref} denotes the reference mass of the vehicle, taken as its initial mass. The parameters n_{ser} and $n_{\text{par,nom}}$ represent the number of battery cells connected in series and the nominal number of cells connected in parallel, respectively. m_{cell} corresponds to the mass of a single battery cell and m_{motor} is the mass of the driving motor. Eq.(9) considers also

$$J_{\text{Driving}} = \frac{\left(\text{f}(\theta_{\text{c,1}}=1, \mu_{\text{n}_{\text{par}}}) - \text{f}(\theta_{\text{c,1}}, \mu_{\text{n}_{\text{par}}})\right)^2}{\text{f}\left(\theta_{\text{c,1}}=1, \mu_{\text{n}_{\text{par}}}\right)}, \quad (11)$$

which is used as a penalty term to satisfy design constraint, ensuring that the vehicles reach a maximum driving range. $J_{\text{EL,m}}$ evaluates the efficiency and effectiveness of the electrical motor, where optimization leads to reduced losses and better reliability. This function is defined as $J_{\text{EL,m}} = \frac{(R_{\text{motor}}\, \text{f}(\theta_{c,2}, \mu_{e_{54}}) I_{\text{motor}}^2)}{R_{\text{motor}} I_{\text{motor}}^2}$.

In this equation, R_{motor} represents the electrical resistance of the motor, while I_{motor} denotes the electrical current supplied to the motor. Last but not least, J_{perf} in Eq.(12) aggregates overall performance measures not explicitly included in the other terms, ensuring balanced system performance.

$$J_{\text{perf}} = \frac{\left(P_{\text{motor,max}}(\theta_{\text{c,2}} = 1) - P_{\text{motor,actue}}\ (\theta_{\text{c,2}})\right)^2}{P_{\text{motor,max}}(\theta_{\text{c,2}} = 1)}, \quad (12)$$

In this formulation, $P_{\text{motor,actuell}}$ denotes the actual motor power as a function of the operating parameter $\theta_{\text{c,2}}$. The term $P_{\text{motor,max}}$ corresponds to the maximum motor power, which is reached when $\theta_{\text{c,2}}$ approaches its limiting value. However, the design variables have been normalized. For $\boldsymbol{\theta} = [\theta_{\text{c,1}}, \theta_{\text{c,2}}, \theta_{\text{c,3}}]$, the bounds are $\mathbf{0} \leq \boldsymbol{\theta} \leq \mathbf{1}$. The framework can now be applied, with the full problem formulated in the same manner as Eq. (5). For the dynamic simulation, the vehicle is driven at a constant velocity of 80 km/h, with the state of charge (SOC) set to 80% for both the high-voltage and low-voltage batteries, and all component temperatures are initialized to the ambient value.

The system dynamics are integrated using MATLAB's ode15s solver. For the optimization, MATLAB's sequential quadratic programming (SQP) algorithm is used to determine the optimal system configuration.

3.4 Results

The design framework is evaluated using three different sets of objective function weights. Test 1 emphasizes minimizing energy losses through the pump ($J_{\mathrm{EL,p}}$), while Test 2 minmizes the mass of the vehicle (J_{mass}) and maximize the driving range (J_{Driving}), which is assumed to be used as design contain in the objective function. Test 3 uses the same objective of optimization of test 2 and places additionally focus in the minimizing of the electric motor ($J_{\mathrm{EL,m}}$) with consideration of the penalty term to the total objective in order to maximize the motor power (J_{perf}). Table 3 presents the weights for each tests. Table 4 presents the design parameter values and the number of iterations for the three tests.

Table 4: Weights for the three test.

Weight	Test 1	Test 2	Test 3
w_1	1	0	0
w_2	0	0.5	0.5
w_3	0	0.09	0.08
w_4	0	0	0.5
w_5	0	0	0.01

The evolution of the objective functions is illustrated in Fig. (6.a). In all cases, the objective function decreases during the optimization process, indicating that SQP converges to an improved design compared to the initial configuration. Test 1 converges after three iterations, whereas Test 3 and Test 4 require five and eight iterations, respectively, due to the higher complexity of the multi-objective optimization.

Test 1 results in an increased pump size, since the design variable $\theta_{\mathrm{c},3}$ reaches its upper bound. This outcome is in line with expectations, since enlarging the pump increases the motor constant, thereby reducing the current required to drive the pump for cooling the liquid. Although a larger pump also leads to higher resistance, the current appears squared in the expression of energy losses, so the overall effect remains beneficial. As a result the used thermal management system will need less power to cool the drive system. In Test 2, the optimizer slightly increases the number of parallel battery cells, reflecting the high weight on the driving-range term w_3. Lowering w_3 reduces the incentive to add parallel cells and thus decreases battery-pack/vehicle mass.

Table 3: Optimization Results

	Test 1		Test 2		Test 3	
	Initial values	Optimized values	Initial values	Optimized values	Initial values	Optimized values
$\theta_{c,1}$	0.0	-	0.5	0.7174	0.5	0.6821
$\theta_{c,2}$	0.0	–	0.5	0	0.5	0.9754
$\theta_{c,3}$	0.5	1	0.0	-	0.5	-
Normalized obj. func	1.58	0.20	1.87	0.009	2.42	1.11
Number of iterations	–	3	-	5	-	8

Test 3 confirms this behaviour: with the same objective structure but a smaller w_3, the optimizer selects a lower mass-scaling parameter, $\theta_{c,1} = 0.6821$, relative to Test 2, indicating a reduced vehicle mass. The results, illustrated in Fig. (6.b), show that battery temperature decreases as the number of parallel cells increases, which also leads to a higher overall mass. While the added mass raises the vehicle's rolling resistance and therefore increases the power demand, this effect is outweighed by the reduction in internal resistance due to cell parallelisation.

However, Test 3 also aims to minimize the energy losses in the driving motor. The results show that the optimizer selected a motor size close to the upper limit of the design variable. Although this increases the overall vehicle mass, the additional motor mass is considered beneficial in this case. This outcome reflects the optimizer's preference for maximizing motor power, since it is explicitly included in the objective function through a penalty term.

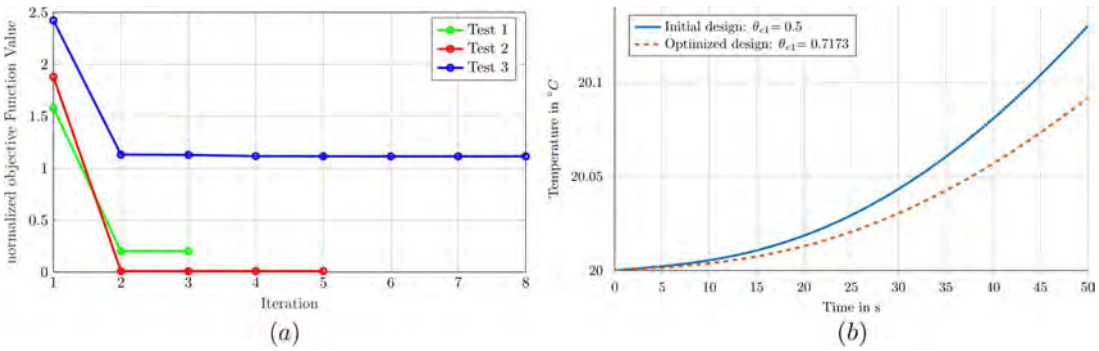

Figure 6: (a) Convergence plot for the three tests, (b) High-Voltage Battery Temperature (Test 2).

4 Conclusion

This work employs a design methodology for optimization that captures the multi-energy domains of dynamic systems. The approach adopts a graph-based modeling technique to represent the physical behaviour and interactions among components. Within this framework, design alternatives, such as component sizing and topology, are systematically integrated.

The case study investigates an electric bus powertrain under a single operational strategy. The results show that variations in component configurations—specifically changes in motor, pump, and battery sizes, significantly affect the thermal behaviour of the system. As a consequence, the energy demand of the thermal management system may either increase or decrease depending on the design choices.

Future work will extend the framework to incorporate multiple operational strategies, with particular focus on evaluating the impact of powertrain design on thermal management requirements during the regenerative braking phases of the electric bus.

5 References

[1] M. Kumar, I. N. Kar and A. Ray, "State Space Based Modeling and Performance Evaluation of an Air-Conditioning System," *HVAC\&R Research,* vol. 14, no. 5, p. 797–816, 2008.

[2] M. Xu, Z. Zhang, X. Wang, L. Jia and L. Yang, "A pseudo three-dimensional electrochemical--thermal model of a prismatic LiFePO4 battery during discharge process," *Energy,* vol. 80, p. 303–317, 2015.

[3] . H. Lindborg, V. Eide, S. Unger, S. Henriksen and H. A. Jakobsen, "Parallelization and performance optimization of a dynamic PDE fixed bed reactor model for practical applications," *Computers \& chemical engineering,* vol. 28, no. 9, p. 1585–1597, 2004.

[4] J. Garcia, G. Dauphin-Tanguy and C. Rombaut, "Modeling and simulating the dynamic electrothermal behavior of power electronic circuits using bond graphs," *PESC Record. 27th Annual IEEE Power Electronics Specialists Conference,* vol. 2, p. 1641–1647, 1996.

[5] G. Rizzoni, L. Guzzella and B. M. Baumann, "Unified Modeling of Hybrid Electric Vehicle Drivetrains," *IEEE/ASME transactions on mechatronics,* vol. 4, no. 3, p. 246–257, 1999.

[6] J. Allison and D. Herber, "Multidisciplinary Design Optimization of Dynamic Engineering Systems," *AIAA journal,* vol. 52, pp. 691-710, 2014.

[7] J. P. KOELN, "Hierarchical Power Management in Vehicle Systems," in *PhD-Thesis*, Urbana, Illinois, University of Illinois at Urbana-Champaign,, 2016.

[8] C. T., Aksland, A. G. and Alleyne, "Hierarchical model-based predictive controller for a hybrid UAV powertrain," *Control Engineering Practice,* vol. 115, no. 0967-0661, p. 104883, 2021.

[9] D. J. Docimo, Z. Kang, K. A. James and A. G. Alleyne, "A Novel Framework for Simultaneous Topology and Sizing Optimization of Complex, Multi-Domain Systems-of-Systems," *Journal of Mechanical Design,* vol. 142, no. 6, pp. 091701-1- 091701-16, 2021.

[10] C. T. Aksland, T. W. Bixel, L. C. Raymond, . M. A. Rottmayer and A. G. Alleyne, "Graph-Based Electro-Mechanical Modeling of a Hybrid Unmanned Aerial Vehicle for Real-Time Applications," in *2019 American Control Conference (ACC)*, IEEE, 2019, p. 4253–4259.

[11] C. Laird, Z. Kang, K. A. James and A. G. Alleyne, "Framework for integrated plant and control optimization of electro-thermal," *Energy,* vol. 258, no. 124855, pp. 1-14, 2022.

[12] J. Koeln, M. A. Williams, C. Pangborn H. and A. ,. G. Alleyne, "Experimental validation of graph-based modeling for thermal fluid power flow systems," *Dynamic Systems and Control Conference,* vol. 50701, no. V002T21A008, p. 1–10, 2016.

[13] D. J. Docimo and A. G. Alleyne, "Graph-Based Hierarchical Control of Thermal-Fluid Power Flow Systems," in *2017 American Control Conference (ACC)*, Washington, IEEE, 201, p. 2099–2105.

[14] P. J. Tannous and A. G. Alleyne, "Fault Detection and Isolation for Complex Thermal Management Systems," *Journal of Dynamic Systems, Measurement, and Control,* vol. 141, no. 6, p. 061008, 2019.

[15] H. Pangborn, J. P. Koeln, W. A. Matthew et A. G. Alleyne, «Experimental validation of graph-based hierarchical control for thermal management,» *Journal of Dynamic Systems, Measurement, and Control,* vol. 140, n° %110, p. 101016, 2018.

[16] H. Schäfer, T. Hellberg et M. Meywerk, «Simulation-Based Investigation and its Experimental Validation of the Thermal Behaviour of a Battery Electric City Bus,» chez *SAE Technical Paper*, Stuttgard, 2025.

Experimental aerodynamic investigation of tire geometries

Aleix Lazaro Prat[1,2], Thomas Schütz[1,2], Holger Gau[2]

[1]Institute for Fluid Mechanics and Aerodynamics (SLA), Technical University of Darmstadt,
Peter-Grünberg-Str. 10, 64287 Darmstadt, Germany

[2]BMW AG,
Knorrstr. 147, 80788 Munich, Germany

aleix.lazaro-prat@bmw.de,
thomas.st.schuetz@bmw.de,
holger.gau@bmw.de

Abstract: The objective of this work is to present the advances in the research of the influence of tire geometry features on the drag coefficient of a car. The aim of this holistic analysis is to encompass wind tunnel testing of market-available tires, the development and wind tunnel testing of a modular tire and the evaluation of external flow CFD simulations of cars with accurately deformed tires. From this extensive groundwork, this current publication focuses on the analysis of different market available 245/45 R18 tires on the BMW 4 series and the 5 series touring in the BMW wind tunnel facilities.

1 Introduction

Aerodynamically, tires account for a meaningful share of the total drag coefficient of a car [Schü17, Witt14]. Simulation results from the BMW 4 series showcase that fact, in which it is observed that 10-15% of the total drag share corresponds exclusively to tires [Inte25]. Furthermore, not only they account for a significant share in the C_d, but their geometry changes yield a notable ΔC_d. In the current work, conducted wind tunnel measurements of current market-available 245/45 R18 tires, a maximum $\Delta C_d = 0{,}011$ is observed (BMW 4 series). However, maximum differences up to $\Delta C_d = 0{,}018$ have been experimentally measured in other vehicles (same rim) [Inte25]. This is not an insignificant effect, given that $\Delta C_d = -0{,}001 \approx \Delta range = 1{,}1 - 1{,}5\ km$ on electric cars [HuSo03]. The reason of this influence is the partial exposition of tires to the incoming air, the angle at which the flow impacts the front tires, and the sensitivity of the surrounding (wheelhouse) and downstream geometries (underbody and rear-end). Moreover, and little-known, tires of the same size have a big geometrical spread, in both contour and tread pattern. This fact is studied, together with the wind tunnel results, in the upcoming sections.

Contribution: 2025 FKFS Conference on Vehicle Aerodynamics and Thermal Management
15 – 16 October 2025 | Leinfelden-Echterdingen

The goal of this contribution is to get a clearer understanding of the influence of geometrical features of tires in the total drag coefficient of a car, by experimental means. Few prior studies approach it similarly [HoSe18a, LJWL12, Schn16]. Most of them, however, rely on CFD to evaluate tire aerodynamics [FuUn21, HoSe18b, HoSL13, MSWS21, NaPa25, ReHI19]. This presents several limitations for this use case, besides the ones inherent to the approximations of the simulation: inaccurate tire geometry representation and rotation conditions. They can be accurately tackled, not without a highly resource-intensive structural-aerodynamic simulation [SGBF23]. Therefore, the standard approach in the automotive industry is to simplify the tire geometry and rotation condition.

The following work is structured as thusly: In the method (Section 2) the aerodynamic setup is described, followed by the listing and geometrical analysis of the tested tires. Section 3 presents the results of the wind tunnel tests. These in the discussion section (Section 4). Lastly, an outlook for the research project is briefly debated in Section 5.

2 Method

2.1 Aerodynamic setup

This study has been performed in the BMW aerodynamic wind tunnel. Two different vehicles are considered: the BMW 4 series and 5 series touring, each evaluated in multiple wind tunnel sessions. Results are always presented in deltas relative to a reference and in every wind tunnel session a common (reference) tire set is evaluated to avoid potential variability coming from the wind tunnel calibration. Nonetheless, the repetition of the same geometrical configuration (car and tire set) in different wind tunnel sessions yields a maximum $\Delta C_d = 0{,}001$. If not otherwise stated, the measurements are performed at 140 km/h, with tire pressure of 2,5 bars and standard tire load and vehicle ride height.

Tested tires are exclusively from the size 245/45 R18. All tests are performed with the same rim styling, which is representative of a non-aerodynamically optimized rim. Further exploration of the aerodynamic behavior of tires on other rim stylings is recommended by the authors.

2.2 Tire geometries

The evaluated tires are listed in Table 1 in no particular order. They represent a subset of all 245/45 R18 acquired tires, but only the ones measured in the wind tunnel with a vehicle are included in this study.

To ease readability, each tire has a unique identification code, or ID, assigned in this work (nomenclature *xya*). It includes information on the type (*x*: Summer (SO) =1,

All Season and Winter (A/S) =2) and structure (*y*: Standard (STD) =1 and Runflat (RSC)=2). The third character (*a*) assigns a unique letter for each model.

Table 1: List of the tested 245/45 R18 tires.

ID	Type	Structure	Manufacturer	Model
11A	Summer	Standard	Continental	EcoContact 6 *
11B	Summer	Standard	Pirelli	P Zero *
11C	Summer	Standard	Michelin	Primacy 3 * MO
11D	Summer	Standard	Bridgestone	Turanza T005 *
11E	Summer	Standard	Kumho	Ecsta PS91 * MO
11F	Summer	Standard	Hankook	Ventus S1evo3 *
11G	Summer	Standard	Goodyear	Eagle F1 Asy3 *
12H	Summer	Runflat	Pirelli	Cinturato P7 * (RSC) MOE
12I	Summer	Runflat	Bridgestone	Turanza T005L * (RSC) MOExtended
12J	Summer	Runflat	Hankook	Ventus S1evo3 * (RSC)
22K	All Season	Runflat	Pirelli	Cinturato P7 All Season * (RSC) MOE
12O	Summer	Runflat	Pirelli	P Zero * (RSC)
22P	All Season	Runflat	Pirelli	P Zero A/S (RSC)
11Q	Summer	Standard	Pirelli	P Zero I *
12R	Summer	Runflat	Pirelli	P Zero I * (RSC)
11V	Summer	Standard	Goodyear	Eagle F1 Asy5
21W	Winter	Standard	Pirelli	Winter Sottozero
21X	Winter	Standard	Goodyear	Ultragrip
22Y	All Season	Runflat	Pirelli	P Zero * A/S (RSC)

The addition of type and structure in the identification code is considered relevant, given their influence on the tread measurements and the stiffness of the tire. These two, together with the contour, fully describe its geometry and mechanical properties. The contour is the general curve that is revolved to create the tire. The tread pattern it defined as the embossed cuts used to move the water out of the contact patch. They are divided in longitudinal and side treads. Finally, the structural stiffness refers to the arrangement of steel strings along the perimeter of the tire, designed to withstand the loads. These three are considered by the authors as the entities that explain the shape and behavior of the tire. They are physical independent features that define the final geometry of the deformed tire, in combination with load, camber, toe, pressure and speed.

The geometrical analysis of tires is enabled by the scanning process and subsequent contour and pattern postprocessing developed algorithms (Figure 6 from the Appendix). This workflow outputs the contour and depth image from the tire, which can be processed for further analysis.

2.3 Tire contours

Evaluated tire contours demonstrate a wide design space, depicted in Figure 1. Not only this, but the taxonomy of the contours is as well diverse. Some have an abrupt profile change in the side wall, others present a balloon-like geometry and a few exhibit a trapezoidal format. No shape appears to be predominant over the others.

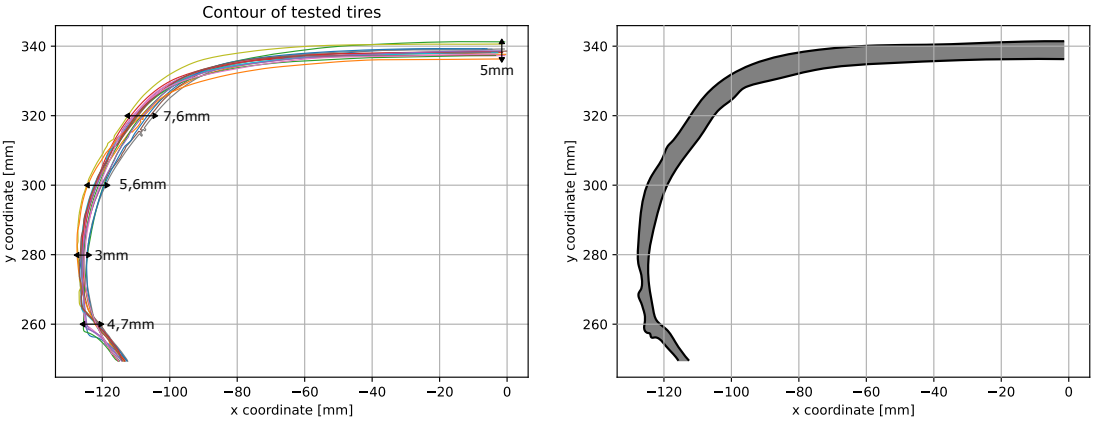

Figure 1: Geometrical variability of the contour of the tested tires, depicted as individual lines on the left-hand side, and their limits on the right-hand side.

Even though most of the contours differ geometrically, a limited number of them are alike. A clustering of the tested tire contours has been performed using a hierarchical agglomerative clustering algorithm. These are: Cluster 1 containing tires 12H and 21W, Cluster 2 with 22P, 12O and 22Y, and Cluster 3 encompassing tires 12J and 11A. They are depicted in Figure 9 from the Appendix. Non clustered geometries do not have comparable contours, emphasizing their diversity. This grouping simplifies the evaluation of drag coefficient delta caused by the tire pattern.

2.4 Tire patterns

Like the contours, the variability in tread patterns designs is substantial, and even more if All Season (or Winter) tires are taken into consideration, like in the presented work.

To enable a characterization of tread geometries that supports the quantitative aerodynamic evaluation of distinct tread components, a feature extraction algorithm is developed. The present approach retrieves exclusively the width and depth of the longitudinal treads. The goal is to identify potential aerodynamic patterns from those, as they dominate the geometry of the pattern. Thus, an automatic vertical line detection algorithm has been implemented. The values for each of the tires, are gathered in Table 2, and the depth maps of the tread patterns are displayed in Figures 7 and 8, all found in the Appendix.

Depending on the pattern shape, the current version of the vertical line detection algorithm might miss a longitudinal tread. This is the case for the foremost left longitudinal tread of the tire 11F, which displays a zigzag silhouette. A more sophisticate approach that embeds the entire pattern shape into a latent space for machine learning-enabled optimization is currently being developed by the researchers.

From the implemented vertical line detecting method, the width and depth distribution of the longitudinal treads are extracted. A simple geometrical analysis shows that, the two parameters do not significantly across tire types. However, the spread in widths is larger for summer standard (SO STD) tires.

Besides the two Winter tires (IDs 21W and 21X), side treads designs do not show apparent geometrical differences. They are slender, shallow similar shapes, positioned at a random (but constrained) distance between each other along the perimeter. This arbitrary distribution avoids the generation of noises, and it adds a layer of complexity in their aerodynamic analysis. In this study they are not considered. In any case, the acoustic requirements of the tires have a higher priority than aerodynamics, and hence any benefit from their aerodynamic optimization in detriment of acoustics would not be justified.

3 Results

This section is structured as follows: First, the base wind tunnel results are discussed. These are tests of the listed tires (Table 1) on the BMW 4 series and 5 series touring under the same inflow velocity (140 km/h) and tire and vehicle conditions (load, tire pressure, rim and ride height). Afterwards, a study on several relevant parameters is presented. Those include tread pattern orientation, ride height, tire pressure, axis position, tire position in vehicle and inflow velocity. In this second part, most of the drag measurements are performed in a reduced number, almost exclusively in the BMW 4 series.

3.1 Base configuration

The results of the aerodynamic evaluation of the tire sets in both the BMW 4 series and 5 series touring are depicted in Figure 2, including the contour clusters highlighted in orange, blue and yellow, respectively. If not otherwise stated, the values are given as deltas relative to the reference tire 12H.

As observed in Figure 2, there is no clear a priori similarity in tire behavior across the two vehicles. Some tires have a similar effect on the ΔC_d (11B, 11G, 11V, 21W, 21X and 22K) and others have not (11C, 11E, 11F, 11Q, 12I). This makes total sense, as the surrounding geometry and flow field are different. However, there might be common geometrical characteristics that on average improve or worsen the C_d.

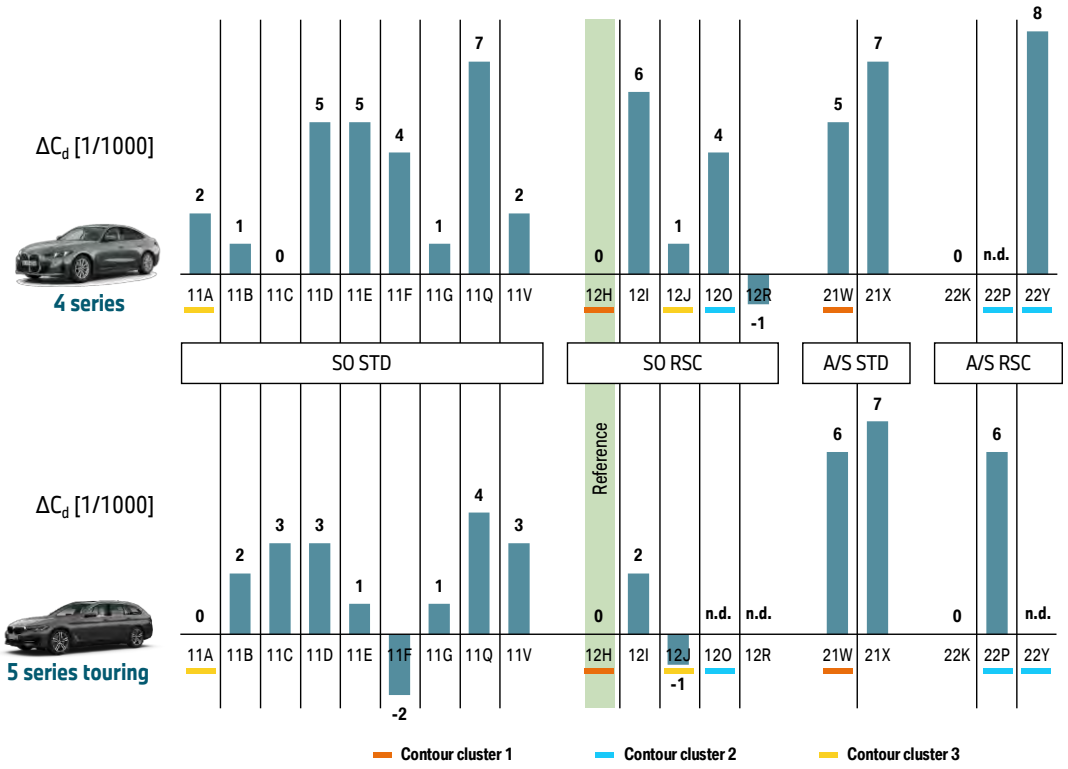

Figure 2: Base wind tunnel results the tested tires with the same rim, tire pressure, load and ride height at 140km/h. Contour clusters are highlighted.

Summer Standard and Runflat tires (SO STD and SO RSC) do not presumably differ in ΔC_d, suggesting that the aerodynamic relevant parameters are embedded in the undeformed shape of the tire. This result does not align with previous tests in different vehicles, in which RSC tires exhibited lower drag due to their stiffer and hence smaller width [Inte25]. Further tests and the analysis of tire scans in the wind tunnel under deformed conditions are required.

Similarly, All Season and Winter tires with both structures (STD and RSC) behave alike in both vehicles. They increase the drag coefficient compared to most of the summer type apart from tire 22K. This model diverges by $\Delta C_d < -0{,}005$ compared to the rest (21W, 21X, 22P and 22Y). Figure 10, located in the Appendix, depicts both contour and tire pattern for such geometries. As observed there, tire 22K has the smallest tire width of the 5 All Season and Winter models, which is expected to be better aerodynamically. Its contour, however, does not considerably differ from tire 21W. In terms of the tread pattern, and with the support of the extracted width and depth, an observation arises: Tire 22K has the maximum longitudinal tread width from them all, and shallow values of depth. These parameters potentially have an influence in the C_d, and thus are further explored.

The results from the contour clusters indicate potential effects caused by the tread pattern. That is the case of Cluster 1. Tire 21W behaves similarly in both vehicles, as tire 12H, but diverge from one another by $\Delta C_d = 0{,}005 - 0{,}006$. Observing 12W, it

contains deeper longitudinal treads than 12H, with a maximum depth of 7,1 mm, fact that seems to be, again, detrimental to the ΔC_d. This effect is observed as well in Cluster 2. Tire 22Y has depths up to 6,6 mm, compared to the 6,1 mm from the 12O. Equally to Cluster 1, deeper grooves seem to not be beneficial for the drag coefficient. Moreover, both geometries from Cluster 2 share the same internal structure (RSC). The opposite however does not seem to strictly hold. The tire with the shallowest longitudinal treads (11A) is not the most aerodynamic one.

If the maximum values of longitudinal depth and width are analyzed, a similar trend is observed: geometries with deeper longitudinal treads yield higher ΔC_d, for both car models. Figure 3 illustrates that trend (colored by contour clusters), alongside the aerodynamic benefit of increasing the width. Note however that these correlations are weak. The experimental analysis of those parameters in an independent manner should be performed to confirm the previous statements.

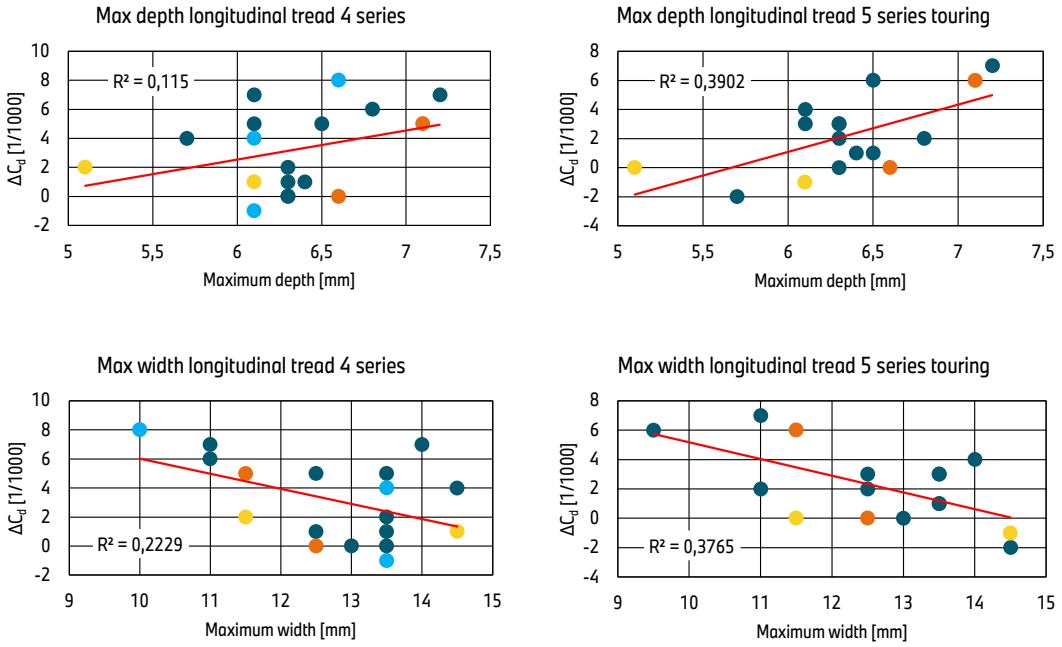

Figure 3: Correlation between maximum width and depth of the longitudinal treads and the ΔC_d, colored by contour cluster.

Analyzing the tires 11Q and 12R, which have similar tread patterns, big differences are observed in the ΔC_d, for the BMW 4 series model. This discrepancy is either originated from the distinct inner structure, or the significant disparity in contour. The second seems the most plausible cause, given the pronounced difference in frontal area. However, the best performing tires (Figure 11, from the Appendix), for both vehicles, share diverse typologies of contours, not necessarily the narrowest ones. They same apply to the contours with tires that produce the highest drag coefficient.

3.2 Pattern orientation

Given the directionality of the tread pattern of tires 21X and 21W, stated by the manufacturer, these have been tested in the opposite configuration in both cars. In doing that, the tire contour and the geometry and position of the longitudinal treads remain constant. The orientation of the side treads is the only modified variable. Results (Figure 6) disguise a clear increase in ΔC_d, clearly exhibiting the relevance of considering these features for aerodynamic optimization. It is unclear if this effect is shared across tire types, as 21X and 21W have a distinguishable deeper side tread layout than the rest. Further tests in other tire types are required to analyze this trend.

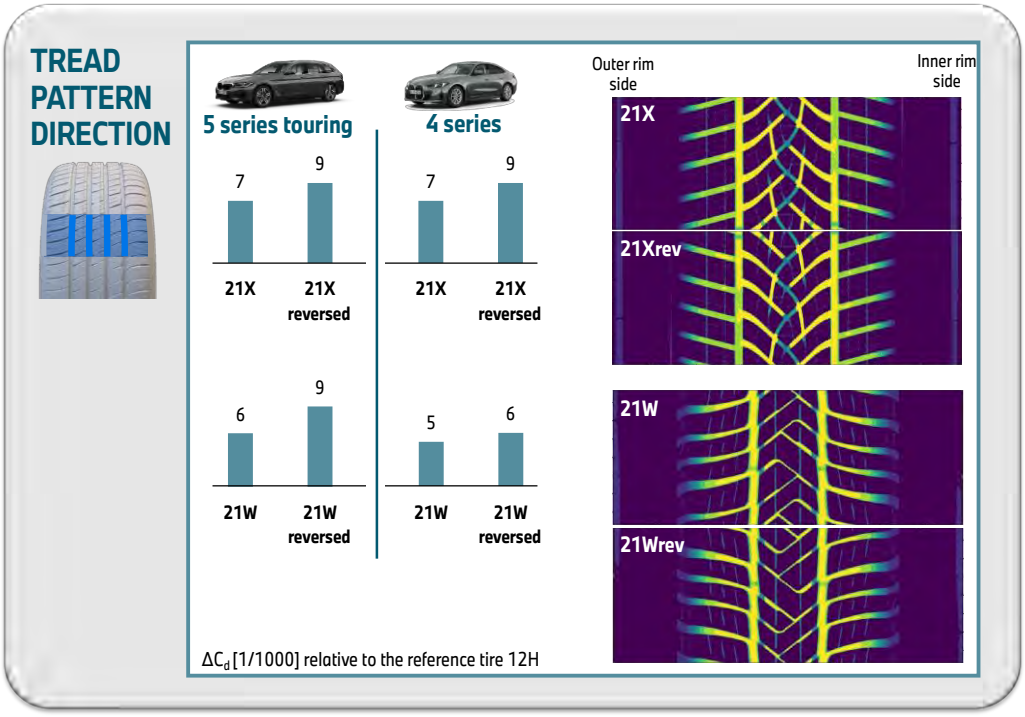

Figure 4: Pattern orientation influence in the ΔC_d.

As tires 21X and 21W in the reverse configuration have the highest recorded drag from the study ($\Delta C_d = 0{,}009$ for both vehicles), they are used to explore the influence of aerodynamically good and bad tires in the front and rear axis (Section 3.6).

3.3 Velocity

Besides the standard testing velocity of 140 km/h, three evaluations have been performed at a reduced speed (100 km/h) in the BMW 4 series. Tires 11A, 21X and 12H have been tested. The objective of this comparison is to assess whether the tires produce a similar outcome at these different speeds. If that is the case, the requirements for the physical modular tire (current under development by the authors) can be lowered.

The results from the experiments show a drag coefficient variation ($\Delta C_{d,140} - \Delta C_{d,100}$) of 0,002, 0 and -0,001, for tires 11A, 21X and 12H, respectively. A more extensive evaluation is required

3.4 Ride height

Tires 12R and 12H have been evaluated under different ride height conditions, to explore the tendency that they follow under the modification of this parameter. Both tires display a very similar behavior, by increasing $\Delta C_d \approx 0{,}005$ every time that the car body is elevated 10 mm.

3.5 Tire pressure

Alongside with the load and the internal structure of the tire, the pressure characterizes the deformation behavior in the contact patch, and in radial due to inertial forces. Hence, the increase in stiffness due to the rise in pressure is expected to cause a reduction in the drag coefficient. Deflated tires exhibit an evidently broader deformation in the contact patch, which increases the frontal area and theoretically generates bigger flow structures that disturb the downstream geometries.

Four different sets have been evaluated in the BMW 4 series (tires 22K, 11B, 12H and 21W), with pressures ranging from 1,8 bars to 3,5 bars. The observed trend is as expected, except for the case of 21W. Nonetheless, all measurements differ by $max\Delta C_d = 0{,}001$, which in the eyes of the authors is not sufficient to generate a statement, and different to previous studies [Inte25]. Like in most of the other variable-studies, the author recommends an extensive analysis of this parameter including scan data from the tire under deformation conditions inside the wind tunnel.

3.6 Axis position

In the following test, two sets of different tires are used: one producing high drag and another a low value of it. Each set is mounted in one of the axes (either the front or the rear), having thus a combined layout. Both BMW 4 series and 5 series touring are included in the experiment. The goal of this evaluation is to determine if there is dominating axis. The selected tires differ 0,007 and 0,009 drag points between them, to better appreciate the effects of the experiment.

A clear dominance of the front axis is observed in the performed measurements, gathered in Figure 7. Front tires receive the impact of the barely disturbed incoming air, which makes their geometry changes more influencing in the aerodynamics of the entire vehicle. Interestingly, the findings are opposite to the wind tunnel results of Landstrom et al. [LJWL12].

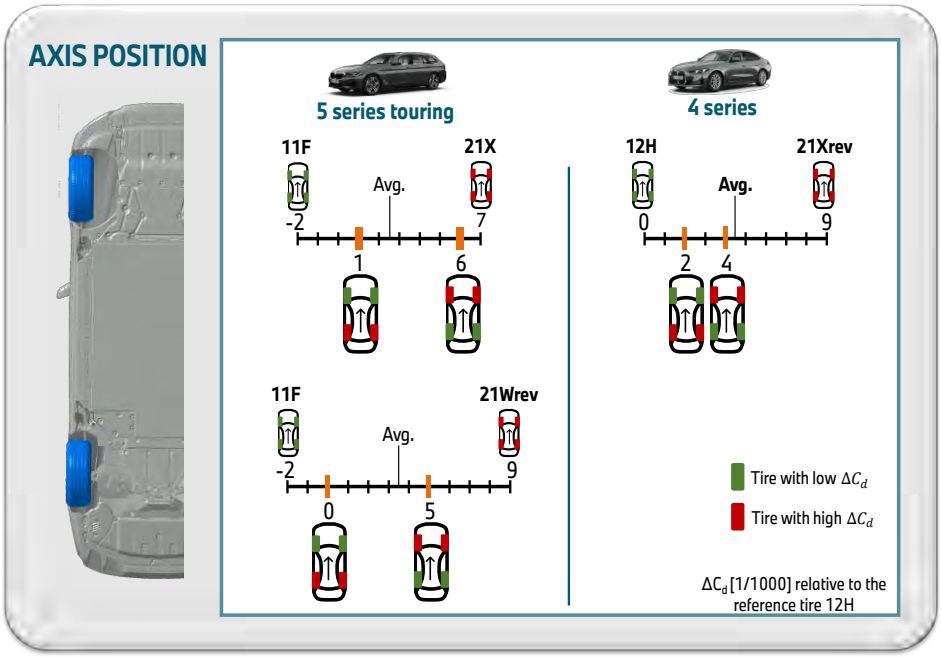

Figure 5: Axis position influence in the ΔC_d.

3.7 Position in the vehicle

Two sets of tires (12H and 12R) are evaluated in the BMW 4 series by placing each individual tire in each of the four positions in the car. This test aims to understand how geometrical tolerances might affect the C_d. Results display a maximum variability of 0,001 in drag coefficient.

4 Conclusions

Tires are multi-parametric multi-requirement complex 3D geometries, that yield a large design space and a substantial spread of drag values. This, complimented by the scarcity of market-available tires from the same size, complicates the aerodynamic evaluation of single geometrical features. However, this work aims to shine some light in the intricate field of tire aerodynamics, from an experimental angle.

The results from the general wind tunnel measurements show a non-equivalence between drag coefficient deltas from the BMW 4 series and the 5 series touring, which is to expect. Most models behave alike, apart from 5 tires (ΔC_d differs by $\geq 0{,}003$).

Summer tires (SO STD and SO RSC) display high variability in both vehicles, with a spread of 0,008 and 0,007 aerodynamic points, for the BMW 4 series and 5 series touring respectively. Winter and All-Season geometries have less spread and a clear higher drag than Summer models, except the ID 22K. This specific geometry exhibits

wide and shallow longitudinal treads, with smaller section area (contour). All these properties could potentially have a beneficial effect in the drag, specially the first two. Further proof is required, as the correlations between these parameters and the ΔC_d are weak. In terms of contour, no design is evidently more beneficial than the rest.

Unexpectedly, no substantial drag difference is observed between STD and RSC across both tire types, nor due to the increase of tire pressure (max. $\Delta C_d = 0{,}001$). This finding should be further studied, as it diverges from previous test [Inte25].

Velocity and ride height behave as expected. The change in air speed and tire rotation modifies slightly the drag coefficient (by $max\Delta C_d = 0{,}002$), and 10mm increments of the ride height increment quite consistently the drag value by approximately 0,005.

Tolerances, which will be always present in the manufacturing, have been briefly evaluated with the testing of tires 12H and 12R in all 4 positions, from the same tire set. Maximum values of 0,001 in drag coefficient have been observed.

Lastly, there is a clear dominance of the front tires on the general trend of the car aerodynamic coefficient. This has been observed in 3 occasions, with $max\Delta C_d = 0{,}005$.

5 Future outlook

Series tires only represent a subset of the design space in which tire manufacturers could potentially manufacture their geometries. Hence, a modular tire is under development by the researchers to fully explore the design space isolating geometrical parameters during the study. The concept intended for the first version of the modular tire is presented in Figure 12. The goal of this prototype is to unveil effects purely coming from the tire tread pattern and not from the contour.

Further research to validate the findings of this work is recommended by the authors. Moreover, a complete description of the tire geometry (including deformation and z-position in the vehicle) could potentially identify features that predominantly govern the drag coefficient. An adequate embedding or parameterization, accounting for of the tire, is therefore vital.

6 Reference list

[FuUn21] Gen Fu, Alexandrina Untaroiu. Investigation of Tire Rotating Modeling Techniques Using Computational Fluid Dynamics. In: *Journal of Fluids Engineering* Bd. 143 (2021), Nr. 11, S. 111206

[HoSe18a] Teddy Hobeika, Simone Sebben. Tyre Pattern Features and Their Effects on Passenger Vehicle Drag. In: *SAE International Journal of Passenger Cars - Mechanical Systems* Bd. 11 (2018), Nr. 5, S. 401–413

[HoSe18b] Teddy Hobeika, Simone Sebben. CFD investigation on wheel rotation modelling. In: *Journal of Wind Engineering and Industrial Aerodynamics* Bd. 174 (2018), S. 241–251

[HoSL13] Teddy Hobeika, Simone Sebben, Christoffer Landstrom. Investigation of the Influence of Tyre Geometry on the Aerodynamics of Passenger Cars. In: *SAE International Journal of Passenger Cars - Mechanical Systems* Bd. 6 (2013), Nr. 1, S. 316–325

[HuSo03] W.-H Hucho, G Sovran. Aerodynamics of Road Vehicles. In: *Annual Review of Fluid Mechanics* Bd. 25 (2003), S. 485–537

[Inte25] *Internal report*: BMW AG, 2025

[LJWL12] Christoffer Landstrom, Linda Josefsson, Tim Walker, Lennart Lofdahl. Aerodynamic Effects of Different Tire Models on a Sedan Type Passenger Car. In: *SAE International Journal of Passenger Cars - Mechanical Systems* Bd. 5 (2012), Nr. 1, S. 136–151

[MSWS21] Mehdi Mortazawy, Richard Shock, Dalon Work, Justin Sacco, James Hoch. Aerodynamic Simulation of a Standalone Round and Deforming Treaded Tire. In: *SAE International Journal of Advances and Current Practices in Mobility* Bd. 3 (2021), Nr. 5, S. 2227–2235

[NaPa25] A Martinez Navarro, G Parenti. Tire Wake Analysis through Unsteady Aerodynamics Simulations. In: *NAFEMS World Congress 2025* (2025)

[ReHI19] Jan Reiß, Lukas Haag, Thomas Indinger. CFD investigation on fully detailed and deformed car tires. In: *International Journal of Automotive Engineering* Bd. 10 (2019), Nr. 4, S. 324–331

[Schn16] Bastian Harald Schnepf. Untersuchung von Einflussfaktoren auf die Umströmung eines Pkw-Rades in Simulation und Experiment (2016)

[Schü17] T. Schütz. Aerodynamische Effizienz von Fahrwerkskomponenten bei zukünftigen Fahrzeugen. In: 2017 — ISBN 978-3-18-102296-2, S. 111–122

[SGBF23] Khaled Sbeih, Arturo Guzman, David Barrera Garcia, Nicolas Fougere, Sam Jeyasingham, Richard Shock, Mehdi Mortazawy, Michael DeMeo. Accurate Automotive Spinning Wheel Predictions Via Deformed Treaded Tire on a Full Vehicle Compared to Full Width Moving Belt Wind Tunnel Results. In: Detroit, Michigan, United States, 2023, S. 2023-01–0843

[Witt14] Felix Wittmeier. *Ein Beitrag zur aerodynamischen Optimierung von Pkw Reifen*. Wiesbaden: Springer Fachmedien Wiesbaden, 2014 — ISBN 978-3-658-08806-4

7 Appendix

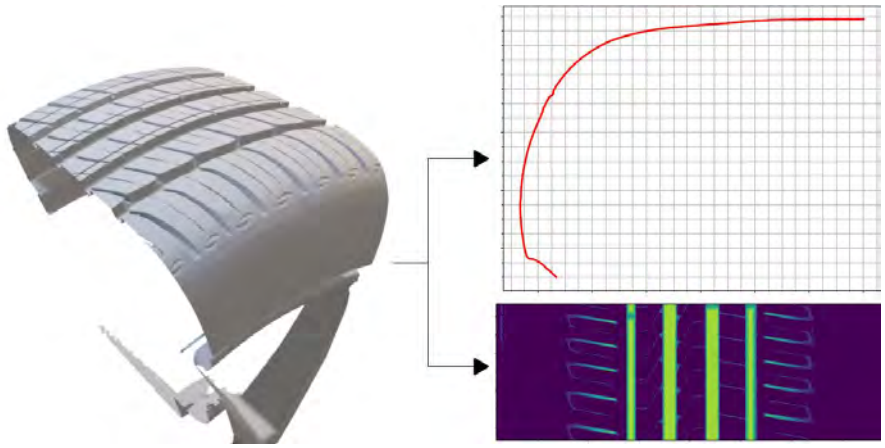

Figure 6: Scanning and geometrical feature identification process.

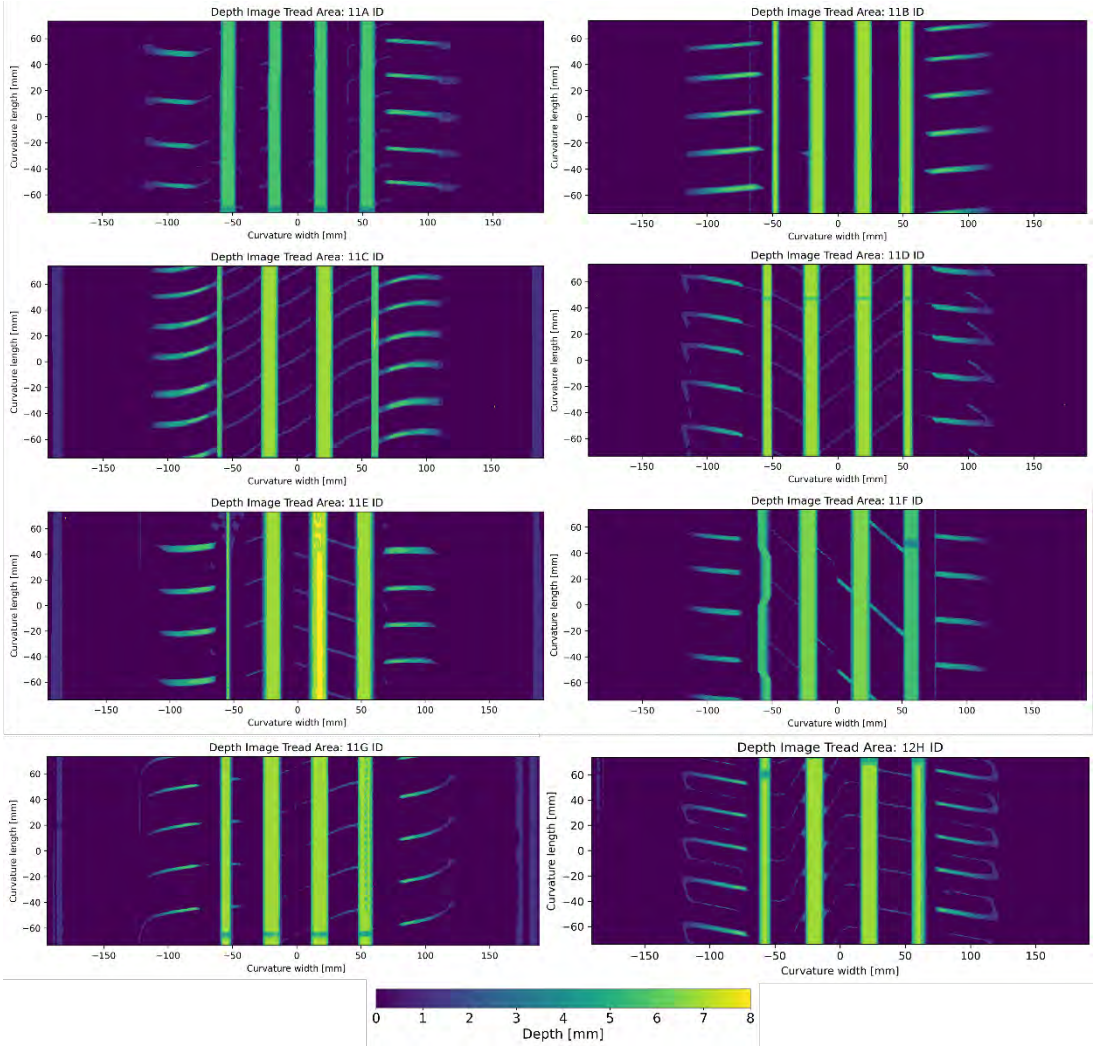

Fig. 7: Tread patterns of tires with IDs from 11A until 12H.

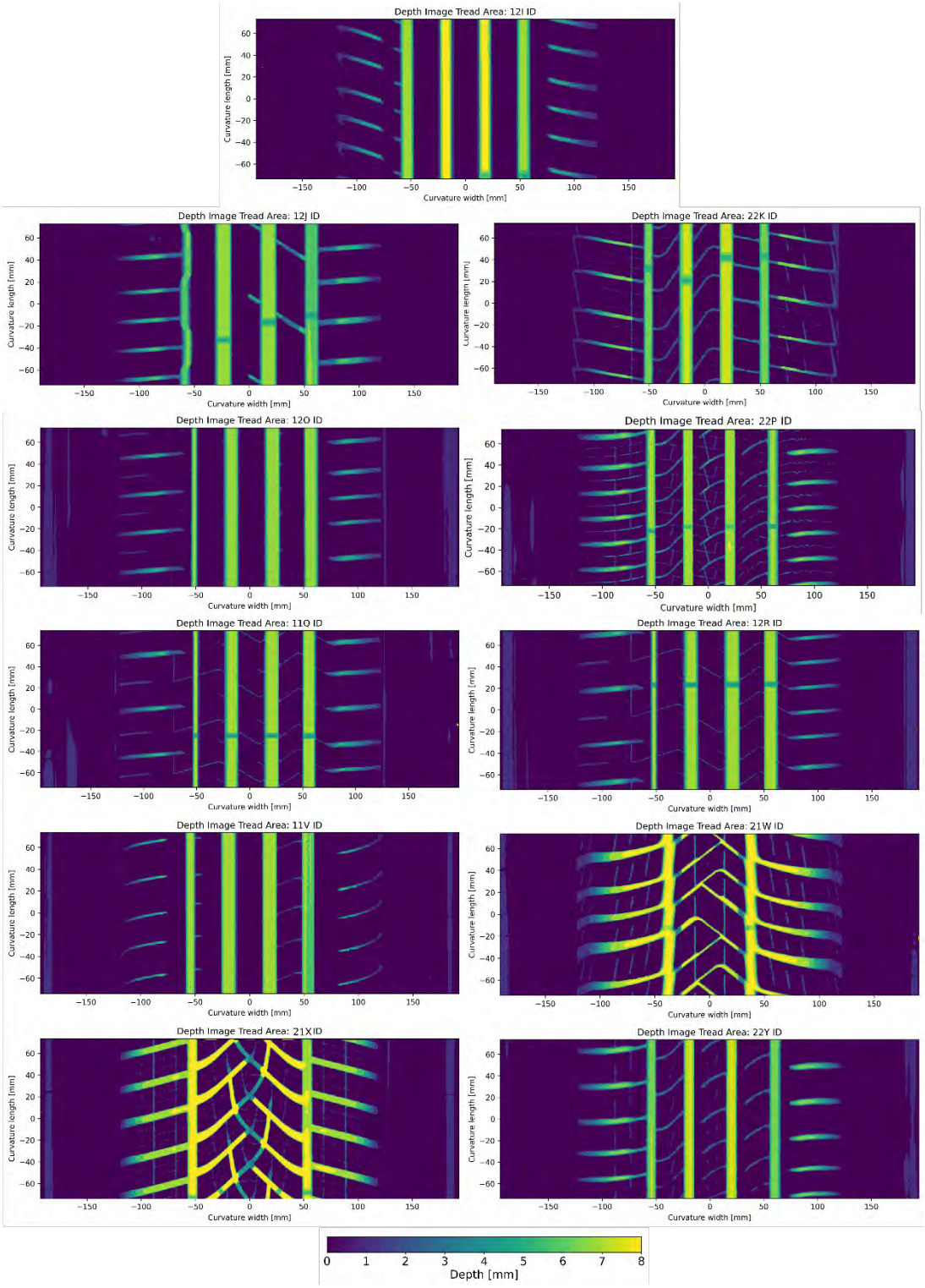

Fig. 8: Tread patterns of tires with IDs from 12I until 22Y.

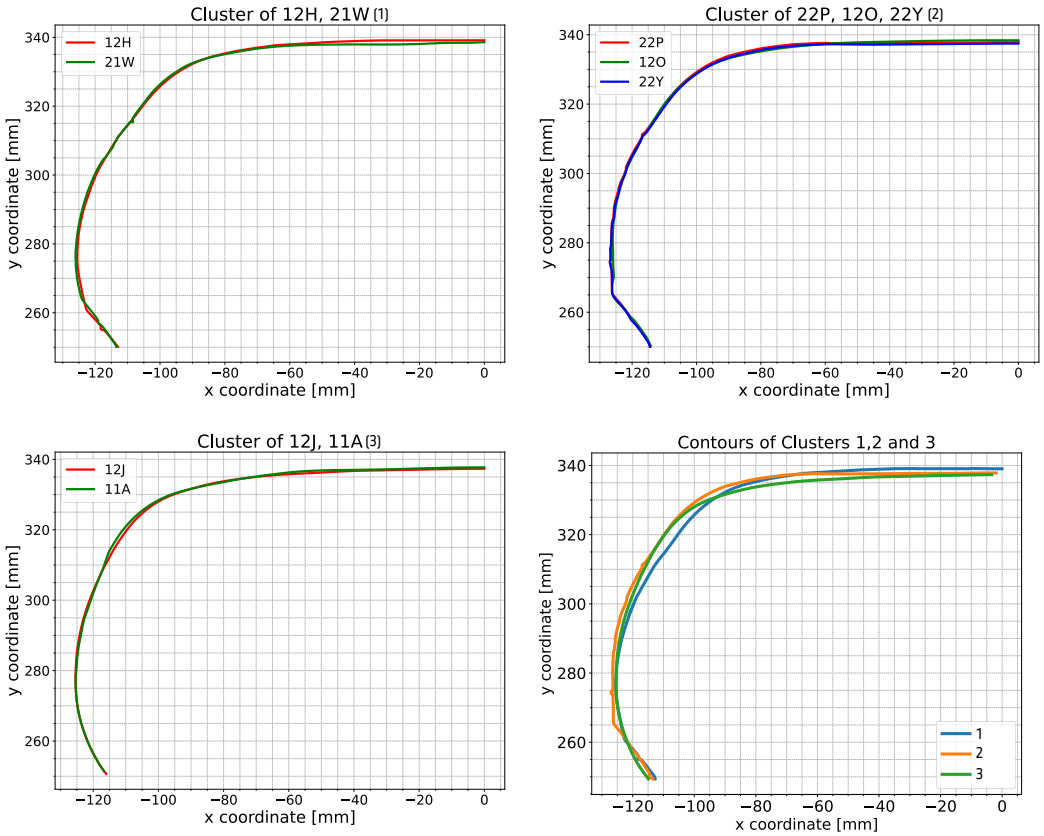

Fig. 9: Contour clusters and comparison between them.

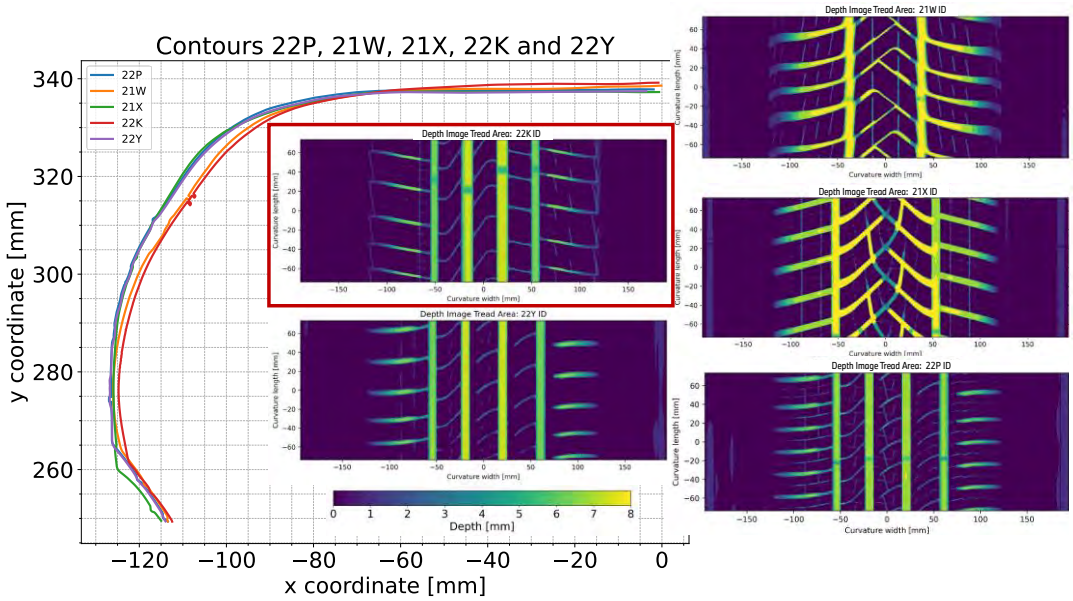

Fig. 10: Comparison of the contours and tread patterns of Winter an All-Season tires.

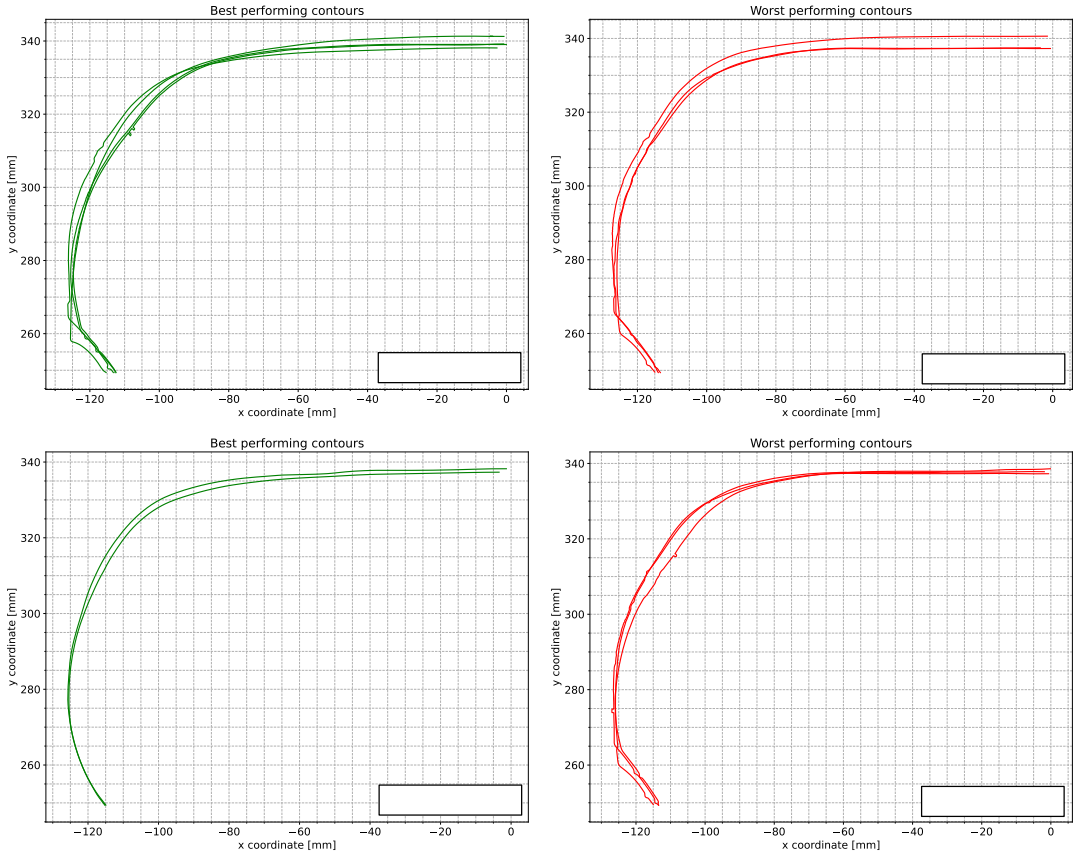

Fig. 11: Best and worst performing tire contours.

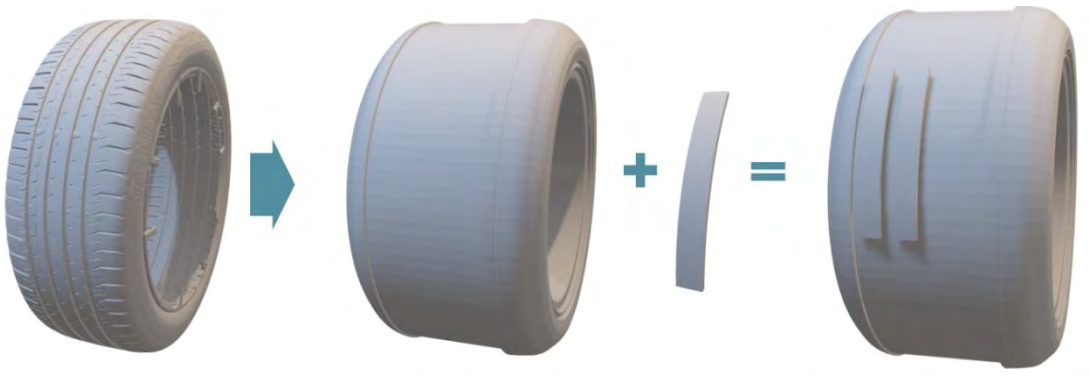

Fig.12: Concept of the modular tire.

Table 2. Base wind tunnel tests, including longitudinal tread width and depth.

Measuring Time-Averaged and Dynamic Surface Pressures on Passenger Car Wheels Using Fast-Response PSP

Jan Marcel Hübner, Dr. Sven Lange, Mathias Hähnel, Dr. Michael Hilfer

Aerodynamics Development
Volkswagen AG
Berliner Ring 2, 38440 Wolfsburg

Institute of Fluid Mechanics
Technische Universität Braunschweig
Hermann-Blenk-Straße 37, 38108 Braunschweig

jan.marcel.huebner@volkswagen.de
sven.lange5@volkswagen.de
mathias.haehnel@volkswagen.de
michael.hilfer@tu-braunschweig.de

Abstract
To enhance passenger car efficiency, reducing aerodynamic drag is crucial, with a significant portion of the drag arising from rotating wheels. Understanding surface pressures on a wheel rim, an area still largely unexplored, is essential for effective development of wheel-related measures. This paper introduces a method for measuring surface pressure on a wheel rim and adjacent body areas both across the whole area and transiently during driving and wind tunnel tests using Fast-Response Pressure Sensitive Paint (PSP). The experimental setup is detailed, covering components, paint characterization, the calibration method using pressure taps, and initial wind tunnel tests at 140 kph using a Volkswagen ID.7 production vehicle with stationary wheels. Measurements are conducted with a high-speed camera at 4000 fps using the intensity-based method with a continuous light source. Results include time-averaged and frequency information, demonstrating the method's capability to capture dynamic pressure distributions. Compared to traditional techniques, PSP offers significant advantages such as high spatial resolution and the elimination of the need for sensors on fast-rotating parts. These findings open new possibilities for understanding flow dynamics around tires, also providing valuable information for improving Computational Fluid Dynamics (CFD) simulations and ground simulation in wind tunnels. Future measurements will focus on rotating wheels in wind tunnel and on-road tests.

Contribution: 2025 FKFS Conference on Vehicle Aerodynamics and Thermal Management
15 – 16 October 2025 | Leinfelden-Echterdingen

1 Introduction

In the automotive industry, increasing environmental awareness, growing demand for electric vehicles with extended range, and stricter regulatory requirements have shifted the focus towards improving vehicle efficiency, particularly by reducing aerodynamic drag coefficients. Since the airflow around the wheels accounts for approximately $20 - 30$ % of the aerodynamic drag of an electric vehicle [1], there is a strong emphasis on gaining a deeper understanding of the flow phenomena around wheels and wheel housings. Due to the rotation and complex geometries (tire tread, rim), accurately capturing these flow phenomena is a complex measurement challenge. Additionally, replicating road-like flow conditions around the wheels in wind tunnels is difficult, especially near the ground. Modern automotive wind tunnels are therefore typically equipped with five-belt systems that simulate ground movement and wheel rotation.

This paper aims to establish a foundation for measuring surface pressures on wheels and adjacent body areas both on the road and in the wind tunnel. The goal is to gain deeper insights into the flow structures around the wheels and to evaluate how closely ground simulation in wind tunnels replicates real road conditions.

Previous studies [2] have for example identified frequencies in the vehicle wake that are attributed to the interaction between wheel rotation and the number of rim spokes. Numerous other works have focused on measuring flow fields around wheels in wind tunnels [1, 3, 4]. These studies revealed that wind tunnel ground simulation, for example through gap flows, influences flow structures around the wheels. However, to the authors' knowledge, surface pressures on rotating rims have not yet been measured, an approach that could provide even deeper insights into the flow field.

To address this gap and achieve a more precise understanding of the flow around rims, this study focuses on developing a measurement methodology capable of capturing high-resolution, time-resolved surface pressures on rims and surrounding body areas. Hilfer [5] demonstrated that pressure fluctuations can be measured on rotating geometries using pressure-sensitive paint. This technique is now being applied to passenger car wheels. Additionally, PSP was previously explored in automotive applications [6], finding it to be a very useful tool for flow diagnostics with an accuracy of $\pm$ 0.2 c_p (at high dynamic pressures between 1914 Pa and 2872 Pa). It is indicated, that for lower dynamic pressures, only qualitative measurements can be conducted. In collaboration with the Institute of Fluid Mechanics at TU Braunschweig, papers by Gregory [7] and Kasai [8] were identified, describing a paint capable of resolving small pressure differences of 30 Pa per brightness level and performing high-frequency measurements up to 2.2 kHz using a 12 bit high-speed camera. Building on that, it is the goal to be able to conduct quantitative measurements also for dynamic pressures around 930 Pa, corresponding to a freestream velocity of 140 kph. Based on simulation results indicating expected pressure ranges between -1200 Pa and 200 Pa in the wheel area, this paint was selected. The basis for the setup used in this work was laid in the master's thesis of Andreas Sieling [9].

2 Development of the Measurement Setup

The development of the setup for pressure-sensitive paint (PSP) measurements focused on ensuring usability both in wind tunnel and on-road tests, while delivering comparable data across both environments. Additionally, the setup should allow measurements at both the front and rear axles.

The measurement setup for PSP includes the paint itself, a high-speed camera, and UV LED spotlights. Both the camera and the UV LEDs must be directed at the surface coated with PSP. Accordingly, a setup was developed that enables both the high-speed camera and UV LED spotlights to be aimed at the wheel rim and adjacent body areas. The development process of this setup is described in the following sections.

2.1 Test Vehicle and Test Facility

The test vehicle used is a Volkswagen ID.7 (see Figure 1). The vehicle is equipped with 19-inch wheels. For the principle tests described in this paper, a 4 mm thick carbon disc was mounted on the front left rim to simplify the geometry.

Figure 1: ID.7 in the AAK.

The experimental investigations were conducted in the Aerodynamics-Aeroacoustics Wind Tunnel (AAK) located in Wolfsburg. The facility is a Göttingen-type aerodynamic wind tunnel specifically designed for full-scale vehicle testing. It features an open test section with a rectangular nozzle cross-section measuring $6.2\ \text{m} \times 3.86\ \text{m}$, corresponding to a cross-sectional area of $23.87\ \text{m}^2$. The maximum flow velocity used during the experiments was 140 kph, which corresponds to a Reynolds number of approximately 1.31×10^7 for a vehicle length of 4.96 m. The flow quality in the measurement section is characterized by a turbulence intensity of less than 0.2 % [10].

To realistically simulate road conditions, the wind tunnel is equipped with a 5-belt system. The central main belt (CMB) beneath the vehicle replicates the relative movement of the road, while four additional wheel drive units (WDU) under each wheel enable correct wheel rotation. Measurements were carried out at a constant air temperature of 22 °C and an ambient pressure of 101007 hPa.

2.2 Measurement Setup Concept

The measurement setup is designed to enable data acquisition at both the front and rear axles. Additionally, it aims to capture flow information upstream and downstream of the wheel, as well as directly on the rim surface. The basic concept of a setup that fulfills these requirements is illustrated schematically for the front axle in Figure 2. The same configuration is intended to be used at the rear axle as well, although the measurements in this study are exclusively conducted at the front axle.

Figure 2: Concept of the measurement setup enabling PSP testing on the road.

The illustrated concept consists of a modular structure comprising a support wing and a measurement pod, allowing for quick installation and removal. The setup can be mounted either in the engine compartment or behind the rear seat. The measurement pod is designed to house both the UV LED spotlights and the high-speed camera. To minimize the frontal area of the pod, the camera is installed longitudinally, and its field of view is redirected via a mirror.

2.3 Design of Support Arm and Measurement Pod

Several factors were considered when determining the distance between the measurement pod and the vehicle, particularly the influence on the airflow around the wheels, which decreases with increasing distance to the vehicle, as well as the torque acting on the vehicle and the measurement pod's proximity to the shear layer of the wind tunnel. In its final configuration, the distance is set to 1100 mm. To minimize aerodynamic interference and reduce vibrations in the measurement pod and support arm, both components were covered with streamlined bodies.

The aerodynamic influence of the setup was also evaluated using CFD simulations (see Figure 3). The results show that while the setup does affect the static pressure field on the vehicle and the rim, especially around the support wing, the pressure difference on the rim and in the upstream and downstream regions is altered by a maximum of $\Delta c_p = \pm 0.02$.

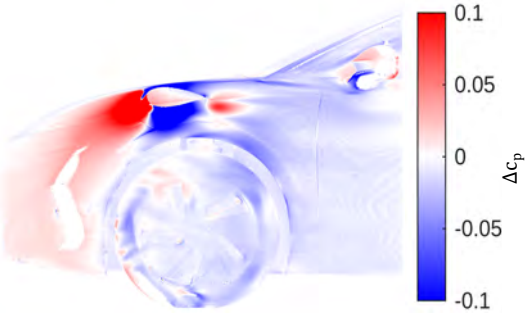

Figure 3: Difference in Δc_p between a CFD simulation with and without the support wing and measurement pod.

2.4 Optics

Inside the measurement pod, the camera and its optics are installed. The camera records at 4000 fps with an exposure time of 247 µs and a 12 bit resolution (4096 brightness levels). Accordingly, one brightness level corresponds to a normalized intensity of 2.44×10^{-4}. Combined with the paint's pressure sensitivity of 0.08 % / 100 Pa, this results in a pressure resolution of approximately 30 Pa per brightness level of the camera. A bandpass filter with a peak transmission at 650 nm is mounted in front of the lens. This ensures that the camera captures only the light emitted by the paint (650 nm). To ensure that the light illuminating the paint originates solely from the LED spotlights (395 nm), bandpass filter glasses are also placed in front of the spotlights, selected for peak transmission at 395 nm.

2.5 Spotlights

For the UV LED spotlights aimed at the measurement area, key requirements include sufficient light output, uniform illumination, and consistent light quality to prevent interference frequencies from being captured by the camera, which could negatively influence unsteady measurement results. To ensure adequate lighting and uniform coverage, four spotlights are positioned to illuminate the measurement area. During reference recordings, where only the UV LED spotlights are active, a frequency analysis using FFT was performed to assess the influence of the spotlights on the measurement results. The resulting amplitudes are plotted against their corresponding frequencies in Figure 4. The analysis shows that the baseline noise generated by the

LED spotlights is below 0.5×10^{-4}, which is five times lower than the resolution threshold (red line in Figure 4).

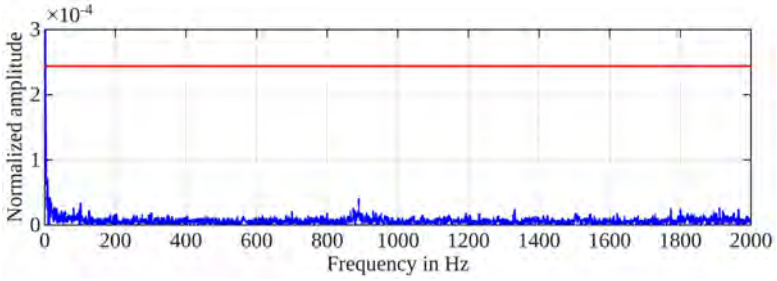

Figure 4: FFT analysis of the UV LED spotlights during a reference measurement. Red line marks normalized intensity of one camera brightness level.

2.6 Wall Pressure Taps

To calibrate the PSP measurements, which only provide relative pressure changes, against absolute values, wall pressure taps are distributed across the wheel arch. The pressure taps, each with a diameter of 0.8 mm, are connected to the pressure measurement system via vinyl tubing.

2.7 Complete Setup

All these components were assembled for the measurements. The complete setup is shown in Figure 5.

Figure 5: ID.7 in the AAK including measurement equipment.

In the right image, the Plexiglas window through which the camera views the measurement area is visible in the center of the pod. Surrounding the window are the four UV LED spotlights. When these are switched on and the wind tunnel lighting is turned off, the setup appears as shown in Figure 6.

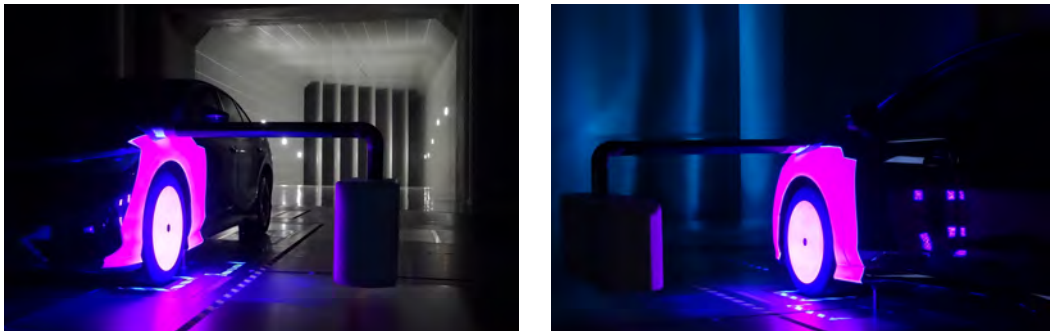

Figure 6: Setup in the AAK with activated UV LED spotlights.

3 Experimental Method

The following section describes the experimental procedure for conducting and evaluating the measurements. First, the test sequence is outlined, followed by the methodology used to analyze the PSP measurements.

3.1 Test Procedure

Once the vehicle is positioned in the wind tunnel as shown in Figure 5, the procedure is as follows: After the airflow velocity reaches 140 kph, pressure measurements via wall pressure taps are initiated, the LED spotlights are switched on, and the camera is triggered to record the measurement (4000 fps, 247 µs exposure time, 4096 frames). After recording, the LED spotlights are turned off and the pressure measurement via taps is stopped. The acquired frames are then saved. It must also be ensured that a reference measurement is recorded under known ambient conditions, which allows the actual frames to be corrected for disturbances such as uneven illumination. For the scope of this paper, all measurements are conducted with stationary wheels.

3.2 Evaluation Method for Pressure-Sensitive Paint

A representative raw image from a recorded measurement is shown in Figure 7. It illustrates that the camera captures only the light emitted from the painted surface, as intended. The following describes the methodology for converting the measurement data into a time-averaged pressure field, followed by the approach used to evaluate initial unsteady results.

Figure 7: Raw image from the PSP measurement.

To obtain the time-averaged pressure field, all frames are aligned, so there is no frame-to-frame movement. Then, both the measurement and reference frames are time-averaged and the measurement is normalized, resulting in a normalized intensity distribution. This distribution is scaled using the time-averaged values from the wall pressure taps (in situ and interea calibration), producing a spatially resolved, time-averaged pressure field. To extract unsteady pressure information, each frame of the measurement is normalized individually. The entire frame-wise normalized measurement is then analyzed using FFT (Fast Fourier Transform). This yields frequency maps, which can be evaluated for each frequency of interest (up to 2000 Hz at 4000 fps). These maps allow the identification of vortex footprints via regions of elevated amplitude, and the assignment of corresponding frequencies to the vortices.

4 Results and Analysis

The following section presents and analyzes the results obtained from the PSP measurements. For scaling and validation purposes, the time-averaged pressures from the wall pressure taps are used. Additionally, simulations (Volkswagen standard setup [11]) are conducted to compare with the experimental results. These simulations are briefly described below.

4.1 CFD-Simulation

In Figure 8 a), the separation zones around the ID.7, including the measurement setup, are identified via CFD simulation. Notable features include the separation at the air curtain (1), the tire wake vortex (2), vortices detaching at the wheel spoiler (3) and (4), and vortices occurring in the upper region of the wheel and wheel housing (5) and (6). In the time-averaged static pressure field shown in Figure 8 b), the footprints of vortices (2), (4), (6), and (7) are particularly visible. These will now be compared with the PSP measurements.

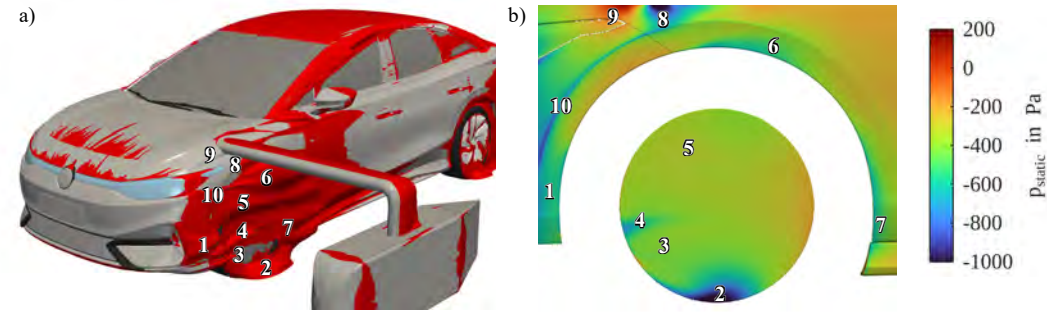

Figure 8: a) Separation zones around the ID.7 with stationary wheels and discs mounted on the rims. b) Static pressure field (both CFD simulations).

4.2 PSP Measurements

The evaluation of the PSP measurements is divided into time-averaged (steady) and unsteady results. The analysis of the time-averaged images follows the procedure described in Section 3.2. The normalized intensity field is scaled using the pressure values from the wall pressure taps. The linear fit used for this scaling is shown in Figure 9, indicating a pressure sensitivity of 0.17 % / 100 Pa. This implies that one brightness level of the camera corresponds to a pressure change of approximately 15 Pa.

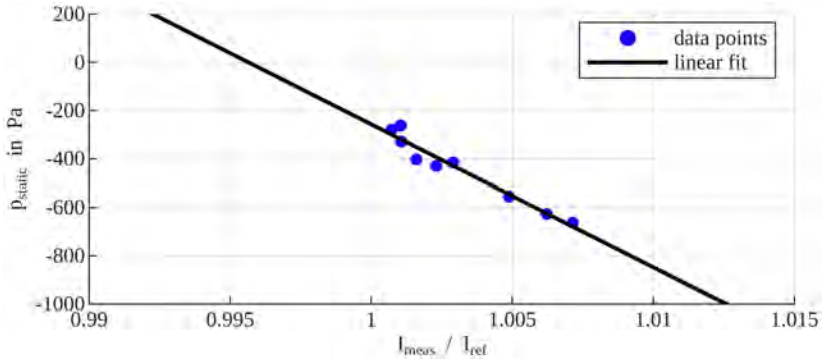

Figure 9 : Linear fit between the static pressure from wall pressure tap measurements and the corresponding normalized light intensity.

The resulting time-averaged static pressure field is shown in Figure 10, with the wall pressure tap values marked (black-bordered points). It is evident that the pressure field measured via PSP closely matches the values obtained from the wall pressure taps. The maximum deviation between a tap and its corresponding PSP value is approximately 50 Pa, which corresponds to a Δc_p of about 0.05.

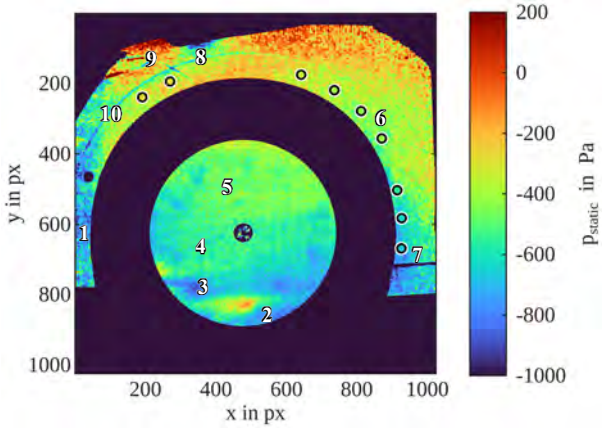

Figure 10: Time-averaged, static pressure field from the pressure-sensitive paint measurement.

When compared to the pressure field from the CFD simulation, key features such as the acceleration of the flow around the wing profile in the upper image area (8), the stagnation pressure region in front of the wing (9), and the low-pressure zone on the edge of the wheel arch to the left of the wheel center (10) show good agreement. The pressure distribution along the wheel arch, moving clockwise, is also comparable, although the exact positions of individual vortex footprints differ slightly between the measurement and simulation. Comparing these vortex footprints reveals that the separation zone around the air curtain (1) is more present in the experiment than in the simulation. Additionally, the separation caused by vortex (6) appears spatially lower in the experiment, and the footprint of vortex (7) is more distinct and extends further downward. These experimental findings on the wheel arch are supported by the wall pressure taps, which align with the PSP intensity gradients. On the disc, another difference between simulation and experiment is observed: while the footprint of vortex (4) is more prominent in the simulation, vortex (3) appears stronger in the experimental data. The origin of these discrepancies is currently unclear and will be the subject of future investigations.

This section focuses on pressure fluctuations to identify vortex footprints and their associated frequencies on the body and disc. As examples, Figure 11 a) shows a region on the body fluctuating at $36 - 37$ Hz, and Figure 11 b) shows a region on the disc fluctuating at $23 - 24$ Hz, demonstrating the setup's capability to detect such phenomena. At $36 - 37$ Hz, a separation is observed in the upper right area of the wheel arch, likely corresponding to vortex (5), assigning it this frequency. At $23 - 24$ Hz, a region of fluctuating pressure is found in the lower right area of the disc, presumably caused by reattachment of flow that separates at the lower front edge of the tire. Detailed evaluations of these phenomena will be addressed in future work.

The yellow areas in the outer body regions in both images (a + b) show a broadband camera noise across all frequencies due to the decrease in signal intensity towards the outer regions.

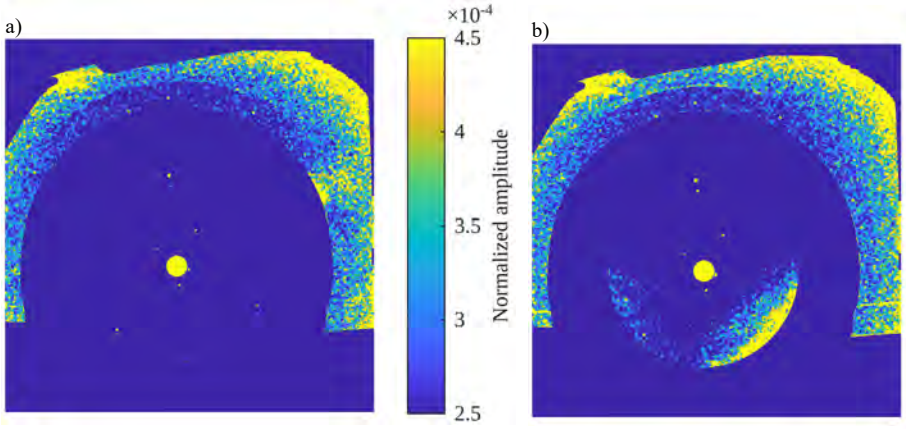

Figure 11: Frequency maps from the PSP measurements:
(a) $36 - 37$ Hz and b) $23 - 24$ Hz.

5 Summary and Outlook

This paper presents a measurement setup that enables the use of pressure-sensitive paint (PSP) to measure surface pressures on the rims of rotating wheels and adjacent body areas of a passenger car, both in wind tunnel and on-road tests. Furthermore, it includes initial evaluated principle measurements with stationary wheels, where a disc was mounted on the rim to simplify the geometry. The PSP was applied to this disc and the surrounding body surfaces.

In summary, the successful use of fast-response PSP in our setup was demonstrated, which opens new possibilities for spatially resolved, time-averaged, and unsteady surface pressure measurements. The accuracy of these initial principle tests was evaluated both qualitatively and quantitatively, with maximum deviations of 50 Pa between wall pressure taps and PSP measurements, which corresponds to $\Delta c_p = \pm 0.05$ for dynamic pressures of approximately 930 Pa. It was shown that PSP can be used not only to measure averaged pressure fields but also to capture unsteady pressure fluctuations, allowing the assignment of frequencies to individual flow structures.

Future work will focus on measurements with rotating wheels to gain detailed insights into surface pressures on the rims and adjacent body areas, both averaged and time-resolved. Building on this, measurements will be conducted in both wind tunnel and road environments to identify, understand, and evaluate differences caused by ground simulation using five-belt systems. Furthermore, this promises high-quality data to further improve CFD simulations.

6 Reference list

[1] J. Hurlbrink, „Analyse der aerodynamischen Verlustmechanismen der Radhausströmung von Pkw und Entwicklung von Maßnahmen zur Luftwiderstandsreduktion," 2022.

[2] Krüger, L., Joksimovic, I., Wegt, S., Burgbacher, J. et al., "Influence of Wheel Wake on Vehicle Aerodynamics: An EddyResolving Simulation Study," SAE Technical Paper 2023-01-0842, 2023, doi:10.4271/2023-01-0842.

[3] D. Möllenbeck, A. Fischer und H. Schmidt, „Impact of Wheel Drive Unit Secondary Flows on the Aerodynamics of Passenger Cars," (2024), In: Kulzer, A.C., Reuss, HC., Wagner, A. (eds) 2024 Stuttgart International Symposium on Automotive and Engine Technology. ISSYM 2024. Proceedings. Springer Vieweg, Wiesbaden. https://doi.org/10.1007/978-3-658-45018-2_3.

[4] E. Josefsson, M. Urquhart und S. Sebben, Influence of Wheel Drive Unit Belt Width on the Aerodynamics of Passenger Vehicles, SAE Technical Paper 2023-01-0657, 2023, https://doi.org/10.4271/2023-01-0657.

[5] M. Hilfer, M. Behn, C. Klein, T. Ahlefeldt, U. Tapken, L. Katzenmeier, L. Koop und L. Enghardt, „Near-field measurements of stationary and rotating in-duct sound sources with pressure sensitive paint," 2022, https://doi.org/10.2514/6.2022-3056.

[6] E. Duell, D. Everstine, R. Mehta, J. Bell und M. Perry, „Pressure-Sensitive Paint Technology Applied to Low-Speed Automotive Testing," SAE International, 2001.

[7] J. W. Gregory, H. Sakaue, T. Liu und J. P. Sullivan, „Fast Pressure-Sensitive Paint for Flow and Acoustic Diagnostics," Annual Review of Fluid Mechanics, 2014, doi: 10.1146/annurev-fluid-010313-141304.

[8] M. Kasai, A. Suzuki, Y. Egami, T. Nonomura und K. Asai, „A platinum-based fast-response pressure-sensitive paint containing hydrophobic titanium dioxide," Sensors and Actuators A: Physical, 2023, https://doi.org/10.1016/j.sna.2022.114140.

[9] A. Sieling, „Entwicklung einer Messmethode zur instationären Messung des Druckfeldes auf einer rotierenden Felge und dem angrenzenden Karosseriebereich im Windkanal- und Freifahrtversuch," 2025.

[10] TÜV NORD Mobilität GmbH und Co. KG, „Inspection of measuring and test equipment Aerodynamik-Aeroakustik-Kanal (AAK) at Volkswagen AG Wolfsburg," 2023.

[11] J. M. Hübner, M. Hähnel, S. Dr. Lange und M. Lemke, „Computational Method to Determine the Cooling Airflow Utilization Ratio of Passenger Cars Considering Component Deformation," SAE Technical Paper 2024-01-2975, 2024, doi:10.4271/2024-01-2975.

Efficient Hybrid Approach for Vehicle Soiling Simulations

MSc, K. Posch

Advanced Engineering
Magna Steyr Fahrzeugtechnik GmbH & Co KG
Liebenauer Hauptstraße 317, 8041 Graz

kevin.posch1@magna.com

Abstract:

Vehicle soiling refers to the accumulation of water, snow, or other contaminants on the surface of a vehicle. Vehicle soiling does not only impact appearance – in fact it can considerably impede safety, for example when the visibility of the exterior rearview mirror is obstructed. Soiling can also have a huge negative impact on the function of sensors resulting in severe impairments or even complete failure of Advanced Driver Assistance Systems (ADAS). Up till now, simulations for soiling were too time-consuming, expensive or inaccurate to be applied to a vehicle project. Soiling tests in the wind tunnel can be performed only at a very late stage of development after initial prototypes of the complete vehicle are available. In an aerodynamic development process that was developed over many years, Magna has integrated new approaches that combine simulations and tests to tackle challenges of the vehicle's passenger safety and system safety successfully. A hybrid simulation approach was deployed to optimize costs and development time while concurrently facilitating a stable basis for vehicle and system functions in complete vehicle development.

1 Simulation of complete vehicle soiling

In complete vehicle development, a differentiation is made when it comes to cause between foreign soiling and soiling caused by the vehicle itself (self-soiling) as is shown in Figure 1. Dirt whirled up by vehicles driving in front as well as snow and rain come under the category of foreign soiling. Self-soiling refers to dirt or precipitation whirled up by the vehicle itself. This differentiation is taken into consideration in the newly developed simulation process and modeled as realistically as possible.

Contribution: 2025 FKFS Conference on Vehicle Aerodynamics and Thermal Management
15 – 16 October 2025 | Leinfelden-Echterdingen

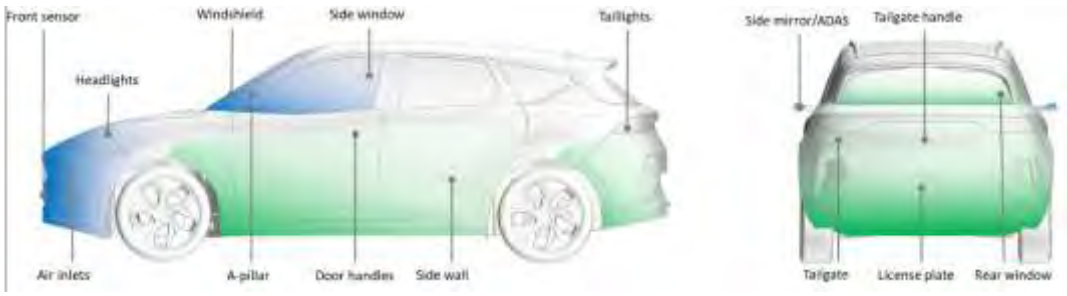

Figure 1: Vehicle areas affected by self-soiling (green) and foreign soiling (blue)

Water is used as a medium for soiling in these investigations. Just like in a wind tunnel test, a matrix of injectors in front of the vehicle is modeled in the simulation of foreign soiling to bring a defined quantity of water into the flow field and distribute it evenly. Modeling the wheel as the source for self-soiling is far more complex. Magna has developed a model for this based on the geometric data of the tire and data from measurements [1, 2] and calculates the mass ratios of different injection areas, injection speed, injection direction and distribution of the diameters of drops at each injection position. To model the trajectories of airborne water drops, this data is used for the injection of Lagrangian particles in the Simcenter Star-CCM+ simulation software. It models the drops as point masses, which are computationally efficient and robust. To validate the model, measurements done by Spruß [3] were used. Figure 2 shows a good match between the model and soiling tests in a wind tunnel.

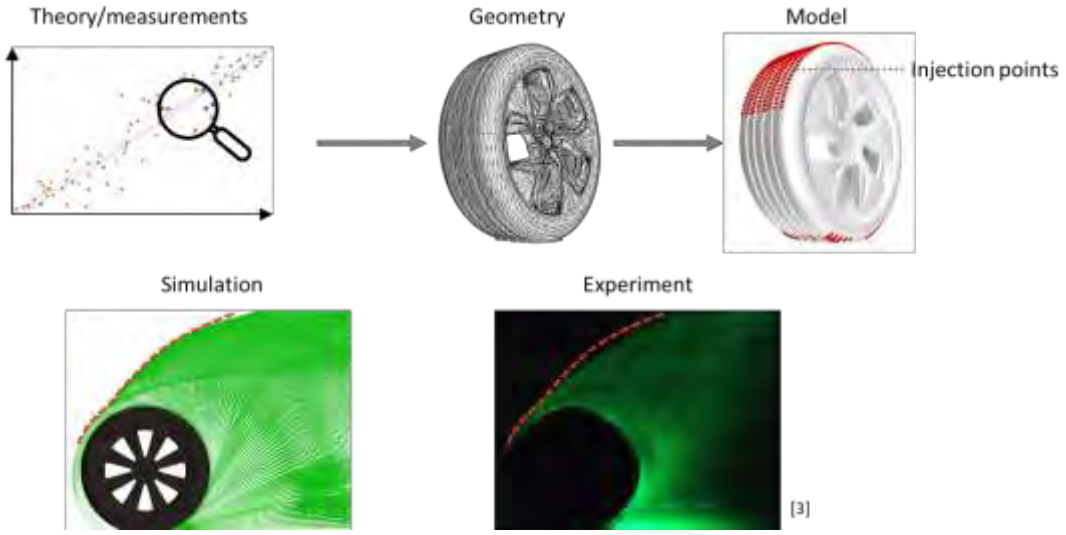

Figure 2: Modelling of the simulation (top) and comparison between simulation and experiment (bottom)

The modeled injectors are integrated in the vehicle aerodynamics simulation. This detailed simulation contains around 200 million cells in which the flow in the boundary layer is tracked accurately using the low Y+ approach and a Detached Eddy Simulation (DES) turbulence model. For the simulation of the soiling, it is essential that the areas close to the wall are tracked as exactly as possible. The injected Lagrangian phase is connected with the Euler phase by a one-way coupling, i.e. the air is not influenced by particles. According to Sommerfeld et al. [4], this simplification is acceptable up to a volume fraction of 1*10-6. In tandem with the aerodynamic forces and momentums, the soiling of the complete vehicle can also be calculated. This increases the simulation time by only 25 %. During the simulation, it is recorded where and how many particles hit the area on average; this in turn allows for calculating the average incident mass flux field across the complete vehicle, Figure 1Figure 3.

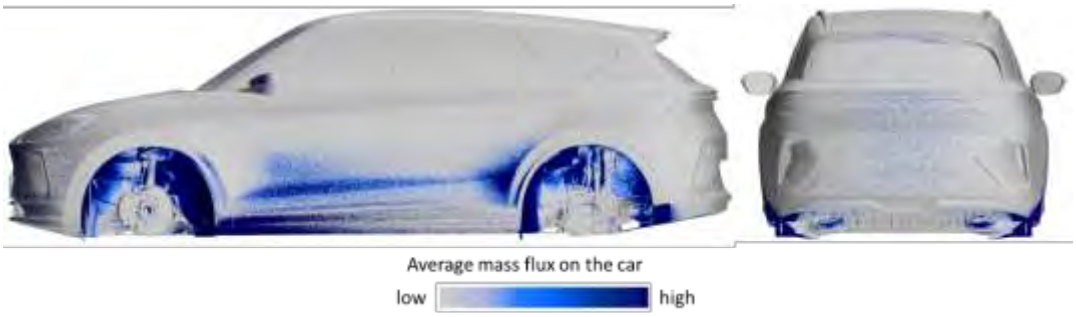

Figure 3: Average mass flux distribution on the body due to self-soiling and foreign soiling.

The slight additional effort makes it possible to compare different variants quickly and easily. Based on these simulation results, the positioning of sensors and cameras can be decided in early project phases, the soiling rate of the rear window and rear lights can be optimized and the side wall and door handle soiling assessed. A huge advantage of the simulation compared to real measurements is the opportunity to do a detailed soiling analysis. By tracking the trajectories of Lagrangian particles the source of the soiling can be determined. This creates a clear trajectory along which measures to improve the resulting pollution can be derived. Moreover, the simulation provides a basis for deciding on what areas a detailed study of the vehicle soiling should be done.

2 Detailed study in the submodel

To analyze the soiling of specific areas in greater detail, submodels are used which use the information gained from the soiling simulation of the complete vehicle and are roughly ten times samller. To illustrate this, the soiling of the side mirror and how it affects the resultant soiling of the side window are considered as an example. The degree of modeling must be significantly increased for these detailed examinations. In addition to the Lagrangian particles/phase and the air as Euler phase from the simulation of the complete vehicle, two more Euler phases are added in the submodel, depicting the water based on different approaches. The first is the fluid film model, a 2-D approximation of wall-bound water [5]. This model is useful in places where the water drops or water films on the surface are small compared to the geometric form of the body. Studies performed at Magna showed that this model provides good results for slightly curved surfaces and, if additional models are used to describe the detachment, also for sharp convex edges. For strong curves, for example the rear edge of a side mirror, the approximations of the fluid film model are no longer valid [6]. The second model is used in these areas: The so-called Volume of Fluid model depicts the flow characteristics of the water far more accurately than the fluid film model, thus providing better results. However, this advantage means heightened requirements for the mesh, smaller time steps and thus a greater calculation effort [7]. A typical side mirror soiling simulation needs around 130000 CPUh to simulate 3s of physical time. The four phases presented together constitute a hybrid simulation approach for solving the complex problem of vehicle soiling as efficiently as possible. This is necessary especially because the iteration cycles are short in the early phases of vehicle development. In addition to the phases, the contact angle of the surface must be taken into consideration. It determines how a surface is wetted by the water and depends a greatly on the material. Especially in concept development, this parameter is still unknown. During this phase, Magna relies on its experience to choose the right values. The trajectory of a water drop on a side mirror is simulated in the hybrid approach as follows: Initially the drop is injected in the submodel as a Lagrangian particle. When the drop hits the surface of the side mirror, several scenarios may occur. The drop can adhere completely to the surface; it may splashes on the surface, partially adhere to the surface and bounce off as smaller droplets; or it bounces off completely. Drops that bounce off can then hit the side window or fly out of the submodel's domain. Drops that adhere to the surface are transformed into a fluid film. On slightly curved surfaces, the drop then flows along the side mirror until it hits a zone where it must be transformed in the Volume of Fluid model. This usually takes place on the rear end of the side mirror. If the drop does not flow back in a fluid film zone and is transformed back, it often accumulates with several drops at the back edge, until the water detaches from the side mirror. After drops have completely detached from the mirror, they are transformed into Lagrangian particles again. From there, the drops then follow the air flow again until they either hit a surface again or fly out of the calculation domain. Figure 4 shows what the phases look like in the simulation.

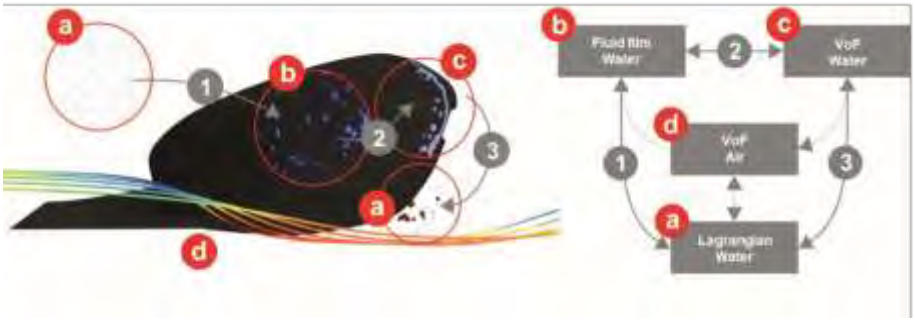

Figure 4:The simulated path of the water on the side mirror is shown on the left. The pattern of couplings and combinations in the hybrid simulation approach is depicted on the right.

With this simulation, local water accumulations and their detachment can be predicted accurately, different geometrical variants can be compared with each other, and risks detected. This provides a good basis for the optimization of soiling behavior. The differences between the variants, for example in the side mirror housing geometry, can be analyzed based on objective factors and thus be analyzed qualitatively. The focus here is on the analysis of the mirror glass and the core areas of the side window. Figure 5 shows the good match of the simulation results with real tests in the soiling wind tunnel. As in the real test, the water accumulates at the rear area of the side mirror and behind the parking assistant camera at the bottom (marked with green circle), flows to the bottom and detaches at the bottom edge of the mirror housing (marked with red ellipse). The soiling of the side window by the splash and spry from the side mirror also matches the real test.

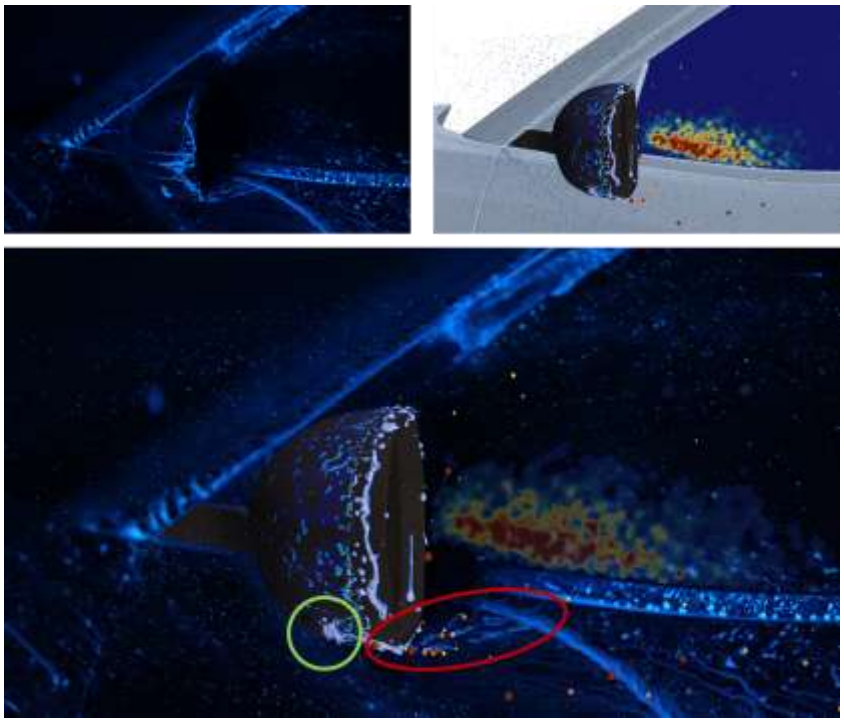

Figure 5: Top: Simulation and test results of side mirror and side window soiling. Bottom: Simulation and test superimposed.

3 Summery and outlook

The complete vehicle simulation presented here offers a good overview of the critical areas of soiling entailing little additional effort in the standard aerodynamics simulation. The multistage simulation process that was developed uses detailed submodels where detailed examination is necessary and simple modeling methods are no longer accurate enough. With this hybrid simulation, Magna has developed an approach that meets the requirements for state-of-the-art vehicle development with respect to quality, time and costs. The virtual development via simulation is supported by wind tunnel tests over various hardware generations. Thus, Magna can develop not only the traditional areas for keeping visibility clear – such as for the side window, side mirror and rear window – but also for side walls, doors, handles, rear lights, ADAS sensors, for example, on the complete vehicle. Thus, development risks continue to be minimized and key functions such as aerodynamics, aeroacoustics and soiling are optimally balanced. The hybrid simulation approach presented here has become possible in recent years because computing power has vastly increased, and new modeling methods have been developed. Yet not all soiling topics can be simulated at present. The simulation of the overflow of the A-pillar as a major cause of side window soiling cannot be done in a reasonable time frame with the method described here. Just how complex such simulations are was shown by Demel [8]. The transition from the traditional, mesh based computational fluid dynamics simulation to the smoothed particle hydrodynamics method might be a possible alternative here.

4 Reference list

[1] Strohbücker, V.: Untersuchung des Tropfenaufwirbelvorganges im Rahmen einer Gesamtfahrzeugeigenverschmutzungssimulation in Versuch und Simulation. Wiesbaden: Vieweg, 2021

[2] Flintsch, G. et al.: Development of a prediction model for splash and spray. Online: https:// vtechworks.lib.vt.edu/server/api/core/bitstreams/ 5457a741-3d30-4c05-96e6-5746b2febfab/ content, access: February 4, 2024

[3] Spruß, I.: Ein Beitrag zur Untersuchung der Kraftfahrzeugverschmutzung in Experiment und Simulation. Wiesbaden: Vieweg, 2015

[4] Sommerfeld, M.; van Wachem, B.; Oliemans, R.: Best practice guidlines for computitional fluid dynamics of dispersed multiphase flows. Online: https://www.ercoftac.org/publications/ercoftac_ best_practice_guidelines/dispersed_multi-phase_ flows_dmpf/, access: February 4, 2024

[5] Siemens (publisher): Simcenter STAR-CCM+ 2306 User Guide. 2023

[6] Posch, K.: Development of a CFD Process to prevent Water Soiling on ADAS Systems. Graz, Technical University, master's thesis, 2022

[7] Ade, M.: Development of a Numerical Methodology for Water Management Simulations of Passenger Cars. Darmstadt, Technical University, dissertation, 2019

[8] Demel, D.: Ein Beitrag zur Simulation der Sichtfreihaltung an Personenkraftwagen. Darmstadt, Technical University, dissertation, 2021

Advancing Wind Tunnel Vehicle Soiling Studies with a Realistic Dynamic Rain Simulation System

[1]Long (Tom) Li, [2]Wing Yi (Roxana) Pao, [1]Eric Villeneuve, [1,2]Keira Wilson, [1]Warren Karlson

[1]ACE Climatic Aerodynamic Wind Tunnel
[2]Faculty of Engineering and Applied Science
Ontario Tech University
2000 Simcoe St N, Oshawa, ON, Canada L1G 0C5

long.li@ontariotechu.ca
wingyi.pao@ontariotechu.net
eric.villeneuve@ontariotechu.ca
keira.wilson@ontariotechu.net
warren.karlson@ontariotechu.ca

Abstract: Rainfall is one of the most prevalent environmental challenges for road vehicles, impacting visibility and sensor performance. As automated features become standard in modern vehicles, ensuring sensor reliability in adverse weather is more critical than ever. Climatic wind tunnels provide controlled environments for vehicle soiling and sensor studies, but traditional spray nozzle systems lack independent control over rain characteristics, limiting their ability to replicate realistic rain conditions. Sensors such as cameras and LiDARs are highly sensitive to these parameters, requiring precise and repeatable testing for real-world validation. This paper presents a novel rain simulation system, the Vectorized Rain Simulation Apparatus (VeRSA), developed at Ontario Tech's ACE Climatic Aerodynamic Wind Tunnel. It employs vectorized water injection and controlled droplet dynamics to generate realistic rain conditions that can be characterized, repeated, and benchmarked. Demonstrations are provided through rain characterization, perception testing of cameras and LiDARs, and early-stage UV dye tracing for vehicle soiling analysis. By overcoming the limitations of traditional systems, VeRSA significantly enhances realism, supporting both academic research and commercial testing. This integrated approach marks a milestone in advancing weather-resilient ADAS and autonomous vehicle development.

Contribution: 2025 FKFS Conference on Vehicle Aerodynamics and Thermal Management
15 – 16 October 2025 | Leinfelden-Echterdingen

1 Introduction

The role of climatic wind tunnels in realistic soiling evaluation

Understanding how vehicles perform under real-world environmental conditions is critical, especially when it comes to visibility and sensor reliability. That's where climatic wind tunnel testing plays a key role. By simulating both aerodynamic forces and perceived precipitation, these facilities allow engineers and researchers to analyze how rain, spray, and dirt accumulate on vehicle surfaces – a process known as vehicle soiling.

There are three main ways soiling occurs, shown in Figure 1: primary soiling from precipitation, secondary soiling from spray generated by nearby traffic, and self-soiling from the vehicle's own tires on wet roads. Each type introduces unique challenges, particularly for ADAS and autonomous sensors that depend on clear, unobstructed views to operate effectively.

Climatic wind tunnels allow engineers to simulate and control a wide range of conditions – from droplet size and precipitation density and intensity. This capability makes it possible to evaluate vehicle and sensor performance under repeatable, realistic conditions, ultimately helping manufacturers design vehicles that stay cleaner, safer, and smarter on the road.

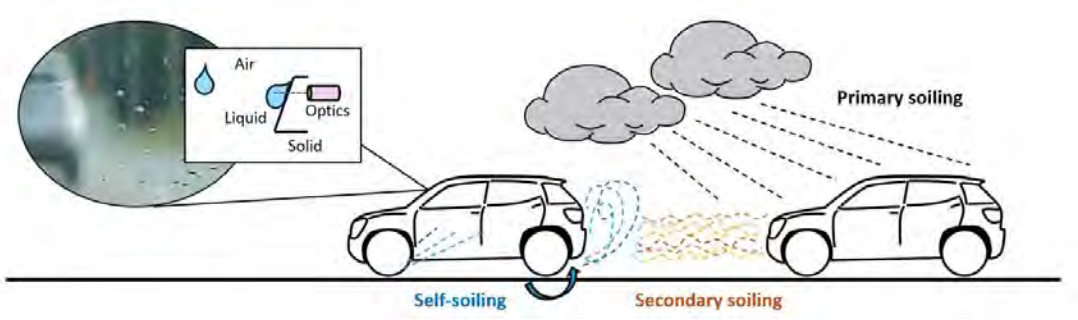

Figure 1: Schematic demonstration of vehicle and sensor soiling.

Why sensor testing in weather matters

Autonomous vehicles rely on a network of sensors to interpret their surroundings and make real-time driving decisions [1]. However, weather conditions can severely impact sensor accuracy and system performance. Cameras and LiDARs are highly sensitive to individual raindrops and water streaks; RADARs and ultrasonic sensors are more affected by snow and ice buildup. When any of these systems are impaired, so are crucial functions like collision avoidance, adaptive cruise control, lane-centering, and auto-steering. That's why it is essential to test these systems in controlled yet realistic conditions, ensuring they perform reliably, not just in perfect weather, but in rain, fog, and snow as well.

Meeting the demands of full autonomy

As industry moves closer to SAE Level 5 autonomy [2], the margin for error narrows. Weather remains one of the most complex variables to solve. To ensure consistent sensor performance, manufacturers must go beyond traditional testing approaches and adopt repeatable methodologies that replicate adverse weather scenarios.

Several testing methods have emerged, ranging from real-world driving to indoor simulation. While field testing provides valuable insights, it is time-consuming and vulnerable to unpredictable variables like wind gusts or sun glare. Outdoor proving grounds face similar limitations. This is where climatic wind tunnels offer a distinct advantage, allowing precise manipulation of wind, droplet size, and intensity, providing a faster and more consistent path toward validating autonomous systems for all-weather performance.

Evolving beyond traditional methods

Climatic wind tunnels have been in use since the mid-20th century, originally focused on simulating rain for aircraft wings, buildings, turbines, and vehicles. But today, the goal has shifted: it is no longer just about measuring water exposure, it is about understanding how rain affects sensor perception. Here, droplet size distribution becomes critical. For instance, tire spray and light rain may have similar overall intensity, but they affect visibility very differently due to the size, shape, and impact area of individual droplets. These characteristics must be captured accurately to reflect real-world driving conditions.

The challenge of creating realistic rain

Simulating rain in a climatic wind tunnel isn't simple. Several types of rain systems are commonly used, each with strengths and limitations: spray nozzle systems can cover large areas, but often produce excessively fine droplets at higher pressures, making them better suited for secondary soiling studies. Sprinkler systems suffer from significant pressure loss and lack fine control over droplet size and flow rate, making them less ideal for consistent sensor testing. Drop former systems create larger and more realistic droplets at lower pressures but often require heavy overhead reservoirs with limited adjustability.

As the demands of autonomous vehicle development continue to grow, so does the need for greater precision and adaptability in rain simulation systems. Addressing these challenges means rethinking how rain studies should be carried out.

Advancing ADAS sensor testing – toward industry benchmarking

To meet these challenges, this paper presents advanced methodologies and improvements to rain study strategies, offering a more robust and realistic framework for testing perception systems in climatic wind tunnels. As part of this contribution, the paper benchmarks best practices for sensor testing in wind tunnels, setting a new standard for evaluating environmental impact on vehicle perception. These advancements lay the groundwork for more weather-resilient, perception-aware vehicles, accelerating progress toward safe and reliable autonomy in all driving conditions.

2 Background Work

Proven methodology for sensor testing in controlled environments

Over the past several development cycles, we have established and refined a wind tunnel-based testing methodology tailored specifically for ADAS and autonomous vehicle sensor evaluation [3]. This work has laid key milestones in the field, combining academic rigor with real-world application to address the growing need for weather-resilient perception systems. There are two core components to this methodology: (1) realistic rain simulation and (2) representative sensor evaluation. This framework has been successfully applied in a number of studies, at the ACE Climatic Aerodynamic Wind Tunnel, focused on sensor soiling, visibility degradation, and performance loss, offering a robust platform for evaluating perception systems across a broad spectrum of use cases.

Bridging outdoor rainfall and controlled testing

To effectively design wind tunnel rain testing conditions, several fundamental questions must be answered – how much rain does a moving vehicle encounter? What are the characteristics of the rain events? – These questions form the basis of what we refer to as perceived precipitation, that is the rainfall conditions experienced by the vehicle as it moves through the environment, rather than simply what falls from the sky. Recreating this perceived precipitation accurately in a controlled environment is essential to producing realistic sensor soiling and performance outcomes.

To support the design of realistic and consistent wind tunnel rain conditions, a perceived precipitation intensity model was developed. This model was built using outdoor validation experiments, combining both dynamic on-vehicle measurements and static reference data from weather towers [4]. The model helps translate real-world rainfall conditions into wind tunnel parameters, considering driving speed, surface orientation and geometry, droplet size distribution, and crosswinds, demonstrated in Figure 2. Representative rain categories – drizzle, light, moderate, heavy, and downpour – were defined based on field data.

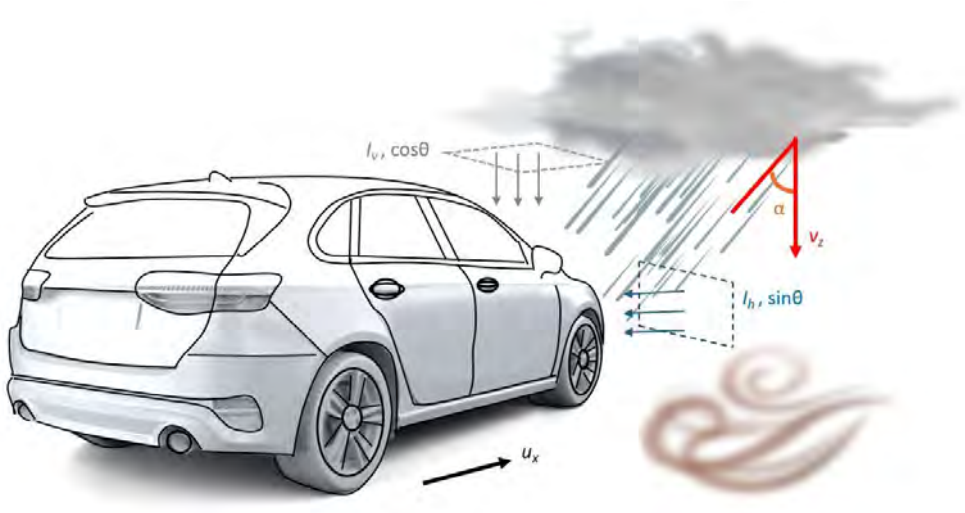

Figure 2: Schematic demonstration of perceived precipitation.

Evaluating sensor soiling and performance in wind tunnel testing

The rain testing methodology developed in our wind tunnel is designed to be scalable and flexible, ranging from sensor-level studies to full-vehicle evaluations with integrated ADAS systems. To quantify performance under rain exposure, we established a suite of objective metrics, tailored to both camera and LiDAR sensors.

A theoretical model was developed to estimate performance degradation based on incoming raindrop size distributions and surface wettability characteristics [5]. This model supports interpretation of experimental results by linking physical parameters to sensor behaviour.

With repeatable, and realistic rain testing capabilities, the test platform enables a variety of parametric studies, including the effect of surface materials on soiling [6], the evaluation of soiling mitigation strategies [7], and even sensor data training under controlled environmental variation [8]. Representative results from these studies are shown in Figure 3.

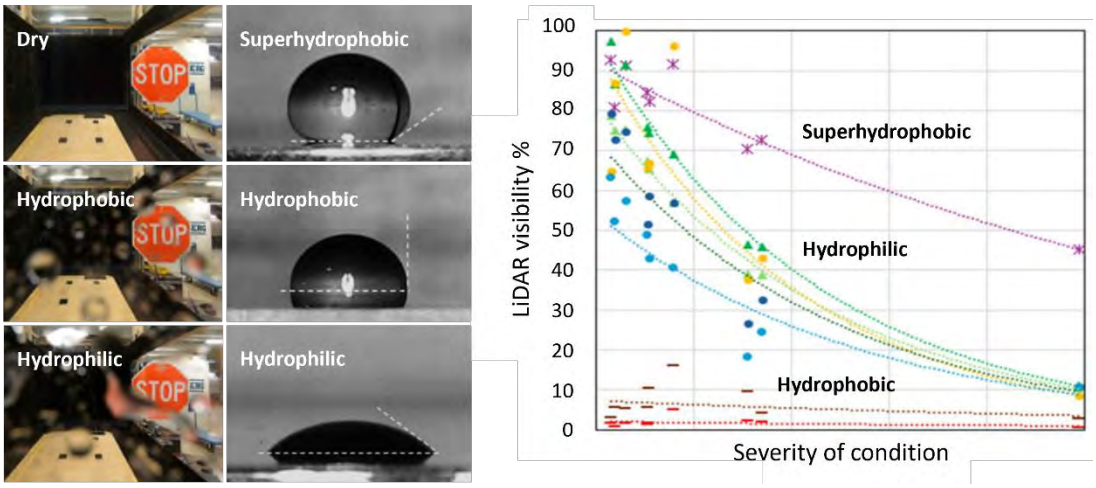

Figure 3: Sensor response varies by surface material in wet conditions.

The overall procedure for conducting ADAS sensor testing in the climatic wind tunnel includes:

1. Selection and calibration of the desired rain condition (based on perceived precipitation model);
2. Application of these calibrated rain profiles onto the vehicle or sensor setup;
3. Recording and analysis of the resulting sensor data.

Further advancements in methodology are discussed in Sections 3 and 4, including expanded rain characterization, integration with moving targets, and development of more advanced testing strategies for sensor evaluation. With growing understanding of both multiphase aerodynamics and sensor-environment interactions, we have broadened our wind tunnel testing capabilities to capture more realistic and complex driving scenarios, such as dynamic camera tracking and LiDAR target discrimination in adverse weather.

The following sections present a full-tunnel rain characterization and highlight practical examples of vehicle soiling and sensor performance evaluation for camera and LiDAR sensors under primary, secondary, and self-soiling conditions.

3 Full Tunnel Rain Characterization

The ACE Climatic Aerodynamic Wind Tunnel is equipped with the Vectorized Rain Simulation Apparatus (VeRSA), a system designed to reproduce realistic precipitation in both vertical and horizontal orientations. The “Ve” in VeRSA highlights the flexibility of this approach, where vertical rain can be combined with horizontal injection to recreate complex weather conditions that vehicles encounter on the road. Together, these systems make it possible to move beyond simplified water spray and deliver controlled, quantifiable rainfall for sensor testing and vehicle development. Figure 4 illustrates the vertical and horizontal rain system in operation, showing rainfall interaction with both the Laser Precipitation Monitor (LPM) and a vehicle positioned in the test section.

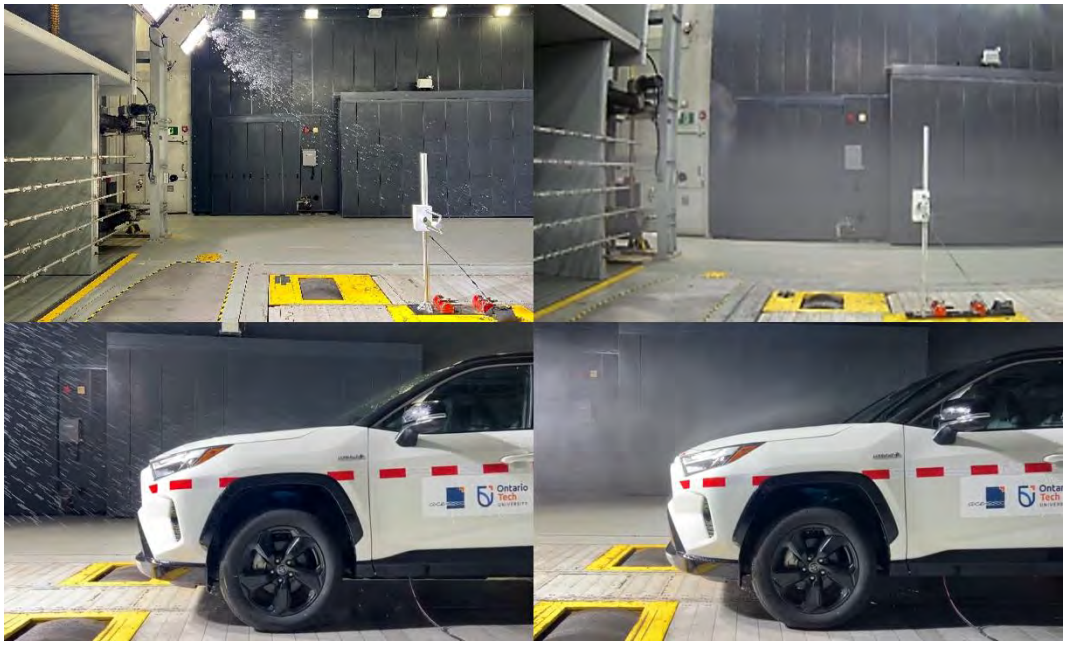

Figure 4: Vertical and horizontal rain system demonstration, with LPM and vehicle.

A full characterization of the rain system has been conducted in the jet symmetry plane, where y = 0 at the tunnel centreline. For the vertical rain configuration, parameters such as nozzle spacing, vertical and horizontal positioning, and flow rate were evaluated. For the horizontal rain configuration, nozzle selection, flow rate, and bar positioning at the nozzle exit plane were assessed. Representative results from these tests are shown in the performance envelopes of intensity and droplet size distribution at 50 km/h, providing a clear picture of how the system can be tuned to match desired conditions, presented in Figure 5.

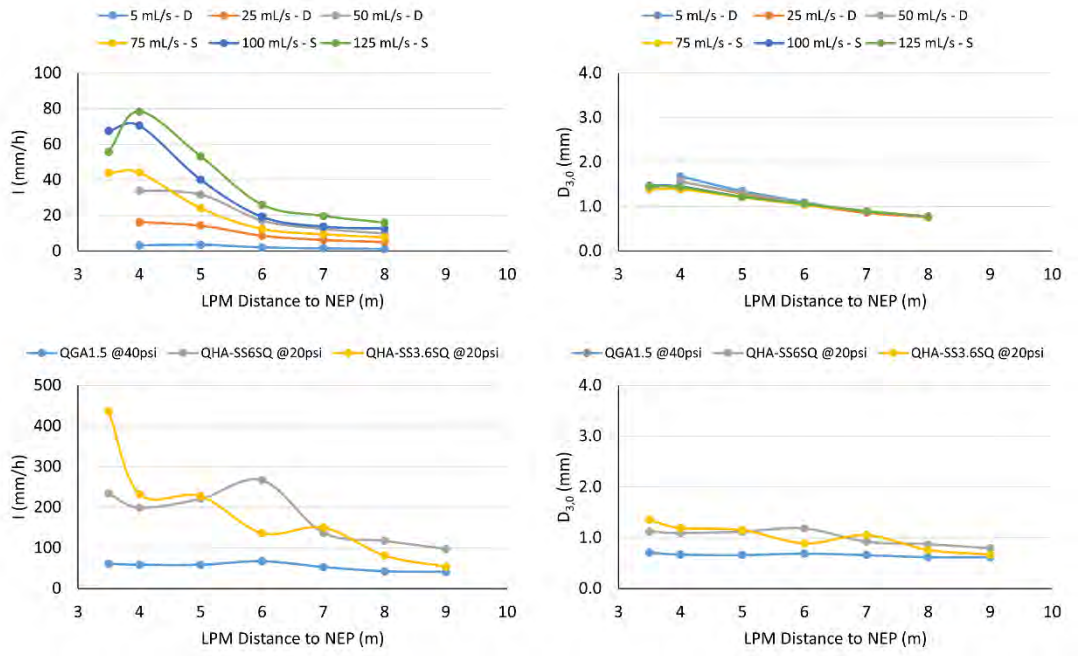

Figure 5: Rain characterization result samples at y = 0 symmetry plane, 50 km/h wind speed, presenting top left: vertical rain system intensity; top right: $D_{3,0}$ (mm); bottom left: horizontal rain system intensity; and bottom right: $D_{3,0}$ (mm).

The vertical system shows strong sensitivity to distance between the nozzle plane and the vehicle. This allows flexible positioning: shifting the vehicle one metre further downstream, for example, can be matched by moving the nozzle plane the same amount, maintaining consistent rain delivery while also opening space for additional equipment such as sensor targets. The horizontal system, in contrast, produces highly uniform droplet size characteristics across the flow field. Because the nozzles are mounted directly at the exit plane, the test vehicle can be positioned precisely where the target rainfall profile is achieved. This combination of adaptability and repeatability makes VeRSA a powerful tool for tailoring rain to different test scenarios.

Another important distinction lies in the behaviour of the two systems. Vertical rain is influenced by transient droplet breakup and coalescence as droplets travel through the air, leading to variations in distribution with distance. This sensitivity creates both challenges and opportunities. Larger droplets tend to arrive at shallower approach angles while smaller droplets follow steeper paths, which reduces uniformity across the full test section. At the same time, these dynamics make it possible to tune rain characteristics at a very specific local position, such as a sensor or windshield, broadening the range of achievable test conditions. By contrast, the horizontal system provides consistent volume mean droplet sizing ($D_{3,0}$) across the test section, enabling stable and predictable exposure conditions. Together, these complementary behaviours allow both realistic variability and highly repeatable uniformity to be recreated, depending on the testing objective.

The results shown here are only a small preview of the system's capability. VeRSA enables a wide range of realistic rain environments, from fine drizzle to heavy downpours, with droplet distributions and intensities that can be characterized, repeated, and benchmarked. In the following sections, sensor data will be presented to demonstrate why these rain characteristics matter, and how the ability to control them is critical for evaluating perception systems under adverse weather.

4 Vehicle and Sensor Soiling Evaluation

In this study, sensors were positioned inside the vehicle behind the windshield to evaluate performance under controlled rain exposure. Both cases, with and without a clearing device, were tested to represent common water management strategies. For each condition, the vehicle surface was first soaked for two minutes to reach a steady-state soiling level before sensor data collection. This ensured consistency across tests and reduced nonlinear effects caused by initial droplet accumulation. Transient performance during accumulation and clearing could also be analyzed in real time, providing a more complete picture of sensor behaviour under rain.

4.1 Camera

Camera evaluation was carried out at 50 km/h under three vertical rain conditions: drizzle at 1.7 mm/h, moderate rain at 24.0 mm/h, and downpour at 186.2 mm/h. Vertical rain was selected to avoid aerodynamic interference from horizontal nozzle bars and to maintain an unobstructed projection field. A GoPro Hero 7 was used as an open-source device to demonstrate methodology without disclosure restrictions. While not representative of commercial ADAS hardware, it provided a consistent platform to showcase the precipitation testing capabilities of the ACE Climatic Aerodynamic Wind Tunnel.

A dynamic projection technique was deployed to create a controlled driving scene within the tunnel, shown in Figure 6. The Berkeley Deep Drive Attention (BDD-A) dataset was projected onto the flow-straightening mesh screen [9], enabling repeatable perception testing under controlled rain conditions. This system is still in early prototyping, with plans for integration into the tunnel infrastructure to support broader testing scenarios.

Figure 6: Dynamic display with physical rain simulation hybrid digital twin platform. Sample object detection quality on dynamic and static targets.

Object detection was performed using YOLOv3 pretrained on the MS-COCO dataset, focusing on road-relevant targets such as a stop sign, car, pedestrian, and bicycle [10, 11]. In parallel, image quality was evaluated using four complementary metrics: mean squared error (MSE), structural similarity index (SSIM), peak signal-to-noise ratio (PSNR), and the MSU Blurring Index with sigma and delta variations. Together, these metrics provide a multidimensional perspective on how rain alters perception.

The results, summarized in Figure 7, show that without any clearing device, detection performance collapsed across all rain intensities. Detection count and model confidence remained near zero even in drizzle, and quality metrics steadily declined as droplets accumulated. With a physical mitigation device activated, perception recovered significantly. Detection count rose to nearly 50% in drizzle with confidence reaching 80%, and partial recovery was observed in moderate and downpour cases. These devices did not eliminate rain effects, but by periodically restoring visibility, they reset perception above a usable threshold and prevented the sensor from sliding into complete blindness.

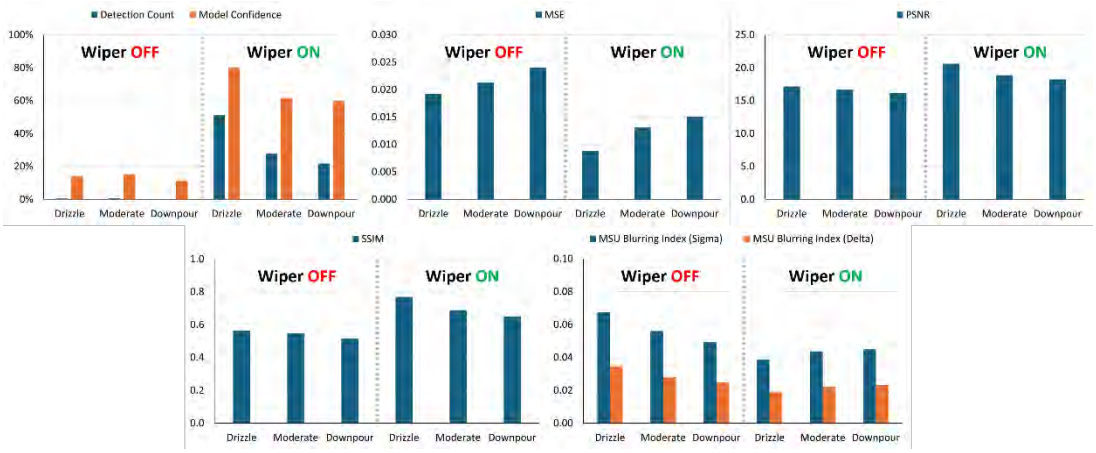

Figure 7: Object detection and image quality evaluation under drizzle, moderate rain, and downpour conditions at 50 km/h, comparing wiper off and wiper on cases.

Frame-by-frame PSNR analysis reinforces this effect. In drizzle without clearing, PSNR values hovered around 17 dB with little variation, reflecting a continuous decline in image fidelity. With clearing engaged, PSNR values reset sharply upward each cycle before gradually decaying again, creating a sawtooth pattern in values. This behaviour illustrates how mitigation works in practice: not by holding visibility constant, but by restoring it in repeated intervals so that sensor perception remains within operational limits.

Image quality metrics further highlight these dynamics. MSE and blurring indices rose quickly without clearing, while SSIM and PSNR dropped, showing degradation of both pixel fidelity and structural features. With clearing, all four metrics improved, particularly in drizzle and moderate rain. Even in downpour, where degradation was strongest, the ability to reset visibility maintained partial functionality that would otherwise have been lost.

The key lesson is that rain intensity alone is not a predictor of performance. Light drizzle without clearing caused near-total blindness, while heavy downpour with clearing allowed intermittent recovery. This underscores the importance of replicating droplet behaviour, film formation, and clearing dynamics, not simply water quantity. Controlled wind tunnel testing enables these effects to be created systematically, providing insights into both sensor limitations and mitigation strategies.

These demonstrations reflect the dual role of the ACE Climatic Aerodynamic Wind Tunnel. As the core research facility of Ontario Tech University, ACE supports academic advances in sensor evaluation and environmental testing. At the same time, ACE operates as a commercial testing facility, providing industry clients with controlled, repeatable environments to validate and improve ADAS performance. The ongoing development of precipitation capabilities, including dynamic projection and coupled perception evaluation, underscores a continuing commitment to advancing both research and industry needs in the automotive sector.

4.2 LiDAR

For LiDAR testing, the vehicle was positioned at X = 7.5 m downstream in the wind tunnel. This location provided sufficient field of view and range for stationary targets, which are necessary since LiDAR relies on reflections from solid objects and does not register projected imagery. Two groups of targets were included for analysis: a close-to-mid field set positioned between 4 and 8 m, and a far field target at 22 m. Bounding boxes were applied around each cluster of points in the point cloud to enable quantitative comparison. The target set included common road objects such as a stop sign, bicycle, pylon, dog silhouette, pedestrian mannequin, passenger car mock-up, and spray bars, presented in Figure 8. In addition, the wind tunnel flow-straightening honeycomb and mesh screens were used as far-field references. The dense mesh screen, in particular, provided a highly consistent reflective surface that served as an effective benchmark for evaluating long-range detection reliability. By combining everyday driving targets with structured reference objects, both practical and controlled scenarios could be studied without overlap in the point cloud.

Both the vertical rain system and the horizontal spray system were employed to evaluate primary rain exposure and secondary soiling. Three intensities of rain and one tire spray case were tested at 50 km/h, providing a range of realistic conditions.

The results highlight how strongly LiDAR performance depends on weather characteristics. Figure 8 illustrates the effect: in dry conditions, the point cloud captured the full set of targets clearly, while in heavy rain much of the detail was lost, leaving only partial object recognition. Quantitative analysis reinforces these visual impressions. Visibility percentages (Figure 9, left) dropped steadily with increasing severity, with tire spray producing the steepest decline. In contrast, normalized reflectivity (Figure 9, right) sometimes increased under degraded conditions, particularly for reflective objects, as droplets magnified their signal returns. These competing effects show why uncontrolled outdoor testing can be misleading: a sensor may appear to perform better in one instance and worse in another, depending on random droplet interactions rather than consistent environmental factors.

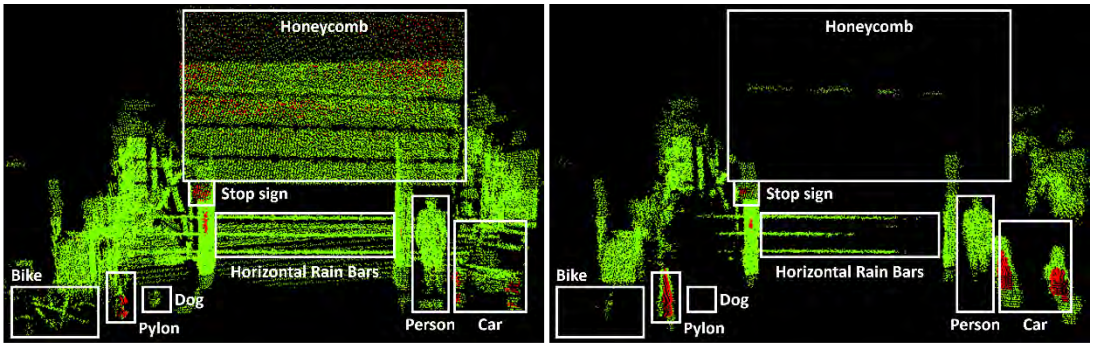

Figure 8: LiDAR point cloud comparison of detection targets in dry (left) and degraded rain conditions (right). Near-field objects include a stop sign, bicycle, pylon, dog silhouette, pedestrian mannequin, car tail gate, and spray bars, while the far-field honeycomb serves as a consistent reference target.

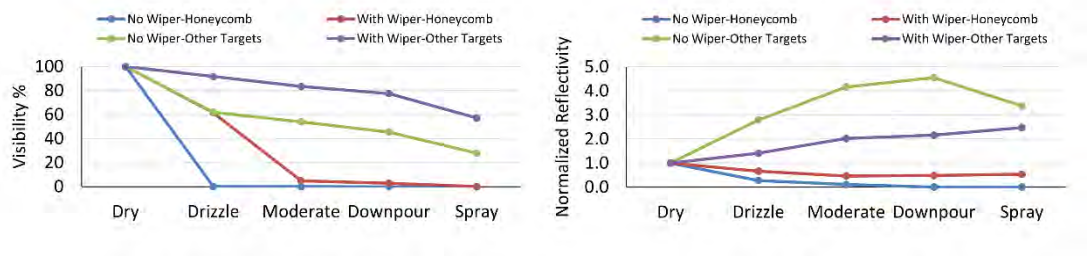

Figure 9: LiDAR visibility percentage (left) and normalized reflectivity (right) for honeycomb and other detection targets under dry, drizzle, moderate rain, downpour, and spray conditions, comparing wiper off and wiper on cases.

Rain quality and droplet dynamics were found to be central to LiDAR perception. Droplet size distribution, number density, and local trajectories each influenced how much of the beam was attenuated before reaching the target. Without control of these parameters, it becomes impossible to separate sensor limitations from environmental variability. By reproducing defined droplet distributions in the tunnel, it becomes feasible to explore practical design trade-offs. Should LiDAR be tuned to capture the broader environment at lower confidence, or accept blind zones while enhancing the detection of reflective objects? Should the sensor be positioned in the aerodynamically cleanest location, or recessed behind a protective surface that alters the field of view? These are real engineering decisions that require quantitative evidence to resolve, and they benefit most from close collaboration between academic research and commercial testing.

Physical mitigation devices add another dimension. Systems such as wipers, shutters, or protective covers can temporarily clear or shield a sensor, but they also introduce brief occlusion. In this demonstration, placing the LiDAR behind a windshield simulated such a device. The results showed that while clearing reduced long-term degradation from droplet accumulation, it also interrupted visibility in short intervals. This mirrors the broader challenge of balancing active and passive mitigation approaches, since neither fully resolves the influence of rain and spray.

Beyond visibility and reflectivity, a wide range of LiDAR behaviours can be studied in a controlled tunnel environment. Material interactions can be evaluated by mounting sensors behind different cover panels or coatings to measure how transmission changes when droplets adhere or shear across surfaces. Local droplet dynamics, including breakup, coalescence, and thin film formation, can be reproduced to study their effect on scattering. Performance can be mapped across conditions that include both uniform rainfall and complex spray patterns, allowing sensitivity to droplet size and number density to be quantified. Tunnel testing also makes it possible to examine placement strategies by shifting sensor position relative to the flow and observing how aerodynamics influence soiling and visibility. Together, these capabilities extend LiDAR evaluation well beyond simple range reduction, enabling systematic exploration of how environment, design, and materials interact to shape perception reliability.

4.3 Soiling Patterns

Ultraviolet dye tracing is a technique where water mixed with fluorescent dye is illuminated under UV lighting and recorded with a camera fitted with a green filter. Areas with greater surface soiling accumulate more dyed water, producing stronger fluorescence that can be quantified through image processing. By converting images into grayscale intensity maps, deposition patterns can be measured and compared across different vehicle regions. Previous work by Gaylard and Gulavani at the FKFS facility in Germany demonstrated the effectiveness of this method [12, 13], particularly in evaluating tire spray-induced soiling.

This capability is now being developed at the ACE Climatic Aerodynamic Wind Tunnel. As an early demonstration, dye tracing was applied to evaluate spray deposition along the side and rear of a test vehicle. Figure 10 shows the front half of the vehicle side, where tire-induced soiling is visible and captured through intensity mapping, as well as results on the tailgate, where deposition is less pronounced due to the absence of UV illumination and filtering, but still detectable through processing. These examples demonstrate how localized accumulations can be visualized and quantified for objective soiling evaluation.

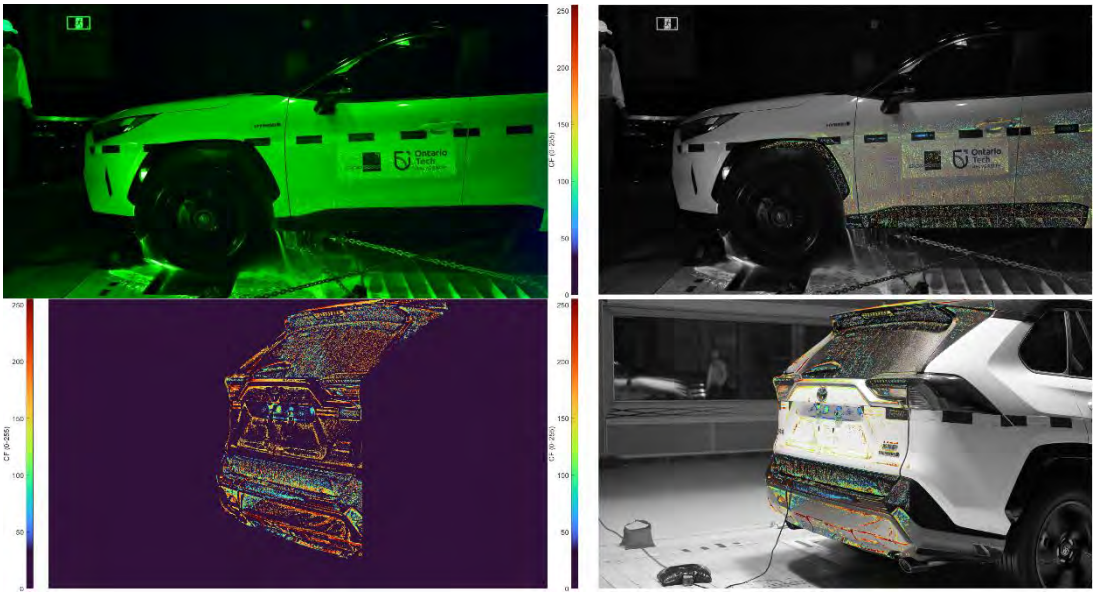

Figure 10: UV dye tracing demonstration. Top: raw side image with UV illumination and filter (left) and processed soiling intensity map (right). Bottom: rear surface overlays without UV illumination or filtering, where reflections appear alongside dyed water deposition.

Unlike FKFS's experiments, which wrapped vehicles in vinyl to reduce reflections, the demonstration was carried out directly on a production vehicle surface. Vinyl wrapping reduces background noise from UV reflections, making dyed particles easier to detect, but it does not represent how real vehicle surfaces interact with water. As shown in Pao's research on material properties, soiling behaviour depends on contact angle and surface energy. On hydrophobic surfaces, droplets may remain as particles, while on hydrophilic regions they may merge into rivulets and run off. Preserving the true surface behaviour is essential for evaluating soiling in a realistic context, even if it introduces additional noise in early-stage processing. At this stage, the results reflect an early attempt to capture vehicle surface soiling intensity, with further refinement underway. The focus is on building the foundation for more robust methods, while acknowledging the pioneering work already carried out at facilities such as FKFS.

The results presented here are preliminary, but they illustrate the potential of dye tracing as a complement to rain and spray simulation. The technique provides a direct, visual method for assessing where water accumulates and how it travels across a vehicle surface. With continued development, dye tracing will expand the range of tools available at ACE for sensor soiling and vehicle cleanliness studies, further strengthening its role as both a research facility of Ontario Tech University and a commercial testing centre for the automotive industry.

5 Conclusions and Future Work

Climatic wind tunnels provide a controlled and repeatable environment for evaluating how precipitation and spray affect vehicles and sensors. The demonstrations presented here highlight both established and emerging capabilities at the ACE Climatic Aerodynamic Wind Tunnel, from full-tunnel rain characterization to camera and LiDAR perception testing, and early-stage UV dye tracing for surface soiling. Together, these methods show how environmental factors can be recreated with precision to reveal sensor behaviours that would be unpredictable in outdoor testing.

As the core research facility of Ontario Tech University and a commercial testing centre for the automotive industry, ACE continues to advance tools and techniques for weather-resilient vehicle development. By combining environmental simulation with sensor evaluation, the facility provides a pathway toward reliable ADAS performance and lays the foundation for broader industry benchmarking in adverse weather conditions.

6 Reference list

[1] P. Pathrose, *ADAS and Automated Driving: A Practical Approach to Verification and Validation*. Warrendale, PA: SAE International, 2022.

[2] *Taxonomy and Definitions for Terms Related to Driving Automation Systems for On-Road Motor Vehicles*, Recommended Practice J3016_202104, S. International, Chicago, IL, 2021.

[3] W. Y. Pao *et al.*, "Wind Tunnel Testing Methodology for Autonomous Vehicle Optical Sensors in Adverse Weather Conditions," in *23. Internationales Stuttgarter Symposium (ISSYM 2023)*. Stuttgart, Germany: Springer Vieweg, Wiesbaden, 2023, pp. 13-39.

[4] W. Y. Pao *et al.*, "Perceived Precipitation Intensity Prediction Model Based on Simultaneous Dynamic and Static Observations for Evaluating Weather Impacts on Vehicle Applications," *Journal of Traffic and Transportation Engineering (English Edition)*, vol. 12, no. 3, pp. 639-651, July 2, 2025 2025, doi: 10.1016/j.jtte.2024.05.003.

[5] L. Li, W. Y. Pao, M. Agelin-Chaab, and J. Komar, "From Raindrops To Pixels: A Novel Model to Predict ADAS Camera Image Degradation in Rain," presented at the 2024 IEEE International Conference on Smart Mobility (SM), Niagara Falls, ON, 2024.

[6] W. Y. Pao, L. Li, and M. Agelin-Chaab, "Perceived Rain Dynamics on Hydrophilic/Hydrophobic Lens Surfaces and Their Influences on Vehicle Camera Performance," *Transactions of the Canadian Society for Mechanical Engineering*, vol. 48, no. 4, pp. 543-553, 2024, doi: 10.1139/tcsme-2023-0156.

[7] W. Y. Pao *et al.*, "Driving in the Rain: Evaluating How Surface Material Properties Affect LiDAR Perception in Autonomous Driving," presented at the WCX SAE World Congress Experience, Detroit, MI, 2025, 2025-01-8016.

[8] L. Li, W. Y. Pao, M. Agelin-Chaab, and J. Komar, "Enhancing ADAS Sensor Vision in Rain Through Machine Learning Training Using Droplet-Influenced Images," presented at the Canadian Society for Mechanical Engineering International Congress 2024, Toronto, ON, 2024.

[9] F. Yu *et al.*, "BDD100K: A Diverse Driving Dataset for Heterogeneous Multitask Learning," presented at the 2020 IEEE/CVF Conference on Computer Vision and Pattern Recognition (CVPR), Seattle, WA, 2020.

[10] J. R. A. Farhadi, "YOLOv3: An Incremental Improvement," 2018.

[11] T.-Y. Lin *et al.*, "Microsoft COCO: Common Objects in Context," presented at the Computer Vision - ECCV 2014, Zurich, CH, September, 2014. [Online]. Available: https://link.springer.com/chapter/10.1007/978-3-319-10602-1_48.

[12] A. Gaylard, K. Kirwan, and D. Lockerby, "Surface Contamination of Cars: A Review," *Proceedings of the Institution of Mechanical Engineers, Part D: Journal of Automobile Engineering*, vol. 231, no. 9, p. 16, 2017, doi: 10.1177/0954407017695141.

[13] R. A. Gulavani, S. Chalipat, and M. Samples, "Assessment of Passenger Car for Surface Dirt Contamination in Wind Tunnel," presented at the Symposium on International Automotive Technology, Sep, 2021, 2021.

CFD Simulations of Vehicle Self-Soiling

Martin Ševčík[1], Rene Devaradja[1], Martin Novák[1], Jacques Papper[1] and Martin Černý[2]

[1]Icon Technology & Process Consulting Ltd.
[2]ŠKODA AUTO a. s.

m.sevcik@iconcfd.com
r.devaradja@iconcfd.com
m.novak@iconcfd.com
j.papper@iconcfd.com
Martin.Cerny2@skoda-auto.cz

Abstract: Self-soiling occurs when dirt and water from the road are lifted by the wheels and deposited onto the vehicle body. This phenomenon affects visibility, sensor functionality, and driving safety. Addressing contamination issues late in the development cycle can result in increased costs and project delays. Computational fluid dynamics (CFD) provides a cost-effective alternative, enabling early identification of contamination patterns through virtual prototyping.

This study investigates vehicle contamination using CFD simulations performed with iconCFD. The external airflow was coupled with a discrete particle phase, where water droplets were modelled as Lagrangian particles, and a film model was applied to track droplet deposition on the vehicle surface.

The CFD results were validated against experimental data from the FKFS climatic wind tunnel by analysing the effects of wheel size, rim design, and mudguards on surface contamination. Different methods for simulating rotating wheels were compared to assess their influence on accuracy. The reliability of airflow predictions was confirmed by comparing CFD-derived pressures with experimental data from sensors positioned at hundreds of locations on the vehicle. Contamination predictions were evaluated by comparing simulated soiling patterns with image data from wet-condition experiments. The findings demonstrate the effectiveness of CFD in predicting vehicle contamination, supporting improved sensor performance and overall cleanliness.

1. Introduction

1.1 Background and Motivation

Vehicle soiling is a critical factor in aerodynamic development, impacting driver visibility, passenger comfort, and, most importantly, safety. Reliable sensor performance and unobstructed sightlines are essential for modern vehicles, particularly those equipped with advanced driver-assistance systems (ADAS). Experimental testing, whether in wind tunnels or on-road, requires a full prototype and specialized facilities, making it costly and often infeasible early in the design cycle. In contrast, virtual simulation methods enable rapid evaluation of design changes from the outset, although they must be validated against experimental data to ensure accuracy.

1.2 Exterior Water Management and Vehicle Soiling Sources

The study of exterior water management (EWM) encompasses multiphase flow involving the carrier airflow, spray particles, surface flows, and their interactions [1]. Vehicle soiling arises from several sources, as illustrated in Figure 1. Wind-driven rain produces relatively large droplets that impact the windshield, side windows, A-pillars, and mirrors. Additional contamination comes from other road users, where smaller droplets are lifted from the road surface by surrounding vehicles and deposit on similar areas as rain. Self-soiling occurs when the vehicle's own wheels generate liquid mist and debris, primarily affecting the wheelhouses, the full side panels, and the rear sections of the vehicle. These sources create characteristic soiling patterns due to differences in droplet size, deposition zones, and fluid dynamics, which must be understood to develop accurate predictive models and effective EWM strategies.

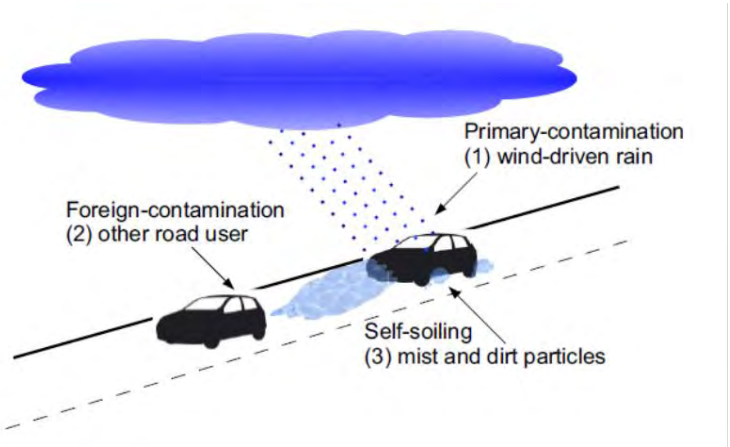

Figure 1 Vehicle soiling sources [1]

1.3 Previous Work and Validation Methods

Research to date has largely focused on external soiling, particularly rain. Novak et al. (2019 [2]) developed a validated Lagrangian–Eulerian methodology, tracking droplets in a Lagrangian frame while resolving airflow in an Eulerian frame.

Upon impact, droplets form a wall film modelled using Bai and Gosman's Continuous Phase Film Model (CPFM) [3], which assumes a quadratic velocity profile in the wall-normal direction, enabling efficient simulation with minimal computational cost.

The model accounts for hydrostatic and capillary pressures, shear stresses from air and wall interactions, gravitational forces, droplet momentum, and partial wetting through a dynamic contact angle with hysteresis and precursor film thickness. Realistic windscreen wiper motion is simulated using an Immersed Boundary Method (IBM), providing accurate wiper-induced water transport with minimal computational overhead as demonstrated in [2].

Coupling between the droplet and airflow phases is handled in two ways. One-way coupling neglects droplet feedback on the airflow, allowing to keep the carrier flow field frozen and computing only droplet and film motion, which is efficient for air-driven film flows such as along A-pillars and side windows. Two-way coupling accounts for droplet feedback on the airflow, providing higher accuracy in areas of high mist density at increased computational cost; this approach is used for predicting mirror contamination and self-soiling.

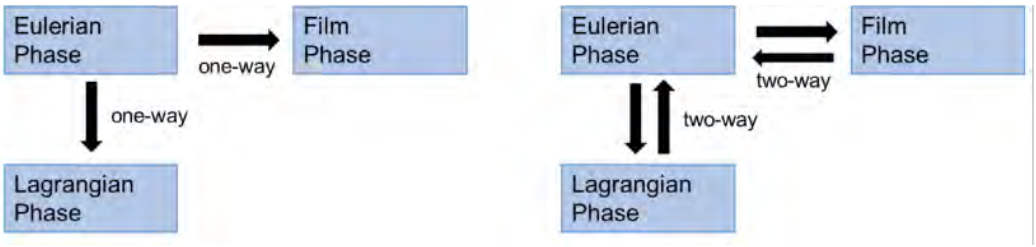

Figure 2 Coupling options between air, particles and film

Self-soiling mechanisms were investigated experimentally by Strohbücker et al. (2019 [4]) using rotating kart tires. Their results shown that tires act as rotary atomizers: water lifted from the road forms ligaments via Rayleigh–Taylor instabilities, which break into droplets through Rayleigh–Plateau mechanisms. The resulting droplet distribution peaks around 0.2 mm, with higher tire speeds increasing the number of smaller droplets while maintaining the most common diameter. Distinct spray zones were observed, as depicted in Figure 3, with the splash/spray region behind the contact patch carrying most of the water mass and larger droplets.

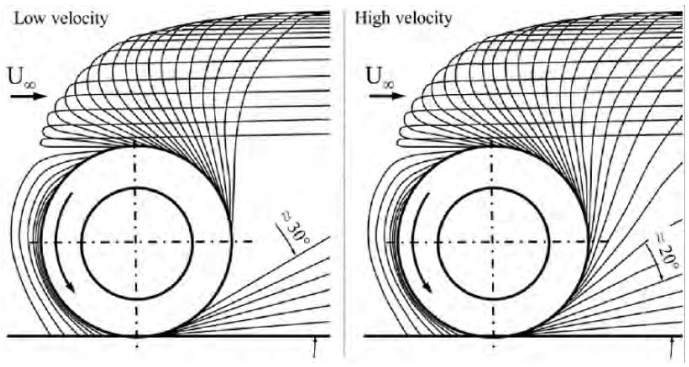

Figure 3 Schematic of droplet field for a free rolling grooved tire at low and high velocities [4]

Tread design significantly affects droplet formation: grooved tires maintain ligament formation at high speeds, whereas slick tires lose water earlier, reducing droplet mass in the second half

of rotation. These experimental findings provide a robust dataset for validating self-soiling simulations and suggest that mechanisms observed in kart tires can be applied to full-scale vehicles under typical operating conditions.

2. Experimental Setup

The FKFS thermal wind tunnel in Stuttgart, represented in Figure 4, was used for experimental validation. This Göttingen-type tunnel features a 2-axis dynamometer test bench but lacks a central belt under the car. The test section dimensions are 15.8 m × 6.8 m × 5.5 m. A water film is applied to rollers beneath the wheels via an irrigation system. The rotating wheels lift the water, generating a droplet field. A UV-tracer fluid is added to the water to visualize its motion on the vehicle surfaces. During testing, tunnel lights are switched off and UV lights illuminate the areas of interest. UV cameras capture the water flow across the vehicle surfaces. Between tests, the vehicle is cleaned with a water jet and dried with compressed air. Nevertheless, fully draining the wind tunnel test section between tests is practically infeasible. This introduces additional, and somewhat arbitrary, sources of water specific to the wind tunnel design, which should be considered when analysing the simulation results.

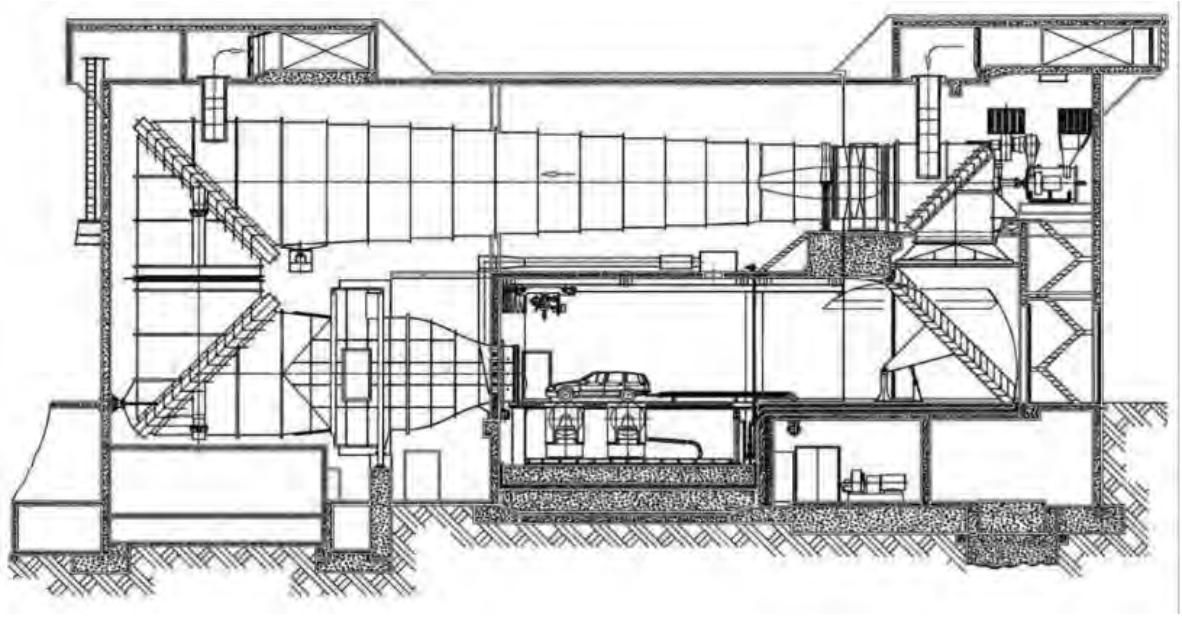

Figure 4 FKFS thermal wind tunnel diagram [5]

Accurate prediction and validation of the flow field are critical for reliable soiling simulations. Therefore, the experiment was divided into two parts: validation of external aerodynamics and validation of soiling. For aerodynamic validation, pressure strips were employed. These MEMS-based digital sensors [6], shown in Figure 5, measure absolute pressure at 100 Hz sampling frequency. The data averaged over the last 15s were used for validation. Their non-intrusive installation eliminates the need for drilling into the vehicle body. Each strip is 255.6 mm long and contains 24 pressure sensors. Ten strips were mounted on the vehicle, with two additional reference strips positioned inside the tunnel test section behind the nozzle.

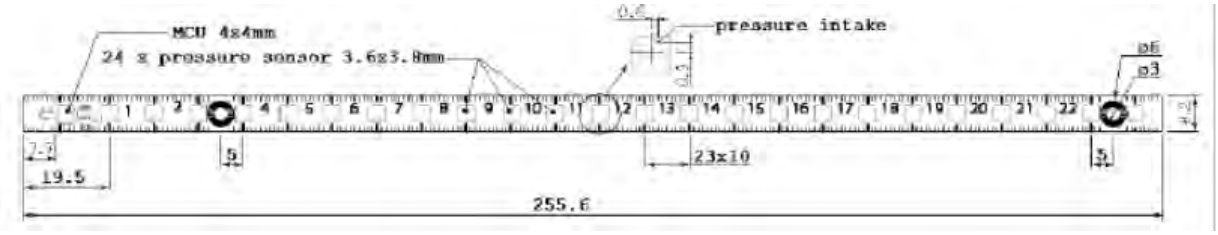

Figure 5 Pressure strip schematics and dimensions [6]

A production Skoda Kodiaq SUV was selected for testing. Since the focus was on self-soiling, different wheel and tire combinations were evaluated. As shown in Figure 6, two wheel sizes R17 (1) and R19 (2) were used and two other wheel variants of R19 were also tested by adding rim covers (3) and optional mud flaps (4). Four airspeeds values 70, 90, 110, and 130 km/h were measured for each configuration.

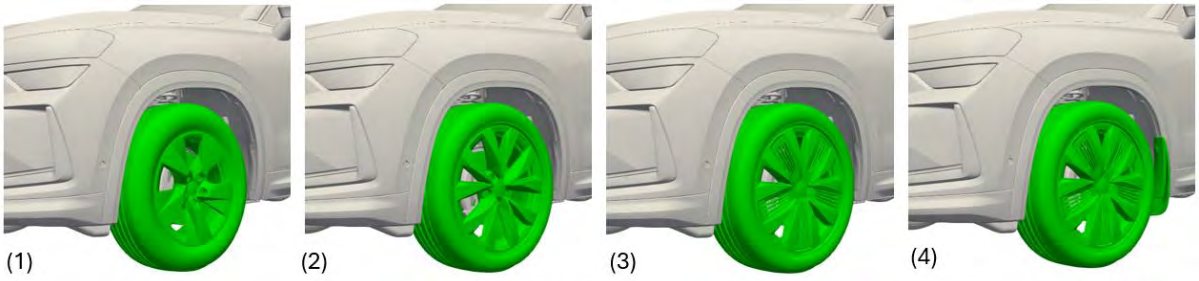

Figure 6 Tested wheel variants

Preliminary CFD simulations, previously validated for A-pillar overflow, were performed to determine optimal pressure strip locations. The first strip (P1) was positioned on the registration plate to capture stagnation pressure and calculate the pressure coefficient. The second strip (P2) was mounted on the leading edge of the roof, just behind the windscreen edge. The remaining strips were distributed across four areas: behind the front left wheel (P3, P4, side panel), underbody left floor covers (P5, P6), inside the front left wheel arch (P7, P8), and around the rear wheel (P9, P10). All these strip positions are shown in Figure 7.

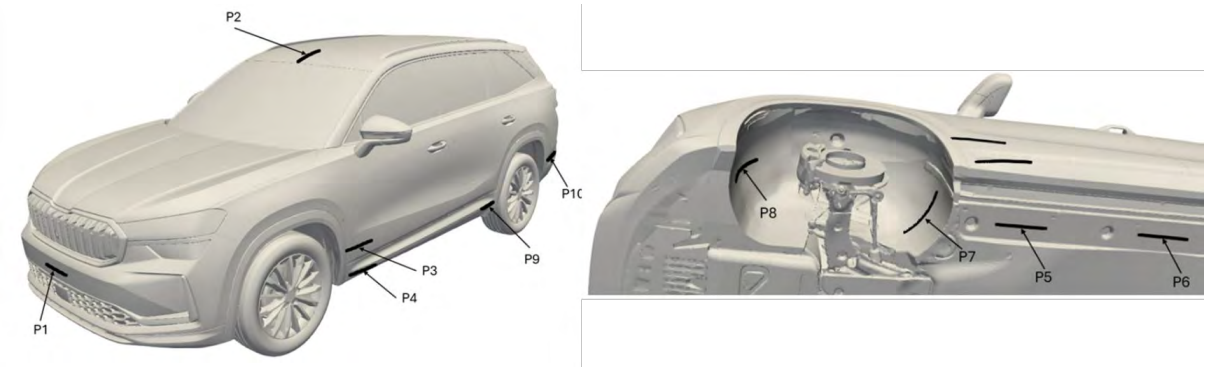

Figure 7 Pressure strip locations on the vehicle

Soiling measurements focused on two main areas: the side doors and rear part of the vehicle. Each area required a dedicated injector configuration and camera placement and was tested separately. Measurement variants differed in wind speed, water mass flow, wheel configuration, and the presence or absence of mudguards. A detailed test matrix is provided in Table 1.

Type	Speed [km/h]	Water amount [l/h]	R17 Mudguards		R19 Mudguards		R19 + inserts Mudguards	
			Yes	No	Yes	No	Yes	No
Side	70	140 (F), 200 (R)					x	x
		200 (F), 250 (R)						
	90	140 (F), 200 (R)	x		x		x	x
		200 (F), 250 (R)					x	x
	110	140 (F), 200 (R)	x		x		x	x
		200 (F), 250 (R)					x	x
	130	140 (F), 200 (R)					x	x
Rear	90	600 (R)	x		x		x	x
		400 (R)						x
	110	600 (R)	x		x		x	x
		400 (R)						x

Table 1 Testing configurations for side and rear soiling analysis

3. CFD Methodology and Setup

The virtual wind tunnel was simulated using the finite volume CFD software iconCFD v4.2.12. The computational domain is a rectangular box with a velocity inlet and pressure outlet, including rolling pads under the wheels to model ground interaction via tangential velocity boundary conditions. The central belt was omitted, matching the FKFS climatic wind tunnel setup. The remaining floor surfaces were modelled as no-slip walls.

The computational mesh is unstructured and hexa-dominant, with 4 prism layers on the vehicle surfaces and 7 prism layers on the wheels. Unsteady simulations are required to capture the external aerodynamics accurately ([2], [7], [8]). The workflow was initialised with a steady-state RANS initialization, followed by a transient DDES simulation using incompressible, pressure-based segregated solvers. The transient phase lasted 1.4 s, with the first 0.4 s used to transition from the RANS solution to a fully transient state, and the remaining 1 s used for averaging the results. Both stages employed the Spalart – Allmaras turbulence model [9].

Previous methodologies focused on the A-pillar and rear-view mirror regions, enabling significant simplifications—such as excluding wheel rotation, engine bay flow, and heat exchanger modeling and underbody flow resolving with reduced detail. These simplifications substantially reduced computational cost without compromising the fidelity of the targeted flow features. For the current self-soiling study, all these features were incorporated: the engine bay was open, heat exchangers were represented as porous media, and airflow through the engine compartment and underbody was fully resolved. Wheel rotation was modelled using two approaches: a Moving Reference Frame (MRF) and physical mesh rotation with an Arbitrary Mesh Interface (AMI). The latter is theoretically more accurate but computationally more expensive. Finally, the tires were deformed to reproduce their realistic shape, as shown in Figure 8. To ensure an accurate representation, the car in the CFD model was positioned according to ride height data obtained from wheel arch apex measurements in the wind tunnel.

Figure 8 Tire deformation on 17″ wheels

The soiling process was modelled using an unsteady multiphase solver with two-way coupling between the Eulerian and Lagrangian phases. Surface wetting was captured using a continuous-phase film model [2], [11]. The wall interaction model assumed that particles adhered upon contact with the surface, and breakup caused by airflow shear forces was modelled using the Reitz–Diwakar approach [10]. The particle equation of motion accounted for gravity, aerodynamic drag, and pressure gradient forces, and detachment from the surface film was represented through mechanisms such as wave stripping, edge shedding, curvature separation, and gravity-induced separation [12]. Together, these processes reproduced realistic droplet behaviour. Water particles were injected from the start of the unsteady simulation via conical injectors placed behind the tire contact patch and on the tire surface itself [4], with particle diameters set to 0.2 mm. Each soiling measurement in the wind tunnel lasted 3 minutes, whereas the CFD simulations were limited to 20 s transient DDES runs initialized with steady-state RANS. To compensate for the shorter simulation duration, the water mass flow rate was proportionally increased, although this adjustment can influence the soiling distribution, as wetted surfaces may absorb more of the dispersed water. It can also be noted that, in the wind tunnel, redeposition from the vehicle, the tunnel floor, or the rolling pads represents a possible additional source of contamination.

4. Validation

4.1 External aerodynamics

Two locations were selected to verify pressure levels in the domain: the registration plate (P1), corresponding to a stagnation point with a pressure coefficient around 1, and the leading edge of the roof (P2), where no separation is expected and the pressure gradient is relatively mild. Experimental and CFD results agreed very well at both locations across all wheel variants. An example for the 17″ wheels at 70 km/h is shown in Figure 9.

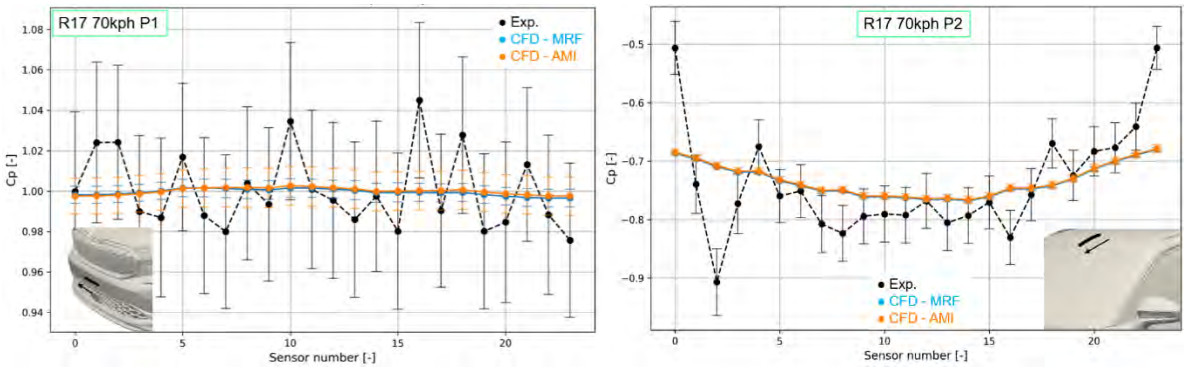

Figure 9 Pressure coefficient prediction for R17 - 70kph - P1 and P2

The main area of interest is the side of the vehicle between wheel arches, where airflow is strongly influenced by wheel rotation. Both the MRF and AMI approaches produced very similar pressure distributions. Agreement with experimental data is excellent in observed locations, as shown in Figure *10*, indicating that the CFD methodology enables accurate airflow prediction, providing a reliable basis for self-soiling analysis.

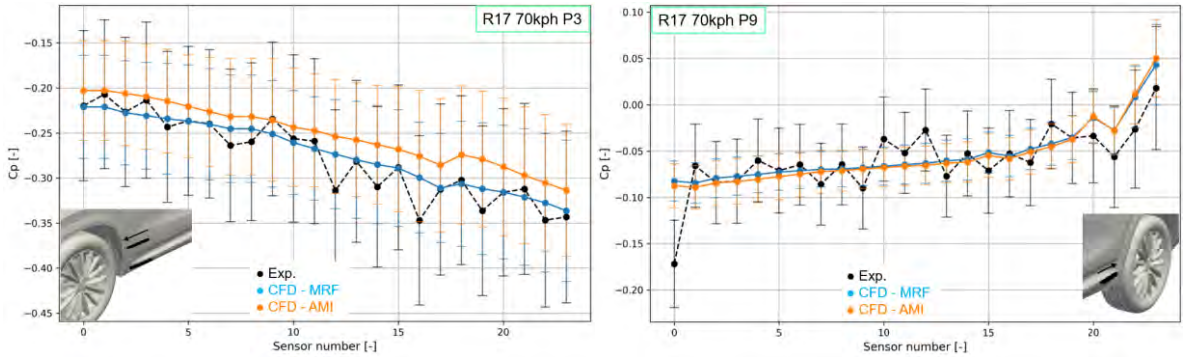

Figure 10 Pressure coefficient prediction for R17 – 70 kph – P3 and P9

In contrast, discrepancies were observed inside the wheel arch and on the floor cover near the wheel, as illustrated in Figure *11*. These differences are likely due to the tire wake from the contact patch not being accurately captured. While the trend matches the experiments, CFD consistently under predicts absolute values of static pressure. Correlation improves further along the floor cover (P6). Additional factors contributing to these discrepancies may include the simplified tire tread geometry, the absence of validated boundary layers on the tunnel floor, and the simplified representation of engine bay airflow.

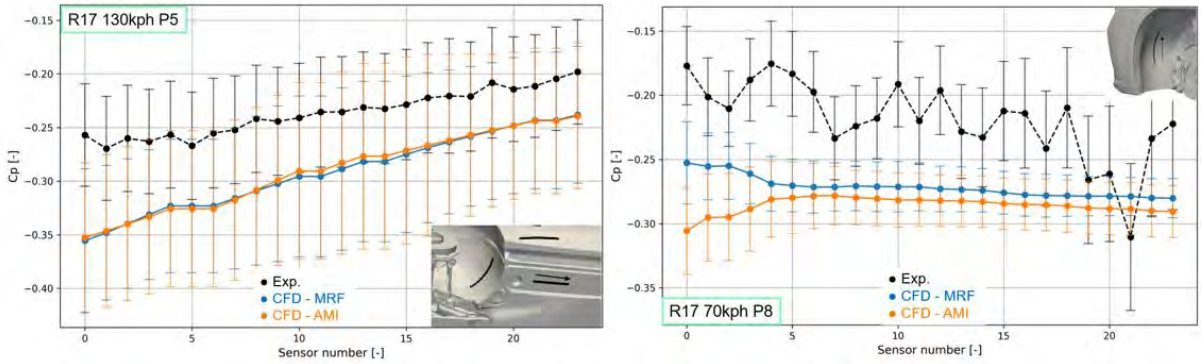

Figure 11 Pressure coefficient prediction for R17 – 130 kph – P5

4.2 Soiling validation

The experimental data from Figure *12* and Figure *13* confirm the findings of Strohbücker et al. (2019, [4]): at higher speeds, the spray angle decreases, leading to reduced surface contamination. To reproduce the same trend in CFD, the injector cone angle was manually adjusted—set to 30° for 70 and 90 kph, and to 20° for 110 and 130 kph. Although this manual adjustment is not ideal for a general self-soiling methodology, it was used as an attempt to replicate the experimental results in CFD and to demonstrate that the injector cone angle has a dominant effect on surface contamination. However, differences in contamination intensity can be observed at all speeds. The experiments also show a larger contaminated area at lower speeds (70 and 90 kph), whereas this effect was not captured in the CFD simulations. This indicates that further adjustments to the cone injector are potentially required. It also highlights

the need for an enhanced water injection method allowing for non-uniform injection distribution from the wheel surface that accounts for the physical phenomena described in [4].

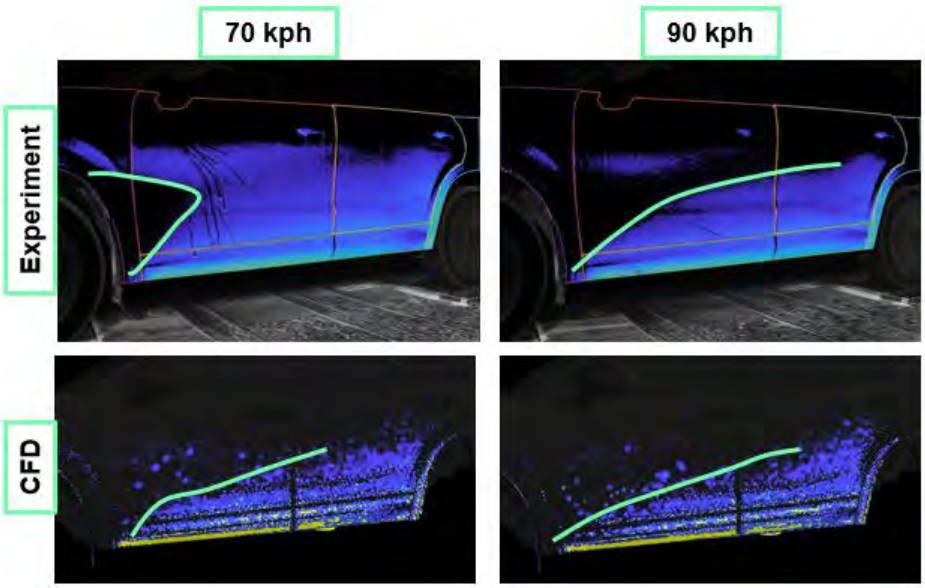

Figure 12 Configuration R19 with covers and mudguards – 70 and 90 kph

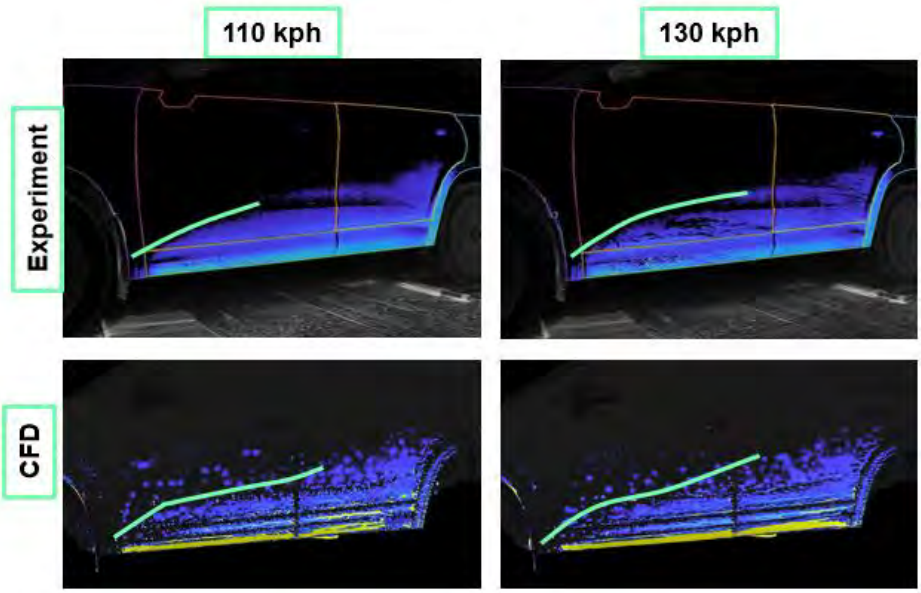

Figure 13 Configuration R19 with covers and mudguards – 110 and 130 kph

The influence of mudguards is also noticeable in Figure *14*. The addition of mudguards reduces the overall contaminated area, while increased contamination intensity can be observed at the edge of the door sill. CFD reproduces this trend moderately, but differences in contamination intensity can still be observed. Additionally, the separation line between the wetted and dry zones without mudguards is slightly lower than in the experiment.

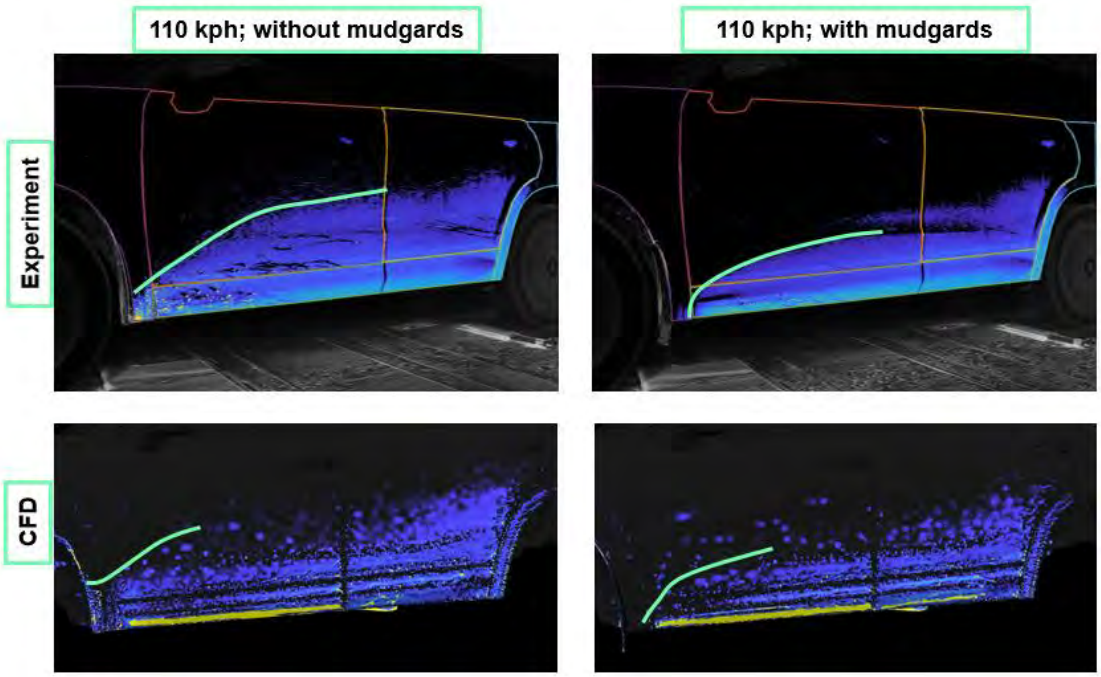

Figure 14 Configuration R19 with covers – mudguards effects

The influence of different wheel designs is also significant, as shown in Figure *15*. The highest level of contamination occurs with the 17" wheels. Adding covers to the 19" wheels alters the shape of the spray-free triangle, but has little effect on the overall contaminated area. Contamination at the edge of the door sill increases with the cover installed. CFD reproduces the change in the shape of the spray-free triangle moderately well, but the overall contamination levels differ from the experiment, being lowest for the 17" wheels. This likely points to the need of the aforementioned advanced wheel surface injector inclusion. It shall be noted that CFD predicts well the dry spots occurring in the bottom half of the front door with 17" wheels

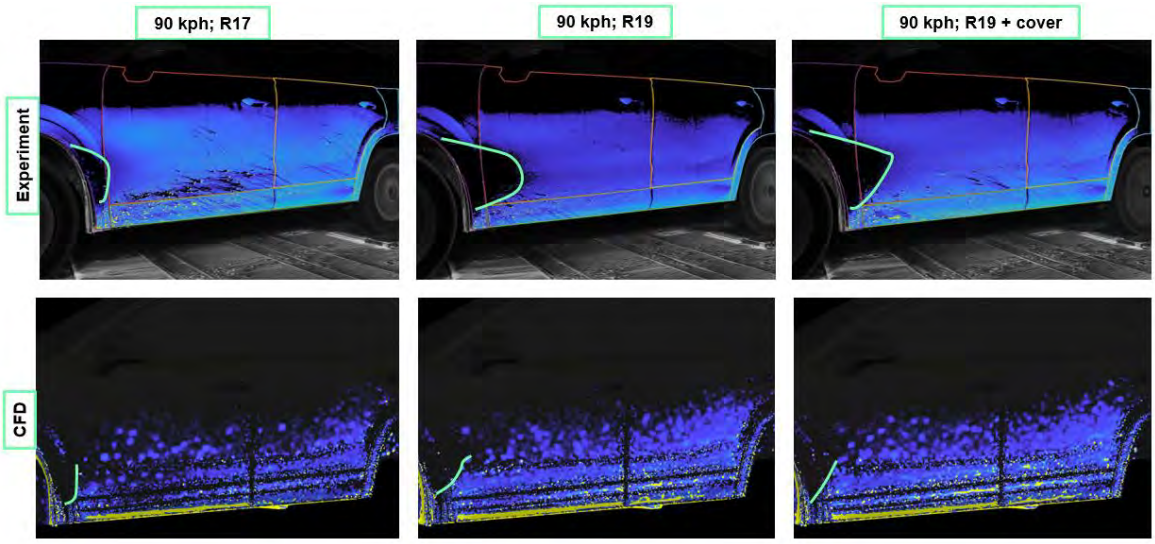

Figure 15 Surface contamination for different wheel designs

Experimentally, the central portion of the rear soiling pattern remained consistent across all tested variants. Among the configurations, the R17 wheels generated the largest contamination-free zones near the rear edges, while the introduction of R19 wheel covers and the addition of mudguards had minimal impact on the soiling patterns at the rear. CFD captures some general trends, predicting similar contamination patterns for the other R19 configurations. However, it

fails to reproduce key features observed in the experiments, such as the differences at the rear bottom-side edges, and exhibits noticeable asymmetry for the R17 configuration that is not present in the measurements. The absence of data in this region does not allow us to determine whether these discrepancies arise from an inaccurate airflow simulation or from limitations in the soiling model itself, highlighting the need for further investigation.

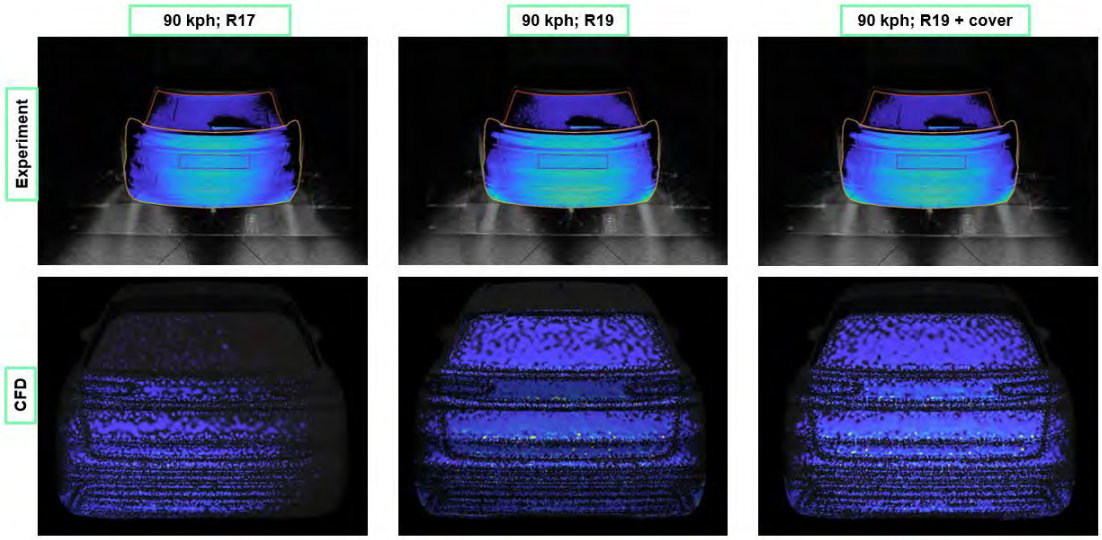

Figure 16 Rear contamination for different wheel designs

5 Summary

The goal of this study was to develop a reliable and experimentally validated simulation methodology for vehicle self-soiling, where water lifted by the wheels contaminates the vehicle body. Simulations were performed using transient Delayed Detached Eddy Simulation (DDES) solver with the Spalart–Allmaras turbulence model, modelling wheel rotation via both Moving Reference Frame and Arbitrary Mesh Interface techniques. Soiling was simulated using a two-way coupled Lagrangian-Eulerian framework, with droplet emission from both conical injectors and tyre surface. Surface film dynamics were captured via the Continuous Phase Film Model.

CFD predictions of external airflow matched experimental data well in most regions, particularly on the side panels and roof. Both MRF and AMI produced comparable results, with MRF chosen for soiling simulations due to lower computational cost. Some discrepancies were noted in the wheel arch and underbody areas, which are less critical for side and rear soiling.

Overall, CFD captured the qualitative trends observed experimentally, including reduced contamination behind the wheels at higher speeds and the effect of mudguards in limiting contaminated areas. Adjusting the injector cone angle successfully replicated the change in spray angle and contamination patterns at different speeds, though discrepancies in contamination intensity remain to be addressed. Accurate modelling of water expelled from the tire, dependent on tread and injection parameters, is still needed.

Wheel design effects were partially reflected in CFD, with some differences between R17 and R19 wheels captured, but the effect of adding R19 wheel covers was not sufficiently

reproduced. Quantitative contamination levels also differed, with CFD underestimating contamination for 17" wheels compared to experiments. These findings highlight the importance of refining injector settings and incorporating a more detailed tire surface representation with keeping in mind much shorter simulations than experiment to improve CFD accuracy in predicting vehicle self-soiling.

6 Acknowledgements

The authors gratefully acknowledge ŠKODA AUTO for granting permission to publish this work and for their excellent collaboration throughout the study.

References

[1] T. Hagemeier, Experimental and numerical investigation of vehicle soiling processes, 2012

[2] M. Novak, R. Devaradja, J. Papper, M. Cerny, Efficient CFD methods for assessment of water management, 2019

[3] C. Bai, A. D. Gosman, Mathematical Modelling of Wall Films Formed by Impinging Sprays. SAE Transactions, 105, 782–796. http://www.jstor.org/stable/44736317, 1996

[4] V. Strohbücker, R. Niesner, D. Schramm, T. Kuthada et al., Experimental Investigation of the Droplet Field of a Rotating Vehicle Tyre, SAE Technical Paper 2019-01-5068, 2019, doi:10.4271/2019-01-5068.

[5] N. Kruse and K.-H. Chen, Exterior Water Management Using a Custom Euler-Lagrange Simulation Approach, in SAE World Congress & Exhibition, 2007

[6] F. Wittmeier, T. Kuthada, J. Filipsky and J. Cizek, New MEMS Pressure Sensors for Transient Aerodynamic Measurements, ATZ worldwide, vol. 120, pp. 38-41, 4 2018.

[7] T. Han, S. Kaushik, K. Karbon, B. Leroy, K. Mooney, S. Petropoulou and J. Papper, Ad-joint-Driven Aerodynamic Shape Optimization Based on a Combination of Steady State and Transient Flow Solutions, 2016.

[8] R. Lietz, L. Larson, P. Bachant, J. Goldstein, R. Silveira, M. Shademan, P. Ireland and K. Mooney, An Extensive Validation of an Open Source Based Solution for Automobile External Aerodynamics, in WCX™ 17: SAE World Congress Experience, 2017.

[9] P.R. Spalart and S.R. Allmaras. A One-Equation Turbulence Model for Aerodynamic Flows. Recherche Aerospatiale, 1:5–21, 1994

[10] R.D. Reitz, R. Diwakar, Effect of Drop Breakup on Fuel Sprays, SAE Paper 860469, 1987.

[11] P.T. Brun, A. Damiano, P. Rieu, G. Balestra, F. Gallaire, Rayleigh-Taylor instability under an inclined plane.Physics of Fluids (1994-present), 27(8), 084107.

[12] K. Meredith, J. Vries and Y. Xin, A numerical model for partially-wetted flow of thin liquid films, 2011.

Reconstruction of Road Vehicle Wake by Physics Informed Neural Networks

Sanghyek Kim*, Jeoungmin Han, Junho Jeong, Yongsu Shin and Sanghyun Park

Aerodynamic Development Team
Hyundai Motor Group
150, Hyundaiyeonguso-ro, Namyang-eup
18280, Hwaseong-si, Gyeonggi-do, Korea
shkim0924@hyundai.com
hanjm@hyundai.com
jh.jeong@hyundai.com
shin.yongsu@hyundai.com
shpark@hyundai.com

Abstract: One of the ways to reduce the aerodynamic drag is by improving the rear wake of the vehicle. To achieve this, accurate measurements of flow velocity and pressure at the rear of the vehicle are essential. In the Hyundai Aero-Acoustic Wind Tunnel (HAWT), a wake measurement system with cobra probe arrays has been installed to measure and analyze the vehicle wake. However, the cobra probe can only properly detect the flows above 10m/s; thus, it cannot create an accurate wake contour within the range of -10m/s to 40m/s. In this paper, a Physics-Informed Neural Network (PINN) is applied to reconstruct the complete vehicle wake from this sparse data. The PINN model fills in the flow where velocities are below a certain threshold, allowing for a precise calculation of micro drag, a quantitative method for vehicle wake analysis. The generic aerodynamic model DrivAer, simulated via CFD, is used to validate the predictive accuracy of the PINN. As a result, the difference in aerodynamic drag coefficient between the ground truth and the PINN prediction is under 1 count ($\Delta C_D < 0.001$). Furthermore, the validated model was successfully applied to live wind tunnel data from the Hyundai IONIQ 5, enabling a quantitative diagnosis that guided a significant drag reduction. The application of PINN is expected to establish a more precise and practical technique for vehicle wake analysis.

Contribution: 2025 FKFS Conference on Vehicle Aerodynamics and Thermal Management
15 – 16 October 2025 | Leinfelden-Echterdingen

1 Introduction

A detailed understanding of the flow field around a vehicle, which is shaped by its geometry and aerodynamic devices, is crucial for reducing aerodynamic drag. The Hyundai Aero-acoustic Wind Tunnel (HAWT) is equipped with a wake measurement system that employs Cobra Probes on an automated traversing system [1-2]. This setup allows for the real-time visualization and analysis of velocity and pressure fields in the vehicle's wake. However, a significant limitation of Cobra Probes, stemming from their structural design (see Section 2.1), is their inability to accurately measure reverse flow. This deficiency introduces distortions in the calculation of the Micro drag (see Section 2.2), a key metric for aerodynamic analysis.

Previous studies have attempted to overcome such data distortion issues arising from instrumentation limits. For instance, J.Jeong et al. applied a Deep Neural Network (DNN) to reconstruct missing data in the temperature field of a flat plate [3]. This work, however, was limited to thermal conduction, a phenomenon significantly less complex and more linear than a turbulent flow field. In another study, D. Kim et al. used an Adaptive Neuro Fuzzy Inference System(ANFIS) to predict the unmeasurable areas in the wake of a side mirror [4]. While successful, the study did not provide a clear rationale for how the ANFIS model learned the underlying physics of the flow.

To address these gaps, this paper introduces Physics-Informed Neural Networks (PINNs) to predict the flow data within the measurable regions of the vehicle wake [5]. By integrating the governing physical equations directly into its loss function, PINNs can learn the flow phenomena in a physically consistent manner. To validate our approach, we evaluate the prediction accuracy of the PINNs using CFD simulation data and benchmark its performance against a standard physics-uninformed neural network. Finally, we employ the Micro drag technique to assess the PINN's predictive accuracy and to perform a quantitative analysis of the complete flow field that results from augmenting the experimental data with the PINN's predictions.

2 Backgrounds

2.1 Cobra probe

The Cobra probe is an instrument designed for flow field measurement. Its operating principle, illustrated in Fig.1, involves measuring pressures at multiple holes on the probe head and then using the pressure differences to calculate the flow direction and three-dimensional velocity components. At HAWT, a 4-hole Fast Response Aerodynamic Probe (FRAP) from Vectoflow GmbH (Germany) is employed. This probe offers high-fidelity data acquisition, capturing pressure and velocity components in real-time at frequencies up to 2kHz.

Despite its capabilities, the Cobra probe has notable limitations. First, as an intrusive instrument (Fig.1), it inevitably disturbs the local flow field it is intended to measure. Second, its four-hole design restricts its effective measurement range to an acceptance angle of ±45 degrees from its central axis. Finally, being a pressure-based sensor, its accuracy significantly degrades at low velocities, particularly below ~10m/s.

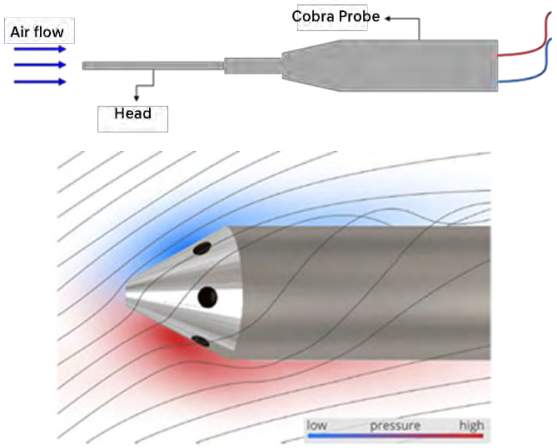

Figure 1: Multi-hole Cobra probe
(Source : vectoflow.de)

2.2 Micro Drag

Micro drag is an analytical technique, originally introduced by Cogotti, for diagnosing the sources of drag in a vehicle's wake [6]. The method is fundamentally based on the Reynolds Transport Theorem and works by calculating the momentum deficit in the flow as it traverses a specified control volume (see Eq.1)

$$C_D \cdot A_x = \int 1 - C_{p,tot} ds - \int \left(1 - \frac{u}{u_\infty}\right)^2 ds + \int \left(\left(\frac{v}{u_\infty}\right)^2 + \left(\frac{w}{u_\infty}\right)^2\right) ds \quad (1)$$

Where C_D is the drag coefficient acting on the vehicle, A_x is the frontal projected area of the vehicle, and $C_{p,tot}$ is the total pressure coefficient calculated from the flow passing through the control surface. u_∞ represents the freestream velocity in the wind tunnel, which corresponds to the driving speed in on-road conditions. The terms u,v, and w are the velocity components in the x,y, and z directions at the measurement points, respectively, and s denotes the control surface.

A primary output of this technique is a Drag map (Fig.2), which provides a visual and quantitative breakdown of how different areas in the wake contribute to the total aerodynamic drag. This allows engineers to pinpoint which flow structures are most responsible for increasing drag. The reliability of this powerful diagnostic tool, however, is critically dependent on the precise measurement of reverse flow regions. This exposes a key limitation in the current experimental setup at HAWT, where the Cobra probe's inability to measure reverse flow undermines the accuracy of the Micro drag analysis.

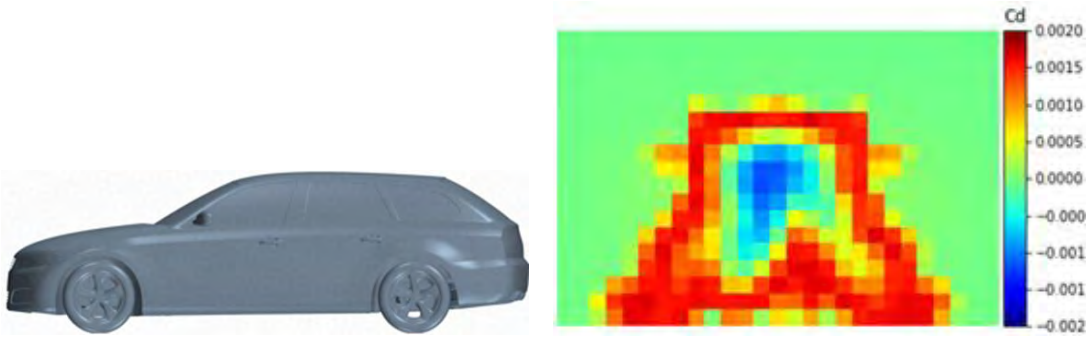

Figure 2: DrivAer Estate Model & Drag map

2.3 Physics Informed Neural Networks

Physics-Informed Neural Networks (PINNs), introduced by Raissi et al., represent a paradigm shift from traditional data-driven models [5]. While conventional neural networks learn exclusively from data, often ignoring the underlying physics, PINNs embed governing physical laws directly into the learning process. This is achieved by formulating a loss function that penalizes predictions for violating these laws, which not only reduces the reliance on large datasets but also accelerates model convergence.

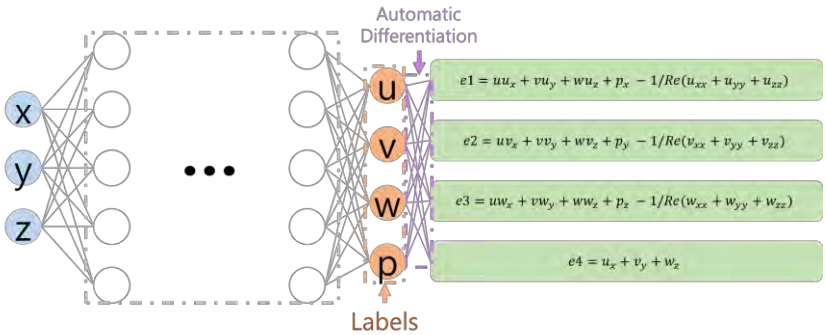

Figure 3: PINNs Architecture

The PINNs architecture, depicted in Fig.3, consists of two primary components. The first is a standard neural network that learns from available data points (left side). The second, and defining, component is the physics-informed part (right side), where the governing equations of fluid dynamics—the Navier-Stokes and Continuity equations—are formulated as a residual term in the loss function. This dual-objective training effectively constrains the solution space, preventing the network from producing physically implausible outcomes.

The model's total loss function L_{model} is therefore a composite of the data loss (L_{data}) and the physics loss ($L_{physics}$), as formulated in Eq.2. A powerful feature of this framework is that L_{data} and $L_{physics}$ need not be evaluated at the same spatial points. This allows the network to make accurate predictions even in regions devoid of measurement data by leveraging the physical laws learned from randomly sampled collocation points throughout the domain, alongside sparse information from actual sensor locations.

$$L_{model} = L_{data} + L_{physics} \tag{2}$$

Building on these capabilities, this study employs PINNs to address the measurement limitations of the Cobra Probe. Specifically, we leverage 1) the enforcement of physical laws and 2) the ability to predict in data-sparse regions to reconstruct the low-velocity airflow (≤10m/s) in the vehicle's wake. This reconstructed flow field is used to perform a quantitative aerodynamic analysis using the Micro drag technique.

3 Model Construction and Validation

This study validates the PINN's predictive capabilities using a semi-synthetic dataset derived from a high-fidelity CFD simulation of the DrivAer Estate model, a widely recognized benchmark in automotive aerodynamics [7]. To mimic the constraints of a real-world experiment, the complete CFD flow field was down-sampled to match the spatial resolution of the HAWT's wake measurement system. The resulting data, which forms the basis for our model training and validation, is shown in Fig.4.

The dataset is defined on a yz cross-sectional plane measuring 2.6m in width and 1.45m in height, situated 0.5m downstream from the vehicle's rear end. The data was partitioned for training and validation as follows:

- Training Data (for L_{data}): The data-driven loss component was trained on points from the "measurable" region, defined as where the axial velocity u > 10m/s. The inputs for the network were the spatial coordinates of these points, while the corresponding labels were the ground-truth velocity components (u,v,w) and pressure (p) from the CFD simulation.
- Collocation Points (for $L_{physics}$): The physics-informed loss component was enforced at collocation points sampled from the "unmeasurable" region (u ≤ 10m/s). The loss at these points was calculated based on the residuals of the governing physical equations, which are detailed in the subsequent section.
- Validation Data: To quantitatively assess the model's accuracy in the target region, a validation set was created using the data points where u ≤ 10m/s. The inputs were the coordinates of these points, and the labels were their true velocity and pressure values from the CFD simulation, serving as the ground truth.

Figure 5 visualizes the initial training data, showing the u, v, and w velocity fields with the target prediction region (u ≤ 10m/s) masked out.

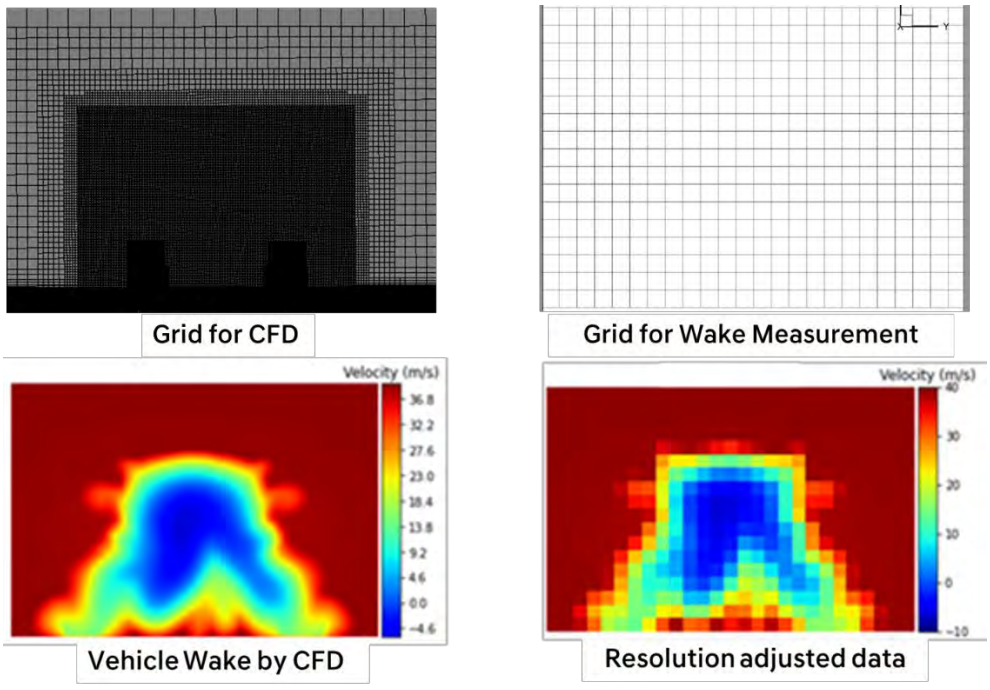

Figure 4. Down-sampling of CFD Wake results

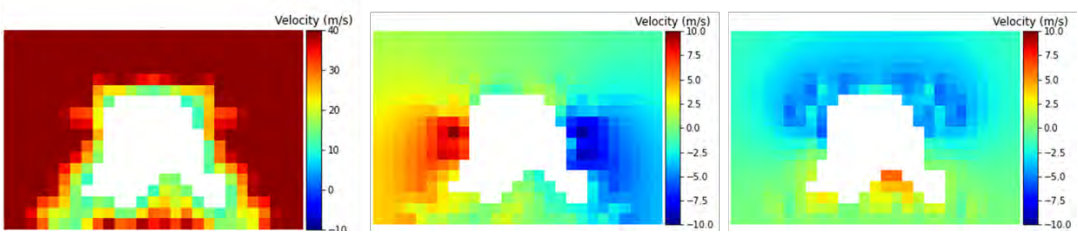

Figure 5. u,v,w velocity flow fields except unmeasurable region

3.1 Hyperparameter tuning

To optimize the model's predictive performance a two-stage tuning process was conducted: first on the neural network architecture, and second on the formulation of the physics-informed loss, $L_{physics}$. Other fundamental hyperparameters were kept constant as detailed in Table 1.

Table 1. Hyperparameter settings for PINN model

Hyperparameter	Value
Activation function	Tanh
Epochs	15,000
Batch size	5,000
Learning rate	1.0e-4

Network Architecture Optimization:

Optimizing the number of layers and neurons is essential for preventing common training pitfalls like overfitting and convergence to poor local minima. For this stage, we used a standard $L_{physics}$ for formulation consisting of the coupled continuity equation (CE) and Navier-Stokes equations (NSE). We evaluated three distinct network architectures, comparing their performance based on the Mean Squared Error (MSE) calculated on the validation data from the unmeasurable region. The results are presented in Table.2

The architecture with 5 hidden layers with 50 neurons each achieved the best performance, exhibiting the lowest MSE. The deepest model (10 layers, 100 neurons) did not overfit within 15,000 epochs but seemed to get trapped in a local minimum. In contrast, the simplest model (5 layers, 10 neurons) was likely too shallow, lacking expressive capacity to accurately model the complex flow field, which resulted in a higher MSE.

Table 2. Results of Network architecture optimization

# of layers	# of neurons	MSE
5	10	0.27
5	50	0.16
10	100	0.36

Physics-Informed Loss ($L_{physics}$) Formulation:

In conventional machine learning, the loss function is not considered a hyperparameter. However, for PINNs, the selection of physical laws that constitute $L_{physics}$ is a critical design choice that can significantly impact accuracy. The canonical choice for fluid dynamics is the coupled NSE and CE. To potentially enhance the physical consistency of the predictions, we investigated the effect of adding a third equation: the Pressure Poisson Equation (PPE). The PPE, derived by taking the divergence of the NSE, acts as a supplementary constraint that reinforces the mathematical compatibility between the pressure and velocity fields. We therefore constructed and compared several cases, each with a different combination of the three governing equations (formulated in Eq.3) and evaluated their performance based on the MSE in the unmeasurable region, as outlined in Table3.

(Navier-Stokes Equation) [8]

$$e1 = -\vec{u} \cdot \nabla\vec{u} - \frac{\nabla p}{\rho} + \mu\nabla^2\vec{u}$$

(Continuity Equation) [8]

$$e2 = \nabla u \tag{3}$$

(Pressure Poisson Equation) [8]

$$e3 = \nabla \cdot (-\vec{u} \cdot \nabla\vec{u} - \frac{\nabla p}{\rho} + \mu\nabla^2\vec{u})$$

Fixing the network architecture to the optimal 5-layer, 50-neuron configuration, we evaluated the performance of different $L_{physics}$ formulations. This evaluation demonstrated that the combination of the Pressure Poisson Equation (PPE) and the Continuity Equation (CE) achieved the lowest Mean Squared Error (MSE). Notably, applying the CE alone as a physical constraint was counterproductive, yielding an even higher MSE than the physics-uninformed baseline model. This result underscores a critical insight: the injudicious application of physical constraints in a PINN can degrade, rather than improve, predictive performance.

Table 3. Combinations of Governing equations

Governing Eqn	# of layers	# of neurons	MSE
CE	5	50	0.24
NSE & CE	5	50	0.16
PPE & CE	5	50	0.12
None	5	50	0.23

Therefore, our final optimized model for this study utilizes a 5-layer, 50-neuron architecture with a physics-informed loss term comprising the PPE and CE to ensure the highest predictive accuracy.

3.2 Analysis of predicted results

While Mean Squared Error (MSE) is a standard metric for regression, it offers limited physical insight into the accuracy of a predicted flow field. To provide a more robust and domain-specific evaluation, we assess the PINN's performance by applying the Micro drag technique (Section 2.2) to the reconstructed wake. We then compare the drag coefficient (C_D) calculated from the PINN's output with the ground truth C_D from CFD simulation. We define our success criterion as a discrepancy of less than 0.001 (1 count), which would validate the model's practical utility for aerodynamic analysis.

Figure 6. visually confirms the high fidelity of the reconstruction, comparing the PINN-predicted flow field in the $u \leq 10$m/s zone with the ground truth. It is remarkable that the model achieved this accuracy without any direct training on the ground truth data within this unmeasurable region, relying solely on surrounding data and physical constraints.

A compelling quantitative comparison is presented in Figure 7., which shows Drag maps for three scenarios: the CFD ground truth, the PINN reconstruction, and the incomplete data mimicking the experimental measurements. The map from the incomplete data fails to capture the crucial drag recovery dynamics (the blue, $C_D < 0$ region), leading to a significant overestimation of the total drag coefficient ($C_D = 0.314$) versus the ground truth ($C_D = 0.294$). Conversely, the PINN-reconstructed map successfully reproduces the drag recovery region, resulting in a highly accurate drag coefficient of 0.295—a deviation of just 1 count from the ground truth.

The excellent agreement, with the C_D difference falling well within our 1-count threshold, confirms that the PINN-based reconstruction is not only accurate but also robust enough for quantitative vehicle wake analysis.

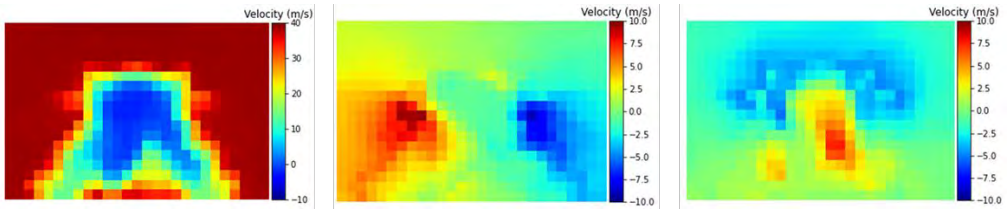

(a) Predicted results by PINNs (u, v, w)

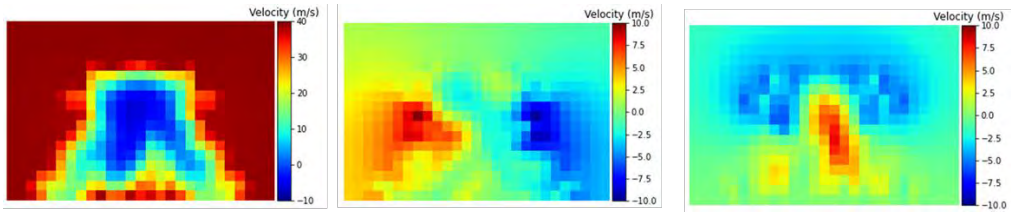

(b) ground truth (u, v, w)

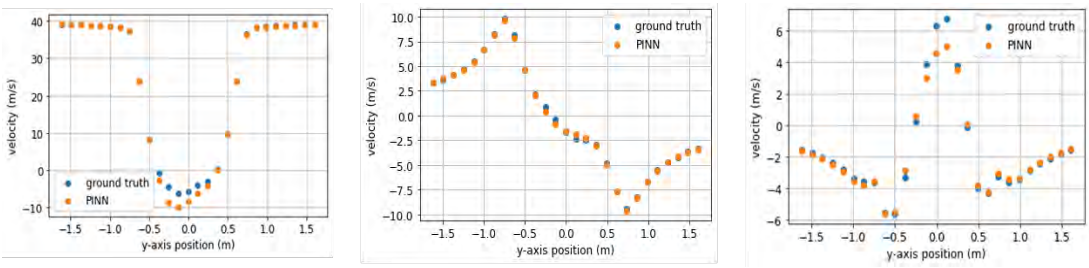

(c) PINNs prediction vs. ground truth: velocity distribution in the u < 10m/s region at z=0.725

Figure 6. PINNs results, ground truth's flow fields & velocity distribution

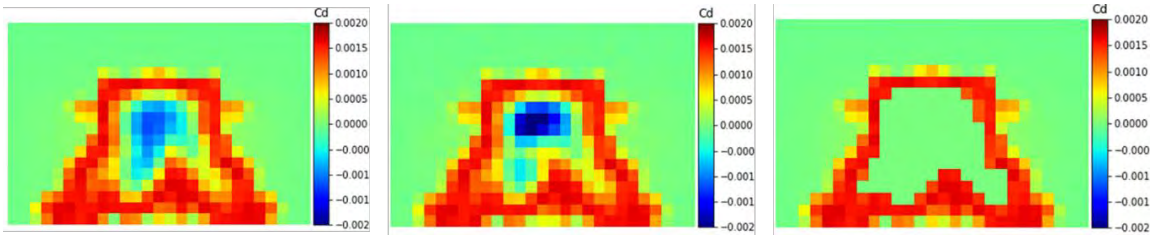

(a) ground truth (b) reconstructed by PINNs (c) Except u < 10m/s

Figure 7. Drag map visualization

3.3 Case Study: Application to Real-World Wind Tunnel Measurements

Having validated our PINNs framework against high-fidelity CFD data, the next critical step was to prove its efficacy on real, incomplete experimental measurements. This section details a case study where the methodology was deployed during development of the new IONIQ 5 (PE), using sparse data gathered directly from wind tunnel test.

The primary engineering goal was to lower the vehicle's drag coefficient (C_D) to increase its All-Electric Range (AER). First, the original IONIQ 5 was evaluated in the wind tunnel. Our PINN model was then applied to its sparse wake measurements to reconstruct a complete flow field. The resulting drag map analysis (Fig8.) provided a crucial insight that was otherwise unobtainable from the raw data: an unusually weak drag recovery region. The quantitative assessment, enabled by our method, pinpointed the roof spoiler (white box) as the primary culprit, responsible for a substantial 18% of the total drag.

Armed with this direct, quantitative feedback from experimental data, engineers redesigned the spoiler for the new IONIQ 5. The modified vehicle was re-tested in the wind tunnel, and the PINN analysis was repeated. The new Drag map (Fig8.) confirmed the success of the modification: the drag contribution from the redesigned spoiler was dramatically reduced to approximately 3%. This case study showcases the framework's successful transition from a validation tool to a powerful diagnostic instrument in an active vehicle development program.

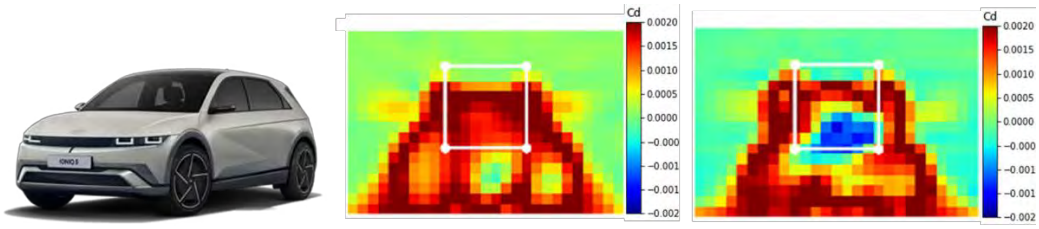

Figure 8. Drag map: IONIQ 5 (left), the new IONIQ 5 (right)

4 Conclusion

This study successfully developed a Physics-Informed Neural Networks (PINNs) framework capable of transforming incomplete, sparse wake measurements into complete, actionable flow fields. We initially validated the model's fundamental accuracy using a semi-synthetic CFD dataset of the DrivAer Estate model, optimizing it to a 5-layer architecture with a PPE-CE physics loss that predicted the drag coefficient to within 1 count (C_D 0.001).

Crucially, this research takes the vital step from validation in a controlled, simulated environment to successful application on real-world experimental data. To prove its practical readiness, the framework was applied directly to sparse data from a wind tunnel test of the new IONIQ 5. This PINN-driven analysis provided unprecedented quantitative insights, identifying a suboptimal roof spoiler as a major contributor to drag. The subsequent design improvements, guided by these findings, yielded a substantial drag reduction. This successful application on genuine experimental data validates our approach as a robust and impactful tool capable of bridging the gap between incomplete measurements and actionable engineering insights in the automotive development cycle. We anticipate that its capabilities can be further extended across diverse vehicle platforms by leveraging techniques like transfer learning.

5 Reference list

[1] Kim, M., Lee, J., Kee, J., and Chang, J: Hyundai Full Scale Aero-acoustic Wind Tunnel, SAE Technical Paper 2001-01-0629, 2001

[2] Heckmeier, Florian: Multi-Hole Probes for Unsteady Aerodynamics Analysis, Dissertation, Technical University of Munich, 2022

[3] Juyong Jeong et al.: Data recovery of 2D Lifetime-Based Phosphor Thermometry Using Deep Neural Networks, Measurement Science and Technology, 2023

[4] Dong Kim et al.: Sound Pressure Level Spectrum Analysis by Combination of 4D PTV and ANFIS method around automotive side view mirror models, Scientific Reports, 2021

[5] M.Raissi, P.Perdikaris, G.E.Karniadakis.: Physics-informed neural networks: A deep learning framework for solving forward and invese problems involving nonlinear partial differential equations, Journal of Computational Physics, 2019

[6] A.Cogotti.: A Strategy for Optimum Surveys of Passenger-Car Flow Fields, SAE, 1989

[7] A.I.Heft, T.Indiger, N.A.Adams.: Investigation of Unsteady Flow Structures in the Wake of a Realistic Generic Car Model, 29th AIAA Applied Aerodynamics Conference, 2011

[8] Munson et al.: Fundamentals of Fluid Mechanics, Wiley

Developments in Drag Reduction Methods and Devices for Road Vehicles

Michael Gerard Connolly*, Alojz Ivankovic and Malachy J. O'Rourke
University College Dublin, Dublin, Ireland

***michael.connolly@ucdconnect.ie**

This work is derived from material originally published in "Developments in Drag Reduction Methods and Devices for Road Vehicles" by Connolly, M. G.; Ivankovic, A.; O'Rourke, M. J., Applied Sciences, 2025 (DOI: 10.3390/app15179693) [1].

Abstract

This study presents new developments into novel drag reduction devices for road vehicles, focusing on the use of inflatable and alternative material rear drag reduction devices that employ both a single and multi cavity approach. The effectiveness of these devices is assessed through on-road testing using constant power measurements to evaluate the resulting drag reductions. Surface pressure measurements collected during testing are compared with CFD predictions, using both RANS and HLES methods to evaluate how accurately pressure changes are modelled when the devices are fitted to the test vehicles. A novel method for analysing vehicle surface flow in real-world conditions is also introduced, involving the capture and processing of video-recorded tuft imagery to determine appropriate means and standard deviations for the surface flow behaviour.

1 Introduction

The need for improved fuel economy and drag reduction in the road transport sector has become critical once again as it was following the oil crisis of the 1970s [2]. This renewed urgency is driven by many factors, which include the ongoing climate crisis [3], the demand for improved electric vehicle driving range [4], and the volatility of fuel prices due to geopolitical situations [5]. One of the most effective ways to improve a vehicle's fuel economy is to reduce the air resistance forces it experiences when on the road. Once a passenger car exceeds a speed of approximately 60 km/h, aerodynamic drag becomes the largest resistance force the vehicle must overcome [6]. The main issue is that the power requirement to overcome this air resistance grows in proportion to the cube of the vehicle's speed, which is one of the primary causes of why substantial fuel economy and range detriments are observed when driving at typical motorway speeds (120 km/h) [7]. Reducing aerodynamic drag on a vehicle reduces fuel consumption; however, the relationship between these reductions is highly dependent on a number of factors, such as vehicle type and driving cycle [6]. In general, when any road vehicle conducts a high-speed long-distance journey, drag is the largest consumer of the fuel used for that journey. A reasonable estimate, commonly used for such a driving cycle, is that a 10% drag reduction would realise a 5% fuel saving [8] [9] [10]. If the driving cycle was different, such as incorporating more city-based or outer city driving, which includes accelerations, starts and stops, then the weighting can be reduced to below 5% [11]. At the higher road speeds (100–120 km/h), aerodynamic drag can significantly exceed rolling resistance, making drag reduction one of the most effective strategies for improving fuel economy and addressing the current needs and challenges in the road transport sector.

2 Literature Review

The rear of a vehicle is particularly well suited for the addition of aerodynamic devices, due to the significant drag caused by the low-pressure wake that forms after flow separation at the end of a bluff body [12]. A comprehensive review of rear and other vehicle-mounted drag-reduction devices was presented in [13], which summarised key developments in the field over the past 50 years. The findings relevant to the present work are summarised next.

A wide variety of rear drag reduction strategies has been assessed in the literature, with performance depending on the shape and size of the device along with the vehicle type. [14] demonstrated a device known as the fluid tail, which redirected air from the rear wheel arches into the rear wake, reducing drag by 18–20% on a production hatchback, while [15] integrated servo-actuated flaps into a base cavity on an SUV to improve yaw-averaged drag performance. [16] outlined work related to the development of an inflatable rear drag reduction device for a road vehicle. The paper outlined drag reduction results for a very simplified body using scale wind tunnel work, without full-scale prototyping or results for the inflatable device on a passenger car. [17] showed that inward-angled deflectors at 20 degrees significantly diminished wake turbulence on a square-back configuration. [18] demonstrated that a tapered rear cavity could more than double the drag reduction achieved by a straight cavity in direct flow. Streamlined tail extensions were studied in [19], reporting up to 60% drag reductions using elongated, tapered designs, which maintained most of the drag reduction performance when truncated. Similarly, [20] showed that truncating a full boat tail on a box van yielded only a marginal performance drop, with drag reductions falling to just 31% from 32%. [21] measured a 3.3% drag reduction with a recessed cavity on an SUV without passive base bleeding, with only a 1% extra performance improvement when the base bleeding was included, highlighting how the initial cavity contributed most of the savings. [12] presented a new type of rear drag reduction device, known as the multi-stage converging cavity, which utilised multiple angled cavities within one another to access a downstream high-pressure zone. The device then redistributed this pressure over the vehicle's base, realising substantial base drag reductions.

In the context of heavy-duty vehicles, [22] examined a boat tail design with a shortened, angled bottom panel and found that excluding the bottom panel halved the overall drag reduction, underscoring the need for bottom surfaces on rear cavities and tails. A study by [23] confirmed that increased cavity length enhanced drag reduction, especially when combined with side skirts, with [24] documenting a 6.5% fuel saving for a road-tested practical cavity device on a heavy truck. Various appendables were studied in [25] for a pick-up truck, where combining a rear boat tail constructed from plates with a partial bed cover led to a drag reduction of 21 counts. Shortened boat tails also performed effectively in the studies outlined by [26] and [27], reporting drag reductions of 10.3% and 10.9% on a heavy and light-duty truck geometry respectively using wind tunnel tests. [28] reviewed various trailer-mounted aerodynamic devices for heavy trucks and recommended boat tail lengths between 24 and 32 inches for a viable trade-off between performance and practicality. The influence of specific panel configurations on rear cavities was explored in [29], which showed a full enclosure with tapering of 10 degrees maximised performance, and that removing lower panels significantly reduced the drag reduction. Overall, these studies highlight that significant drag and fuel savings are realisable through the integration of a rear tail or cavity device appended to the base of a road vehicle.

3 Road Testing Methodology

3.1 Measuring a Drag Change on-Road

The method described next for measuring a drag change on-road was first described in [30], therefore only a brief summary of the technique will be provided next. The method involves fixing the vehicle's throttle pedal across two vehicle configurations. For a given, fixed, throttle position, a road vehicle will reach a constant equilibrium speed for its configuration on a long flat straight road. This happens because by fixing the vehicle's throttle pedal, the fixed power output from the engine is used to counteract both the drag and the rolling resistance force on the vehicle. It was confirmed in [30] that fixing the vehicle's throttle pedal across configurations does produce a fixed power output from the engine, which was confirmed via three different power measurements remaining constant for multiple different configurations with two different vehicles. An example to demonstrate the method is as follows: The baseline standard vehicle has its throttle pedal fixed at 35% compression, the vehicle will then reach a constant speed on a long, flat, straight road, V_1. The vehicle is then configured in some way, such as by adding a kayak to its roof. When this configured vehicle travels down the same road with the same throttle pedal compression it will reach a new speed, V_2. The resulting speed delta measured on the road, V_1 - V_2, can then be used with the equation set discussed next to determine the percentage drag change on the vehicle.

3.1.1 Governing Equations

The derivation for the percentage drag change equation begins from the constant power statement (Equation 1), which becomes Equation 2, as the only two forces acting on a vehicle once it reaches its equilibrium speed for a given power input are drag and rolling resistance.

$$P_1 = P_2 \tag{1}$$

$$(D_1 + R_1)(V_1) = (D_2 + R_2)(V_2) \tag{2}$$

A reasonable assumption to apply is that the rolling resistance force between the two configurations at the speeds V_1 and V_2 remains constant. This is valid as the measured speed delta is often less than 10 km/h, and the rolling resistance force change across such a speed delta would be minimal [31]. Applying this assumption to Equation 2, the power balance then becomes Equation 3.

$$\frac{1}{2}\rho V_1^3 C_{D1} A_1 + RV_1 = \frac{1}{2}\rho V_2^3 C_{D2} A_2 + RV_2 \tag{3}$$

Equation 3 can then be rearranged to isolate the drag area of the vehicle in its second configuration, which can then be subbed into the percentage drag change formula to produce Equation 4. This is the final equation of the derivation, which is used to determine the percentage change in drag for a baseline vehicle caused by any given configuration change.

$$C_{D2}A_2 = \frac{\frac{1}{2}\rho V_1^3 C_{D1} A_1 + R(V_1 - V_2)}{\frac{1}{2}\rho V_2^3}$$

$$\%Drag\ Change = \frac{D_2 - D_1}{D_1} = \frac{C_{D2}A_2 - C_{D1}A_1}{C_{D1}A_1} = \frac{C_{D2}A_2}{C_{D1}A_1} - 1$$

$$\%Drag\ Change = \left(\left(\frac{V_1}{V_2}\right)^3 + \frac{2R(V_1 - V_2)}{\rho V_2^3 C_{D1}A_1} - 1\right) 100 \tag{4}$$

The percentage drag change determined by Equation 4 is primarily determined by the values inputted for the road-measured speeds, V_1, and V_2. To apply the formula, an approximate estimate of the baseline vehicle's drag area and rolling resistance is required. It was shown in [30] via a sensitivity analysis, that only general estimates of these values are required, as the formula is relatively insensitive to the values used for the drag area, $C_{D1}A_1$, and R. The formula's primary sensitivities are related to the values inputted for V_1 and V_2, highlighting the need for the accurate determination of the road-measured speeds using GPS to gain representative results.

3.1.2 Test Track & Testing Conditions

A 3.5 km section of public road was used as the test track which can be seen in Figure 1. The test track was comprised of a main test section and two pretest sections which led into the main test section from either side. To ensure minimal interference from external traffic, all road tests were conducted between the hours 1–4 am. The vehicle's throttle pedal was fixed at the start of the pretest section after which the vehicle begins to reach its equilibrium speed, which usually occurs just prior to entering the main test section. At the centre of the main test section, the vehicle's speed is recorded using dual frequency GPS, which has a speed measurement accuracy of 0.25 km/h based on the number of satellites the GPS can access along the test track. The vehicle's speed is recorded using several runs travelling in both directions. Testing was conducted only on dry calm nights, where the external wind speed was measured to be less than 2 km/h using a handheld hot wire anemometer at the centre of the test track over a period of 90 s. In general, the external wind speed for most test nights was less than 1 km/h, and any slight wind was accounted for by recording the vehicle's speed when coming from both directions. The track has substantial tree cover either side which added additional protection from any slight external wind which came perpendicular to the track. In general, the averaged speeds recorded when coming from both directions were approximately the same, or varied by at most 1-2 km/h due to any slight external wind conditions during testing. Any runs which encountered traffic interference that would have affected the equilibrium speed recorded at the speed record point were scrapped, however scrapping a run was uncommon due to the minimal traffic interference along the test track during the testing hours stated.

3.1.3 Testing Procedure & Test Vehicles

The throttle pedal position for the test vehicles was monitored using an OBD II Bluetooth scanner (OBDLink MX+). This scanner also provided information on the vehicle's power output based on measurements from quantities such as mass air flow rate and fuel injection data. As stated previously, the power output measured using three different power indicators during testing confirmed that the engine's power output remained constant across configuration changes for a fixed throttle pedal. Prior to any speeds being recorded, the test vehicle was warmed up for approximately 20–30 minutes by

Figure 1: Images of the test track with details of the main and pretest sections. Adapted from [30].

driving it along the test track. This allowed the vehicle's engine, tires and other moving components to reach normal operating temperatures. In general, a given vehicle configuration required 6–10 runs until the vehicle's constant equilibrium speed could be determined. This was done by observing a modal speed for the runs in each direction. Once the modal speed was recorded in each direction after the required number of runs, an average of these two speeds was taken, which resulted in the overall equilibrium speed recorded for a given vehicle configuration. The two test vehicles used for the study were a 2017 VW Golf Mk7 1.6 L diesel, and a 2018 Citroen Berlingo commercial van 1.6 L diesel L1 H1. Both these vehicles are shown in Figure 2.

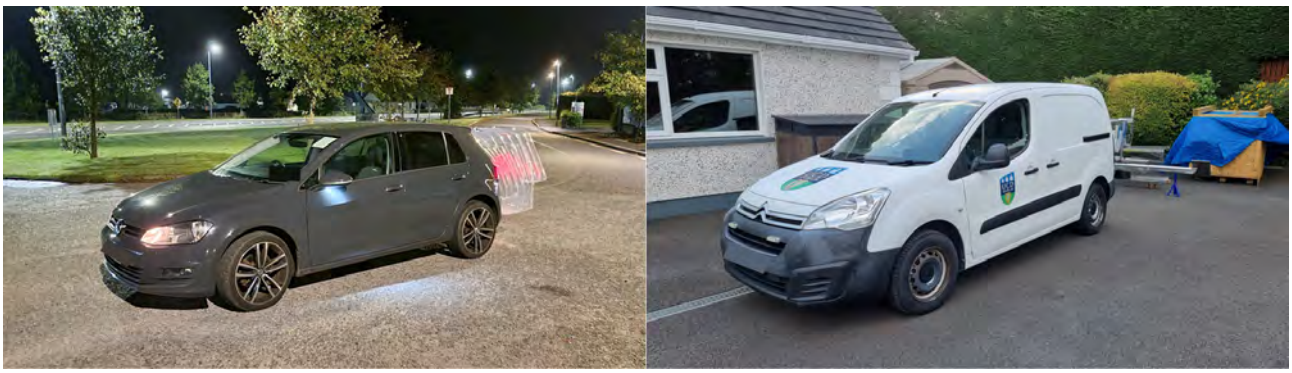

Figure 2: The two test vehicles used in the study which included a VW Golf Mk7 (shown left with an inflatable device) and a Citroen Berlingo L1 H1 van (right).

As stated previously, to use Equation 4 a rough estimate of the test vehicle's baseline drag area and rolling resistance were required. The VW Golf Mk7 was taken to have a C_D value of 0.305 based on CFD results [30] and outline values based on online sources where the manufacturer claims the vehicle to have a C_D value between 0.3 - 0.31 depending on spec [32] [33]. The rolling resistance value for the VW Golf Mk7 was taken as 150 N, which was based on its mass and the road surface of the test track. This value is typical for a hatchback vehicle of this size, based on an example in [6] which outlines a similar value for a Mercedes Benz B-Class. The drag coefficient for the van was based on an online source stating it to be 0.35 [34], and the rolling resistance value was taken as 200 N, which accounts

for the van's larger mass, and condition based on a service life as a commercial van with over 100,000 km travelled. These values match those used in [30] for the same vehicles. The VW Golf Mk7 was used for this study on account of its availability to the authors as a personal vehicle and the Citroen Berlingo van was provided by the University of the authors to assist with research activities. The frontal areas for the vehicles were measured using a CAD frontal area projection tool using highly detailed STL files for both vehicles. The frontal areas for the car and van were measured as 2.113 m^2 and 2.800 m^2 respectively.

To ensure a fair comparison of the drag force deltas between road measurements and CFD predictions, the denominators in the percentage drag change formulas for the CFD data use the same reference values as those used for the road data. This means that in the percentage drag change formula for the van and car, the deltas are always divided by 0.35 and 0.305, respectively, when the areas for the vehicle configurations remain constant. For both the car and van, the frontal projected areas remained constant across all rear drag reduction device configurations, including when no devices were fitted.

4 Results & Discussion

4.1 On-Road Drag Change Measurements

All CFD-predicted drag changes stated in this section are based on the RANS methodology disucssed in [1]. The air density used for the CFD simulations was 1.2215 kg/m^3. When calculating the road-measured drag change using Equation 4, the same density value was applied. Although the most appropriate value for ρ is that measured on the testing night when V_1 and V_2 are recorded, the formula is highly insensitive to ρ. Therefore, for simplicity and consistency across tests with slightly varying air densities, and for direct comparison with CFD, a single value of 1.2215 kg/m^3 was used. To demonstrate this insensitivity, if a value of 1.25 kg/m^3 were used for ρ when calculating the road-measured drag change in Table 1, the result would shift only from 13.52% to 13.48%, confirming the suitability of using a single air density value.

An important consideration when interpreting the CFD-predicted drag changes for the inflatable and foam cavity devices is that the simulations are based on idealised CAD geometries. In practice, discrepancies existed between the CAD models supplied to the manufacturer and the final manufactured devices. The degree of sealing between each device and the vehicle rear also has a significant impact on the drag reduction achieved, with tighter seals generally producing greater benefits. Accurately representing the exact level of sealing in CAD is difficult due to the shape uncertainties when working with such devices. Therefore, the CFD-predicted drag changes for the inflatable and foam devices should be viewed as idealised indicators for the performance achievable under optimal manufacturing and sealing conditions.

4.1.1 Van with Inflatable Triple Cavity

A rigid triple cavity device for the Citroen Berlingo van was first outlined in [30]. An inflatable version of this device was developed in an attempt to preserve similar performance, while offering the added benefits of reduced weight, lower cost, and easier storage. Figure 3 outlines the final manufactured version of this device. A key limitation of inflatable devices is that their section thickness must be significantly greater than that of rigid devices. By having a thickened section for the cavities, the rear projected surface area on the multi cavity device is increased, which can negatively affect the drag reduction, as those rear surfaces are subjected to pressures below ambient static pressure. This is especially the case for the outer and middle cavity, but less so for the inner cavity which can have a positive pressure exerted on its rear face as it makes contact with a downstream high-pressure bubble. Details on how a multi cavity device reduces drag using this downstream high-pressure bubble are outlined in detail in [12] and [30]. The contrast between the manufactured inflatable and the idealised inflatable is shown in Figure 4, where the idealised version is free from any rippled surfaces and, most importantly, the end of the outer cavity features a taper. This taper was omitted from the real inflatable by the manufacturer due to the difficulty of incorporating it into the inflatable design. This tapered surface is needed to help the device converge the wake and reduce drag. By not having the taper, the drag reduction realised by the manufactured device was always going to be less than that for the idealised version.

Figure 3: A collection of images highlighting the inflatable triple cavity device for the van. This figure demonstrates the inflation process, how it is protected from hot exhaust gases (with an image of the shield on the VW Golf Mk7 for a better visual), and how it looks on the road from an aerial view.

One other interesting feature outlined in Figure 3, is that the device uses a silver reflective heat shield on its underside in the vicinity of the vehicle's exhaust pipe. This triple cavity device was one of the first inflatable devices to be manufactured and road tested in this study. On the first attempt at road testing with this device, the device was punctured due to the heat from the exhaust gases after approximately 30 minutes of driving. Following this incident, all subsequent inflatable devices were fitted with a heat shield in this area. This heat shield solution was very effective at protecting the devices, as no future ruptures of any inflatables due to exhaust heat occurred. This device can be inflated in approximately 2 to 3 minutes using a high-power, high-flow-rate pump (shown in Figure 3). The device attaches to the vehicle via hooks that engage the panel gap between the doors and body, with straps linking the hooks to O-rings on the inflatable's surface. Brake lights, indicator signals, and the rear licence plate are still visible when the device is attached to the vehicle.

Configuration Name	V_1 (km/h)	V_2 (km/h)	Road-Measured $\Delta Drag$	CFD Predicted $\Delta Drag$
Van Inflatable Triple Cavity	99	103.25	-13.5%	-16.3%*

Table 1: Drag change results for the van with the inflatable triple cavity.
(*) CFD prediction based on idealised geometry for the device.

Table 1 outlines the drag reduction results for this device on the van. The road-measured drag reduction based on the road-measured speeds V_1 and V_2 was 13.5%. When driving on the road with

this inflatable device, the van is noticeably much quieter, as the level of turbulence in the van's wake is significantly reduced due to the presence of the device. It was also observed to handle better in corners, likely due to a more stable base wake in the slightly yawed flow encountered during cornering. The CFD predicted drag change using an idealised model for the device was found to be 16.3%. This was based on the delta between the CFD predicted C_D for the baseline van (0.297) and that for the inflatable device (0.240), divided by the road value for the van's C_D, 0.35, outlined previously in Section 3.1.3. To quantify the effect the level of sealing between the device and the vehicle has on the drag reduction, an additional CFD simulation was performed. This showed that if the device was perfectly sealed against the van, the C_D value for the device drops to 0.228, producing a drag reduction of 19.7%. This highlights the need for caution when comparing road-measured results with CFD predictions for flexible or slightly deformable devices.

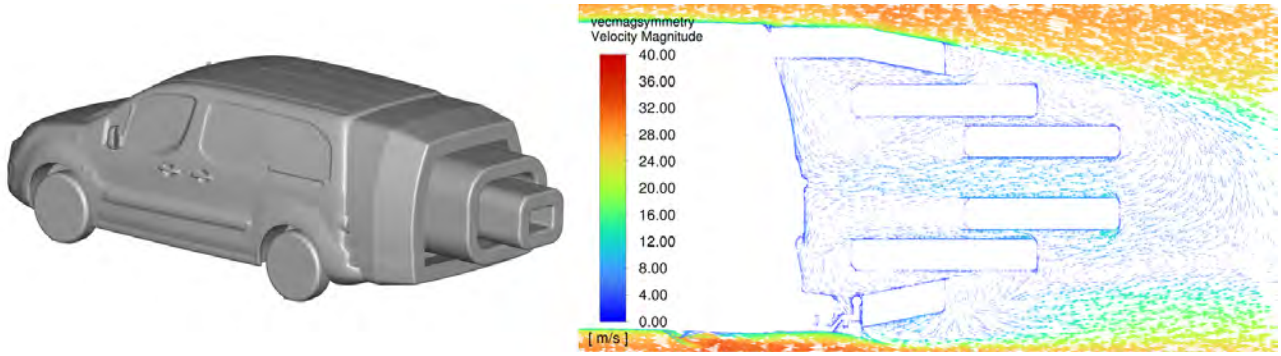

Figure 4: Outline of the CFD model and idealised shaped for the van's inflatable triple cavity (left) with the velocity flow field inside the device along the vehicle's symmetry plane (right).

4.1.2 Van with Inflatable Single Cavity

Having demonstrated that an inflatable triple cavity device could be constructed, a single cavity device was developed to offer similar performance. This was achieved mainly by changing the shape of the bottom section, removing the taper and raising it slightly from the bottom trailing edge of the van. This change was made because the bottom taper on the triple cavity device did not have attached flow, and it reduced performance by increasing the rear projected surface area exposed to underpressured flow. Additionally, removing the inner two cavities reduced the rear projected area, which helped further increase drag reduction, as the device now carried less self drag. Figure 5 outlines the manufactured inflatable single cavity, while Table 2 details the road-measured and CFD predicted drag reductions. It is notable that the CFD predicted drag reduction for the single cavity (-18.0%) is greater than that for the triple cavity (-16.3%), this is mainly due to the single cavity's improved outer cavity design. If another inner cavity were designed to go inside this single cavity, the drag reduction would further improve, however, the improvement would not be as substantial as that seen when working with rigid thin section cavities. Therefore, because of the added self drag associated with the thicker sections of inflatable devices, implementing them as single cavities is generally more practical, as the marginal gains from using multiple cavities are not large enough to justify the extra material and size.

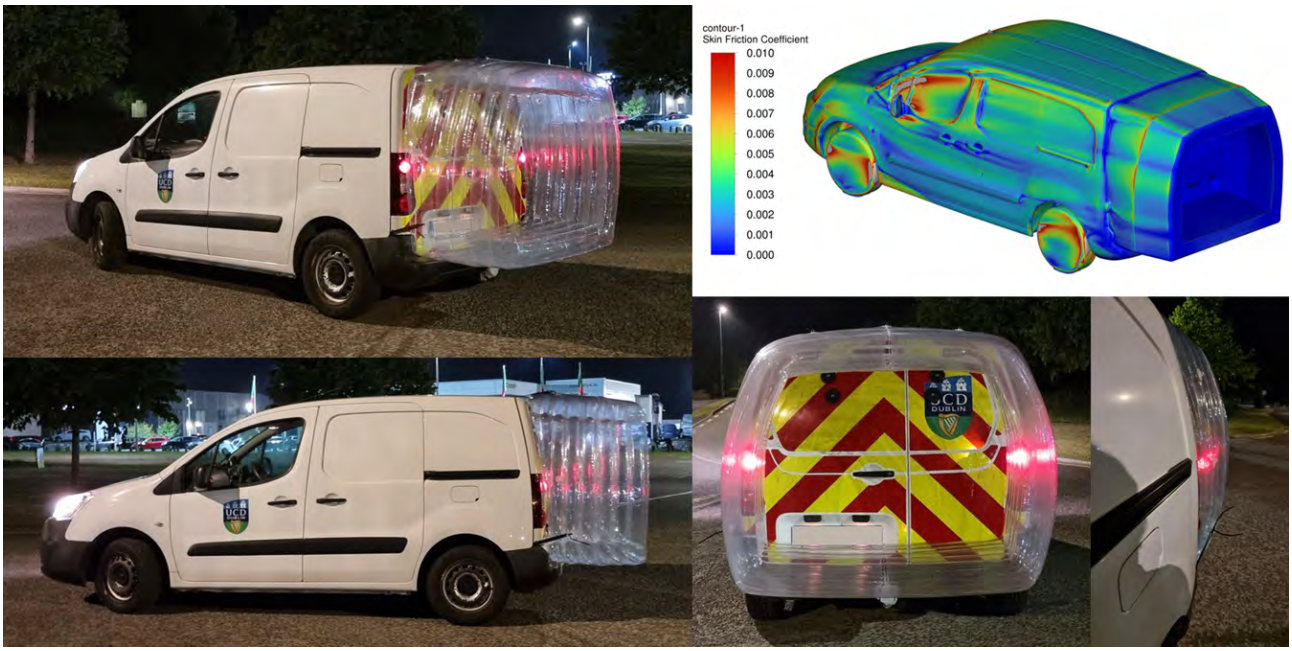

Figure 5: Images highlighting the inflatable single cavity device on the van. Shown top right is a skin friction coefficient contour plot along the configuration's surface.

The road-measured speed, V_1, for the unconfigured van outlined in Table 2, is notably much higher than that detailed in Table 1. This was because the road testing associated with the triple cavity device was performed with 35% throttle compression across configurations, while 37% was used for the single cavity device. The 35% throttle compression was chosen for the triple cavity testing in order to keep the recorded road speeds closer to 100 km/h, as it was expected that the V_2 for the triple cavity device would be quite large if testing was performed at 37% throttle compression. The road-measured drag reduction for the inflatable single cavity device (-9.0%) was notably much lower than that predicted by the CFD (-18.0%) for an idealised device. The cause of the deviation was primarily due to the sizing of the manufactured device, which was slightly too large for the base of the vehicle. This over-sizing issue can be observed in Figure 5, where the top and sides of the inflatable slightly protrude out past the base of the van into the flow. Additionally, the stated CFD predicted value is based on a tightly sealed inflatable against the rear of the van. This level of sealing was not present on the real device, particularly on the side sections near the van's lights. Another major cause of the discrepancy is the shape deviations, particularly the rippled surface and the general absence of tapering on the top and sides, which differ significantly from the idealised device.

Configuration Name	V_1 (km/h)	V_2 (km/h)	Road-Measured $\Delta Drag$	CFD Predicted $\Delta Drag$
Van with Inflatable Single Cavity	106.75	109.75	-9.0%	-18.0%*

Table 2: Drag change results for the van with the inflatable single cavity.
(*) CFD prediction based on idealised geometry for the device.

4.1.3 Car with Foam Cavity

One of the main disadvantages of inflatable devices is the difficulty in making their shape match the desired form drawn and studied in CAD and CFD. A solution to this was to construct a single cavity device from foam for the VW Golf, CNC milled to allow a closer match between the CAD geometry and the real device. The foam device shown in Figure 6 was constructed from EPS foam, wrapped in aluminium tape, and coated in polyurea paint to provide added strength, waterproofing and general weather resistance. The final device was a very close match with the CFD model in terms of its overall shape. The CFD model for this device predicted a drag reduction of 27.5% as detailed in Table 3. This idealised reduction is based on a perfect seal between the device and the rear of the car, combined with perfect alignment of the device. The main discrepancies between the real device and the CFD model were related to a reduced level of sealing, and the alignment of the device. On the night when this device was road tested, the device was slightly misaligned, such that the device was tilted backwards slightly. This can be partially seen in the top left image of Figure 6. This was only observed when reviewing the images of the road tested device after the testing and comparing them with how the CFD model had the device aligned.

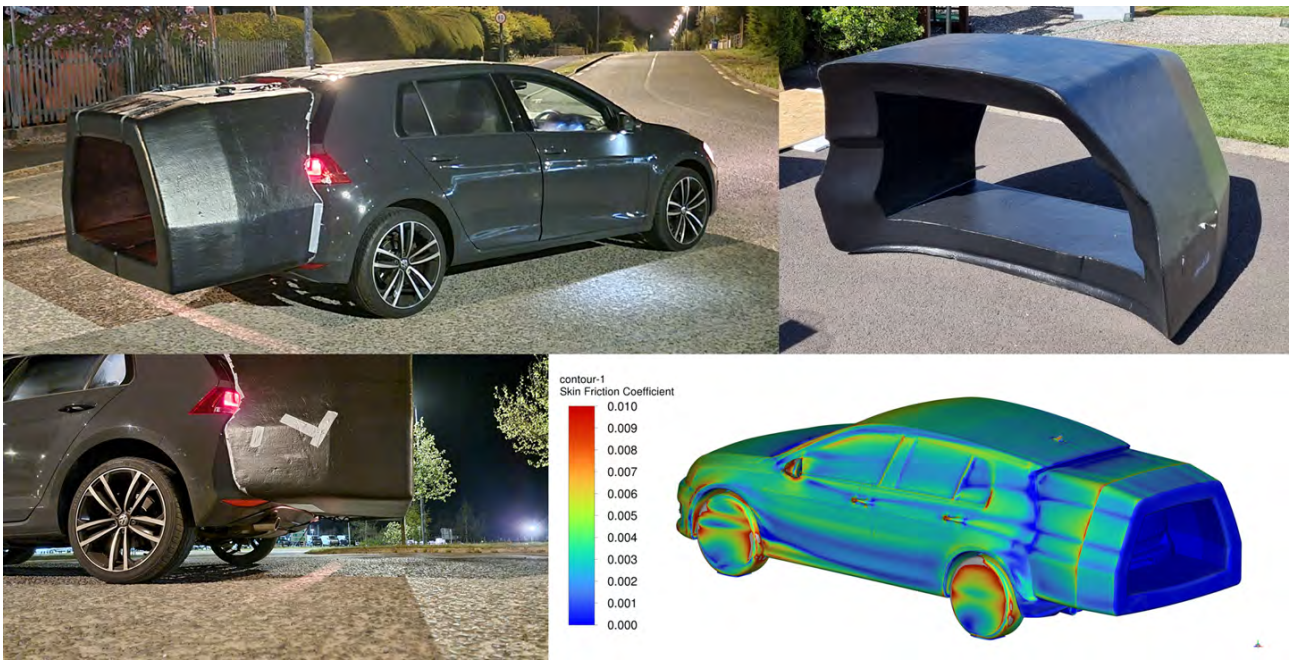

Figure 6: Images highlighting the foam single cavity device for the car with a skin friction coefficient contour plot along the configuration's surface shown bottom right.

Even with these deviations, the road-tested device still achieved an appreciable 17.4% drag reduction. If the device were better sealed and correctly aligned it would be very likely to produce a drag reduction in excess of 20%. Driving with this device on the VW Golf had a very noticeable effect on its speed and acceleration, with the car reaching highway speeds with substantially less throttle effort. The device was light enough to be installed on the vehicle by a single individual. Additionally, when viewed from the rear, both the licence plate and rear lighting systems were visible with only minor obstruction.

This device could be further refined by reducing its section thickness, taking its current size down from approximately 150 mm to 75 mm. This would improve both rear visibility and the realised drag reduction, as reducing the rear projected surface would lower the self drag on the cavity's rear face.

Configuration Name	V_1 (km/h)	V_2 (km/h)	Road-Measured $\Delta Drag$	CFD Predicted $\Delta Drag$
Car with Foam Cavity	99	104.5	-17.4%	-27.5%*

Table 3: Drag change results for the car with the foam cavity.
(*) CFD prediction based on idealised geometry for the device.

4.1.4 Car with Inflatable Double Cavity

As the rear of the VW Golf was smaller than that of the Citroen Berlingo van, constructing a triple cavity inflatable device for it was not feasible given the required section thickness for each cavity when made from inflatable material. Therefore, to demonstrate a multi cavity inflatable device on the passenger car, a double cavity variant was designed and manufactured, as shown in Figure 7. This device was made primarily to study its usability instead of pursuing a maximum drag reduction. This was due to the van inflatable device results, which indicated that when manufacturing rear devices from inflatable material, the gains from using multi cavity variants are only marginal due to manufacturable shape constraints. A major issue with this device was the lack of support for the inner cavity when connected to the outer cavity. To help support it, a cable tie chain was used to connect the ends of the top surfaces of the outer and inner cavity, which can be seen in the images of Figure 7. Even with this support, the inner cavity was observed to bounce/oscillate slightly in the vertical direction when on the road during testing.

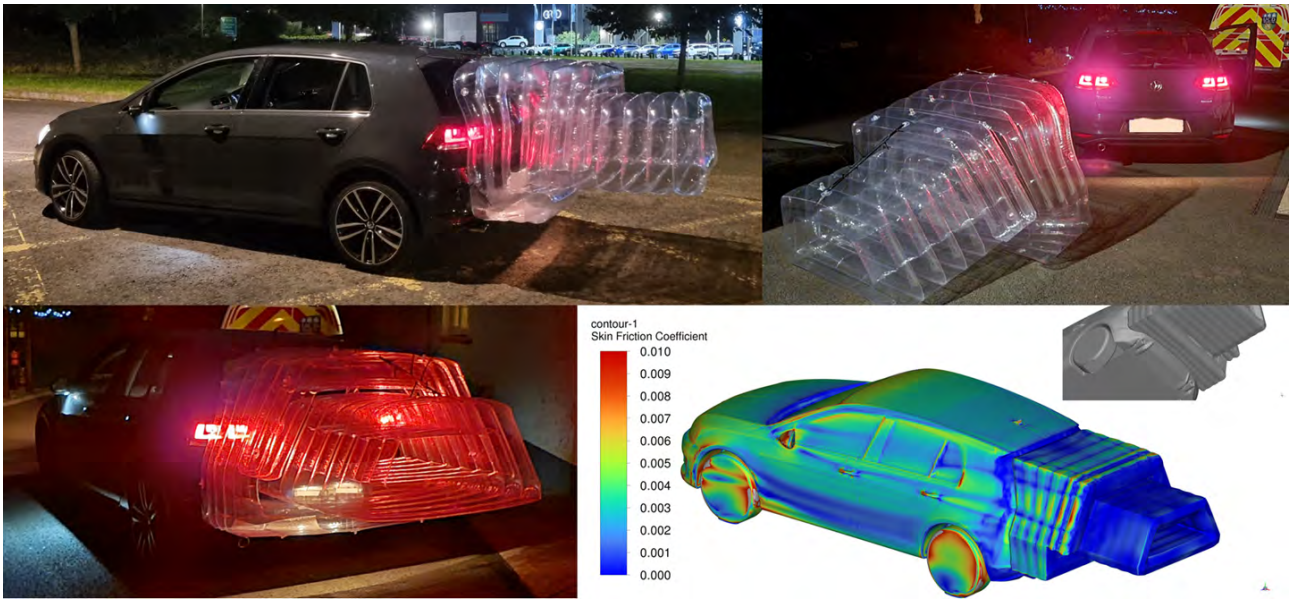

Figure 7: Images highlighting the inflatable double cavity device for the car with a skin friction coefficient contour plot along the configuration's surface shown bottom right.

Therefore, the road-measured drag reduction presented in Table 4 was always unlikely to match that predicted with the CFD model. The bouncing issue combined with a general lack of sealing between the device and the lower rear of the VW Golf is primarily what caused the road-measured reduction to realise just 8% compared to the 16.4% predicted with CFD. Figure 7 includes an image showing the level of sealing between the underside of the device and the car for the CFD model, which was tightly sealed. This contrasted with the manufactured device, which had a noticeable gap in this region.

Configuration Name	V_1 (km/h)	V_2 (km/h)	Road-Measured $\Delta Drag$	CFD Predicted $\Delta Drag$
Car with Inflatable Double Cavity	102.5	105	-8.0%	-16.4%*

Table 4: Drag change results for the car with the inflatable double cavity.
(*) CFD prediction based on idealised geometry for the device.

4.1.5 Car with Adapted Inflatable Double Cavity

Given that the inner cavity of the car's inflatable double cavity was prone to bouncing, an adapted version was created by cutting it away. This effectively made a single cavity device for the car using just the outer section of the original double cavity. Figure 8 shows this device, while Table 5 presents its road-measured results. Removing the inner cavity did reduce the device's performance, demonstrating just a 5% drag reduction for its adapted single cavity variant in comparison to its original 8% drag reduction as a double cavity. While the realised drag reduction was smaller, the adapted version of this device was significantly more practical and user-friendly. This is shown in the lower images of Figure 8, which illustrate how the device can be easily manoeuvred to allow access to the vehicle's rear storage space.

Figure 8: Images highlighting the adapted (inner-removed) inflatable double cavity device for the VW Golf. Shown is an outline for how the inner cavity was cut away and how the device can be manoeuvred to facilitate access to the rear boot space and how it can be easily deflated and stored.

Reaching through the centre of the device to open the boot was made easier with the inner cavity removed. Additionally, the device can be easily flipped onto the roof of the car to access the boot, or it can remain attached to the hatch as the boot opens. Another benefit of this smaller device is that it can be quickly deflated and easily stored in the boot, taking up less space as a result of the reduced material. The original double cavity can be stored and manoeuvred in a similar way, but it requires more effort and must be fully deflated to fit in the boot, whereas the single variant requires only partial deflation.

Configuration Name	V_1 (km/h)	V_2 (km/h)	Road-Measured $\Delta Drag$
Car with Adapted Inflatable Double Cavity	102	103.5	-5.0%

Table 5: Drag change results for the car with the adapted (inner-removed) inflatable double cavity.

4.2 Surface Pressure Measurements

4.2.1 Van with Rigid Triple Cavity

The inflatable triple cavity device for the Citroen Berlingo van previously detailed in Section 4.1.1 was based on a rigid triple cavity device which was first studied in [30]. This rigid device (shown in Figure 9) was used in this present study to quantify the changes to the van's base pressure map once the device was fitted. Six base pressure patches, labelled A–F, were fitted to the van's rear, which was divided horizontally into three sections, with patches A–B, C–D, and E–F representing the top, middle, and lower sections, respectively. Table 6 outlines the recorded pressure deltas on each of the six patches for the three measurement methods. The road-measured pressure deltas show that the largest base pressure increase occurred on the lower section of the van once the device was fitted, with patches E and F reporting increases of 64 Pa and 75 Pa respectively. The next largest pressure increase was recorded on the middle section, with the top section showing the lowest pressure rise.

Figure 9: Images showing the locations of the six base pressure patches fitted to the Citroen Berlingo van (left) and the rigid triple cavity device fitted to the van for testing (right).

Patch Pressure Difference ΔP (Pa)	A	B	C	D	E	F
Road-Measured	24	20	34	52	64	75
RANS	58	63	52	91	36	49
HLES	23	32	30	46	69	87
RANS Error	34	43	18	39	-28	-26
HLES Error	-1	12	-4	-6	5	12

Table 6: Pressure deltas recorded at each of the six patches shown in Figure 9 using the three different measurement methods, with an outline for the errors between the CFD methods and the experiment.

The HLES method successfully predicted this trend with relatively high accuracy, with four out of the six patches demonstrating an error of 6 Pa or less. In contrast, the RANS methodology predicted a noticeably different change to the van's base pressure map, predicting a greater pressure increase in the upper section compared to the lower section. The limitations of RANS in accurately predicting base pressure distributions for squareback geometries are well documented in the literature. Notably, the AutoCFD workshops [35] [36] provide a relevant example, where simulations on a squareback Windsor body using RANS models showed significant discrepancies compared to experimental results, whereas scale-resolving methods demonstrated improved agreement. While RANS struggles to predict the exact shape change to the base pressure map as a result of the rear device, it remains valuable in predicting overall changes in C_D during development. For this device, the RANS method predicted a total drag reduction of 65 counts once fitted to the van, while the HLES method predicted a slightly higher 76 counts.

[30] demonstrated that predictions of drag force changes using RANS showed a high level of agreement with on-road measurements when appendable devices were fitted to road vehicles. For example, the road-measured drag reduction for this device on the van reported in [30] was 17.5%, which correlated closely with the 18.6% reduction predicted using RANS. In contrast, the HLES method would have predicted a notably higher reduction. When working with CAD models of vehicles that have smooth undersides and no internal flows, RANS can produce results that more closely match road measurements due to a potential beneficial cancellation of errors. A rear drag reduction device is likely to produce a greater drag reduction when fitted to a vehicle with a smooth underside, as the lower turbulence and improved flow attachment in the underside flow interact more effectively with the device, leading to enhanced downstream pressure recovery and increased base pressure. Vehicles with messy undersides will experience the opposite effect, reducing the effectiveness of the device. Therefore, the lower drag reductions predicted using RANS are more likely to align with on-road measurements due to a beneficial cancellation of errors when simulating such CAD geometries.

4.2.2 Car with Foam Cavity

The foam cavity device fitted to the VW Golf Mk7, outlined in Section 4.1.3, was equipped with six base pressure patches, as shown in Figure 10. This was done to correlate the road-measured drag reduction of 17.4% with a corresponding average base pressure increase resulting from the device. Due to the difficulty in CAD modelling the exact level of sealing between the car and the device, no comparisons are made to the CFD pressure changes, as the CFD base pressure measurements are highly sensitive to the represented/modelled level of sealing between the device and the car. Table 7 outlines the road-measured patch pressures for each of the six patches for both vehicle configurations. The rear of the car experiences a substantial base pressure increase with the device, as it taps into a higher downstream pressure and distributes this over its base. The cavity, particularly with its end tapers, enhances downstream static pressure recovery, benefiting the overall base pressure increase on the car's rear. The top (A-B) and middle (C-D) sections experienced the largest pressure increase, with reported deltas of approximately 50 Pa over both sections.

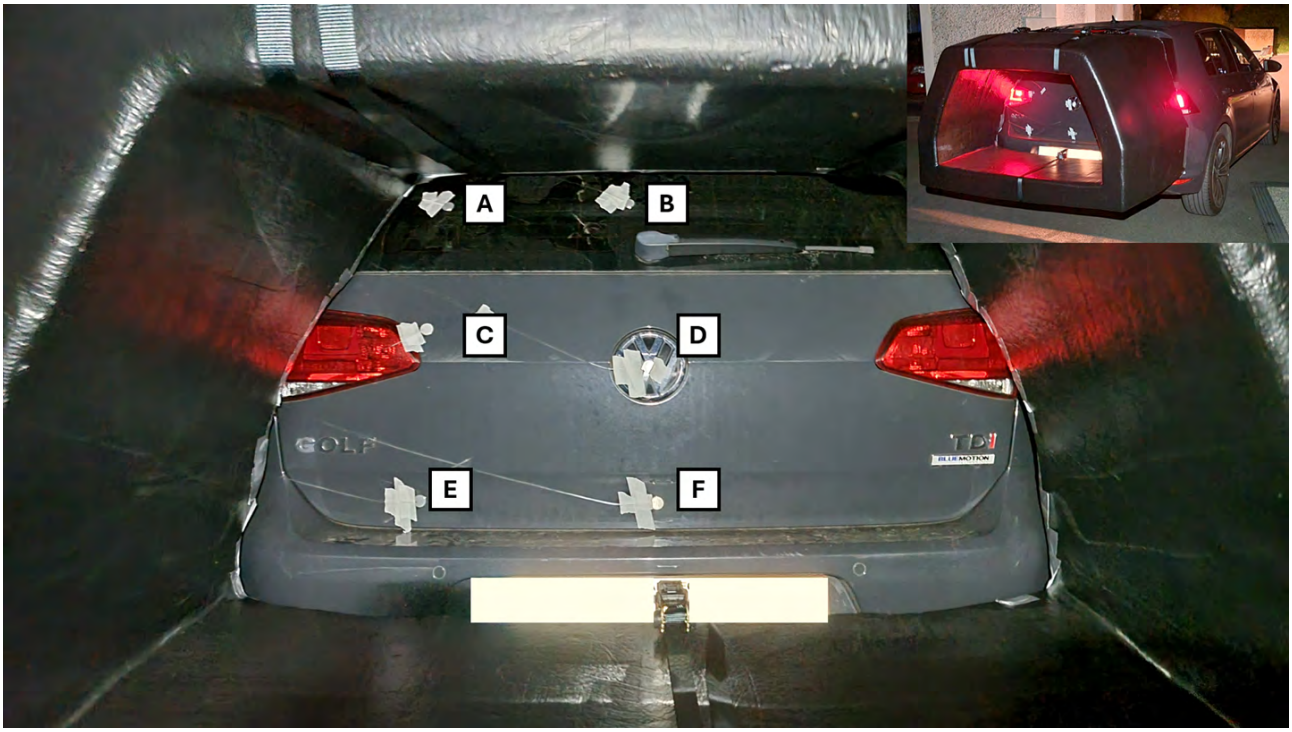

Figure 10: Locations of the six base pressure patches fitted to the VW Golf Mk7 during the surface pressure testing with the foam cavity device.

Based on the percentage base pressure increases for the six patches in Table 7, the overall average base pressure rise for the rear is likely between 40% and 50% as a result of the device. A CFD analysis of the baseline car revealed that approximately 50% of the total drag force is carried by the rear alone. For the real vehicle, this value is likely slightly less when accounting for the vehicle's internal flows, detailed wheels, and less smooth underside. Therefore, the true portion of the total drag force carried by the VW Golf's rear is likely between 40-50%. Taking this as 45% for the purpose of applying a

weighting to the measured base pressure increase of 40-50%, the estimated drag reduction for this base pressure rise is likely between 18% and 22.5%. This estimate does not account for the additional self drag present on the foam cavity, particularly on its angled tapers and end faces, due to their rear-projected surfaces. When accounting for this, the drag reduction is likely closer to the 18% estimate rather than the higher value of 22.5%. Therefore, the road-measured drag reduction of 17.4% shows reasonably good agreement with the estimated drag reduction, based on the measured base pressure increases.

Road-Measured Patch Pressure (Pa)	A	B	C	D	E	F
VW Golf Mk7	-107	-110	-114	-111	-100	-94
VW Golf Mk7 with Foam Cavity	-59	-58	-58	-63	-58	-61
Delta	48	52	56	48	42	33
|% Base Pressure Increase|	45%	47%	49%	43%	42%	35%

Table 7: Pressure measurements from each of the six pressure patches (as shown in Figure 10) for the VW Golf Mk7, with and without the foam cavity.

4.3 Surface Flow Measurements - Car with Taxi Sign

As outlined by the surface flow measurement methodology detailed in [1], averaged images of tufts produced from video-recorded imagery provide a better understanding of surface flow in transient regions compared to reviewing instantaneous single images. The wake of the taxi sign is one such region, where instantaneous images reveal little about the overall surface flow behind the sign. Figure 11 presents an averaged image of the surface flow in the wake of the taxi sign, alongside CFD predictions of the same flow. Four distinct regions, labelled 1–4, are identifiable in the averaged image and show good agreement with the CFD. Region 1 highlights how the flow begins to wrap inwards far downstream in the wake of the taxi sign. Region 2 illustrates how some of the flow is able to pass beneath the centre of the taxi sign at high speed, which is captured by the very straight alignment of the tufts in the top image of Figure 11. This compares well with the lower CFD skin friction plot, where a green/orange-coloured zone is clearly identifiable in this region, highlighting this fast-moving, attached flow.

Region 3 is identified as the end of a recirculation bubble directly behind the taxi sign along the vehicle's centreline, indicated by the vertical standing tufts. Identifying Region 3 using only instantaneous images was difficult and generally inconclusive. In contrast, the averaged image clearly reveals its presence. The CFD predicts this feature effectively, as shown by the vector plot along the symmetry plane in the lower image of Figure 11. Finally, Region 4 shows a zone of reversed flow in the wake of the taxi sign, extending along the centre of the roof noticeably far downstream. This extensive reversed flow region is also visible in the CFD vector plot, which indicates a similar downstream extent. Overall, Figure 11 demonstrates the usefulness of averaged tuft imagery in understanding overall surface flow patterns in highly transient regions, providing a reliable basis for meaningful, validatable comparisons against CFD-predicted surface flow behaviour.

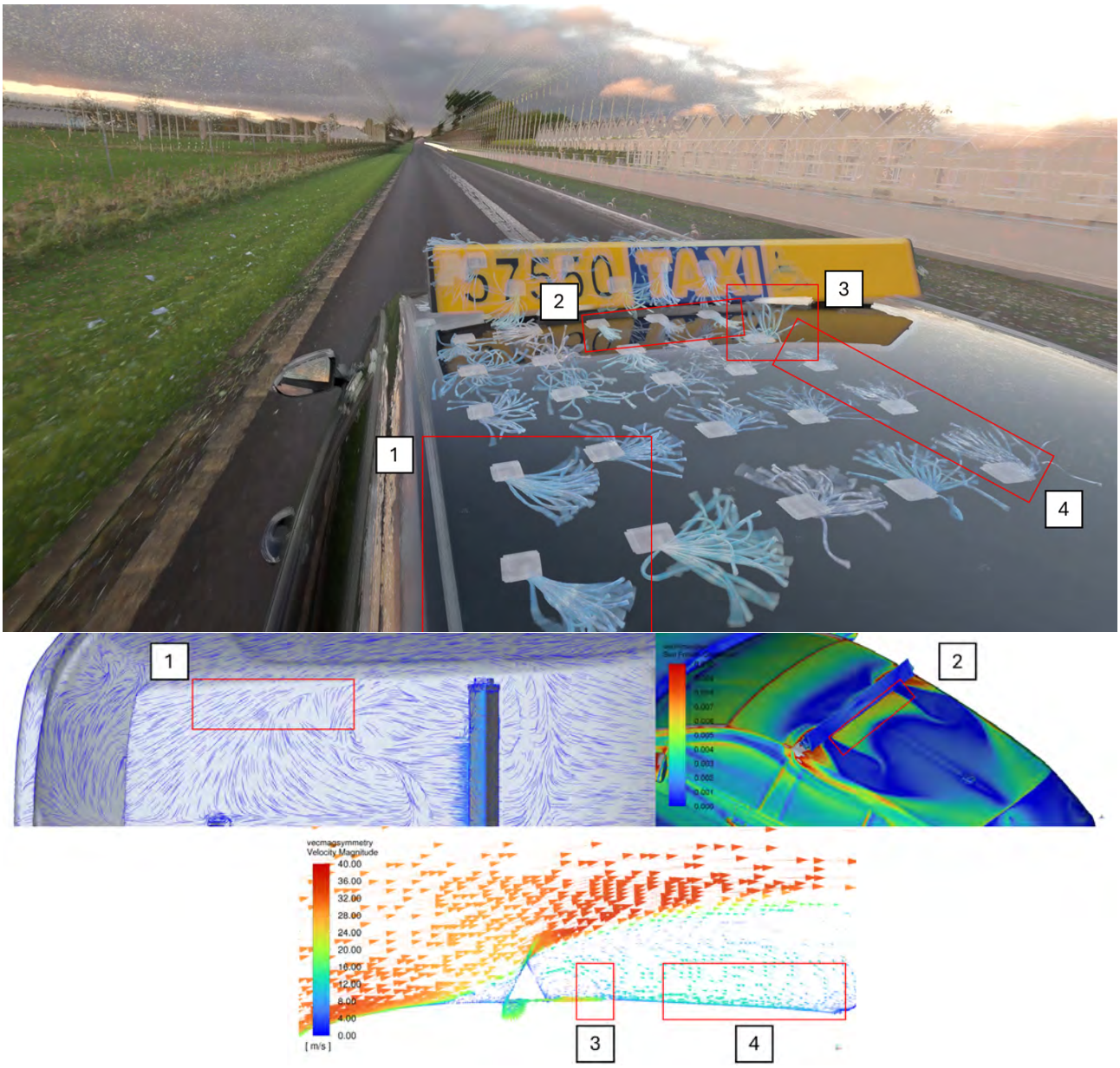

Figure 11: Comparison between the road-measured surface flow and that predicted using CFD for the VW Golf Mk7 fitted with the Irish taxi sign.

5 Conclusions

- A detailed look at some of the latest developments in appendable drag reduction technology for road vehicles was outlined, presenting results on inflatable rear cavity devices, one foam device, and a rigid triple-cavity device. Of the inflatable devices presented, these include findings for single, double, and triple cavity variants. These devices were road tested and simulated using CFD on two road vehicles: a VW Golf Mk7 and a Citroen Berlingo van.

- The best-performing road-tested inflatable device was a triple cavity mounted to the van, which reduced drag by 13.5%. Overall, inflatable devices were found to have practical benefits over rigid devices, such as easier storage and mounting. However, their drag reduction performance was closely linked to their manufactured shape and the level of sealing between the inflatable and the rear of the vehicle. Producing an inflatable device that matches the CAD model used in the CFD studies during development can be difficult, and performance degradation was observed due to shape deviations such as rippled surfaces, thickened sections, lack of tapering, and incomplete sealing with the vehicle.

- Due to the thickened section required when working with inflatable devices, an additional self drag penalty is incurred, as the increase in rear-projected surface area results in an added rearward drag force. This contrasts with thin-section rigid devices, where a panel can have near-negligible self drag. This led to the conclusion that implementing inflatable devices as multi cavity variants offers only marginal benefits, as the added drag reduction can be offset by the increased self drag from the thicker cavity sections.

- The observed driving properties of the test vehicles when fitted with a rear drag reduction device were noticeably improved over the standard vehicles. Clear increases in acceleration, reduced throttle effort for maintaining road speeds, and improved handling while cornering were all observed when driving with some of the most effective rear devices outlined in this article.

- Road testing with a foam cavity device mounted to the VW Golf Mk7 was found to reduce drag by nearly 20%, with corresponding base pressure measurements indicating the device offered a near 50% increase in base pressure inside the cavity. Additionally, base pressure measurements taken from a van fitted with a rigid triple cavity device also showed substantial base pressure increases. When compared with CFD, scale-resolving methods such as Hybrid-LES were found to offer much closer agreement with the road-measured pressure deltas than the RANS methods, even though both CFD approaches predicted similar overall drag deltas for the device.

Funding

This research was funded by The Irish Research Council grant number EPSPG/2022/213 and Science Foundation Ireland grant number 22/NCF/EI/11277.

Acknowledgments

The support of UCD SONIC and ICHEC for the use of their HPC resources.

References

[1] Michael Gerard Connolly, Alojz Ivankovic, and Malachy J. O'Rourke. Developments in Drag Reduction Methods and Devices for Road Vehicles. *Applied Sciences*, 15(17):9693, January 2025. ISSN 2076-3417. doi: 10.3390/app15179693. URL https://www.mdpi.com/2076-3417/15/17/9693. Publisher: Multidisciplinary Digital Publishing Institute.

[2] Noraini Zulkifli and Daniel Haqeem. The Opec Oil Shock Crisis (1973): An Analysis. *Asian Journal of Research in Business Economics and Management*, 4:136–148, March 2022. doi: 10.55057/ajrbm.2022.4.1.12.

[3] David Banister. The climate crisis and transport. *Transport Reviews*, 39(5):565–568, September 2019. ISSN 0144-1647. doi: 10.1080/01441647.2019.1637113. URL https://doi.org/10.1080/01441647.2019.1637113. Publisher: Routledge _eprint: https://doi.org/10.1080/01441647.2019.1637113.

[4] Sudarshan Gnanavendan, Senthil Kumaran Selvaraj, S. Jithin Dev, Kishore Kumar Mahato, R. Srii Swathish, G. Sundaramali, Oussama Accouche, and Marc Azab. Challenges, Solutions and Future Trends in EV-Technology: A Review. *IEEE Access*, 12:17242–17260, 2024. ISSN 2169-3536. doi: 10.1109/ACCESS.2024.3353378. URL https://ieeexplore.ieee.org/document/10398193.

[5] Caroline Kuzemko, Mathieu Blondeel, Michael Bradshaw, Gavin Bridge, Erika Faigen, and Louis Fletcher. Rethinking Energy Geopolitics: Towards a Geopolitical Economy of Global Energy Transformation. *Geopolitics*, 30 (2):531–565, March 2025. ISSN 1465-0045. doi: 10.1080/14650045.2024.2351075. URL https://doi.org/10.1080/14650045.2024.2351075. Publisher: Routledge _eprint: https://doi.org/10.1080/14650045.2024.2351075.

[6] Thomas Christian Schuetz. *Aerodynamics of road vehicles*. Sae International, 2015. ISBN 0-7680-8253-6.

[7] Chun Li, Fan Yang, and Zhenchong Wang. Experimental study on high-speed endurance of electric vehicle at normal temperature (25℃). volume 268, page 01032. EDP Sciences, 2021. ISBN 2267-1242.

[8] Transport Canada. Review of Aerodynamic Drag Reduction Devices for Heavy Trucks and Buses, May 2018. URL https://tc.canada.ca/en/programs/non-funding-programs/ecotechnology-vehicles-program/review-aerodynamic-drag-reduction-devices-heavy-trucks-buses. Publisher: AHEC.

[9] The Effect of Aerodynamic Drag on Fuel Economy | ARC, . URL https://www.arcindy.com//effect-of-aerodynamic-drag-on-fuel-economy.html.

[10] K. Chow. Improving vehicle rolling resistance and aerodynamics. In Richard Folkson and Steve Sapsford, editors, *Alternative Fuels and Advanced Vehicle Technologies for Improved Environmental Performance (Second Edition)*, Woodhead Publishing Series in Energy, pages 459–481. Woodhead Publishing, January 2022. ISBN 978-0-323-90979-2. doi: 10.1016/B978-0-323-90979-2.00009-3. URL https://www.sciencedirect.com/science/article/pii/B9780323909792000093.

[11] Hyeonjik Lee and Kihyung Lee. Comparative Evaluation of the Effect of Vehicle Parameters on Fuel Consumption under NEDC and WLTP. *Energies*, 13(16):4245, January 2020. ISSN 1996-1073. doi: 10.3390/en13164245. URL https://www.mdpi.com/1996-1073/13/16/4245. Number: 16 Publisher: Multidisciplinary Digital Publishing Institute.

[12] Michael Gerard Connolly, Malachy J. O'Rourke, and Alojz Ivankovic. Reducing Aerodynamic Drag on Flatbed Trailers for Passenger Vehicles Using Novel Appendable Devices. *Fluids*, 8(11):289, November 2023. ISSN 2311-5521. doi: 10.3390/fluids8110289. URL https://www.mdpi.com/2311-5521/8/11/289. Number: 11 Publisher: Multidisciplinary Digital Publishing Institute.

[13] Michael Gerard Connolly, Alojz Ivankovic, and Malachy J. O'Rourke. Drag reduction technology and devices for road vehicles - A comprehensive review. *Heliyon*, 10(13):e33757, July 2024. ISSN 2405-8440. doi: 10.1016/j.heliyon.2024.e33757. URL https://www.sciencedirect.com/science/article/pii/S2405844024097883.

[14] Alberto Morelli. A New Aerodynamic Approach to Advanced Automobile Basic Shapes. SAE Technical Paper 2000-01-0491, SAE International, Warrendale, PA, March 2000. URL https://www.sae.org/publications/technical-papers/content/2000-01-0491/. ISSN: 0148-7191, 2688-3627.

[15] Magnus Urquhart and Simone Sebben. Optimisation of Trailing Edge Flaps on the Base Cavity of a Vehicle for Improved Performance at Yaw. *Flow, Turbulence and Combustion*, 109(2):309–326, August 2022. ISSN 1573-1987. doi: 10.1007/s10494-022-00323-z. URL https://doi.org/10.1007/s10494-022-00323-z.

[16] Kathleen M. McNamara, Jamey D. Jacob, Ben Loh, Ryohei Tsuruta, Taro Tsukada, Eiji Itakura, and Umesh Gandhi. Experimental Investigation of Drag Reduction on Automobiles With an Inflatable Boat-Tail. In *2018 Applied Aerodynamics Conference*, AIAA AVIATION Forum. American Institute of Aeronautics and Astronautics, June 2018. doi: 10.2514/6.2018-3964. URL https://arc.aiaa.org/doi/10.2514/6.2018-3964.

[17] Alessandro Capone and Giovanni Paolo Romano. Investigation on the effect of horizontal and vertical deflectors on the near-wake of a square-back car model. *Journal of Wind Engineering and Industrial Aerodynamics*, 185: 57–64, February 2019. ISSN 0167-6105. doi: 10.1016/j.jweia.2018.12.011. URL https://www.sciencedirect.com/science/article/pii/S0167610518306445.

[18] Magnus Urquhart, Max Varney, Simone Sebben, and Martin Passmore. Drag reduction mechanisms on a generic square-back vehicle using an optimised yaw-insensitive base cavity. *Experiments in Fluids*, 62(12):241, November 2021. ISSN 1432-1114. doi: 10.1007/s00348-021-03334-0. URL https://doi.org/10.1007/s00348-021-03334-0.

[19] Jeff Howell, Max Varney, Martin Passmore, and Daniel Butcher. The Aerodynamic Effects of a 3D Streamlined Tail on the Windsor Body. *Fluids*, 8(2):59, February 2023. ISSN 2311-5521. doi: 10.3390/fluids8020059. URL https://www.mdpi.com/2311-5521/8/2/59. Number: 2 Publisher: Multidisciplinary Digital Publishing Institute.

[20] R. L. Peterson. *Drag Reduction Obtained by the Addition of a Boattail to a Box Shaped Vehicle*. PhD thesis, August 1981. URL https://ntrs.nasa.gov/citations/19810020556. NTRS Author Affiliations: California Polytechnic State Univ. NTRS Report/Patent Number: NASA-CR-163113 NTRS Document ID: 19810020556 NTRS Research Center: Legacy CDMS (CDMS).

[21] Y. A. Irving Brown, S. Windsor, and A. P. Gaylard. The Effect of Base Bleed and Rear Cavities on the Drag of an SUV. SAE Technical Paper 2010-01-0512, SAE International, Warrendale, PA, April 2010. URL https://www.sae.org/publications/technical-papers/content/2010-01-0512/. ISSN: 0148-7191, 2688-3627.

[22] Eui Jae Lee and Sang Joon Lee. Drag reduction of a heavy vehicle using a modified boat tail with lower inclined air deflector. *Journal of Visualization*, 20(4):743–752, November 2017. ISSN 1875-8975. doi: 10.1007/s12650-017-0426-6. URL https://doi.org/10.1007/s12650-017-0426-6.

[23] Joshua P. Kehs, Kenneth D. Visser, Jeff Grossman, Jared Niemiec, Andrew Smith, and Charles M. Horrell. A Comparison of Full Scale Aft Cavity Drag Reduction Concepts With Equivalent Wind Tunnel Test Results. *SAE International Journal of Commercial Vehicles*, 6(2):486–497, September 2013. ISSN 1946-391X, 1946-3928. doi: 10.4271/2013-01-2429. URL https://www.sae.org/publications/technical-papers/content/2013-01-2429/. Number: 2013-01-2429.

[24] J Kehs, K Visser, J Grossmann, C Horrell, and A Smith. Experimental and full scale investigation of base cavity drag reduction devices for use on ground transport vehicles. pages 269–283. Springer, 2010.

[25] Kuo-Huey Chen and Bahram Khalighi. A CFD Study of Drag Reduction Devices for a Full Size Production Pickup Truck. SAE Technical Paper 2015-01-1541, SAE International, Warrendale, PA, April 2015. URL https://www.sae.org/publications/technical-papers/content/2015-01-1541/. ISSN: 0148-7191, 2688-3627.

[26] Drew Landman, Richard Wood, Whitney Seay, and John Bledsoe. Understanding Practical Limits to Heavy Truck Drag Reduction. *SAE International Journal of Commercial Vehicles*, 2(2):183–190, October 2009. ISSN 1946-391X, 1946-3928. doi: 10.4271/2009-01-2890. URL https://www.sae.org/publications/technical-papers/content/2009-01-2890/. Number: 2009-01-2890.

[27] Drew Landman, Matthew Cragun, Mike McCormick, and Richard Wood. Drag Reduction of a Modern Straight Truck. *SAE International Journal of Commercial Vehicles*, 4(1):256–262, September 2011. doi: 10.4271/2011-01-2283. URL https://saemobilus.sae.org/articles/drag-reduction-a-modern-straight-truck-2011-01-2283. Publisher: SAE International.

[28] Marc Belzile, Jeff Patten, P Eng, Brian McAuliffe, William Mayda, and Bernard Tanguay. Technical Report Review of Aerodynamic Drag Reduction Devices for Heavy Trucks and Buses. *Project*, 54:A3578, 2012.

[29] G. M. R. Van Raemdonck and M. J. L. Van Tooren. Numerical and wind tunnel analysis together with road test of aerodynamic add-ons for trailers. In *International Conference on Engineering Conferences International*, pages 237–252. Springer, 2010.

[30] Michael Gerard Connolly, Alojz Ivankovic, and Malachy J. O'Rourke. A Novel Method for Evaluating on-Road Drag Changes Using Constant Power Measurements. SAE Technical Paper 2025-01-8764, SAE International, Warrendale, PA, April 2025. URL https://www.sae.org/publications/technical-papers/content/2025-01-8764/. ISSN: 0148-7191, 2688-3627.

[31] Lisa Ydrefors, Mattias Hjort, Sogol Kharrazi, Jenny Jerrelind, and Annika Stensson Trigell. Rolling resistance and its relation to operating conditions: A literature review. *Proceedings of the Institution of Mechanical Engineers, Part D: Journal of Automobile Engineering*, 235(12):2931–2948, October 2021. ISSN 0954-4070. doi: 10.1177/09544070211011089. URL https://doi.org/10.1177/09544070211011089. Publisher: IMECHE.

[32] Pavel Niederle. ssp537 golf gte.pdf (4.79 MB) - Repair manuals - English (EN), October 2024. URL https://en.volkswagenclub.net/manual_download.php?id=1740.

[33] VW USA Press Release. 2015 Volkswagen Golf GTI Mk7 (US-Spec). URL https://www.caricos.com/cars/v/vw/2015_volkswagen_golf_gti_us/.

[34] Detailed specs review of 2016 Citroen Berlingo Multispace BlueHDI 100 model for Europe, October 2024. URL https://www.automobile-catalog.com/car/2016/2227385/citroen_berlingo_multispace_bluehdi_100.html.

[35] Gary J. Page and Astrid Walle. Towards a Standardized Assessment of Automotive Aerodynamic CFD Prediction Capability - AutoCFD 2: Windsor Body Test Case Summary. SAE Technical Paper 2022-01-0898, SAE International, Warrendale, PA, March 2022. URL https://www.sae.org/publications/technical-papers/content/2022-01-0898/. ISSN: 0148-7191, 2688-3627.

[36] AutoCFD4 | AutoCFD5, . URL https://autocfd.org/autocfd4/.

Development of aerodynamics of the facelifted Enyaq and Enyaq Coupe models

Jiri Novak

Technical Development
Skoda Auto a. s.
Tr. Vaclava Klementa 869, Mlada Boleslav II, 293 01 , Czech Republic

jiri.novak33@skoda-auto.cz

Abstract: The thesis summarizes the development of aerodynamics of the facelifted Enyaq and Enyaq Coupe models (MY 2025) in the technical development department of Skoda Auto. Through the gradual optimization of selected parts, aerodynamics has been improved, with a positive impact on the car's range. Several features and modifications contributed to improving Enyaq's already good aerodynamics, such as the new front end with the Modern Solid design, which features a slimmer Tech-Deck Face with an optimized transition to the hood, sealing the air duct behind the radiator grille, improved flow around the front wheels thanks to new air curtains and new alloy wheels on offer. CFD simulations and validation measurements were widely used during the development.

1 Introduction

Automotive aerodynamics is a technical discipline focused on the interaction between airflow and vehicle shape. Its optimization directly affects energy consumption, driving stability, noise levels, and overall comfort. Škoda Auto, as an established manufacturer of passenger vehicles, systematically integrates aerodynamic principles into the design of its models. The Enyaq, the brand’s first fully electric vehicle built on the MEB platform, underwent structural and visual updates as part of its 2025 facelift. Although primarily aimed at design enhancement, these changes also led to measurable improvements in aerodynamic performance. The aim of this article is to describe the technical aspects of these modifications and their impact on the vehicle’s aerodynamic efficiency.

Contribution: 2025 FKFS Conference on Vehicle Aerodynamics and Thermal Management
15 – 16 October 2025 | Leinfelden-Echterdingen

2 Škoda Enyaq and Enyaq coupé

The successful electric vehicle Škoda Enyaq has been offered in a new form since 2025. The updated model features a design aligned with the Modern Solid language and improved aerodynamics resulting in extended driving range. The drag coefficient (Cx) of the Enyaq model decreased from 0.256 to 0.245 compared to the previous version, while the Enyaq Coupé improved from 0.234 to 0.225. These are among the best values in this segment. Thanks to the improved aerodynamic drag coefficient and other changes, the vehicle's range increased by up to 7 km (WLTP cycle).

2.1 Project and Timeline

The project began in 2021 and followed a timeline that included several key phases—from initial design concepts through testing to final approval. It was classified as a "minor facelift," focusing on changes to the front section of the vehicle, primarily using virtual methods without physical prototypes. During development, 1,600 CFD simulations of external aerodynamics were conducted. The project also included extensive validation and later homologation measurements in the FKFS wind tunnel, totaling 110 hours of testing.

2.2 Aerodynamic Optimization within the Facelift

The improvement in the aerodynamic drag coefficient is the result of changes in the shape and function of several components across different areas of the vehicle. The design modifications were limited to the front of the car, and thus most aerodynamic enhancements are concentrated there. The optimized elements include:

- *Air Curtain* – The shape of the front bumper corner was refined to ensure optimal airflow around the front wheels while preventing air from entering the rear wall of the wheel arch. A central island surrounds the driver assistance sensor within the wheel cutout trim.
- *Upper Grille Transition* – The upper grille, now referred to as the Tech-Deck, features a smooth, frameless design that transitions seamlessly into the hood without causing flow separation. The hood latch lever within the gap is now better sealed.
- *Tighter Airflow Management* – Air passage to the heat exchangers has been further sealed using two-component air guides. The soft sections of these guides press more tightly against surrounding parts, minimizing unwanted leaks.
- *Wheel Portfolio* – As part of the facelift, several wheel designs were replaced with new, aerodynamically optimized versions. These improvements include reshaped aluminum rims or the addition of plastic covers.

- *Rear Underbody Deflector* – Although the rear section of the vehicle remained unchanged in terms of component shape, a new underbody cover with a rubber deflector was developed for the wagon variant to further harmonize the wake flow. However, this part was ultimately not included in the final production phase.

Figure 1: Overview of Optimized Areas within the Facelift

Attention was also given to tests and simulations concerning snow accumulation on the vehicle, aimed at protecting sensor functionality under winter conditions. To assess the impact on driving range, various accessories were tested and simulated, including roof boxes and towbar-mounted cargo boxes.

2.3 CFD simulations

The data center in Mladá Boleslav is designed to handle demanding aerodynamic simulations, the development of assistance systems, electromobility, and digital twins. Its computing capacity is equivalent to the performance of more than 60,000 standard PCs. According to the latest ranking [1], Škoda Auto a.s.'s corporate supercomputer placed 138th among the most powerful systems globally. With a performance exceeding 8.4 petaflops/s, it represents the most powerful computing infrastructure in the commercial sector in Central and Eastern Europe.

2.4 Experimental measurements in the aerodynamic tunnel

Experiments in the aerodynamic tunnel focused on validating Computational Fluid Dynamics (CFD) methods, determining sensitivity to changes, and fine-tuning virtual techniques for further application. This phase involved advanced measurement techniques – dynamic surface pressure sensing on the car body using in-house developed pressure strips, video recording of yarn movement with subsequent image analysis to visualize wake regions and flow separation boundaries, as well as wake traversing behind the wheels and rear of the vehicle using a multi-directional probe arm. Additionally, airflow through heat exchangers was monitored, enabling a detailed comparison between virtual simulation and actual flow behavior in the engine compartment.

Figure 2: Př Overview of optimized areas within the facelift (A – wake traversing zone, B – traversing arm monitoring the wake behind the front wheel, C – visualization of the measured total pressure field behind the front wheel, D – visualization of measured flow fluctuations using video analysis of yarn oscillation, E – overall view of the experimental vehicle in the aerodynamic tunnel)

In the final phase of the project, an additional set of aerodynamic measurements was conducted, this time focused on obtaining aerodynamic data for determining the vehicle's homologation values. Various equipment configurations were tested to assess their impact on the drag coefficient (Cx) and, consequently, on the vehicle's range within the WLTP process.

2.5 Summary

The Škoda Enyaq model has positioned itself among the top electric vehicles in terms of aerodynamics. The Coupe version, achieving a drag coefficient of Cx = 0.225 [2] in its facelifted form, currently stands as the best-performing slanted back BEV with the hight of over 1.6m (SUV). Even the standard Enyaq variant performs excellently with a Cx = 0.245 [3], confirming Škoda's strong emphasis on efficient airflow around the vehicle and its impact on energy consumption and driving range.

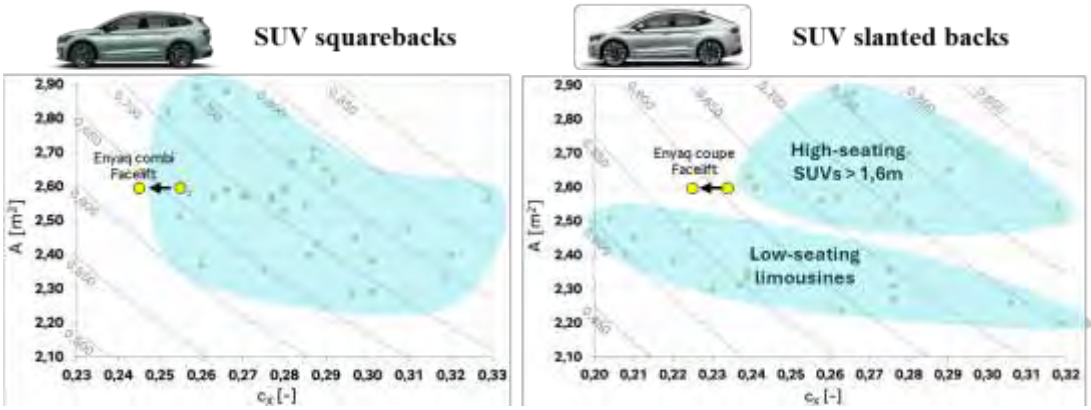

Figure 3: Overview of drag coefficient and frontal area values among competitors

3 Reference list

[1] List of largest HPC https://www.top500.org

[2] Press-kit for the Enyaq Coupe Facelift MY2025 model on Skoda Auto website https://www.skoda-auto.com/models/range/new-enyaq-coupe

[3] Press-kit for the Enyaq Facelift MY2025 model on Skoda Auto website https://www.skoda-auto.com/models/range/new-enyaq

Optimisation of Chassis Dynamometer Force Variability for Floor Anchor Restraint Systems

Luke Williams

Vehicle Efficiency – Thermal Energy Management
JLR
Banbury Road Gaydon, Lighthorne Heath, Warwick CV35 0RR

lwilli36@jaguarlandrover.com

Abstract: To ensure sufficient axle load correlation can be achieved between Climatic Wind Tunnel (CWT) chassis dynamometer testing and track testing, coast match methodology such as that seen in SAE J2264 should be utilised to ensure any facility-imposed forces are negated. Such methodology introduces increased test preparation time to carry out a coast match test prior to starting CWT testing. With increased pressure to reduce financial and environmental impact of CWT testing, an investigation into the repeatability of CWT vehicle installations was conducted. The investigation aimed to understand if a coast match test was required for subsequent installations of a vehicle into a CWT having completed an initial coast match test. An experiment was conducted to evaluate potential influencing factors, including tyre type, tyre pressure, dynamometer position and loading applied through the vehicle restraints. Analysis concluded that tyre pressure and loading applied through vehicle restraints led to the highest variability in applied force to the vehicle axles. Implementation of control techniques through inclusion of strain gauges to vehicle restraints reduced variability of axle loading normalised by track road load from a range of 13.2% - 4.5% down to 5.6 % - 1.8 % across speeds of 0-100 kph. Leveraging an improvement in vehicle installation repeatability allowed a singular coast match test to be utilised for subsequent vehicle tests, reducing both financial and environmental impact of CWT testing.

Contribution: 2025 FKFS Conference on Vehicle Aerodynamics and Thermal Management
15 – 16 October 2025 | Leinfelden-Echterdingen

1 Introduction

As part of the vehicle development cycle, Climatic Wind Tunnel (CWT) testing provides a crucial role in validating the thermal performance, robustness and efficiency of a vehicle. There are two main aspects of CWT testing, with the first being the control of environmental conditions, including Ambient Temperature, Relative Humidity, Solar Irradiation and Wind Speed. The second main factor is the force applied to the vehicle wheels via a chassis dynamometer. This is often referred to as the vehicle road load and is applied to the wheels via the chassis dynamometer rolling drums (often referred to as "rollers") located directly below each wheel. Figure 1 below shows an example of a chassis dynamometer within a CWT.

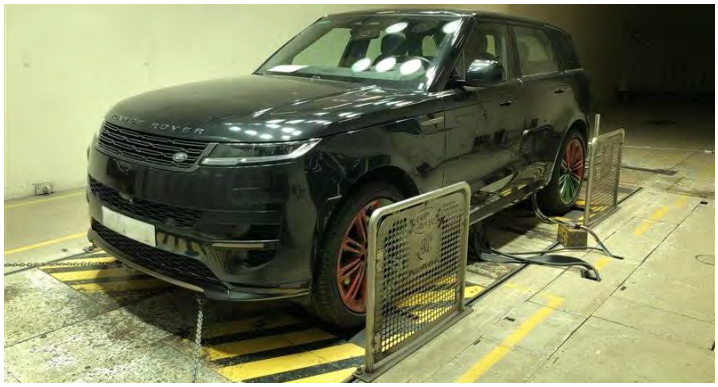

Figure 1 – Image of a chassis dynamometer within a CWT

A vehicle restraint system is utilised to maintain the vehicle in a stationary position on the chassis dynamometer, while ensuring the forces generated by the vehicle are transferred from the wheels to the power absorbers connected to the dynamometer rollers. To restrain the vehicle, a number of solutions are available. These include hub mounted, recovery point and floor anchor restraints. For this investigation only floor anchor restraint systems were evaluated due to the wider prevalence of those systems within UK based climatic facilities used for development.

As thermal system behaviour is highly influenced by the loading applied to the vehicle wheels, care must always be taken to ensure that the forces applied on a chassis dynamometer accurately reflect the real-world condition aimed to be evaluated. Coastdown match methodology, consisting of a ~1hr test prior to vehicle testing, is often utilised in line with best practices [1], to allows the differences in force between real world road load and dynamometer road load to be compensated.

To ensure all testing is carried out at the correct road load, a coastdown match test would be required at every instance a vehicle is installed onto a chassis dynamometer due to the variable vertical drive-axle static suspension deflection associated with lower control arm mounted floor anchor restraints. With increased financial and environmental pressures on vehicle development cycles, an investigation was highlighted to determine the level of variability between vehicle installations to evaluate if a singular coast match test could be utilised for subsequent vehicle installations.

If suitable control actions could be identified, a potential reduction in facility utilisation could be achieved through a reduction in the number of coast match tests required, both reducing the financial and environmental impact of vehicle development.

2 Investigation

2.1 Restraint System Methodology

A floor anchor restraint system commonly utilises four floor anchors and chains that connect to steel straps fitted around the lower control arms of the vehicle. Typically, the floor anchors are connected to steel straps on the opposite side of the vehicle to reduce lateral vehicle movement. Figure 2 & Figure 3 below shows a floor anchor restraint system within a CWT, applied to a Range Rover Sport.

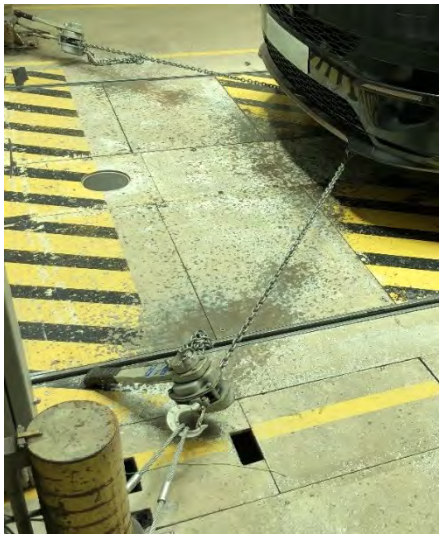

Figure 2– Front view of floor anchor restraint system applied to a Range Rover Sport.

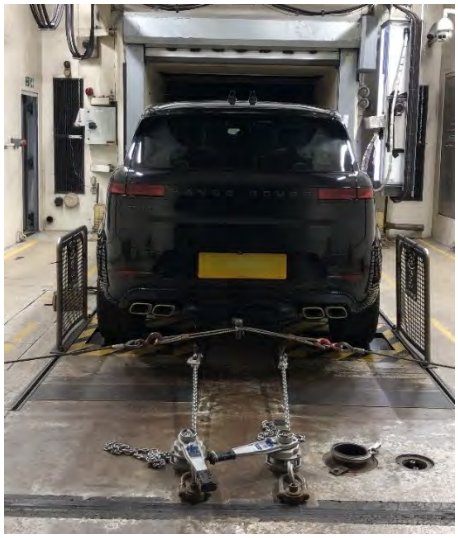

Figure 3 – Rear view of floor anchor restraint system & safety restraints applied to a Range Rover Sport

As can be seen in Figures 2 & 3, the tension of the vehicle restraints can be adjusted using the ratchet mounted next to the floor anchor point. A typical vehicle installation process involves positioning the vehicle on the dynamometer, setting the roller spacing to match the vehicle wheelbase and then restraining the vehicle to the dynamometer via the chains connected to the floor anchor restraints and lower control arm steel straps. The chain restraints are tensioned until deemed suitably pre-loaded by the facility operator. During this tensioning event, often static suspension deflection greater than 5mm is noted.

Post installation, the facility operator would inspect the vehicle and restraint arrangement before allowing a coast match test to be carried out.

2.2 Coastdown Match Methodology

To conduct a coast match test, a number of different methods can be utilised. For the purposes of this investigation, the Environmental Protection Agency (EPA) adopted process as detailed in SAE J2264 was utilised [2]. The methodology consists of the following process as shown below in Figure 4.

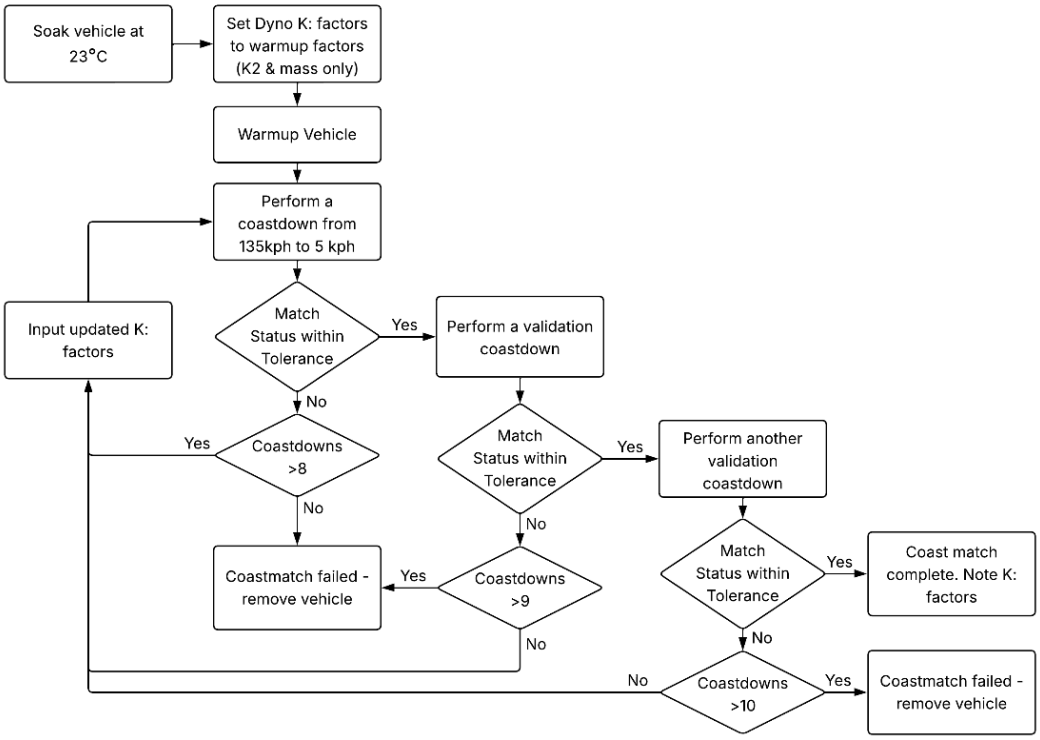

Figure 4 - EPA Coast Match Process

As seen in Figure 4, the coast match procedure consists of an iterative process, starting with a warmup phase followed by an iterative matching phase. The warmup phase is utilised to ensure driveline fluid temperatures are stabilised at a nominal running temperature prior to completing the matching process. The outcome of the matching process is a set of K: factors matched to the target road load and compensated for the additional imposed resistances of the vehicle test arrangement.

As detailed in SAE J2264 4.2.3, the coast match test completed may only be re-used for subsequent testing if the static suspension deflection is less than 5mm. As the deflection is often greater than 5mm for a floor anchor restraint system, a repeat coast down match test would be required to ensure the correct vehicle loading is applied for subsequent testing, aligned with best practices detailed in SAE J2777_202211 4.2 [1].

For testing the thermal performance of an Internal Combustion Engine (ICE) vehicle, the addition of a coastdown match test is relatively easy to contain as a stabilisation period for the driveline fluids is required prior to the test commencement, therefore no soak condition is required. However, for a Battery Electric Vehicle (BEV) or ICE efficiency testing, a pre-test soak is required during which time the vehicle cannot be driven, such as during test schedules shown in SAE J1634_202104 [3].

As a result, for BEV testing, a coast match test must be carried out prior to the vehicle soak in the CWT, leading to facility underutilisation as the vehicle cannot be soaked in a separate facility, which can result in over 9.5 hours of non-productive CWT time. Figure 5 below shows the process flow of carrying out BEV CWT testing from a soaked condition when a pre-test coast match test is required.

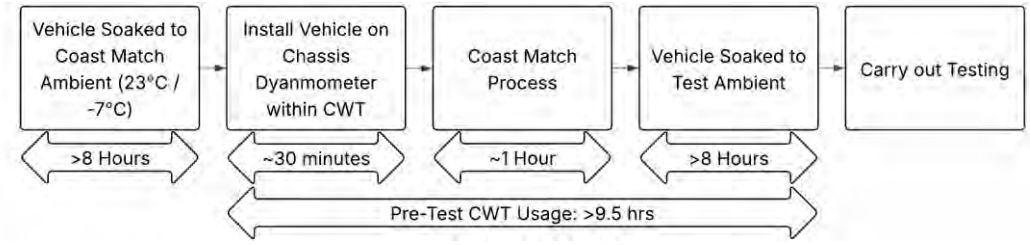

Figure 5 - BEV CWT Pre-Test Schedule with Coast Match

2.3 Repeatability Investigation

To determine the change in force applied to the vehicle between installations, an investigation into the major influencing factors was devised. A review of existing literature highlighted a number of key factors likely to influence the force applied to the vehicle, namely vehicle tyre pressure, tyre temperature, vertical loading and dynamometer wheelbase alignment. [3][4].

2.3.1. Test Equipment

For this investigation, a Range Rover Sport was used. The vehicle was fitted with supporting instrumentation and logging equipment to capture vehicle driveline fluid temperatures, powertrain torque, wheel and engine speed alongside tyre temperature and pressure. Table 1 below details the key vehicle attributes.

Vehicle Parameter	Test Vehicle
Vehicle Model	Range Rover Sport
Powertrain	Petrol Turbocharged Inline 6-cylinder MHEV
Driveline	4WD with fixed centre transfer case
Tyre Size	275/40 R22 108Y
Nominal Inflation Pressure	36 PSI
Vehicle Test Mass	2405 kg

Table 1 - Test Vehicle Details

The facility utilised for the investigation was a Climatic Wind Tunnel located at JLR Gaydon in the UK, with a schematic shown below in Figure 6.

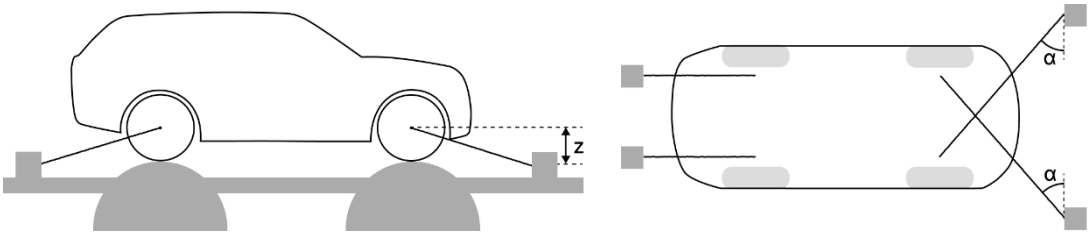

Figures 6 - Chassis Dynamometer Side & Top Profile Schematics

As shown in Figure 6, the z-height between the floor anchor point and vehicle lower control arm mounting point can vary dependent on the vehicle that is being tested and the location of the suspension lower control arms. The specification of the vehicle chassis dynamometer can be seen in Table 2.

Facility Parmeter	**Facility Specification**
Roller Surface	Anti-Slip Coating
Roller Type	Twin Axle Single Roller
Roller Width	0.6 m
Roller Diameter	1.70 m
Maximum Wheelbase	3.20 m
Restraint Type	Floor Anchored Chains
Fan Nozzle Outlet Area	6.75 m^2

Table 2 - Climatic Wind Tunnel Dynamometer Specifications

2.3.2. Influencing Parameter Evaluation

Having reviewed surrounding literature and the physical vehicle installation, a number of key influencing parameters were identified as shown in Table 3 below [3][4][5].

Variable	**Constant / Varied**
Tyre Temperature	Constant
Tyre Type	Constant
Tyre Pressure	Varied
Dynamometer Roller Positioning	Varied
Restraint Tension	Varied
Ambient Temperature	Constant

Table 3 - Influencing Parameter Type

Tyre temperature, tyre type and ambient temperature were all determined to be constant as they would be expected to remain consistent between coast match tests. To evaluate the impact of each variable on the outcome of the coast match test, a fixed procedure was utilised as seen below in Figure 7.

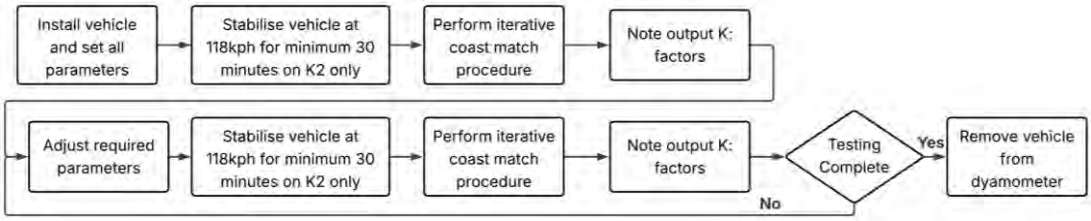

Figure 7 - Test Process Methodology

As in Figure 7, the procedure included a warmup duration of a minimum of 30 minutes at 118 kph to ensure consistent pre-test driveline fluid and tyre temperatures, aligning with standard JLR practices for WLTP type approval as per GBR-20171151 [6]. To ensure reliability of results generated, repeat testing was carried out for each test condition and an average of results taken with the exception of variation of the restraint tension whereby each test condition was considered individually. Table 4 below shows the test conditions evaluated.

Test Number	Tyre Pressure	Dynamometer Roller Position	Restraint Tension	Repeats
1	36 PSI	Centred	Baseline	4
2	36 PSI	-60 mm from centre	Baseline	2
3	36 PSI	-30 mm from centre	Baseline	2
4	36 PSI	-10 mm from centre	Baseline	2
5	36 PSI	+10 mm from centre	Baseline	2
6	36 PSI	+30 mm from centre	Baseline	2
7	36 PSI	+60 mm from centre	Baseline	2
8	16 PSI	Centred	Baseline	2
9	26 PSI	Centred	Baseline	2
10	46 PSI	Centred	Baseline	2
11	36 PSI	Centred	Configuration 1	2
12	36 PSI	Centred	Configuration 2	2
13	36 PSI	Centred	Configuration 3	2
14	36 PSI	Centred	Configuration 4	2
15	36 PSI	Centred	Configuration 5	2
16	36 PSI	Centred	Configuration 6	2
17	36 PSI	Centred	Configuration 7	2
18	36 PSI	Centred	Configuration 8	2

Table 4 – Repeatability Test Matrix

As seen in Table 4, to determine the repeatability of restraint tension, 9 technicians were chosen to set the restraint tension on the dynamometer as per normal setup process. This was captured in the baseline restraint tension and 8 subsequent restraint tension configurations.

2.3.3. Baseline Results

To assess baseline repeatability of the process without altering any test variables, four consecutive baseline tests were conducted. Analysis of the data collected indicated a baseline force variation, normalised by track road load, of ~0.4% - 1.2% over a range of 0-100 kph as shown in Figure 8, demonstrating low test to test force variation. Dynamometer position was then evaluated as shown in Figure 9.

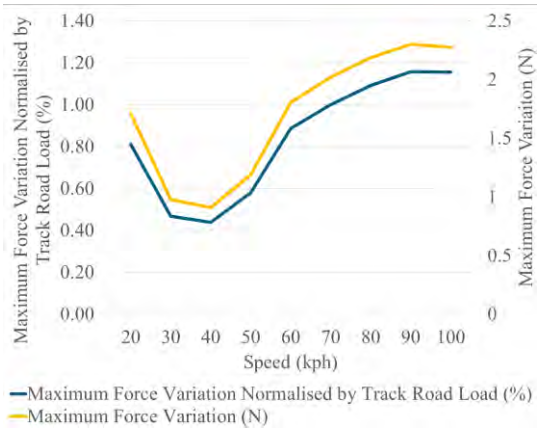

Figure 8 – Baseline Testing Force Variation

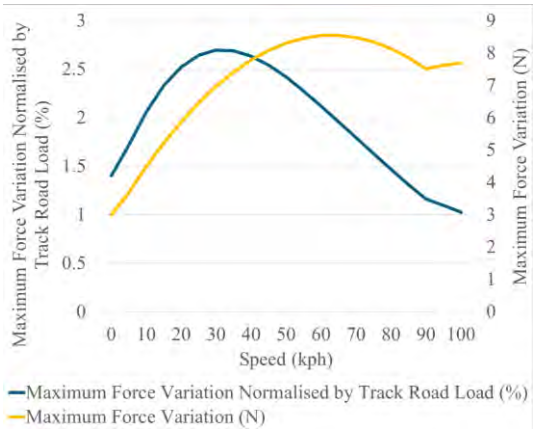

Figure 9 – Dynamometer Position Testing Force Variation

As seen in Figure 9, dynamometer position change of -60mm to +60mm from nominal led to a maximum force variation of 2.7% - 1.0% of track road load across a speed range of 0-100 kph. Whilst this was greater than the normal test to test variation, this was deemed of lower significance to overall load variation.

As shown in Figure 10, the evaluation of tyre pressure from 16 PSI to 46 PSI yielded a significant maximum force variation of 59.3% - 19.8% of the track road load over a speed range of 0-100 kph.

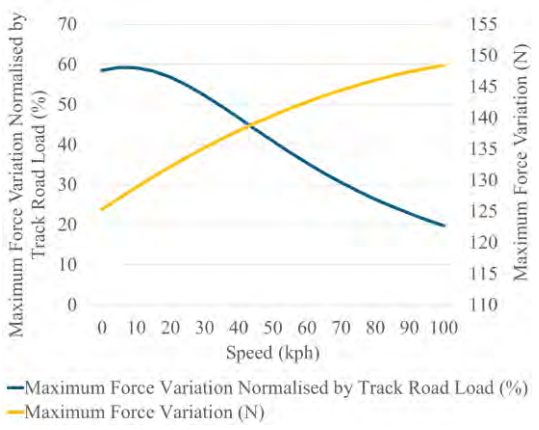

Figure 10 – Tyre Pressure Testing Force Variation

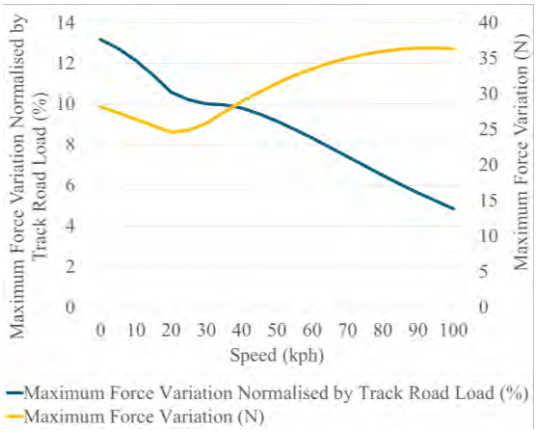

Figure 11 – Restraint Tension Testing Force Variation

To evaluate the effect of restraint tension, the force applied through the restraints was varied, with the vehicle maximum force variation shown in Figure 11 above.

This was achieved by asking nine technicians to each follow the normal installation process, whilst keeping the chain mounting location on the vehicle consistent.

The effect of varying chain tension through the normal installation process led to a variation in force of 13.2% - 4.5% over a speed range of 0-100 kph. This was deemed a significant variation in force applied to the vehicle between vehicle installation conditions. The combined results of the maximum force variation normalised by track road load over a range of 0-100 kph can be seen in Figure 12 below.

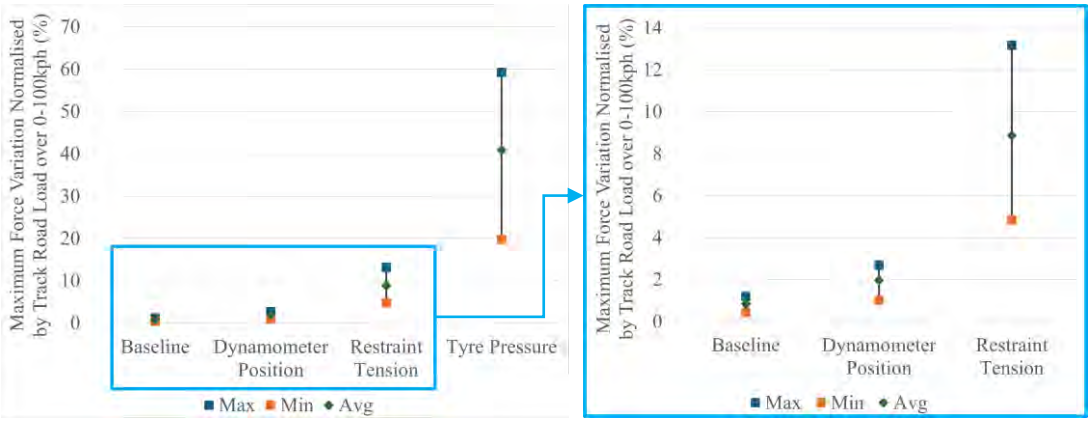

Figure 12 – Combined Maximum Force Variation

Overall, the initial results indicated that tyre pressure and restraint position had the most significant influence on tractive force applied to the vehicle. Additional plots can be seen in Appendix A – Baseline Test Results.

3 Control Measures

Having conducted baseline testing, a series of control measures were proposed to reduce to the variability in force between coast match tests. In line with facility best practice, a process to ensure tyre pressure and dynamometer positioning consistency between tests was implemented. To address dynamometer restraint forces applied, a more novel solution was required.

3.1 Restraint Tension Control Methodology

A series of z-axis load cells, commonly used in lifting applications, were proposed to be implemented at the floor anchor point of the vehicle restraint system. This would allow measurement of the axial forces imposed on the restraint system chains and ensure the user could replicate a previous coast match installation. For this application, Applied Measurements Z-Beam load cells and IPEtronik measurement equipment were chosen [7]. Figure 13 below shows the implementation of the load cells at the base of the restraint system.

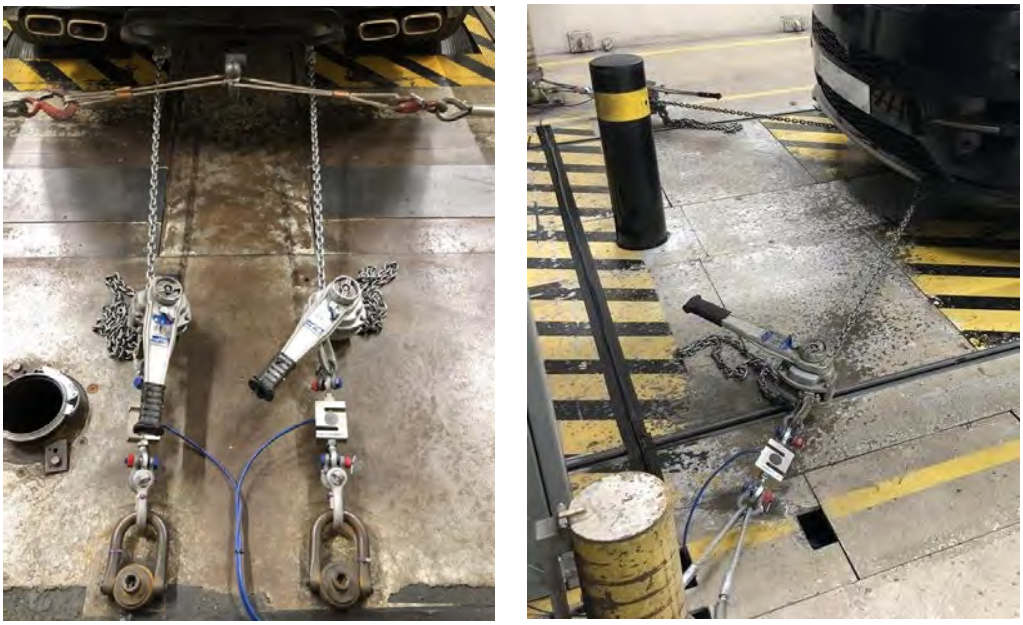

Figure 13 – Z-Beam load cells fitted at the anchor points of a chassis dynamometer restraint at the front and rear of a Range Rover Sport.

As can be seen in Figure 13, the load cells were located at the anchor point of the chassis dynamometer restraints. The axial force imposed on the restraint system could be decomposed as the combination of the vertical and longitudinal applied loading to the vehicle.

To ensure that the measurements from the load cells could be utilised to control the vertical loading applied via the restraints, an iterative process for vehicle installation, aiming to match the initial installation force, was devised as seen in Figure 14,

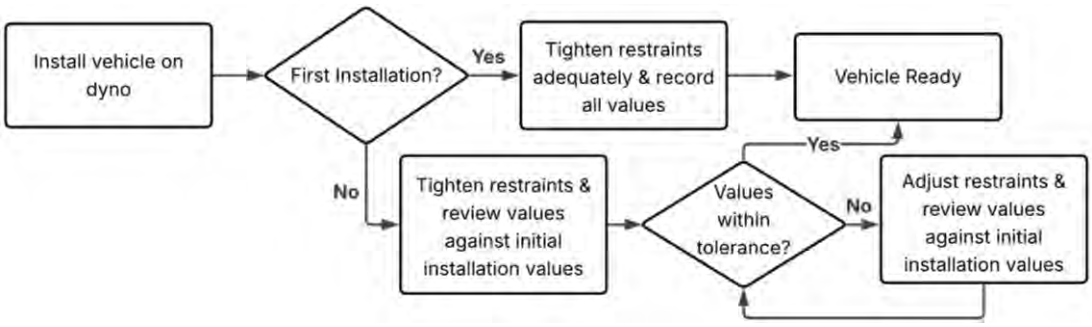

Figure 14 – Vehicle Installation Process Flow

To determine the process tolerance, an exercise was conducted with several facility technicians to ascertain an achievable tolerance within the tight timeframe required to install a a vehicle. The result of this exercise led to an agreed achievable tolerance of ±0.5 kN per restraint. Subective feedback from the technicians involved in the activity was that this tolerance could be more easily achieved by setting slightly higher tension in the restraints during the initial installation. This was deemed acceptable due to the low effect of restratint tension on vehicle wheel slip [8].

4 Control Testing & Results

To determine the impact of the addition of the vehicle restraints control process, a test matrix was devised, utilising test cases 10-18 of Table 4. As per the original baseline testing, 9 fitters were utilised, with the first vehicle installation being utilised to generate the reference restraint loading and the subsequent installations targeting a tolerance of 0.5 kN per restraint. Carrying out the test process as described in 2.3.2 yielded the results shown in Figure 15 below.

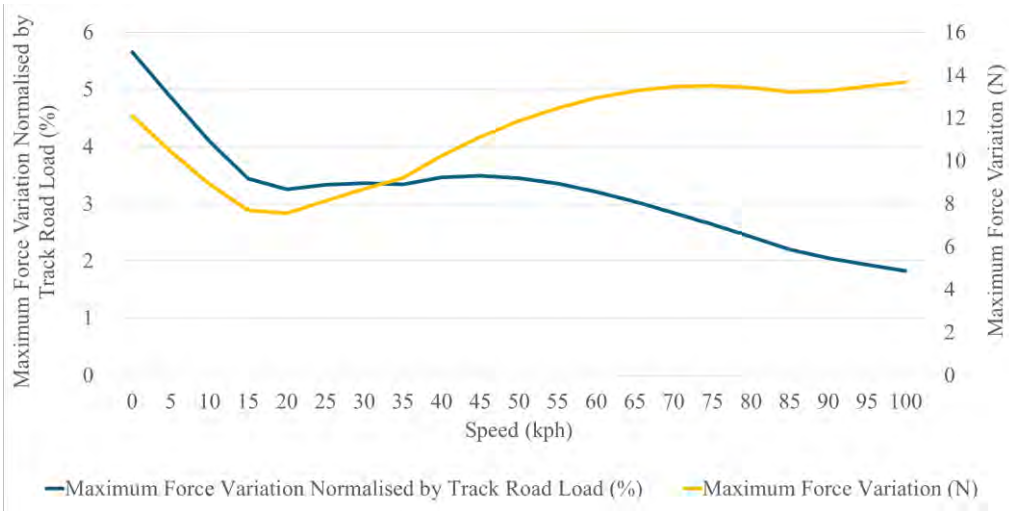

Figure 15 - Restraint Tension Control Process Force Variation

As can be seen in Figure 15, the implementation of the restraint tension control process yielded a maximum force variation of 5.6% - 1.8% of the track road load over a speed range of 0-100 kph. This result was compared to the initial baseline test results for restraint tension control test cases 8-18. The comparison showed a reduction of force variation between 3.0% - 7.0% of the track road load over a speed range of 0-100 kph as seen below in Figure 16.

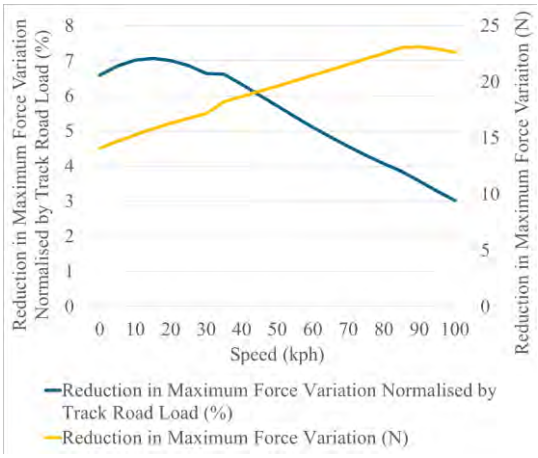

Figure 16 – Restraint Tension Baseline to Control Process Force Variation Change

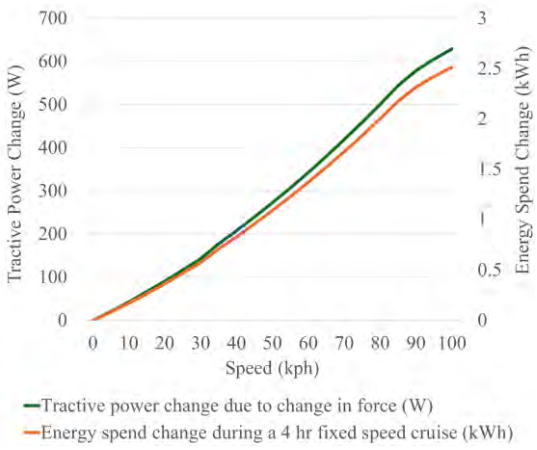

Figure 17 – Power & Energy Change between Baseline and Control Process

The effect of the force reduction shown in Figure 16 was applied to a 4-hour cruise cycle, where the resulting change in vehicle force was reflected in the change in power and energy consumption as seen above in Figure 17.

The implementation of the control process for restraint tension demonstrated a reduction in tractive power of up to 628 W at 100 kph, which applied to a 4-hour cruise use case would result in an expected reduction in tractive energy of ~2.5 kWh.

5 Conclusion & Recommendations

Overall, an investigation was conducted to assess the variability of tractive force applied to a vehicle when influenced by normal operating parameters of a climatic wind tunnel with a floor anchor restraint system. Baseline testing yielded results indicating a significant variance in tractive force due to changes in restraint tension applied to the vehicle. A novel solution was proposed to implement restraint tension monitoring equipment and a process devised to ensure consistent vehicle restraint tension upon installation of a vehicle into a climatic wind tunnel. Validation testing of applied control techniques demonstrated a reduction in variability of axle loading normalised by track road load from a range of 13.2% - 4.5% down to 5.6% - 1.8% across speeds of 0-100kph. As applied to a 4-hour cruise use case at 100 kph, a change in tractive energy of up to ~2.5 kWh was noted for a Range Rover Sport with the reduction in tractive effort.

Overall, the process implemented provided sufficient confidence in the repeatability of the installation process to allow all thermal performance and feature development testing to be carried out with a singular coast match test, without the requirement for subsequent coast match tests. This improvement in operational efficiency was estimated to save ~20 hrs of climatic wind tunnel time per ICE vehicle test programme and ~190 hrs per BEV vehicle test programme. Deployment of the control process demonstrated an active improvement in facility operational efficiency with negligible impact on vehicle installation time and facility maintenance requirements.

Overall, the author recommends that climatic wind tunnels utilising a floor anchor restraint system adopt the methodology described in this paper to reduce variability in axle loading due to restraint tension, allowing optimisation of facility time and reduction in environmental impact of vehicle development. Going forward, the author recommends further work to review the tolerance value associated with the use of the restraint monitoring process and to define if any further reduction in installation variability can be achieved through a tighter tolerance.

6 Reference list

1. SAE International Recommended Practice, Recommended Best Practice for Climatic Wind Tunnel Correlation, SAE Standard J2777_202211, Revised November 2022, Issued January 2007, https://doi.org/10.4271/J2777_202211.

2. SAE International Recommended Practice, Chassis Dynamometer Simulation of Road Load Using Coastdown Techniques, SAE Standard J2264_202301, Revised January 2023, Issued April 1995, https://doi.org/10.4271/J2264_202301.

3. SAE International Recommended Practice, Battery Electric Vehicle Energy Consumption and Range Test Procedure, SAE Standard J1634_202104, Revised April 2021, Issued May 1993, https://doi.org/10.4271/J1634_202104.

4. Nakajo, T., and Tsuchiya, K., "Factors Affecting Driving Force Characteristics of 4WD Vehicles on a 4WD Chassis Dynamometer," SAE Technical Paper 2009-01-1350, 2009, https://doi.org/10.4271/2009-01-1350.

5. Mayer, W., and Wiedemann, J., "The Influence of Rotating Wheels on Total Road Load," SAE Technical Paper 2007-01-1047, 2007, https://doi.org/10.4271/2007-01-1047.

6. GB Transposed Version of Commission Regulation (EC) 2017/1151 of June 1, 2017 Supplementing Regulation (EC) No. 715/2007 of the European Parliament and of the Council on Type Approval of Motor Vehicles with Respect to Emissions from Light Passenger and Commercial Vehicles (Euro 5 and Euro 6) and on Access to Vehicle Repair and Maintenance Information, Amending Directive 2007/46/EC of the European Parliament and of the Council, Commission Regulation (EC) No. 692/2008 and Commission Regulation (EU) No. 1230/2012 and Repealing Commission Regulation (EC) No. 692/2008.

7. Applied Measurements (2025) Z-Beam Load Cell. Available at: https://appmeas.co.uk/products/load-cells-force-sensors/s-beam-load-cell-dbb/ (Accessed: 05 September 2025).

8. Baker, N., and Presnell, K., "Investigation of the Effects of Wheel Slip on Vehicle Emissions and Fuel Economy," SAE Technical Paper 2006-01-1358, 2006, https://doi.org/10.4271/2006-01-1358.

7 Appendix A – Baseline Test Results

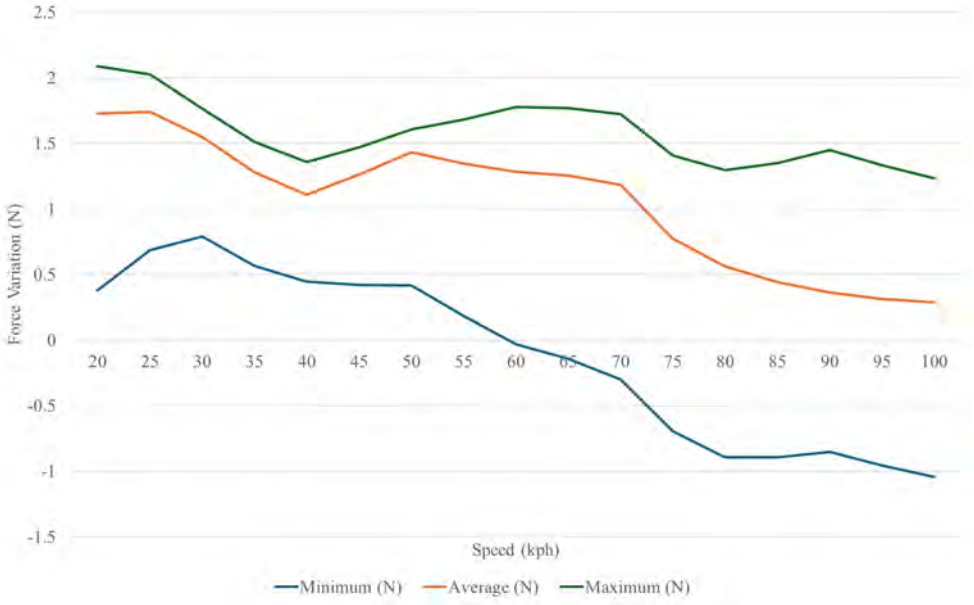

Figure 18 - Baseline Testing Force Variation Min, Max, Avg

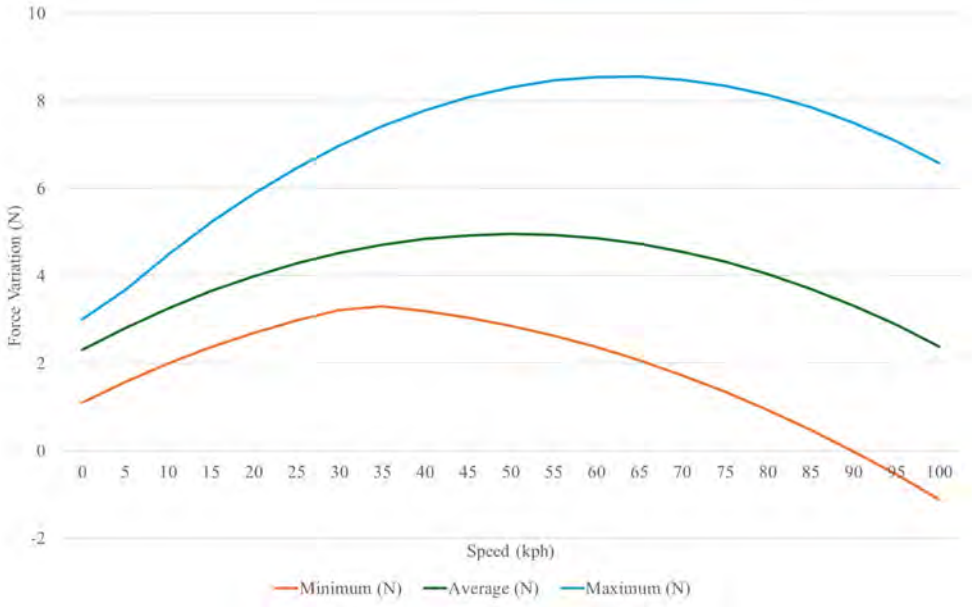

Figure 19 - Dynamometer Position Testing Force Variation Min, Max, Avg

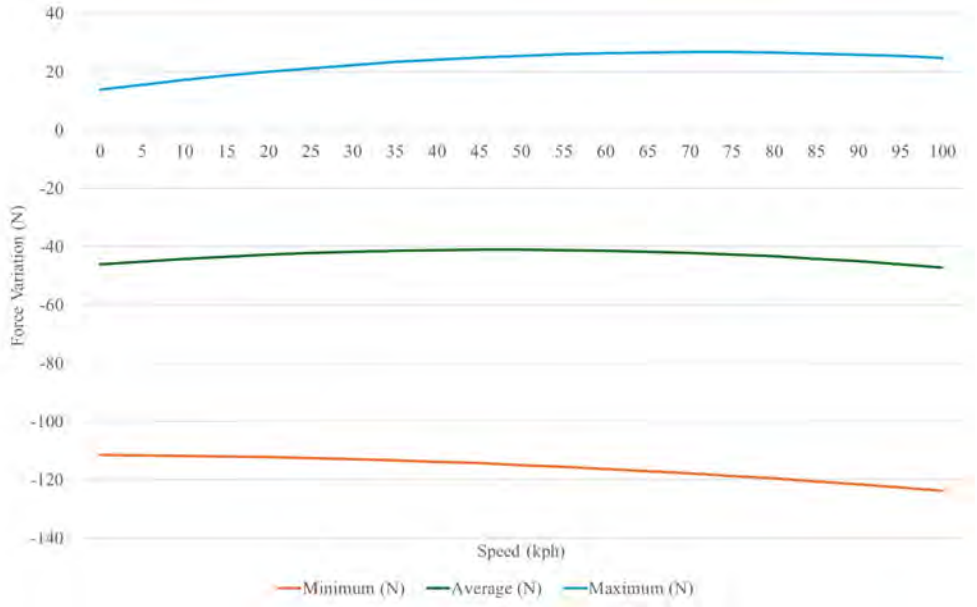

Figure 20 - Tyre Pressure Testing Force Variation Min, Max, Avg

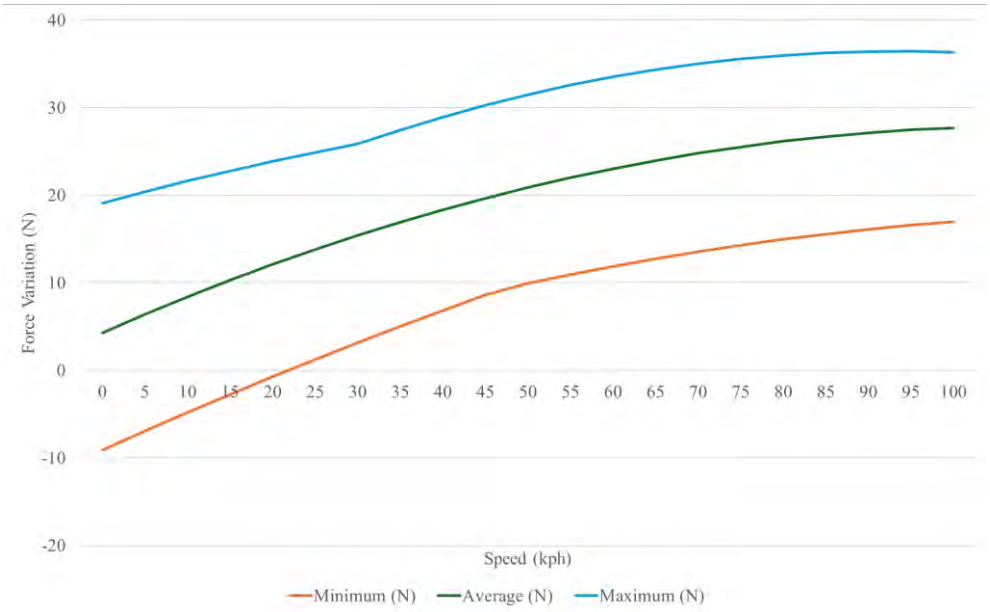

Figure 21 - Restraint Tension Testing Force Variation Min, Max, Avg

8 Appendix B – Control Process Test Results

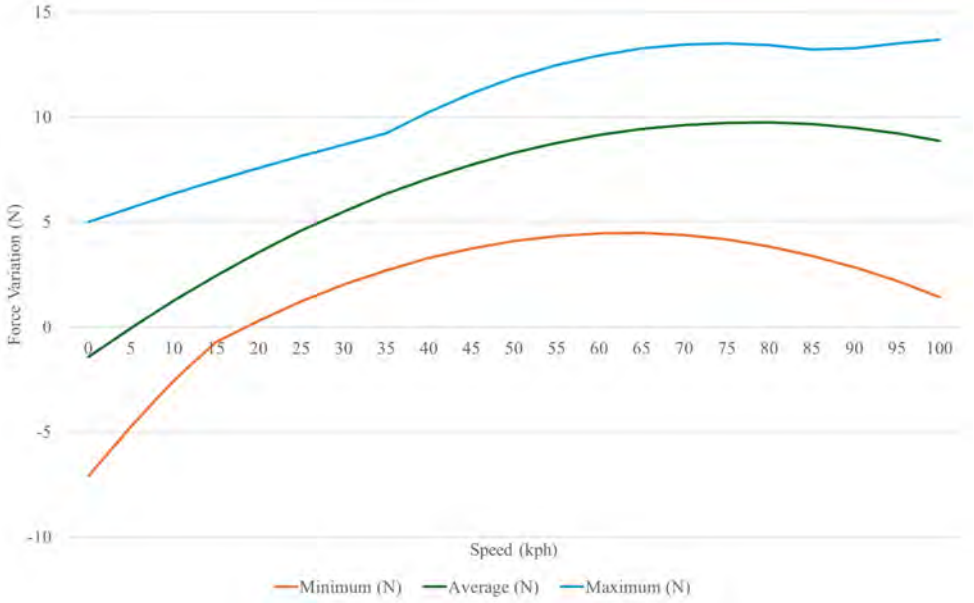

Figure 22 - Restraint Tension Control Process Force Variation Min, Max, Avg

Multi element integration technology for thermal hazard simulation calibration based on full-scale automotive climate numerical wind tunnel

Dan Wang[1], Xuelong Liu[1],Liansong Mu[1],Haiyang Wang[1],Ziming Yan[1]
1.China Automotive Technology and Research Center Co., Ltd.

wangdan@catarc.ac.cn

liuxuelong@catarc.ac.cn

Abstract: With the rapid development of the automotive industry, the optimization of automotive thermal management systems is crucial for improving overall vehicle performance, safety, and reliability. This article focuses on the multi-dimensional integration technology in the full-scale automotive climate numerical wind tunnel, and elaborates on how to use this technology to accurately simulate and calibrate automotive thermal hazards. By constructing an accurate heat damage simulation model and combining it with the real working conditions simulated in wind tunnels, the heat damage situation of automobiles in different environments is simulated and analyzed, and strict calibration verification is carried out based on experimental data. The research results indicate that the multi-dimensional integration technology based on full-scale automotive climate numerical wind tunnel can effectively improve the accuracy of thermal hazard simulation, provide strong support for the optimization design of automotive thermal management systems, and help the automotive industry make further breakthroughs in energy conservation, emission reduction, and improving driving comfort.

This article delves into the difficult problem of automatic calibration for full-scale automotive climate numerical wind tunnel thermal damage simulation. The vehicle thermal management simulation model for automobiles contains a large number of parameters, and accurate numerical values are difficult to obtain. Parameter calibration is crucial. Therefore, this article constructs an automated optimization process and adopts a dual track technical path: one is manual calibration based on experimental data comparison and expert experience, and the other is intelligent calibration with the help of multiple technical means. At the key technical level, a parametric simulation process is built through graphical software, integrating multiple DOE algorithms, conducting sensitivity analysis, clarifying the sensitivity ranking of input parameters,

Contribution: 2025 FKFS Conference on Vehicle Aerodynamics and Thermal Management
15 – 16 October 2025 | Leinfelden-Echterdingen

and using artificial intelligence algorithms to generate and train proxy models, significantly reducing simulation computation time. The above method ensures that the temperature error between the simulation model and the corresponding position of the test measurement point is controlled within an acceptable engineering range of 5% under the premise of accurately loading the simulation boundary conditions, significantly improving the accuracy and reliability of the simulation results of automotive thermal management and greatly enhancing the calibration efficiency.

1 Introduction

1.1 Research background and significance

In the actual operation of automobiles, heat damage seriously affects the performance, reliability, and service life of vehicles[1-3]. When a car is in motion, components such as the engine and exhaust pipe generate a large amount of heat. If they are not dissipated in a timely and effective manner, it can lead to high temperatures in the components, causing a series of problems such as increased wear and tear, decreased lubricating oil performance, electronic component failure, and even endangering driving safety[4-6]. In addition, in high temperature environments, the driving comfort inside the car will also be greatly reduced. Therefore, it is of great practical significance to conduct in-depth research on the problem of automobile heat damage and seek effective solutions.

Traditional research methods for automobile heat damage often rely on actual vehicle testing. However, actual vehicle testing is not only expensive and time-consuming, but also limited by environmental conditions, testing sites, and other factors, making it difficult to comprehensively and systematically study heat damage issues under various working conditions[7,8]. The emergence of full-scale automotive climate numerical wind tunnels has brought new opportunities for the study of automotive thermal hazards. It can simulate various complex climate conditions and driving conditions, and through multi-dimensional integration technology, couple and analyze multiple physical fields, providing a more realistic and accurate simulation environment for automobile heat damage simulation, which helps to deeply understand the mechanism of heat damage and provide scientific basis for the optimization design of automobile thermal management systems[9-11].

1.2 Current research status at home and abroad

In the field of automotive heat damage research, foreign research started early and achieved fruitful results. Developed countries in the automotive industry, such as Europe, America, and Japan, are leading in thermal damage testing and simulation with advanced full-scale automotive climate wind tunnel laboratories and numerical wind tunnel simulation models[12,13].Mercedes Benz conducted research on engine compartment heat damage under different climatic conditions through numerical simulation technology, optimized the layout of heat dissipation channels, and reduced the high-temperature failure rate of engines by 18%. BMW Group utilizes wind tunnel testing and finite element method to simulate the thermal degradation process of the braking system. By improving the material and structural design of the brake disc, the high-temperature stability of the braking system has been effectively enhanced[14].In the research of simulation algorithms, Stanford University in the United States proposed an improved finite volume method, which increases the computational efficiency of fluid solid coupling by 30%, significantly enhancing the real-time and accuracy of thermal damage simulation[15].

Although the research on automobile heat damage started relatively late in China, it has developed rapidly. The Shanghai Ground Transportation Wind Tunnel Center relies on advanced wind tunnel equipment to conduct research on thermal flow problems in automotive engine compartments[16].The Automotive Wind Tunnel Laboratory of China Automotive Center conducted in-depth analysis of the flow field in the pure motor compartment through a combination of experiments and simulations, and optimized the matching design of the cooling fan and radiator[17].In terms of research institutions, Tsinghua University has made progress in handling boundary conditions for thermal hazard simulation, proposing a dynamic boundary setting method based on actual road conditions, which has improved the fit between simulation results and real vehicle road tests[18].Despite numerous achievements in domestic and international research, there are still significant pain points. Firstly, the deep application of multivariate integration technology in thermal hazard simulation is insufficient. Existing research mainly focuses on single physical fields or simple coupling analysis, and the simulation accuracy of multi physical field coupling effects such as fluid, heat transfer, and thermal radiation under complex working conditions is limited. Secondly, the accuracy and universality of simulation model parameters are poor, with significant differences in material characteristics among different vehicle models and components. Existing model parameters are difficult to adapt to diverse scenarios, resulting in simulation result errors generally exceeding 15%. Thirdly, the collaborative calibration efficiency between experiments and simulations is low, traditional wind tunnel test data acquisition and processing take a long time, and simulation model parameter adjustment relies on empirical trial and error, which cannot meet the rapid iteration requirements of automotive research and development.

2 Full scale automotive climate numerical wind tunnel test

2.1 Structure and Function of Full Scale Automotive Climate Numerical Wind Tunnel

The full-size automotive climate wind tunnel is a large-scale testing facility that can simulate the real driving environment of automobiles. Its structure mainly includes the tunnel body, driving system, measurement and control system, and climate simulation system. The tunnel body is the core part of a wind tunnel, usually adopting a closed or semi closed structure, with sufficient internal space to accommodate a complete car for testing. The driving system uses a powerful motor to drive the fan, generating stable and controllable airflow, simulating the wind speed during car driving. The measurement and control system is responsible for accurately measuring and controlling parameters such as airflow velocity, temperature, and pressure inside the wind tunnel, ensuring the accuracy and stability of the test conditions. The climate simulation system can simulate various complex climate conditions, such as high and low temperatures, solar radiation, rainfall, snowfall, etc., providing a diverse experimental environment for the study of automobile heat damage[19].The function of the full-size automotive climate wind tunnel is very powerful, which can deeply study the thermal management performance of automobiles under high and low temperature, wind, frost, rain, snow, fog and other climate conditions, as well as cloudy and tunnel environments[20].By installing different sensors and measuring devices in wind tunnels and vehicles, real-time monitoring of temperature changes, airflow distribution, and heat dissipation performance parameters of various components of the car can be achieved, providing rich data support for research on car heat damage. In addition, wind tunnels can also be integrated with other testing equipment, such as road load simulation systems, thermal road simulation systems, etc., to further expand their testing functions and achieve comprehensive simulation of complex automotive operating conditions.

The following figure shows the structure of the horizontal reflux 3/4 opening full-size climate wind tunnel of China Automotive Technology Research Center:

Figure 2.1-1: Climate Wind Tunnel Laboratory of China Automotive Technology Research Center

The various parameter indicators of the wind tunnel are shown in the following table:

Table 2.1.1-1: Climate Wind Tunnel Parameter Indicators

Parameter	Specification
	130 km/h with the large nozzle (13.2 m2 nozzle)

Maximum wind speed	250 km/h with the small nozzle (8.25 m2 nozzle)
Velocity uniformity	1σ(U/Umean) ≤ 0.5% (Small nozzle: X= 1 m, Y=±1.2 m, Z=0.2 m to
Flow angularity	1σ(Δα) ≤ 0.5° 1σ(Δβ) ≤ 0.5° (Small nozzle: X= 1 m, Y=±1. 1 m, Z=0.2 m to
Turbulence Intensity Uniformity	Tu ≤ 0.5 % (f = 20 Hz to 4 kHz) (Small nozzle: X= 1 m, Y=±1.0 m, Z=0.2 m to
Wind speed controllability	Under steady state conditions, the wind speed
Boundary Layer	δ * ≤ 4 mm at X = 1 m
Axial Static Pressure Gradient	dCp/dx ≤ 0.002 m- 1 (X=1 m to 9 m, Y= 0, Z=1 m)
Static Pressure Pulsations	Cprms ≤ 0.02 (X = 7 m, Y = 4.5 m)
Air temperature range	-40ºC to +60ºC
Air temperature uniformity	1σ(T) ≤ 0.5°C
Air temperature	Under steady state conditions, the air temperature
Air temperature transition time limits (at 110 km/h)	+ 10ºC to +45ºC in less than 43.75 minutes +45ºC to +10ºC in less than 43.75 minutes
Humidity range	5% RH to 95% RH (non-condensing, maximum dewpoint = 36.7°C)
Humidity controllability	Under steady state conditions, the humidity shall
Humidity transition time limits	20%RH to 80%RH in 30 minutes at 35ºC 80%RH to 20%RH in 30 minutes at 35ºC
Background Noise Level	80 dB(A) at 100 km/h (measured out-of-flow)

Numerical wind tunnel is a 1:1 reconstruction of a physical wind tunnel, establishing a virtual simulation wind tunnel, reproducing various climate conditions in the physical wind tunnel on a computer, and using CFD methods to obtain low-cost, fast, and accurate thermal performance results of vehicles. Due to the main testing area being located in the chamber, in order to reduce computational costs, the numerical wind tunnel intercepts the flow channels between the chamber and the front and rear corners. The main retained components include the contraction section, evaporator, honeycomb device, chamber, nozzle, boundary layer suction porous plate, sunlight simulation device, chassis dynamometer hub, vehicle fixing device, collection port, and collection section flow channel. As shown in the following figure:

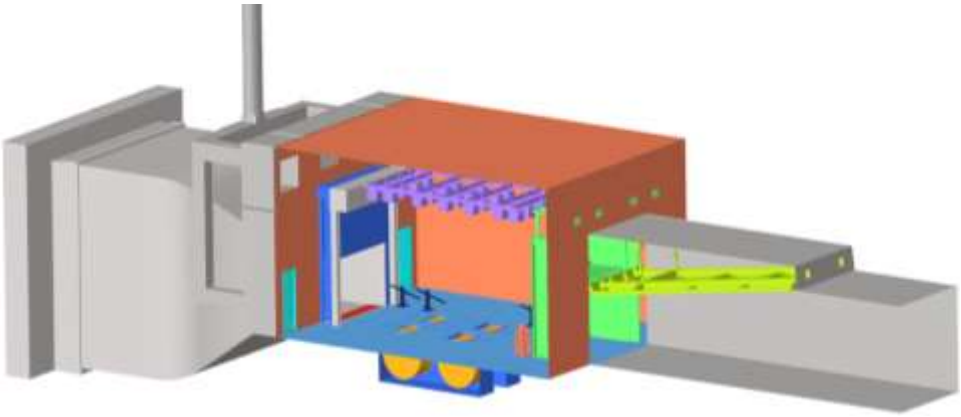

Figure 2.1.3: Climate Numerical Wind Tunnel

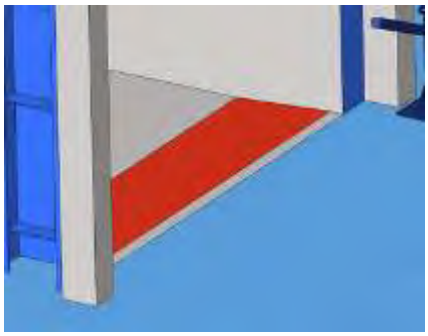

Figure 2.1.4: Boundary layer suction device

Figure 2.1.5:Adjustable nozzle

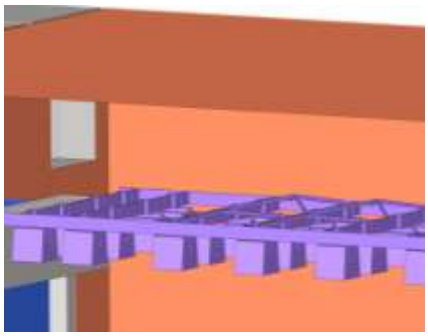

Figure 2.1.6: Sunshine Simulation Device

Figure 2.1.7: Chassis dynamometer hub

2.2 Experimental equipment and instruments

The equipment required for full-scale automotive climate numerical wind tunnel testing mainly includes the wind tunnel body, climate simulation system, measuring instruments, etc. The wind tunnel body provides a stable and controllable airflow environment, and its fan system can generate airflow of different wind speeds to simulate the working conditions of a car at various speeds; The climate simulation system can adjust environmental parameters such as temperature, humidity, and solar radiation intensity inside the wind tunnel to simulate different climate conditions. The parameters of the wind tunnel equipment are shown in the following table:

Table 2.2-1: Parameters of Climate Wind Tunnel Equipment

No.	Equipment	Parameter
1	Master Nozzle	8.25m2
2	Master Nozzle Max. Wind Speed	250km/h
3	Truck Nozzle	13.2m2
4	Truck Nozzle Max. Wind Speed	170km/h
5	Reverse Wind Max. Speed	20km/h
6	Wind Speed Control Tolerance	≤±0.5km/h
7	Vehicle Speed Range	0~250km/h
8	Temperature Range	-40~+60℃
9	Temperature Control Tolerance	≤±0.5 ℃
10	Humidity Range	5~95%
11	Humidity Control Tolerance	≤±3%
12	Solar Simulation Intensity	300~1200W/ m2
13	Other abilities	Hot Road Simulation
		Rain & Snow Simulation

Measuring instruments are used to obtain various physical parameters during the experimental process, mainly including temperature sensors, wind speed sensors, flow sensors, radiation sensors, etc. The temperature sensor uses high-precision thermocouples or platinum resistors to measure the surface temperature of various components of the car, engine coolant temperature, air temperature, etc; Wind speed sensors typically use pitot tubes, cobra probes, or impeller anemometers to measure the airflow velocity distribution inside the wind tunnel and the airflow distribution on the surface of the cooling module. Pressure sensors are used to measure parameters such as high and low pressure in refrigerant systems, tire pressure, etc. Radiation sensors are used to measure the thermal radiation intensity of the car roof, providing boundary inputs and reference targets for thermal hazard analysis. The main focus of this analysis is on the temperature target of vehicle heat damage, using two types of temperature sensors: high temperature and low temperature. The model parameters are shown in the table below:

Table 2.2-2: Temperature Sensor Parameter Table

No.	Model	Lengh(m)	Measuring range(℃)	Temperature resistance limit of cables(℃)
1	Armored K-	5	-200℃~1000℃	-200℃~400℃
2	Type K	5	-50℃~260℃	-50℃~260℃

The temperature measuring points of ordinary thermocouples are rolled into a coil shape and attached to the surface of the object being measured with cloth tape. The cables are fixed at room temperature along the way with tape. Finally, the sensor wire harnesses at similar positions are tied and tied with zip ties, and the other end is connected to the data acquisition instrument. High temperature thermocouples are armored and not easily bent. The measuring point is glued to the surface of the object being measured with iron, and the high-temperature resistant section behind the measuring point is fixed to the nearby pipe section with a metal clamp to ensure the stability of the measuring point during testing. It should be noted that when pasting

measuring points, the beginning and end of each sensor should be uniformly marked with label paper to avoid confusion in measuring point output after multiple cables are tied together. After connecting all measuring points to the data acquisition equipment, open the testing software to check the signal status and ensure that all sensors can output temperature values in a timely and accurate manner. The layout methods of two types of sensors on the vehicle are shown in the following figure:

Figure 2.2-1: Layout of Type K

Figure 2.2-2: Layout of Armored K-type

2.3 Test conditions and results

During the experiment, various physical parameter data were collected in real-time using measuring instruments, and stored and transmitted through a data acquisition system. The temperature data collection frequency is 1HZ. The collected data needs to be preprocessed, including data filtering, outlier removal, and other operations, to improve data quality. Then, use data analysis software to perform statistical analysis on the processed data. By analyzing the experimental data, the temperature distribution information of various components of the car under different working conditions is obtained, providing a basis for the calibration of the thermal damage simulation model. The following table shows the average temperature values of each thermal equilibrium stage after data processing in this experiment. Among them, the ambient temperature, vehicle speed, and surface temperature of the heat source are used as simulation input conditions, and the surface temperature of the target component is the target value calibrated by simulation.

Table 2.3-1: Surface Temperature Values of Heat Sources for Vehicle Thermal Balance Test

No.	Heat source components	Surface measurement point temperature(℃)		
		Medium speed climbing(60kph)	High speed climbing(110kph)	Maximum speed(150kph)
1	Cylinder head	101.23	89.46	85.63
2	Cylinder linder	106.40	93.71	90.23
3	Cylinder block	119.55	102.69	96.00
4	Oil pan	117.81	107.11	104.45

5	Engine side cover	112.93	101.07	98.92
6	exhaust manifold	121.00	110.88	108.07
7	Cold end of	83.38	87.92	91.36
8	Hot end of	639.89	625.19	629.28
9	Pre urging	643.98	611.77	618.88
10	Pre urging	240.39	165.45	139.52
11	Front pipe of	542.29	503.56	502.60
12	Corrugated pipe	213.29	142.09	132.29
13	Main reminder	525.67	487.18	484.15
14	Main reminder	355.96	299.11	287.67
15	Front	434.70	380.29	375.56
16	Front	153.78	111.97	97.86
17	Front	427.97	382.03	384.25
18	Central muffler	180.38	131.76	129.00
19	Front pipeline of	358.76	307.95	306.20
20	Rear muffler	277.37	229.09	227.77
21	Tail pipe	281.44	239.20	271.57

Table 2.3-2:Temperature Table of Target Components for Whole Vehicle Thermal Balance Test

Target component	Surface measurement point temperature(℃)		
	Medium speed climbing(60kph)	High speed climbing(110kph)	Maximum speed(150kph)
Exhaust lifting ear	110	85	80

3 Construction of Automotive Thermal Damage Simulation Model Based on Multivariate Integration Technology

3.1 Modeling and Grid Division

Grid partitioning is one of the key steps in constructing a simulation model for automotive thermal hazards, and the quality of the grid directly affects the accuracy and computational efficiency of the simulation results. In the thermal hazard simulation of full-scale automotive climate numerical wind tunnel, due to the complex structure of the automotive model and the drastic changes in the flow and temperature fields, a mixed grid partitioning method is usually used. For key parts such as the car body and engine compartment, high-precision unstructured hexahedral grids are used for partitioning to accurately capture complex geometric shapes and physical phenomena; For areas far away from cars, use sparser grids to reduce computational complexity. At the same time, boundary layer mesh division is carried out at the interface between fluid and solid, and in areas with large temperature gradients, with local mesh refinement to ensure computational accuracy. In addition, in order to

improve the quality of the grid, it is necessary to perform smoothing treatment on the grid to avoid problems such as distortion and distortion. The following table shows the mesh division parameters of the wind tunnel:

Table 3.1-1: Grid Parameter Setting Table

No.	Project	Parameter
1	Body mesh type	Trimmer
2	Total thickness of boundary layer	2 mm
3	Boundary layers	2层
4	Boundary layer growth rate	1.3
5	Total number of body grids	7674万

The grid division is shown in the following figure:

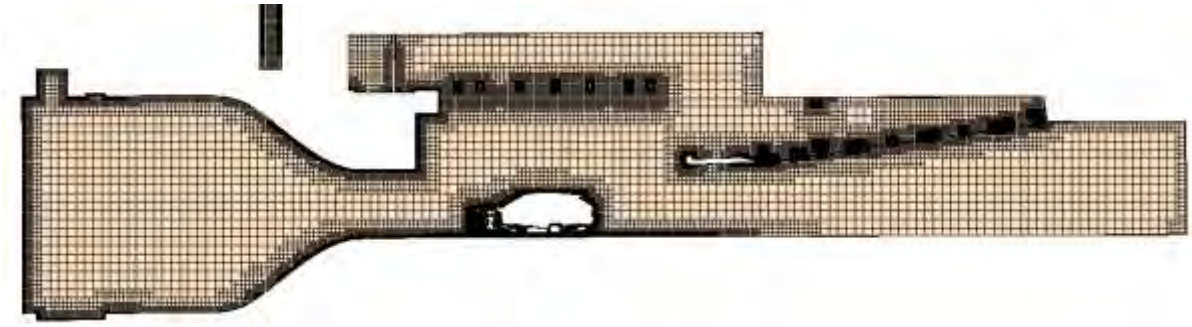

Figure 3.1-1: Longitudinal section mesh of the whole vehicle and wind tunnel

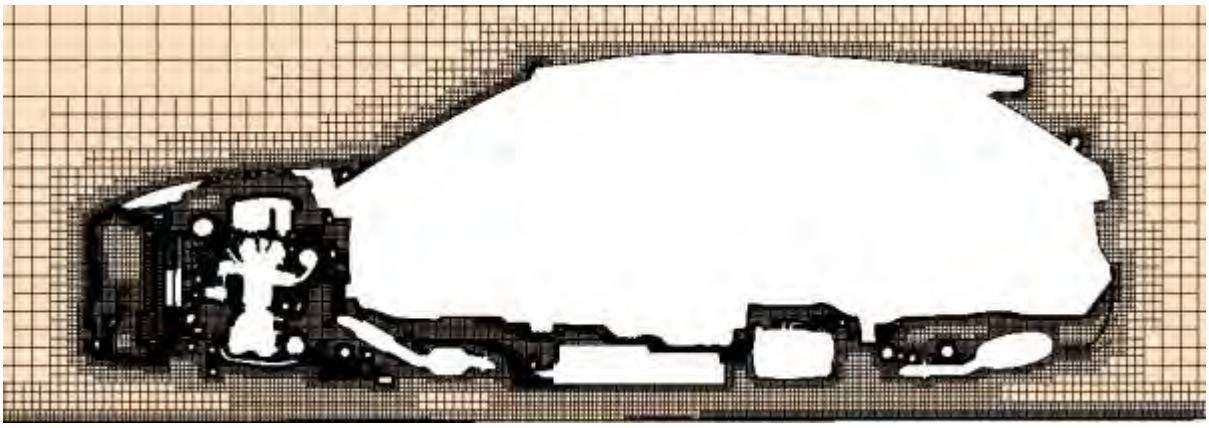

Figure 3.1-2: Vehicle Grid Encryption Zone

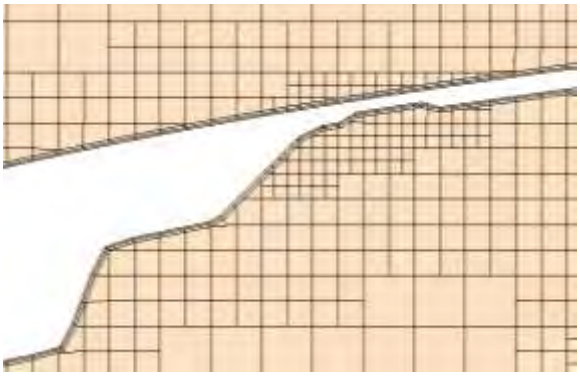

Figure 3.1-3:Grid of Body Surface Layer

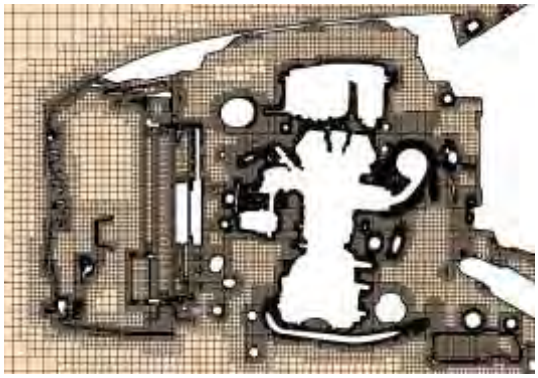

Figure 3.1-4:Engine Compartment Grid

3.2 Boundary condition setting

The accurate setting of boundary conditions is an important prerequisite for ensuring the reliability of simulation results. In the thermal hazard simulation of a full-scale automotive climate numerical wind tunnel, the boundary conditions mainly include the following categories:

- 1. Entrance boundary conditions: Set the air flow velocity and temperature parameters based on the simulated working conditions in the wind tunnel. For the driving conditions of automobiles, the wind tunnel nozzle is usually set as the air flow inlet, with the speed direction opposite to the direction of the car's travel. For simulations of different climate conditions, the temperature and density parameters of the inlet air are adjusted.

- 2. Export boundary conditions: generally set as pressure outlet, with a value of atmospheric pressure. On the premise of ensuring stable calculation, the setting of outlet pressure should be as close as possible to the actual working conditions to avoid problems such as reflux caused by improper outlet pressure setting affecting the calculation results.

- 3. Wall boundary conditions: For solid walls such as car bodies and engine compartment components, non slip boundary conditions are adopted, which means that the air flow velocity at the wall is zero. For heating components such as engines and exhaust pipes, their surface temperature needs to be set according to the test values. In addition, for moving parts such as wheels and cooling fans, a rotating coordinate system is used to simulate the effects of their rotational motion on the surrounding flow field and temperature field.

- 4. Boundary conditions for heat exchangers: Tube fin heat exchangers such as condensers and radiators use air to carry away heat from the fluid medium for heat exchange. In CFD, they are simplified as porous media, with inertial and viscous drag coefficients set, and the gas-liquid heat transfer under vehicle operating conditions set.

The boundary parameters of the entire vehicle are shown in the following table:

Table 3.2-1: Vehicle Boundary Parameter Setting Table

No.	Boundary	Medium speed climbing (60kph)	High speed climbing (110kph)	Maximum speed (150kph)
1	Wind tunnel nozzle airflow	151.5kg/s	277.8kg/s	378.9kg/s
2	Relative export pressure	0 Pa	0 Pa	0 Pa
3	Ambient temperature	38℃	40℃	40℃
4	Air density	1.119kg/m^3	1.110kg/m^3	1.110kg/m^3
5	Wheel speed	431.3rpm	790.7rpm	1078.3rpm
6	Cooling fan speed	2300rpm	2300rpm	2300rpm
7	Hub speed	167.1rpm	306.3rpm	417.7rpm
8	Condenser ventilation resistance inertia coefficient	216.93kg/m^4	216.93kg/m^4	216.93kg/m^4
9	Condenser ventilation resistance viscosity coefficient	685.45kg/m^3-s	685.45kg/m^3-s	685.45kg/m^3-s
10	Ventilation resistance inertia coefficient of radiator	195.39kg/m^4	195.39kg/m^4	195.39kg/m^4
11	Ventilation resistance viscosity coefficient of radiator	595.85kg/m^3-s	595.85kg/m^3-s	595.85kg/m^3-s
12	Condenser heat exchange	7kw	7kw	7kw
13	Heat exchange of radiator	32.7kw	34.5kw	35.9kw

4 Calibration and Verification of Thermal Damage Simulation Model under Dual track Technology

4.1 Manual calibration based on experimental data comparison and expert experience

4.1.1. Calibration method and process

The calibration of the heat damage simulation model is the process of adjusting the model parameters to make the simulation results consistent with the experimental data. The calibration method in this section mainly adopts traditional manual calibration. Firstly, manual parameter screening is conducted based on experience to identify key parameters that have a significant impact on the simulation results of the target, such as the heat source near the target component and the thermal conductivity and emissivity of the target component itself. By changing the values of these key parameters and observing the trend of simulation results, identify the components and parameters that have a significant impact on the simulation results and sort them. Then, within a reasonable range of parameters, arrange and combine calculations until the error between the simulation results and experimental values is within ± 8 ℃, which is considered to meet the standard. The calibration process is shown in the following figure:

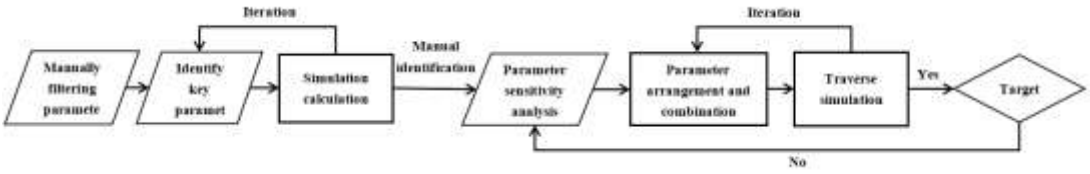

Figure 4.1.1-1: Manual Calibration Process

The target value for this study is the surface temperature of the exhaust hanging ear. Due to its proximity to the exhaust pipe heat source, the thermal emissivity of this pipe section is selected as the key parameter. The hanging ear itself is made of black rubber material, and the thermal emissivity of the hanging ear and the thermal conductivity of the rubber material are also selected as key parameters. Based on simulation experience, heat sources and metal surfaces near the target component may also have an impact on it. Therefore, the thermal emissivity and aluminum material thermal conductivity of the front suspension, chassis, engine, and exhaust pipe surfaces are selected as key parameters. The key parameters of other components are selected using the same method. The thermal emissivity ranges from 0 to 1, the thermal conductivity of rubber materials varies from 0.6 to 1.5, and the thermal conductivity of aluminum materials varies from 225 to 249. The following table shows the key parameters identified manually and their values during preliminary simulation calculations:

Table 4.1.1-1: emissivity Values in Simulation Model

Variable	Front suspension	Floor panel	Engine	Exhaust pipe	Heat Shield	Exhaust lifting ear

Emissi-vity	Base	0.80	0.80	0.80	0.80	0.80	0.80
	Case1	0.95	0.95	0.95	0.95	0.95	0.95
	Case2	0.90	0.90	0.90	0.90	0.90	0.90
	Case3	0.70	0.70	0.70	0.70	0.70	0.70
	Case4	0.60	0.60	0.60	0.60	0.60	0.60
	Case5	0.50	0.50	0.50	0.50	0.50	0.50
	Case6	0.40	0.40	0.40	0.40	0.40	0.40
	Case7	0.30	0.30	0.30	0.30	0.30	0.30
	Case8	0.20	0.20	0.20	0.20	0.20	0.20
	Case9	0.10	0.10	0.10	0.10	0.10	0.10

Table 4.1.1-2: Thermal conductivity values in the simulation model

Variable		Heat Shield	Exhaust lifting ear
Thermal conductivity (W/m-K)	Case10	235.0	0.85
	Case11	233.0	0.80
	Case12	231.0	0.75
	Case13	229.0	0.70
	Case14	227.0	0.65
	Case15	225.0	0.60
	Case16	239.0	1.00
	Case17	241.0	1.10
	Case18	243.0	1.20
	Case19	245.0	1.30
	Case20	247.0	1.40
	Case21	249.0	1.50

After calculating in a full-scale climate numerical wind tunnel, the extracted surface measurement point temperature of the target component is:

Table 4.1.1-3: Simulation Results

CFD result	Temperature measurement point of exhaust suspension ear(℃)		
	Medium speed climbing(60kph)	High speed climbing(110kph)	Maximum speed(150kph)
Base	114.28	89.84	79.32
Case1	118.00	92.99	82.50
Case2	116.91	92.74	81.42
Case3	112.29	87.68	77.35
Case4	109.18	85.53	75.48
Case5	107.24	83.70	73.72
Case6	104.06	82.13	72.14
Case7	101.67	81.19	70.81
Case8	98.60	79.70	69.77
Case9	95.21	78.99	69.02
Case10	114.50	90.03	79.48

Case11	114.72	90.24	79.65
Case12	114.97	90.45	79.84
Case13	116.16	90.41	80.03
Case14	116.47	90.63	80.24
Case15	116.22	90.87	80.47
Case16	114.68	89.48	79.02
Case17	114.28	89.75	78.76
Case18	113.52	88.86	78.51
Case19	112.83	88.44	78.28
Case20	112.84	88.33	78.08
Case21	112.65	87.97	77.88

Comparing the simulation and experimental results, Case 3, Case 4, and Case 5 under medium speed conditions are close to the measured values. Under high-speed conditions, in addition to Case 3, Case 4, and Case 5 approaching the measured values, Case 19 to Case 21 also show a clear trend towards approaching the target temperature. At the highest speed, Case 13 is optimal, and the errors of other cases are also less than 10%. From this, it can be concluded that under low wind speed conditions, the sensitivity of parameters in CFD simulation is ranked from high to low as follows: emissivity>thermal conductivity>convective heat transfer. However, in high wind speed simulations, convective heat transfer becomes more important.

Next, we will arrange and combine the parameter variables from the highly sensitive cases, resulting in a total of 72 sets of parameters and 72 simulation examples. Submit calculations to a 448 core CPU server, taking a total of 288 hours. Select one set of parameters from the 72 sets with an error within 8 ℃ compared to the experimental results, as shown in the table below:

Table 4.1.1-4: Combination of Standard Parameters

Variable		Front suspension	Floor panel	Engine	Exhaust pipe	Heat Shield	Exhaust lifting ear
T-Case 107	Emissivity	0.70	0.60	0.60	0.70	0.30	0.90
	Thermal conductivity(W/m-K)	/				249.0	1.50

4.1.2. Verification method and result analysis

Model validation is an important step in verifying the accuracy and reliability of calibrated simulation models. The verification method mainly adopts comparative analysis to compare the simulation results of the calibrated simulation model under new experimental conditions with the actual experimental data. Select test conditions

different from the calibration conditions, conduct wind tunnel tests, and obtain test data. Then, the calibrated simulation model is used to simulate and calculate the new operating conditions, and the simulation results are compared and analyzed with the experimental data. Evaluate the error between simulation results and experimental data. If the error between the simulation results and the experimental data is within an acceptable range, it indicates that the calibrated simulation model has high accuracy and reliability, and can effectively simulate the problem of automobile heat damage. If the error is large, further analysis of the reasons is needed to check whether there are problems in model construction, parameter settings, experimental data, etc., and re calibrate and verify until the model meets the accuracy requirements.

The same vehicle, same measuring point, and 80kph working condition heat balance experiment were conducted in the same climate wind tunnel. The environmental conditions and heat sources are shown in the following table:

Table 4.1.2-1: Test Environment Conditions

No.	Boundary	Speed 80kph
1	ambient temperature	40℃
2	air density	1.110kg/m^3
3	Cooling fan speed	2300rpm
4	Condenser heat exchange	7kw
5	Heat exchange of radiator	30.2kw

Table 4.1.2-2: Test Heat Source Temperature

No.	Heat source components	Speed 80kph
1	Cylinder head	85.32
2	Cylinder linder	90.40
3	Cylinder block	98.56
4	Oil pan	100.03
5	Engine side cover	87.20
6	exhaust manifold	100.09
7	Cold end of turbocharger	83.50
8	Hot end of turbocharger	621.09
9	Pre urging pipeline	608.70
10	Pre urging	130.39
11	Front pipe of corrugated pipe	497.80
12	Corrugated pipe	150.40
13	Main reminder front pipe	477.59
14	Main reminder	285.06
15	Front consumption front pipe section	369.15
16	Front consumption	100.10
17	Front consumption rear pipe section	380.12
18	Central muffler	150.00
19	Front pipeline of rear muffler	300.87

20	Rear muffler	225.06
21	Tail pipe	233.64

Table 4.1.2-3: Test Target Temperature

Target component temperature(℃)	Speed 80kph
Exhaust lifting ear	74.5

Set the simulation model according to the parameters in Table 4.1.1-4, and obtain the CFD results as shown in the following table:

Table 4.1.2-4: Simulation Results

Target component temperature(℃)	Experimental value	Simulated value	Absolute error	Relative error
Exhaust lifting ear	74.5	69.3	5.2	7%

The result meets the absolute error requirement of less than ± 8 ℃, and the relative error is also within an acceptable range.

However, in actual engineering development, there are 30-60 target components for thermal damage in a vehicle, and key parameters also have mutual influence. Manually calibrating them one by one will consume a lot of manpower, computing power, and time, which is difficult to achieve in tight engineering development. Therefore, it is necessary to find a fast and efficient automatic calibration method to accelerate the progress of vehicle development.

4.2 Intelligent calibration based on multiple technologies

4.2.1. Calibration method and process

The calibration method in this section mainly adopts a combination of parameter sensitivity analysis and optimization algorithms. Firstly, conduct parameter sensitivity analysis to determine the key parameters and their impact coefficients that have a significant impact on the simulation results. Build a response surface model, optimize with experimental data as the objective function, and find parameter combinations with an error of less than 3%. The calibration process is as follows:

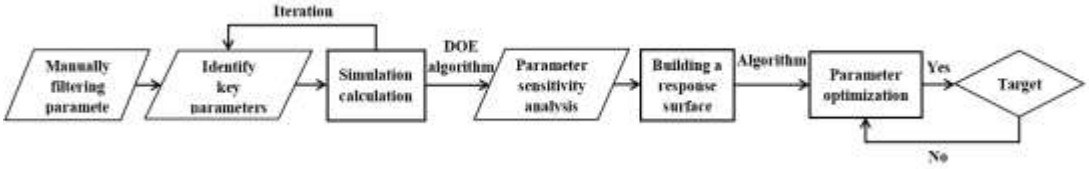

Figure 4.2.1-1: Intelligent Calibration Process

This study aims to simulate and benchmark the surface temperature measurement points of exhaust suspension ears. Select the heat source, heat shield, and its own emissivity and thermal conductivity near the target component as variables. The thermal emissivity ranges from 0 to 1, the thermal conductivity of rubber materials varies from 0.6 to 1.5, the thermal conductivity of stainless steel materials varies from 50 to 80, and the thermal conductivity of aluminum materials varies from 225 to 250.

Using the results of the first round of 66 simulation examples as the initial dataset, a graphical software was called to perform parameter sensitivity analysis. The sorting is shown in the following figure:

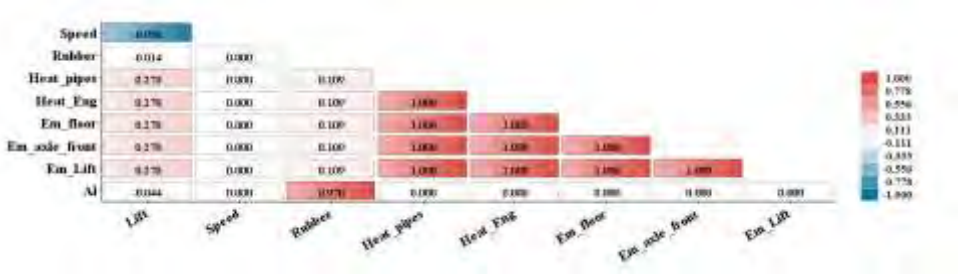

Figure 4.2.1-2: Parameter Sensitivity Statistical Chart

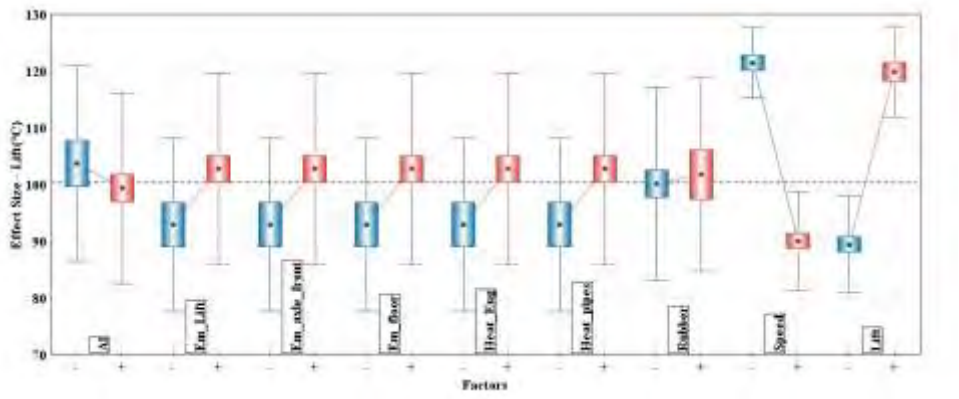

Figure 4.2.1-3: Parameter Sensitivity Box Diagram

In the figure, Speed represents the vehicle speed, Rubber represents the thermal conductivity of the suspension lug rubber material, Heat_pipes represents the emissivity of the exhaust pipe heat source near the suspension lug, Heat_Eng represents the emissivity of the engine heat source near the suspension lug, Em_foor represents the emissivity of the bottom plate, Em_axle_front represents the thermal emissivity of the front suspension, Em_Lift represents the thermal emissivity of the suspension lug, Al represents the thermal conductivity of the exhaust pipe aluminum heat shield, and Lift represents the target temperature on the surface of the suspension lug.

From the parameter sensitivity statistics in Figures 4.2.1-2 and 4.2.1-3, it can be seen that vehicle speed has the greatest impact on the surface temperature of the lifting lug, and the influencing factor is negative. This is because vehicle speed directly affects the convective heat transfer coefficient on the surface of the lifting lug. The higher the vehicle speed, the faster the surface air flow, resulting in faster convective heat transfer. Next are the emissivity of nearby components, the thermal conductivity of the heat shield, and the thermal conductivity of the material of the lifting ear itself.

Data training, due to the consistent dimensions of different temperature measurement points but significant differences in numerical ranges, for example, the surface temperature range of a fan motor is 96 ℃~166 ℃, while the range of a fuel filler tube is 46℃~53℃. This article normalizes the input using Z-score normalization and the output using Z-score normalization to eliminate anisotropy and accelerate network convergence. Both sets of Scalers are serialized and saved to ensure consistency between offline training and online deployment. The use of ensemble learning methods for prediction combines the ability of multi-layer perceptrons (MLPs) to capture nonlinear relationships and complex patterns with the advantages of random forests in handling noisy data. After training the MLP and random forest models separately, use a weighted voting strategy to obtain the final output results.

We first constructed a three-layer feedforward neural network to capture the nonlinear mapping between 8-dimensional temperature characteristics and 4-dimensional thermal properties parameters. The number of hidden layer units is 64 and 32 respectively, and all hidden layers use ReLU activation functions to ensure gradient sparsity and computational efficiency. To suppress overfitting, the model adds a dropout layer after each hidden layer and incorporates L2 weight decay into the loss function. The optimizer uses Adam with an initial learning rate 1×10^{-3}. During the training phase, 10% of the samples are randomly selected from the original training set as the internal validation set, and an early stopping strategy is adopted to avoid overfitting, with a maximum of 500 epochs of training.

Additionally, construct a random forest regressor to utilize its integrated variance reduction and robustness to outlier measurement points. The base learner uses CART regression tree and constructs diversity through self sampling and random subspace strategy. To prevent excessive growth of a single tree, set $\text{max\_depth} = 3$ and $\text{min\_samples\_split} = 2$ for strong regularization.

The optimal number of n_estimators trees within the range of $\{10,20,50,100,200\}$ is determined through grid search using 5-fold cross validation MSE as the evaluation metric, and the final optimal number of trees is 100. This hyperparameter combination performs best in the bias variance trade-off, maintaining sufficient model complexity to capture nonlinear interactions between temperature and thermal properties, while significantly reducing prediction variance through ensemble averaging. Extract the training result data and perform curve fitting, as shown in the following figure:

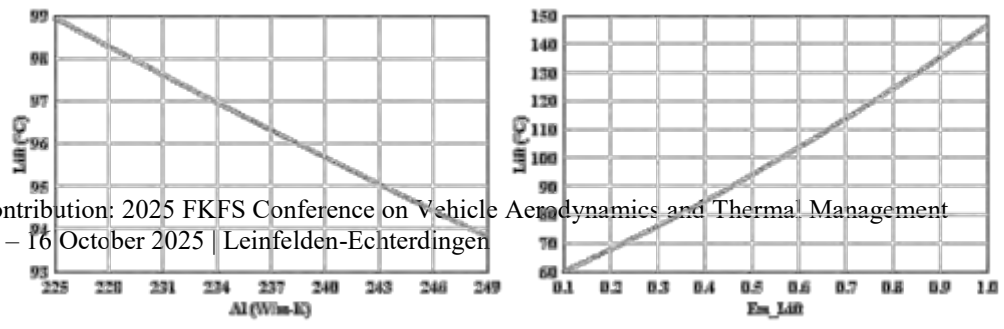

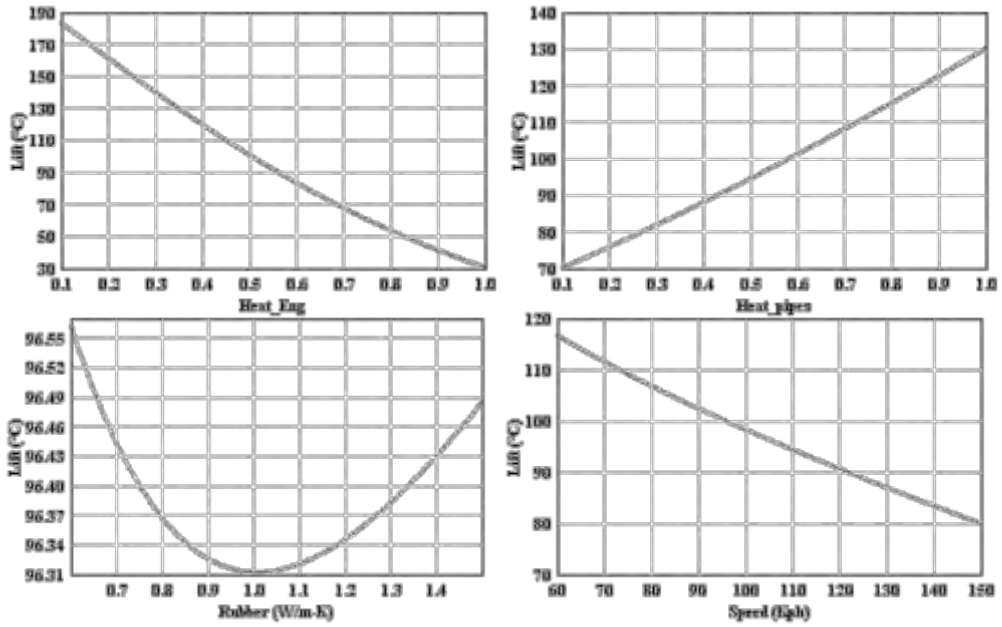

Figure 4.2.1-4: Relationship Curve between Variables and Target Temperature

From Figure 4.2.1-4, it can be seen that the relationship between the thermal conductivity of the hanging ear and the surface temperature is not monotonic. The same surface temperature can be obtained when the thermal conductivity is 0.8 and 1.3, and the minimum surface temperature can be obtained when the thermal conductivity is 1.0.

The random grid search method is selected for parameter optimization, with the aim of finding the optimal parameter combination to maximize the temperature of the 8 target surfaces, including the fan motor surface, rear suspension cushion, corrugated pipe rear suspension ear, fuel tank outer surface, ECU surface, left side surface of the rear bumper, the closest point of the fuel pipe to the exhaust pipe, and the center point of the lower surface of the battery pack, to the experimental values.

After obtaining MLP and random forest models, this paper proposes a weighted voting strategy of "output dimension correlation". Firstly, extract 30% from the training set as an independent validation set, and then use a grid search strategy to select MLP weights with a weight range of {0,1} and a step size of 0.05. With the goal of minimizing the MSE of the validation set, the optimal weights for each dimension are determined as shown in the table below:

Table 4.2.1-1: Optimal Weights

Fusion algorithm	Emissivity	Al-Conductivity	Rubber-Conductivity
MLP Weight	0.85	0.20	0.15
Random Forest Weight	0.15	0.80	0.85

Merge the outputs of two models on the test set according to their corresponding weights. This strategy not only retains the dominance of MLP over the emissivity, but also makes full use of the stable estimation of RF for the three thermal conductivities to avoid a single model bias. The following table shows the performance results of two separate models and the ensemble model on the test set:

Table 4.2.1-2: Test Results

MSE / R^2	MLP	RF	Ensemble
Emissivity	0.0021/0.9231	0.0048/0.7815	0.0012/0.9791
Al-Conductivity	26.3592/0.1129	21.9873/0.1635	19.7467/0.1958
Rubber-Conductivity	0.0681/0.1546	0.0401/0.2838	0.0371/0.3042

Overall, the fusion model showed an average improvement of 18.75% and 17.26% in MSE and R^2 com/pared to the best performing individual model in the three output indicators of ear radiation coefficient, exhaust pipe heat shield thermal conductivity, and exhaust ear thermal conductivity, respectively, verifying the effectiveness of the weighted voting strategy. The Intel Xeon 8358 was used for training in terms of computational efficiency, with the MLP model taking a total of 4.5 seconds and the random forest model taking 2.7 seconds. The overall training of the model can be completed within 10 seconds, and the iterative development efficiency is high.

The optimal parameter combination obtained is shown in the following table:

Table 4.2.1-3: Optimal Parameter Combination

Variable	Front suspension	Floor panel	Engine	Exhaust pipe	Heat Shield	Exhaust lifting ear
Emissivity	0.690	0.763	0.522	0.677	0.270	0.948
Thermal conductivity(W/m-K)		/			237.101	1.405

4.2.2. Verification method and result analysis

Verify according to the method in section 4.1.2, set the simulation model according to the parameters in Table 4.2.1-3, and obtain the CFD results as shown in the following table:

Table 4.2.2-1: Simulation Results

Target component temperature(℃)	Experimental value	Simulated value	Absolute error	Relative error

Exhaust lifting ear	74.5	71.2	3.3	4%

The result meets the absolute error requirement of less than ± 5 ℃, and the relative error is also within an acceptable range. Compared to manual simulation results, the absolute error was reduced by 1.9 ℃ and the simulation accuracy was improved by 2.5%. As the number of training samples increases, the accuracy will further improve.

The comparison between manual calibration technology and multivariate integration technology is shown in the following table:

Table 4.2.2-2: Comparison between Multivariate Integration Technology and Manual Calibration Technology

	Absolute error	Relative error	Time consumption for single target optimization	Feasibility of multi-objective optimization
Manual calibration technology	5.2 ℃	7%	288 hours	Low
Multivariate integrated calibration technology	3.3 ℃	4%	10 seconds	High

5 Conclusions and Prospects

5.1 Research findings

- 1. Based on the multi-dimensional integration technology of full-scale automotive climate numerical wind tunnel, a simulation model of automotive heat damage has been successfully constructed. Through reasonable simplification of modeling, grid division, coupling simulation, and benchmarking analysis, it can accurately simulate physical phenomena such as convective heat transfer, heat conduction, and heat radiation involved in automotive heat damage problems.

- 2. Through climate wind tunnel testing and data collection, real and reliable test data were obtained. Scientific calibration methods were used to calibrate the simulation model. After verification, the calibrated simulation model has high accuracy and reliability, which can provide effective analysis methods and design optimization basis for the study of automotive thermal hazards.

- 3. Adopting multivariate integration technology has the advantage of improving simulation accuracy compared to manual calibration, and has significant efficiency advantages in dealing with multivariate and multi-objective problems in engineering.

5.2 Research Prospects

- 1. Further improve the accuracy of the simulation model, consider the mutual influence between more component parameters, in order to more accurately simulate the problem of automobile heat damage.
- 2. Strengthen the integration of diversified integration technology with advanced technologies such as artificial intelligence and machine learning, achieve automatic optimization and rapid prediction of simulation models, and improve research efficiency.
- 3. Expand the research scope and apply this technology to new fields such as battery thermal management and fuel cell thermal damage in new energy vehicles, providing technical support for the development of new energy vehicles.

Acknowledgements

This work was sponsored by the National Key R&D Program of China (Project Number: 2022YFE0208000). The authors would like to thank the China Automotive Technology and Research Center team on the wind tunnel for their support and the colleagues from the vehicle aerodynamics and thermal management department for the assisting discussions.

6 Reference list

[1] Kang Tingting, Li Yantao The impact of extended range vehicle heat damage on battery packs[J]. battery, 2025, 55 (01): 124-128. DOI:10.19535/j.1001-1579.2025.01.020.

[2] Fan Peng, Ma Dehui, Deng Xiang, etc Thermal Management Design and Typical Problem Analysis Application of Extended Range Electric Vehicles[J]. Shanghai Automotive, 2025, (01): 9-14.

[3] Yihu City, Fu Wenqi, Ma Mingjun, etc Study on the Influence of Geothermal Radiation on High Temperature Testing of Whole Vehicles[J]. auto electric, 2024, (12): 81-84.

[4] Liu Chunlei Design and Analysis of Exhaust System for a Certain Vehicle Model Based on CFD Method [D]. Nanchang University, 2023.DOI:10.27232/d.cnki.gnchu.2023.002997.

[5] Sun Xiaogang Thermal Management Analysis of Exhaust System in Extended Range Hybrid Vehicles [J]. Automotive Practical Technology, 2023, 48 (09): 23-28. DOI: 10.16638/j.cnki. 1671-7988.2023.09.005.

[6] Sun Quanhai, Gao Dayi, Chen Chuanzhen, etc Research on Thermal Damage of Hidden Exhaust Duct Vehicle Rear Bumper Skin [C]//China Society of Automotive Engineers, Automotive Aerodynamics Committee of China SAE. Proceedings of the 2022 Annual Conference of the Automotive Aerodynamics Committee of China Society of Automotive Engineers - Thermal Management Sub venue FAW Volkswagen Automotive Co., Ltd; , 2022: 76-80. DOI:10.26914/c.cnkihy.2022.035469.

[7] Yihu City, Huang Yin, Mei Zheng, etc Research on Deviation of Environmental Chamber Test Results Based on Environmental Wind Tunnel [J]. Automotive Practical Technology, 2020, 45 (21): 148-151. DOI: 10.16638/j.cnki. 1671-7988.2020.21.047.

[8] Qin Zhijun Simulation Optimization and Experimental Study on Thermal Damage Protection of Hybrid Electric Vehicles [D]. Northeastern University, 2021 DOI:10.27007/d.cnki.gdbeu.2021.001916.

[9] Ghani A A A S ,Aroussi A ,Rice E .Simulation of road vehicle natural environment in a climatic wind tunnel.[J].Simul. Pr. Theory,2001,8(6-7):359-375.

[10] Song Xin, Li Shuya, Yan Jie, etc Research on the correlation between numerical wind tunnel simulation and open road simulation [J]. Automotive Engineering, 2020, 42 (06): 759-764. DOI: 10.19562/j. cinasae. qcgc. 2020.06.008.

[11] Tao H ,Jinsheng L ,Xianzhong H , et al.Extended Study of Full-Scale Wind Tunnel Test and Simulation Analysis Based on DrivAer Model[J].Proceedings of the Institution of Mechanical Engineers, Part D: Journal of Automobile Engineering,2022,236(10-11):2433-2447.

[12] Ljungskog E ,Sebben S ,Broniewicz A .Inclusion of the physical wind tunnel in vehicle CFD simulations for improved prediction quality[J].Journal of Wind Engineering & Industrial Aerodynamics,2020,197104055-104055.

[13] Engineering - Wind Engineering; New Wind Engineering Data Have Been Reported by Researchers at Chalmers University of Technology (Inclusion of the Physical Wind Tunnel In Vehicle Cfd Simulations for Improved Prediction Quality)[J].Energy Weekly News,2020.

[14] Parsa N ,Abolghasemi H ,Kamkari B .Experimental and numerical investigation of thermal performance enhancement in shell-and-tube latent heat storage

systems: effects of fins, eccentricity, and shell geometry[J].Journal of Energy Storage,2025,128117159-117159.

[15] Guedri K ,Al-Ghamdi S A .Improved Finite Volume Method for Three-Dimensional Radiative Heat Transfer in Complex Enclosures Containing Homogenous and Inhomogeneous Participating Media[J].Heat Transfer Engineering,2018,39(15):1364-1376.

[16] Wang Hongchao, Dan Xizhuang, Yang Zhigang Numerical and Experimental Study on Thermal Management of a Passenger Car Engine Cabin [C]//Proceedings of the 2017 Academic Annual Meeting of the Automotive Aerodynamics Branch of the Chinese Society of Automotive Engineers Tongji University Shanghai Ground Transportation Wind Tunnel Center; ,2017:271-279.

[17] Wang Dan, Xu Junfang, Zhang Yilun, etc The Influence of Front end Module Design on Cooling System of Electric Vehicles [J]. Equipment Manufacturing Technology, 2022, (02): 5-7+17.

[18] Yang Sheng Research on Semi Physical Simulation Test Platform for Automotive Thermal Management System [D]. Tsinghua University, 2004.

[19] Xu Xiang, Wang Yuan, Yu Yilong, etc Numerical simulation and experimental study of the flow field of automobiles in environmental wind tunnels [J]. Automotive Engineering, 2024, 46 (03): 536-545. DOI: 10.19562/j.cinasae. qcgc. 2022.03.018.

[20] Tobias E ,Matthias E ,David K , et al.Snow Contamination of Simplified Automotive Bluff Bodies: A Comparison Between Wind Tunnel Experiments and Numerical Modeling[J].SAE International Journal of Advances and Current Practices in Mobility,2022,4(6):2120-2134.

A novel approach to highly integrated thermal management rig and facility for vehicle applications

Paul Cromback-Dugény

Vehicle Efficiency

Jaguar Land Rover Ltd.
Gaydon
Warwickshire CV35 0RR United Kingdom

pcromba1@jaguarlandrover.com

Abstract: vehicle system requires the use of hardware/software/control strategy to provide cooling/heating of the cabin, powertrain system and electrical devices. All functions have to be delivered on cost for the customer but also on weight and efficiency to lower energy consumptions and maintain human comfort at all ambient temperature. Thermal Energy Management (TEM) optimisation is critical as ambient temperature variation proves to have a large effect on vehicle energy consumptions for the different types of propulsion systems [1].

Thermofluid system based on highly integrated coolant, refrigerant and air subsystem which are highly integrated require deep level development. They are responsible for enabling energy transfer between sub system to limit heat waste and maximize energy efficiency

This is usually performed using Computational Aided Engineering (CAE) methods during development and validated on rigs and prototype. While component and subsystem rigs are essentials in validation steps, they cannot enable super system level validation. Prototypes on the other hand do but can lack robustness, maturity and their operational time requirement might not be compatible with engineering development cycle and certifications timing. A thermofluid system rig, based on Hardware in the Loop (HiL), is the key to make the link between these two validation stages of the components but also of the system while reducing the development time and accelerate time-to-market.

Contribution: 2025 FKFS Conference on Vehicle Aerodynamics and Thermal Management
15 – 16 October 2025 | Leinfelden-Echterdingen

This paper introduces a novel approach of a highly integrated HiL rig which combines the entire thermofluid super system – under – test (SUT) of the vehicle. The faster than real time digital twin approach enables eliminating all propulsion systems with thermal emulators designed to replicate the heating & cooling into the thermal system plant. Multiple distributed controllers are also integrated part of this rig, within the scope of the SUT. A novel approach of digital twin use for front end airflow emulation is also introduced in this complex thermo-fluid rig. This rig enables sign off entire thermofluid system hardware & its associated control systems with time to test reduced by up to 94%.

1 Thermofluid system within vehicle applications

Within vehicles, thermofluid systems are comprised of the coolant, refrigerant and HVAC sub system. They are supported by LV/HV architectures, and also by the mechanical engine duty in some case like with engine driven coolant pumps. It has the duty of transferring energy across the different vehicle subsystems and it is responsible for cooling and heating the vehicle cabin, the powertrain sub system and diverse electronic components.

Thermofluid system approach enables combining the different individual loops to optimize the energy transfer within the vehicle but also with the surrounding ambient. Such complexity requires the use of highly intelligent control and calibration. This is key to fulfil thermal comfort within the cabin but also to maximize powertrain efficiency leading to improved range and lower emissions.

The current automotive industry shows a wide range of thermal strategies and methods to provide heating and cooling to the thermofluid system. Coolant heating can be achieved through the High Voltage Coolant Heater (HVCH), through the high voltage compressor or by harvesting powertrain wasted energy. The cabin heating can be performed by harvesting Internal Combustion Engine (ICE), using an electric cabin heater, a cabin heater core combined with a high voltage coolant heater or ambient air heat recovery system (heat pump).

While the system performance is a key aspect for choosing the best system, the weight, complexity and cost need to be balanced. Another aspect is the ambient range expected on the market where the vehicle is sold: while some vehicles are dedicated to specific market with more favourable environmental condition, some are sold to market with more extreme weather (i.e cold and/or hot). This will affect the energy consumption [1]. The jaguar I-Pace released in 2018 relies for example on HVCH to heat the coolant system, a coolant heater core to transfer the coolant heat to the cabin through the Heating, Ventilation, and Air Conditioning system (HVAC), two dedicated Low Temperature Radiators (LTR) for the battery and the propulsion system, a refrigerant arrangement with a high voltage compressor and the associated components that enables a heat pump mode. This mode enables the harvest of heat from low ambient temperature and to transmit it to the cabin in order to reduce the energy consumption while heating the cabin. In cold ambient condition, this helps maximizing the range.

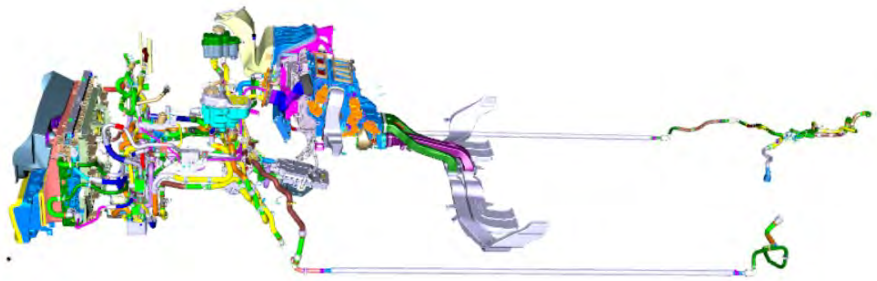

Figure 1: Jaguar I-Pace thermofluid system

As shown in the figure 1, we associate to the system components dedicated to deliver the airflow to the different air to coolant and air to refrigerant heat exchangers such as the cooling fan, the ducting, the grille shutters and the related ducting.

In a recent study that compiled Jaguar I-Pace customer data [1], it was shown that despite using a heat pump system, the average energy consumption at 0deg C ambient is 50% higher than at 20deg C. The energy consumption relation to the ambient temperature for this vehicle is shown in the figure 2. This low and high temperature drives for additional load on the TEM system. Optimising the hardware, control and calibration is therefore key to lower energy consumption and maximize the EV range.

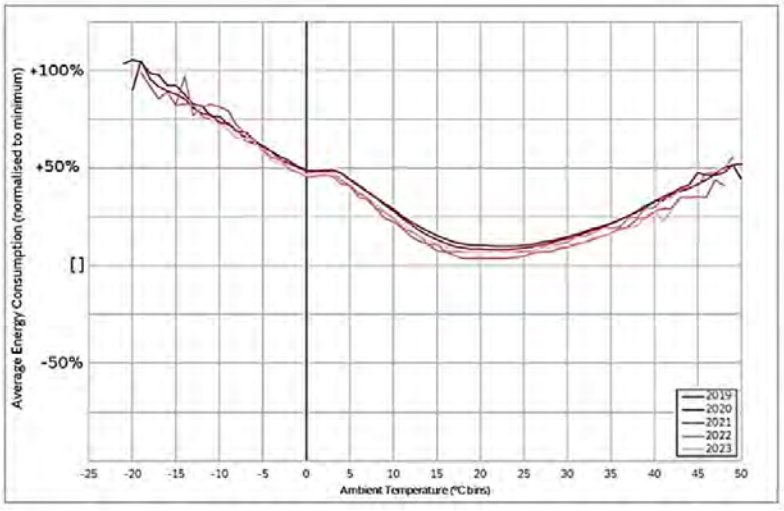

Figure 2: Energy usage as a function of the ambient temperature on the Jaguar I-Pace [1]

2 V system and development cycle

Typical automotive development follows the V model of system engineering. It is split in two main steps. The left branch relates to the requirement/attribute target definition followed by designing stages of the systems, sub-systems and components. These stages rely mostly on CAE development that can be performed using 1d and 3d modelling.

During the second stage, the aim is to verify and validate the components, sub-systems, systems and finally the attributes performance. While components performance and sub-systems can be tested on physical rigs, the industry relies mostly on testing full vehicle with different level of component maturities. This can prove challenging when relying on in-market testing and the test facilities availabilities.

Beside hardware testing, another important part of the testing relates to the software, control and calibration. This is critical to ensure the system functions are delivered efficiently and robustly. For the example of the thermofluid, control and calibration are important with regards to the arbitration of the cabin and powertrain heating/cooling delivery. Although the system might be sized based on the thermal performance load cases with high loads and extreme temperatures, the system needs to deliver the required output for the lowest amount of energy to optimize the powertrain and overall vehicle efficiency.

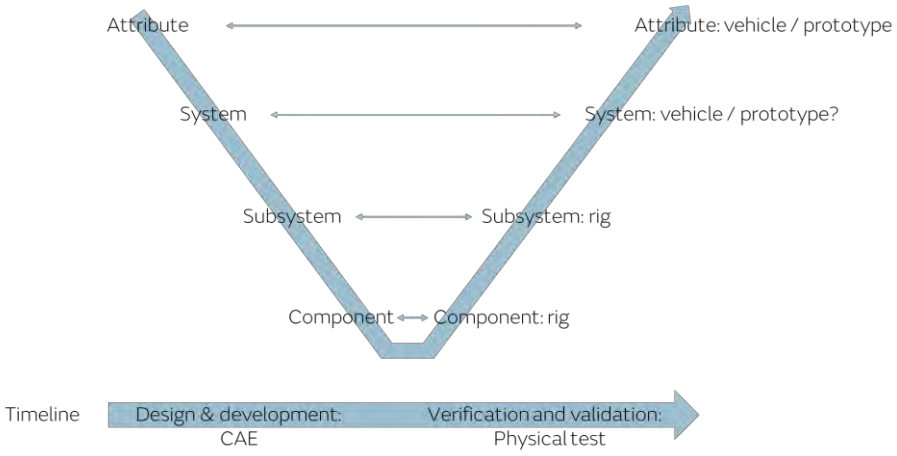

Figure 3: V shape of engineering

One of the downfalls of relying on prototype vehicle testing for system validation and verification can be the maturity level of the vehicle, some of the lengthy time required by specific load case and sometimes the reliability of the properties. Changing critical components to update a vehicle can lead to significant downtime in the development process due to part retrofitting periods, the possible re-instrumentation requirements and the associated challenges. For specific drive cycles, preconditioning, and testing can take up to thirty six hours per drive cycle.

For all these reasons, having the possibility to test thermofluid system on a dedicated HIL bench test apparatus is critical. The use of such physical approach is an area of development for automotive applications [2][3][4]. The following section introduces the newly developed highly integrated rig.

3 New Hardware in the Loop (HiL) test rig approach

The so called “thermofluid level 5 rig” has been developed with the aim of enabling the full thermofluid system testing for a wide range of environmental conditions on steady state and transient load cases. It intends at testing all the refrigerant, HVAC, coolant and air subsystem so that it allows the testing of the controller and fluids interactions as it is shown on the figure 1.

To allow flexibility and to remove sensitivity to part, a number of sub-systems and components are emulated: this includes the heat and cold sinks such as the engine, battery, the front and rear Electric Drive Units (EDU), the electrical components that require heating/cooling and the cabin. This is possible by making the bench working alongside vehicle 1d models that have been developed in the prior phase of the design. Such models need to be real time capable.

The commissioned test bench is composed of an environmental chamber that contains its own conditioning unit. It is capable of controlling the ambient condition within -20 to 50°C. The chamber is sized so it can contain the vehicle labcar that holds the vehicle thermofluid unit. The Heat Exchangers (HX) can be mounted in the vehicle line position on the labcar or on a dedicated front end unit that is designed to replicate real airflow distribution as seen by the vehicle on the road. This apparatus is critical as airflow distributions have an impact on the performance of the air to coolant or air to refrigerant as shown in [5][6][7]. The delivery of the air to the front end unit is performed by the main air handling unit. It is capable of delivering air mass flow representative a high speed load case to the cooling pack for a range of temperature of -20 °C up to 75 °C and an adjustable relative humidity between 10 % and 90 %. Similarly, airflow conditioning to the front and rear HVAC units are handled by separate Air Handling Unit (AHU) and are capable of replicating recirculation mode or fresh inlet from the surrounding environment. The labcar is instrumented with all the required sensors. This includes current and voltage sensors to capture energy usage over cycles, temperature sensors on the different fluid networks but also refrigerant and coolant flow rate sensors. The rig is capable of supporting Low and High voltage components like electrical compressors, but it can also be associated with a dedicated bench that enables the use of mechanical compressors that are used in ICE and hybrid vehicles.

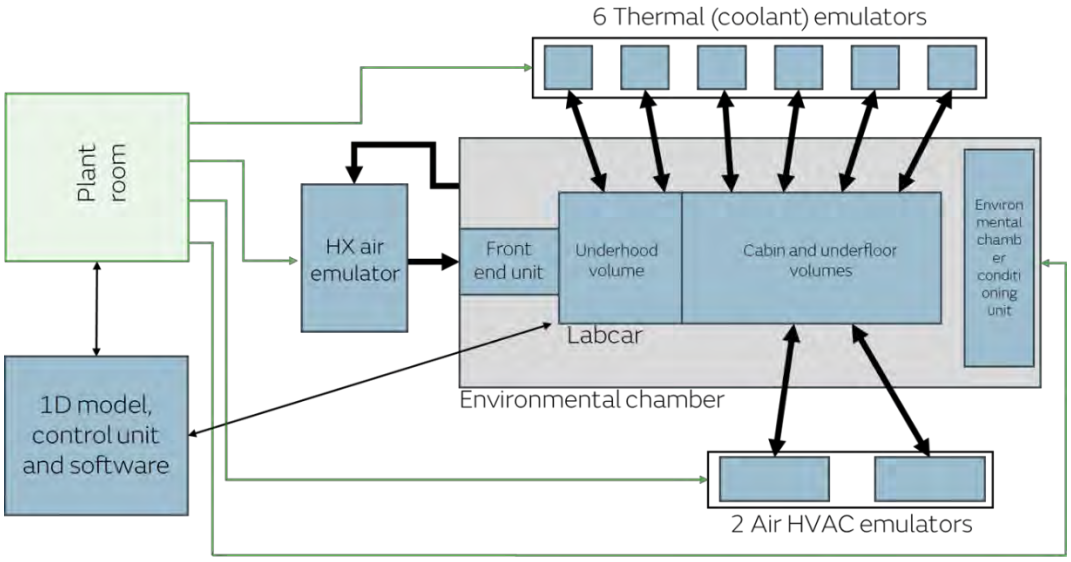

Figure 4: Schematic of the thermofluid level 5 rig

The vehicle components that are handled by the 1d model and emulated on the rig with heating and cooling loads are handled by six individual coolant emulators. They can be used to replicate the components interacting with the fluid network that are not on the labcar like the powertrain units. These coolant emulators have the capability to be controlled through heating or cooling loads (from -12kW to +20kW each) or based on temperature profiles. If individual emulator heat loads are not sufficient, they can also be connected and run in series to increase the cooling or heat delivered to the labcar. Adjustable pressure valves are used when connected to the labcar to be representative with the vehicle expected coolant loop characteristics and pipe connections to the labcar are designed to replicate the total vehicle coolant volume.

Figure 5: -1: Coolant emulators -2: Plant room -3: Coolant emulators secondary -4: Environmental chamber

The labcar contains some of the vehicle ECUs while some can be modelled within the 1d model that is used on the rig. It is made of two volumes to enable temperature control: the larger one contains the components that sit in the cabin volume, and the smaller one represents the underhood volume. The underhood side is connected to the front end unit. This unit is designed to enable the emulation of the airflow distribution onto the cooling pack and represents a novelty.

Figure 6: Labcar

4 Novel approach to air to HX emulation within a rig

One of the key aspects to this rig is the particular attention brought to the air emulated to the front end unit containing the vehicle cooling pack. This system is made of the main air handling unit, the pipe connecting it to the front end unit, the front end unit, the labcar and the return pipe. As shown on the figure 7, it starts from the main AHU which is controlled to provide a specific mass flow and temperature. The air is delivered to the front end unit through some piping into the environmental chamber. This unit contains the vehicle cooling pack and is then connected to the labcar underhood volume.

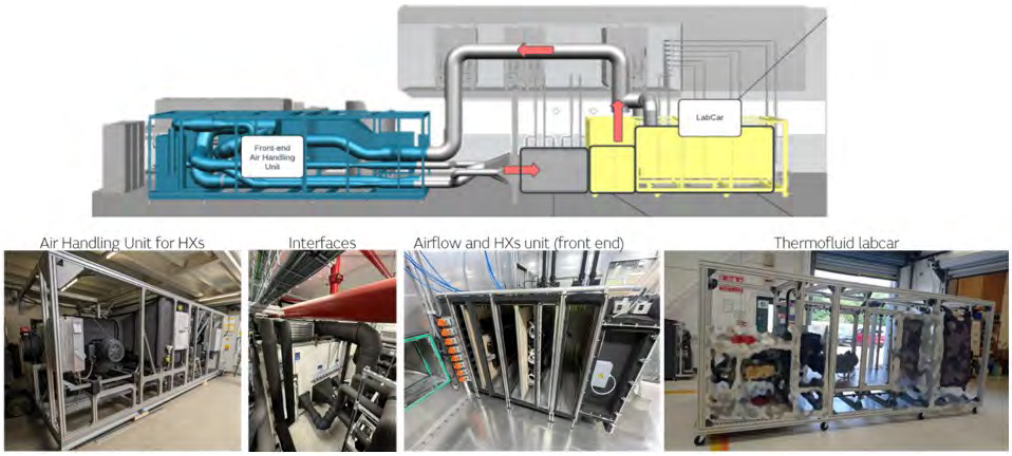

Figure 7: The main AHU flow path

On a typical drive cycle, the main air handling unit is capable of following the transient air mass flow trace from specific drive cycle while taking into account the dynamic movement of the active air system such the active grille shutter and the electric cooling fan. The figure 8 represents a typical Thermal Energy Management drive cycle and the air mass flow input to the rig and its response.

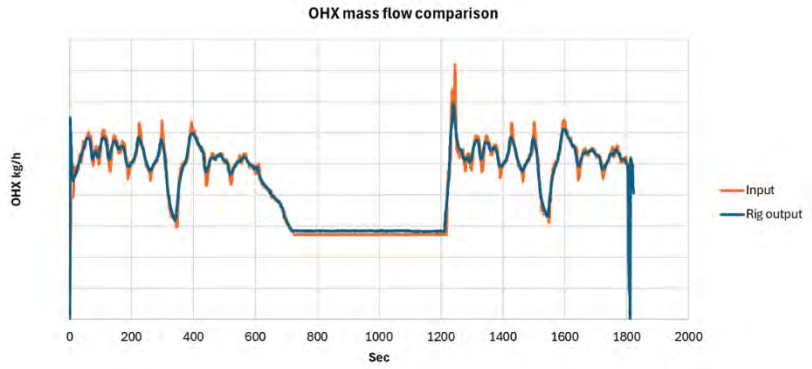

Figure 8: transient air mass flow trace input and output

Beside the total air mass flow, the airflow distribution influences the amount of heat transfer exchanged between the air and the coolant/refrigerant heat exchanger. This is a function of the front end design of the vehicle, the active grille shutter position and the fan power and it is a well-documented phenomenon. [6] shows the impact of airflow blockage onto the refrigerant performance and energy usage. [5] [7] shows that for a typical coolant to air heat exchanger with a uniformity index of 0.6, 10%, or even 20% to 30% of heat rejection decrease can be expected from a perfect uniform airflow performance. This loss of heat transfer performance needs to balance with additional airflow which either means additional fan power or increase active grille shutter opening. Both methods are equivalent to an increase of energy consumption of the thermal system. The following figure shows typical air mass flow distribution onto the HX inlet faces for different vehicle speeds.

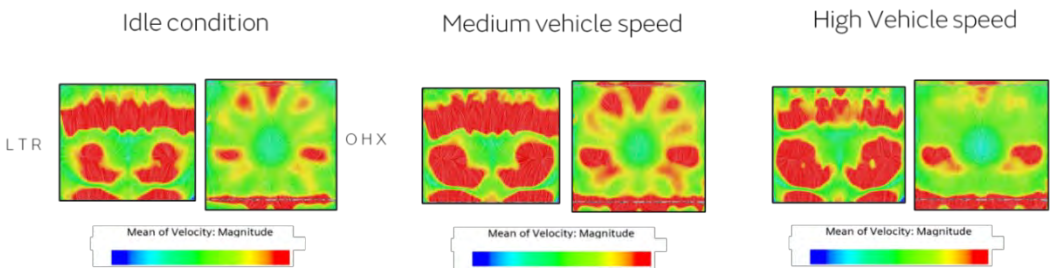

Figure 9: Air velocity distribution for different vehicle speeds

One of the requirements of the test bench is to enable the replication of this airflow condition on the test bench within the front end unit. The front end unit within the environmental chamber is composed of four volumes: two to emulate the airflow distribution and two to integrate the vehicle cooling hardware, as shown on the figure 10. The first airflow distribution emulator system is the most upstream section and is composed of eight horizontal individually actuated vanes which influences the airflow distribution on the height axis. Downstream, the dynamically actuated vehicle vanes are fitted and are controlled through either the vehicle ECU or the vehicle model. It is followed by a static blockage that adds an element of control to the distribution ahead of the vehicle cooling pack.

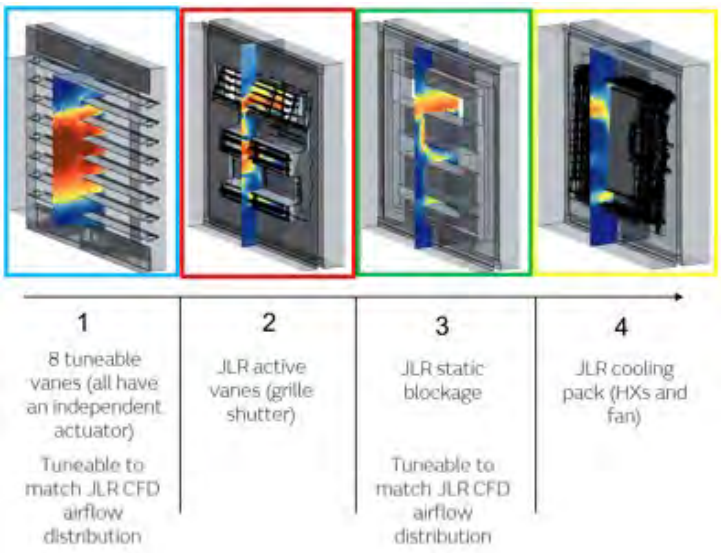

Figure 10: Front end unit description

The tuning of the rig is performed through the use of a correlated CFD model of the airflow system of the bench. It can be used to investigate the airflow distribution within the rig and be used to tune the test bench, so it provides the same airflow as expected on the vehicle. The test rig CFD model includes the air handling unit inlet to the front end unit up to the labcar entry.

The whole thermal vehicle CFD model output is used to describe the airflow distribution for different active system configurations and vehicle speed range. A DoE is then performed using the correlated test bench CFD model which enables the selection of the best blockage which can then be manufactured and integrated onto the front end unit.

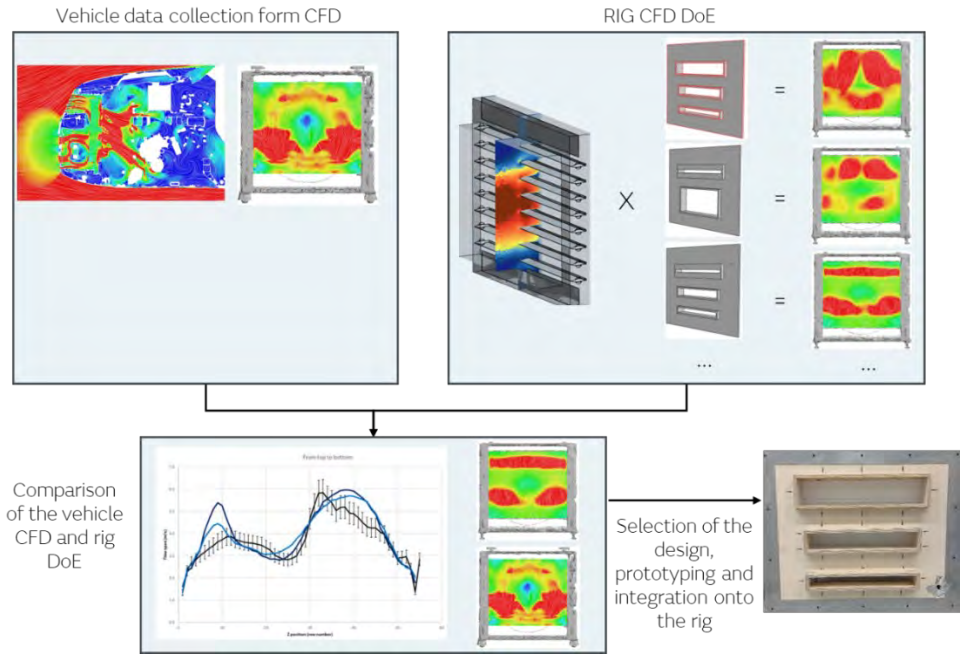

Figure 11: Airflow distribution mapping from vehicle CFD to the front end unit

The different sections of the front end unit can be integrated through a system of sliders to easily access the components while insuring it is possible to connect them to the low or high voltage, coolant and refrigerant system while also maintaining a good seal one the components are in place in the unit.

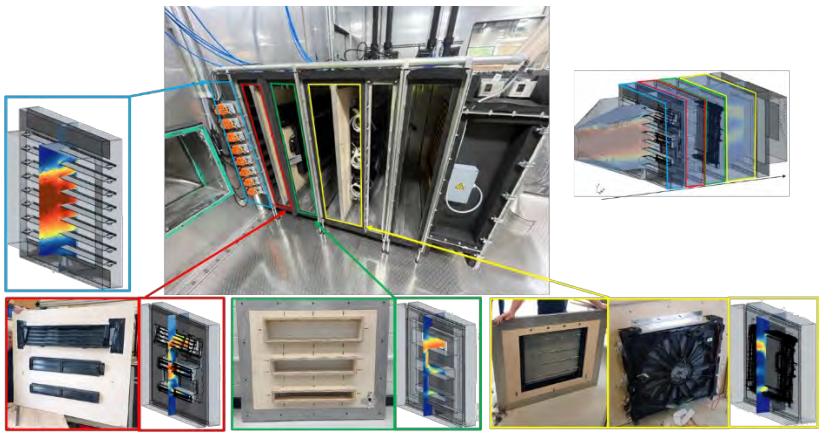

Figure 12: Front end unit and its CFD representation

5 Development and test benefits

The use of the thermofluid rig enables a faster approach to system testing and validation ahead of classical vehicle testing. This supports the Thermal Energy Management performance measurement and control optimisation while allowing the flexibility to easily replace specific hardware and save development time. Full vehicle testing also require extended preconditioning period which can be minimize on the rig thanks to the fast dynamic control of the plant room. Typically, for EPA and WLTP physical testing, this pre-test soak and conditioning can last up to thirty six hours while they can be performed in under one hour on the rig. This is similar with OEM specific and other real world driving replicated drive cycle which might have to be performed a number of times over the thermal system development and validation.

Beside this, although it could take days for replacing physical components on a vehicle prototype leading to extended property downtime, this can be performed quickly on the associated propulsion 1d model.

Based on these typical examples, we believe such rig enables sign off entire thermofluid system hardware & its associated control systems with time to test reduced by up to 94% compared to traditional method

6 Conclusions

The aim of this paper was to demonstrate the application and benefits of a HiL rig for thermofluid applications This is possible by eliminating all propulsion system with a combination of air and coolant emulators. This includes the overall main specifications, operations method and benefits for the aim of validating and investigating the performance of physical hardware and the associated control and calibration.

It also includes a novel method to emulate airflow conditions on the inlet of the heat exchangers as per the expected vehicle condition through the use of vehicle and test bench CFD. This enables adding the air system for the overall thermal energy management system approach on a physical test rig.

This paper introduces a novel approach of a highly integrated HiL rig which combines the entire thermofluid super system – under – test (SUT) of the vehicle. The faster than real time digital twin approach enables eliminating all propulsion systems with thermal emulators designed to replicate the heating & cooling into the thermal system plant. Multiple distributed controllers are also integrated part of this rig, within the scope of the SUT. A novel approach of digital twin use for front end airflow emulation is also introduced in this complex thermo-fluid rig. This rig enables sign off entire thermofluid system hardware & its associated control systems with time to test reduced by up to 94%.

7 Acknowledgment

The author would like to thank the JLR leadership team for enabling the progress on this project, including Nilabza Dutta, Wilko Jansen and Chris Chatham. As well, some of this work would not have been possible without the support of the technical team such as Abdalla Elabd, Barry Aston and many more.

8 Reference list

[1] Dutta, N., Evans, D., and Sapte, A., “A Percipient Analysis of Jaguar I-PACE Electric Vehicle Energy Consumption Using Big Data Analytics,” SAE Technical Paper 2024-01-2879, 2024, doi:10.4271/2024-01-2879.

[2] Leighton, Daniel. Combined Fluid Loop Thermal Management for Electric Drive Vehicle Range Improvement, No. 2015-01-01709. SAE Technical Paper, 2015.

[3] Chowdhury, S., Leitzel, L., Zima, M., Santacesaria, M. et al., “Total Thermal Management of Battery Electric Vehicles (BEVs),”SAE Technical Paper 2018-37-0026, 2018, doi:10.4271/2018-37-0026.

[4] Bires, M,. “Driving Tomorrow’s Vehicles: AVL’S Software Thermal Management Developing Process to Ensure Calibration on System Level”, No. 24TMSS_0064. TMSS, 2024.

[5] Baskar, S. and Prince Arockia Doss, S., “Investigation on Underhood Airflow Management - Effect of Airflow Statistics,”SAE Technical Paper 2018-28-0024, 2018, doi:10.4271/2018-28-0024.

[6] Kumar Reddy, J., Deopa, S., Sharma, A., and Aggarwal, P., "Impact of Condenser Opening Area on A/C Performance of the Automotive HVAC System," SAE Technical Paper 2015-01-0368, 2015, doi:10.4271/2015-01-0368.

[7] Johnson, A,. Vaddiraju, S., and Solomon, J., “Impact of Airflow Non-Uniformity on Heat Exchanger Performance”, GT Conference 2020, 2020.